Evaluation of Engineered Barrier Systems FY20 Report

Spent Fuel and Waste Disposition

Prepared for US Department of Energy
Spent Fuel and Waste Science and Technology

E.N. Matteo, T. Dewers, S. Gomez, T. Hadgu,
Sandia National Laboratories

L. Zheng, L. Lammers, P. Fox, C. Chang, H. Xu, S.
Borglin, M. Whittaker, C. Chou, C. Tournassat, N.
Subramanian, Y. Wu, P. Nico, B. Gilbert, T. Kneafsey,
Lawrence Berkeley National Laboratory

F. Caporuscio, K.B. Sauer, M.J. Rock, A. Kalintsev,
A. Migdissov, C. Alcorn, Los Alamos National Laboratory

E.C. Buck, X-Y Yu, J. Yao, J. Son,S.L. Reichers,
Pacific Northwest National Laboratory

O. Klein-BenDavid, G. Bar-Nes,
Nuclear Research Center of the Negev, Israel

J.C.L. Meeussen, Nuclear Research and Consultancy
Group (NRG), the Netherlands

C. Gruber, M. Steen, K.G. Brown, R. Delapp, A. Taylor,
J. Ayers, D.S. Kosson, Vanderbilt University

August 31, 2020
M2SF-20SN010308042
SAND2020-11452 R

U.S. DEPARTMENT OF ENERGY

NNSA National Nuclear Security Administration

Sandia National Laboratories

Sandia National Laboratories is a multi-mission laboratory managed and operated by National Technology & Engineering Solutions of Sandia, LLC., a wholly owned subsidiary of Honeywell International, Inc., for the U.S. Department of Energy's National Nuclear Security Administration under contract DE-NA0003525.

APPENDIX E

NFCSC DOCUMENT COVER SHEET[1]

Name/Title of Deliverable/Milestone/Revision No. Evaluation of Engineered Barrier Systems FY20 Report / M2SF-20SN010308042

Work Package Title and Number Engineered Barrier System R&D - SNL

Work Package WBS Number 1.08.01.03.08

Responsible Work Package Manager Edward Matteo
(Name/Signature)

Date Submitted

Quality Rigor Level for Deliverable/Milestone[2]	☐ QRL-1 ☐ Nuclear Data	☐ QRL-2	☐ QRL-3	☐ QRL-4 Lab QA Program[3]

This deliverable was prepared in accordance with Sandia National Laboratories
(Participant/National Laboratory Name)

QA program which meets the requirements of
☒ DOE Order 414.1 ☐ NQA-1 ☐ Other

This Deliverable was subjected to:

☒ Technical Review

☐ Peer Review

Technical Review (TR)
Review Documentation Provided
☐ Signed TR Report or,
☐ Signed TR Concurrence Sheet or,
☒ Signature of TR Reviewer(s) below
below

Peer Review (PR)
Review Documentation Provided
☐ Signed PR Report or,
☐ Signed PR Concurrence Sheet or
☐ Signature of PR Reviewer(s)

Name and Signature of Reviewers
Carlos F. Jové Colón

NOTE 1: *Appendix E should be filled out and submitted with the deliverable. Or, if the PICS:NE system permits, completely enter all applicable information in the PICS:NE Deliverable Form. The requirement is to ensure that all applicable information is entered either in the PICS:NE system or by using the NFCSC Document Cover Sheet.*

- *In some cases there may be a milestone where an item is being fabricated, maintenance is being performed on a facility, or a document is being issued through a formal document control process where it specifically calls out a formal review of the document. In these cases, documentation (e.g., inspection report, maintenance request, work planning package documentation or the documented review of the issued document through the document control process) of the completion of the activity, along with the Document Cover Sheet, is sufficient to demonstrate achieving the milestone.*

NOTE 2: *If QRL 1, 2, or 3 is not assigned, then the QRL 4 box must be checked, and the work is understood to be performed using laboratory QA requirements. This includes any deliverable developed in conformance with the respective National Laboratory / Participant, DOE or NNSA-approved QA Program.*

NOTE 3: *If the lab has an NQA-1 program and the work to be conducted requires an NQA-1 program, then the QRL-1 box must be checked in the work Package and on the Appendix E cover sheet and the work must be performed in accordance with the Lab's NQA-1 program. The QRL-4 box should not be checked.*

This page is intentionally left blank.

SUMMARY

This report describes research and development (R&D) activities conducted during fiscal year 2020 (FY20) specifically related to the Engineered Barrier System (EBS) R&D Work Package in the Spent Fuel and Waste Science and Technology (SFWST) Campaign supported by the United States (U.S.) Department of Energy (DOE). The R&D activities focus on understanding EBS component evolution and interactions within the EBS, as well as interactions between the host media and the EBS. A primary goal is to advance the development of process models that can be implemented directly within the Generic Disposal System Analysis (GDSA) platform or that can contribute to the safety case in some manner such as building confidence, providing further insight into the processes being modeled, establishing better constraints on barrier performance, etc.

The FY20 EBS activities involved not only modeling and analysis work, but experimental work as well. Despite delays to some planned activities due to COVID-19 precautions, progress was made during FY20 in multiple research areas and documented in this report as follows: (1) EBS Task Force: Task 9/FEBEX Modeling Final Report: Thermo-Hydrological Modeling with PFLOTRAN, (2) preliminary sensitivity analysis for the FEBEX in-situ heater test, (3) cement-carbonate rock interaction under saturated conditions: from laboratory to modeling, (4) hydrothermal experiments, (5) progress on investigating the high temperature behavior of the uranyl-carbonate complexes, (6) in-situ and electrochemical work for model validation, (7) investigation of the impact of high temperature on EBS bentonite with THMC modeling, (8) sorption and diffusion experiments on bentonite, (9) chemical controls on montmorillonite structure and swelling pressure, (10) microscopic origins of coupled transport processes in bentonite, (11) understanding the THMC evolution of bentonite in FEBEX-DP—coupled THMC modeling, (12) modeling in support of HotBENT, an experiment studying the effects of high temperatures on clay buffers/near-field, and (13) high temperature heating and hydration column test on bentonite.

The R&D team represented in this report consists of individuals from Sandia National Laboratories, Lawrence Berkeley National Laboratory (LBNL), Los Alamos National Laboratory (LANL), Pacific Northwest National Laboratory (PNNL), the Nuclear Research Center of the Negev in Israel, the Nuclear Research and Consultancy Group (NRG) in the Netherlands, and Vanderbilt University. In addition, the EBS R&D work leverages international collaborations to ensure that the DOE program is active and abreast of the latest advances in nuclear waste disposal. For example, the FY20 work on modeling coupled THMC processes at high temperatures relied on the bentonite properties from the Full-scale Engineered Barrier EXperiment (FEBEX) Field Test conducted at the Grimsel Test Site in Switzerland.

Overall, significant progress has been made in FY20 towards developing the modeling tools and experimental capabilities needed to investigate the performance of EBS materials and the associated interactions in the drift and the surrounding near-field environment under a variety of conditions including high temperature regimes.

This page is intentionally left blank.

ACKNOWLEDGEMENTS

This work was supported by the U.S. Department of Energy Office of Nuclear Energy, through the Office of Spent Fuel and Waste Science and Technology (SFWST) Research and Development Campaign (DOE NE-81) within the Office of Spent Fuel and Waste Disposition.

The authors acknowledge contributions in the form of discussions on technical and integration issues from the following people from Sandia National Laboratories: R. Chris Camphouse, Emily Stein, David Sassasni, Ernie Hardin, Carlos Jové-Colón, Yifeng Wang, and Peter Swift (retired). In addition, the authors thank Jorge Monroe-Rammsy (DOE NE-81), Bill Spezialetti (DOE NE-81) (retired), Prasad Nair (DOE NE-81), Tim Gunter (DOE NE-81) and William Boyle (DOE NE-8) for their discussions, oversight, and guidance on topics covered in this report.

The authors thank Jeralyn Prouty (Sandia) for assistance with formatting and proofing of this document.

Lastly, the authors thank Carlos Jové-Colón (Sandia) for providing a careful and thorough technical review of this document.

This page is intentionally left blank.

CONTENTS

LIST OF FIGURES

LIST OF TABLES

ACRONYMS

1D	one-dimensional
2D	two-dimensional
3D	three-dimensional
AFM	atomic force microscope (microscopy)
APS	advanced photon source
ASPECT	Advanced Solver for Problems in Earth's ConvecTion
ASTM	American Society for Testing and Materials
BBM	Barcelona Basic Model
BExM	Barcelona Expansive Model
BGR	Bundesanstalt für Geowissenschaften und Rohstoffe
BRGM	The Bureau De Recherches Géologiques Et Minières, France
BSE	backscattered electron
C(A)SH	calcium aluminum silicate hydrate
CE	counter electrode
cec	cation exchange capability
CET	cryo-electron tomography
CG	conjugate gradient
CIEMAT	Centro de Investigaciones Energéticas, Medioambientales y Tecnológicas, Spain
COD	Crystallography Open Database
COLVARS	Collective Variables
CPU	central processing unit
CSH	calcium silicate hydrate
CT	computed tomography
CUDA	Compute Unified Device Architecture
CV	cyclic voltammogram
DAKOTA	Design Analysis Kit for Optimization and Terascale Applications
DC	direct current
DCM	double-crystal monochromator
DECOVALEX	DEvelopment of COupled Models and their VAlidation against Experiments
DLVO theory	theory named after Boris Derjaguin and Lev Landau, Evert Verwey and Theodoor Overbeek
DOC	dissolved organic carbon

DOE	Department of Energy, USA
DPC	dual-purpose canister
DRS	dielectric relaxation spectroscopy
DRZ	disturbed rock zone
EBS	engineering barrier system
E-cell	electrochemical cell
EDS	energy-dispersive X-ray spectroscopy
ELSM	Extended Linear Swelling Model
EMP	electron microprobe
ENRESA	National Radioactive Waste Corporation, Spain
EPA	Environmental Protection Agency, USA
ERT	electrical resistivity tomography
ERT-CT	electrical resistivity tomography-computed tomography
EXAFS	extended X-ray absorption fine structure
FCRD	Fuel Cycle Research and Development
FEBEX	Full-scale Engineered Barrier Experiment
FIB	focused ion beam
FLAC	Fast Lagrangian Analysis of Continua
FT	Fourier transform
FWHM	full width at half maximum
FY	fiscal year
GBM	granular bentonite mixture
GCMC	Grand Canonical Monte Carlo
GDSA	Generic Disposal Systems Analyses
GG	Grimsel granodiorite
GNU	GNU is not Unix
GPU	Graphics Processing Unit
HDF5	Hierarchical Data Format version 5
High T	high temperature
HLW	high-level radioactive waste
HotBENT	High Temperature Effects on Bentonite
HPC	High Performance Computing
HPLC	high-performance liquid chromatography
IC	ion chromatography
ICP-MS	inductively coupled plasmas – mass spectrometry

ICP-OES	inductively couple plasma-optical emission spectrometry
ID	inner diameter
IP	intellectual property
L/S	liquid-to-solid ratio
LA-ICP-MS	laser ablation inductively coupled plasma mass spectrometry
LAMMPS	Large-scale Atomic/Molecular Massively Parallel Simulator
LANL	Los Alamos National Laboratory
LBNL	Lawrence Berkeley National Laboratory
LC	loading-collapse
LCS	low carbon steel
LHS	Latin Hypercube Sampling
LLW	low-level radioactive waste
LSP	liquid-solid partitioning
LSTM	long-short term memory
LXO	LeachXS/Orchestra
mAESTRO	Australian Extreme SpecTROscopy
MAXS	medium-angle X-ray scattering
MD	molecular dynamics
MDL	minimum detection limit
MGC	Modified Guoy-Chapman
MIP	mercury intrusion porosimetry
MMT	montmorillonite
NAGRA	National Cooperative for the Disposal of Radioactive Waste, Switzerland
NDIR	catalytic oxidation/nondispersive infrared detection
NPT	constant number, pressure, and temperature
NRG	Nuclear Research and Consultancy Group, the Netherlands
NS	natural system
NUMO	Nuclear Waste Management Organization of Japan
NVT	constant number, volume, and temperature
OD	outer diameter
OPC	Ordinary Portland Cement
PCTFE	polychlorotrifluoroethylene
PDMS	polydimethylsiloxane
PEEK	polyether ether ketone
PETSc	Portable, Extensible Toolkit for Scientific Computation
PFLOTRAN	Parallel subsurface FLOw and reactive TRANport code
PMF	potential of mean force
PMMA	polymethyl methacrylate
PNNL	Pacific Northwest National Laboratory

PWR	pressurized water reactor
QXRD	quantitative X-ray diffraction
R&D	research and development
RE	reference electrode
RWM	Radioactive Waste Management Limited, Quintessa Ltd (United Kingdom)
SALVI	System for Analysis at the Liquid Vacuum Interface
SAXS	small-angle X-ray scattering
SE	secondary electron
SEM	scanning electron microscope
SFWD	Spent Fuel and Waste Disposition
SFWST	Spend Fuel and Waste Science and Technology
SIMS	secondary ion mass spectrometry
SKB	Swedish Nuclear Fuel and Waste Management Company
SMD	steered molecular dynamics
SOWAT	SOdium chloride WATer
SPC/E	extended simple point charge
SRM	Standard Reference Material
SS	stainless steel
STEM	scanning transmission electron microscope
SURAO	Radioactive Waste Repository Authority, Czech Republic
TEM	transmission electron microscope
TGA	thermogravimetric analysis
TH	thermal-hydrologic
THC	thermal-hydrologic-chemical
THM	thermal-hydrologic-mechanical
THMC	thermal-hydrologic-mechanical-chemical
ToF-SIMS	time-of-flight secondary ion mass spectrometry
TOUGH	Transport of Unsaturated Groundwater and Heat
U.S.	United States
UFD	Used Fuel Disposition
URL	underground research laboratory
UV-VS	ultraviolet-visible spectroscopy
WAXS	wide-angle X-ray scattering
WB	Wyoming bentonite
WE	working electrode
WHAM	Weighted Histogram Analysis Method
WIPP	Waste Isolation Pilot Plant
XANES	X-ray absorption near edge structure
XAS	X-ray absorption spectroscopy

XRD	X-ray diffraction

This page is intentionally left blank.

SPENT FUEL AND WASTE DISPOSITION EVALUATION OF ENGINEERED BARRIER SYSTEMS FY20 REPORT

1. INTRODUCTION

This report describes research and development (R&D) activities conducted during fiscal year 2020 (FY20) specifically related to the engineered barrier system (EBS) R&D Work Package in the Spent Fuel and Waste Science and Technology (SFWST) Campaign supported by the United States (U.S.) Department of Energy (DOE). It fulfills the SFWST Campaign deliverable M2SF-20SN010308042. The R&D team consists of individuals from Sandia National Laboratories, Lawrence Berkeley National Laboratory (LBNL), Los Alamos National Laboratory (LANL), Pacific Northwest National Laboratory (PNNL), the Nuclear Research Center of the Negev in Israel, the Nuclear Research and Consultancy Group (NRG) in the Netherlands, and Vanderbilt University.

The R&D activities described in this report focus on understanding EBS component evolution and interactions within the EBS, as well as interactions between the host media and the EBS. A primary goal is to advance the development of process models that can be implemented directly within the Generic Disposal System Analysis (GDSA) platform or that can contribute to the safety case in some manner such as building confidence, providing further insight into the processes being modeled, establishing better constraints on barrier performance, etc.

The FY20 EBS activities involved not only modeling and analysis work, but experimental work as well. While some planned activities were delayed because of COVID-19 precautions, progress was still made in a number of different research areas during FY20, as described in this report and summarized below:

- **EBS Task Force: Task 9/FEBEX Modeling Final Report: Thermo-Hydrological Modeling with PFLOTRAN (Section 2)**

  This section outlines modeling studies applied to Stage 1 and Stage 2 of the Full-scale Engineered Barriers Experiment in Crystalline Host Rock (FEBEX) in-situ test for the SKB EBS Task Force Task 9. The FEBEX test was a full-scale test conducted over ~18 years at the Grimsel, Switzerland Underground Research Laboratory (URL). Past modeling studies generally used two-dimensional (2D) axisymmetric meshes, ignoring three-dimensional (3D) effects, gravity and asymmetric wetting and dry out of the bentonite engineered barrier. The studies described in Section 2 investigate these effects with use of the PFLOTRAN (Parallel subsurface FLOw and reactive TRANport) THC code (Hammond et al., 2014) with massively parallel computational methods in modeling FEBEX Stage 1 and Stage 2 results. The discussion includes the modeling approach and associated results as well as a comparison of those modeling results to the field results. The simulation results show good agreement with some FEBEX measurements including the measured temperatures near Heater 1 for Stage 1 and near Heater 2 for Stage 2 as well as the liquid saturations after the first dismantling. Other simulated results tended to be underpredicted compared to the FEBEX measurements.

- **Preliminary Sensitivity Analysis for the FEBEX In-situ Heater Test (Section 3)**

  As a complement to the information in Section 2, Section 3 presents additional preliminary modeling work on sensitivity and uncertainty analysis applied to Stage 1 of the Full-scale Engineered Barriers Experiment in Crystalline Host Rock (FEBEX) in-situ test for the EBS Task Force, Task 9. The intent of this analysis is to determine the parameters that are important to defining the thermal-hydrologic (TH) condition in the bentonite buffer and the host rock. In particular, temperature and relative humidity were examined to identify possible sensitivities to various parameters. To allow multiple simulations for sensitivity analysis, a 2D TH model with reduced mesh size was used, a method that is consistent with most of the previous modeling studies on the FEBEX experiment. The analysis indicates that the stronger correlations are between Heater 1 temperature and Heater 1 power, and between relative humidity and buffer van Genuchten parameters. The strong correlation between Heater temperature and Heater power is expected as the power directly controls the temperature. The correlation between relative humidity and van Genuchten parameters is also consistent with the matching exercise described in Section 3.2. Matching of relative humidity is very sensitive to the values of the reciprocal of the air entry pressure and the parameter λ.

- **Cement-Carbonate Rock Interaction under Saturated Conditions: From Laboratory to Modeling (Section 4)**

  The Israel Atomic Energy Commission is examining the possibility of locating a geological waste disposal site within the carbonate Ghareb and Nezer Formations in the northern Negev, Israel (Klein-BenDavid et al., 2019). Therefore, the goal of the present study is to simulate the long-term performance of interfaces between cementitious materials (CEM I, selected as a bounding case for alkaline cement-rock interactions, and a low pH cement) with carbonate geologic strata (limestone, chalk, marl, oil shale, low organic phosphorite and high organic phospharite) of the northern Negev, Israel. The objectives for this work are presented in Section 4 and include the following: (1) demonstrate how laboratory characterization methods results are used as input data in reactive transport simulations; (2) simulate short-term scenarios (5 years) of interfaces between carbonate rocks (limestone and marl) and OPC paste; and (3) provide preliminary long-term performance assessments (100 and 1,000 years) of these interfaces based on simulations results. The simulation results show the change in the carbonation front location with time. Preliminary estimates of carbonation depth for OPC paste were estimated for 100 and 1,000 years when in contact with limestone and marl. After 1,000 years, the carbonation depth for marl/OPC cement is about an order of magnitude deeper than for limestone/OPC paste interface.

- **Hydrothermal Experiments (Section 5)**

  The work presented in Section 5 develops concepts related to mineral and geochemical changes that may occur in the near field of high temperature for a nuclear waste repository hosted in crystalline rock. The core samples used for the experimental program consist of granodiorite from the Grimsel Test Site, a well-characterized lithology, to mimic a generic crystalline rock environment. This section presents the results from FY20 research, which characterized (1) how EBS components (stainless steel/low carbon steel, Wyoming bentonite, Ordinary Portland Cement (OPC)) react and change in the presence of Grimsel granodiorite wall rock and synthetic Grimsel granodiorite groundwater and (2) steel-bentonite interface mineralogy at high temperature and pressure (250°C, 150 bars) in-situ repository conditions.

  The FY 20 experimental work yielded multiple concepts of interest: (1) illitization of montmorillonite in Wyoming bentonite in a Grimsel granodiorite wall rock environment may be restricted due to the bulk chemistry of the overall system (i.e., low potassium) and/or kinetics, (2) montmorillonite structural alterations were not observed in the Wyoming bentonite + Grimsel granodiorite + cured OPC experiment, (3) the inclusion of a cured Portland cement chip did not dramatically increase the solution pH but lead to the formation of diverse secondary mineral formation, (4) analysis of clay mineral structural changes reveals that montmorillonite alteration did not occur, (5) newly crystallized Fe-saponite forms at the steel-bentonite interface and grows perpendicular to the steel surface, (6) Fe enrichment in the bentonite due to interaction with steel corrosion products does not migrate far from steel (<50 μm), (7) calcium aluminum silicate hydrate (C(A)SH) minerals formed within the Wyoming bentonite-Grimsel granodiorite system, (8) zeolite-forming reactions are not favored in the Wyoming bentonite-Grimsel system, and (9) general steel corrosion is observed and thicknesses/rates of Fe-rich clay formation were measured.

- **Progress on Investigating the High Temperature Behavior of the Uranyl-Carbonate Complexes (Section 6)**

  Section 6 provides the preliminary results of ongoing work investigating the aqueous complexation of uranium at elevated temperatures conducted during FY20. The primary focus of this study was to determine the formation constants of uranyl-carbonate complexes at elevated temperatures such that any future models of uranium transport in high temperature fluids would be based on experimentally determined data rather than data extrapolated from room temperature to those conditions. The experiments involve application of the autoclave solubility, in-situ ultraviolet-visible spectroscopy (UV-VS), and synchrotron-based in-situ XAS techniques. The autoclave solubility experiments were performed at 200°C and 250°C and concentrations of carbonate ranging from 0 to 0.5 m. Solutions with carbonate concentrations ranging from 0.02–525 M and total dissolved U of 6 or 2 mM were investigated using in-situ UV-VS at 100°C to 250°C. In order to acquire a molecular level of understanding of the structure and co-ordination of uranyl-carbonate complexes, in-situ XAS synchrotron-based spectroscopy was applied to two solutions containing 0.86 m $NaHCO_3$ with one containing an additional ~0.9 m NaOH.

  Preliminary data suggest that currently available thermodynamic data for uranyl carbonate complexes are inadequate for predicting behavior at elevated temperatures. It appears that extrapolations of room temperature data greatly overestimate the stability of these complexes at elevated temperatures with the discrepancy between theory and reality evidently increasing with higher temperatures and carbonate concentrations.

- **In-situ and Electrochemical Work for Model Validation (Section 7)**

  The aim of this work is to investigate the corrosion of UO_2 in situ in the scanning electron microscope (SEM). The corrosion potential (E_{corr}) is measured using an electrochemical workstation and a unique microfluidic reactor containing three electrodes and compatible for multiple analytical platforms, termed System for Analysis at the Vacuum Liquid Interface (SALVI) electrochemical cell (E-cell). This approach aims to provide real-time and in operando monitoring of UO_2 electrode stability and morphological change and to study the UO_2 corrosion process at the microscale. Several new approaches have been developed to attach particles to working electrodes (WEs) in the microfluidic E-cell and to enable in operando analysis of UO_2. Several types of powders including metal and metal oxide materials were used to demonstrate the feasibility. These new methods are described, and validation results are provided in Section 7. The experimental results show that in operando and in-situ study of UO_2 particles using the modified SALVI E-cell platform is possible using one of the illustrated methods. These new approaches are easy to implement and cost effective, permitting UO_2 corrosion potential studies in a wide range of conditions.

- **Investigation of the Impact of High Temperature on EBS Bentonite with THMC Modeling (Section 8)**

Section 8 presents the results of the development and application of thermal-hydrologic-mechanical-chemical (THMC) modeling to evaluate the EBS bentonite characteristics in argillite repository under different temperature (100°C and 200°C). This section contains three parts. The first part presents some new results, using the dual structure model (Barcelona Expansive Model, BExM) to conduct a parametric study of the effect of the pre-consolidation pressure. With this study, a distinct elasto-plastic behavior of bentonite was obtained, revealing that the spatial heterogeneity of the sample may induce uneven performance inside the material. The second part includes a description of the progress of the development of the simulator (TReactMech) with new libraries, modified the coupling strategy from iterative two-way coupling to a sequential coupling method, and used it to simulate the high temperature in nuclear waste disposal sites. A good agreement between numerical simulations and analytical solutions is obtained, but in the THM simulation of high T case, the hydrological calculation failed to converge due to phase changes. The third part of Section 8 provides a summary of using reduced-order models for investigation of new constitutive relationships for bentonite.

- **Sorption and Diffusion Experiments on Bentonite (Section 9)**

  Section 9 presents the results of sorption and diffusion experiments on bentonite samples, with the focus being on the diffusion of ^{3}H, U, and Se through compacted smectite. Specifically, the section presents results from ^{3}H and U diffusion experiments from field-heated (95°C, 18 years) and cold-zone (20°C) FEBEX bentonite under different chemical conditions, plans for studying Se(VI) diffusion through compacted montmorillonite under different background electrolyte compositions, and plans for modeling the diffusion experiments. The results revealed that the average normalized 3H flux at steady state (≥50-hr) for 3H through-diffusion was not significantly different across samples, with values ranging from $1.38 \pm 0.13 \times 10^{-3}$ m/day to $1.73 \pm 0.17 \times 10^{-3}$ m/day. U(VI) in-diffusion experiments conducted in the presence of 2 mM Ca showed the diffusive loss of U(VI) from the high concentration reservoir was indistinguishable for the heated and cold-zone bentonite, and U(VI) traveled less than 1 mm into the clay over the 30-day diffusion period. While lower U(VI) adsorption was previously measured on the heated-zone FEBEX bentonite compared to the cold-zone bentonite, it is possible that differences in U(VI) diffusion due to differences in adsorption may only become apparent over much longer time periods than can be realistically tested in the laboratory.

- **Chemical Controls on Montmorillonite Structure and Swelling Pressure (Section 10)**

  Section 10 presents the progress on an integrated set of experiments, molecular simulations, and thermodynamic modeling to develop a predictive understanding of ion exchange-driven swelling and collapse of montmorillonite clay. We report on the development of an X-ray transparent micro-oedometer system for the measurement of montmorillonite swelling pressure as a function of the dry bulk density and the aqueous solution composition. Initial work focused on pure homoionic NaCl and KCl solutions as well as NaCl+KCl mixtures. Preliminary data are presented from in-situ X-ray scattering experiments. To develop a theoretical understanding of microstructural evolution, we applied our newly published structural model for cis-vacant smectite clay (Subramanian et al., 2020) to simulate the free energy of mixing crystalline layer states and find that highly unfavorable mixing energetics can drive phase separation in mixed layer state systems. Ongoing simulations of swelling free energy are being conducted using a potential of mean force (PMF) calculation method. Finally, these results are integrated into a thermodynamic model to predict swelling pressure as a function of pore fluid composition in compacted bentonite.

- **Microscopic Origins of Coupled Transport Processes in Bentonite (Section 11)**

  Section 11 presents a research plan for a newly added research activity on the development and validation of a microscopic model of coupled transport processes in bentonite and using this model to determine cost effective augmentation strategies to increase the bulk thermal conductivity of hydrated bentonite. Because this activity was added in March 2020, we only report a research plan and some preliminary results, which will serve as a foundation for a larger scale effort in FY20–21 to stably increase the thermal conductivity of bentonite above 2 W/(m·K) at temperatures relevant to modern nuclear waste storage design concepts.

Our model predicts two important consequences for the thermal conductivity of bentonite. The first is that a local equilibrium is not possible without macroscopic rearrangement of mineral layers, and therefore microscopic gradients of ions and water are pervasive in bentonite unless or until the mineral is chemically altered to redistribute structural charge. The second is that a 'turbostratic' rearrangement of layers, as is observed in natural bentonites, may minimize the free energy of a given local arrangement, but that any structural fluctuations away from this arrangement will alter the energetic landscape and drive ion and water fluxes. These phenomena represent two important couplings between the chemistry and mechanical deformation of mineral layers in bentonite whose ultimate consequence is to create microscopic fluxes that generate entropy, and therefore, heat. It is anticipated that this model can be used to quantify the specific interactions/fluctuations through which heat is transferred and make predictions about deliberate chemical or structural alteration that may augment heat conduction.

- **Understanding the THMC Evolution of Bentonite in FEBEX-DP—Coupled THMC Modeling (Section 12)**

  Section 12 presents the results of coupled THMC modeling for understanding the THMC evolution of bentonite in FEBEX-DP. From FY16 to FY19, extensive model calibrations were conducted, which provided a coherent explanation of THMC data collected at the FEBEX in-situ test. In FY20, the modeling work included the use the THMC model to explore the long-term alteration of bentonite. In addition, a long-term THC model was also used to assess the necessity of using the THMC model for studying the long-term alteration of bentonite, especially geochemical alteration.

  The following simulation results were obtained: (1) in terms of the hydrological behavior, the THMC and THC modeling results are similar for the period of 50 years despite of a remarkable difference for the first 30 years, (2) the evolution of conservative chemical species (e.g., chloride) based on the results of THMC and THC modeling is similar, (3) the evolution of reactive species (e.g., potassium) based on the results of THMC and THC modeling is different, indicating that the reaction history in THMC and THC models in the early time (<30 years) have a long-term effect, (4) bentonite will become fully saturated in 30–40 years based on the model with a heat decay function, and the bentonite barrier is expected to homogenize in most areas, (5) high chemical concentrations in bentonite near the heater, which were observed in the field test, are predicted to disappear after bentonite becomes fully saturated, and (6) illitization will continue for 50 years, but won't proceed. However, for the sixth point, the THC model shows more illitization in area near the heater compared to the THMC model.

- **Modeling in Support of HotBENT, an Experiment Studying the Effects of High Temperatures on Clay Buffers/Near-field (Section 13)**

  Section 13 presents the results of modeling in support of the HotBENT (High Temperature Effects on Bentonite) field test that is currently under construction in Grimsel, Switzerland. In April 2020, the design for HotBENT was finalized in terms of the type of bentonite and the designed conditions of bentonite barrier. In addition, a THC model was developed to predict the evolution of one of the bentonites (Wyoming bentonite) that will be used in the HotBENT.

  Modeling of coupled THC processes affected by high temperature, relatively high permeability, and high hydraulic pressure, combined with the effect of artificial hydration, generated simulated results that have not been observed in FEBEX in-situ test (Zheng et al., 2018). For example, with a heater temperature of 200°C, the temperature at the bentonite/granite interface is expected to reach 87°C. In about 3 years, most of bentonite would become fully saturated, but a narrow zone about 3 cm thick in the close vicinity of heater would remain unsaturated with a water saturation degree from 95% to 98% until 20 years. Another example focuses on the expectation that the most remarkable chemical changes will occur in a narrow unsaturated zone because of the continuous strong evaporation (referred as "evaporation zone"). Ion concentrations are expected to increase up to 2–3 mol/kg due to the dissolution of smectite, precipitation of illite, anhydrite, quartz and cristobalite, very high exchange Na and Mg and very low exchange of Ca and K at the cation exchangeable sites. However, modeling showed the development a chemically active area a little further away from the heater and right next to the narrow unsaturated zone. It is referred to as the "condensation zone," in which chemical changes are induced by continuous condensation of vapor that is generated in the "evaporation" zone. In this area, the model showed a significant dilution of the bentonite pore water, dissolution of most aluminum-silicate minerals, except muscovite, very high exchange of Ca and K, and very low exchangeable Na and Mg at the cation exchangeable sites.

- **High Temperature Heating and Hydration Column Test on Bentonite (Section 14)**

  Section 14 presents a summary of the benchtop-scale laboratory experiment, HotBENT-Lab, which provides a laboratory analog of the HotBENT experiment, to obtain a more comprehensive set of characterization and monitoring measurements. The primary goal of this laboratory experiment is to obtain well-characterized datasets for (1) understanding bentonite THMC processes under heating and hydration for model parameterization and benchmarking, (2) comparison with field-scale test results from HotBENT, and (3) development of a prototype experimentation platform for future studies of bentonite under conditions of high temperature.

  Results obtained until March 2020 show steady state hydration for both columns, with some density, hydration and chemistry differences between the heated and non-heated conditions. Major observational results from the column tests are threefold. First, computed tomography (CT) imaging and electrical resistivity tomography (ERT) of clay hydration clearly showed the hydration front moving radially inward. Density measurements from CT images indicated that hydration caused clay swelling, which, in turn, caused localized compaction, closed flow paths created from column packing heterogeneities, and swelling along the clay/sand interface. Second, in the center of the heated column, the clay hydration was lower, but the density increased due to mineral precipitation. Third, effluent chemistry showed differences between the heated and non-heated columns, specifically, sulfate, calcium, potassium and magnesium reduction and silicon and potassium production occurred in the heated column.

2. EBS TASK FORCE: TASK 9/FEBEX MODELING FINAL REPORT: THERMO-HYDROLOGICAL MODELING WITH PFLOTRAN

2.1 Introduction

This report outlines Sandia National Laboratories modeling studies applied to Stage 1 and Stage 2 of the Full-scale Engineered Barriers Experiment in Crystalline Host Rock (FEBEX) in-situ test for the SKB EBS Task Force Task 9. The FEBEX test was a full-scale test conducted over ~18 years at the Grimsel, Switzerland Underground Research Laboratory (URL) managed by NAGRA. It involved emplacing simulated waste packages, in the form of welded cylindrical heaters, inside a tunnel in crystalline granitic rock and surrounded by a bentonite barrier and cement plug. Sensors emplaced within the bentonite monitored the wetting-up, heating, and drying out of the bentonite barrier, and the large resulting data set provides an excellent opportunity for validation of multiphysics TH, thermal-hydrologic-chemical (THC), and thermal-hydrologic-mechanical (THM) modeling approaches for underground nuclear waste storage and the performance of engineered bentonite barriers. The present status of the EBS Task Force is finalizing Task 9, which follows years of modeling studies of the FEBEX test, by many notable modeling teams (Gens et al., 2009; Sánchez et al. 2010; 2012; Samper et al., 2018). These modeling studies generally use 2D axisymmetric meshes, ignoring 3D effects, gravity and asymmetric wetting and dry out of the bentonite engineered barrier. This study investigates these effects with use of the PFLOTRAN THC code with massively parallel computational methods in modeling FEBEX Stage 1 and Stage 2 results. The PFLOTRAN numerical code is an open source, state-of-the-art, massively parallel subsurface flow and reactive transport code operating in a high-performance computing environment (Hammond et al., 2014).

Section 2 describes the applied partial differential equations describing mass, momentum and energy balance used in this study, considerations derived by assuming phase equilibrium between gas and liquid phases, constitutive equations for granite, cement plug, and bentonite domains, and specific approaches for use in the PFLOTRAN code. Section 3 describes the geometry, meshing, and model set-up. Section 4 describes modeling results, Section 5 compares modeling results to field testing data, and Section 6 gives conclusions.

2.2 General Modeling Approach

2.2.1 Balance Equations

Fundamental first principles for TH modeling are expressions for mass and energy conservation. Here we outline partial differential equations commonly used in porous media compositional two-phase, two-component modeling for air and water components (denoted by "*a*" and "*w*" respectively) in gas and aqueous liquid phases (denoted by "*g*" and "*l*" respectively), where the solid phase is denoted by 's'. The benefits of the compositional approach in modeling multiphase problems is that terms representing mass transfer between phases cancel, simplifying the equations and reducing the "stiffness" associated with solving kinetic terms, which is equivalent to assuming local equilibrium between liquid water and water vapor. We assume that the solid phases (granite, cement, and bentonite) are inert, and ignore shrink-swell changes in the bentonite barrier associated with wetting and drying. This amounts to an assumption of constant porosity in all solid phases.

A general mass or energy density balance equation with density d of component α in phase β takes the form

$$\frac{\partial d_\beta^\alpha}{\partial t} + \nabla \cdot \boldsymbol{q}_\beta^\alpha - Q_\beta^\alpha \qquad \textit{Equation 2-1}$$

where **q** is the total flux density with respect to a frame of reference and Q is a source/sink term. In multiphase problems, the total mass density is a function of porosity, phase saturation S_β, and component density (component α in phase β) ρ_β^α ($d_\beta^\alpha = \phi S_\beta \rho_\beta^\alpha$), where the relative phase flux includes an advective term with relative phase velocity $\boldsymbol{v}_r$ relative to a fixed reference frame and diffusive/dispersive flux $\boldsymbol{J}$ such that

$$\boldsymbol{q}_{r,\beta}^{\alpha} = \phi S_\beta \rho_\beta^\alpha \boldsymbol{v}_{r,\beta} + \boldsymbol{J}_\beta^\alpha \qquad \textit{Equation 2-2}$$

We denote the Darcy velocity as $\boldsymbol{V}_\beta$

$$\boldsymbol{V}_\beta = \phi S_\beta \boldsymbol{v}_\beta \qquad \textit{Equation 2-3}$$

Expressing the mass balance of air (a) and water (w) components in a non-deformable inert porous medium is expressed as (see, e.g. Martinez and Stone, 2008)

$$\frac{\partial}{\partial t}\left(\rho_l^w S_l \phi + \rho_g^w S_g \phi\right) + \nabla \cdot \left(\boldsymbol{q}_{r,l}^w + \boldsymbol{q}_{r,g}^w\right) + Q^w = 0 \qquad \textit{Equation 2-4a}$$

$$\frac{\partial}{\partial t}\left(\rho_l^a S_l \phi + \rho_g^a S_g \phi\right) + \nabla \cdot \left(\boldsymbol{q}_{r,l}^a + \boldsymbol{q}_{r,g}^a\right) + Q^a = 0 \qquad \textit{Equation 2-4b}$$

where the Q are source/sink terms not including kinetic expressions or mass transfer between phases. Here ρ_l^w is the mass density of water component in the liquid phase, ρ_g^w is the mass density of the water component in the gas phase (water vapor), ρ_l^a is the mass density (or concentration) of air dissolved in the liquid phase, and ρ_g^a is the mass density of dry air in the gas phase such that, with mass fractions Y_β^α and ρ_l and ρ_g being the liquid and gas phase densities respectively,

$$\rho_l^w = Y_l^w \rho_l,\ \rho_g^w = w\rho_g,\ \rho_l^a = Y_l^a \rho_l,\ \rho_g^a = Y_g^a \rho_g \qquad \textit{Equation 2-5}$$

The saturations of both phases must sum to unity, so that

$$S_g = 1 - S_l \qquad \textit{Equation 2-6}$$

The total fluxes include both advective (with Darcy velocities V_β for each phase β) and diffusive fluxes (the latter denoted $\boldsymbol{J}$)

$$\boldsymbol{q}_{r,l}^w = \rho_w \boldsymbol{V}_l$$

$$\boldsymbol{q}_{r,g}^w = \rho_g^w \boldsymbol{V}_g + \boldsymbol{J}_g^w$$

Equation 2-7

$$\boldsymbol{q}_{r,l}^a = \rho_l^a \boldsymbol{V}_l + \boldsymbol{J}_l^a$$

$$\boldsymbol{q}_{r,g}^a = \rho_a \boldsymbol{V}_g + \boldsymbol{J}_g^a$$

Darcy fluxes for phase β are given by

$$\boldsymbol{V}_l = -K_w k_{rw}/\mu_l(\boldsymbol{\nabla} P_l - \rho_l g \boldsymbol{z})$$

Equation 2-8

$$\boldsymbol{V}_g = -K_g k_{rg}/\mu_g(\boldsymbol{\nabla} P_g - \rho_g g \boldsymbol{z})$$

Later we will give expressions for relative permeability and phase saturation in terms of a suction or capillary pressure given by

$$P_c = P_g - P_l$$

Equation 2-9

For binary diffusion of water and air components in the gas phase, we follow Gens et al. (2009) and use

$$\boldsymbol{J}_g^w = -J_g^a = -\phi(1 - S_l)\tau D_g^w \rho_g \boldsymbol{\nabla} Y_g^w$$

and *Equation 2-10*

$$\boldsymbol{J}_l^a = -\phi(S_l)\tau D_l^a \rho_w \boldsymbol{\nabla} Y_l^a$$

The internal energy balance equation for the solid plus pores with two fluid phases has been derived previously, and here we use the approach of Martinez and Stone (2008)

$$\frac{\partial}{\partial t}\left(e_s\rho_s(1-\phi) + e_l\rho_l S_l\phi + e_g\rho_g S_g\phi\right) + \boldsymbol{\nabla}\cdot\boldsymbol{q_e} = Q^e$$

Equation 2-11

where the total heat flux vector includes terms for heat conduction, convection relative to a deforming solid frame, and heat transport due to binary diffusion in the gas phase:

$$\boldsymbol{q}_e = -\lambda_T \boldsymbol{\nabla} T + \rho_l \boldsymbol{V}_l h_l + \rho_g \boldsymbol{V}_g h_g + h_g^w \boldsymbol{J}_g^w + h_g^{wa} \boldsymbol{J}_g^a$$

Equation 2-12

Here h_β is the enthalpy of phase β, and h_g^α is the enthalpy of component α in the gas phase. We explore phenomenology for the thermal conductivity λ in terms of saturations and other parameters later in Section 2.3.

2.2.2 Equilibrium Considerations for Air-Water and Air-Water-Bentonite Systems

With the assumption of phase equilibrium comes the application of the familiar expressions of Henry's, Dalton's Law, and Kelvin's Law, which permit the interrelationship between pressure and density variables. Henry's Law expresses the equilibrium between dissolved air in the liquid phase and dry air in the gas phase

$$\rho_l^a = H_a \rho_a$$

Equation 2-13

where Ha is Henry's law constant and ρ_a is dry air density. A further common assumption in air-water systems is that the gas phase is an ideal mixture of air and water vapor components, such that

$$P_g = P_a + P_v$$

Equation 2-14

where P_a is the partial pressure of dry air in the gas phase and P_v is the partial pressure of water vapor in the gas phase. It is convenient to introduce the relationships between the partial pressures and densities used in the conservation laws where (M_a and M_v are molecular weights of dry air and water vapor, respectively, and R is the gas constant)

$$\rho_g^a = \rho_a = \frac{M_a}{RT} P_a \text{ and } \rho_g^w = \rho_v = \frac{M_v}{RT} P_v \qquad \textit{Equation 2-15}$$

For water vapor in contact with bentonite, Kelvin's Law expresses the psychrometric relationship between state of suction, s (= P_g - P_l or capillary pressure) in the bentonite and vapor pressure of water P_v in the gas phase (with M_w being the molecular weight of water component):

$$P_v = P_v^0 e^{-sM_w/RT\rho_w} \qquad \textit{Equation 2-16}$$

This expression is used to calculate the relative humidity (RH) within the bentonite, where

$$RH = 100\% \, {}^{P_v}\!/_{P_v^0} \text{ and } P_v^0 = 136075 \ e^{-5239.7/T} \qquad \textit{Equation 2-17}$$

P_v^0 is the saturated vapor pressure of water in MPa, and the expression we use here is from Gens et al. (2009).

For the two-phase flow portions of the above model, we have multiple variables: four ρ_β^α for the two components in the two phases, the liquid and gas pressures P_l and P_g, and the liquid and gas saturations S_l and S_g. The equilibrium conditions and the compatibility condition between saturations reduce the number of variables to two (so-called primary variables), with added algebraic calculations between the calculated primary variables and the secondary variables being necessary (in compositional modeling, these are sometimes called "flash" calculations associated with the appearance of gas phase, e.g. steam flashing). During numerical simulation, it is common to calculate one of the pressures and liquid saturation, for example. Problems arise when phases appear or disappear, leading to various approaches for multiphase flow. For the PFLOTRAN simulations, we use P_g and S_l as primary variables.

2.2.3 Constitutive Equations for Granite, Bentonite, and Cement

2.2.3.1 Bentonite, Cement, and Granite Water Retention

Water retention properties for FEBEX bentonite have been studied by many authors, notably by Pintado et al. (2002) and Villar and Lloret (2004). We use a bentonite water retention curve following the familiar van Genuchten formulation

$$S_{el} = \left[1 + \left(\frac{s}{P_0}\right)^{\frac{1}{1-\lambda_0}}\right]^{-\lambda_0} \qquad \textit{Equation 2-18}$$

where $S_{el} = \frac{S_l - S_{lr}}{S_{ls} - S_{lr}}$, where S_{lr} is residual liquid saturation and S_{ls} is the maximum saturation, taken as unity. For relative permeability, PFLOTRAN has the option of the Mualem functions for liquid (k_{rl}) and gas-phase (k_{rg}) relative permeability, which are adopted here:

$$k_{rl} = \sqrt{S_{el}} \left\{1 - \left(1 - S_{el}^{\lambda}\right)^{1/\lambda}\right\}^2 \qquad \textit{Equation 2-19a}$$

$$k_{rg} = \sqrt{1 - S_{eg}} \left\{1 - S_{eg}^{1/\lambda}\right\}^{2\lambda} \qquad \textit{Equation 2-19b}$$

where $S_{eg} = 1 - \frac{S_l - S_{lr}}{1 - S_{lr} - S_{gr}}$, with S_{gr} being the residual gas saturation taken as zero.

2.2.3.2 *Water Equation of State*

We use a simple equation of state for liquid water,

$$\rho_l = \rho_l^0 e^{\{\beta(P_l - P_l^0) + \alpha_T(T - T^0)\}} \qquad \textit{Equation 2-20}$$

where β is the water compressibility at standard conditions and α_t is the volumetric expansion coefficient of water at standard conditions.

2.2.3.3 *Vapor Diffusion*

The gas phase binary diffusional fluxes of vapor and dry air are expressed in terms of the vapor mass fraction gradient and take the form

$$J_g^w = -J_g^a = -\varphi(1 - S_r)\tau D_g^w \rho_g \nabla Y_g^w \qquad \textit{Equation 2-21}$$

where τ is tortuosity, and the diffusion coefficient (m^2/s) is temperature and gas pressure dependent, in the form from Philip and de Vries (1957):

$$D_g^w = 5.9\ x\ 10^{-12} \frac{T^{2.3}}{P_g} \qquad \textit{Equation 2-22}$$

2.2.3.4 *Effective Thermal Conductivity and Heat Capacity*

Thermal conductivity was assumed to be a function of liquid saturation following the form of Somerton et al., 1974:

$$k_{th} = k_{dry} + \sqrt{S_l}(k_{sat} - k_{dry}) \qquad \textit{Equation 2-23}$$

where k_{th} = thermal conductivity, k_{dry} = dry thermal conductivity, and k_{sat} = fully saturated thermal conductivity.

2.3 Thermal-Hydrologic Modeling with PFLOTRAN

2.3.1 Stage 1 Modeling

TH modeling was conducted for Task 9, Stage 1 FEBEX in-situ test, up to first dismantlement (5 years). A 3D modeling domain was developed based on project specifications Figure 2-1) with domain size 60 × 20 × 40 m in the x, y and z directions, respectively. To reduce mesh size an axisymmetric boundary condition was applied (Figure 2-2).

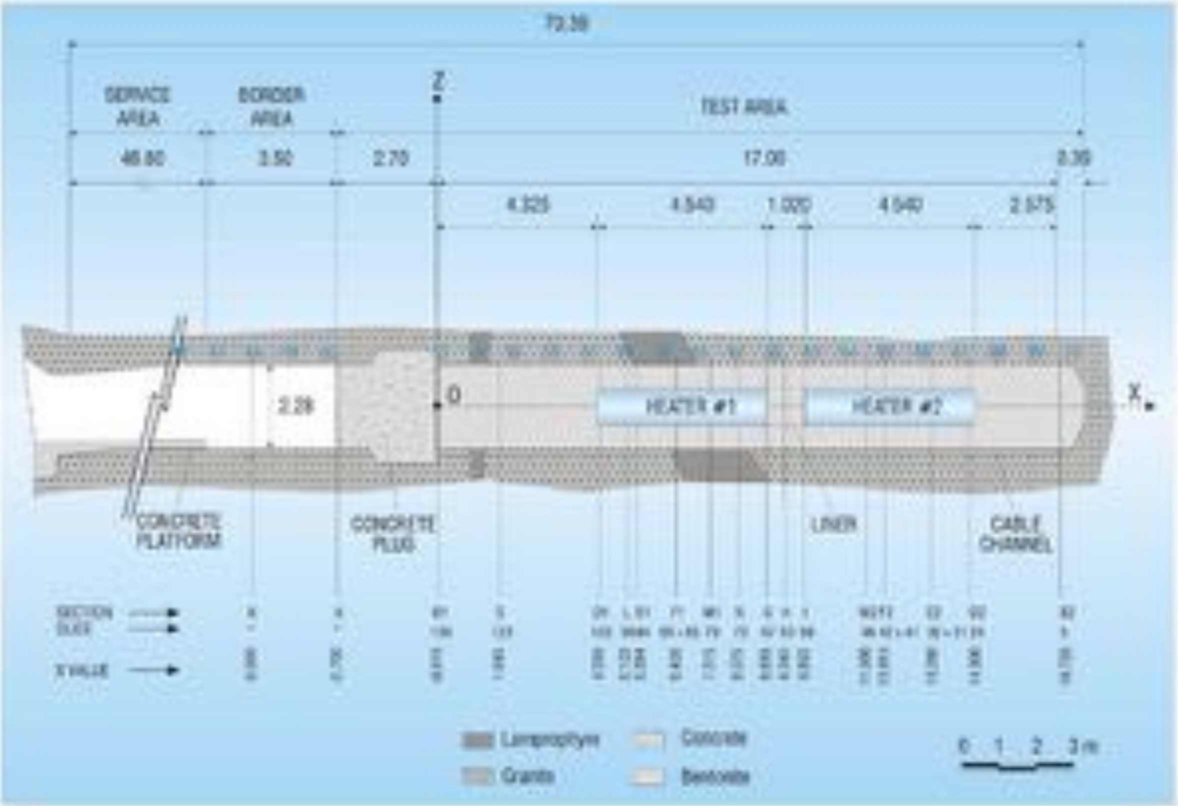

Source: Bárcena et al. 2003.

Figure 2-1. General layout of the FEBEX in-situ test for Stage 1.

For TH simulations using PFLOTRAN numerical code the domain was discretized using an unstructured grid with fine discretization around the heaters and the buffer (Figure 2-3). Figure 2-4 shows discretization of the buffer. The mesh size for Stage 1 is 125,824 grid blocks. The buffer is represented by a total of 4,096 grid blocks (elements), with 46 grid blocks (elements) across the bentonite barrier. The simulation domain includes details of various regions representing different materials including granite, disturbed rock zone (DRZ), bentonite buffer, heaters, plug, liner, micro-annulus, lamprophyre and fracture at back of test area. For this report, we have assumed that the DRZ, lamprophyre dikes and fracture zones have the same properties as the granite domain.

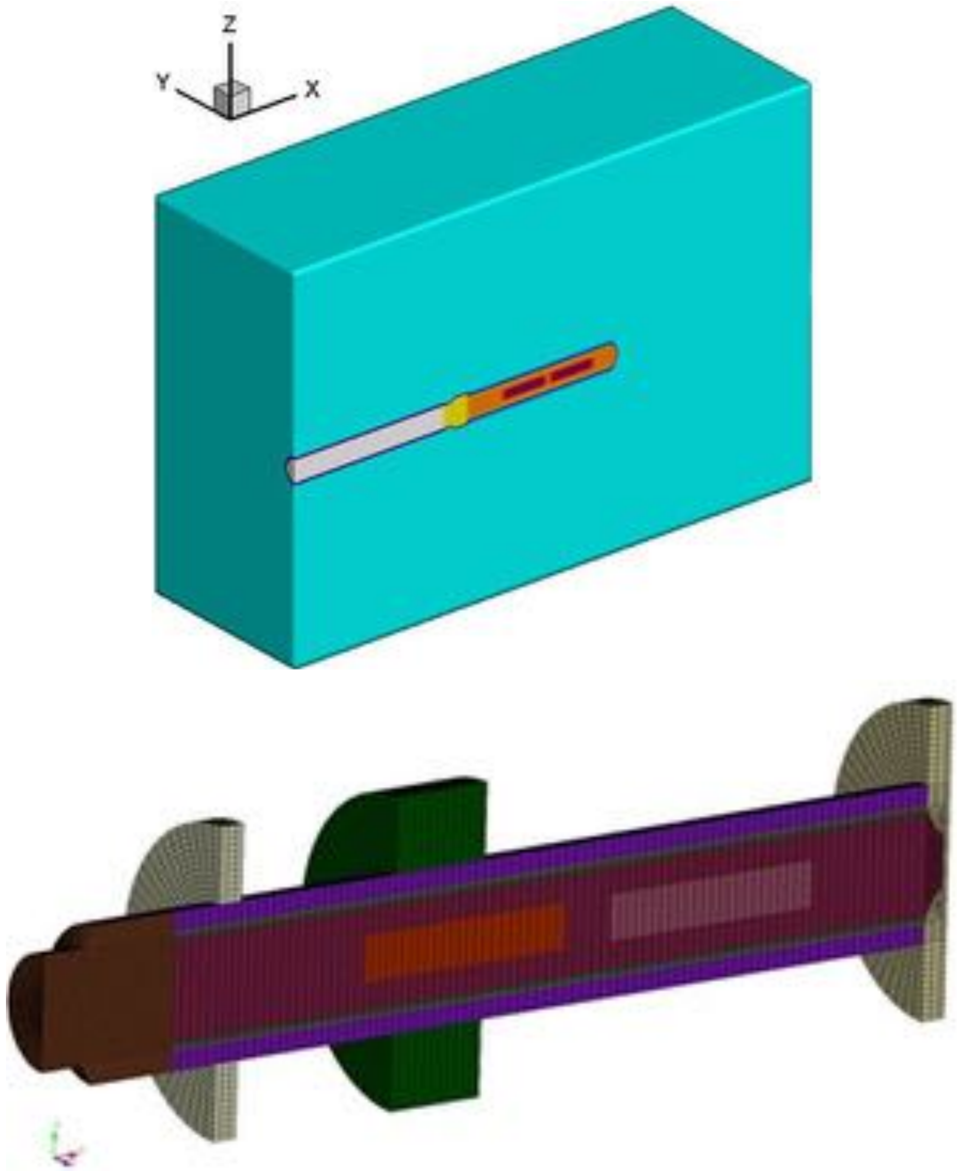

Figure 2-2. 3D modeling domain with axisymmetric meshing for Stage 1.

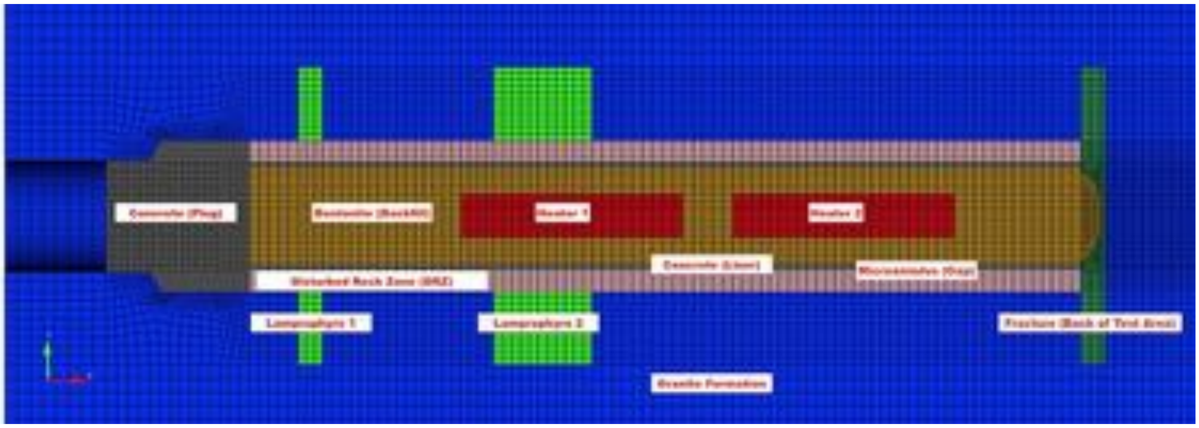

Figure 2-3. Meshing of the TH modeling domain for Stage 1.

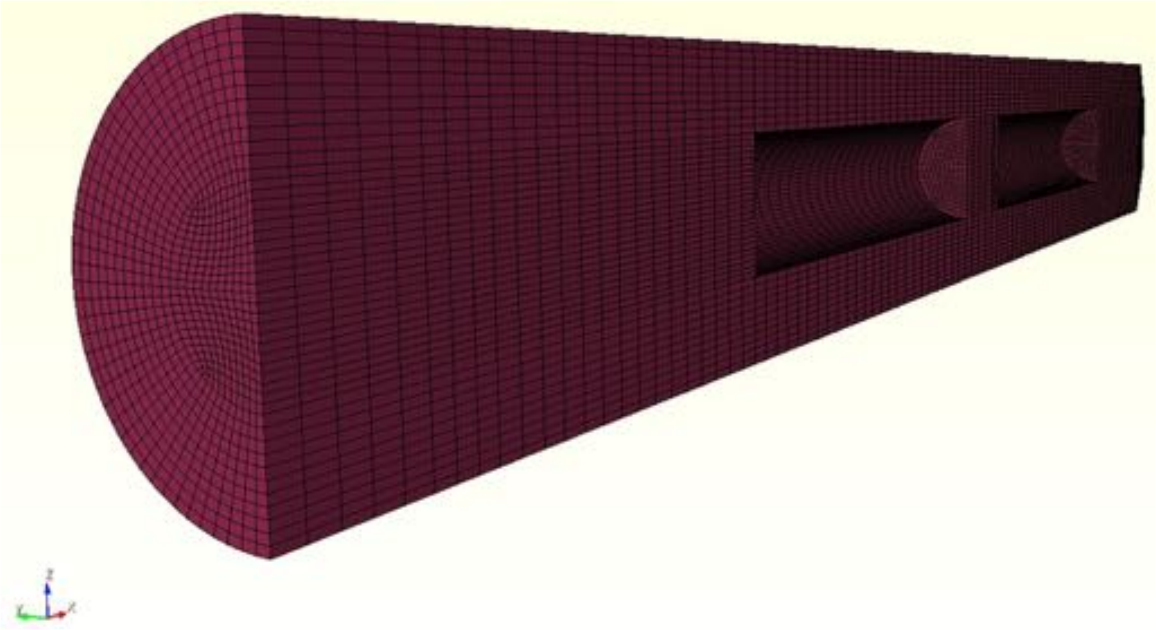

Figure 2-4. Meshing of the bentonite buffer for Stage 1.

2.3.1.1 TH Model Setup

Dates of important events in the FEBEX heater test that are examined in this report are given in Table 2-1. The system is assumed to be at 12°C at the beginning of the simulation. When the bentonite buffer is emplaced in the test area, a pressure of one atmosphere and a liquid saturation of 0.36 were applied. At the beginning of the heating phase the bentonite is assumed to be at a higher liquid saturation of 0.65 due to hydration from the formation. Hydrostatic pressure boundary condition was assigned on the sides of the modeling domain with a pressure of 0.7 MPa at the top of the domain. Based on the project specification, a 1,200 W heat was applied at the two heaters for the first 20 days of simulation time. The power was raised to 2,000 W per heater between Day 20 and Day 60. For the rest of the simulation time in Stage 1, time varying heat was applied at the two heaters to maintain a temperature of 100°C.

Table 2-1. Sequence of events in the FEBEX in-situ test.

Event	Date (Month/Day/Year)	Interval/Days	Cumulative Days
Start of Tunnel Excavation	09/25/95	—	—
End of Tunnel Excavation	10/30/95	35	35
Start of Installation	07/01/96	245	280
End of Installation	10/15/96	106	351
Heaters Switched On	02/27/97	135	241
Heater 1 Switched Off	02/28/02	1,827	1,962
End of 1st Dismantling	07/19/02	141	1,968
Heater 2 Switched Off	04/20/05	1,006	1,147
End of 2nd Dismantling	07/20/15	3,743	4,749

Material properties of main components selected for modeling are specified in Table 2-2. Retention curve parameters are given in Table 2-3. Molecular diffusion of vapor in free air of 2.0×10^{-5} m^2/s and diffusion coefficient in liquid of 2.0×10^{-9} m^2/s were used.

Table 2-2. Material properties used in the TH simulations.

Property	Units	Granite	Buffer	Concrete Plug
Permeability	m^2	1.26×10^{-19}	1.60×10^{-20}	2.0×10^{-20}
Porosity	—	0.01	0.375	0.01
Density	kg/m^3	2,750	1,600	2,600
Thermal Conductivity dry/wet	W/(m·K)	3.2/3.3	0.6/1.3	3.0/3.0
Specific Heat	kJ/kg	793	1,091	1,000.0

Table 2-3. Retention curve parameters used in the TH simulations.

Parameter	Units	Granite	Buffer	Concrete Plug
P_0	MPa	0.0021	25.0	0.0021
l	—	0.7	0.2	0.7
S_{lr}	—	0.0	0.1	0.01
S_{gr}	—	0.0	0.1	0.01
S_{ls}	—	1.0	1.0	1.0

2.3.2 Stage 2 Modeling

TH modeling was conducted for Task 9, Stage 2 FEBEX in-situ test, between the first and second dismantlement as listed in Table 2-1. Because of change in domain geometry, and the complexity of the mesh used in Stage 1 modeling, the same mesh could not be used for Stage 2. A different 3D mesh was needed to include all the changes that occurred after the first dismantlement. This also meant that Stage 1 modeling output at the end of simulation time could not be transferred to the Stage 2 TH modeling. Thus, for Stage 2, modeling is performed for 18 years with Heater 2 only operating to obtain reasonable initial conditions for the Stage 2 modeling. This neglects the contributions of Heater 1 for Stage 2.

A 3D modeling domain was developed based on project specifications (Figure 2-5) with domain size 60 × 20 × 40 m in the x, y and z directions, respectively. To reduce mesh size an axisymmetric boundary condition was applied (Figure 2-6). For TH simulations using PFLOTRAN numerical code the domain was discretized using an unstructured grid with fine discretization around the heaters and the buffer (Figure 2-6). The mesh size for Stage 2 is 329,828 grid blocks and includes a total of 1,052 grid blocks (elements). The simulation domain includes details of various regions representing different materials including granite, DRZ, bentonite buffer, heaters, old concrete plug, new shotcrete plug, liner, micro-annulus, lamprophyre and fracture at back of test area. For modeling purposes the new shotcrete plug was assigned the same material properties as the old concrete plug.

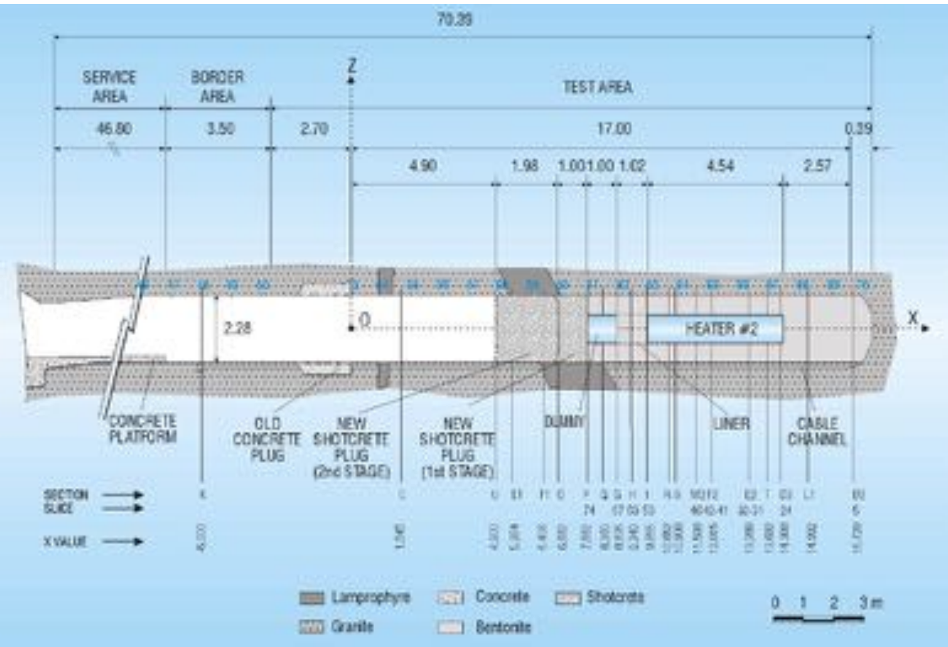

Figure 2-5. General layout of the FEBEX in-situ test after first dismantlement.

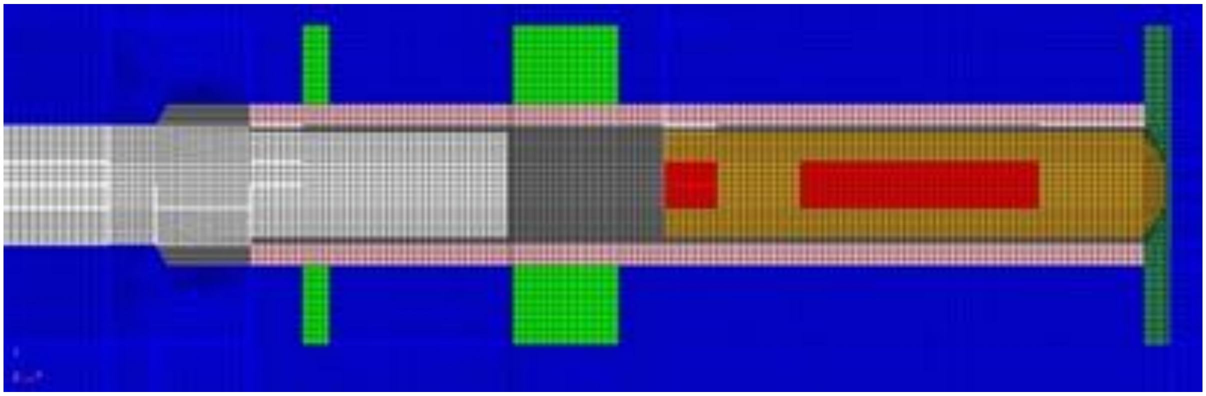

Figure 2-6. Meshing of the TH modeling domain for Stage 2.

2.3.2.1 TH Model Setup

As stated above, Stage 2 modeling starts at the beginning of heating. As for Stage 1 the system is assumed to be at 12ºC at the beginning of the simulation. At the beginning of heating the bentonite buffer is at pressure of one atmosphere and a liquid saturation of 0.65. Hydrostatic pressure boundary condition was assigned on the sides of the modeling domain with a pressure of 0.7 MPa at the top of the domain. Based on the project specification, a 1,200 W heat was applied at Heater 2 for the first 20 days of simulation time. The power was raised to 2,000 W between Day 20 and Day 60. For the rest of the simulation time, time varying heat was applied at Heater 2 to maintain a temperature of 100ºC. The PFLOTRAN numerical code was used for the simulation in a high-performance computing environment. The same material properties specified in Table 2-1 were used for Stage 2 modeling.

2.4 Modeling Results

PFLOTRAN runs were made using up to 160 processors per run using High Performance Computing (HPC) facilities at Sandia National Laboratories. For Stage 1, simulations were run for a total of 1,800 days with both heaters operating and parameter values described in Section 2.3. In addition, simulations were conducted with a cooling period for 141 days. For Stage 2, simulations were run for a total of 6,700 days with Heater 2 only operating and using the same parameter values as in Stage 1. Stage 2 simulations were conducted with a cooling period for 128 days. Analysis of simulation results and comparison with experimental data for Stage 1 and Stage 2 are described in Section 2.5.1 and Section 2.5.2, respectively.

Figure 2-7 shows initial system pressure before heating is applied. The system is at hydrostatic pressure conditions except across the buffer barrier. The buffer is at a liquid saturation of 0.65 and gas pressure of one atmosphere. The corresponding suction is 167 MPa with relative humidity at 27%.

TH modeling results at the end of the Stage 1 are shown in Figure 2-8 and Figure 2-9. Figure 2-8 shows distribution of temperature along the axis of the tunnel, a perpendicular cross-section at the location of Heater 1 and a horizontal cross-section. The figure shows migration of heat into the buffer and host rock. Figure 2-9 shows the corresponding distribution of liquid saturation.

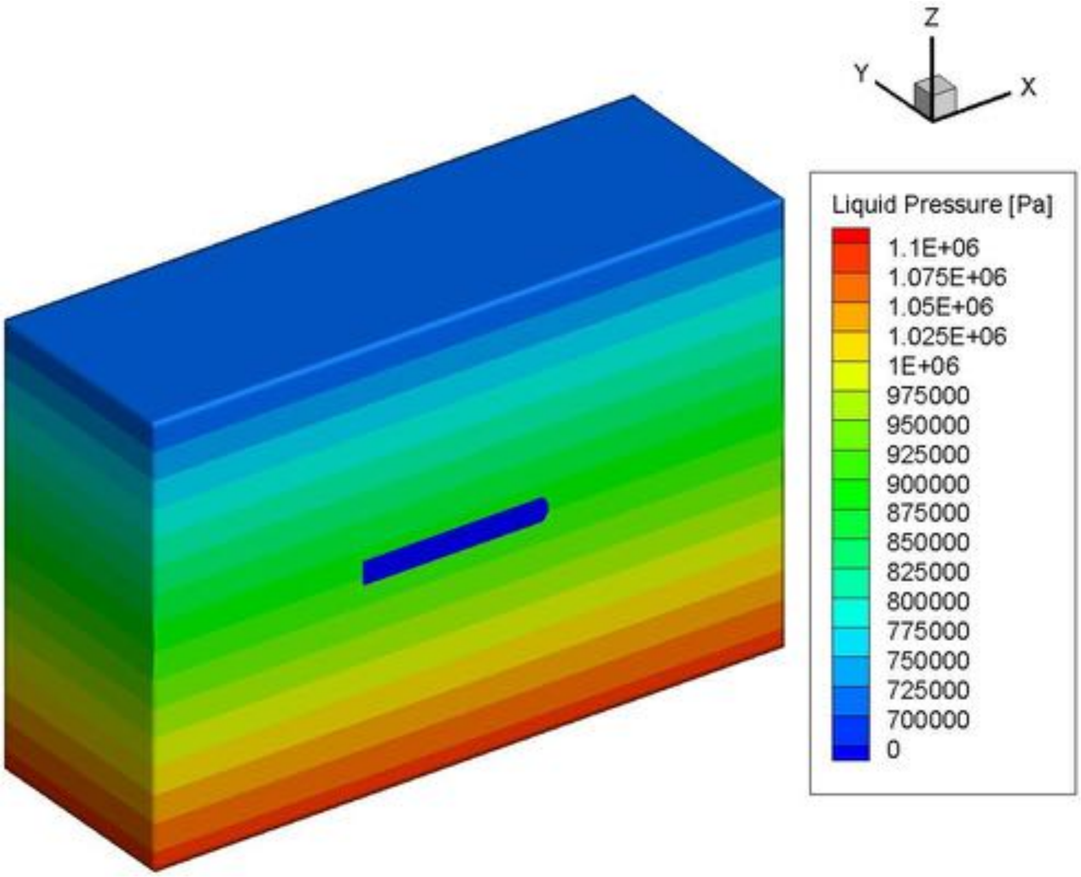

Figure 2-7. Initial condition for both Stage 1 and Stage 2 simulations. Note that negative liquid pressures in the buffer related to suction have not been included in the figure.

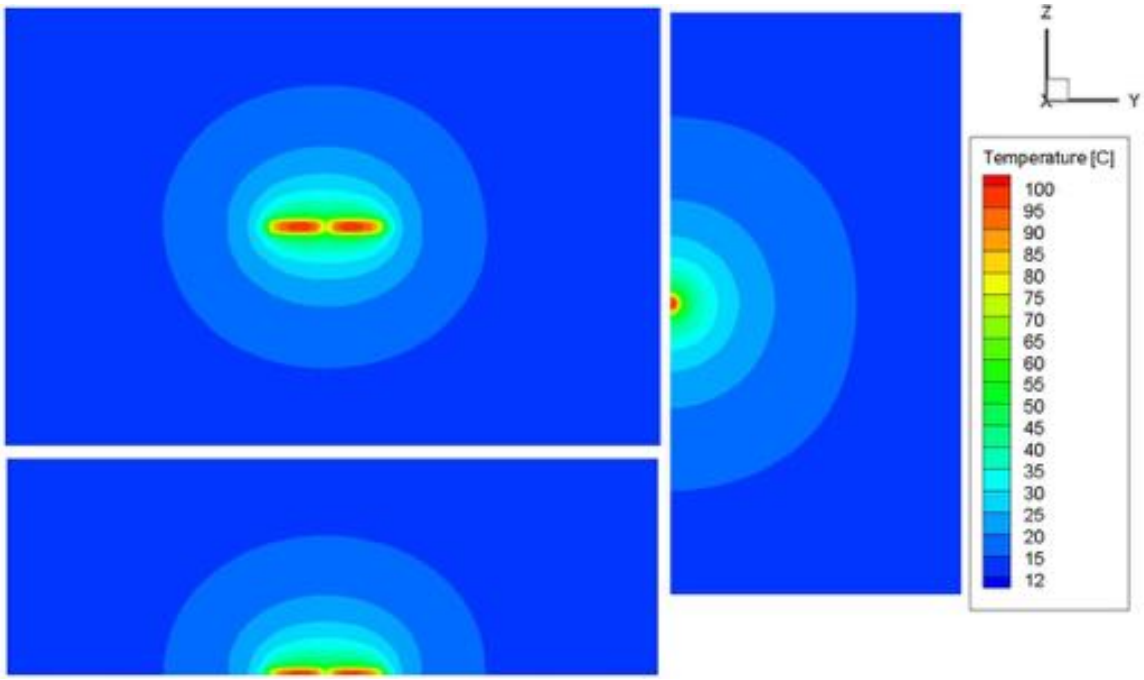

Figure 2-8. Predicted temperature distribution for Stage 1 at 1,800 days.

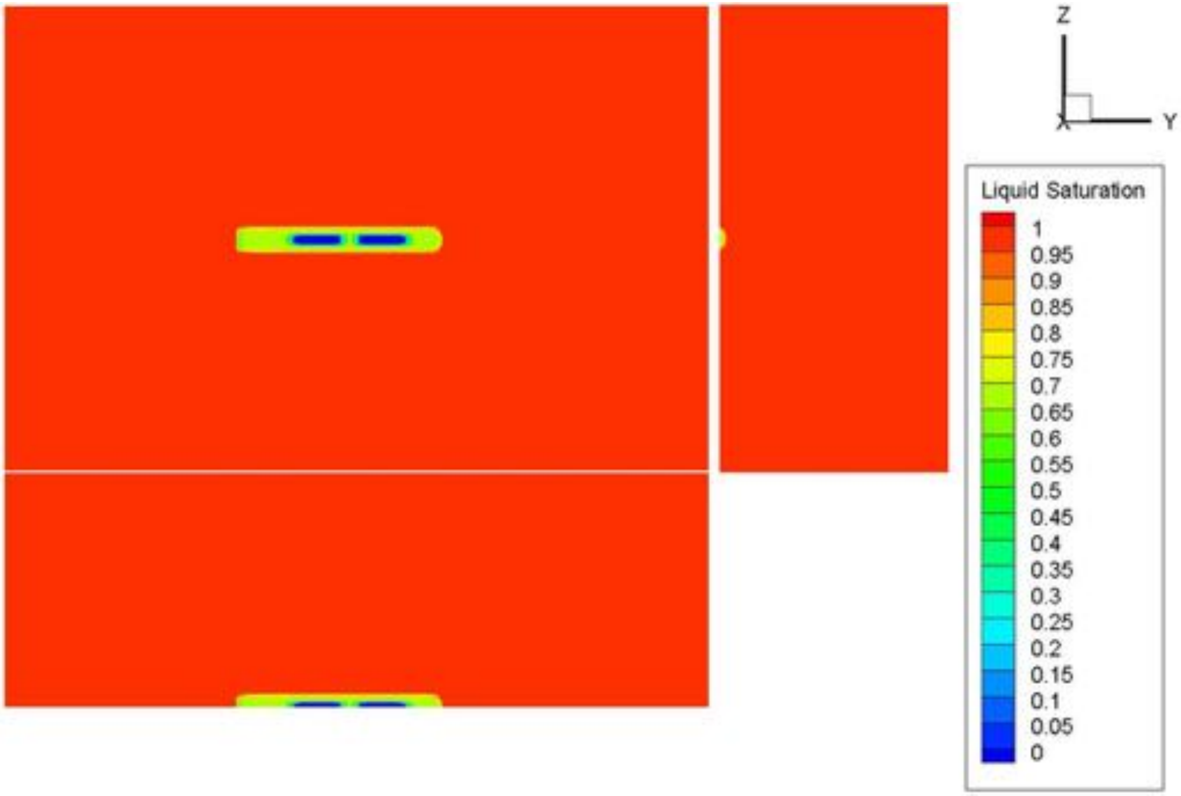

Figure 2-9. Predicted liquid saturation distribution for Stage 1 at 1,800 days.

2.5 Comparison to Field Results

2.5.1 Stage 1: Analysis of Results

2.5.1.1 Evolution of Heating Power

For Stage 1 simulations to maintain 100ºC at the heaters the power applied to both heaters was kept at 2,000 W for the rest of the simulation time. Figure 2-10 and Figure 2-11 show comparison of the measured and simulated results for heating power. The predicted power is close to experimental for Heater 1. For Heater 2 the predicted power is lower by up to 10%.

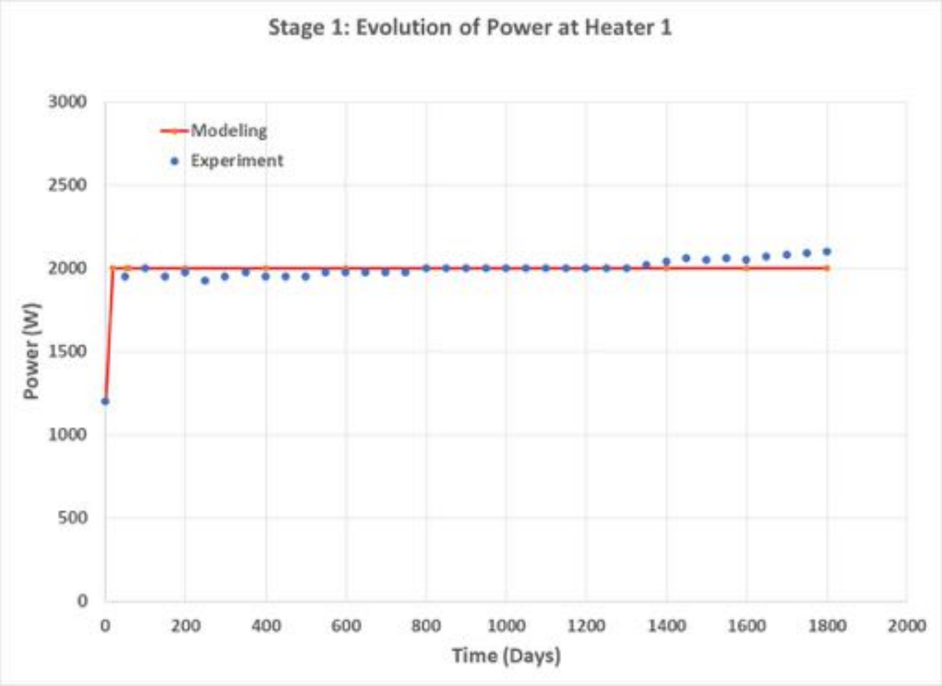

Figure 2-10. Predicted evolution of power at Heater 1 for Stage 1.

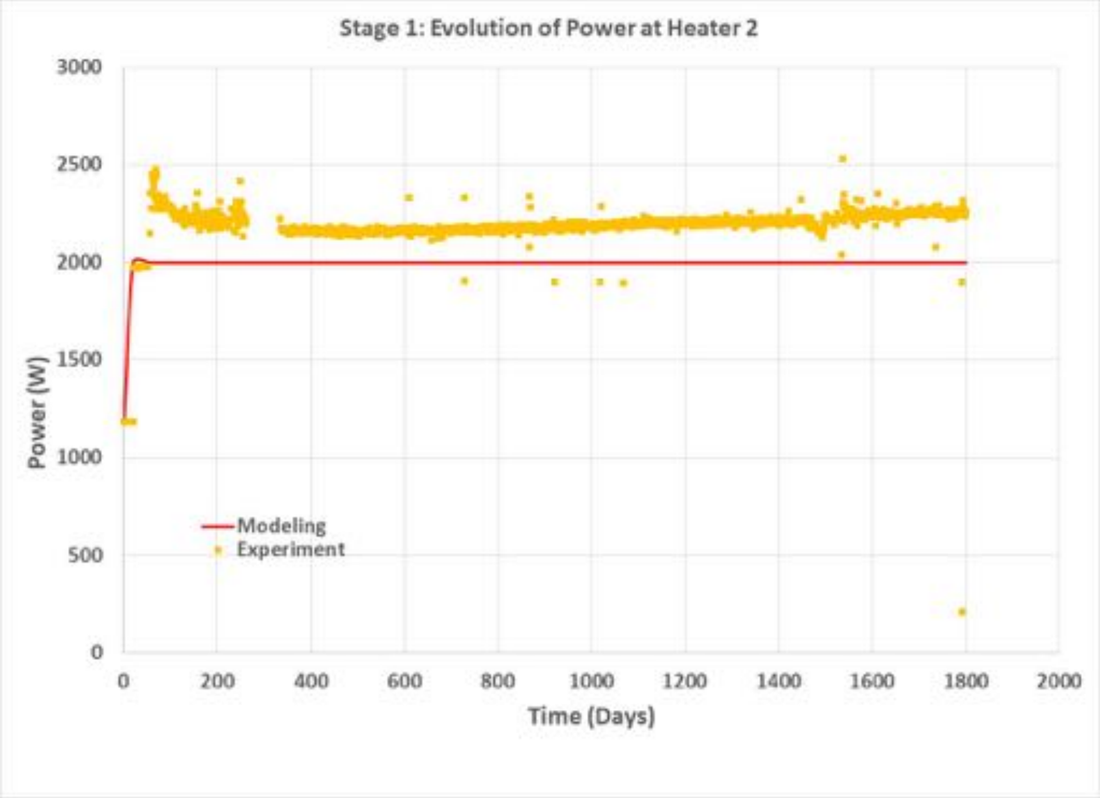

Figure 2-11. Predicted evolution of power at Heater 2 for Stage 1.

2.5.1.2 Prediction of Temperature

Prediction of distribution of temperature along radial segments on Section D1 at 90 days and 1,800 days simulation times are shown in Figure 2-12 and Figure 2-13, respectively, along with experimental data. Section D1 is close to Heater 1 and thus temperatures are higher at radial distances close to the heater. Experimental temperatures are lower away from the heater. At 90 days simulation time predicted temperatures are lower than experimental close to the heater. For the rest of the radial locations the model results are close to experimental. Results at 1,800 days are similar to those at 90 days with slightly lower predicted temperatures near the heater but excellent matching at other radial locations.

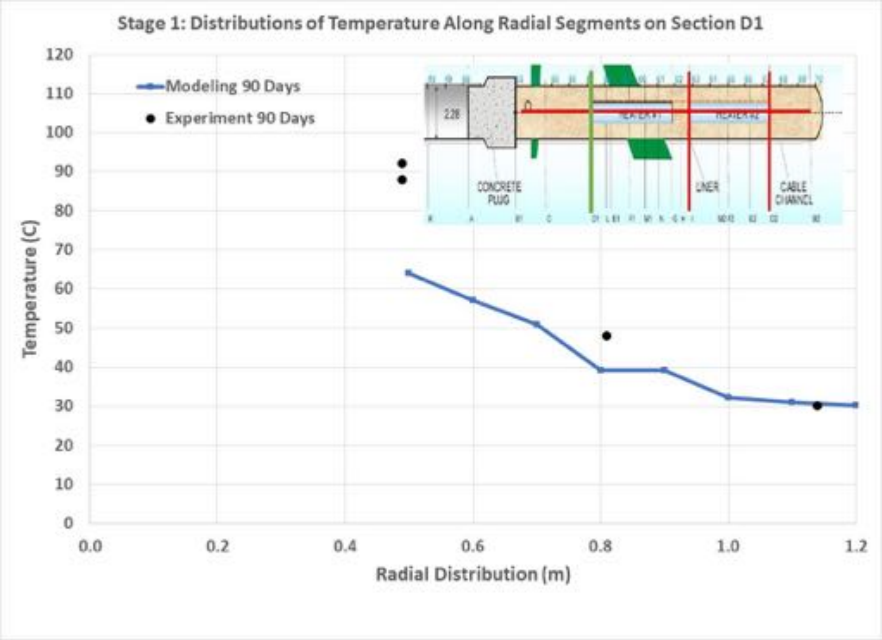

Figure 2-12. Stage 1: Predicted distributions of temperature along radial segments on Section D1 at 90 days simulation time.

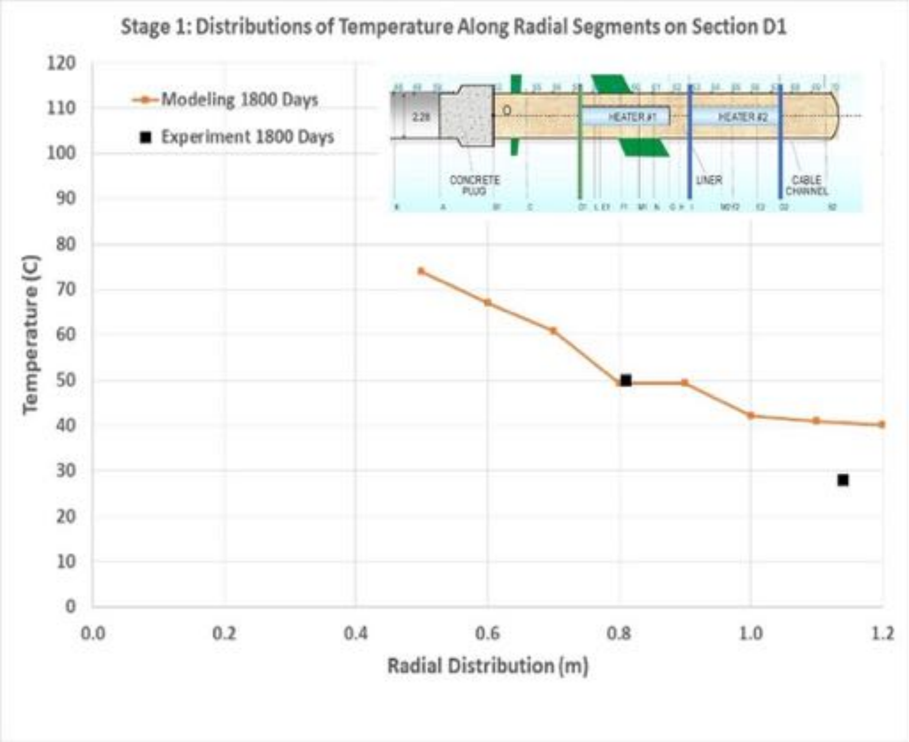

Figure 2-13. Stage 1: Predicted distributions of temperature along radial segments on Section D1 at 1,800 days simulation time.

Prediction of distribution of temperature along radial segments on Section D2 at 90 days and 1,800 days simulation times are shown in Figure 2-14 and Figure 2-15, respectively, along with experimental data. Section D2 is close to Heater 2 on the other end from Section D1. The simulation results are similar to those of Section D1. At both 90 days and 1,800 days predicted temperatures are slightly lower than experimental near the heater. Better matching is obtained at other radial locations.

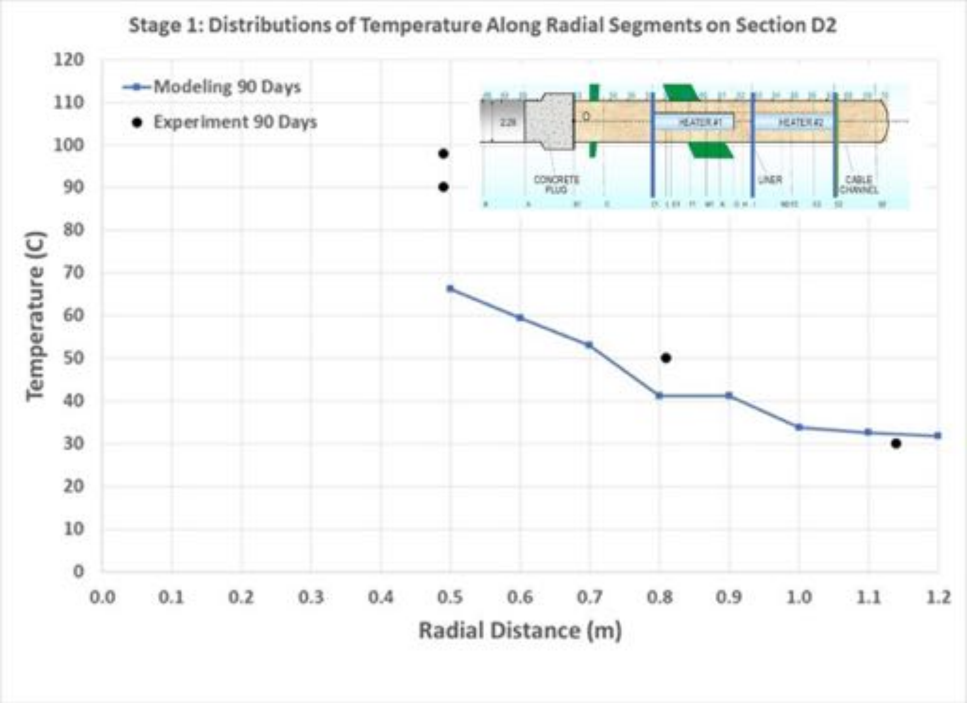

Figure 2-14. Stage 1: Predicted distributions of temperature along radial segments on Section D2 at 90 days simulation time.

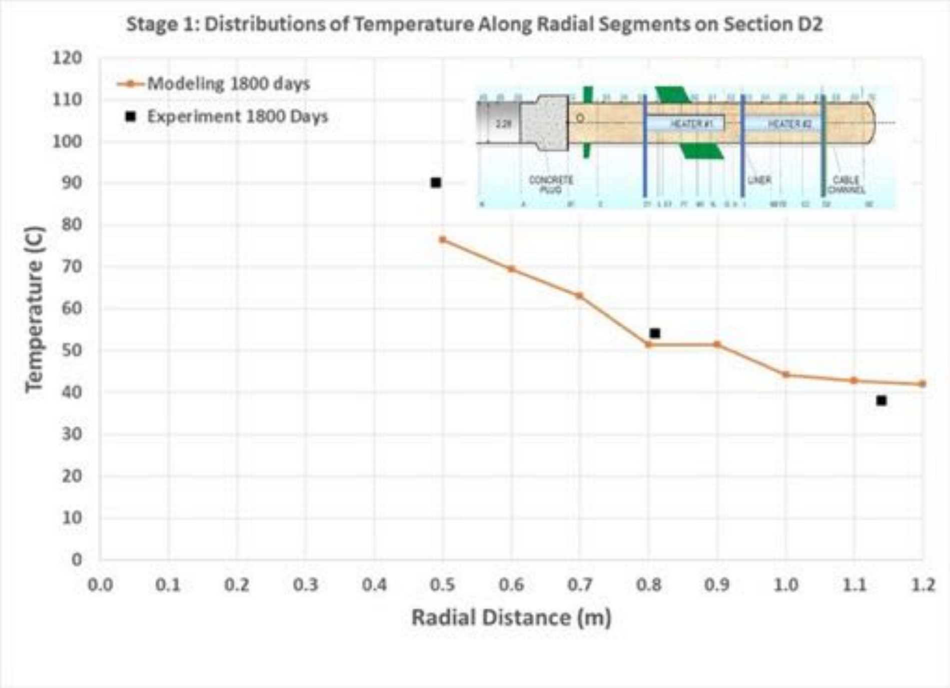

Figure 2-15. Stage 1: Predicted distributions of temperature along radial segments on Section D2 at 1,800 days simulation time.

Predictions of distribution of temperature along axial segments AS1 and AS2 (Table 2-4) are shown in Figure 2-16 to Figure 2-19 at 90 days and 1,800 days along with experimental data. The predictions are very close to the experimental data. As would be expected temperatures rise close to the heaters and decrease away from the heaters. The dip in temperature in the middle of the figures is related to the area between the heaters. Temperature is lower there because the measurement point is away from the heaters. Segment AS1 is closer to the heaters than AS2 and thus temperatures are higher at AS1.

Table 2-4. Locations of the axial segments AS1 and AS2.

Segment	Origin (x, y, z)	End (x, y, z)	Remarks
AS1	(0.00, –0.81, 0.00)	(17.00, –0.81, 0.00)	Parallel to x-axis, between heaters and granite
AS2	(0.00, –1.14, 0.00)	(17.00, –1.14, 0.00)	Parallel to x-axis, near granite

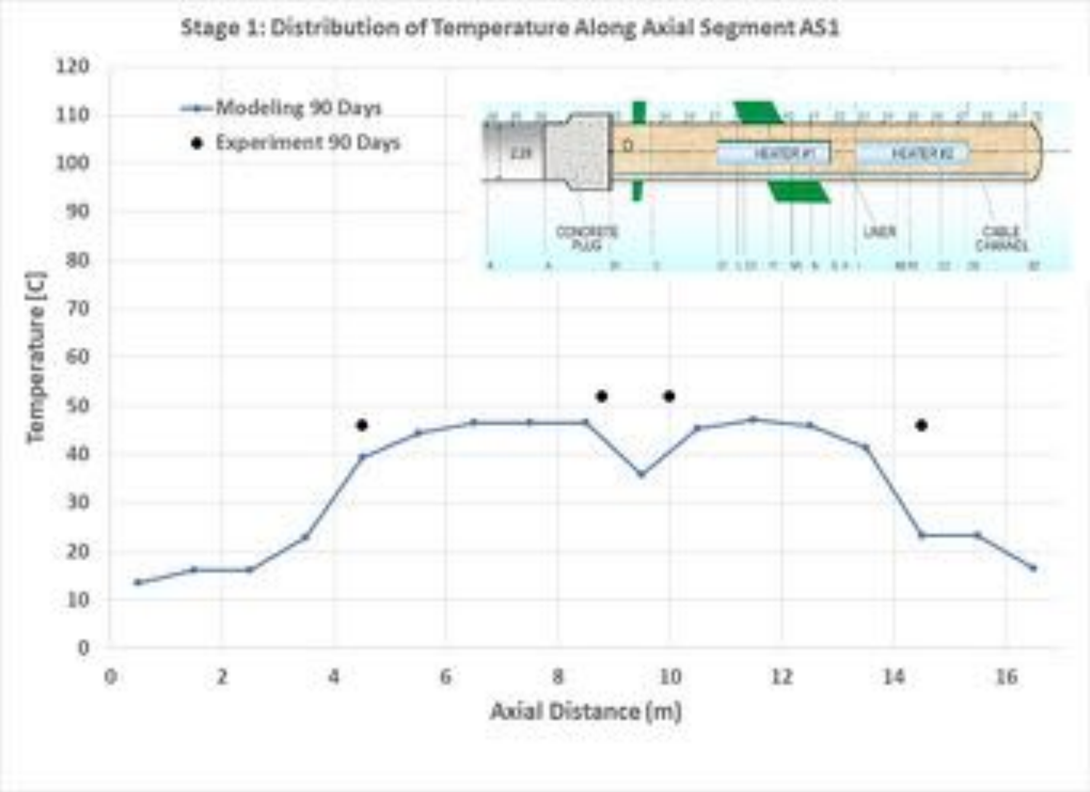

Figure 2-16. Stage 1: Predicted distributions of temperature along axial segment AS1 at 90 days simulation time.

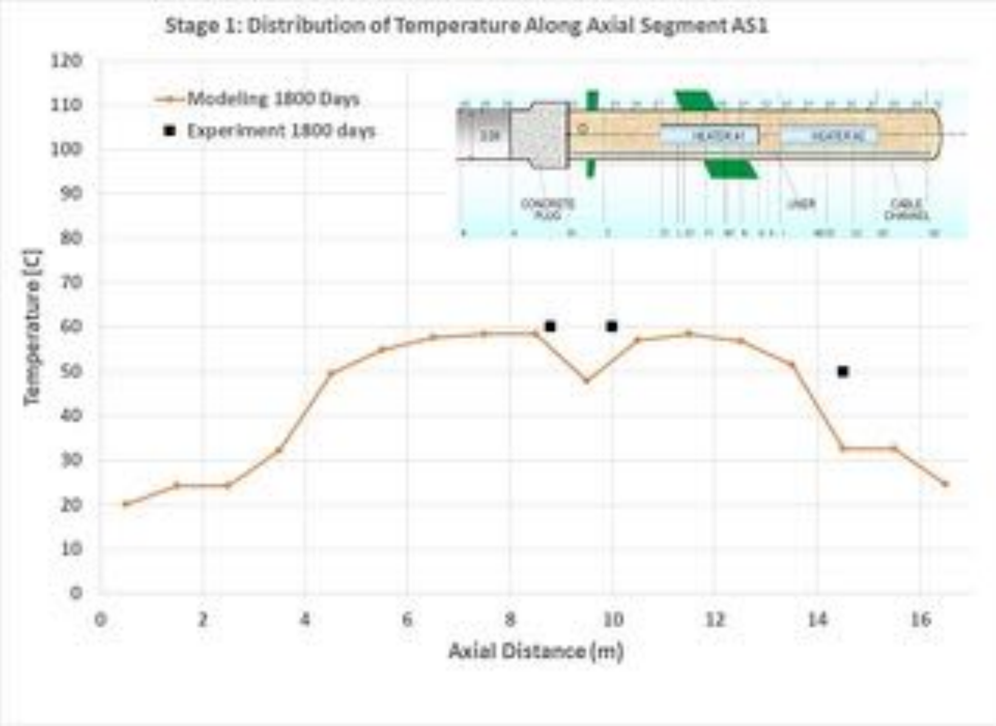

Figure 2-17. Stage 1: Predicted distributions of temperature along axial segment AS1 at 1,800 days simulation time.

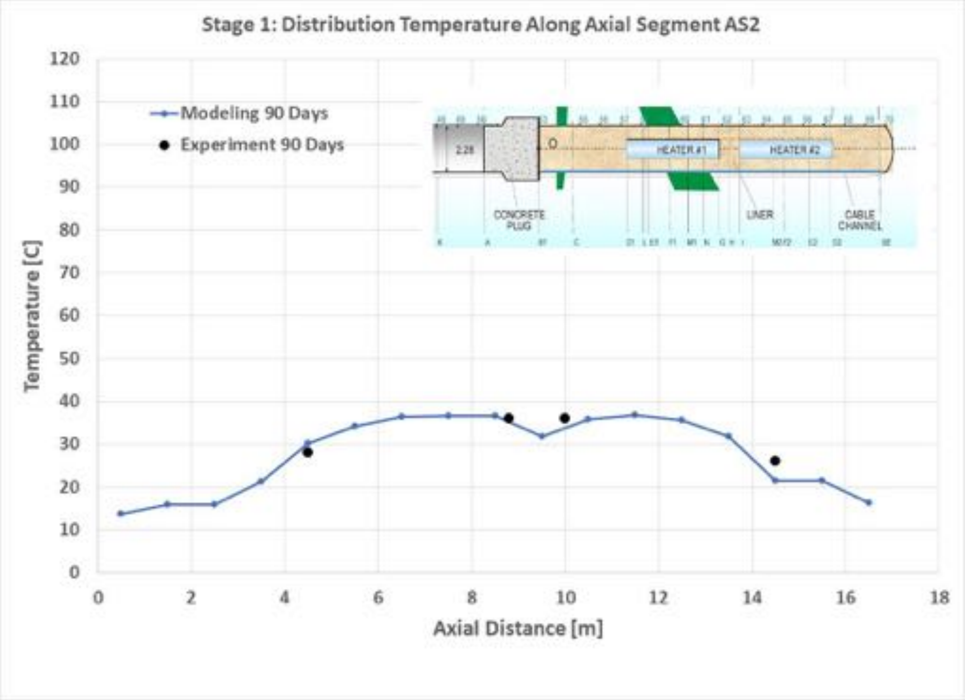

Figure 2-18. Stage 1: Predicted distributions of temperature along axial segment AS2 at 90 days simulation time.

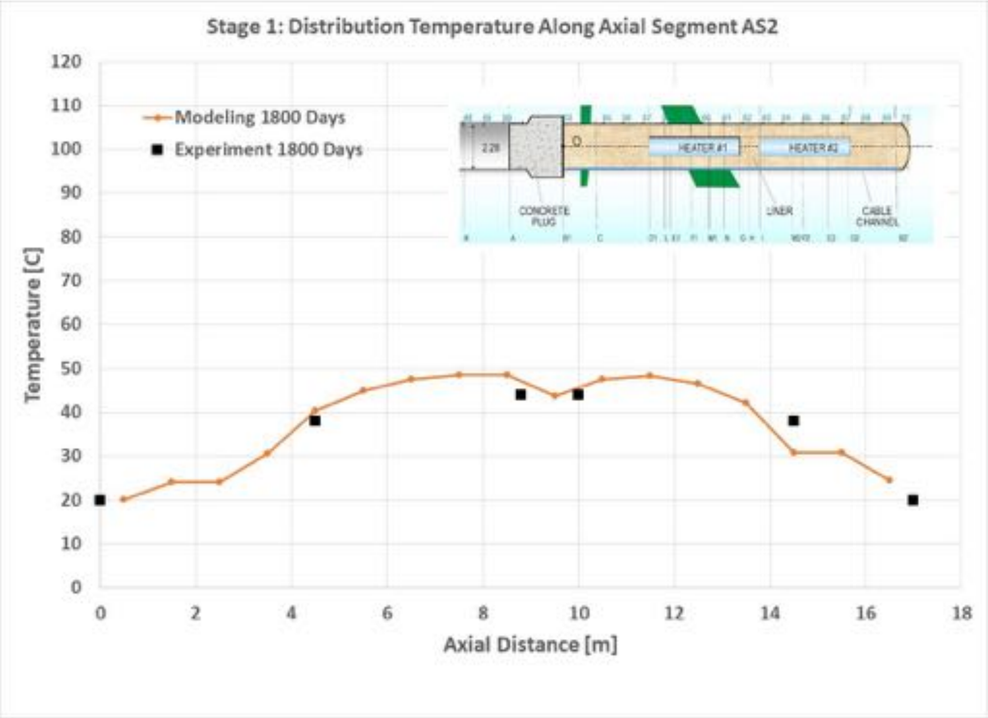

Figure 2-19. Stage 1: Predicted distributions of temperature along axial segment AS2 at 1,800 days simulation time.

Predicted evolution of temperature at Point P1 on Section D1 (Table 2-5) is shown in Figure 2-20 along with experimental data. Point P1 is away from Heater 1, close to the wall. Thus, temperatures are lower. Predicted temperatures are close to the experimental values everywhere, except at early time where predicted temperatures are slightly higher. Figure 2-21 shows results for Point P1 on Section D2 (Table 2-5). The results are similar to those at D1. The slight temperature over prediction maybe explained by careful observation of the experimental method, location of observation points and with sensitivity analysis.

Table 2-5. Locations of points on Sections D1 and D2.

Segment	Origin (x, y, z)	Remarks
SD1P1	(4.42, –1.14, 0.00)	Negative y-axis, near granite
SD2P2	(14.38, –1.14, 0.00)	Negative y-axis, near granite

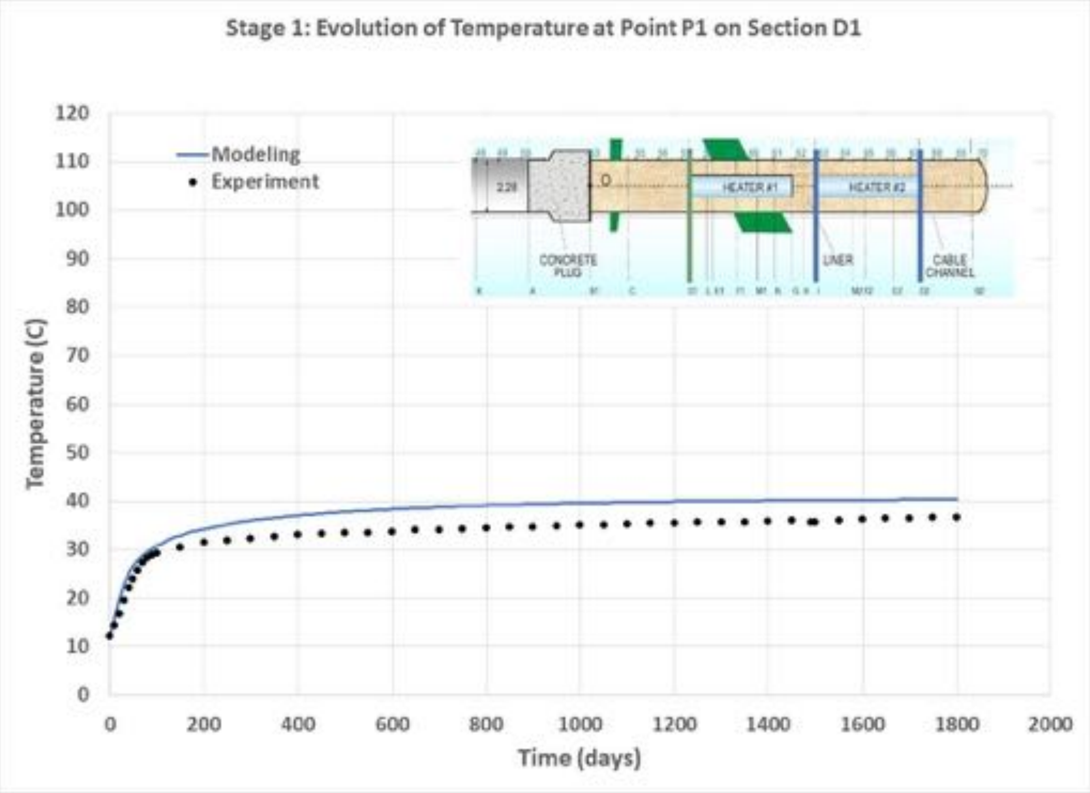

Figure 2-20. Stage 1: Predicted evolution of temperature at Point P1 on Section D1.

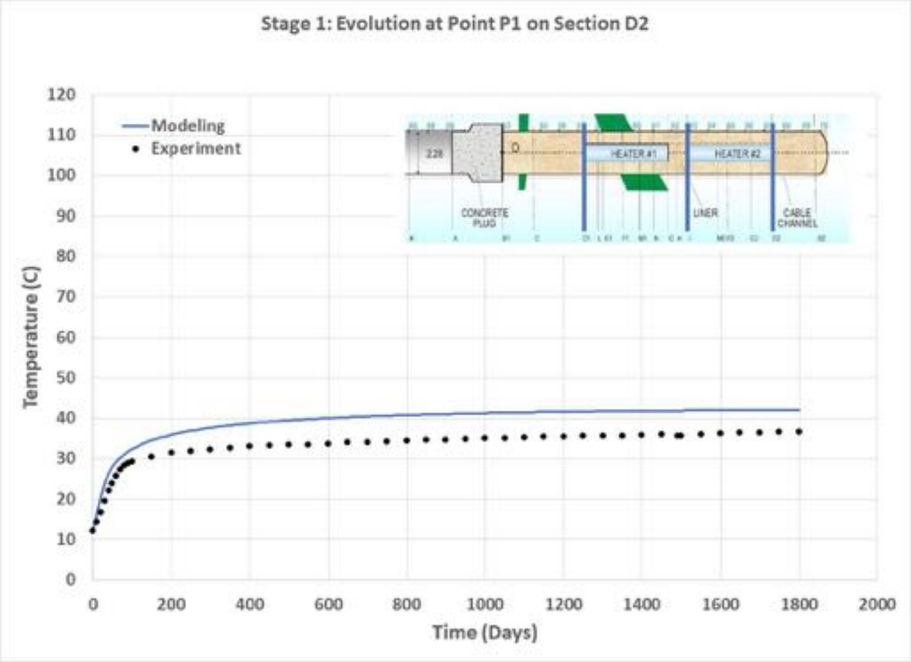

Figure 2-21. Stage 1: Predicted evolution of temperature at Point P1 on Section D2

2.5.1.3 Prediction of Relative Humidity

Predicted evolution of relative humidity at Points P1, P2 and P3 on Section E1 (Table 2-6) are shown in Figure 2-22. At early times predicted results at Point P1 are higher than the experimental. Predicted and experimental results are equivalent at later times. At Point P2 the predicted values are close to the experimental at early times but are lower at later times. The predicted results at Point P3 match the experimental data. A sensitivity analysis showed that predictions at Points P1 and P2 improve at higher granite permeability.

Table 2-6. Locations of points on Section E1.

Segment	Origin (x, y, z)	Remarks
SE1P1	(5.53, –0.52, 0.00)	Negative y-axis, near steel liner
SE1P2	(5.53, -0.81, 0.07)	Negative y-axis, near middle of bentonite
SE1P3	(5.53, -1.10, -0.17)	Negative y-axis, near granite

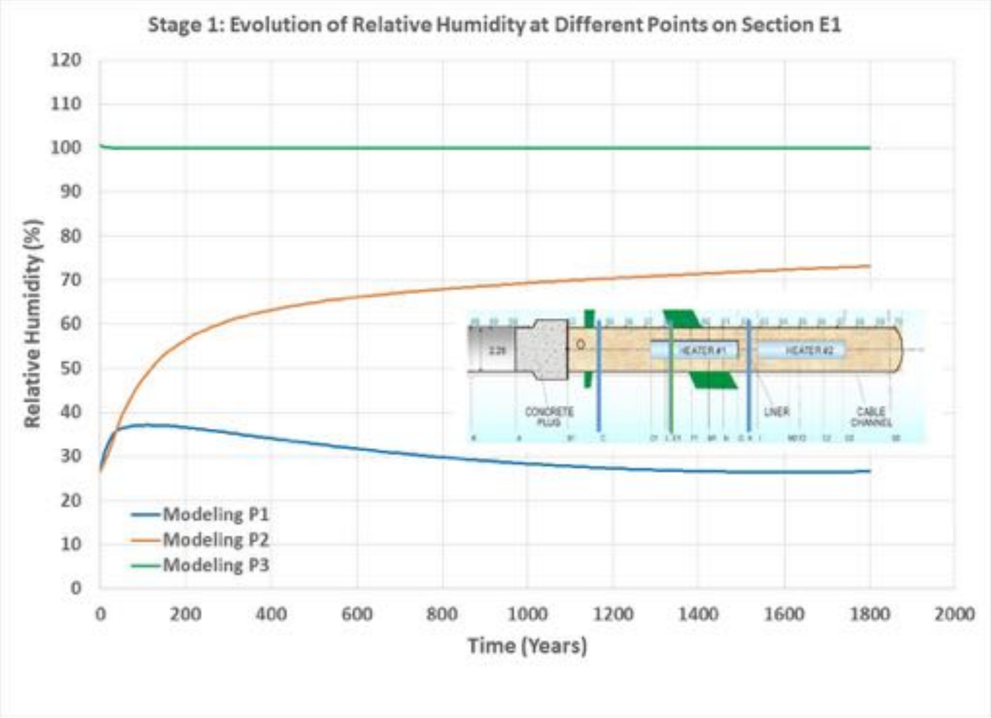

Figure 2-22. Stage 1: Predicted evolution of relative humidity at Points P1, P2 and P3 on Section E1.

Predicted evolution of relative humidity at Points P1, P2 and P3 on Section H (Table 2-7), which is located between the two heaters, are shown in Figure 2-23 together with experimental data. For Points P1 and P2 predicted results are lower than the experimental at later times. Predicted results for Point P3 match the experimental. Predicted evolution of relative humidity at Points P1, P2 and P3 on Section C (Table 2-8), which is located close to the concrete plug, are shown in Figure 2-24 together with experimental data. For Points P1 and P2 the predicted results are lower than the experimental. Predicted results for Point P3 are close to the experimental values. The discrepancies may be explained from careful investigation of the experimental data collection, location of observation points, and statistical analysis.

Table 2-7. Locations of points on Section H.

Segment	Origin (x, y, z)	Remarks
SHP1	(9.50, –0.52, 0.05)	Negative y-axis, near steel liner
SHP2	(9.50, -0.81, 0.05)	Negative y-axis, near middle of bentonite
SHP3	(950, -1.17, -0.16)	Negative y-axis, near granite

Table 2-8. Locations of points on Section C.

Segment	Origin (x, y, z)	Remarks
SCP1	(1.81, 0.0, 0.00)	Negative y-axis, near steel liner
SCP2	(1.81, -0.60, 0.07)	Negative y-axis, near middle of bentonite
SCP3	(1.81, -1.10, 0.07)	Negative y-axis, near granite

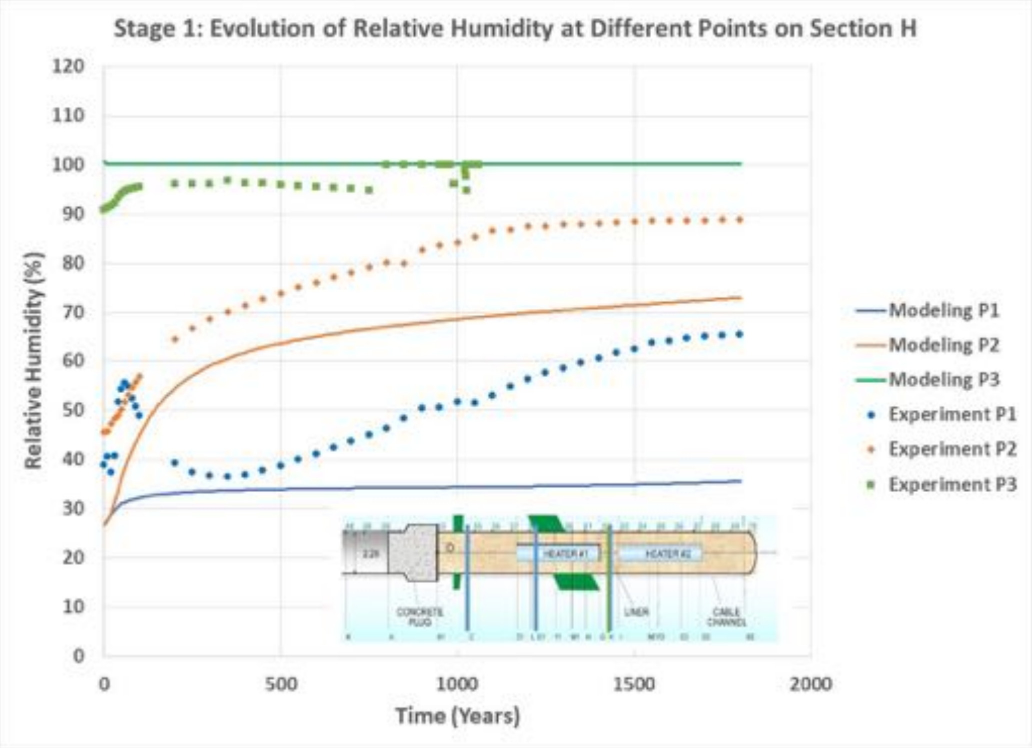

Figure 2-23. Stage 1: Predicted evolution of relative humidity at Points P1, P2 and P3 on Section H.

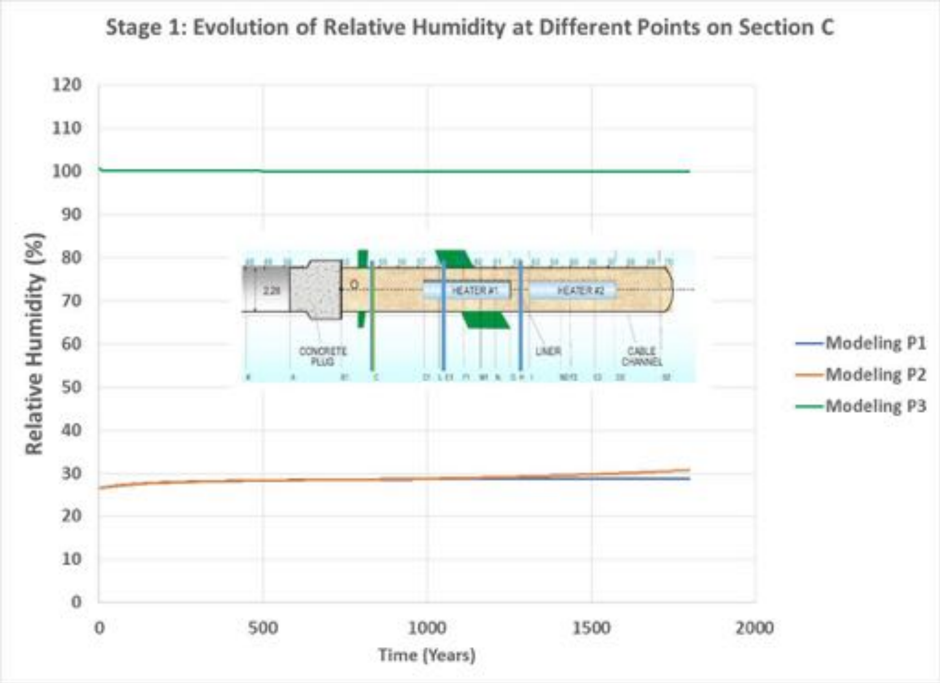

Figure 2-24. Stage 1: Predicted evolution of relative humidity at Points P1, P2 and P3 on Section C.

Figure 2-25 shows predicted distribution of relative humidity along radial segments on Section E1 at 90 days, 300 days and 1,800 days simulation times. For all specified times the results are close to experimental. Figure 2-26 shows predicted distribution of relative humidity along radial segments on Section H at 90 days, 300 days and 1,800 days simulation times. For all specified times the predicted results are lower than the experimental data. Figure 2-27 shows predicted distribution of relative humidity along radial segments on Section C at 90 days, 300 days and 1,800 days simulation times. For 90 days and 300 days results are close to experimental data. Results for 1,800 days are lower than experimental data. Some of the differences between simulation results and experimental data could be attributed to mislocation of observation points. Careful observation of the experimental method, location of observation points and sensitivity analysis may help.

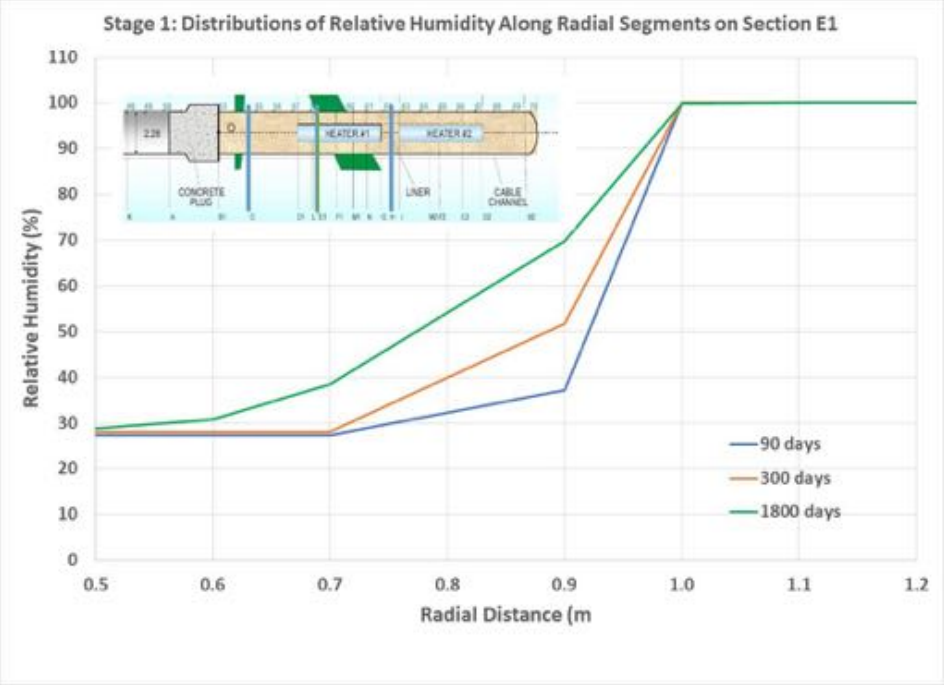

Figure 2-25. Stage 1: Predicted distribution of relative humidity along radial segments on Section E1 at different times.

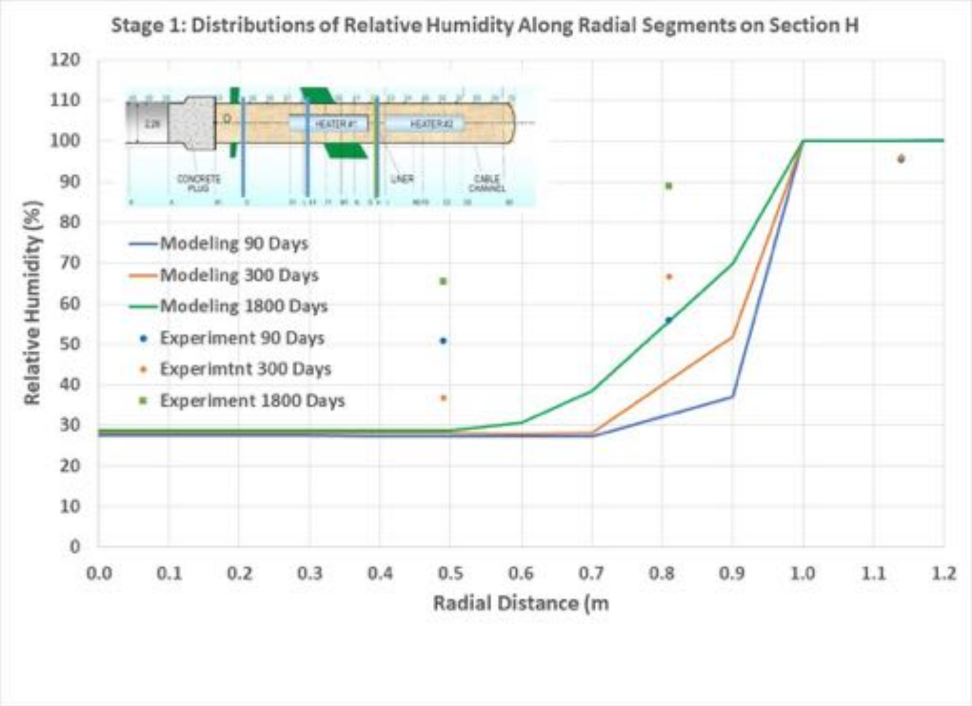

Figure 2-26. Stage 1: Predicted distribution of relative humidity along radial segments on Section H at different times.

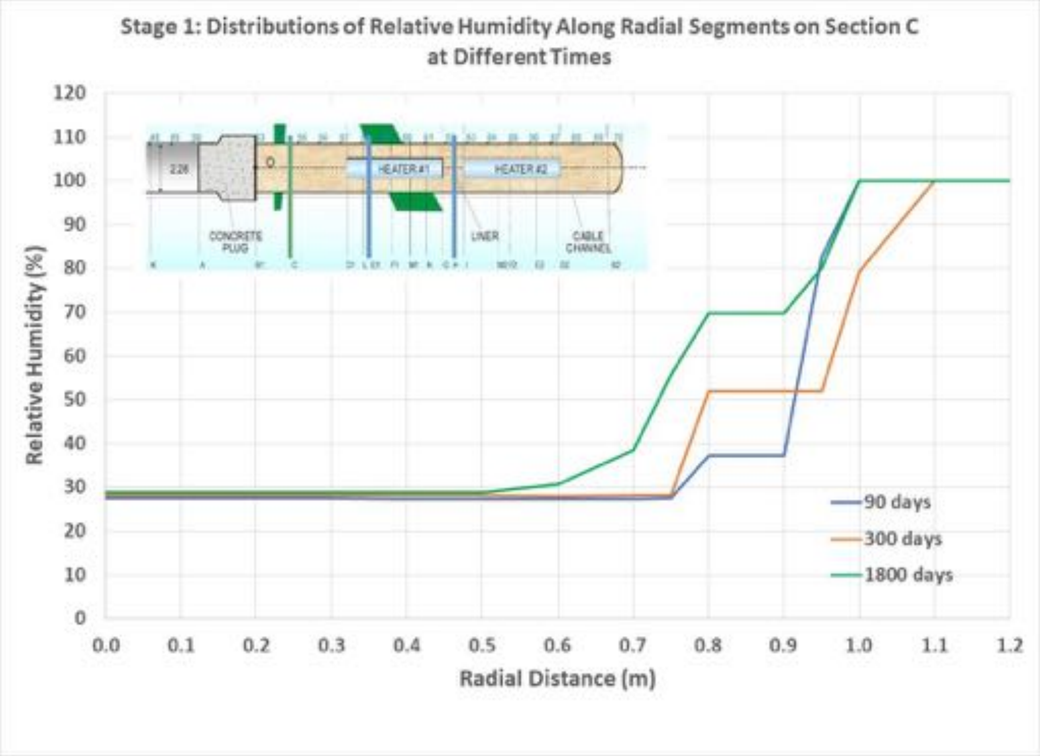

Figure 2-27. Stage 1: Predicted distribution of relative humidity along radial segments on Section C at different times.

2.5.1.4 Stage 1 Dismantling Results

Simulations were conducted for 141 days for the period after Heater 1 was shut off. Heat was applied at Heater 2 only. For TH simulations with PFLOTRAN bentonite swelling was not modeled. Thus, only liquid saturation results at specified locations are reported. Figure 2-28 shows locations of the three sections where results are provided (Sections 15, 27, and 31). These locations are close to Heater 1 and are described below.

Section 15: x = 3.27 m (between concrete plug and heater H1)

Table 2-9. Definition of the radial segments on dismantling Section 15.

Segment	Origin (x, y, z)	End (x, y, z)	Remarks
S15RS1	(3.27, 0.00, 0.00)	(3.27, 0.87, 0.73)	Angle with pos. y-axis = 40°
S15RS2	(3.27, 0.00, 0.00)	(3.27, –0.48, 1.03)	Angle with pos. y-axis = 115°
S15RS3	(3.27, 0.00, 0.00)	(3.27, 0.00, –1.13)	Angle with pos. y-axis = 270°

Section 27: x = 6.85 m (on heater H1)

Table 2-10. Definition of the radial segments on dismantling Section 27.

Segment	Origin (x, y, z)	End (x, y, z)	Remarks
S27RS1	(6.85, 0.37, 0.31)	(6.85, 0.87, 0.73)	Angle with pos. y-axis = 40°
S27RS2	(6.85, –0.17, 0.46)	(6.85, –0.39, 1.07)	Angle with pos. y-axis = 110°
S27RS3	(6.85, 0.00, –0.49)	(6.85, 0.00, 1.13)	Angle with pos. y-axis = 270°

Section 31: x = 7.74 m (on heater H1)

Table 2-11. Definition of the radial segments on dismantling Section 31.

Segment	Origin (x, y, z)	End (x, y, z)	Remarks
S31RS1	(7.74, 0.47, –0.17)	(7.74, 1.10, –0.29)	Angle with pos. y-axis = –15°
S31RS2	(7.74, –0.17, 0.46)	(7.74, –0.39, 1.07)	Angle with pos. y-axis = 110°
S31RS3	(7.74, –0.32, –0.37)	(7.74, –0.73, –0.87)	Angle with pos. y-axis = 270°

Figure 2-29 shows prediction of distributions of liquid saturation along radial segments on Section 15 along with experimental data. Section 15 is in the buffer between the original concrete plug and Heater 1. The predicted results are slightly lower at lower radial distances while better matching with experimental data is observed for the rest of the radial distances. Figure 2-30 and Figure 2-31 show results at Sections 27 and 31. Both the sections are close to Heater 1. For both locations excellent matching of predicted and experimental data was obtained.

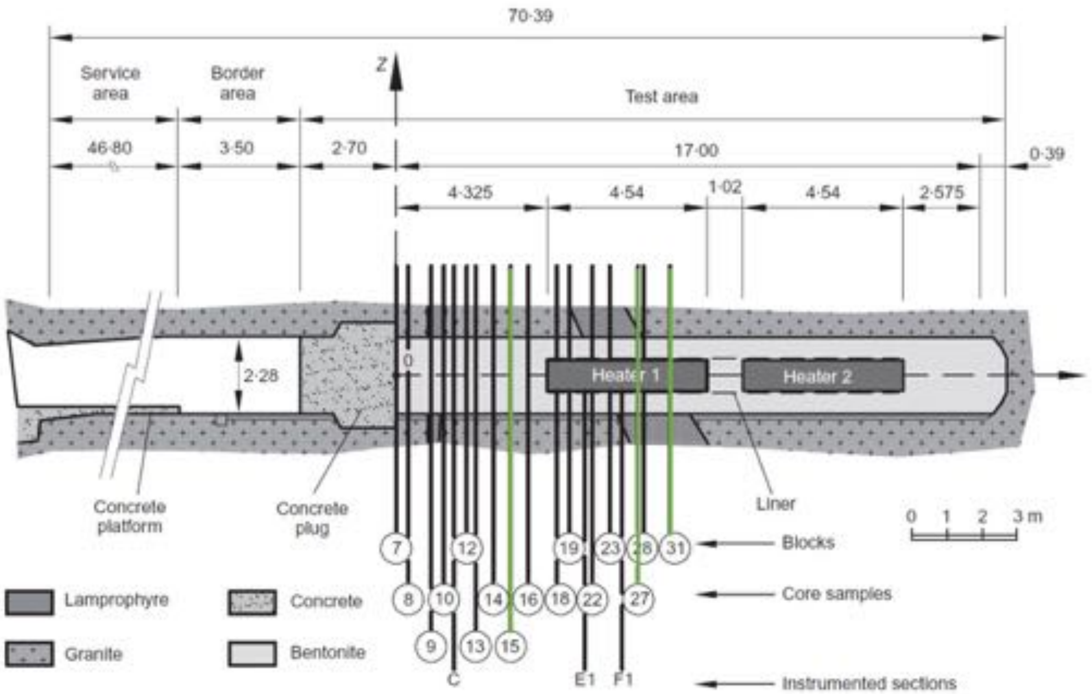

Figure 2-28. Stage 1: Locations of three dismantling sections for requested results for distributions of liquid saturation after dismantling (Sections 15, 27 and 31 are shown in green).

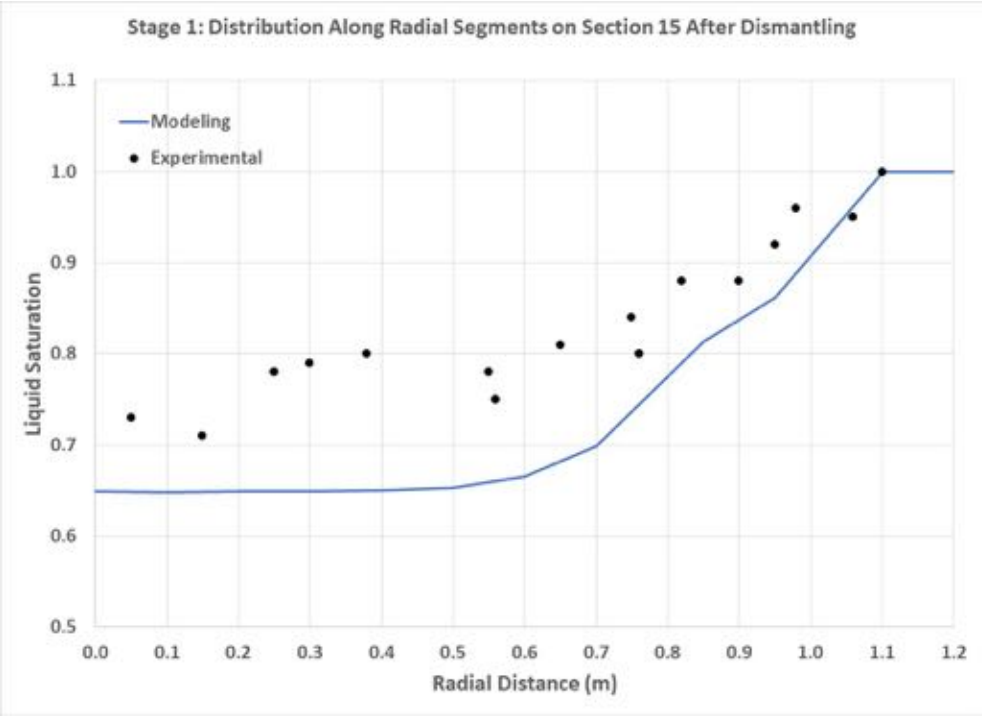

Figure 2-29. Stage 1: Predicted distribution of liquid saturation along radial segments on Section 15 after dismantling.

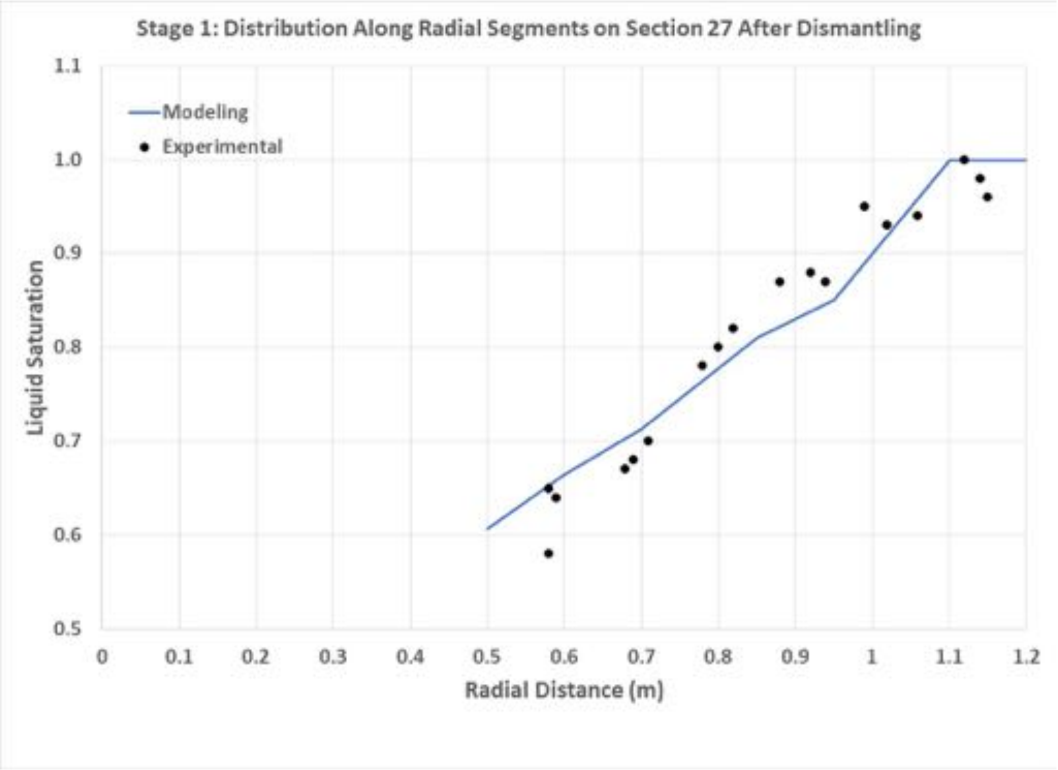

Figure 2-30. Stage 1: Predicted distribution of liquid saturation along radial segments on Section 27 after dismantling.

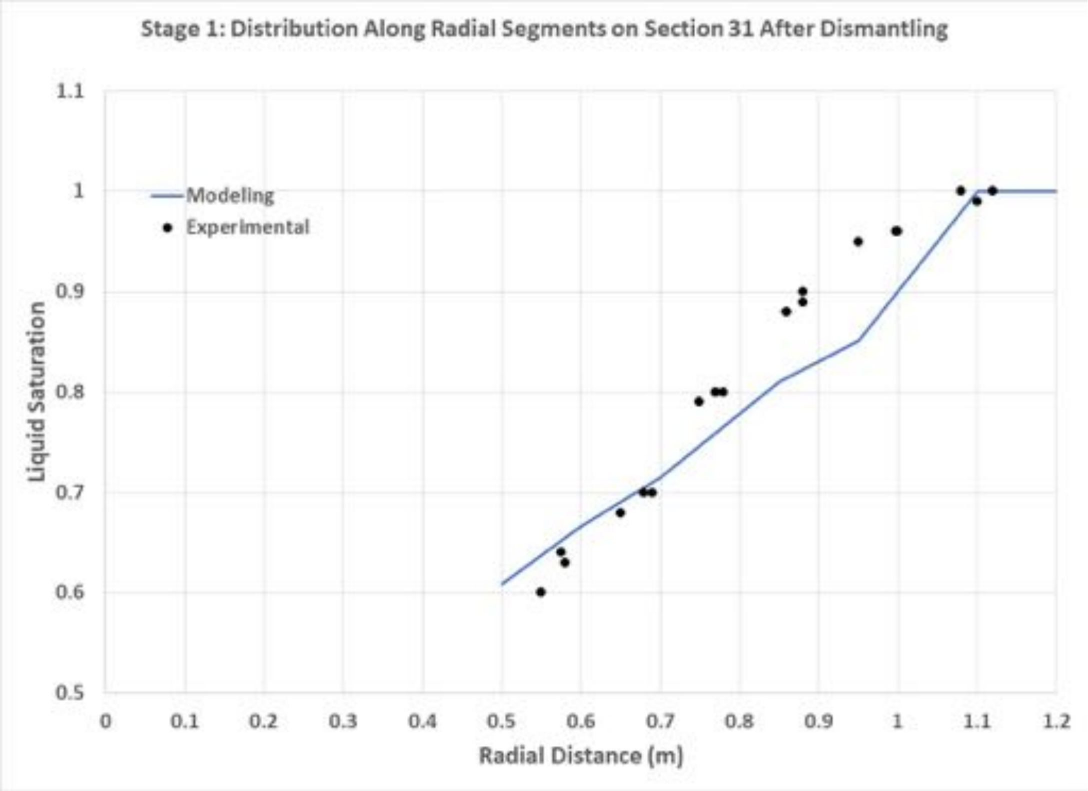

Figure 2-31. Stage 1: Predicted distribution of liquid saturation along radial segments on Section 31 after dismantling.

2.5.2 Stage 2: Analysis of Results

2.5.2.1 Evolution of Heating Power

For Stage 2 simulations, power was kept at 2,200 W between the first dismantling and the final dismantling to maintain 100°C at Heater 2. Figure 2-32 shows comparison of the measured and simulated results for heating power. As in the Stage 1 simulations the predicted power for Heater 2 is underpredicted. Future work in the form of a statistical analysis could provide the main factors that control the predicted heating power.

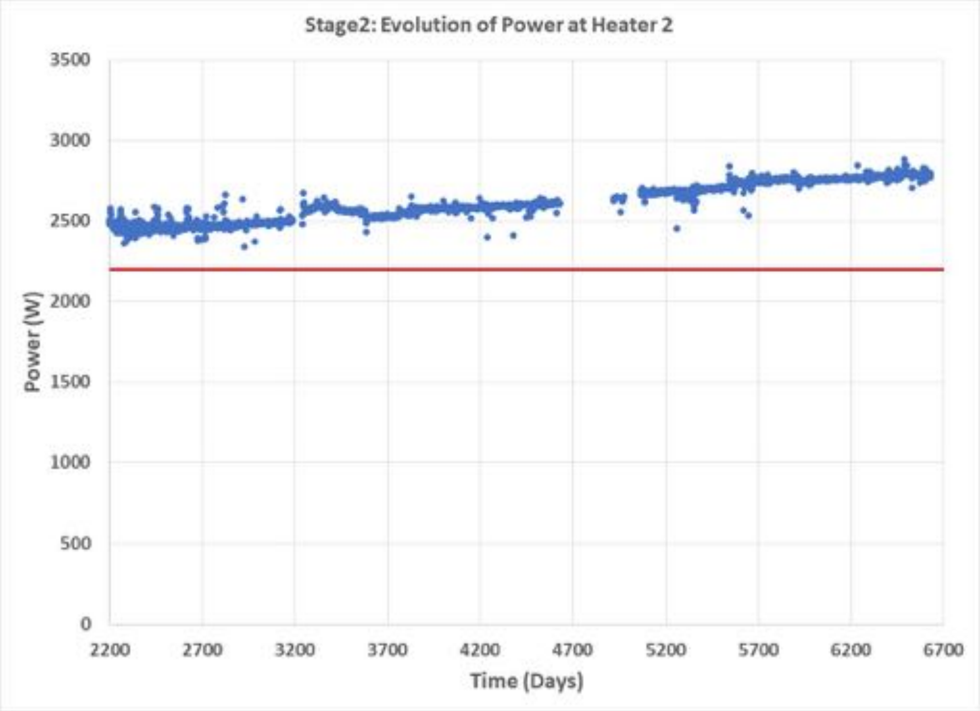

Figure 2-32. Predicted evolution of power at Heater 2 for Stage 2.

2.5.2.2 Prediction of Temperature

Prediction of distribution of temperature along radial segments on Section D2 at 5,600 days simulation time is shown in Figure 2-33, along with experimental data. The predicted temperatures are very close to the measured. Predictions of distribution of temperature along axial segment AS1 are shown in Figure 2-34 at 5,600 days along with experimental data. The predictions are very close to the experimental data. Differences at lower axial distances could be due to discrepancies in the location of observation points.

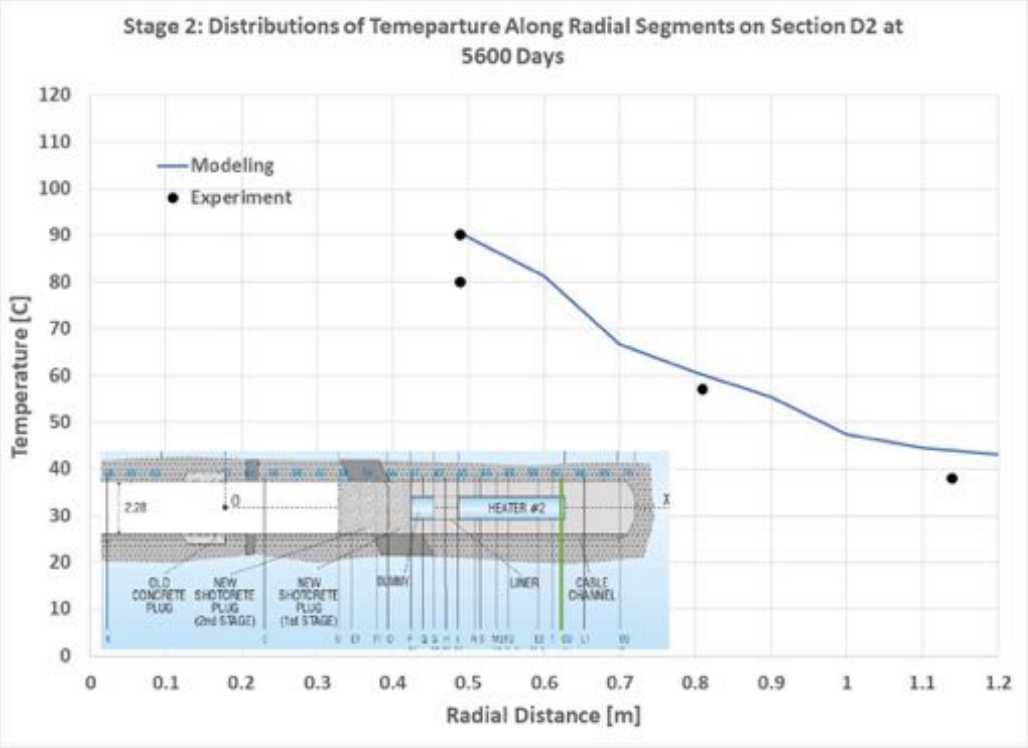

Figure 2-33. Stage 2: Predicted distributions of temperature along radial segments on Section D2 at 5,600 days simulation time.

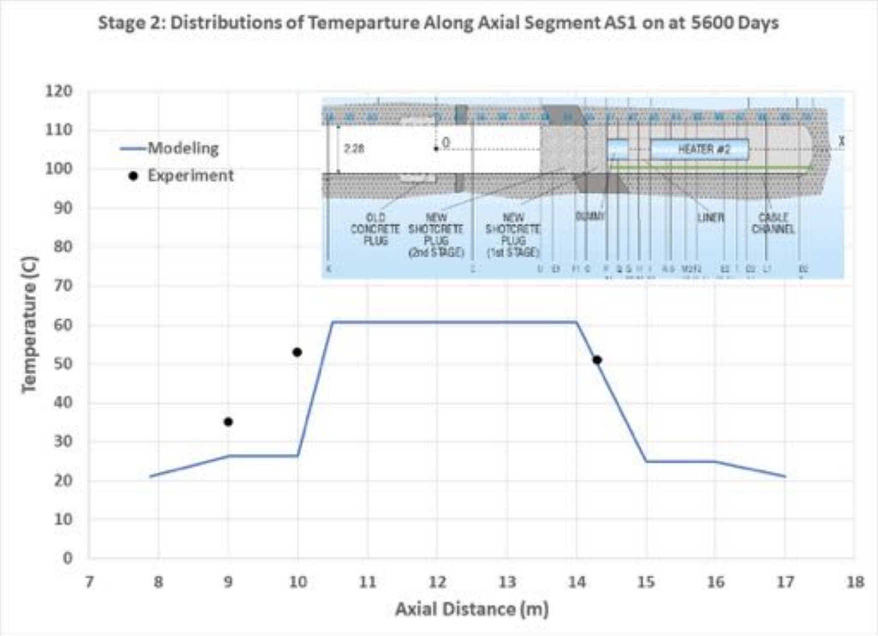

Figure 2-34. Stage 2: Predicted distributions of temperature along axial segment AS1 at 5,600 days simulation time.

Predicted evolution of temperature at Point P1 on Section D2 is shown in Figure 2-35 along with experimental data. Point P1 is away from Heater 1, close to the wall. Thus, temperatures are lower. Predicted temperatures are slightly higher but close to experimental data.

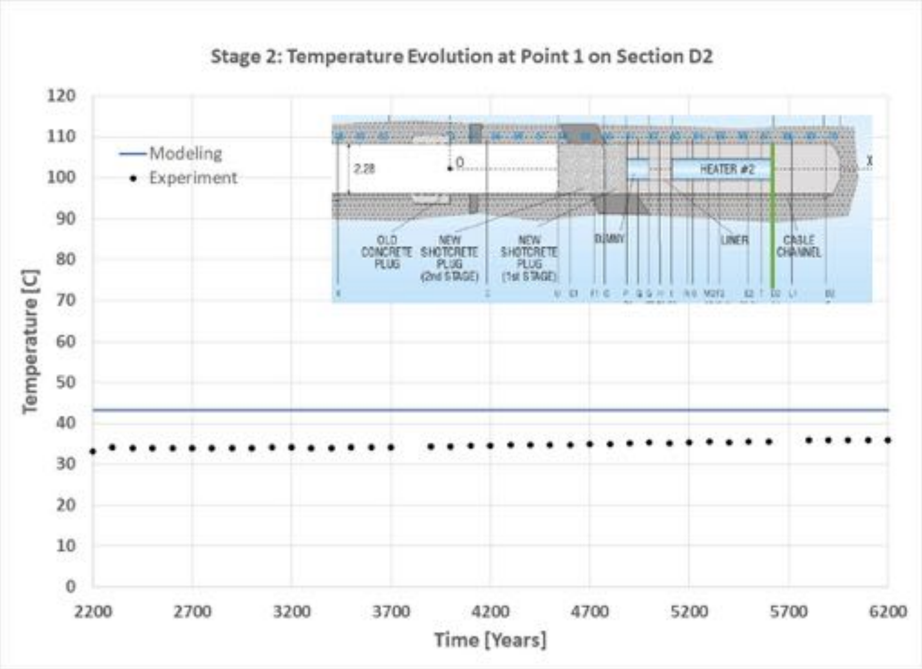

Figure 2-35. Stage 2: Predicted evolution of temperature at Point P1 on Section D2.

2.5.2.3 Prediction of Relative Humidity

Predicted evolution of relative humidity at Points P3 and P5 on Section F2 (Table 2-12) are shown in Figure 2-36. The simulation results for P3 and P5 are similar. The predicted relative humidity for P3 is very close to the experimental. The predicted relative humidity for P5 is lower that the experimental. Further study will be needed to account for the difference.

Table 2-12. Locations of points on Section F2 (near the middle of Heater 2).

Segment	Origin (x, y, z)	Remarks
SF2P3	(12.30, -0.27, -0.52)	Near Heater 2
SF2P5	(12.30, 0.53, 0.24)	Near Heater 2

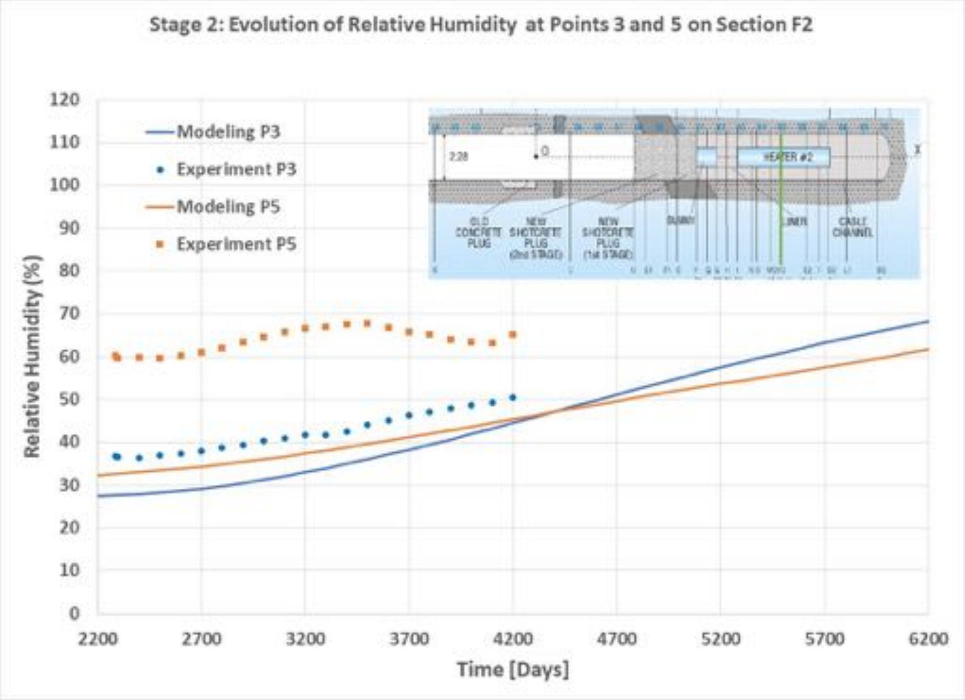

Figure 2-36. Stage 2: Predicted evolution of relative humidity at Points P3 and P5 on Section F2

2.5.2.4 *Stage 2 Dismantling Results*

Simulations were conducted for 128 days for the period after Heater 2 was shut off with no heat applied. For TH simulations with PFLOTRAN bentonite swelling was not modeled. Thus, only liquid saturation results at specified locations are reported. Figure 2-37 shows locations of the four sections where results are provided (Sections 43, 49, 56 and 61). These locations are close to Heater 2 and are described below.

Section 43: x = 10.12 m (on heater H2, near its end closest to concrete plug)

Table 2-13. Definition of the radial segments on dismantling Section 43.

Segment	Origin (x, y, z)	End (x, y, z)	Remarks
S43RS1	(10.12, 0.00, 0.49)	(10.12, 0.00, 1.14)	Angle with pos. y-axis = 90°
S43RS2	(10.12, –0.37, –0.31)	(10.12, –0.87, –0.73)	Angle with pos. y-axis = 220°
S43RS3	(10.12, 0.42, –0.24)	(10.12, 0.98, –0.57)	Angle with pos. y-axis = 330°

Section 49: x = 12.27 m (on heater H2, near its center)

Table 2-14. Definition of the radial segments on dismantling Section 49.

Segment	Origin (x, y, z)	End (x, y, z)	Remarks
S49RS1	(12.27, 0.42, 0.24)	(12.27, 0.98, 0.57)	Angle with pos. y-axis = 30°
S49RS2	(12.27, –0.42, 0.24)	(12.27, –0.98, 0.57)	Angle with pos. y-axis = 150°
S49RS3	(12.27, 0.00, –0.49)	(12.27, 0.00, –1.14)	Angle with pos. y-axis = 270°

Section 56: x = 14.56 m (on bentonite buffer, near end of heater H2 closest to tunnel end)

Table 2-15. Definition of the radial segments on dismantling Section 56.

Segment	Origin (x, y, z)	End (x, y, z)	Remarks
S56RS1	(14.56, 0.00, 0.00)	(14.56, 0.98, 0.57)	Angle with pos. y-axis = 30°
S56RS2	(14.56, 0.00, 0.00)	(14.56, –1.03, 0.48)	Angle with pos. y-axis = 155°
S56RS3	(14.46, 0.00, 0.00)	(14.56, 0.00, –1.14)	Angle with pos. y-axis = 270°

Section 61: x = 16.87 m (on bentonite buffer, near to tunnel end)

Table 2-16. Definition of the radial segments on dismantling Section 61.

Segment	Origin (x, y, z)	End (x, y, z)	Remarks
S61RS1	(16.87, 0.00, 0.00)	(16.87, 0.00, 1.14)	Angle with pos. y-axis = 90°
S61RS2	(16.87, 0.00, 0.00)	(16.87, –0.93, –0.65)	Angle with pos. y-axis = 215°
S61RS3	(16.87, 0.00, 0.00)	(16.87, 0.98, –0.57)	Angle with pos. y-axis = 330°

Figure 2-38 shows prediction of distributions of liquid saturation along radial segments on Section 43 along with experimental data. Section 43 is located near Heater 2 but close to the dummy heater. The predicted results are lower than the experimental. Figure 2-39 shows results for Section 49, which is also close to the middle of Heater 2. The predicted results are better for this location. Figure 2-40 are the results for Section 56, which is in the buffer close to the end of Heater 2. The predicted results for this section are close to the experimental data. Results for Section 61 are shown in Figure 2-41. Section 61 is close to the wall. For this location excellent matching of predicted results and experimental data was obtained.

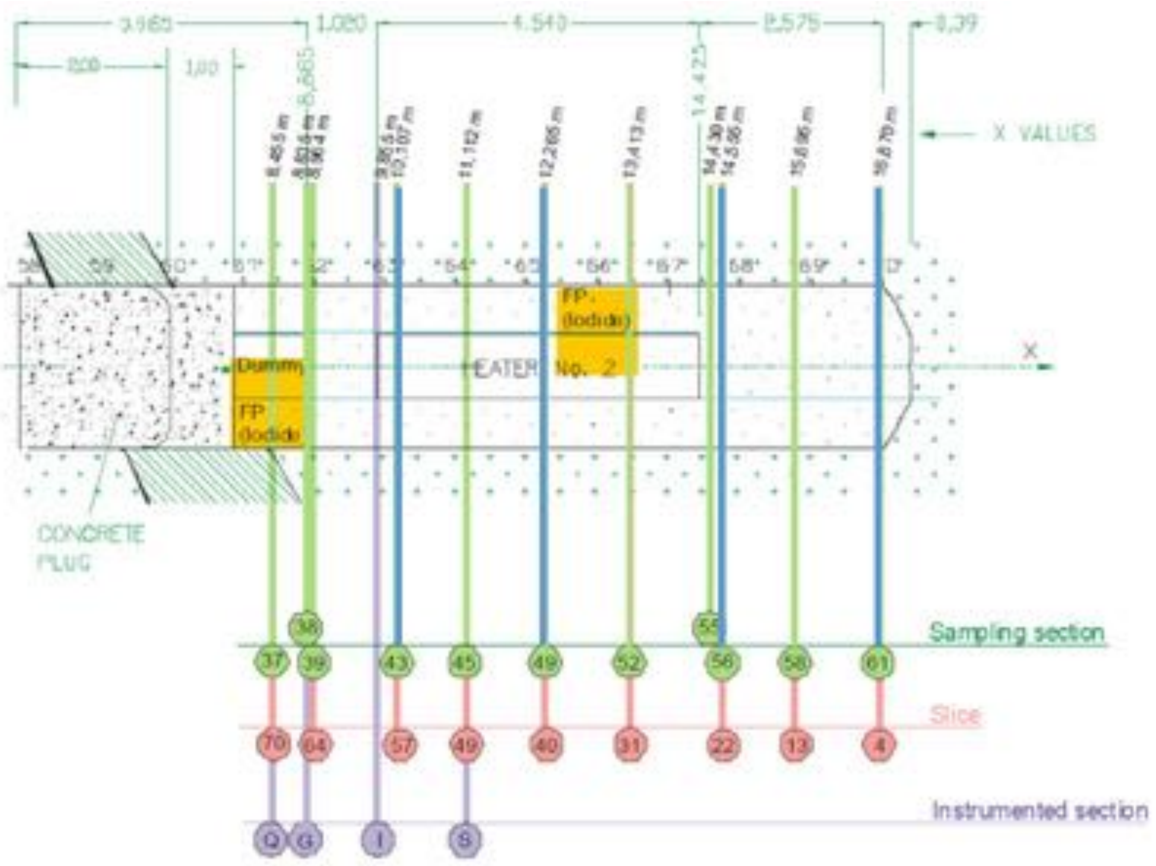

Figure 2-37. Stage 2: Locations of four dismantling sections for requested results for distributions of liquid saturation after final dismantling (Sections 43, 49, 56 and 61 are shown in blue).

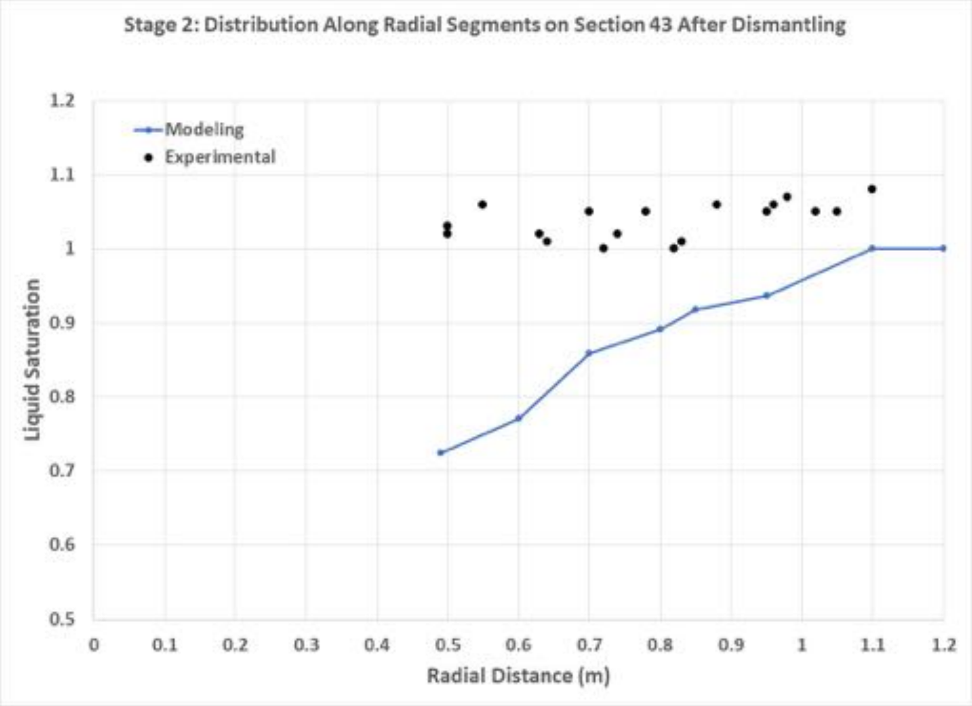

Figure 2-38. Stage 2: Predicted distribution of liquid saturation along radial segments on Section 43 after final dismantling.

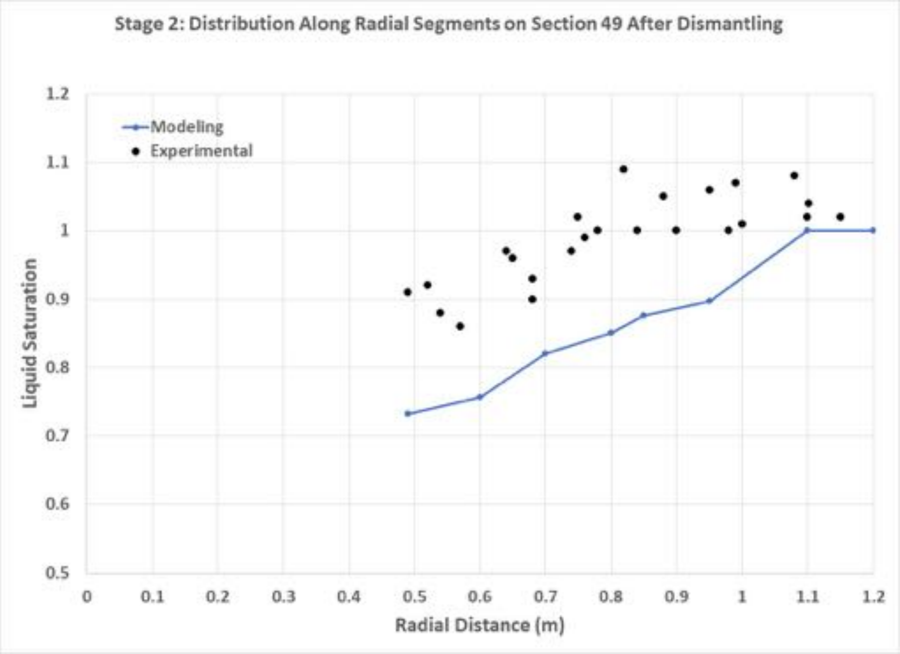

Figure 2-39. Stage 2: Predicted distribution of liquid saturation along radial segments on Section 49 after final dismantling.

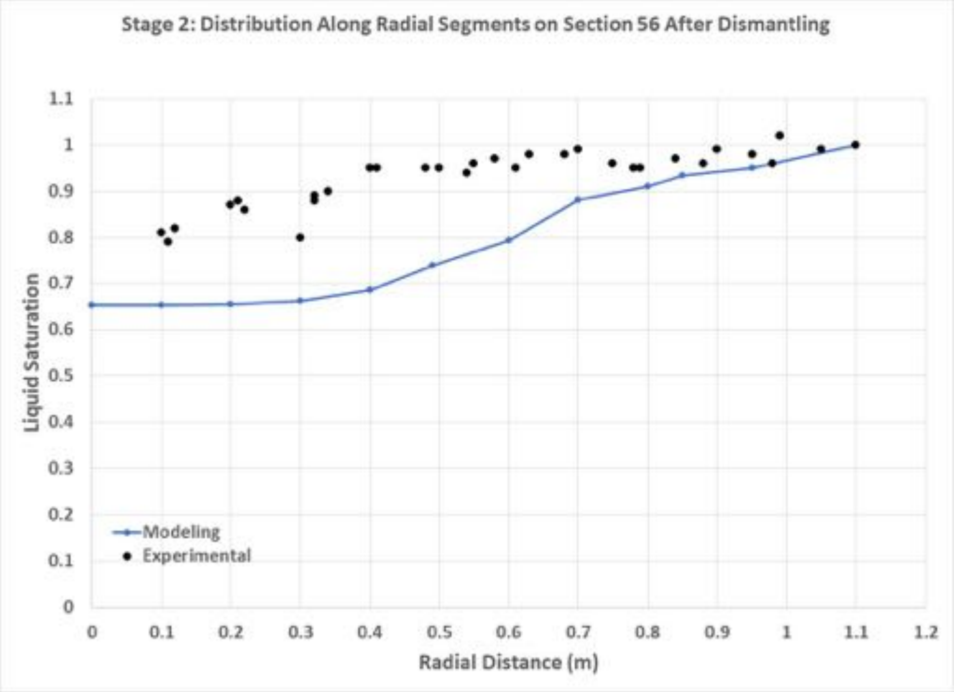

Figure 2-40. Stage 2: predicted distribution of liquid saturation along radial segments on Section 56 after final dismantling.

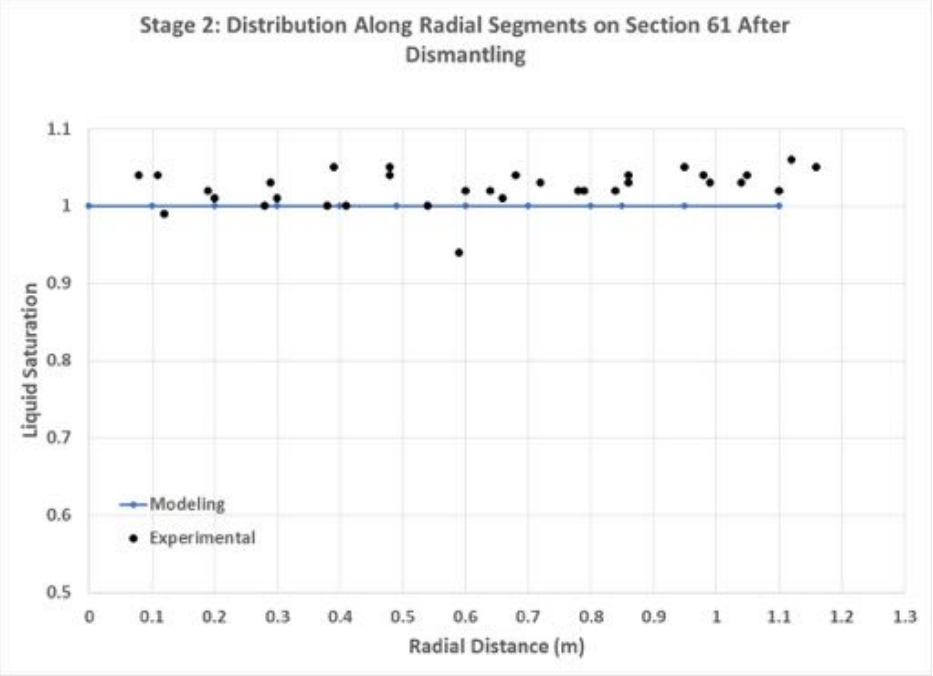

Figure 2-41. Stage 2: predicted distribution of liquid saturation along radial segments on Section 61 after final dismantling.

2.6 Conclusions

TH modeling of the Stage 1 and Stage 2 FEBEX in-situ experiment using the massively parallel reactive transport code PFLOTRAN was accomplished using HPC facilities at Sandia National Laboratories. Being TH modeling only, we neglected shrink/swell aspects and other structural deformational aspects of the bentonite barrier. Nonetheless the simulation results show good agreement with some FEBEX measurements, while some disagreement with others. In general, the modeling results show:

- Good agreement with temperature measurements near Heater 1, while slightly underpredicting temperatures measured near Heater 2 for Stage 1.
- Good agreement with measured liquid saturations after the first dismantling.
- Good agreement with measured temperatures during Stage 2 (Heater 2).
- Underprediction of liquid saturations at the end of Stage 2.

In general, the modeling under-calculated humidity measurements, which may have been a consequence of the spatially constant initial conditions for bentonite wetting assumed in the modeling.

3. PRELIMINARY SENSITIVITY ANALYSIS FOR THE FEBEX IN-SITU HEATER TEST

3.1 Introduction

This section describes additional preliminary modeling work on sensitivity and uncertainty analysis applied to Stage 1 of the Full-scale Engineered Barriers Experiment in Crystalline Host Rock (FEBEX) in-situ test for the EBS Task Force, Task 9. It complements the detailed 3D TH simulations conducted by the Sandia team (Hadgu et al., 2020). This analysis is designed to determine parameters that are important to define the TH condition in the bentonite buffer and the host rock. To allow multiple simulations for sensitivity analysis, a 2D model with reduced mesh size was used. This is in line with most of the previous modeling studies on the FEBEX experiment.

The FEBEX test was a full-scale test conducted over ~18 years at the Grimsel, Switzerland Underground Research Laboratory (URL) managed by NAGRA. It involved emplacing simulated waste packages, in the form of welded cylindrical heaters, inside a tunnel in crystalline rock and surrounded by a bentonite barrier. A multitude of sensors emplaced within the bentonite monitored the wetting-up, heating, and drying out of the bentonite barrier, and allow for validation of multiphysics TH, THC, and THM modeling approaches. Stage 1 of the in-situ test involved operation of two heaters for a period of 5 years, until dismantling of one of the heaters. Further description of the experiment and previous modeling effort can be found in Huertas et al. (2000), Bárcena et al. (2003), Gens et al. (2009) among others.

Figure 3-1 shows schematic diagram of the FEBEX experimental setup which includes specifications of components.

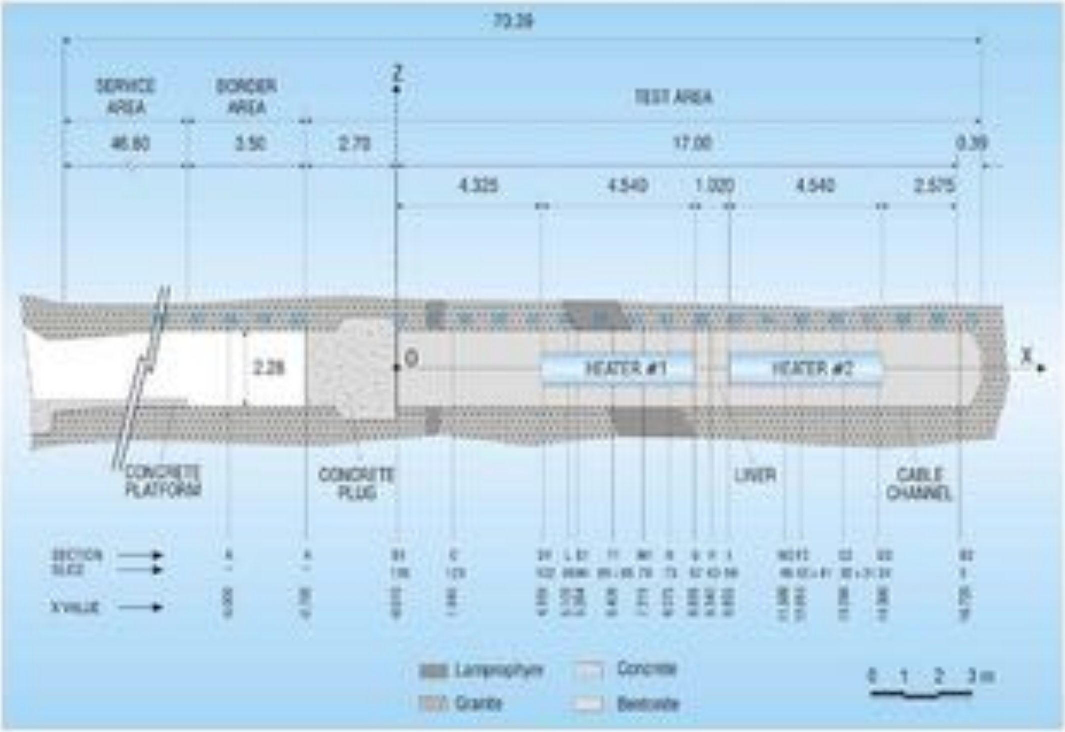

Source: Bárcena et al., 2003.

Figure 3-1. General layout of the FEBEX in-situ test for Stage 1.

3.2 Thermal-Hydrologic 2D Modeling of Stage 1 FEBEX In-situ Test

TH modeling was conducted for Task 9, Stage 1 FEBEX in-situ test, up to first dismantlement (5 years). A 2D modeling domain was developed based on project specifications (Figure 3-1) with domain size 206.09 m × 94.54 m in the x and y directions, respectively. To reduce mesh size an axisymmetric boundary condition was applied (Figure 3-2).

For TH simulations using PFLOTRAN numerical code the domain was discretized using an unstructured grid with fine discretization around the heaters and the buffer (Figure 3-3). The mesh size for Stage 1 is 3,780 grid blocks. The simulation domain includes details of various regions representing different materials including granite, DRZ, bentonite buffer, heaters and concrete plug. For this report, the DRZ was assumed to have the same properties as the granite domain.

3.2.1 TH Model Setup

For the TH simulations similar setup as in Hadgu et al. (2020) was used. The system was assumed to be at 12°C at the start of the simulation. When the bentonite buffer is emplaced in the test area, a pressure of one atmosphere and a liquid saturation of 0.36 were applied. At the beginning of the heating phase the bentonite is assumed to be at a higher liquid saturation of 0.6 due to hydration from the formation. For the 2D simulation the far field was assigned a pressure of 0.7 MPa. Based on the project specification, a 1,200 W heat was applied at the two heaters for the first 20 days of simulation time. The power was raised to 2,000 W per heater between Day 20 and Day 60. For the rest of the simulation time in Stage 1, time varying heat was applied at the two heaters to maintain a temperature of 100°C.

Material properties of main components selected for modeling are specified in Table 3-1. Retention curve parameters are given in Table 3-2. The original van Genuchten retention curves were used. Molecular diffusion of vapor in free air of 2.0×10^{-5} m^2/s and diffusion coefficient in liquid of 2.0×10^{-9} m^2/s were used.

Table 3-1. Material properties used in the 2D TH simulations

Property	Units	Granite	Buffer	Concrete Plug
Permeability	m^2	2.5×10^{-18}	3.2×10^{-20}	1.0×10^{-22}
Porosity	—	0.01	0.375	0.01
density	Kg/m^3	2750	1600	2,600
Thermal Conductivity dry/wet	W/(m·K)	3.2/3.3	0.6/1.3	3.0/3.0
Specific Heat	J/(kg·K)	793	1,091	1,000.0

Table 3-2. Retention curve parameters used in the 2D TH simulations

Parameter	Units	Granite	Buffer	Concrete Plug
P_0	MPa	0.0021	20.0	0.0021
λ	—	0.7	0.2	0.7
S_{lr}	—	0.0	0.1	0.01
S_{gr}	—	0.0	0.1	0.01
S_{ls}	—	1.0	1.0	1.0

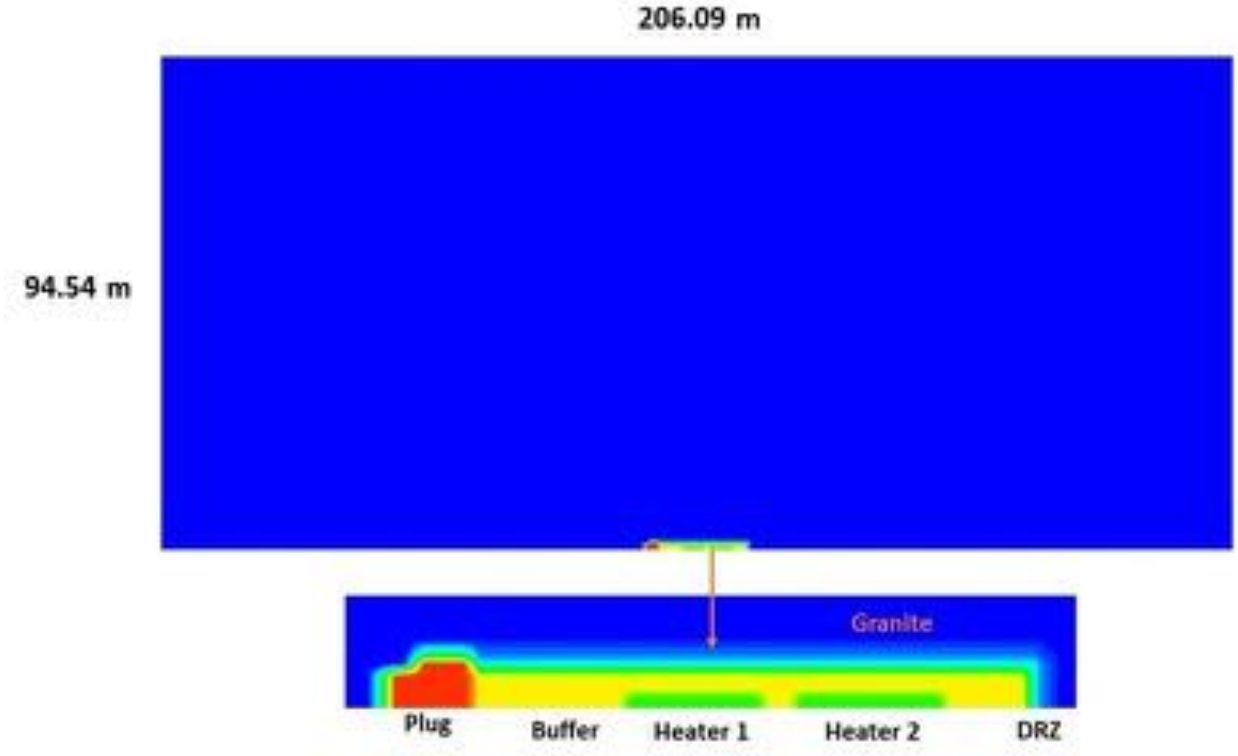

Figure 3-2. Schematic representation of the 2D modeling axisymmetric domain used for Stage 1.

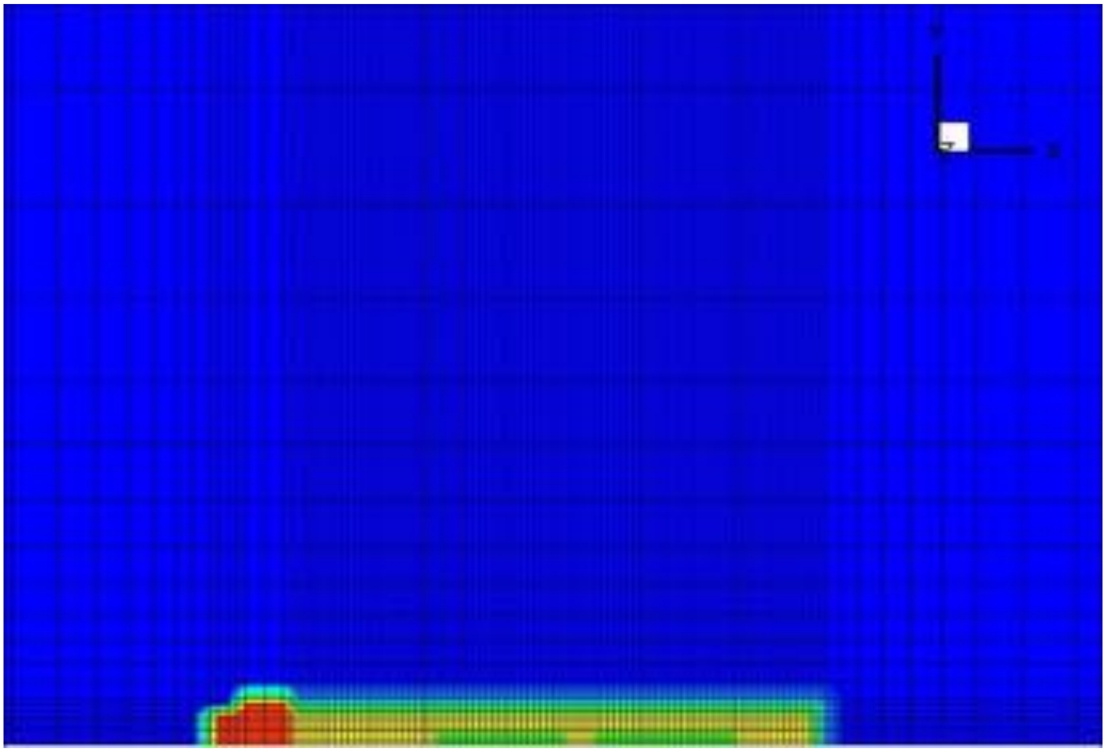

Figure 3-3. 2D modeling axisymmetric meshing for Stage 1.

3.2.2 Modeling Results of 2D TH Simulations

TH simulations were made using PFLOTRAN to match experimental data. For Stage 1, simulations were run for a total of 1,800 days with both heaters operating and using parameter values described in Table 3-1 and Table 3-2. Simulation results and comparison with experimental data are described below.

At initial time the buffer is at a liquid saturation of 0.60 and gas pressure of one atmosphere. The far-field is at saturated conditions.

TH modeling results at the end of Stage 1 are shown in Figure 3-4 and Figure 3-5. Figure 3-4 shows temperature distribution at the end of the simulation time of 1,800 days. The applied heat at Heater 1 and Heater 2 results in transport of heat into the buffer and the host rock. The temperature distribution evolves during the 5 years heating period in Stage 1. Figure 3-5 shows the corresponding liquid saturation distribution, which is largely confined to the bentonite buffer, with slight drying out on the edges of the rock. The saturation distribution evolves at different periods during Stage 1.

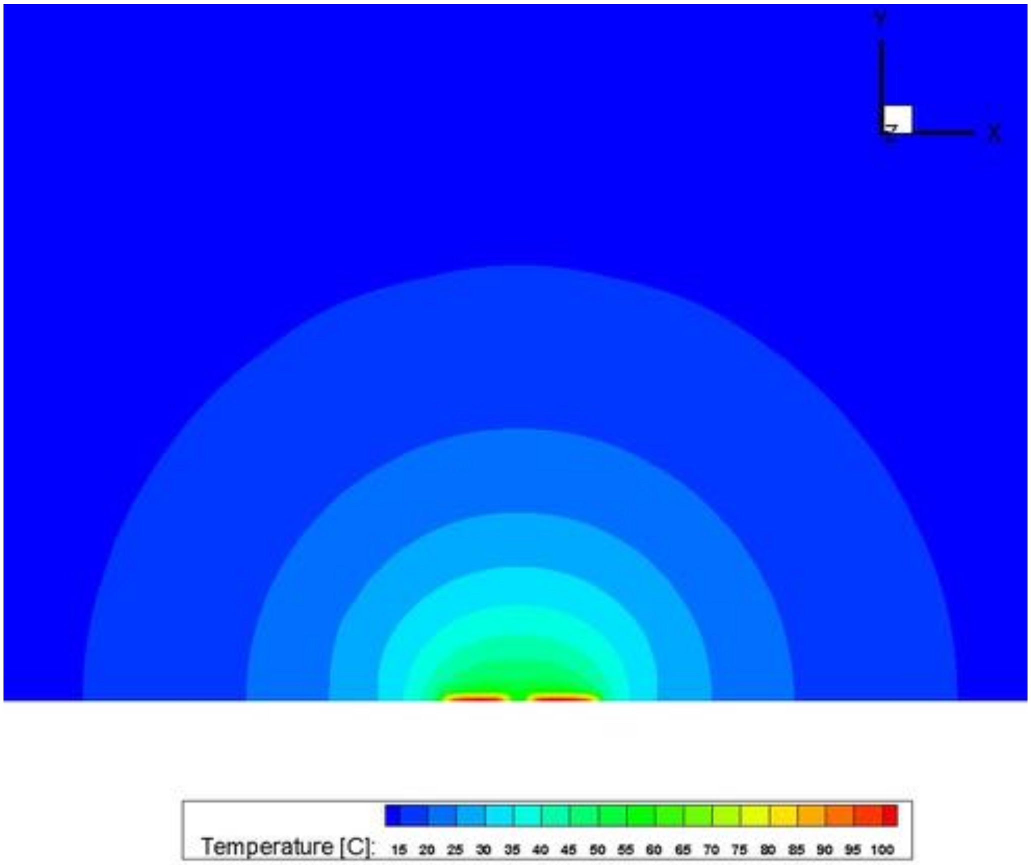

Figure 3-4. Simulated temperature distribution at 1,800 days simulation time.

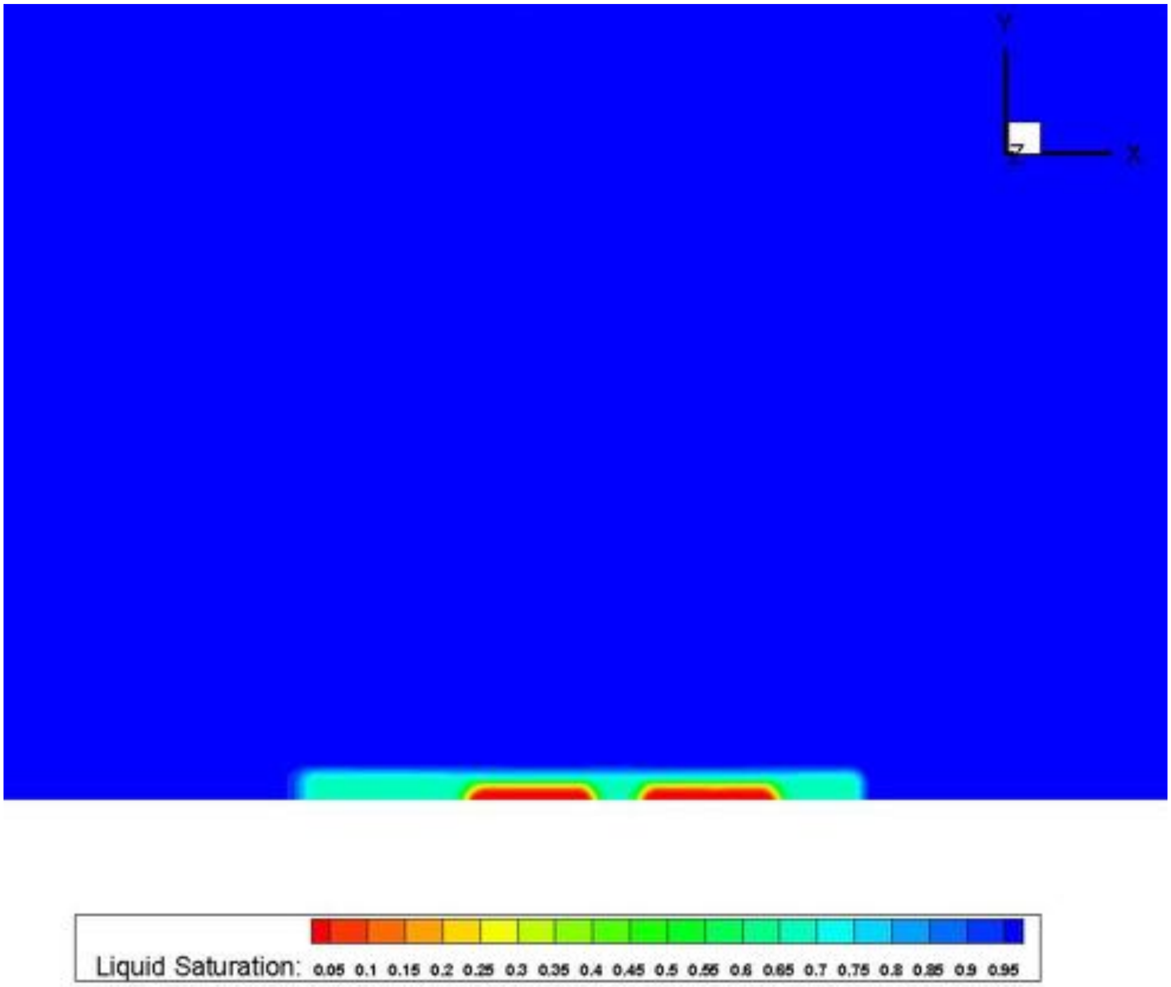

Figure 3-5. Simulated liquid saturation distribution at 1,800 days simulation time.

For Stage 1 simulations to maintain 100°C at the heaters the power applied to both heaters would need to be varied. For this analysis the heating power at both heaters was kept constant at 2,000 W to simplify the simulations. Figure 3-6 shows comparison of the measured and simulated results for temperature at Heater 1. The predicted heater temperature is close to the experimental values at later time but is lower than experimental values at early times.

Locations of points P1, P2 and P3 on Section E1 are shown in Table 3-3. Figure 3-7 shows a schematic diagram of the experimental setup with location of Section E1 indicated. Predicted evolution of relative humidity at Points P1, P2 and P3 on Section E1 are shown in Figure 3-8. For Point 1 predicted and experimental results are equivalent. At Point P2 the predicted values are lower than the experimental at early times but are closer at later times. The predicted results at Point P3 match the experimental data.

Table 3-3. Locations of points on Section E1

Segment	Origin (x, y, z)	Remarks
P1	(5.53, −0.52, 0.00)	Negative y-axis, near steel liner
P2	(5.53, −0.81, 0.07)	Negative y-axis, near middle of bentonite
P3	(5.53, −1.10, −0.17)	Negative y-axis, near granite

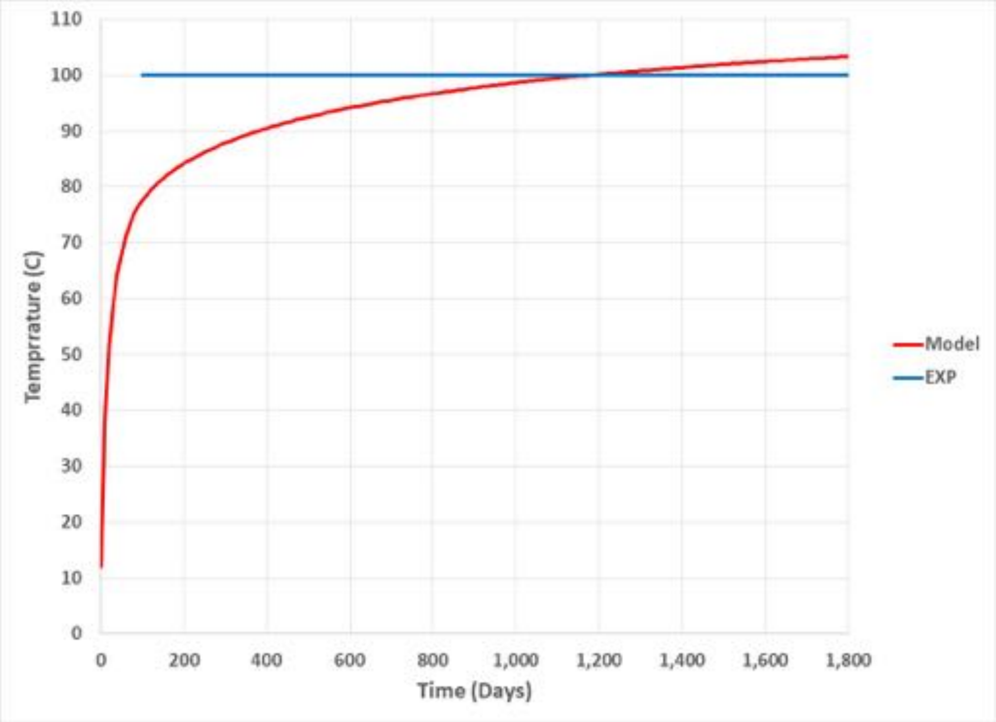

Figure 3-6. Simulated temperature evolution at Heater 1 together with experimental data.

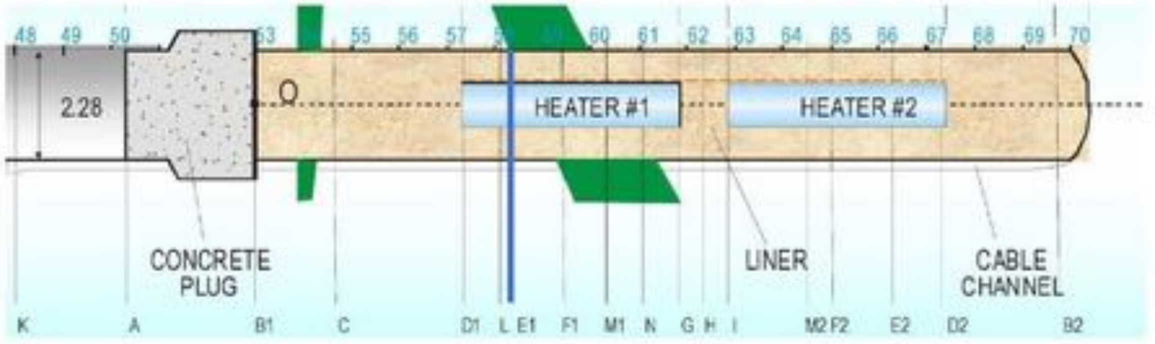

Source: Huertas et al., 2000.

Figure 3-7. Schematic diagram with locations of Heater 1 and Section E1.

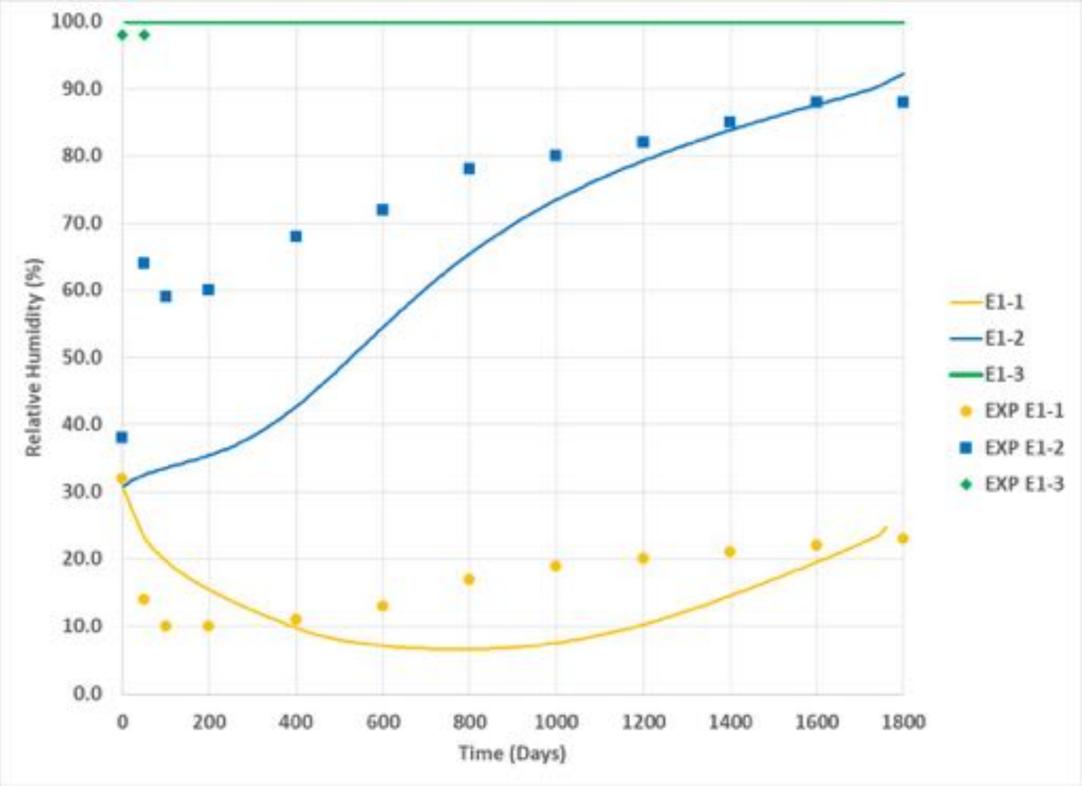

Figure 3-8. Prediction of evolution of relative humidity at Points P1, P2 and P3 on Section E1 together with experimental data.

3.3 Preliminary Statistical Analysis and Uncertainty Quantification for Stage 1 Simulations

Preliminary sensitivity analysis and uncertainty quantification was conducted by wrapping PFLOTRAN with an uncertainty quantification and optimization code (DAKOTA) as shown in Figure 3-9. The analysis follows the work of Wang et al. (2010) on the use of coupled DAKOTA-TOUGH2 (TOUGH refers to “Transport of Unsaturated Groundwater and Heat”) for the analysis of carbon sequestration.

The PFLOTRAN numerical code is an open source, state-of-the-art, massively parallel subsurface flow and reactive transport code operating in a high-performance computing environment (Hammond et al., 2014).

DAKOTA (Design Analysis Kit for Optimization and Terascale Applications) is a software toolkit that provides a flexible and extensible interface between simulation codes and iterative analysis methods used in large-scale systems engineering optimization, uncertainty quantification, and sensitivity analysis (Adams et al., 2019). The DAKOTA toolkit can perform parameter optimization through the use of gradient and nongradient-based methods. It can also be used to conduct sensitivity analysis with the purpose of investigating variability in response to variations in model parameters using sampling methods such as Latin Hypercube Sampling (LHS), among others. Further capabilities of the toolkit include uncertainty quantification with sampling, analytic reliability, and stochastic finite element methods; and parameter estimation with nonlinear least squares methods. These capabilities may be used on their own or as components within system models. By employing object-oriented design to implement abstractions of the key components required for iterative systems analyses, the DAKOTA toolkit provides a flexible and extensible problem-solving environment for design and performance analysis of computational models on high performance computers. For this analysis, DAKOTA version 6.12 was utilized.

For the analysis a DAKOTA based nondeterministic sampling algorithm is implemented for the FEBEX modeling task, similar to what was done in Wang et al. (2010). The overall sampling flow involves embedded PFLOTRAN functional evaluations within a DAKOTA run. First, a set of uncertain parameters with assigned probability distributions is specified in the DAKOTA input parameter file. A sample is drawn using LHS. The sample is processed by an input filter routine to transcribe each sample element, comprising a value for each uncertain parameter, into a formatted template file that is compatible with PFLOTRAN. After each sample element is executed, an output filter extracts the pertinent output values via an output filter routine and returns these to DAKOTA

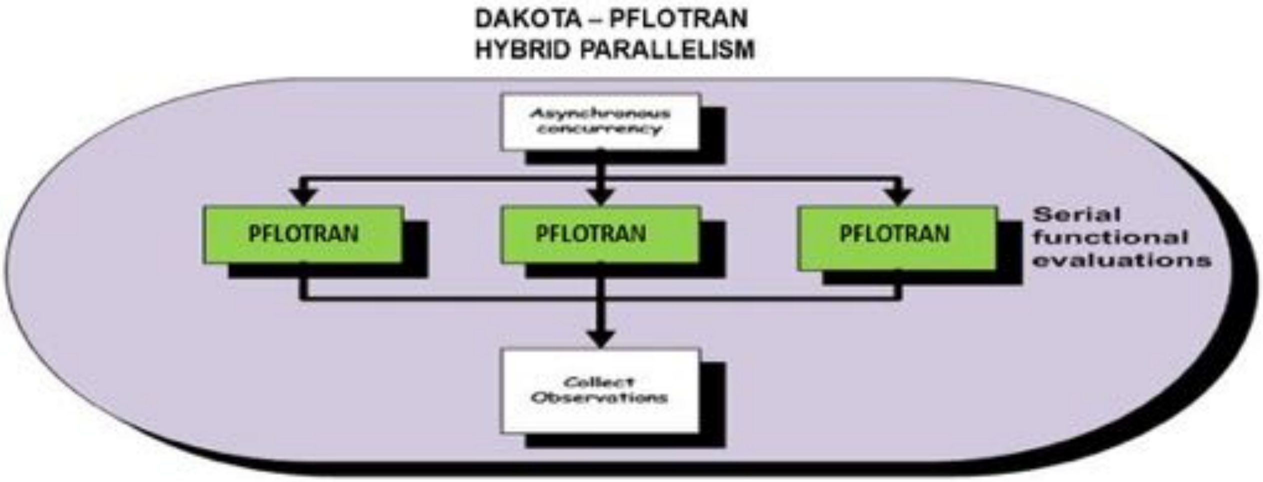

Figure 3-9. Schematic diagram of DAKOTA-PFLOTRAN hybrid parallelism.

3.3.1 Description of the Sensitivity Analysis Method

For the analysis ten uncertain input parameters were selected shown in Table 3-4. Typical distribution types were used for each of the parameters. The values of these parameters were selected based on previous modeling experience, such as shown in Section 3.2. The output of interest for the analysis are temperature at Heater 1 and relative humidity at Points 1, 2 and on Section E1 at simulation time of 1,800 days. Relative humidity is calculated using Equation 3-1, using outputs of PFLOTRAN. For this exercise 25 LHS samples (realizations) were selected.

$$RH\,\% = 100exp\left(\frac{-s \cdot V_w}{10^{-6} R \cdot T}\right) \qquad \textit{Equation 3-1}$$

where

RH = relative humidity (%)

s = suction (MPa)

V_w=molar volume of water (1.8×10^{-5} m^3/mol)

R = universal gas constant (8.3143 J/(mol·K))

T = temperature in Kelvin

The DAKOTA-PFLOTRAN simulations were conducted using the uncertain input parameters described in Table 3-4.

Table 3-4. Uncertain input parameters.

Input Parameter	Distribution Type	Value
Granite permeability, m^2	lognormal	Mean: −18.0; Stand. Dev.: 1.0
Buffer permeability, m^2	lognormal	Mean: −20.0; Stand. Dev.: 1.0
Plug permeability, m^2	lognormal	Mean: −20.0; Stand. Dev.: 2.0
Po, MPa	uniform	Range: 20.0–200.0
van Genuchten λ	uniform	Range: 0.1–0.3
Heater Power, W	uniform	Range: 1740.0–2390.0
Granite thermal conductivity, W/(m·K)	lognormal	Mean: 3.0; Stand. Dev.: 0.5
Buffer thermal conductivity dry, W/(m·K)	lognormal	Mean: 0.7; Stand. Dev.: 0.3
Buffer thermal conductivity wet, W/(m·K)	lognormal	Mean: 1.5; Stand. Dev.: 0.3
Plug thermal conductivity, W/(m·K)	lognormal	Mean: 3.0; Stand. Dev.: 0.5

3.3.2 Results of the Sensitivity Analysis

The DAKOTA-PFLOTRAN coupled codes were run for the specified 25 realizations. Selected results of the simulations are shown below. Figure 3-10, Figure 3-11, and Figure 3-12 show plots of the specified results versus time together with experimental data. Figure 3-10 shows predictions of Heater 1 temperature for all the realizations together with the experimental data. The experimental temperature is in the middle of the distribution of predicted temperatures. There is still a need to produce better predictions at early time.

Matching of relative humidity are not as easy as those of temperature because of the non-linear relations involved. Figure 3-11 shows prediction for Point 1 of Section E1. Most of the realization are close to the experimental data. Figure 3-12 shows prediction for Point 2 of Section E1. Most of the realization are lower than the experimental data.

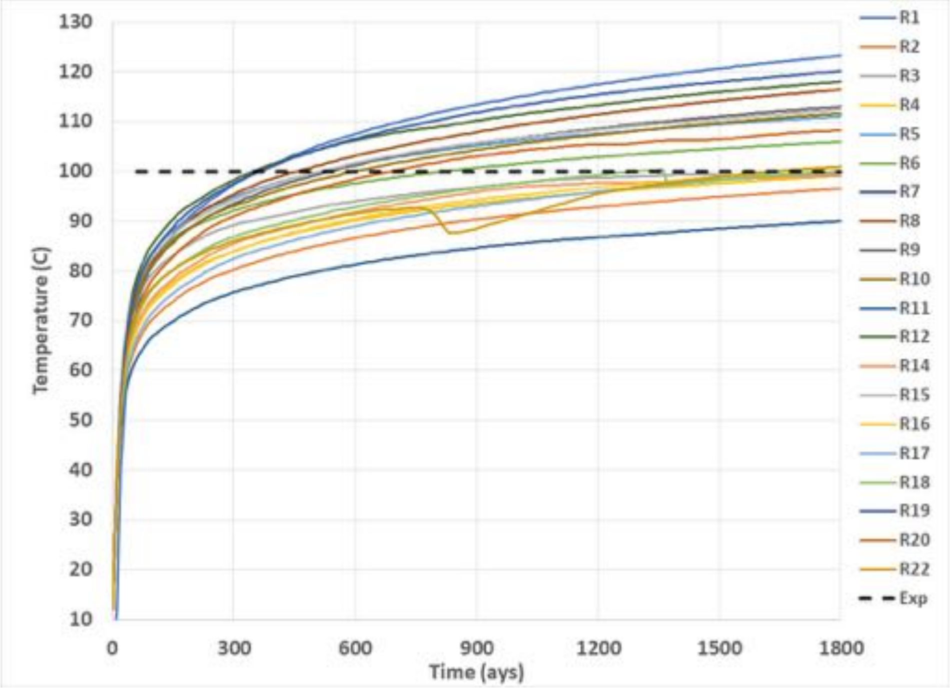

Figure 3-10. Simulated temperature evolution for all realizations at Heater 1 together with experimental data.

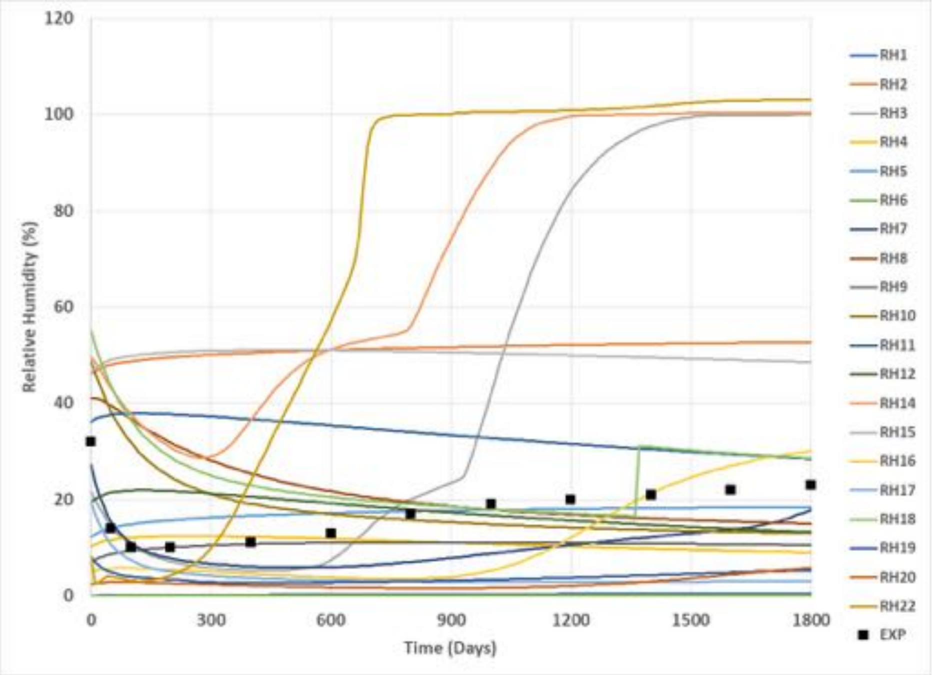

Figure 3-11. Simulated relative humidity evolution at Point 1 in Section E1 for all realizations together with experimental data.

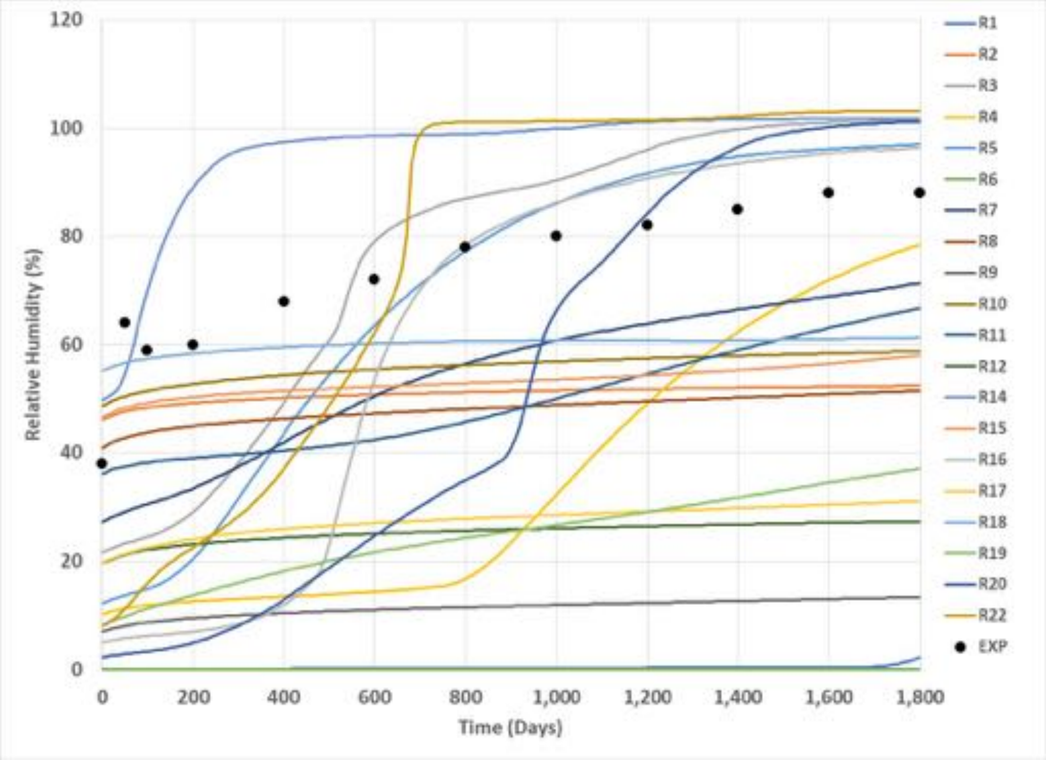

Figure 3-12. Simulated relative humidity evolution at Point 2 in Section E1 for all realizations together with experimental data.

Figure 3-13 to Figure 3-18 show selected results of the sensitivity analysis for the specified number of realizations. Figure 3-13 to Figure 3-16 show plots of temperature of Heater 1 versus Heater 1 power, buffer dry thermal conductivity, buffer saturated thermal conductivity and granite thermal conductivity, respectively. Figure 3-17 and Figure 3-18 show plots of relative humidity at Point 1 on Section E1 versus air entry pressure (Po) and buffer van Genuchten parameter λ, respectively. The stronger correlations are between Heater 1 temperature and Heater 1 power, and between relative humidity and buffer van Genuchten parameters. The strong correlation between Heater temperature and Heater power is expected as the power directly controls the temperature. The correlation between relative humidity and van Genuchten parameters is also consistent with the matching exercise described in Section 3.2. Matching of relative humidity is very sensitive to the values of the reciprocal of the air entry pressure and the parameter λ. Further analysis will be needed to obtain a complete interpretation of the results.

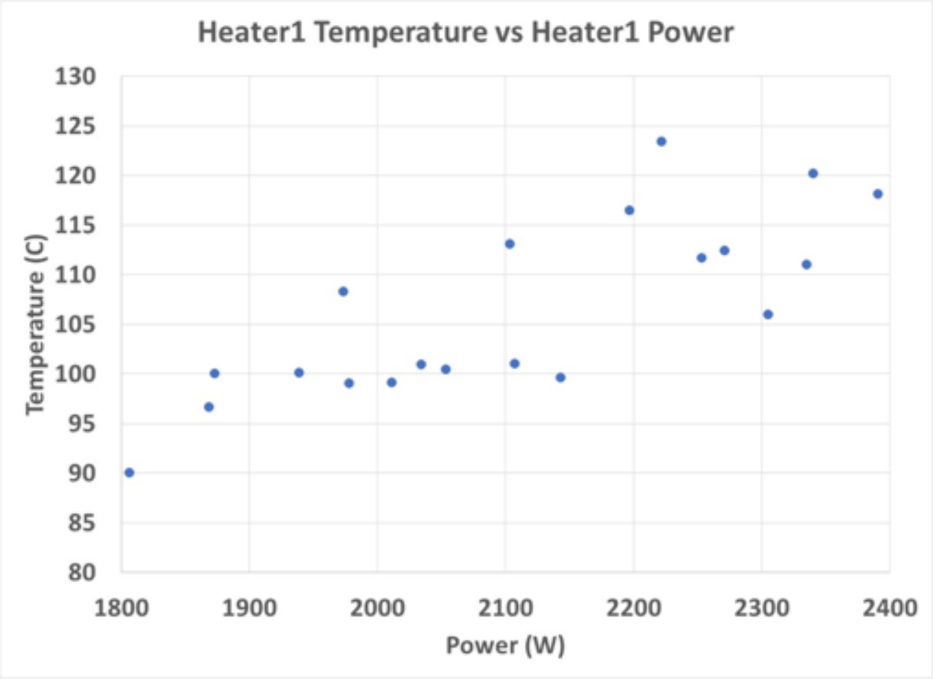

Figure 3-13. Sampled values of Heater 1 power versus temperature at Heater1 after 1,800 days simulation time.

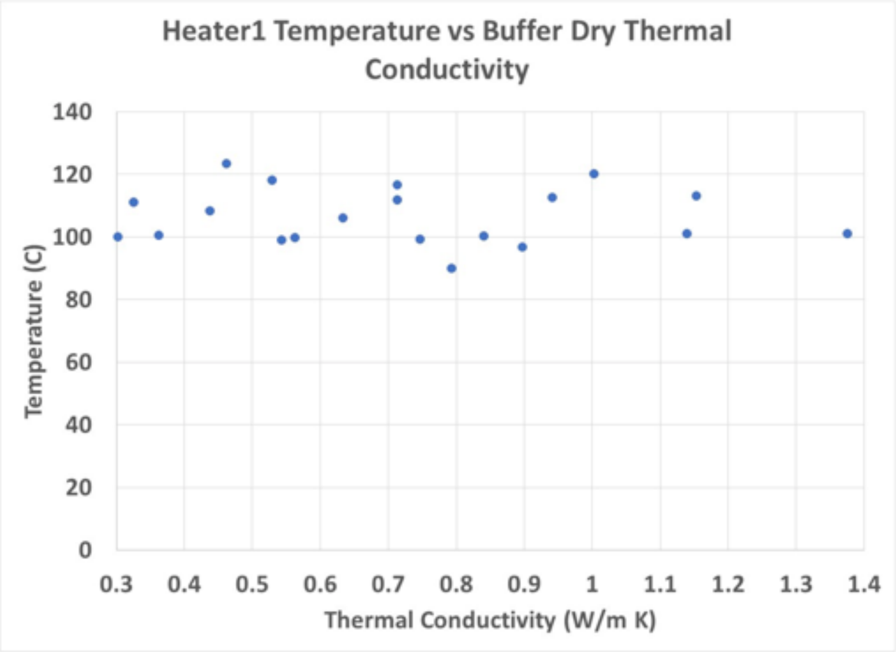

Figure 3-14. Sampled values of buffer dry thermal conductivity versus temperature at Heater1 after 1,800 days simulation time.

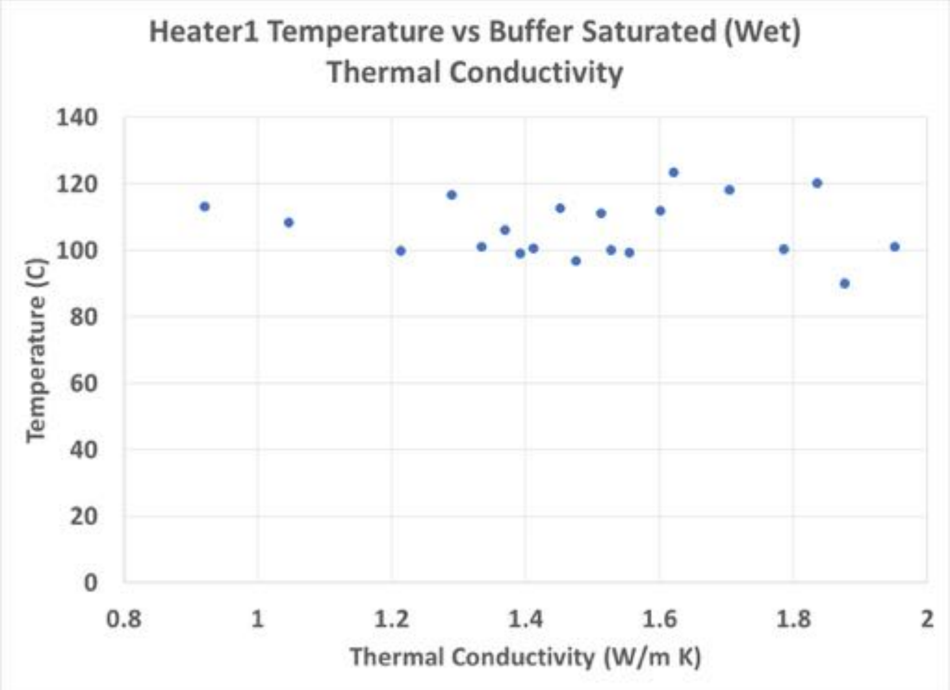

Figure 3-15. Sampled values of buffer saturated thermal conductivity versus temperature at Heater1 after 1,800 days simulation time.

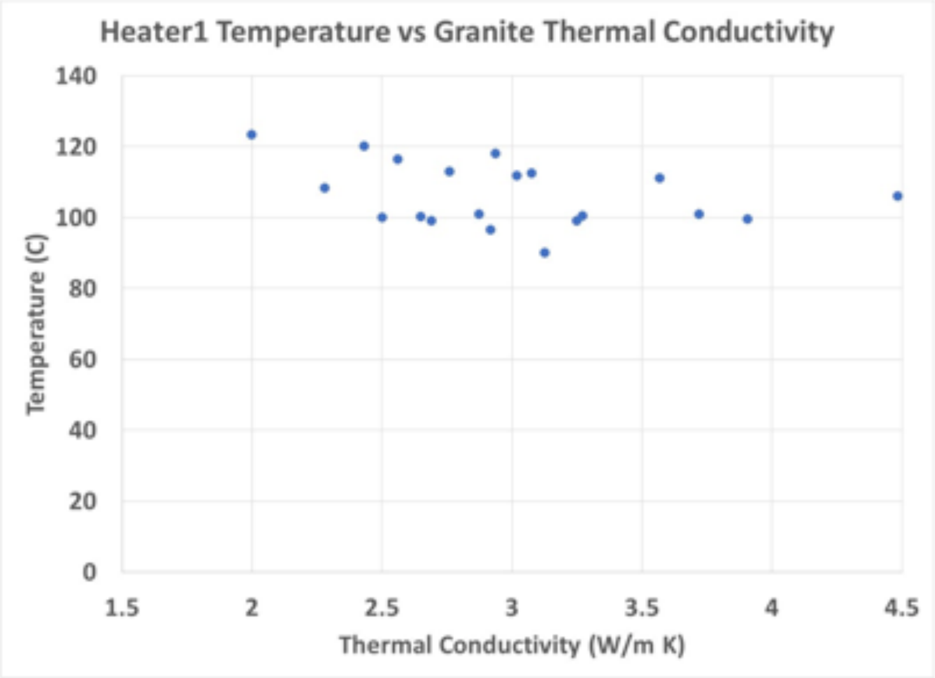

Figure 3-16. Sampled values of granite thermal conductivity versus temperature at Heater1 after 1,800 days simulation time.

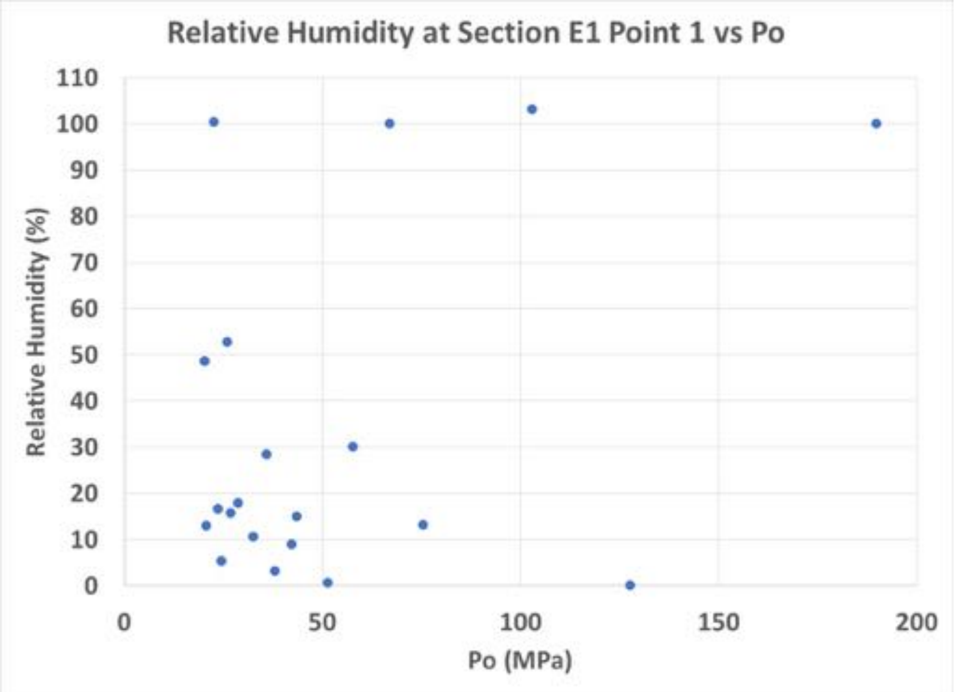

Figure 3-17. Sampled values of buffer air entry pressure (Po) versus relative humidity at Point 1 on Section E1 after 1,800 days simulation time.

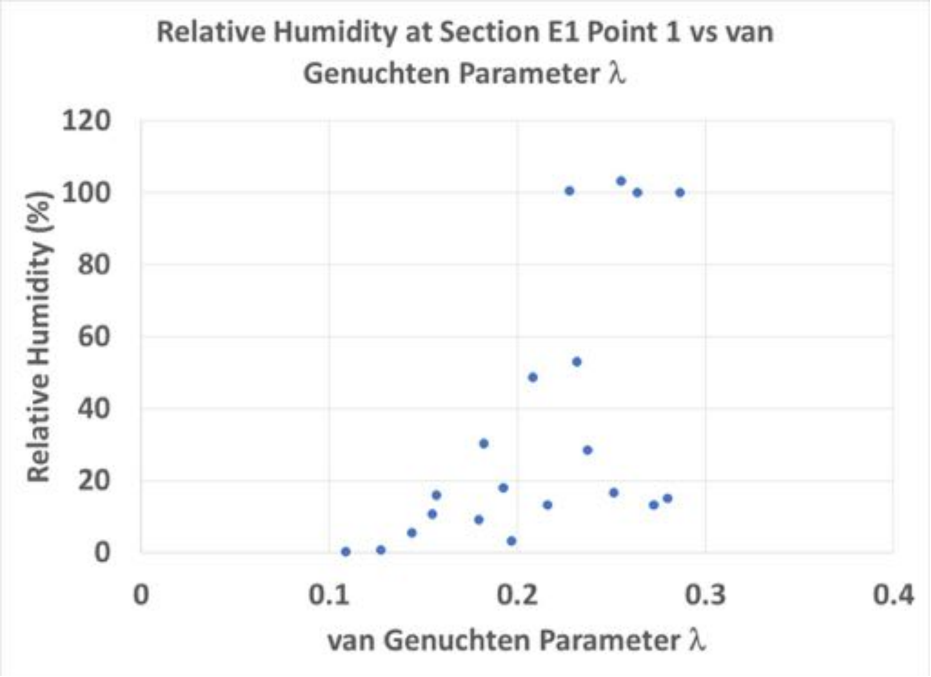

Figure 3-18. Sampled values of buffer van Genuchten parameter λ versus relative humidity at Point 1 on Section E1 after 1,800 days simulation time.

4. CEMENT-CARBONATE ROCK INTERACTION UNDER SATURATED CONDITIONS: FROM LABORATORY TO MODELING

4.1 Introduction

4.1.1 Background

Quantification and prediction of chemical interactions along interfaces between cementitious materials and host rocks have important implications for many applications, such as: (1) deep geological repositories (Gaucher and Blanc, 2006; Ishikawa et al., 2005); (2) deep boreholes for radioactive waste, carbon dioxide sequestration or gas and oil wells (Crossland, 2017; Hangx et al., 2016; Ingraffea et al., 2014; Jackson, 2014); (3) engineered barriers (Ewing et al., 2016; Gaucher and Blanc, 2006; Ingraffea et al., 2014); and (4) engineered structures (Gaucher and Blanc, 2006; Hangx et al., 2016; Ingraffea et al., 2014; Ishikawa et al., 2005). Such interfaces may lead to chemical and structural alteration of both the cement and the host rock caused by diffusion and reaction driven by gradients in porewater pH and composition, pore structure, and mineralogical differences between the different materials.

For example, carbonation of the cement hydration products (e.g., portlandite, C-S-H, and ettringite) and changes in rock mineralogy from alkali interaction are expected in the case of an interface between cement paste and carbonate rocks. Dissolved carbon dioxide (CO_2) originates from the atmosphere, soil microbial activity, or dissolution products of carbonate bearing rock phases (e.g., $CaCO_3$) and diffuses into the saturated pore space of the cement paste. The interaction of dissolved carbon dioxide products (mostly aqueous CO_3^{2-} and HCO_3^-) with soluble hydroxides in the pore solution leads to a series of reactions that result in carbonation of the cement paste. Carbonation is the formation of calcium carbonate ($CaCO_3$) solid phases at the expense of hydrated cement products. Depletion of portlandite results in subsequent decalcification of C-S-H that leads to changes in the cement strength and may lead to structural failure. The conversion of hydroxide-bearing cement hydration products (e.g., portlandite, C-S-H, and ettringite) leads to a decrease in pH of the pore solution. Also as a result of carbonation, the mobility of some trace constituents (e.g., radionuclides) may increase or decrease in response to changes in pH, porosity, and mineralogical gradients. While cements are predominantly carbonated, the porosity of rocks near the interface may be increased due to reaction with highly alkali solutions that have migrated from the cement into the rock's pores (Lorek et al., 2016). Furthermore, the distinct pH and chemical composition of the cement's pore solution compared to the rock pore water results in etched surfaces of solid phases in the rock (e.g., calcite), which increases the chemical reactivity of these phases (Monteiro and Mehta, 1986).

A significant number of studies on rock-cement interfaces have been conducted on geological disposal of radioactive waste in several low permeability rock types such as salt, clay, granite, and tuff (Ewing et al., 2016; Grambow, 2016; Hedin and Olsson, 2016; Ström et al., 2008; Swift and Bonano, 2016; von Berlepsch and Haverkamp, 2016). These sites usually include interfaces between cementitious materials and host rocks. Previous studies focused on interfaces such as: (1) between clayey geological formations and cement (Fernández et al., 2006; Gaboreau et al., 2011; Gaucher and Blanc, 2006; Jenni et al., 2014), where the clay and cement media have very contrasted chemistries that will interact and lead to a degradation of both types of material. These studies used laboratory experiments and in-situ field observations to monitor cement degradation; and (2) between granite, basalt and cement paste (Kong and Du, 2015). Using laboratory experiments, Kong and Du (2015) demonstrated that Ca^{2+}, K^+, and Na^+ were absorbed by multiple types of aggregates from the cement solution and, furthermore, granite and basalt also absorb significant amounts of OH^- and release significant amounts of Si into cement solution.

Research-based laboratory experiments and field observations on rock-cement interfaces require complementary models that capture key mechanisms to provide useful scenario-based projections of long-term performance. Chemical and physical properties of both materials that form the interface change with time. Typically reactive-transport models that directly include detailed descriptions of materials and processes or abstractions are used for performance simulations. In turn, reactive transport model simulations provide input for a performance assessment as part of a system safety evaluation (Steefel and Maher, 2009):

- Watson et al. (2013) described the performance of existing boreholes (cement-clay interface) filled with concrete and cement that were in contact with the natural mudstone for 15–20 years. They observed, both in the model and in the boreholes, porosity variations and precipitation of carbonates, K-feldspar, ettringite and calcite.
- (Kosakowski and Berner (2013) showed that for cement/clay interfaces, regardless of the high pH gradient between the two materials, the zone in which the pH increased in the host rocks was limited. They also presented calculations that show substantial change in porosity near the interface as a result of dissolution/precipitation of minerals phases.
- Lichtner et al. (1997) simulated an interface between cement and tuff. Their calculations predicted porosity reduction and calcification.
- Trotignon et al. (2007) evaluated the effect of sulfate attack on an interface between a concrete engineered barrier and a mudrock by simulating a 10^6 year contact interval. Their simulations predicted the host rock (mudstone) to be altered due to ingression of high pH fluid from the concrete barrier.

However, the Achilles' heel of the existing reactive transport models is the limited testing conditions range (e.g., pH, liquid/solid ratio and mineral phases) of the input parameters and materials that describes fairly well a specific lab/field scenario but does not account for all possibilities in future scenarios. Consequently, the long-term performance predictions can be inaccurate.

In countries where low permeability rocks are not accessible at appropriate depths or under stable geological settings, other low permeability rock types, such as sedimentary carbonate rocks, are considered. Moreover, because few geological disposal sites of radioactive waste are active to date (e.g., Waste Isolation Pilot Plant (WIPP) (U.S. Congress, 1996)), radioactive waste is being stored in interim storage facilities over a wide range of lithologies, including within carbonate rocks. Hence, the interaction of cementitious materials with carbonate lithologies is important for short-lived radionuclides under interim storage conditions and long-term geological disposal for extended time frames.

4.1.2 Objectives and Approach

The Israel Atomic Energy Commission is examining the possibility of locating a geological waste disposal site (Figure 4-1) within the carbonate Ghareb and Nezer Formations in the northern Negev, Israel (Klein-BenDavid et al., 2019). Therefore, the goal of the present study is to simulate the long-term performance of interfaces between cementitious materials (CEM I and a low pH cement) with carbonate geologic strata (limestone, chalk, marl, oil shale, low organic phosphorite and high organic phospharite) of the northern Negev, Israel. Interface performance will be evaluated with respect to (1) changes in abundance of major phases for primary constituents, (2) the anticipated reaction front depths as a function of time for each material, and (3) changes in physical, mass transport and mechanical properties. In this report, the interface between OPC paste (CEM I) and two carbonate rock types, limestone and marl, were chosen to illustrate the methodology developed to-date and observations regarding the specific cases.

CEM I was selected as a bounding case for alkali cement-rock interactions because of its highly alkaline pore water (pH≈13). First, physical, chemical and mineralogical characterization was carried out on samples of representative types of carbonate rocks. Second, equilibrium leaching tests as a function of pH and liquid-to-solid (L/S) ratio were completed on rock and cement samples and the results were used to select a set of minerals and other parameters for use in equilibrium geochemical speciation simulations. Third, mass transport leaching tests (monolith diffusion tests) were carried out on rock and cement samples, with the results used to estimate tortuosity for diffusive mass transport in each material and to verify the mineral set and simulation parameters selected based on equilibrium leaching tests. Fourth, the mineral set and transport parameters derived for each material were used in a series of cement-rock interface simulations, where diffusion and reaction across the interface were simulated to elucidate expected reaction front depths and mineral changes over extended contact intervals. For each cement-rock interface combination, a series of experiments were designed and initiated to provide multi-year interactions between materials under saturated conditions followed by detailed characterization.

The specific objectives of this report are the following: (1) demonstration of how laboratory characterization methods results are used as input data in reactive transport simulations; (2) simulating short-term scenarios (5 years) of interfaces between carbonate rocks (limestone and marl) and OPC paste; and (3) to provide preliminary long-term performance assessments (100 and 1,000 years) of these interfaces based on simulations results.

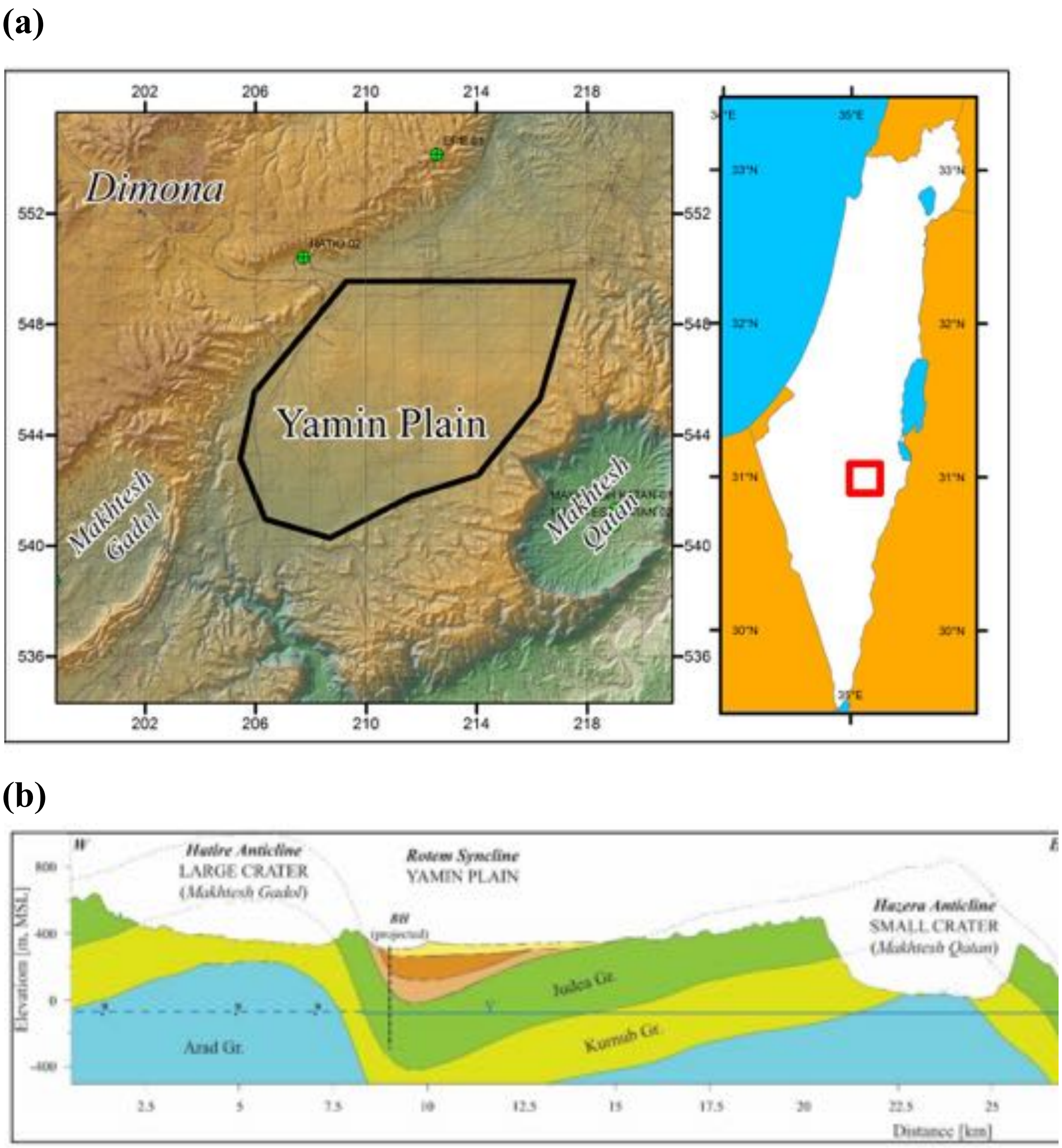

Source: Calvo et al. 2019.

Figure 4-1. (a) Location of the proposed area, Yamin Plain (left) for geological waste disposal site in Israel (right), and (b) Schematic cross-section through Yamin Plain, showing the stratigraphy.

4.2 Experimental Methods

4.2.1 Materials

4.2.1.1 Ordinary Portland Cement Paste

OPC paste was prepared using the following formula: 1092 g CEM 1, 12 g superplasticizer (glenium), and 466 g water (w/b=0.4). The blend was cast into 10 cm by 5 cm tubes and then was cured in an environmental chamber at a temperature of 30°C and 100% relative humidity for 90 days.

4.2.1.2 Rock Properties and Selected Samples

Large bulk samples of limestone and marl, approximately 48 cm by 20 cm were obtained from the northern Negev desert in Israel. The samples are from the carbonate-rich Judea Group and Mount Scopus Group, respectively. Both groups are of Upper Cretaceous to early Paleocene age and are found in the Yamin Plateau (northeastern Negev Desert), several hundred meters below surface, and above the regional water table and outcrops at the margins of the Plateau. Netzer Formation (*ca.* 40 m of limestone) forms the top of the Judea Group. The Ghareb Formation (*ca.* 50 m) forms the top of the Upper Cretaceous and consists of a marl unit overlying an oil shale unit. A more detailed description of the geological settings can be found in the supplementary information.

4.2.2 Solids Characterization for Model Parameterization

4.2.2.1 X-ray Diffraction

Limestone and marl crystallographic characterization for both bulk and clay fractions was performed by X-ray diffraction (XRD). Semi-quantitative clay abundances were estimated from the relative peak areas of illite-smectite, kaolinite, illite, and chlorite following the method of Biscaye (1965). The mineralogical compositions of the limestone, chalk, marl, oil shale, low organic phosphorite and high organic phosphorite are listed in Table 4-1.

Table 4-1: Rock type and mineralogical composition (from XRD)

Sample Name and Rock Type	Formation/Group	Mineralogy			
		Dominant	Major (20%–50%)	Minor (5%–20%)	Trace (<5%)
Marl	Ghareb/ Mount Scoups	Calcite	—	Phyll	Quartz Halite Goethite
Oil Shale	Ghareb/ Mount Scoups	Calcite	—	Fluorapatite Kaolinite Gypsum	Quartz
Chalk	Menucha/ Mount Scoups	Calcite (>80%)	—	—	Quartz
Limestone	Nezer/Judea	Calcite (>80%)	—	—	Quartz
Low Organic Phosphorite	Ghareb/ Mount Scoups	Fluorapatite	Calcite	Phyll	Quartz
High Organic Phosphorite	Ghareb/ Mount Scoups	Fluorapatite	Calcite	—	Quartz

NOTE: Phyll = Phyllosilicate: illite/smectite, kaolinite, and mica.

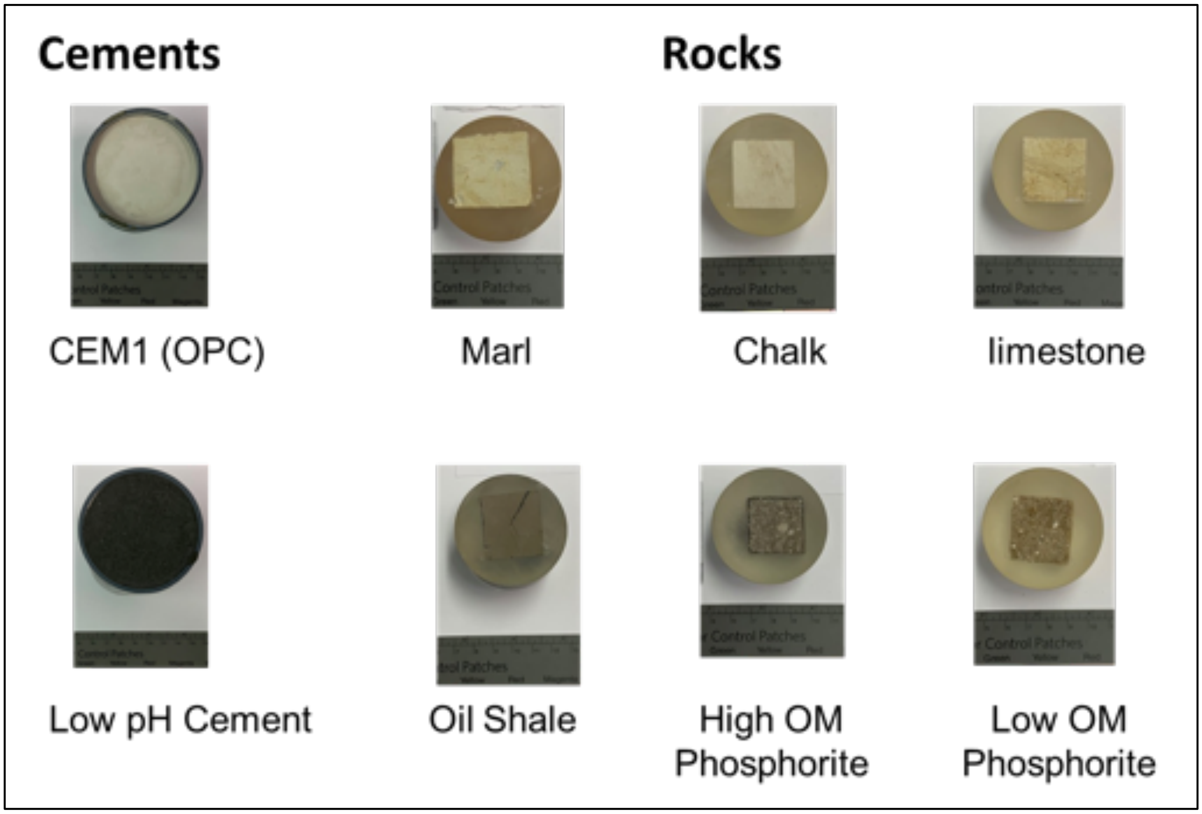

Figure 4-2. Rocks and cements samples.

4.2.2.2 *Mercury Intrusion Porosimetry*

Mercury intrusion porosimetry (MIP) was carried out by Micromeritics Instrument Corporation (Atlanta, GA) according to American Society for Testing and Materials (ASTM) D4404-18 (ASTM International (2010)) to determine sample pore size distribution, percent porosity, and total pore volume for pore sizes from 500 µm to 3.5 nm (Table 4-2).

Table 4-2. Materials characterization results

Rock	BET Surface Area (m^2 g^{-1})	Porosity (%)	Average Pore Diameter (µm)	Total Pore Area (m^2 g^{-1})	Total Intrusion Volume (ml g^{-1})	Bulk Density (g m^{-1})	Cumulative Pore Volume (ml g^{-1})
Limestone	0.64	6.8	0.1	1	0.03	2.47	0.25
Marl	5.55	31.7	0.14	5	0.17	1.85	0.13
Oil Shale	12.9	33	0.03	25	0.17	1.88	0.12
LOM	15.1	35	0.04	26	0.24	1.44	0.1
Chalk	Not Measured	19.3	0.11	3	0.09	2.15	0.09

NOTE: LOM = Low organic material phosphorite. High organic material phosphorite (HOM) sample was not measured.

4.2.2.3 Thermogravimetric Analysis (TGA)

A TA Instruments Q600 SDT analyzer (New Castle, Delaware, USA) was used to estimate the mass fraction of total carbonate in the rock and cement samples. For each material, TGA was conducted on duplicate subsamples of approximately 40 mg. Each TGA run was heated up to a temperature of 989°C at a heating rate of 10.0°C/min. The chamber was continuously flushed with nitrogen throughout the heating process with a flow rate of 100 $\text{mL}\cdot\text{min}^{-1}$.

4.2.3 Major Constituent Solubility as a Function of pH (EPA Method 1313)

U.S. EPA Method 1313 (U.S. EPA, 2017a) is a pH-dependence leaching test method that provides the liquid-solid partitioning (LSP) of species of interest under near equilibrium conditions. Eluate solutions are prepared with final pH ranging from <2 to 13 using particle-size reduced subsamples of test materials. Particle-size reduction facilitates the approach to solid-liquid equilibrium. In the present work, for each one of the materials (limestone, marl, and OPC paste) two sets of parallel batch extractions of a solid material at specified end-point pH conditions were done: (1) at a L/S of 10 mL/g-dry and (2) at L/S of 1. The additional L/S of 1 was done to approach the low L/S in the rocks and cement pore water. Concentrations of species of interest in the eluate were determined by inductively couple plasma-optical emission spectrometry (ICP-OES) following U.S. EPA Method 6010D (U.S. EPA, 2018). The results of EPA Method 1313 are pH titration and response curves of LSP of constituents as a function of pH (Table 4-3 and Figure 4-3). The results of the EPA Method 1313 are used to select a reaction set of minerals and related parameters to represent the material by fitting LSP curves of constituents as a function of pH at equilibrium (Section 4.2.6) in conjunction with other material information. Further details on EPA Method 1313 procedure and application of this method can be found elsewhere (A. Garrabrants et al., 2012; A.C. Garrabrants et al., 2010; U.S. EPA, 2017a).

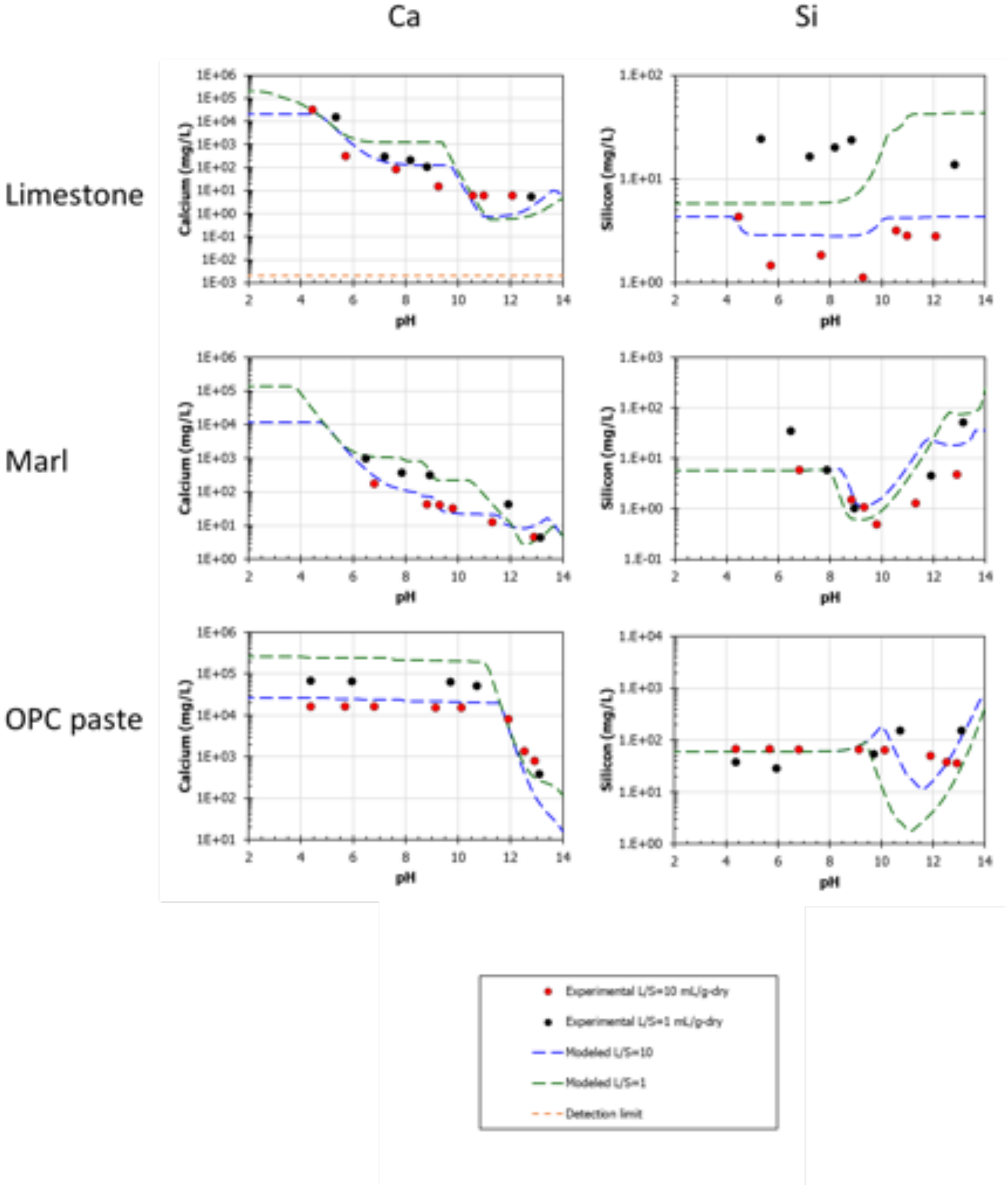

Figure 4-3. Results of EPA Method 1313 tests and the prediction of LSP curves

Table 4-3. Available content evaluation using EPA method 1313

Constituent (mol/kg)	Limestone	Marl	OPC Paste
	Available Content L/S = 10	Available Content L/S = 10	Available Content L/S = 10
$Al[OH]_4^-$	5.14E-04	1.24E-02	6.30E-01
Ca^{+2}	4.99E+00	3.52E+00	3.74E+00
$CO3^{-2}$	4.99E+00	3.50E+00	1.00E-06
$Fe[OH]_4^-$	1.28E-03	1.45E-03	2.44E-02
$H_2SiO_4^{-2}$	1.54E-03	3.11E-02	3.84E-01
K^+	2.27E-03	8.18E-03	7.65E-02
Mg^{+2}	6.13E-02	3.68E-02	3.27E-01
Na^+	3.61E-03	1.15E+00	3.31E-01
$PO4^{-3}$	2.34E-05	1.65E-02	5.37E-03
SO_4^{-2}	9.86E-03	3.60E-02	3.61E-01

4.2.4 Monolith Leaching Test (EPA Method 1315)

EPA Method 1315 is a mass transfer rate, tank leaching test (U.S. EPA, 2017b). The test consists of continuous leaching of water-saturated monolithic material with periodic renewal of the eluent at predetermined intervals. The concentration of constituent in each interval eluate is used to calculate the interval mass flux across the exposed surface area ($mg \cdot m^{-2} \cdot sec^{-1}$) and the cumulative mass release ($mg \cdot m^{-2}$) to the eluate. After each eluant exchange, the eluate is analyzed for pH, conductivity, E_h, elemental analysis by ICP-MS (EPA Method 6020B) and inductively coupled plasma optical emission spectroscopy (ICP-OES; EPA Method 6010D, U.S. EPA (2018)), dissolved organic carbon (DOC), and other parameters of interest. DOC was analyzed using Shimadzu TOC-V CPH/CPN (Shimadzu Scientific Instruments, Inc., Columbia, MD) by catalytic oxidation/nondispersive infrared detection (NDIR) following EPA Method 9060A (U.S. EPA, 2004).

Test samples for Method 1315 were prepared by cutting approximately 2.5 cm cubes from the larger rock specimens utilizing a rock saw with diamond blade. The 2.5 cm cubes were then cast in epoxy utilizing 5 cm by 10 cm tubes for molds and epoxy resin and hardener (Figure 4-4). After the samples were set, they were demolded and polished. Samples were polished using 140 grit paper for coarse polishing to expose the surface of the sample and 240 grit paper for finer polishing. Samples were then exposed under 100% relative humidity at 30°C in an environmental chamber for approximately three weeks to achieve water saturation through capillary condensation of water vapor. Samples were weighed approximately every 48 hours until constant weight indicated that saturation was achieved (approximately 2 weeks).

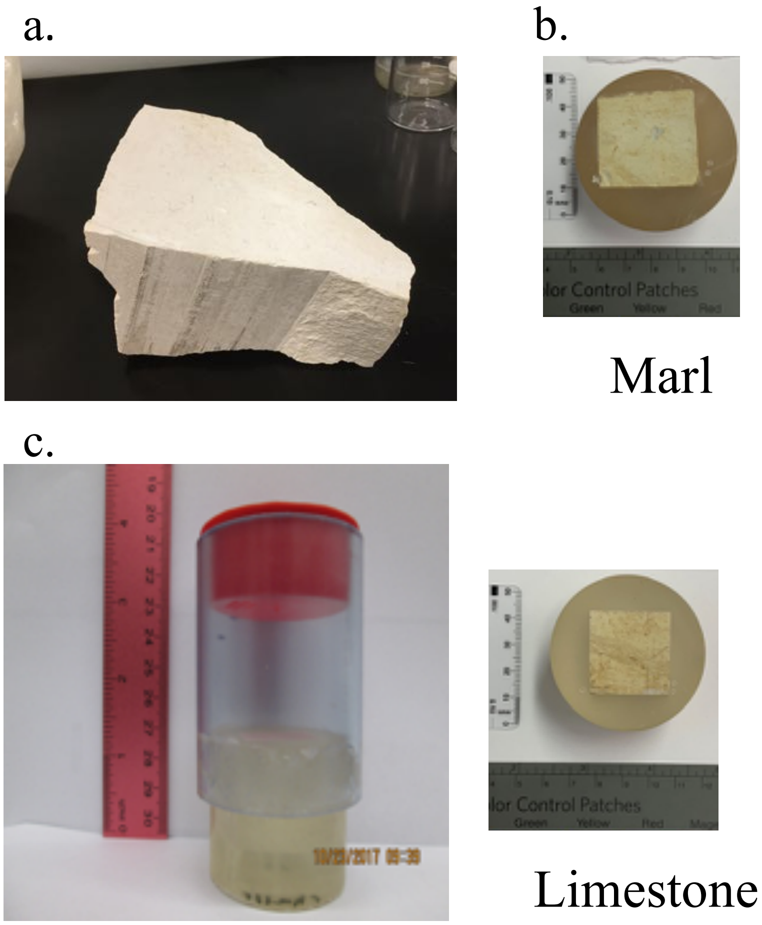

Figure 4-4. (a) Example of bulk sample, (b) processed samples used for 1315, and (c) example of experimental set up for 1315 test apparatus.

The results of the EPA method tests for limestone, marl, and OPC paste are shown in Figure 4-5. The results of the EPA Method 1315 are used in conjunction with the reactive transport model to estimate tortuosity (Section 4.2.7) of the materials as well as for validation of the selected mineral reaction set (Section 4.3.3).

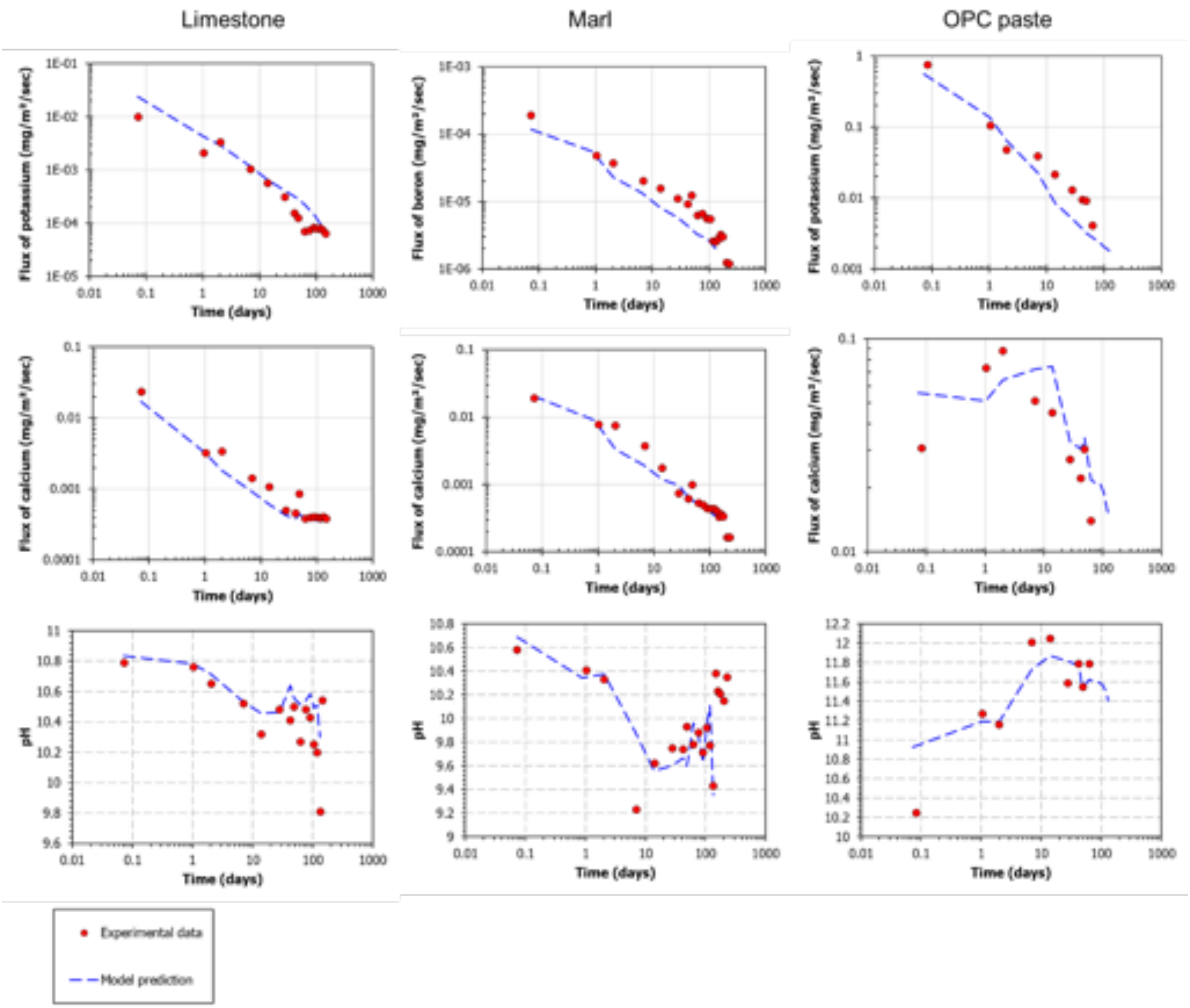

Figure 4-5. Results of EPA Method 1315

4.2.5 Geochemical Speciation and Reactive Transport Models

The LeachXS (Van der Sloot et al., 2008) with ORCHESTRA (Meeussen, 2003) embedded for geochemical speciation and reactive mass transport (hereafter LeachXS/Orchestra, LXO) was used to develop a geochemical reactive transport model that considers geochemical speciation, liquid/solid partitioning, and multi-ionic diffusion (Arnold et al., 2017; ECN, 2019; Meeussen, 2003). Geochemical speciation modeling was used to simulate the equilibrium LSP of constituents obtained from EPA Method 1313 (i.e., pH-dependent LSP model) and the mass transfer release of constituents in EPA Method 1315 (i.e., monolith diffusion-controlled leaching model). The resulting geochemical speciation model and mass transfer model were used to simulate rock-cement interface behavior.

4.2.6 Geochemical Speciation and Thermodynamic Dataset

The ion activities and LSP were calculated with equilibrium constants (logK) at 30°C and 1 bar. The aqueous phase speciation and mineral reaction set used in modeling were from the thermodynamic databases, Minteq.v4 (U.S. Environmental Protection Agency, 1998) and CEMDATA18 (Lothenbach et al., 2019). Activity coefficients were calculated by adopting the approach of Samson et al. (1999) for ionic strength higher than the range of the extended Debye-Hückel and Davies equations. LogK values of modeled solid phases were calculated for 30°C (Table 4-4) using the temperature dependency reported in the MinteqV.4 (U.S. Environmental Protection Agency, 1998) and CEMDATA18 (Lothenbach et al., 2019) datasets.

A set of minerals (i.e., mineral reaction set) that may be present in the system was derived by fitting LSP curves of constituents as a function of pH at equilibrium. Minerals were selected based on (1) identified phases from the XRD analyses (for rocks samples only); (2) minimizing the residuals between the modeled and measured LSP curves by selecting phases that are likely to be initially present or form under the experimental EPA 1313 test experimental conditions (i.e., pH, temperature, and experiment duration); and (3) by confirming portlandite, CSH, and ettringite phases form under the natural pH of the OPC paste. The mineral reaction sets used to describe limestone, marl, and OPC paste are shown in Table 4-4.

Table 4-4. Calibrated mineral reaction set

Mineral	Notation	Mineral Dissolution Reaction	Log $K_{30°C}$	Materials Used To Be Calibrated	Reference	Database
$AlOHSO_4$	$\mathrm{AHS}\overline{\ 2}$	$AlOHSO_{4(s)} + 3H_2O_{(aq)}$ <--> $Al[OH]_4^{-}{}_{(aq)} + 3H^{+}{}_{(aq)} + SO_4^{-2}{}_{(aq)}$	25.918	Limestone, OPC paste	(U.S. Environmental Protection Agency, 1998)	MinteqV4
$BaSO_4$	Barite	$BaSO_{4(s)}$ <--> $Ba^{+2}{}_{(aq)} + SO_4^{-2}{}_{(aq)}$	9.913	Limestone. OPC paste and Marl	(U.S. Environmental Protection Agency, 1998)	MinteqV4
SiO_2	CEM18_Amor_SI	$SiO_{2(s)} + 2H_2O_{(aq)}$<--> $2H^{+}{}_{(aq)} + H_2SiO_4^{-2}{}_{(aq)}$	25.533	Limestone, OPC paste and Marl	(Lothenbach et al., 2019)	CEMDATA18
$Mg[OH]_2$	CEM18_Brc	$Mg[OH]_{2(s)} + 2H^{+}{}_{(aq)}$ <--> $Mg^{+2}{}_{(aq)} + H_2O_{(aq)}$	-16.509	Limestone, OPC paste	(Lothenbach et al., 2019)	CEMDATA18
$CaCO_3$	CEM18_Cal	$CaCO_{3(s)}$ <--> $CO3^{-2}{}_{(aq)} + Ca^{+2}{}_{(aq)}$	8.514	Limestone, OPC paste and Marl	(Lothenbach et al., 2019)	CEMDATA18
$SrSO_4$	CEM18_Cls	$SrSO_{4(s)}$ <--> $SO_4^{-2}{}_{(aq)} + Sr^{+2}{}_{(s)}$	6.637	Limestone and Marl	(Lothenbach et al., 2019)	CEMDATA18
$Al[OH]_3$	CEM18_Gbs	$Al[OH]_{3(s)}$ <--> $Al[OH]_4^{-}{}_{(aq)} + H^{+}{}_{(aq)} + H_2O_{(aq)}$	14.718	Limestone and Marl	(Lothenbach et al., 2019)	CEMDATA18
$CaSO_4{\cdot}2H_2O$	CEM18_Gp	$CaSO_4{\cdot}2H_2O_{(s)}$ <--> $Ca^{+2}{}_{(aq)} + 2H_2O_{(aq)} + SO_4^{-2}{}_{(aq)}$	4.586	Limestone and Marl	(Lothenbach et al., 2019)	CEMDATA18
CaO	CEM18_Lim	$CaO_{(s)} + 2H^{+}{}_{(aq)}$ <--> $Ca^{+2}{}_{(aq)} + H_2O_{(aq)}$	-32.028	Limestone	(Lothenbach et al., 2019)	CEMDATA18
$CaMg[CO_3]_2$	CEM18_Ord_Dol	$CaMg[CO_3]_{2(s)}$ <--> $Ca^{+2}{}_{(aq)} + Mg^{+2}{}_{(aq)} + 2CO_3^{-2}{}_{(aq)}$	17.201	Limestone and Marl	(Lothenbach et al., 2019)	CEMDATA18
$Ca(OH)_2$	CEM18_Portlandite	$Ca(OH)_{2(s)} + 2H^{+}{}_{(aq)}$ <--> $Ca^{+2}{}_{(aq)} + 2H_2O_{(aq)}$	-22.424	Limestone and Marl	(Lothenbach et al., 2019)	CEMDATA18
SiO_2	CEM18_Qtz	$SiO_{2(s)} + 2H_2O_{(aq)}$ <--> $2H^{+}{}_{(aq)} + H_2SiO_4^{-2}{}_{(aq)}$	26.548	Limestone and Marl	(Lothenbach et al., 2019)	CEMDATA18
$AlO[OH]$	Diaspore	$AlO[OH]_{(s)} + 2H_2O_{(aq)}$ <--> $Al[OH]_4^{-}{}_{(aq)} + H^{+}{}_{(aq)}$	15.815	Limestone	(U.S. Environmental Protection Agency, 1998)	MinteqV4
$Fe[OH]_3$	Ferrihydrite	$Fe[OH]_{3(s)} + H_2O_{(aq)}$ <--> $Fe[OH]_4^{-}{}_{(aq)} + H^{+}{}_{(aq)}$	18.609	Limestone	(U.S. Environmental Protection Agency, 1998)	MinteqV4

Mineral	Notation	Mineral Dissolution Reaction	Log $K_{30°C}$	Materials Used To Be Calibrated	Reference	Database
NaCl	Halite	$NaCl_{(s)} \longleftrightarrow Na^+_{(aq)} + Cl^-_{(aq)}$	-1.610	Limestone	(U.S. Environmental Protection Agency, 1998)	MinteqV4
$[Fe_2O_3]Ca_3O_3[SiO_2]_{0.84}[H_2O]_{4.32}$	CEM18_C3AS0_41H5_18	$[Fe_2O_3]Ca_3O_3[SiO_2]_{0.84}[H_2O]_{4.32(s)} + 3.18H^+_{(aq)} \longleftrightarrow 2Al[OH]_4^-{}_{(aq)} + 3Ca^{+2}_{(aq)} + 3.18H_2O_{(aq)} + 0.41H_2SiO_4^{-2}{}_{(aq)}$	-19.353	OPC paste	(Lothenbach et al., 2019)	CEMDATA18
$CaOAl_2O_3[H_2O]_{10}$	CEM18_CAH10	$CaOAl_2O_3[H_2O]_{10(s)} \longleftrightarrow 2Al[OH]_4^-{}_{(aq)} + Ca^{+2}_{(aq)} + 6H_2O_{(aq)}$	7.130	OPC paste	(Lothenbach et al., 2019)	CEMDATA18
$[H_2O]_2Ca_6Al_2[SO_4]_3[OH]_{12}[H_2O]_{24}$	CEM18_ettringite	$[H_2O]_2Ca_6Al_2[SO_4]_3[OH]_{12}[H_2O]_{24(s)} + 4H^+_{(aq)} \longleftrightarrow 2Al[OH]_4^-{}_{(aq)} + 6Ca^{+2}_{(aq)} + 30H_2O_{(aq)} + 3SO_4^{-2}{}_{(aq)}$	-11.450	OPC paste	(Lothenbach et al., 2019)	CEMDATA18
$Ca_2Al_2SiO_7[H_2O]_8$	CEM18_straetlingite	$Ca_2Al_2SiO_7[H_2O]_{8(s)} \longleftrightarrow 2Al[OH]_4^-{}_{(aq)} + 2Ca^{+2}_{(aq)} + 5H_2O_{(aq)} + H_2SiO_4^{-2}{}_{(aq)}$	18.497	OPC paste	(Lothenbach et al., 2019)	CEMDATA18
Fe_2O_3	Maghemite	$Fe_2O_{3(s)} + 5H_2O_{(aq)} \longleftrightarrow 2Fe[OH]_4^-{}_{(aq)} + 2H^+_{(aq)}$	36.790	OPC paste	(U.S. Environmental Protection Agency, 1998)	MinteqV4
$[CaO]_{12}[Al_2O_3]_7$	CEM18_C12A7	$[CaO]_{12}[Al_2O_3]_{7(s)} + 10H^+_{(aq)} + 23H_2O_{(aq)} \longleftrightarrow 14Al[OH]_4^-{}_{(aq)} + 12Ca^{+2}_{(aq)}$	-165.417	Marl	(Lothenbach et al., 2019)	CEMDATA18
$Al[OH]_{3(am)}$	CEM18_AlOHam	$Al[OH]_{3(am)} \longleftrightarrow Al[OH]_4^-{}_{(aq)} + H^+_{(aq)} + H_2O_{(aq)}$	13.3773	Marl	(Lothenbach et al., 2019)	CEMDATA18
$(AlFeO_3)[Ca_3O_3(SiO_2)_{0.84}(H2O)_{4.32}]$	CEM18_C3AFS0_84H4_32	$(AlFeO_3)[Ca_3O_3(SiO_2)_{0.84}(H2O)_{4.32}]_{(s)} + 2.32H^+_{(aq)} \longleftrightarrow Al[OH]_4^-{}_{(aq)} + 3Ca^{+2}_{(aq)} + Fe[OH]_4^-{}_{(aq)} + 1.48H_2O_{(aq)} + 0.84H_2SiO_4^{-2}{}_{(aq)}$	-2.13594	Marl	(Lothenbach et al., 2019)	CEMDATA18
$K_{0.6}Mg_{0.25}Al_{2.3}Si_{3.5}O_{10}[OH]_2$	Illite	$K_{0.6}Mg_{0.25}Al_{2.3}Si_{3.5}O_{10}[OH]_2 + 11.2H_2O \longleftrightarrow 2.3Al[OH]_4^- + 8.2H^+ + 3.5H_2SiO_4^{-2} + 0.6K^+ + 0.25Mg^{+2}$	39.0951	Marl	(Parkhurst and Appelo, 2013)	phreeqc.dat
SiO_2	SiO2[am-ppt]	$SiO_2 + 2H_2O \longleftrightarrow 2H^+ + H_2SiO_4^{-2}$	-25.56	Marl	(U.S. Environmental Protection Agency, 1998)	MinteqV4
$Ca_5[PO_4]_3[OH]$	Hydroxylapatite	$Ca_5[PO_4]_3[OH]_{(s)} + H^+_{(aq)} \longleftrightarrow 5Ca^{+2}_{(aq)} + H_2O_{(aq)} + 3PO_4^{-3}{}_{(aq)}$	44.333	Marl	(U.S. Environmental Protection Agency, 1998)	MinteqV4
$FeO[OH]$	Goethite	$FeO[OH]_{(s)} + 2H_2O_{(aq)} \longleftrightarrow Fe[OH]_4^-{}_{(aq)} + H^+_{(aq)}$	21.2721	Marl	(U.S. Environmental Protection Agency, 1998)	MinteqV4
$CaHPO_4$	CaHPO4[s]	$CaHPO_{4(s)} \longleftrightarrow Ca^{+2}_{(aq)} + H^+_{(aq)} + PO_4^{-3}{}_{(aq)}$	19.1854	Marl	(U.S. Environmental Protection Agency, 1998)	MinteqV4

Mineral	Notation	Mineral Dissolution Reaction	Log $K_{30°C}$	Materials Used To Be Calibrated	Reference	Database
$CaHPO_4{:}2H_2O$	CaHPO4:2H2O	$CaHPO_4{:}2H_2O_{(s)}$ <--> $Ca^{+2}{}_{(aq)} + H^+{}_{(aq)} + 2H_2O_{(aq)} + PO_4^{-3}{}_{(aq)}$	18.9285	Marl	(U.S. Environmental Protection Agency, 1998)	MinteqV4
$Ca_3[PO_4]$	Ca3[PO4]2[beta]	$Ca_3[PO_4]_{(s)}$ <--> $3Ca^{+2}{}_{(aq)} + 2PO_4^{-3}{}_{(aq)}$	28.764	Marl	(U.S. Environmental Protection Agency, 1998)	MinteqV4
$Ca_3[SiO_3][SO_4][CO_3] \cdot 15H_2O$	CEM18_thaumasite	$Ca_3[SiO_3][SO_4][CO_3] \cdot 15H_2O_{(s)}$ <--> $CO_3^{-2}{}_{(aq)} + 3Ca^{+2}{}_{(aq)} + 15H_2O_{(aq)} + H_2SiO_4^{-2}{}_{(aq)} + SO_4^{-2}{}_{(aq)}$	23.7155	Marl	(Lothenbach et al., 2019)	CEMDATA18
$Na_2Al_2Si_3O_{10} \cdot 2H_2O$	CEM18_natrolite	$Na_2Al_2Si_3O_{10} \cdot 2H_2O_{(s)} + 5H_2O_{(aq)}$ <--> $2Al[OH]_4^-{}_{(aq)} + 6H^+{}_{(aq)} + 3H_2SiO_4^{-2}{}_{(aq)} + 2Na^+{}_{(aq)}$	97.9651	Marl	(Lothenbach et al., 2019)	CEMDATA18
$Mg_4Al_2O_7[H_2O]_{10}$	CEM18_hydrotalcite	$Mg_4Al_2O_7[H_2O]_{10(s)} + 6H^+{}_{(aq)}$ <--> $2Al[OH]_4^-{}_{(aq)} + 9H_2O_{(aq)} + 4Mg^{+2}{}_{(aq)}$	-27.6721	Marl	(Lothenbach et al., 2019)	CEMDATA18
$[SiO_2]_{2.4}[CaO]_2[H_2O]_{3.2}$	CEM18_Tob_I	$[SiO_2]_{2.4}[CaO]_2[H_2O]_{3.2(s)}$ <--> $2Ca^{+2}{}_{(aq)} + 0.8H^+{}_{(aq)} + 2.8H_2O_{(aq)} + 2.4H_2SiO_4^{-2}{}_{(aq)}$	28.4296	Marl	(Lothenbach et al., 2019)	CEMDATA18
$M_{1.5}S_2H_{2.5}$	CEM18_M075SH	$M_{1.5}S_2H_{2.5(s)}$ <--> $H^+{}_{(aq)} + 2H_2O_{(aq)} + 2H_2SiO_4^{-2}{}_{(aq)} + 1.5Mg^{+2}{}_{(aq)}$	32.7025	Marl	(Lothenbach et al., 2019)	CEMDATA18
$Al_2Si_2O_5[OH]_4$	CEM18_Kln	$Al_2Si_2O_5[OH]_{4(s)} + 3H_2O_{(aq)}$ <--> $2Al[OH]_4^-{}_{(aq)} + 6H^+{}_{(aq)} + 2H_2SiO_4^{-2}{}_{(aq)}$	83.154	Marl	(Lothenbach et al., 2019)	CEMDATA18
$CA_{5/32}N_{11/32}S_{38/32}H_{42/32}$	INFCNA	$[CaO]_{1.25}[SiO_2][Al_2O_3]_{0.125}[Na_2O]_{0.25}[H_2O]_{1.375}$<--> $0.3125Al[OH]_4^- + Ca^{+2} + 1.875\ H_2O + 1.1875H_2SiO_4^{-2} + 0.6875Na^+$	10.149	OPC Paste	(Lothenbach et al., 2019)	CEMDATA18

4.2.7 Transport Modeling (multi-ionic diffusion)

The modeled materials were represented by sets of well-mixed cells having successively larger thickness with increasing distance from the interfaces (water-monolith and rock-cement interfaces). Conceptual models for simulating Method 1315 results and cement-rock interfaces are diagrammed in Figure 4-6. Constituent diffusion from each cell is based on the fully explicit finite volume scheme described in Meeussen and Brown (2018). In all simulations, local equilibrium assumption conditions were met, i.e., the chemical reactions are much faster within each cell than the transport process between cells (Samson et al., 1999).

A multi-ionic diffusion approach (Arnold et al., 2017) was used to model constituent specific diffusivity in both monolith diffusion-controlled leaching and rock-cement interface models. The approach uses free liquid diffusivity coefficients, D_i^0, for specific constituents to calculate the diffusivity of the constituent on a per primary-entity basis. When D_i^0 could not be found for a particular constituent, the geometric mean of D_i^0 per electron of all the known D_i^0 values was used to calculate the D_i^0 of the constituent. The D_i^0 used for each primary entity and corresponding constituent is summarized in Table 4-5.

Table 4-5. List of free liquid diffusivity coefficients (D_i^0) that were used in the transport models

Constituent	Primary entity	D_i^0 (10^{-9} m²/s)	Reference
Al	$Al[OH]_4^-$	3.120	(Mackin and Aller, 1983)
CO_3^{-2}, DIC	CO_3^{-2}	1.846	(Vany´sek, 2018)
Ca	Ca^{+2}	1.584	(Vany´sek, 2018)
Fe	$Fe[OH]_4^-$	1.257	(Arnold et al., 2017)
H^+	H^+	5.273[a]	(Vany´sek, 2018)
H_2O	H_2O	2.299	(Mills, 1973)
Si	$H_2SiO_4^{-2}$	1.697	(Arnold et al., 2017)
K	K^+	1.957	(Vany´sek, 2018)
Mg	Mg^{+2}	1.412	(Vany´sek, 2018)
Na	Na^+	1.334	(Vany´sek, 2018)
PO	PO_4^{-3}	2.472	(Vany´sek, 2018)
SO	SO_4^{-2}	2.130	(Vany´sek, 2018)
e	e^-	2.130	—

NOTE: [a] D_i^0 of OH^- used because system is alkaline.

Tortuosity factors (τ), representing physical retention of constituents moving through a tortuous pore network, were calibrated for each material (rocks and cement samples) based on sodium, boron, and potassium eluate flux from Method 1315 results. The dependency of the effective diffusivity on tortuosity is described by

$$D_{i,eff} = D_i^0 \frac{\emptyset}{\tau^2} \qquad \text{Equation 4-1}$$

where $Di,_{eff}$ is the effective diffusivity ($m^2 \cdot sec^{-1}$) and $\emptyset$ is the porosity (fraction). Calibration was achieved by minimization of residuals between the simulated and measured values. Arithmetic residuals were calculated as

$$R = |\, y - \hat{y}| \qquad \textit{Equation 4-2}$$

where R is the residual, y is the observed value, and $\hat{y}$ is the predicted or modeled value.

4.2.8 Modeling Rock/Cement Interface

A one-dimensional (1D) LXO model (Figure 4-6b) was used to simulate the interface between carbonate rocks and cement. The model was set up with one interface (rock-cement) and 2-materials (limestone or marl and OPC paste). The chemical properties determined using EPA Method 1313 and the calibrated mineral reaction set were used to describe initial pore water and solids compositions of the limestone, marl, and OPC paste. Measured porosity and calibrated tortuosity were used to describe the physical properties of the solid materials. The model was set up assuming no flux at the external boundaries (only diffusion was allowed within the materials and across the interface) and 100% water saturation. The overall thickness of each material in the model was selected such that the boundary conditions would not affect results over the simulated time frame of 5 years. Greater material thicknesses will be used to simulate longer time intervals relevant to field conditions (e.g., up to 1,000 years). Appropriate material thickness for simulation was determined by introducing a conservative spike (NaCl) at the interface cells (first cell on each side of the interface) and monitoring the diffusion of the spike over the simulated time. The thicknesses of rocks and OPC paste in the interface models were set up to be 66 cm and 23 cm, respectively.

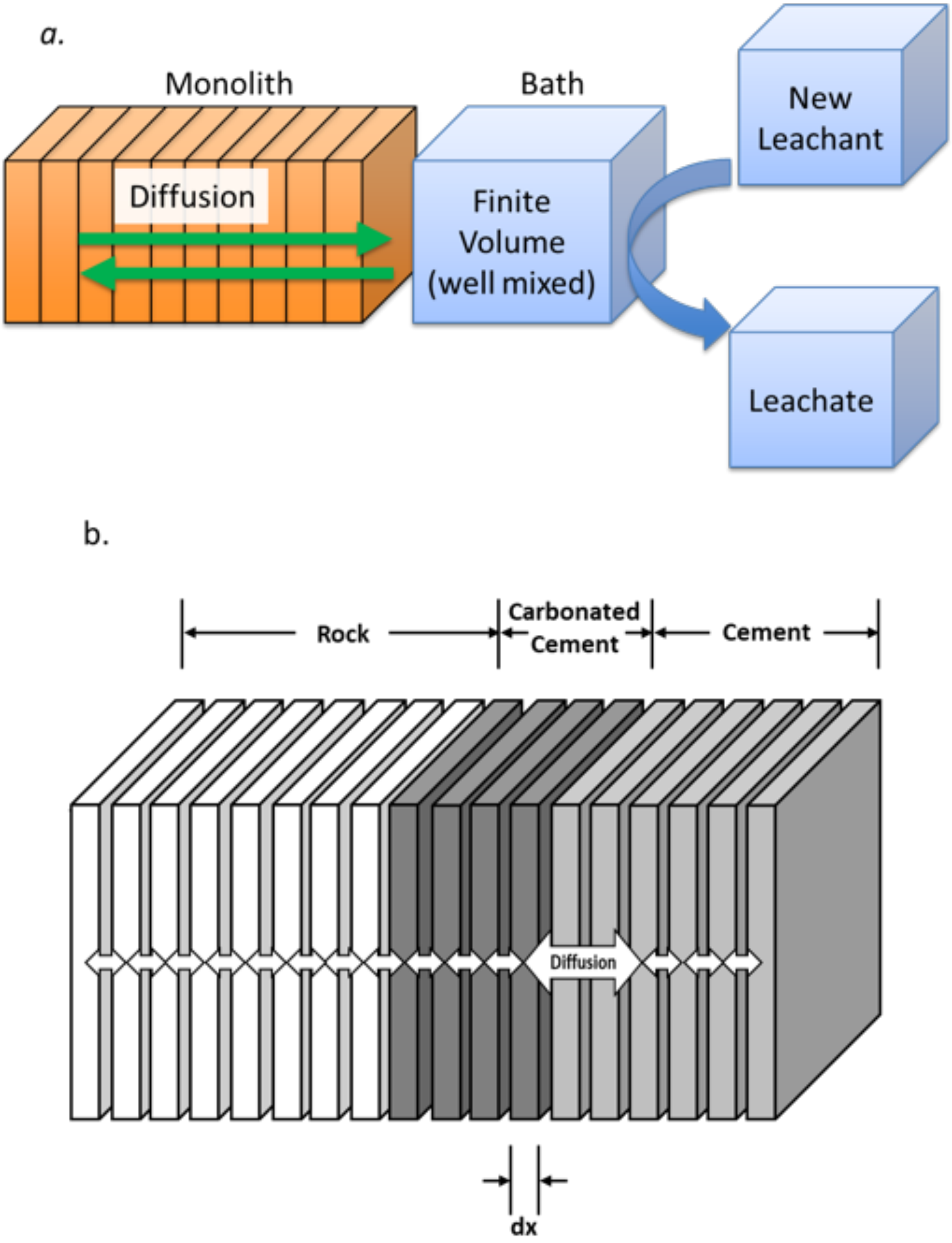

Figure 4-6. Conceptual models for (a) modeling EPA Method 1315 and (b) rock-cement interface

4.3 Results

4.3.1 Chemical Characterization of Limestone, Marl and OPC Paste Samples and Calibration of Mineral Reaction Set

Results from EPA Method 1313 pH-dependent leaching tests for limestone, marl, and OPC paste at L/S=10 mL/g dw were compared to the results at L/S=1 mL/g dw (Figure 4-3). The measured natural pH (no addition of acid or base) values for the limestone, marl, and OPC paste samples were the following: limestone—9.26 and 8.18, marl—8.82 and 7.86, and OPC paste—12.93 and 13.11, for L/S =10 mL/g dw and L/S=1 mL/g dw, respectively. For both the limestone and marl samples, the dominant solid phase is calcite, and the measured natural pH values reflect dissolved carbonate which buffers the solution pH to a slightly alkaline pH range (7.8–9.3). In contrast, the natural pH of the OPC paste sample is controlled by the formation of portlandite in the cement.

The solubility curves of various constituents from Method 1313 can be classified into two categories: reactive and conservative. Solubility curves of aluminum, calcium, magnesium, and silicon show a reactive behavior as a function of pH. The reactive pH dependency reflects the participation of these constitutes as reactants or products in reactions with solid material (one phase or more). The ability to predict the solubility of these constituents has a strong influence on the ability to predict pH during EPA Method 1315 tests (Section 4.3.3) and the interface simulations (Section 4.3.4). For the rock samples, the aluminum and silicon concentrations show a minimum solubility under slightly alkaline conditions, reflecting the low solubility of aluminum and silicon bearing phases like gibbsite, kaolinite, diaspore, and amorphous silica. Aluminum and silicon do not show a minimum for the OPC paste as they are both tied to major cement phases, such as C-S-H and ettringite that have low solubility under highly alkaline pH conditions (9–13).

The calcium LSP curve is very similar for the rocks and cement, mostly reflecting the solubility of calcite and portlandite as a function of pH. Under acidic conditions (pH<5), calcite is not stable and, therefore, calcium concentration is at a maximum. With the increase of pH, calcite is formed until the solutions' pH is in the range of 13. Above pH of 13, the solubility of portlandite is lower than of calcite and calcium is tied to portlandite. Unlike the limestone and marls samples where the pore water pH is strongly controlled by carbonate dissolved from calcite, the solid phases in cements like portlandite and C-S-H are highly sensitive to the pore water pH. Therefore, the reproducibility of the LSP curves by representing the solid materials with robust mineral reaction sets over the anticipated field pH domain as bounded by the two initial materials and potential external influences is crucial for a defensible predictive reactive-transport model.

Constituents that show a conservative behavior (not reactive) are potassium, sodium, and boron. These constituents were used to quantify the diffusion-controlled transport in the porous media as their leaching concentration is reasonably assumed to be solely dependent on the physical parameters of the solid materials (e.g., saturation, porosity, and tortuosity) and, therefore, used to calibrate the tortuosity of the solid materials (Section 4.3.2).

Using LXO, a set of minerals (i.e., mineral reaction set, Table 4-4) was selected to describe the LSP curves for the limestone, marl, and OPC paste both at L/S=10 mL/g dw and at L/S=1 mL/g dw (dashed lines in Figure 4-3). Then, an iterative process of changing the mineral reaction set was carried out to minimize the residuals between the predicted LSP at L/S=10 mL/g dw and the experimental data from EPA Method 1313 at L/S=10 mL/g dw. The comparison between the predicted LSP and experimental data at L/S=1 mL/g dw then was used to validate the ability of the mineral reaction set to describe the pore water composition under low L/S conditions.

For interface simulations, the union of the mineral reaction sets (rock and cement) was used as a single mineral reaction set. Then the union mineral reaction set was used to simulate the LSP of each one of the materials (limestone, marl, and OPC cement) to test if predicted LSP was affected. None of the predicted LSP curves was affected from using the union mineral reaction set.

4.3.2 Physical Characterization of Limestone, Marl, and OPC Paste Samples

The measured porosities of the limestone and marl samples are 6.8% and 31.7%, respectively. The measured porosities are within the typical reported range for these type of rocks (Bf Miglio, 2000; Cardoso and Alonso, 2009; Moshier, 1989). The porosity of the OPC paste was not measured and was assumed to be 15%, which is about the median value of typical a OPC paste porosity (Cui and Cahyadi, 2001; Li et al., 2006).

Results of EPA Method 1315—The results of EPA Method 1315, a mass transfer rate test for potassium, calcium, and pH, are shown in Figure 4-5. During the first 63 days of the test, potassium flux from limestone, marl, and OPC paste shows conservative constituent characteristics as its flux appears controlled by diffusion. The slopes of the log-flux with log-time are −0.6 for limestone, −0.5 for marl, and −0.6 for OPC paste. These values are very close to the theoretical slope (−0.5) expected from a diffusion-controlled process. Calcium shows slopes that are close to the theoretical slope of q diffusion-controlled process (−0.6 for limestone and marl during the first 63 days and for OPC paste between day 1 and 43); however, calcium is pH dependent and is partitioning between the liquid and the solid phases (mainly calcite, portlandite, C-S-H, and ettringite). Potassium, unlike calcium, is not incorporated into any of the solid phases and, therefore, can be used for tortuosity calibration. During the first 14 days of limestone and marl tests, the pH decreases (10.8 to ~10.5 and 10.6 to ~9.8 for the limestone and marl, respectively) and then it stabilizes until day 63. The decrease in pH can be a result of calcium calcite precipitation on the sample surface or near it. The refresh solutions that were introduced to the experimental tank were highly alkaline (10.8 in average), where under these pH conditions, the solubility of carbonate is higher than the solubility under the natural pH values of the limestone and marl samples. Mixed with the high calcium concentration of pore water, precipitation of calcium carbonate is possible that would decrease pH. After 14 days, the refresh intervals are long enough to allow the refresh solution to approach equilibrium with respect to solid calcium carbonate and atmospheric CO_2, and, therefore, the pH values stabilize until day 63 of the test. During the first 7 days of the OPC paste test, the pH increased from 11.2 to 12. The pH increase reflects dissolution of portlandite (one of the main components of OPC paste). During dissolution of portlandite, calcium and hydroxide are released to solution and as a result, the pH increases. After day 7, the contact time of the experimental solutions with the solid material is long enough for the experimental solution to approach equilibrium with respect to portlandite and, therefore, the solution's pH stabilizes at a higher pH value (~11.7).

Tortuosity Calibration—The diffusion of constituents in these materials and during EPA Method 1315 testing is strongly dependent on tortuosity (Equation 4-1). Unlike other porous media physical characteristics, measurement of tortuosity is not straightforward and dependent on measurement method and scale (Gaboreau et al., 2011; Steefel and Maher, 2009). Tortuosity calibration using a relatively large sample allows avoiding microscale heterogeneities that may affect the measured tortuosity using MIP, SEM, or micro-CT methods, which focus on a relatively small volume unit of porous material. Moreover, tortuosity that is calibrated using measured diffusion fluxes accounts for variations in diffusion rates that are not observed using scanning instruments, for example, intraparticle routes (Schaefer et al., 1995).

Potassium was used as a conservative constituent for calibrating tortuosity by fitting the predicted potassium flux calculated using the LXO model to the measured flux from EPA Method 1315 test (Figure 4-5). The flux of a conservative constituent under the experimental conditions is dependent on concentration gradients, porosity and tortuosity. As the initial concentration gradients are known from EPA Method 1313 and porosity, is measured, the fitting of the modeled flux to the experimental dataset can be done solely by changing tortuosity values until the best fit is achieved. The fitting was done for the time intervals where the flux of potassium was diffusion controlled. Potassium flux is controlled by surface effects during the first days of the tests (as a result of fractures near surface and higher porosity of surface layer as from the sample preparation process). To get good agreement between the model predictions and experimental data at the first day of EPA method 1315 tests, it was necessary to increase the porosity and decrease the tortuosity of the top cells (i.e., those close to solution/surface contact) for each of the models. The change was in the upper 2.4 mm for limestone, 1 mm for marl, and 2.5 mm for OPC paste compared to about 26 mm in total for the samples. The calibrated internal tortuosity values are 10 for both limestone and marl and 30 for OPC paste. The reported values for sedimentary carbonate rocks are within the range of 3 to 100 (Boving and Grathwohl, 2001). Lower tortuosity values reflect more highly fractured rock with lower resistance for diffusion. The high tortuosity values are for rocks without a primary fracture network. Tortuosity values range for OPC cements varies between 30 and 80 (Branch, 2018).

4.3.3 Validation of Mineral Reaction Set and Tortuosity Calibrations

While the calibrations of mineral reaction sets and tortuosity values are independent of each other, the ultimate goal is to combine them together to predict the concentrations and fluxes of constituents that are controlled by both diffusion and chemical reactions within the porous solids. The ability to predict independent datasets (e.g., fluxes of nonconservative constituents) that have not been used for calibration is crucial for validating the calibration. Calcium and pH are highly sensitive for both diffusion and chemical reactions process and, therefore, were selected for validation purposes. For the rock samples, the concentration of calcium and pH are primarily controlled by dissolution and precipitation of calcium carbonate. On the other hand, C-S-H, portlandite, and ettringite are the solid phases that control the concentration of calcium and pH at equilibrium. Using the calibrated mineral reaction set and tortuosity values, the LXO model was used to predict the flux of calcium and pH during EPA Method 1315 tests (Figure 4-5, blue line). For all three materials, the model successfully predicted the flux of calcium during the entire tests and followed the same trends as the experimental data. The greatest deviation of the predicted flux from experimental is less than 50%, Despite of the test time span and several orders of magnitude change in fluxes during the tests. Moreover, except for a single data point in each dataset, the model predicted the pH during the entire tests within 0.2 pH units range from the measured pH of the experimental solution.

4.3.4 Rock/Cement Interfaces

The results of interface simulations (limestone/OPC paste and marl/OPC paste) are shown in Figure 4-7 and Figure 4-8, respectively. For both interfaces, after a simulated time of 5 years, most of the change in the phase distributions occurred in calcium bearing phases and, therefore, only the calcium-bearing phases are shown in Figure 4-7 and Figure 4-8. The dominant calcium-bearing phase(s) in both rocks is calcite (100%) and in the OPC paste are portlandite (60%), C-S-H phases (20%), and ettringite (20%).

After 5 years of simulated limestone/OPC paste interface, ~1 mm of OPC paste was altered as a result of chemical interactions. The relative amount of portlandite was slightly depleted (3%) compared to the initial amount in cement. On the other hand, C-S-H phases show mixed changes. While C3AS0.41H5.18 was depleted by more than 20%, CNASH was increased by 13%. The relative amount of ettringite increased by 13%. The process of portlandite depletion accompanied with C-S-H phase changes represents the onset of cement carbonation. While the solid phases in the cement were altered, no significant changes in solid phase compositions were observed in the limestone. For this study, the diffusion distance of the NaCl tracer is defined as 90% reduction compared to the initial concentration at the interface. In 5 years the diffusion distance of Cl^{-} was 16 cm and 3 cm into the rock and cement, respectively. During the simulation, limestone pore water pH changed significantly up to 20 cm from the interface and increased from 9.26 (natural value) to ~12.5 at the interface. However, the pH in the cement pore water did not decrease dramatically and changed about 0.2 pH units 6 cm from the interface and the pH at the interface changed from 13 to ~12.5.

After 5 years of simulated marl/OPC paste interface, 4.5 mm of OPC paste was fully carbonated. Extensive calcite formation filled the altered zone up to 92% of the total calcium bearing phases.

Portlandite, C-S-H phases, and ettringite were completely depleted. Formation of ordered dolomite ties down the rest of the calcium in the carbonated cement. Like the limestone, the solids phases in the marl were not significantly impacted by the interaction with the cement. In 5 years the diffusion distance of Cl^- was 2 cm and 3 cm into the rock and cement, respectively. After 5 years, marl pore water pH changed slightly up to 25 cm from the interface and increased from 8.82 (natural value) to ~8.9 at the interface. However, the pH in the cement pore water changed dramatically up to 7 cm from the interface. The pore water pH at the interface changed from 13 to ~8.9.

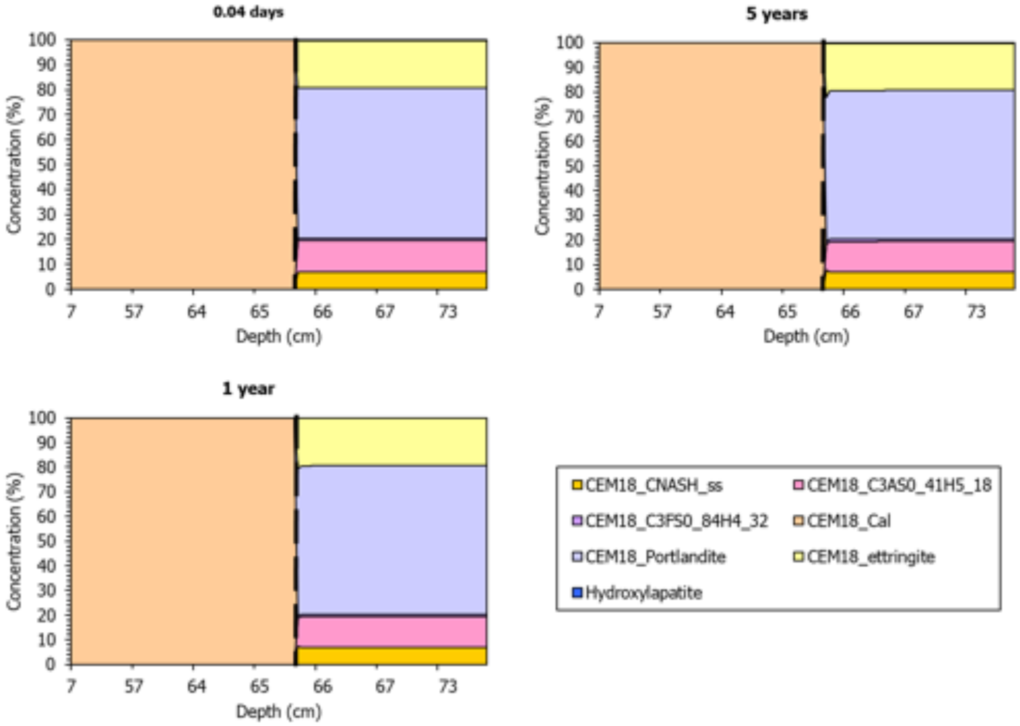

Figure 4-7. Distribution of calcium-bearing phases during limestone/OPC paste simulation. Vertical black dashed line represents the initial location of the interface at the beginning of the simulation. On the left side of the interface is the rock and on the right is the cement.

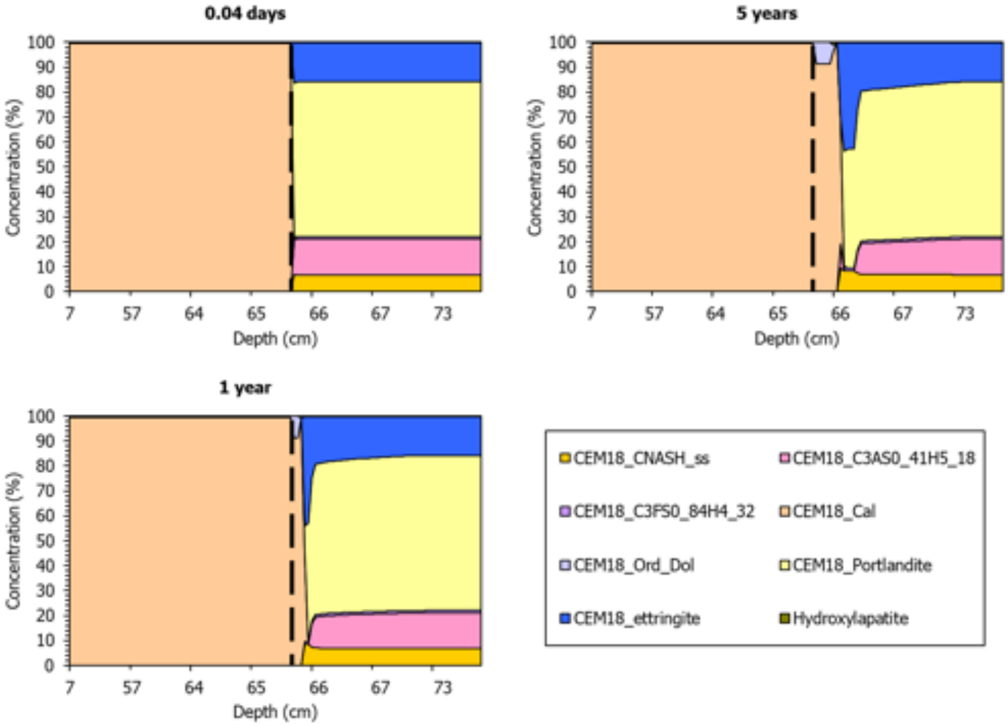

Figure 4-8. Distribution of calcium-bearing phases during marl/OPC paste simulation. Vertical black dashed line represents the initial location of the interface at the beginning of the simulation. On the left side of the interface is the rock and on the right is the cement.

4.4 Discussion

4.4.1 Limestone Versus Marl

The carbonation front advanced from the interface 1 mm in 5 years when the rock was limestone compared to 4.5 mm for marl. Regardless of the difference in predicted carbonation depths, the overall redistribution of calcium bearing phases is nearly the same. In both scenarios, calcite precipitation replaced cementitious phases (portlandite, C-S-H, and ettringite). However, in the marl/OPC paste scenario, the maximum depth of calcite precipitation was significantly deeper (4.5 mm), where in the case of limestone it was closer to the interface (~1 mm). Within the carbonated layer in the limestone/OPC paste scenario, the cementitious phases were slightly depleted and still dominated the carbonated cement layer. In contrast, after 5 years of interaction with marl, most of the OPC paste carbonated layer was depleted of cementitious phases that were replaced with calcite and dolomite. Dolomite formed in the simulation with marl and not with limestone. While the available content of magnesium is similar for both rocks, it is most likely that the formation of dolomite in the limestone scenario happens after longer interaction periods with the OPC paste. As the available content of calcium, magnesium, and carbonate of the two rocks are very similar (Table 4-3), it is reasonable that the results of marl/OPC paste interface scenario are a reflection of advanced carbonation that may happen to the OPC paste after longer interaction periods with the limestone. Moreover, the differences between the two interfaces long-term performances are likely due to physical differences between the two rocks and not chemical differences.

4.4.2 Carbonation Depth as a Function of Porosity/Tortuosity Ratio

The main differences between the physical parameters of limestone and marl are in porosity and calibrated tortuosity. Together, these parameters control the fluxes of constituents through diffusion across the interface. As the cement pore water is relatively enriched in calcium, the thickness of the carbonated cement layer may be controlled by bicarbonate flux from the rock's pore water to the cement's pore water. Constituent fluxes are controlled by (1) the ratio of porosity to tortuosity ($\emptyset/\boldsymbol{\tau}^2$) and (2) concentration gradients. For both interfaces, the concentration of bicarbonate in the rock's pore water is six orders of magnitude greater than in the cement and about 40% higher in the limestone pore water compared to the marl pore water. Thus, the concentration gradient cannot account for most of the difference in thickness of the carbonate layer between the two interfaces. As both concentration gradients are steep, the resistance ($\emptyset/\boldsymbol{\tau}^2$) of the carbonate rock to bicarbonate diffusion can account for differences in the flux. The value of $\emptyset/\boldsymbol{\tau}^2$ is about 4.6 times greater for the marl than the limestone (0.0032 compared to 0.0007). The factor of 4.6 is almost the ratio between the thicknesses of the two carbonated layers (4.5). The relative ratios of $\emptyset/\boldsymbol{\tau}^2$ factors can account for most of the difference between the two rock-cement interface results.

As the carbonation layer thickness is almost independent of the chemical composition of the carbonate rock, it is possible to use the ratio of porosity to tortuosity ($\emptyset/\boldsymbol{\tau}^2$) to estimate the extent of the carbonated layer in other carbonate rich rocks and OPC paste interface. Other common carbonate rocks are chalk, oil shale and phosphorite. Assuming typical porosity values for the rock (40%, 33%, and 353 for chalk, oil shale, and phosphorite, respectively) and tortuosity of 10, the thickness of the carbonated cement layer will be after 5 years of interaction 6 mm, 5 mm, and 5 mm for chalk, oil shale, and phosphorite respectively. These estimates will be independently confirmed through experiments and simulations as described for the limestone-cement and marl-cement cases described here.

4.4.3 Preliminary Long-Term Estimates of OPC Paste

The propagation of the cement carbonation front as a function of time can be described using a mechanistic model of Papadakis and Fardis that considers mass transport, cement chemistry, and reaction kinetics (Papadakis et al., 1989). The aforementioned mechanistic model is complex, but it can be simplified to represent carbonation as a sharp moving front. A simple analytical expression for the location, X_C (m), of the moving carbonation front as a function of cement composition and conditions, when the relative humidity is above 50%, is (Papadakis et al., 1989):

$$X_c = A\sqrt{t} \qquad \text{Equation 4-3}$$

where A is the proportionality constant and t is time. The linear trend of the carbonation front in Figure 4-9a was fitted using Equation 4-3. The proportionality constants for marl and limestone were estimated by a "minimum least squares" linear regression, using the LINEST function of Microsoft® Office Excel. The A parameter was found to be 16 and 2 (mm $\mathrm{yr}^{-0.5}$) for the marl and limestone, respectively. Using the fitted A and Equation 4-3, it is possible to estimate the location of carbonation front as a function of time (Figure 4-9b). After 100 and 1,000 years, the carbonation front within the cement will be 166 mm and 507 mm from the initial location of the interface between marl and the OPC paste and for limestone OPC paste interface the carbonation front will be 17 mm and 63 mm after 100 and 1000 years, respectively.

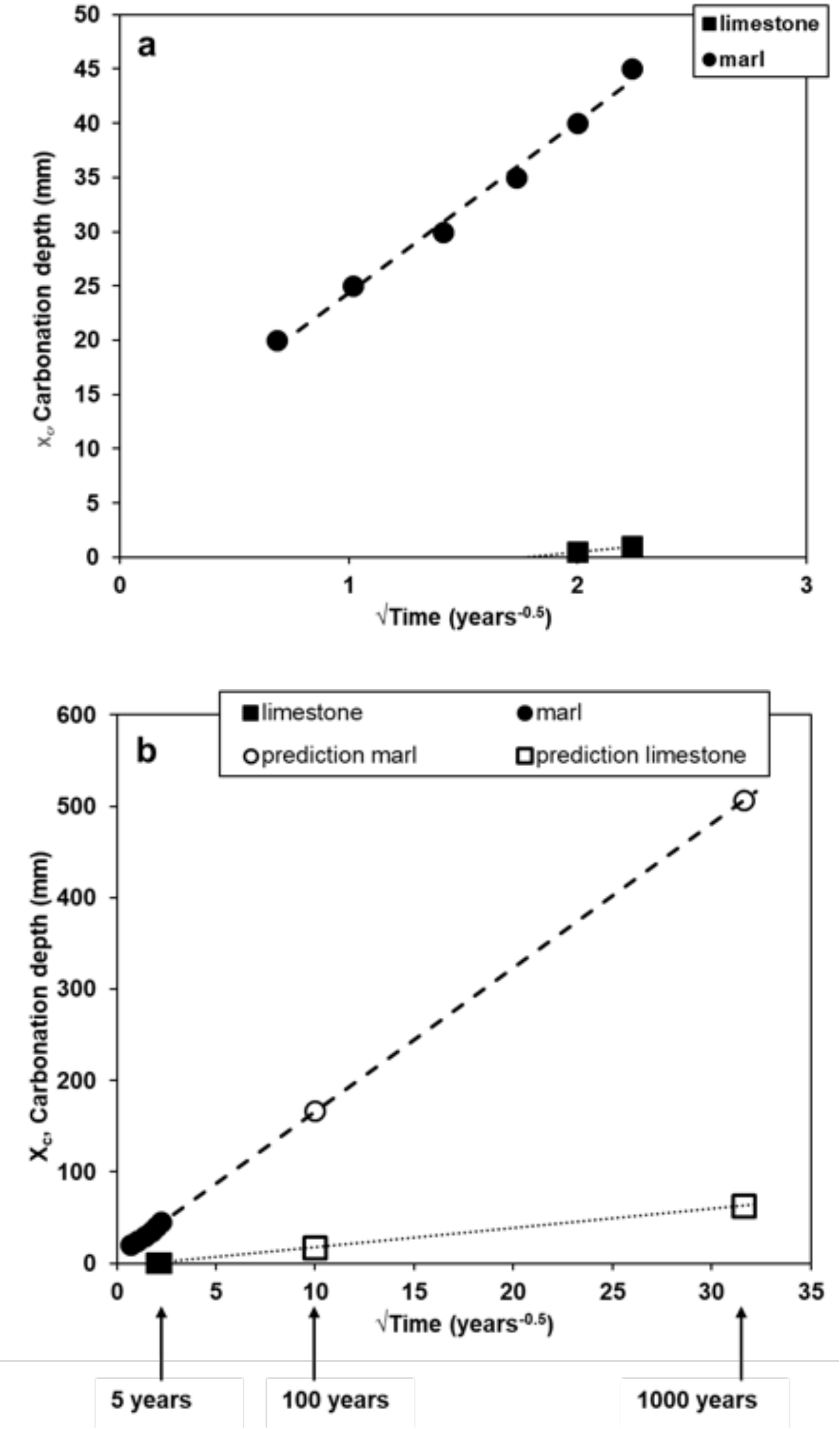

Figure 4-9. (a) The location (X_C) of carbonation front as a function of square root of time. The lines are fitting lines based on Equation 4-3 to the carbonation results from the LXO model. (b) extrapolation of Equation 4-3 to estimate carbonation depths after 100 and 1,000 years.

4.5 Summary and Future Work

The present work demonstrates how the integration of laboratory characterization methods with reactive transport simulations (LXO) as a set of tools allows assessment of the performance of interfaces between two materials with chemical and physical gradients over long periods of time. Moreover, the present work shows how this set of tools can be used for performance assessment of carbonate rocks and OPC paste interfaces. Based on simulation results, it was possible to determine what are likely to be the key parameters for best cement integrity when in contact with carbonate rocks. The porosity to tortuosity ratio ($\emptyset/\boldsymbol{\tau}^2$) was found to control the thickness of the carbonated cement layers, as the thickness of carbonated layers after a given time interval were proportional to $\emptyset/\boldsymbol{\tau}^2$ ratio between the two rocks. When choosing a geological formation for geological disposal site, it is recommended to choose a target formation with the lowest $\emptyset/\boldsymbol{\tau}^2$ available. However, macro scale features in the rock, such as fractures and karst were not considered, and when they exist in the host rock they potentially can dominate bicarbonate and other constituent fluxes from the rock to cement and vice versa.

Based on simulation results, a dependency of carbonation front location on time was found. Using this relationship, preliminary estimates of carbonation depth for OPC paste were estimated for 100 and 1,000 years when in contact with limestone and marl. It was found that after 1000 years, carbonation depth for marl/OPC cement is about an order of magnitude deeper than for limestone/OPC paste interface (507 mm compared 63 mm).

The findings of this work are not limited to engineered barriers used in geological waste disposal sites but may also be useful for assessing the long-term performance of cements used in wellbores for oil/gas and geological carbon sequestration. The latter is often planned to store and seal carbon dioxide for thousands of years. The findings of the present work may help in designing the appropriate cements for wellbore as well as choosing subsurface areas with geological formation with minimal degradation effect on sealing cements.

Future work on simulations will be used for long-term behavior estimates. Simulations will include (1) interfaces of other typical carbonate rocks such as chalk, oil shale, and phosphorite with OPC paste cement and low pH cement; (2) the geochemical speciation and transport of radionuclide simulants; (3) the effect of organic material content on interface integrity and the partitioning and transport of radionuclide simulants; and (4) unsaturated reaction, moisture transport, and temperature variations.

In parallel with simulations, interface experiments of carbonate rocks with cements are being carried out in the laboratory. Samples from these experiments are in early stages of chemical and physical characterization. Characterization methods include (1) interface characterization using laser ablation inductively coupled plasma mass spectrometry (LA-ICP-MS), SEM energy-dispersive X-ray spectroscopy (EDS), and micro-CT and (2) nano indentation to measure changes in material mechanical properties as a result of interface reactions.

5. HYDROTHERMAL EXPERIMENTS

5.1 Introduction

The United States Department of Energy's Spent Fuel and Waste Disposition (SFWD) program is investigating the design and safety function of generic nuclear geologic repositories in a variety of geologic settings (salt, argillite, and crystalline rock). The U.S. DOE is also interested in exploring options for the direct disposal of dual-purpose canisters (DPCs), which are large waste canisters designed for storage and transportation of spent nuclear fuel and waste. Directly disposing of as-loaded DPCs has benefits, including the reduction of potential worker dose and costs related to waste repackaging, as well as disadvantages, including significant increases in repository ventilation time and/or peak temperatures (e.g., Hardin et al., 2015).

The work presented here develops concepts related to mineral and geochemical changes that may occur in the near field of high temperature for a nuclear waste repository hosted in crystalline rock. Repository designs in crystalline rock typically include nuclear waste encapsulated in a metal canister, surrounded by bentonite blocks, which is emplaced in an excavated drift lined with cementitious materials (Figure 5-1). These components all have favorable properties related to repository function to isolate radionuclides under ambient temperature conditions. With heat generated from the decay of spent nuclear fuel and the infiltration of natural groundwaters, interactions between the EBS components will likely occur that may affect the long-term performance and safety of the repository system (e.g., Nutt et al., 2011; Jove-Colon et al., 2011). Several foreign repository programs are exploring concepts related to disposal of spent nuclear fuel (e.g., Japan, Canada, Finland, Switzerland, Sweden, and Korea). Sweden and Finland in particular have selected disposal sites in variably metamorphosed granitic rock (Forsmark and Olkiluto, respectively). Full-scale EBS demonstrations in crystalline rock have been conducted and are ongoing, for example, at the Grimsel Test Site in Switzerland (FEBEX, HotBENT) and Äspö URL (Sweden).

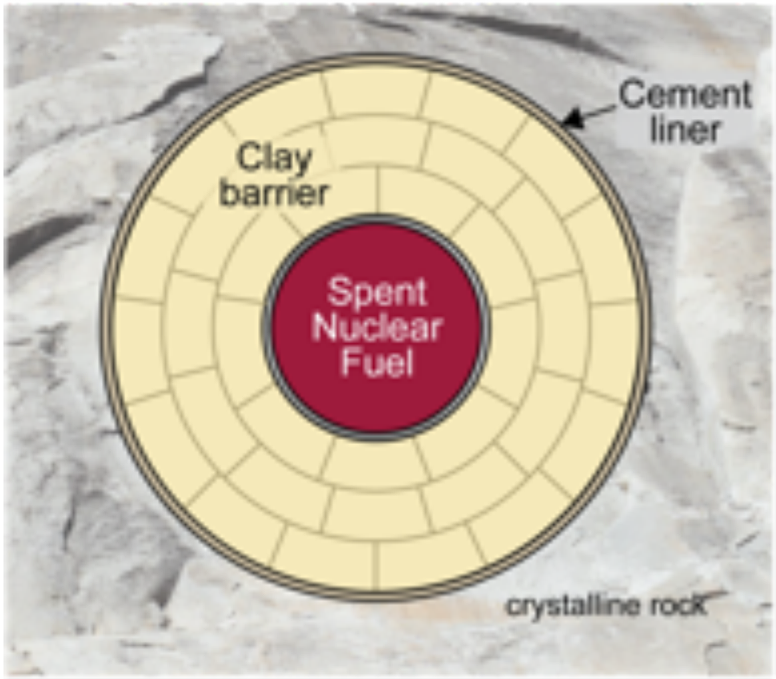

Figure 5-1. Schematic of a generic EBS concept in crystalline host rock. Bentonite blocks surround a waste canister (approximate diameter = 1 m) emplaced in a horizontal tunnel lined with cement.

Our experimental program uses core samples of granodiorite from the Grimsel Test Site, a well-characterized lithology, to mimic a generic crystalline rock environment. One experiment was completed in FY20, with several others in planning, due to the COVID-19 pause in laboratory work. This report will present the results from our research program for FY20, which characterized 1) how EBS components (stainless/low carbon steel, Wyoming bentonite, OPC) react and change in the presence of Grimsel granodiorite wall rock and synthetic Grimsel granodiorite groundwater and 2) steel-bentonite interface mineralogy at high temperature and pressure (250°C, 150 bar) in-situ repository conditions.

5.1.1 Background

5.1.1.1 EBS Concepts in Crystalline Rock

The EBS in crystalline rock consists of the waste canister overpack, bentonite buffer, cement liner, and host rock (Figure 5-1), similar to designs for argillite-hosted repositories. Crystalline rock has many favorable characteristics that contribute to waste package longevity, including stability of excavated tunnels, favorable (i.e., reducing) chemical conditions, and low porosity/groundwater fluxes (e.g., Andersson et al., 2013). Unique concerns for repositories hosted in crystalline rock are related to the physical properties of the host rock, which allow for the sustained presence of natural and manmade fractures. Interconnected networks of fractures can create pathways for radionuclide transport away from the repository near field (e.g., Figueiredo et al., 2016); therefore, the waste canister overpack and bentonite buffer are relied on for radionuclide retention for long term repository function (e.g., Mariner et al., 2011).

Colloid-mediated transport of radionuclides has been identified as a possible concern for crystalline rock hosted repository systems. Colloids, 1 to 1000 nm suspended particles, are present in natural groundwaters and can be formed from bentonite erosion. The hydraulic conductivity of the bentonite buffer when fully saturated is expected to be sufficiently low to prevent transport of radionuclides away from the canister and colloids are expected to be filtered by the low porosity of the bentonite (Missana and Geckis, 2006). However, bentonite colloid formation at the outer edge of the EBS, adjacent to the host rock, and in contact with a fracture or flow pathway, may lead to transport of radionuclides away from the repository near field (Figure 5-2; Missana et al., 2003; Möri et al., 2003; Missana and Geckis, 2006). Therefore, colloid-facilitated transport must be considered in assessments of crystalline-rock hosted repository systems and has been examined in experiments at URL sites (e.g., Möri et al., 2003; Missana and Geckis, 2006; Kurosawa et al., 2006; Reimus, 2012) and laboratory scale experiments (Missana et al., 2008; Dittrich et al., 2015; Telfeyan et al., 2020).

Crystalline rock repository concepts have been evaluated in long-term, full-scale, in-situ demonstrations at underground research facilities and laboratory experiments, mostly at temperatures <100°C. Foreign repository programs have extensively vetted repository designs, especially Sweden and Finland who have each submitted license applications for repository operations in crystalline rock. Buffer temperature limits in these cases are 100°C. The FEBEX heater test at the Grimsel Test Site was an 18-year long full-scale EBS demonstration in crystalline rock, which included a heater that maintained a temperature of 100°C at the dummy canister surface. In the FEBEX experiment, smectite alteration was only observed close to the heater surface (~10 cm) and included recrystallization to saponite and chlorite, accumulation of magnesium near the heater, and decrease in clay mineral cation exchange capacity and surface area (Fernández et al., 2018).

To address the temperatures involved with the disposal of DPCs, there is a need for higher-temperature, full-scale experiments to characterize the changes in bentonite physical and chemical properties. The planned HotBENT (High Temperature Effects on Bentonite) experiment performed by NAGRA at the Grimsel Test Site in the same drift as the FEBEX experiment, is in its initial stages and was scheduled to begin in the spring of 2020. The experiment will run for 15 to 20 years and will be dismantled over five years (AMBERG, 2019). The peak temperatures will be between 175°C to 200°C. Results will be very useful for evaluating potential alterations to bentonite mineralogy and physical properties in a high temperature crystalline rock repository setting.

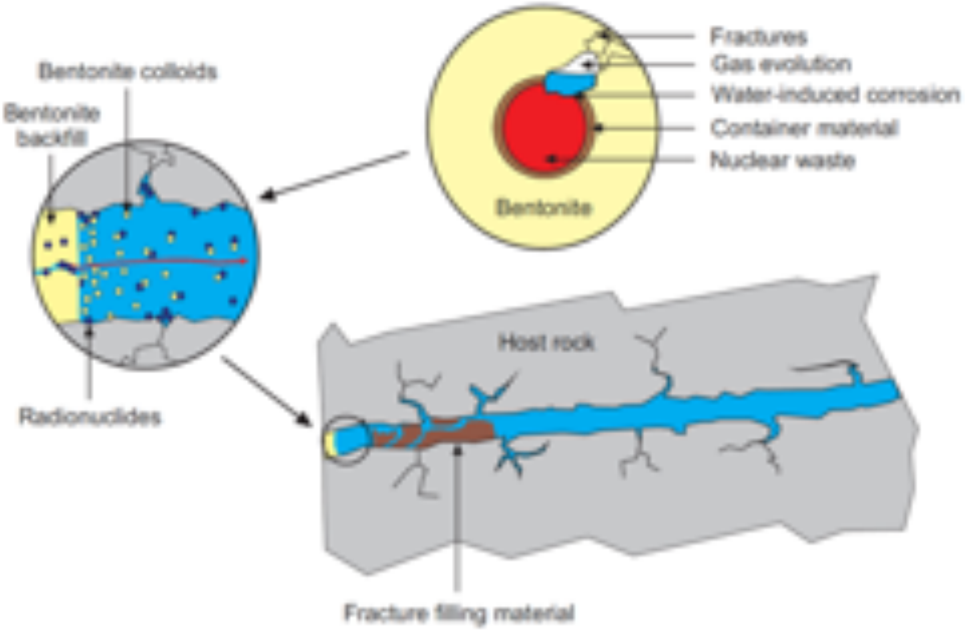

Source: Missana and Geckeis 2006.

Figure 5-2. Possible scenario for bentonite-colloid facilitated transport of radionuclides away from a corroded waste package. Waste package breach coincides with fracture formation in the bentonite buffer and the formation of bentonite colloids at the buffer-host rock interface. Radionuclides sorbed to colloids are transported away from the EBS via fractures in the host rock.

5.1.1.2 Previous research in bentonite–Portland cement interaction

There have been many studies on the interaction of bentonite and cementitious materials in EBS systems as both materials are integral to most repository designs (e.g., Karnland, 1997; Cuevas et al., 2006; Savage et al., 2007; Watson et al., 2009; Fernández et al., 2009; Savage et al., 2010; Watson et al., 2018). Cementitious materials, such as shotcrete, cast-in-place, and/or pre-formed cement blocks, are necessary elements of repository infrastructure and provide ground support to maintain drift integrity and prevent collapse. However, the reaction of cement with water may have a significant chemical effect on the repository system through the dissolution of portlandite ($Ca(OH)_2$), alkali-rich phases, calcium silicate hydrate (CSH) minerals, and other reactive components of the cement (e.g., sulfates). Thus, cement reactions have the potential to release significant amounts of OH^- and Ca^{2+} into the groundwater migrating into the EBS system, leading to increase in pore water pH in the bentonite buffer, montmorillonite dissolution, and the formation of diverse secondary mineral phases (e.g., Ca-zeolites, CSH phases, feldspars). Cement-bentonite interaction is observed to be a non-linear system that involves multiple coupled processes that occur simultaneously and affect each other (e.g., Savage et al., 2007). These processes include the reaction of concrete to release Ca^{2+} and OH^-, transport of hydroxide and cations into bentonite, montmorillonite ion exchange and dissolution, precipitation of secondary phases, dissolution of accessory minerals, and porosity and swelling changes (Savage et al., 2007).

The potential for significant and wide-ranging geochemical and mineralogical effects of bentonite-cement interaction has led repository programs to implement a pH limit for cement porewater (e.g., SKB, pH < 11). The pH limit is achievable using low pH cements that replace traditional cement components (e.g., limestone aggregate) with siliceous materials (e.g. fly ash and silica fume) resulting in the reduced abundance of portlandite in the cured product and a lower Ca/Si ratio in the CSH minerals (Calvo et al., 2010; Lothenbach et al., 2011). Due to the potential for bentonite degradation in alkaline pore waters, low pH cement formulations are becoming increasingly standard for repository concepts. The experimental work presented in this report focuses on the effects of cured OPC; next phases will evolve to include low pH formulations.

Observations from long-term, full-scale, in-situ demonstrations at underground research facilities provide insight into cement-bentonite interactions in the natural environment, including potential effects on groundwater geochemistry, host-rock properties, and hydrologic processes. Several full-scale experimental studies at underground research laboratories (URLs) in crystalline rock have been conducted, including the prototype repository at the Äspö Hard Rock Laboratory in Sweden (Johannesson et al., 2007) and FEBEX at the Grimsel Test Site (Martin et al., 2006). Observations of cement-bentonite interaction after 13 years in the FEBEX demonstration are reported in Alonso et al. (2017) and Fernández et al. (2017). The FEBEX experiment consisted of a heater that was held at 100°C resulting in an observed maximum temperature of 28°C in the concrete liner (Martinez et al., 2016). Therefore, the observed alteration was likely due only to water-rock interaction, and not temperature effects. Important observations, reported in Alonso et al. (2017) and Fernández et al. (2017), include that both the shotcrete plug and bentonite experienced alteration due to groundwater interaction. In the concrete, portlandite dissolution occurred at the host rock-concrete interface and CSH phases in the concrete were altered due to the incorporation of aluminum, sulfur, and magnesium. At the bentonite-concrete interface, the main alteration mineral observed was ettringite ($Ca_6Al_2(SO_4)_3(OH)\cdot 26\ H_2O$), indicating that the breakdown of sulfur-rich phases in the bentonite, concrete, and/or sulfur sourced from the groundwater resulted in mineral precipitation (Alonso et al., 2017). In the bentonite, alteration was mostly limited to the immediate interface zone, mostly in the form of precipitation of Mg-rich phases and the change in exchangeable cations in the bentonite (Fernández et al., 2017). These results highlight the potential for alteration at the cement-bentonite interface at ambient temperatures in a realistic crystalline rock repository scenario.

5.1.1.3 Steel Canister-Clay Interface Zone Alteration in a Crystalline-Hosted Repository

As discussed above, the U.S. DOE is interested in exploring the disposal of larger waste packages with higher thermal loads. The large amount of spent nuclear fuel in the waste packages, therefore, has the potential to generate temperatures at the waste package surface in excess of 200°C for long periods of time. The interface between the metal canister and the bentonite barrier in a backfilled repository EBS concept will likely undergo chemical reactions due to the elevated temperatures and infiltration of groundwater. The effect of these high thermal loads and the presence of an aqueous fluid will produce corrosion of the surface of the metal canister, and likely mineral reactions between the steel corrosion products and the bentonite in close proximity to the canister.

This report focuses on the interaction of the EBS and candidate steel overpack materials in a crystalline rock environment. Design concepts for a crystalline rock repository in the United States are still being explored, but the current base case in crystalline rock includes stainless and carbon steel (Matteo et al., 2016). In comparison, all foreign repository designs in crystalline rock include a copper waste package overpack with cast iron inserts to maintain canister structure. Crystalline rock is thought to be a less robust natural barrier in comparison to other host rock lithologies, such as clay and salt. Therefore, in crystalline rock, the waste package is relied on as the primary mechanism to prevent radionuclide release. Copper is selected in repository designs developed by foreign countries due to its corrosion-resistant nature under anoxic conditions, and is thought to provide a long-term barrier. Copper, however, will be susceptible to corrosion due to chloride and sulfide, which must be accounted for in the groundwater, EBS, and host rock.

5.1.1.4 Formation of the Fe-Oxide Layer on Steel

The steel will corrode at the bentonite buffer interface in the presence of oxygen according to one of the following reactions (aerobic corrosion) (Kursten et al., 2004):

$$4\ Fe^{o} + 3\ O_2 \rightarrow 2\ Fe_2O_3 \qquad \textit{Equation 5-1}$$

$$2\ Fe + 2\ H_2O + O_2 \rightarrow 2\ Fe(OH)_2 \qquad \textit{Equation 5-2}$$

The corrosive reaction (Equation 5-2) can be fairly fast for carbon steel, whereas corrosion can be slowed for stainless steels by an oxide film (i.e., Fe-oxide). The oxide film will act as a protective coating against further corrosion in the effect called passivation. In an alkali solution where a porous $Fe(OH)_2$ develops, a passive layer may not form, but $Fe(OH)_2$ may still decrease the corrosion rate (Kursten et al., 2004). Therefore, stainless steel and carbon steel are protected against corrosion by the presence of a thin "passive" layer in environments with cement that are highly alkaline conditions (Kursten et al., 2004).

Oxide passive films can break down at lower pHs and/or by reactions with aggressive species, e.g., chlorides (Kursten et al., 2004). The passive film overlaying carbon steel can more easily be broken down by chloride corrosion than on stainless steel. Carbon steel, therefore, tends to suffer for general/uniform corrosion, whereas stainless steel tends to be highly localized (i.e. pitting corrosion, stress corrosion) (Smart et al., 2004).

Previous laboratory studies (25°C–100°C) have shown the formations of the Fe-oxide layer at the steel-bentonite interface (i.e. Álvarez et al., 2008; Bourdelle et al., 2014; Kursten et al., 1996; 1997; Pignatelli et al., 2014; Smailos et al., 1997). A range of different Fe-oxide/hydroxides are observed to precipitate on the steel surface in the laboratory experiments, dependent on experimental conditions. The main corrosion products observed are magnetite (Fe_3O_4) and goethite ($FeO(OH)$) in experiments below 100°C, with hematite (Fe_2O_3) occurring in the experiments at 100°C.

5.1.1.5 Mineral Reactions at Steel-Bentonite Interface

The interface of the waste canister overpack and the EBS represents a chemical boundary at which material interactions may affect bentonite properties and the canister surface (e.g., Gaudin et al., 2013; Wilson et al., 2006a,b). After initial repository closure and when the boundary is experiencing the thermal peak, this boundary will likely be dry. Under dry conditions, bentonite mineralogy will likely be stable (e.g., Wersin et al., 2007) and corrosion will be minimal. However, the saturation of the bentonite buffer will occur over time due to the infiltration of groundwater, leading to: canister corrosion, potential alteration of the bentonite, and reactions between corrosion products and the bentonite.

The assessment of the interactions occurring at the steel-bentonite interface is important to consider in the evaluation of the long-term repository function for waste isolation. For example, iron mobilized by corrosion of the steel canister may affect the properties of the bentonite. In the event of a canister failure, significant changes in the bentonite immediately adjacent to the breached area (i.e., the steel-bentonite interface) will affect the movement of radionuclides and the sealing properties of the bentonite. Higher temperatures at the clay/canister interface may cause a local increase in Fe-activity and dissolved SiO_2. The resulting chemical gradient causes migration of dissolved species radially away from the canister towards the colder rock, potentially leading to the silicification throughout the buffer during the cooling phase (Pusch and Madsen, 1995; Svemar, 2005).

Interaction of carbon steel and bentonite was examined in the 18-year FEBEX full-scale EBS heater test at the Grimsel Test Site (Martin et al., 2006). Metal corrosion and chemical changes in bentonite chemistry at the buffer-steel interface occurred and is described in Kober et al. (2017) and Hadi et al. (2019). The bentonite in contact with steel examined by Hadi et al. (2019) likely was heated to temperatures of 30°C to 60°C. They observe that corrosion of carbon steel leads to a >140 mm layered zone of iron enrichment extending radially into the bentonite. In the ~30 mm closest to the canister, iron is hosted in newly formed goethite ($Fe^{3+}O(OH)$) within the bentonite. The remainder of the Fe-enriched zone is interpreted to be a result of the diffusion and sorption to the clay mineral edge site of Fe^{2+} (Hadi et al., 2019). This layering is interpreted to be related to the initial diffusion of Fe^{3+} during oxidizing conditions, followed by diffusion of Fe^{2+} when oxygen becomes depleted. Clay mineral alteration was not observed, likely due to the low temperatures achieved.

High-temperature, full-scale experiments are needed to characterize the steel-bentonite interface evolution under conditions relevant to DPC disposal. HotBENT (High Temperature Effects on Bentonite), an experiment conducted by NAGRA in the same drift as the FEBEX experiment, is in its initial stages and was scheduled to begin in the spring of 2020. The experiment will run for 15 to 20 years and will be dismantled over five years (AMBERG, 2019). The peak temperatures will be between 175°C to 200°C. Results will be very applicable to understanding steel-bentonite interaction in a crystalline rock repository setting.

Lab-scale experiments, in comparison to full-scale demonstrations, lack the long timeframes, realistic scales, and water/rock and clay/steel ratios that are unique to in-situ experiments, such as FEBEX (described above), but can provide insight to potential reaction pathways at higher temperatures. To date, many lab-scale experiments have been completed on the interaction of clay minerals/bentonite with steel/Fe-oxide/native iron at temperatures between 25°C and 300°C (e.g., Lantenois, 2003; Perronnet, 2004; Lantenois et al., 2005; Cathelineau et al., 2005; Wersin et al., 2008; Mosser-Ruck et al., 2010; Pignatelli et al., 2013; Bradbury et al., 2014; Kaufhold et al., 2015; Bourdelle et al., 2014; 2017; Cheshire et al., 2018). These studies show that steel corrosion has the potential to have wide ranging effects on the physical and chemical properties of the bentonite buffer, likely dependent on bulk system chemistry.

In low temperature repository settings (<100°C), iron released through steel corrosion will be likely absorbed by the surrounding clay through cation exchange. This exchange will reduce the self-sealing ability in the clay (i.e., swelling capacity) and cause the buffer to become stiff (Pusch et al., 2015). Fe^{3+}, generated under initial oxidizing conditions, may replace Al^{3+} in the octahedral sheet of montmorillonite, which can accelerate the alteration to non-swelling phases, due to high crystal stresses and mineral instability due to the large cation size (Nguyen-Thanh et al., 2014). In addition, the combination of heating and the ion exchange between the Na^{2+} in the clay with the Fe^{2+} produced from corrosion under reducing conditions (anoxic) promotes the development of channel-type transport pathways for solutions migrating through the bentonite buffer (Gueven and Huang, 1990; Nguyen-Thanh, et al., 2014; Pusch et al., 2012).

In > 100°C experimental systems that utilize reaction solutions with circumneutral pH values (i.e., porewaters buffered by clay and silicate minerals), $Fe^{2+/3+}$ is transferred from either iron shavings or steel coupons to clay minerals in the bentonite to form different Fe-rich phyllosilicate minerals (chlorite, Fe-saponite, berthierine, serpentine phase) (e.g., Guillaume et al., 2004; Mosser-Ruck et al. 2010; Cheshire et al., 2018; Caporuscio et al., 2019; Jove-Colon et al., 2019). For example, in 300°C hydrothermal experiments that include steel coupons embedded in bentonite, stainless steel corrodes to produce a chromite-like ($FeCr_2O_4$) passivation layer above unaltered steel, whereas a magnetite-like phase forms on the surface of low carbon steel (Cheshire et al., 2018; Jove Colon et al., 2019). Attached to the corroded surface is a < 100 µm zone of Fe-rich smectite (Fe-saponite) (Cheshire et al., 2018). Results from lab-scale studies indicate that the formation of Fe-rich silicate phases as mantle on the steel surface may provide corrosion protection (e.g, Kaufhold et al., 2015; Cheshire et al., 2018); however, this finding should be confirmed in full-scale/long term experiments.

5.2 Methods: Experimental Design

Hydrothermal experiments were designed to understand geochemical and mineralogical changes that may occur in the EBS of a high-temperature crystalline repository. Different combinations of materials found in the hypothetical repository setting, including wall rock (Grimsel granodiorite from the Grimsel Test Site), bentonite buffer (unprocessed Wyoming bentonite), waste canister overpack (316SS [stainless steel], 304SS, LCS [low carbon steel]), cement liner (cured OPC), and groundwater (synthetic Grimsel granodiorite groundwater) were included in the experiments.

Experiments were conducted under water-saturated conditions. Reactants (listed in Table 5-1) were loaded into a flexible gold reaction cell and fixed into a 500 mL gasket confined closure reactor (Seyfried et al., 1987). The redox conditions for each system were buffered using a 1:1 mixture (by mass) of Fe_3O_4 and Fe° added at 0.07 wt.% of the bentonite mass. Coupons of steel (316SS, 304SS, or LCS), were added to the experiments at approximately 15 to 25 wt. % of the mass of the solid reactants to mimic the presence of a waste canister. Experiments were pressurized to 150 to 160 bar and were heated isothermally to 250°C for 6 to 8 weeks. Reaction liquids were extracted periodically during the experiments and analyzed to investigate the aqueous geochemical evolution in relationship to mineralogical alterations. The sampled reaction liquids were split into three aliquots for unfiltered anion, unfiltered cation, and filtered (0.45 µm syringe filter) cation determination. All aliquots were stored in a refrigerator at 1°C until analysis.

Reaction products and starting materials were characterized using XRD, electron microprobe (EMP), and scanning electron microscopy. Detailed analytical methods are listed in Appendix A.

Table 5-1. Initial components and reaction conditions for IEBS experiments in the presence of Grimsel granodiorite. Abbreviations: LCS, low carbon steel; PC, Portland cement; GG, Grimsel granodiorite; SS, stainless steel; WB, Wyoming bentonite.

Exp.	Components	Temp (°C)	Run time	Synthetic GW (g)	Grimsel Granodiorite (g)	WY bentonite (g)	Cured Portland cement (g)	Steel type	EBS metal (g)	Fe° (g)	Fe_3O_4 (g)	Water:Rock
IEBS-1	GG + WB	250	6 weeks	144	3.47	10.91	-	-	-	0.49	0.50	10:1
IEBS-2	GG+ WB + 316SS	250	6 weeks	182	3.19	11.02	-	316SS	nm	0.49	0.50	13:1
IEBS-3	GG + WB + 304SS	250	6 weeks	110	3.41	11.05	-	304SS	2.74	0.50	0.59	8:1
IEBS-4	GG + WB + LCS	250	6 weeks	185	3.28	11.00	-	LCS	5.06	0.50	0.51	13:1
IEBS-5	GG + WB + 316SS	250	8 weeks	150	3.29	11.01	-	316SS	5.07	0.50	0.50	10:1
IEBS-6	GG + WB + PC	250	8 weeks	126	2.11	6.60	2.07	-	-	0.50	0.50	10:1

*nm= not measured

5.3 Results

5.3.1 Starting Material Characteristics

Synthetic Grimsel Groundwater—A synthetic groundwater was mixed to mimic fluids found at the Grimsel Test Site after the recipe reported in Kersting et al. (2012). Chemistry of the synthetic fluid is presented in Table 2. The groundwater at the Grimsel Test Site is a Na-CO_3 type water and has a pH of ~8.6 to 8.8.

Wyoming Bentonite—The bentonite used in the present study is unprocessed and was provided by Bentonite Performance Minerals LLC from Colony, Wyoming, U.S.A. It is composed dominantly of Na-montmorillonite (general composition: $Na_{0.33}(Al,Mg)_2(Si_4O_{10})(OH)_2 \cdot nH_2O$), lesser clinoptilolite and feldspar, and minor biotite, pyrite, quartz, opal, and sulfide minerals. The QXRD results from unheated bentonite are presented in Table 3.

Grimsel Granodiorite—The granodiorite used in the experiments was sourced from a drill core from the Grimsel Test Site. Major mineral phases include K-feldspar, plagioclase, and quartz. Minor phases are muscovite and biotite. Trace phases are allanite, zircon, titanite, and apatite. The QXRD results from unheated granodiorite are presented in Table 3.

Cured Portland Cement Chip—Chips consisting of a mix of 100% OPC and water were cast in November of 2018. Major mineral phases observed in the XRD pattern the cured cement chip include portlandite ($Ca(OH)_2$), belite (calcio-olivine, Ca_2SiO_4), alite (Ca_3SiO_5), dolomite ($CaMg(CO_3)_2$), and vaterite ($CaCO_3$) with trace amounts of iron- and phosphate-bearing phases.

Table 5-2. Initial groundwater chemical composition from Kersting et al. (2012) and the synthetic groundwater used in these experiments (Missana and Geckeis, 2006).

	Target Solution (Kersting et al., 2012) (mg/L)	Synthetic Grimsel GW (this study) (mg/L)
Na^+	127	116
K^+	3	3
Ca^{2+}	5	7
Mg^{2+}	13	12
Cl^-	11	14
CO_3^{2-}	219	203
SiO_2	21	34
SO_4^{2-}	97	87
pH	8.6–8.8	8.5

Table 5-3. Quantitative X-Ray Diffraction (QXRD) analyses of the buffer clay (Wyoming bentonite). the wall rock (Grimsel granodiorite), and experiments run products.

SAMPLE ID	**Wyoming Bentonite**	**Grimsel Granodiorite**	**80 WB: 20 GG**	**IEBS-1**	**IEBS-2**	**IEBS-3**	**IEBS-4**	**IEBS-5**
NON-CLAY FRACTION								
Quartz	1.5	24.1	6.9	11.4	8.2	8.2	8.2	9
K-Feldspar	0.7	10.3	3	3.5	3.7	4.2	4.4	4.4
Plagioclase	6.2	39.3	14.1	13.6	14.8	12.7	13.9	13.4
Apatite	0	0.5	0.1	0.4	0.4	0.3	0.2	0.4
Pyrite	0.2	0.3	0.2	0.1	0.1	0.1	0.1	0.2
Calcite	0	0.8	0.2	0.1	0.1	0.1	0.1	0.1
Dolomite	0	2.3	0.6	0.4	0.4	0.1	0.2	0.1
Amphibole	0.1	0.9	0.3	0	0	0	0	0
Gypsum	0	0	0	0	0	0	0	0
Clinoptilolite	13	0	9.9	8	6.4	5.1	3.8	5.5
Cristobalite	1.5	0	1.1	0	0	0	0	0
TOTAL	23.2	78.4	36.4	37.4	34	30.8	30.9	33.1
CLAY FRACTION								
Smectite	71	5.5	55.3	58.7	64.3	66.4	63.2	62.4
Mica	3.8	14.3	6.3	3.4	1.5	2.5	5.7	4.3
Chlorite / Kaolinite	2	1.8	2	0.4	0.2	0.3	0.2	0.2
TOTAL	76.8	21.6	63.6	62.6	66	69.2	69.1	66.9
GRAND TOTAL	100	100	100	100	100	100	100	100

316SS—(NIST SRM 160b) is an iron alloy primarily with 18.37 wt.% Cr, 12.35 wt.% Ni, 2.26 wt.% Mo, 1.619 wt.% Mn, 0.5093 wt.% Si, and 0.175 wt.% Cu.

304SS—An ion alloy which differs from 316SS in Cr/Ni ratio. Along with Fe, it contains 18 wt.% Cr, 8 wt.% Ni, < 2 wt.% Mn, < 1 wt.% Si, < 0.045 wt. % P, and < 0.03 wt.% S, and < 0.08 wt.% C.

Low Carbon Steel (LCS)—Composed of Fe along with ~0.2 wt.% C, 0.9 wt.% Mn, < 0.04 wt.% P, and < 0.05 wt.% S.

5.3.2 Aqueous Geochemistry (EBS-23 to -28)

The pH and concentrations of cations and anions in reaction fluids evolved during the experiment, likely reflecting mineral-brine reactions. The starting solution, synthetic Grimsel granodiorite groundwater, has a pH of ~8.5. The pH, measured at 25°C, of the fluids extracted weekly from the reaction vessels dropped over the course of all experiments. The pH of IEBS-1 initially dropped to ~7, and then remained ~6.5 for the experiment duration. Experiment IEBS-2 had a slightly more acidic solution during the middle of the experiment: the pH dropped to ~5 by week 3 and then increased to ~6.2 by the end of the experiment. IEBS-3 dropped to 6.8 in the first week and continued to gradually decrease to almost 6.0. The pH of IEBS-4 dropped to 6.5 in the first two weeks and remained around similar values for the remainder of the experiment. Finally, IEBS-5 dropped to a pH of 6.3 before gradually increasing to 6.6 (Figure 5-3). The pH values observed in IEBS-6, which contained a cured Portland Cement chip, evolved to slightly higher pH values (i.e., ~7–7.5) (Figure 5-3).

Water:Rock—Experiments were performed at a range of water:rock ratios (8:1 to 13:1). As experiments progressed, fluids were gradually extracted from the reaction vessel during sampling, which slightly lowered the water:rock ratio with every fluid extraction.

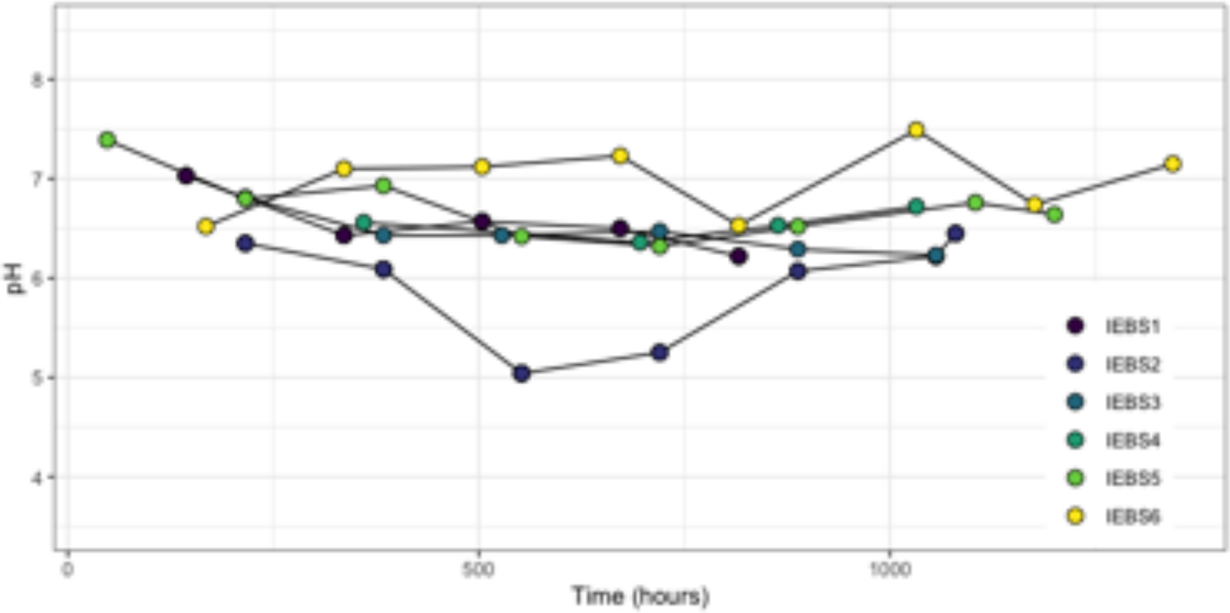

Figure 5-3. Measured pH values (at 25°C) for reaction fluids extracted from experiments IEBS-1 through IEBS-6.

5.3.2.1 Cations

Alkali/Alkaline Earth Metals—Major alkali and alkaline earth metal cations (K^+, Na^+, Ca^{2+}, Mg^{2+}) follow similar trends in concentrations measured throughout each experiment (Figure 5-4). In the unfiltered and filtered results, concentrations typically decrease slightly from values observed at the first sampling. No significant differences in measured values between the filtered and unfiltered results are observed. For IEBS-1 through IEBS-5, initial K^+ and Ca^{2+} values are observed to be close to concentrations in the starting Grimsel granodiorite synthetic groundwater (~3 and 7 mg/L, respectively). Calcium concentrations in IEBS-5, are observed to be slightly elevated in comparison to the other experiments. Observed sodium values in all experiments cover a wide range (100–200 mg/L) but are similar in magnitude to the [Na^+] observed in the starting solution (116 mg/L). Magnesium concentrations drop from starting solution values (~12 mg/L) to < 0.5 mg/L in the unfiltered aliquot by the first sampling, and remain at similar values for the duration of all experiments. Results for K^+, Na^+, Ca^{2+}, Mg^{2+} from IEBS-6 (experiment with the cured Portland cement chip) are elevated with respect to all other experiments at the first sampling, but drop to similar concentrations by the second week of the experiment.

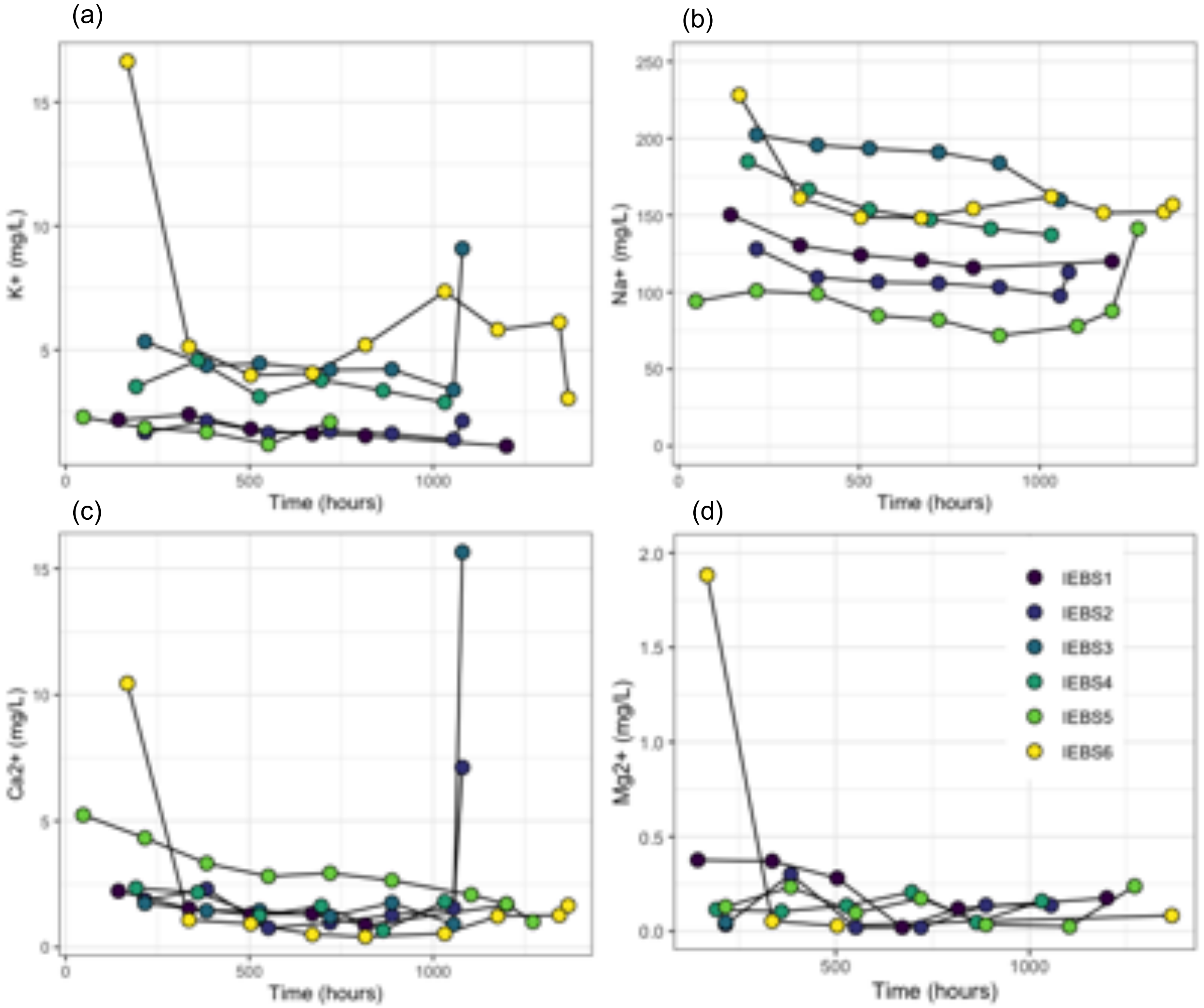

Figure 5-4. Concentration in mg/L of (a) potassium, (b) sodium (c) calcium, and (d) magnesium in the unfiltered reaction fluids during each IEBS experiment.

SiO_2—Measured concentrations in the six completed experiments cover a wide range of values between ~350 and 800 mg/L (Figure 5-5). Starting silica values in the synthetic Grimsel groundwater are ~34 mg/L; values observed in the experiments all increase rapidly during the first week of experiment time. In the individual experiments, comparison of results from unfiltered and filtered aliquots show little difference in concentrations. Comparing between experiments, the aqueous silica concentrations do not follow consistent trends. For example, values in IEBS-1, IEBS-2, and IEBS-4 decrease after the first sample, before values increase by the third or fourth sample. Concentrations in IEBS-3 and IEBS-6 initially increased before leveling off around the middle of the experiment, and slightly decreasing over the last two weeks. Concentrations in IEBS-5 remained relatively constant before slightly increasing at the end of the experiment.

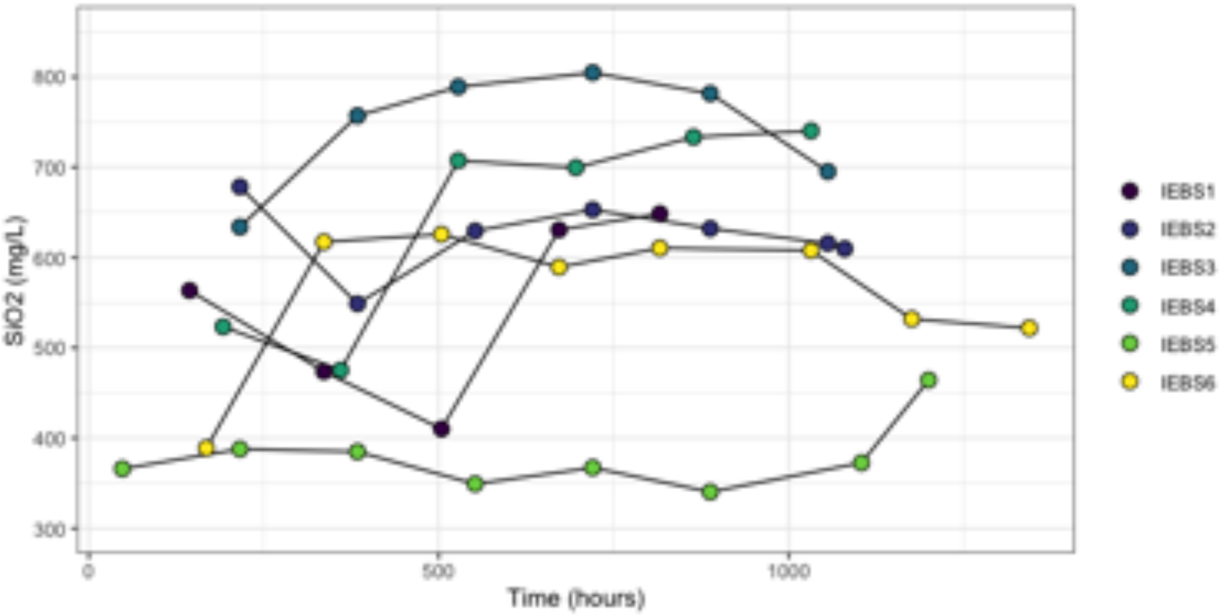

Figure 5-5. Concentration in mg/L of aqueous silica in the unfiltered reaction fluids during each IEBS experiment.

Fe^{2+}—The [Fe^{2+}] in all IEBS experiments remains below ~1 mg/L in the filtered and unfiltered cation samples for the duration of the experiments (Figure 5-6a). A jump to ~10 mg/L is observed around 500 hours experiment time in IEBS-6 in the unfiltered results; this is likely the result of particulate matter present in the sample. The final sample from IEBS-1 that was collected before experiment cooling has Fe concentrations of ~4 mg/L for both filtered and unfiltered samples. Quench samples (collected after experiment cooling) from IEBS-2 and IEBS-3 show sharp increases to >20 mg/L in the unfiltered aliquot (Figure 5-6a).

Al^{3+}—Aluminum concentrations in the unfiltered fraction from experiments IEBS-1 through IEBS-5 reached concentrations of ~4 to 5 mg/L by the first weeks of experiment time (Figure 5-6b). Concentrations slightly decreased or remained near constant for the remainder of the experiment. Quench samples from IEBS-2 and IEBS-3 exhibit a spike in [Al^{3+}] concentrations. In comparison, the [Al^{3+}] concentrations were notably higher in IEBS-6, reaching ~10 mg/L after one week of reaction time, before decreasing steadily to ~6 mg/L by the end of the experiment (Figure 5-6b). Filtered results mirrored the trends observed in all six experiments, but have concentrations that were lower by about 2 to 3 mg/L.

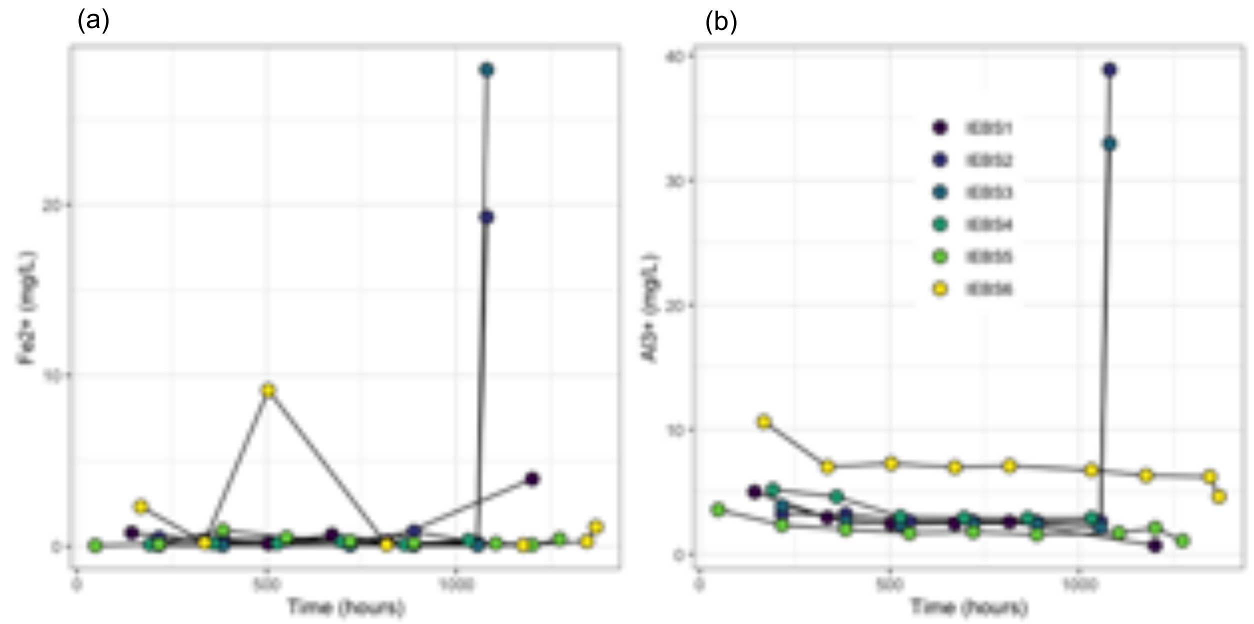

Figure 5-6. Concentration in mg/L of aqueous (a) iron and (b) aluminum in the unfiltered reaction fluids during each IEBS experiment.

5.3.2.2 Anions

Cl^-—Chloride concentrations are observed to decrease gradually during the six experiments. Values are initially slightly elevated with respect to the starting concentrations (20–35 mg/L versus 15 mg/L, respectively). By the end of each experiment, measured concentrations are between 10 and 20 mg/L (Figure 5-7a).

SO_4^{2-}—Sulfate concentrations in the six experiments are variable throughout each experiment (Figure 5-7b). Observed initial values are between ~150 and 350 mg/L, which shows an increase from the starting solution values (87 mg/L). The majority of experiments end at concentrations of 100 to 175 mg/L, with the exception of IEBS-3, which ended around 275 mg/L (325 mg/L quench).

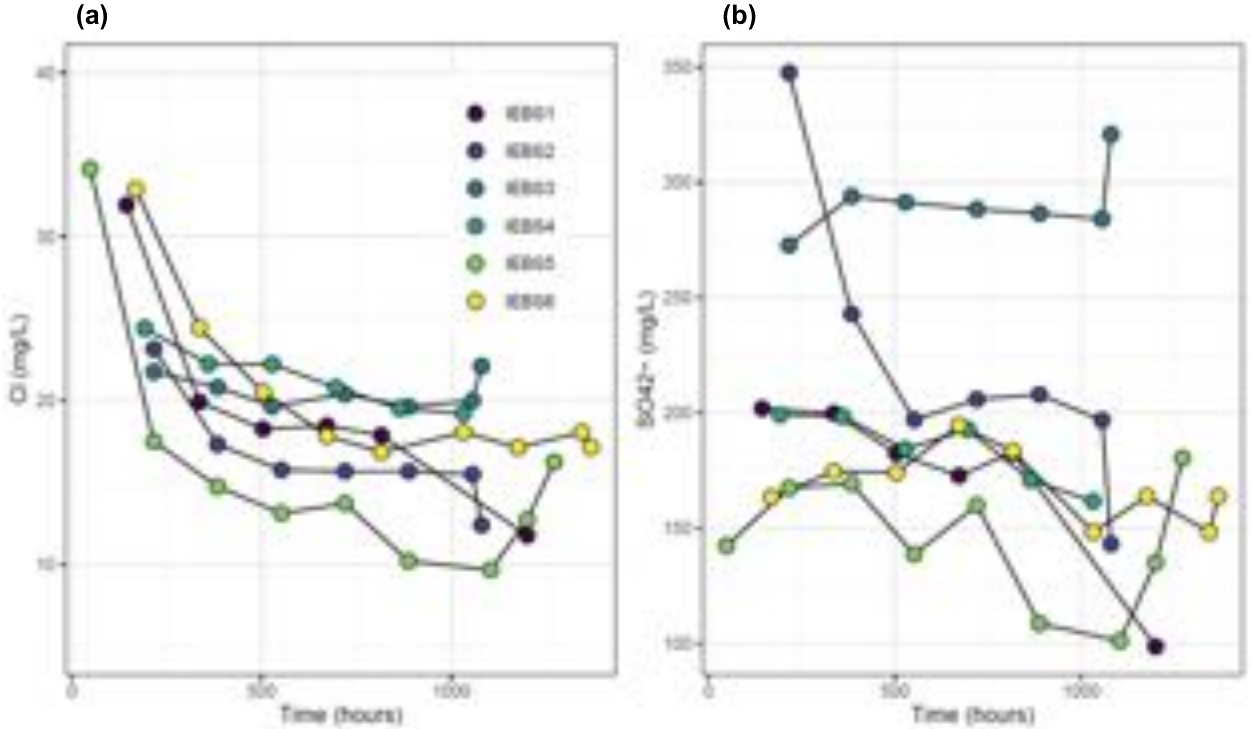

Figure 5-7. Concentration in mg/L of (a) chloride and (b) sulfate anions in the unfiltered reaction fluids during each IEBS experiment.

5.3.3 Quantitative X-ray Diffraction Results

New QXRD analyses of the starting material mixture and the bulk reaction products from IEBS-1 through IEBS-5 were acquired in FY20 (Table 5-3). The results show changes in bulk mineralogy as the result of the hydrothermal reaction. Analysis of the reaction products from IEBS-6 (experiment with the cured cement chip) was delayed due to the COVID-19 pause in lab work and will be included in the next FY report.

The approximate starting reaction mixture for each experiment was 20% Grimsel granodiorite chips and powder and 80% Wyoming bentonite powder and granules. The bulk mineralogy of a representative sample of Wyoming bentonite, Grimsel granodiorite, and the starting mixture is reported in Table 5-3.

Results from the experiment product indicate that mineral dissolution, precipitation, and recrystallization reactions likely occurred. For example, in the results from all samples, the abundance of quartz increases by ~1 to 7 wt.%. Clinoptilolite dissolution likely occurred based on the decrease in abundance by 1 to 6 wt.%. Smectite abundance increases by 3 to 11 wt.% and the amount of mica and chlorite decreases by about 5 wt.%. Changes in clay mineralogy were further investigated by detailed clay mineral structural studies, discussed in the next section. CSH minerals, which were identified in thin section and in SEM images, were not identified via XRD, likely due to their low bulk abundance or poorly crystalline nature.

5.3.4 Clay Mineral XRD

The clay-size fraction (<2 µm) was separated via density separation from a gently crushed portion of the reaction products from each experiment. While crushing, discrete particles of Grimsel granodiorite were removed. In the case of IEBS-6, the cement chip was separated before the sample was selected. The XRD patterns of the ethylene glycol saturated, oriented clay fractions can be used to determine alterations to the clay mineral structure (i.e., peak position shifts), which can be used to calculate clay mineral expandability. The ethylene glycol saturated peak positions are presented in Table 5-4 and the XRD patterns are plotted in Figure 5-8.

Peak positions from IEBS-1 through IEBS-5 show slight shifts in the position of all ethylene glycol saturated smectite peaks in comparison to unheated Wyoming bentonite, and calculated expandabilities based on the difference between the d002 and d003 peaks from these samples show an increase in clay expansion. In comparison, results from IEBS-6, which included the cured cement chip, show lower expandabilities than the clay fraction from experiments without cement, but still slightly increased in comparison to unreacted Wyoming bentonite.

Table 5-4. Ethylene glycol saturated smectite peaks from the <2 µm fraction from unheated Wyoming and the clay groundmass of the six completed IEBS experiments. Expandability (%Exp) is calculated based on the difference between the d002 and d003 peaks using Equation 5-1 to Equation 5-3.

Sample	1		2		3		5		002/003	1	2	3
EG-smectite	2Θ	d (Å)	2Θ	d (Å)	2Θ	d (Å)	2Θ	d (Å)	$\Delta 2\theta$	%Exp	%Exp	%Exp
WY Bentonite	5.18	17.04	10.4	8.5	15.66	5.65	26.3	3.39	5.22	102	105	105
IEBS-1	5.22	16.92	10.38	8.52	15.6	5.68	26.24	3.39	5.16	105	109	109
IEBS-2	5.32	16.6	10.44	8.47	15.7	5.64	26.22	3.4	5.12	108	112	111
IEBS-3	5.18	17.05	10.32	8.57	15.58	5.68	26.2	3.4	5.14	107	111	110
IEBS-4	5.18	17.05	10.32	8.56	15.6	5.68	26.22	3.4	5.14	107	111	110
IEBS-5	5.22	16.92	10.36	8.53	15.62	5.67	26.24	3.39	5.14	107	111	110
IEBS-6	5.2	16.98	10.38	8.51	15.68	5.65	26.34	3.38	5.18	104	107	107

NOTE: 1: $\%Exp = 973.76 - 323.45\Delta + 38.43\Delta^2 - 1.62\Delta^3$ (Eberl et al., 1993).

2: $\%Exp = 1517.8 - 548.49\Delta + 68.35\Delta^2 - 2.90\Delta^3$ (Eberl et al., 1993)

3: $\%Exp = 766.01 - 194.10\Delta + 12.924\Delta^2$ (Moore and Reynolds, 1997)

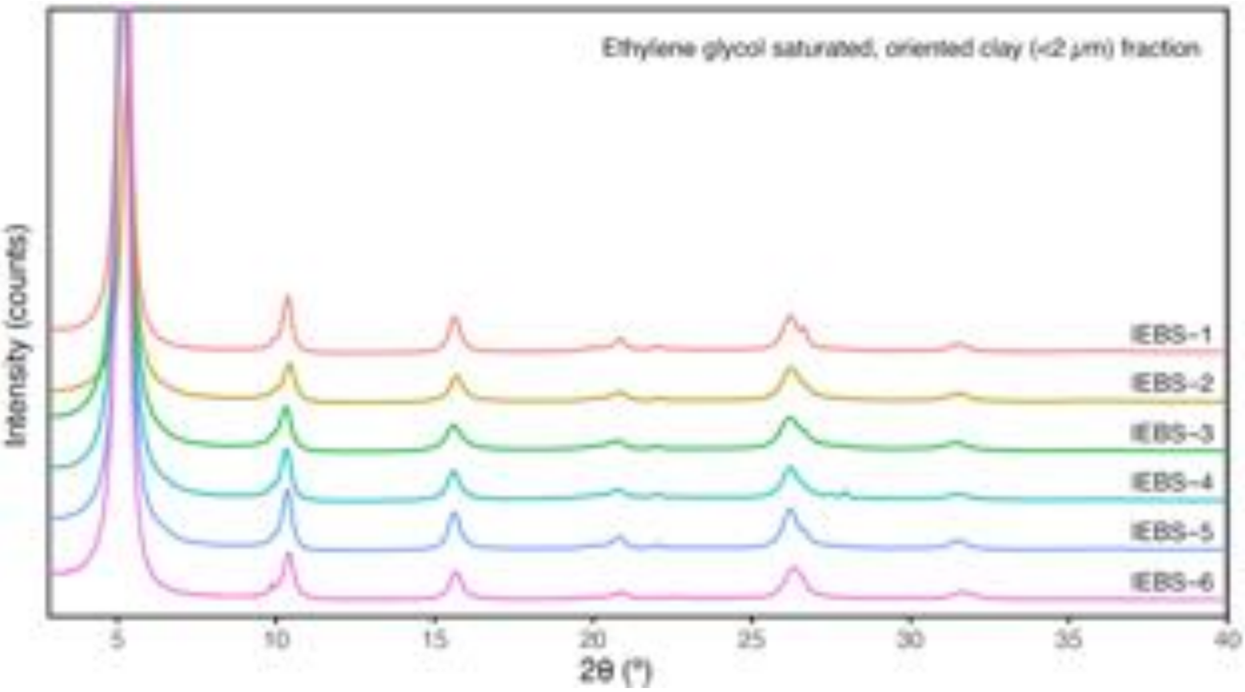

Figure 5-8. XRD patterns the oriented, ethylene glycol saturated <2 µm fraction from IEBS-1 through IEBS-6 showing no significant shifts in smectite peaks.

5.3.5 Electron Microprobe Analyses

Reaction products were analyzed via EMP to determine the major element composition of mineral phases. The EMP analyses primarily targeted the clay matrix, steel alteration products, altered glass shards, and other authigenic minerals. Analysis of the reaction products from IEBS-6 (experiment with the cured cement chip) was delayed by the COVID-19 pause in lab work and will be included in the next report. The EMP results of the previous experiments are reported in Appendix B and described below.

Clay Matrix—The fine-grained groundmass of the reaction products of the IEBS experiments have similar major element compositions. All contain 60 wt.% SiO_2, ~22 wt.% Al_2O_3, 4 to 6 wt.% FeO and 1 to 2% MgO, and 1 to 3% of Na_2O, ~0.3 K_2O, 0.2 to 0.5 wt.% CaO, and 0.1 to 0.2 wt.% F.

Calcium (aluminum) Silicate Hydrates (tobermorite)—In the experiments, <10 µm round mineral grains were observed with the fine-grained matrix. The grains in IEBS-1 were too small to analyze, but some grains in IEBS-2, 4 and 5 were large enough to target (Figure 5-9). However, the small size and beam sensitivity of this mineral made obtaining EMP analyses difficult. The collected data indicate low SiO_2 wt.% (~10–15 wt.%) and Al_2O_3 (1–5 wt.%) and very high CaO (~41–48%). The low SiO_2 content may be due to sample decrepitation in the beam line prior to SiO_2 analysis. These minerals could be seen actively being destroyed during analysis. Fluorine is present in trace amounts (~0.2–1.2%). Low oxide totals (~60%) indicate the likely presence of H_2O. In addition, EDS analyses demonstrate presence of CO_3. Based on the composition and rounded crystal form, this mineral is likely a calcium (aluminum) silicate hydrate (C(A)SH) and may be identified as mineral tobermorite ($Ca_5Si_6O_{16}(OH)_2 \cdot 4(H_2O)$), with a small carbonate component.

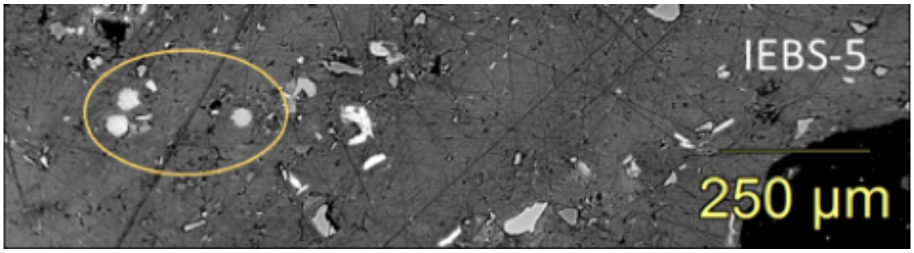

Figure 5-9. Back scattered SEM image of circular tobermorite grains (circled in yellow) in the fine-grained smectite matrix from a thin section of sample IEBS-5.

Clinoptilolite—Clinoptilolite was present in the unheated, precursor bentonite clay as partial replacement phases in volcanic glass shards. Upon heating, remnant glass was recrystallized to clinoptilolite. The Si/Al ratios for the clinoptilolite from the unheated bentonite and experiment products are dominantly between 4.0 and 6.0. The Na/(Na+Ca) values in the clinoptilolite range from 0.5 to 0.8, whereas glass values are closer to 1.0 (Figure 5-10).

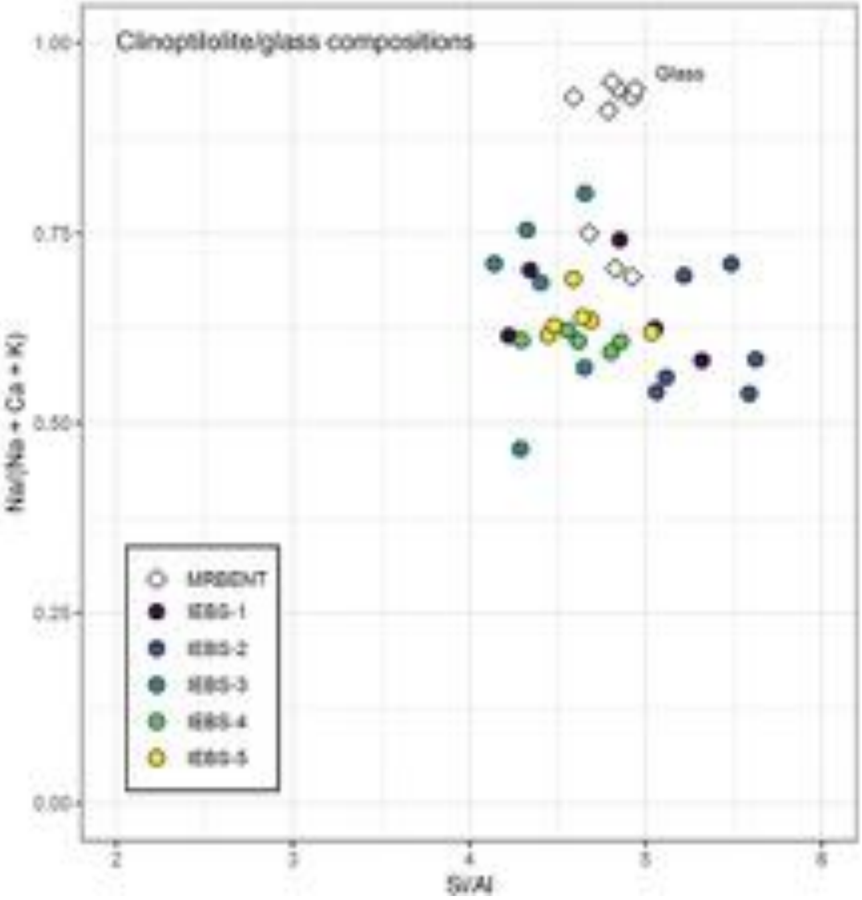

Figure 5-10. Clinoptilolite compositions analyzed by EMP. Each point is an individual analysis and MRBENT is the clinoptilolite/glass from the unreacted Wyoming bentonite.

Feldspars—The feldspars from the individual IEBS experiments have varying compositions (Figure 5-11). The plagioclase observed in IEBS-2, 3, and 5 are all depleted in K^+. However, there is a range of Ca^{2+} and Na^+ in the samples. Na^+ ranges from 35 to 91% in the sample and Ca^{2+} between 8 to 80%. The K-feldspar in IEBS-3, 4 and 5 show similar compositions. IEBS-5 has one sample more enriched in K^+. The rest of the samples cluster around 70% K^+, 30% Na^+ and no Ca^{2+}.

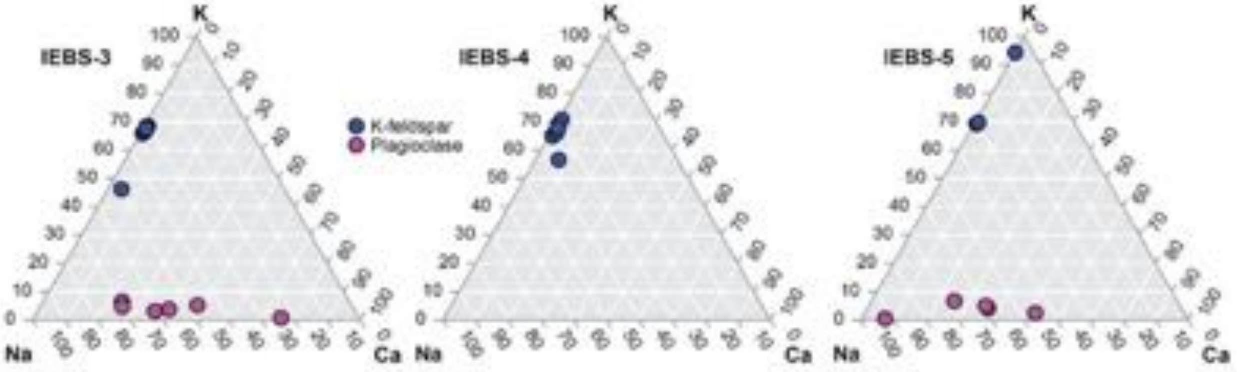

**Figure 5-11. Varying feldspar composition for IEBS-3 to 5.
Note the wide range of compositions observed.**

Steel/Fe Alteration—Mineral growth is observed at the surface of the steel coupons in IEBS-2 through 5 (Figure 5-12). Fe-saponite is observed to form on the steel interface, and a thin chlorite rim forms outside of the saponite in IEBS-2. The iron content in the saponite is ~20 wt.% in all the experiments.

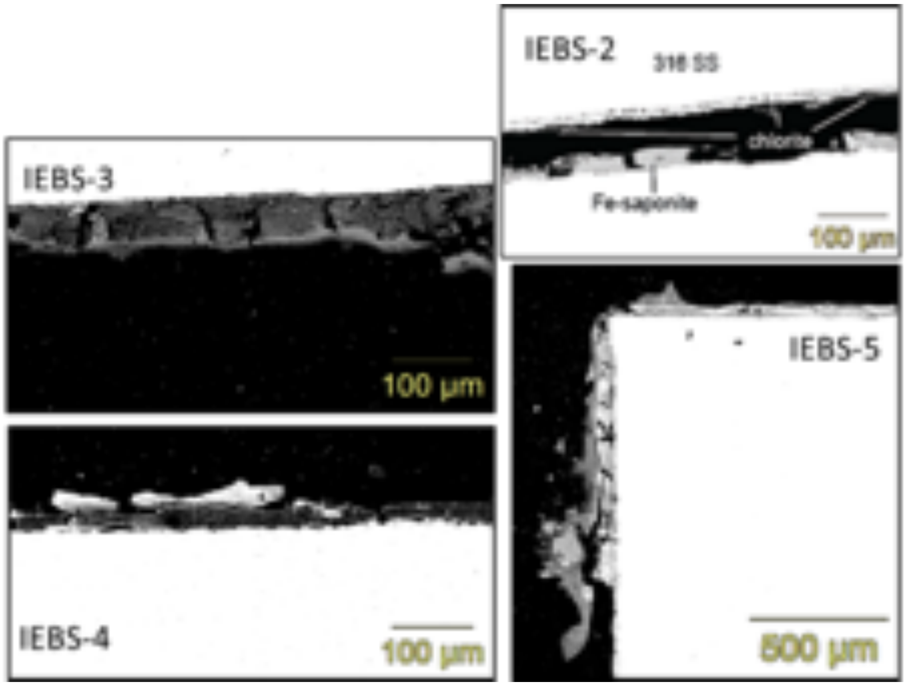

**Figure 5-12. Backscattered electron images of thin sections
of the post-reaction polished steel coupons.**

5.3.6 SEM/EDS Results

Reaction products, including loose powder, epoxy mounts, and thin sections, from the IEBS experiments were characterized using the SEM and qualitative elemental abundances were evaluated using EDS. The SEM images are presented in Appendix C and described below.

5.3.6.1 Clay

The reaction products show similar features. In all the experiments, montmorillonite clay has a foily texture (i.e., Figure C-1A, B; Figure C-4A, B; Figure C-7A). Spherical crystals are embedded in the fine-grained clay matrix (i.e., Figure C-1C, D, E; Figure C-2C, D; Figure C-3A, C; Figure C-4B, C, D, E; Figure C-6B, C). The EDS analyses of these crystals reveal large Ca peaks, with smaller Si, Al, and C peaks, likely corresponding to C(A)SH minerals. The composition of these phases is discussed further in the previous section (5.3.5 Electron Microprobe Analyses).

5.3.6.2 Grimsel Granodiorite

Feldspar surfaces are observed to be variably pitted, indicating dissolution may have occurred at the edge of the grains (Figure 5-13). No significant authigenic mineral precipitation is observed to form rims on the feldspar grains. Further, fragments of Grimsel granodiorite included in the experiments did not experience any significant mineral reactions. For example, Figure 5-14 shows an intact Grimsel fragment composed of biotite, apatite, and quartz. No alteration textures or new mineral growth is observed within the boundaries of the Grimsel fragment.

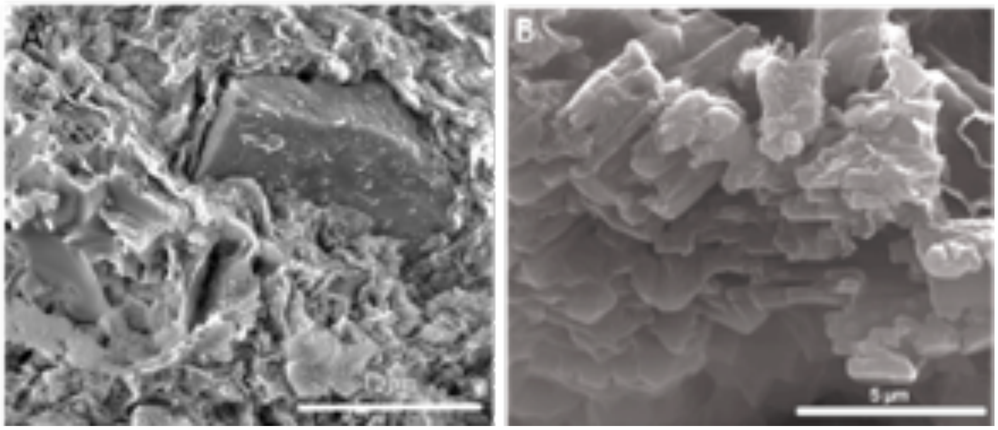

Figure 5-13. Feldspar dissolution textures observed in secondary electron (SE) SEM images from (A) IEBS-5 and (B) IEBS-1.

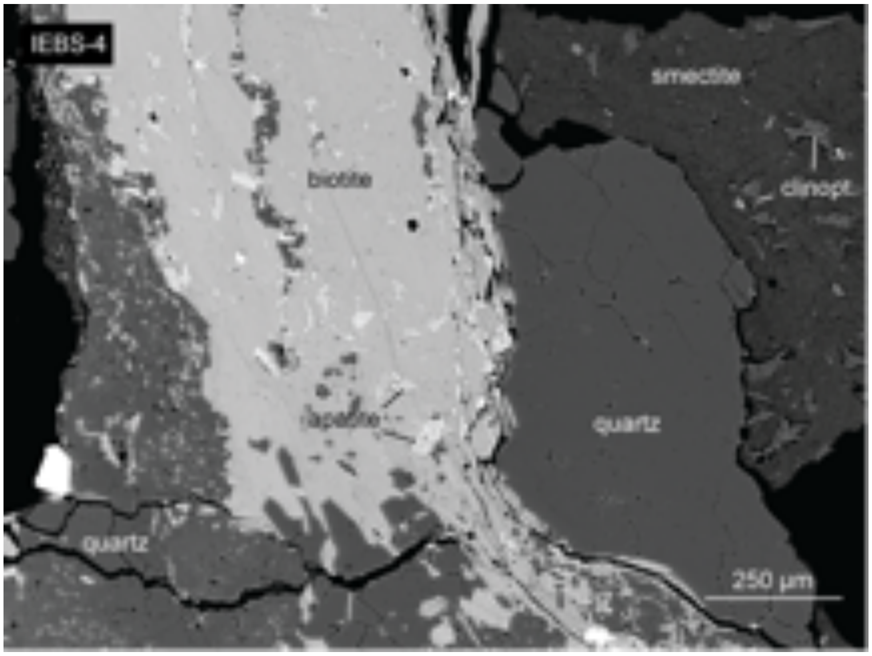

Figure 5-14. Backscattered electron SEM image of a post-reaction fragment of Grimsel granodiorite from IEBS-4. Authigenic mineral growth/alteration is not apparent within the fragment. Abbreviation: clinopt., clinoptilolite.

5.3.6.3 Post-Reaction Gel

At the conclusion of the experiments, a gel-like slurry was present on the top of the reaction product for IEBS-3, 4, and 5 (Figure 5-15A). The dried gel was analyzed with EDS and is Si- and Al-rich with minor amounts of Fe (1.4 – 4.3 wt.%) and Na^{2+} (3 – 6 wt.%). The dried gel texture consisted of linear and cross-linked morphology (Figure 5-15B, C).

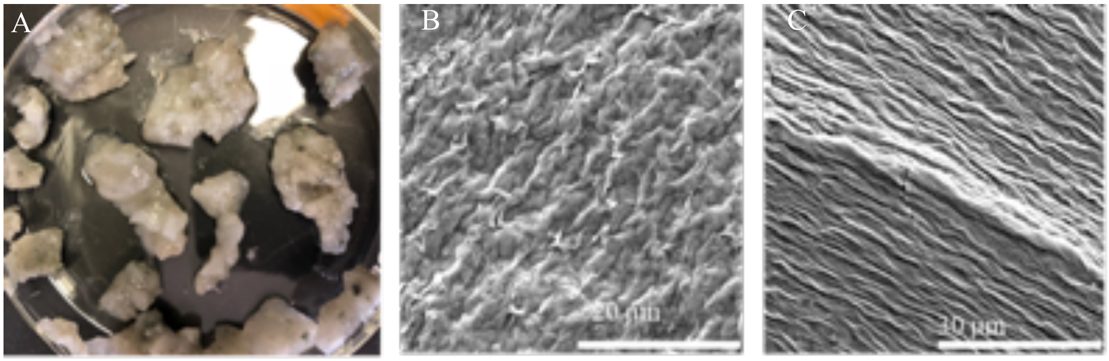

Figure 5-15. [A]. Post-reaction gel mixed with clay from IEBS-4. [B & C]. SEM images of the dried gel. Two different textures were observed: cross-linked and linear.

5.3.6.4 Experiment with Cement

In the IEBS-6, containing cured Portland cement, (Figure C-12A, B) Na-rich analcime was prevalent throughout the reaction product (Figure 16) along with minor erionite-Ca and garronite (Figure C-11A). The fragments of the Grimsel granodiorite did not experience significant alterations and only occasional dissolution texture on the surface of feldspar grains was observed (Figure C-11B). The cured Portland cement chip placed in IEBS-6 had a layer of clay with zeolite embedded on the surface (Figure 5-16; Figure C-10A, B). A thin section showing a cross section of the cement chip was created and will be characterized in the next FY.

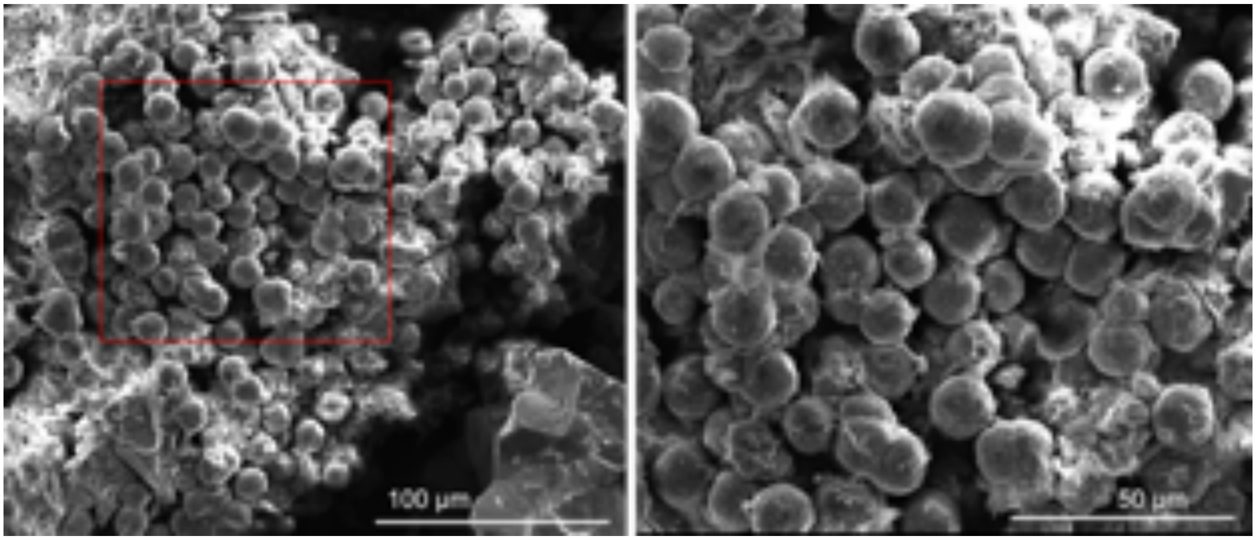

Figure 5-16. Cluster of Na-rich analcime grains from experiment IEBS-6, which included a cured chip of OPC. The image on the right is a magnification of the red box in left image.

5.3.7 Colloid Formation

A gel phase was observed on experiment cooling in IEBS-3, IEBS-4, and IEBS-5. When suspended in DI water, particles remained suspended in solution. A dried film of the suspension from IEBS-5 was analyzed via XRD; the colloid phase was identified as montmorillonite. A portion of the suspension fluid from IEBS-5 was also analyzed with a Zetasizer at Los Alamos National Laboratory, in order to assess particle size and colloid stability. The measured zeta potential values centered around −38.9, indicating moderately stable colloids. The average particle size diameter was ~237 nm and the diameters were distributed between ~30 and 1,000 nm (Figure 5-17). Further characterization of colloid phases from the remaining experiments will be completed in the next FY.

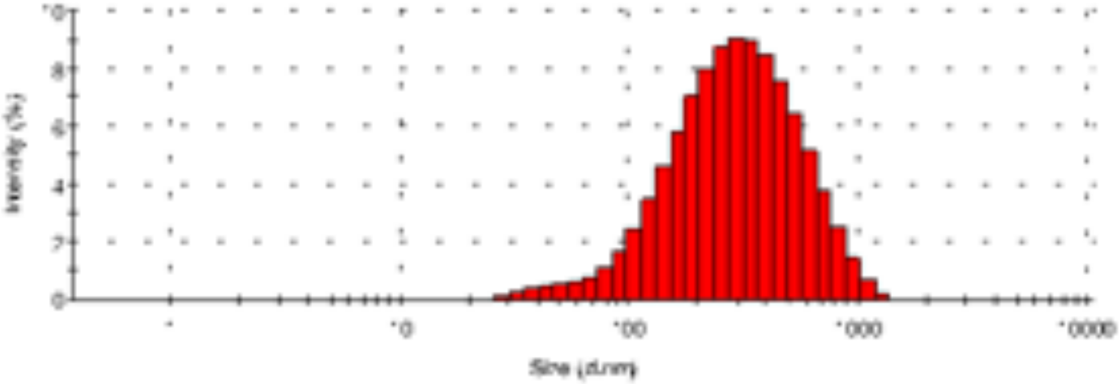

Figure 5-17. Distribution of colloid diameters from sample IEBS-5 measured via Zetasizer.

5.3.8 Steel-Bentonite Interface Mineralization

Steel coupons (316SS, 304SS, and LCS) were included in IEBS-2 through IEBS-5 (Table 5-5). All of the experiments contained Wyoming bentonite, Grimsel granodiorite, and synthetic Grimsel granodiorite groundwater. Experiments were run at 250°C and 150 bar for a period of 6 or 8 weeks. The mineralogy and chemistry of phases that formed on the surface of the steel coupons was characterized and measured via SEM and electron probe micro analysis.

304SS: IEBS-3—The surface of the 304SS coupon included in IEBS-2 was coated in Fe-saponite with a honeycomb texture. Fe-Ni-Cr sulfides are observed embedded in the Fe-saponite and unaltered smectite is observed attached to the underlying Fe-saponite (Figure 5-12; Figure C-7A-F).

316SS: IEBS-2 and -5—Images of the 316SS coupons from IEBS-2 show two layers of mineral growth that formed perpendicular to the steel surface (Figure 12). Fe-saponite forms directly adjacent to the pitted steel surface (Figure 5-12; Figure C-9C,D) and chlorite is observed to form a thin layer locally adjacent to the steel surface, inside of the Fe-saponite. Sulfide minerals, such as pyrrhotite are also observed (Figure 5-12).

The 316SS from IEBS-5 shows two layers of mineral growth similar to IEBS-2. A thin layer of chlorite is observed locally attached to the steel surface and Fe-saponite rosettes form outboard of the chlorite (Figure 5-12; Figure C-8C,D).

LCS: IEBS-4—The post-reaction LCS was coated by a layer of Fe-saponite rosettes. Fe,Ni,Cr-sulfide or other Fe-rich alteration products were not observed.

5.3.8.1 Growth Rates of Fe-Rich Layer on the Steel Surface

Width measurements of precipitation products perpendicular to the surface of 316SS, 304SS, and LCS coupons were measured for experiments containing stainless-steel coupons. Precipitation thicknesses (Table 5-5) were measured on backscattered electron (BSE) images of two coupons per experiment. Fifty measurements were taken at regular intervals from each long side at equal intervals and eight measurements on each short side. Measurements were made in Adobe Photoshop using the measurement tool. Mineral growth rates (Table 5-5) were determined by dividing the average precipitation thickness by the number of experimental run days.

Table 5-5. Precipitation thickness and rates. Rates are represented in µm per day. Three steel types were examined: 304SS, 316SS and LCS from IEBS-2 through IEBS-5. The water:rock ratios were calculated without the stainless steel. All experiments contained Wyoming bentonite and Grimsel granodiorite

Sample	Steel	Matrix	Temp	Time	Water: Rock	Average Precip. (µm)	Precip./Day (µm/day)
IEBS-3	304	Bent + GG	250°C	6 weeks	7.1	31.60 (±27.01)	0.88
IEBS-2	316	Bent + GG	300°C	6 weeks	11.9	2.27 (±1.40)	0.06
IEBS-5		Bent + GG	300°C	8 weeks	9.4	38.72 (±27.76)	0.69
AVERAGE:						20.50	0.38
IEBS-4	LCS	Bent + GG	300°C	6 weeks	5.6	40.17 (±30.17)	1.12

NOTE: Bent = Wyoming bentonite; GG = Grimsel granodiorite.

The mineral growth rates were the highest IEBS-4 containing LCS (1.12 µm/day), followed by the 304SS in IEBS-3 (0.88 µm/day). The precipitation rates were the slowest in the experiment containing 316SS. The six-week experiment, IEBS-2, had a lower precipitation rate (0.06 µm/day) versus the 8-week experiment, IEBS-5, at the same conditions (0.69 µm/day). The length of time may have an impact on the thickness of the precipitation, but the difference in the water to rock ratio may be more significant.

5.4 Discussion

5.4.1 Hydrothermal Interaction of Wyoming Bentonite and Grimsel Granodiorite

The reaction products formed in the IEBS experiments include a fine-grained, recrystallized clay matrix with phenocrysts derived from the starting Grimsel granodiorite and accessory minerals in Wyoming entonite, such as feldspars, micas, and quartz. Newly formed mineral phases include calcite, quartz, gypsum, and a C(A)SH phase. The following describes our preliminary observations on hydrothermal mineralization and alteration in the Wyoming bentonite + Grimsel granodiorite experiments.

Montmorillonite—Secondary electron (SE) SEM imaging of loose powder mounts of the reaction products show the development of a foily texture in the fine-grained clay matrix. Recrystallization of montmorillonite to non-swelling phases, such as illite or muscovite, is not observed. The XRD patterns from the oriented clay fraction show no alteration to the montmorillonite structure or expansion capacity (Figure 5-8, Table 5-4). In addition, the QXRD analyses of the reaction products from IEBS-1 through IEBS-5 show increased abundance of montmorillonite.

The EMP analyses from the clay matrix of all the IEBS experiments have very similar compositions (Appendix B). In terms of alkali elements, the matrix is most enriched in Na (0.15–0.17 atoms per formula unit) in comparison to K (0.02–0.03 apfu) and Ca (0.02–0.03 apfu). The bulk chemistry of the starting materials (i.e., Na-rich montmorillonite in the unheated Wyoming bentonite) may prevent illitization due to low K^+ content in the system. Stability of Na-montmorillonite in hydrothermal experiments with low bulk system potassium has also been observed in our experimental work with Wyoming bentonite ± Opalinus Clay, in which illitization was prohibited by the bulk chemistry of the system (Cheshire et al., 2014; Sauer et al., 2020)

Feldspars—Low temperature feldspars have been identified in all the experimental runs; however, further characterization is needed in future experiments to understand their significance.

Calcium (aluminum) Silicate Hydrates—In all the experiments with Grimsel granodiorite and Wyoming bentonite, spherical, C(A)SH phases formed within the fine-grained clay matrix. Small amounts of this mineral are observed in IEBS-1, and it is abundant in IEBS-2 through 5 (Figure 5-7). Based on the composition of this mineral (Appendix B), it is likely a hydrated calcium silicate, such as tobermorite ($Ca_5Si_6O_{16}(OH)_2 \cdot 4(H_2O)$).

The formation of C(A)SH minerals contrasts with the products of previous experiments with Wyoming bentonite ± Opalinus Clay host rock in which zeolite phases (analcime–wairakite solid solution) formed. The EMP analyses of the spherical minerals formed in the IEBS experiments had significantly lower SiO_2 and Al_2O_3 content and very high CaO in comparison to the analcime–wairakite. Further, analcime–wairakite is interpreted to crystallize from dissolution/precipitation of clinoptilolite and/or clay minerals in Opalinus Clay (Cheshire et al., 2013; Sauer et al., 2020). In the Grimsel system, clinoptilolite is observed to survive the hydrothermal experiment (e.g., Figure 5-14). Tobermorite crystals are embedded in the clay matrix of the IEBS reaction products, and may form from the dissolution/precipitation of smectite. Other studies have identified the formation of tobermorite from montmorillonite during lower temperature (<120°C) hydrothermal reactions (e.g., Fernández et al., 2016). Tobermorite has also been observed in experiments involving bentonite and cement with highly alkaline bulk chemistries and pH > ~10 (Savage et al., 2007). In comparison, the solution pH over the course of the IEBS experiments did not exceed ~7 (Figure 5-3) and the experiments did not involve cement. Future investigations will focus on CSH mineral reactions in the IEBS experiments with Grimsel granodiorite and Wyoming bentonite.

H_2S Generation—Fluid extraction from the IEBS experiments was accompanied by strong $H_2S_{(aq,g)}$ smells during the course of the 250°C experiments. The $H_2S_{(aq,g)}$ is most likely related to pyrite solubility from the starting Wyoming Bentonite in a chloride-bearing solution (Crerar et al., 1978; Ohmoto et al., 1994) and the sulfate concentration in the synthetic Grimsel groundwater solution. The reducing nature of the experimental system likely preserved the $H_2S_{(aq,g)}$ species. Pyrite contents obtained by QXRD analyses for the Colony Wyoming bentonite (0.4 wt.%) are listed in Table 5-3. Grimsel granodiorite lacks pyrite, but the synthetic Grimsel groundwater contains appreciable SO_4^{2-} (Table 5-2). The QXRD results show a slight decrease in the abundance of pyrite in the reaction products; however, the low bulk abundance likely resulted in some uncertainty in the result.

Sulfide-induced corrosion of the waste canisters is the primary concern for the Swedish repository systems (Börjesson et al., 2010), therefore the Swedish Nuclear Fuel and Waste Management Company (SKB) have emplaced fairly strict sulfur specifications (sulfide content <0.5 wt.%; total sulfur <1 wt.%) for the bentonite buffer used in their repositories (Börjesson et al., 2010).

pH Effects—In IEBS-1 through IEBS-5, the solution starts with a pH of 8.5 and ends between 6 and 7.5. All the experiments drop in pH in the middle of the experiment to less than 6.7 before slightly rebounding (Figure 5-2). Many of the mineral-forming reactions described above are strongly influenced by the pH of the system. Most mineral reaction rates that are of concern to a repository are increased under high pH systems. Chermak (1992) showed that under pH conditions of 11 to 13, Na-rectorite was formed at 150 to 200°C within 17 days. Fully formed Na-mica (paragonite) developed after 32 days. Work from Eberl and Hower (1977) and Eberl (1978) do not show illitization until 260°C to 400°C at quenched pH's ranging from 4 to 5. These observations are consistent with the current IEBS research; illitization was not observed and Na-rich phyllosilicates formed.

The formation of C(A)SH minerals may also affect the pH of the system. Savage et al. (2002) describe the formation of tobermorite with the generalized reaction:

$$Ca^{2+} + SiO_{2(aq)} + H_2O \rightarrow \text{tobermorite} + H^+ \qquad \textit{Equation 5-3}$$

in which H^+ is produced. Thus, the formation of C(A)SH minerals, such as tobermorite, may buffer the solution to lower pH values. Savage (1997) reported that zeolite formation within bentonite in contact with cement occurs at lower pH values and C(A)SH mineral formation is favored at high pH (> 11.5). In the IEBS experiments, C(A)SH minerals formed, but solution pH values remained below ~7 for the duration of the run. The formation of C(A)SH minerals at low pH (<7) in the IEBS experiments is at odds with previous experiments and will be the subject of our future investigations.

Summary—The mineralogical and geochemical changes observed in the Wyoming bentonite-Grimsel granodiorite experiments can be applied to understanding potential material interactions in a high-temperature, crystalline repository. Montmorillonite remained stable in the 250°C hydrothermal experiments, indicating the bulk composition of the system likely prevented smectite illitization. Quartz precipitation occurred, likely related to breakdown of precursor zeolite (clinoptilolite) in the Wyoming bentonite. Minor CSH phases were observed and may be precursor phases to zeolites. Preliminary findings suggest that the clay barrier may only experience slight alteration in the initial thermal pulse in a repository setting, but this finding should be supported by longer term experiments and full-scale demonstrations (e.g., HotBENT).

5.4.2 Colloid Generation

The formation of bentonite colloids is likely significant for process models of repository function, as colloid-facilitated transport of radionuclides may occur in a crystalline system (e.g., Missana and Geckeis, 2006). Moderately stable colloids were observed in re-suspensions of gel formed in IEBS-5, and likely are present in the other experiments that are yet to be characterized. Colloid stability at the high temperatures utilized in this experimental study is not well known. According to the DLVO theory (named after Boris Derjaguin and Lev Landau, Evert Verwey and Theodoor Overbeek), colloids are likely not stable in solution at the temperature of the experiment (250°C) due to reduction in surface charge density and electric double layer thickness of the colloid particles (e.g., Garcia-Garcia et al., 2009). Therefore, in our reaction products, colloids were likely stabilized in solution to form a gel phase upon experiment cooling. Future work will investigate if colloids are present in aqueous samples extracted while the experiment is at temperature and the effects of hydrothermal treatment on the physical properties of bentonite colloids.

5.4.3 Effects of Ordinary Portland Cement

One experiment containing a cured chip of OPC was completed in FY20. Characterization results are still in progress; preliminary interpretations are presented here. The inclusion of the cured cement chip introduced multiple mineral phases and chemical species that were reactive at the temperature and pressure conditions of the experiment. The cement chip represented 18 wt.% of the total solid reactants and resulted in slightly increased solution pH values and diverse mineral reaction products in comparison to the results from IEBS-1 through IEBS-5 described above.

The effect on the system pH was not dramatically different from the experiments without cement (e.g., pH = ~7.5 versus pH = 6–7, respectively). It appears that OH^- derived from the cement chip was either quickly consumed by mineral-forming reactions and/or the system was buffered by zeolite/clay mineral forming reactions. Local changes in mineralogy (e.g., stability of portlandite) and chemistry from the edge to the interior of the cement chip will be evaluated via SEM and EDS analysis of a thin section of a cross section of the cement chip and XRD techniques.

In full-scale EBS demonstrations, such as FEBEX, the alteration zone in the bentonite at the cement-bentonite interface (at ambient temperatures) only extends several cm into the buffer (Fernández et al., 2017). Characterization of the reaction products from IEBS-6 is in progress, but it appears that zeolite and secondary mineral formation occurred throughout the clay mineral groundmass of the reaction products, not just in the clay observed attached to the reacted cement chip (Figure C-12A,B). Quantitative XRD results from the clay groundmass will show the proportion of clay and other precursor mineral phases that were consumed in zeolite and CSH mineral-forming reactions, which will provide insight to potential volume decreases/porosity development at the cement-bentonite interface.

5.4.4 Steel-Bentonite Interface Mineral Precipitation and Steel Corrosion

The results from these experiments show a dynamic environment in the experimental systems at the bentonite-metal interface. The bulk chemistry likely controls the alteration mineralogy, as demonstrated by the similarities in mineral precipitation in the experiments. The new growth of surface-bound minerals is likely due to direct crystallization in the localized environments surrounding the metal with the steel material acting as a substrate for mineral growth in response to corrosion.

The findings of our previous investigations on mineral precipitation at the steel-bentonite interface in hydrothermal experiments mimicking a crystalline rock environment have been described in Caporuscio et al. (2018; 2019). These previous reports describe the layered alteration sequence observed on the surface of steel coupons included in experiments with Wyoming bentonite, Grimsel granodiorite, and synthetic Grimsel groundwater. In general, an Fe-oxide layer is observed to form an alteration layer on the surface of the steel coupons after six to eight weeks of hydrothermal treatment. The Fe-oxide layer is followed by a thin layer of chlorite and sulfides precipitated from sulfide-bearing fluids, likely from pyrite dissolution in the bentonite/host rock. This thin layer is followed by a ~0.30 to 150 μm thick layer of newly crystallized Fe-saponite. The Fe-enriched phyllosilicate minerals observed are interpreted to be the results of the interaction of Fe supplied by steel corrosion and clay minerals in the bentonite (i.e., montmorillonite). Locally, chlorite and CSH minerals are also observed attached to the steel surface. The following describes our finding from a general crystalline rock environment.

5.4.4.1 Steel-Bentonite Interface Reactions

The steel corrosion products from the interaction with bentonite produced four layers onto the steel substrate: (1) general corrosion, (2) Fe-oxide, (3) CSH and/or chlorite (if present), and (4) Fe-saponite outer layer with occasional minor sulfides. The post-experiment steel shows uniform corrosion at the conditions of these experiments. The occurrence of the Fe-saponite is associated with the corrosion of the steel, but there is no significant alteration of the bentonite away from the steel surface (>100 μm) (Figure 5-18). The precipitation of sulfides, such as pentlandite, formed at early stages of corrosion and is likely due to pyrite decomposition in the bentonite. The occurrence of the sulfides is closely associated with the Fe-saponite at the steel interface. Fe-saponite formation is related to the interaction of the Fe-bearing/Si-rich fluids from the leaching of the steel and bentonite dissolution (Cheshire et al., 2018; Jove-Colon et al., 2019). The surface-bound Fe-rich minerals likely directly crystallized from solution in the local environments surrounding the metal plates as these phases are not observed elsewhere in the clay reaction products. The localized presence of the newly formed Fe-rich phases together with the lack of significant increase in aqueous Fe in the reaction fluids indicate that steel coupon reactions did not influence solution chemistry of the bulk system. Further testing needs to be performed (i.e. Raman spectroscopy or XRD) to identify the Fe-oxide phase of the steel surface.

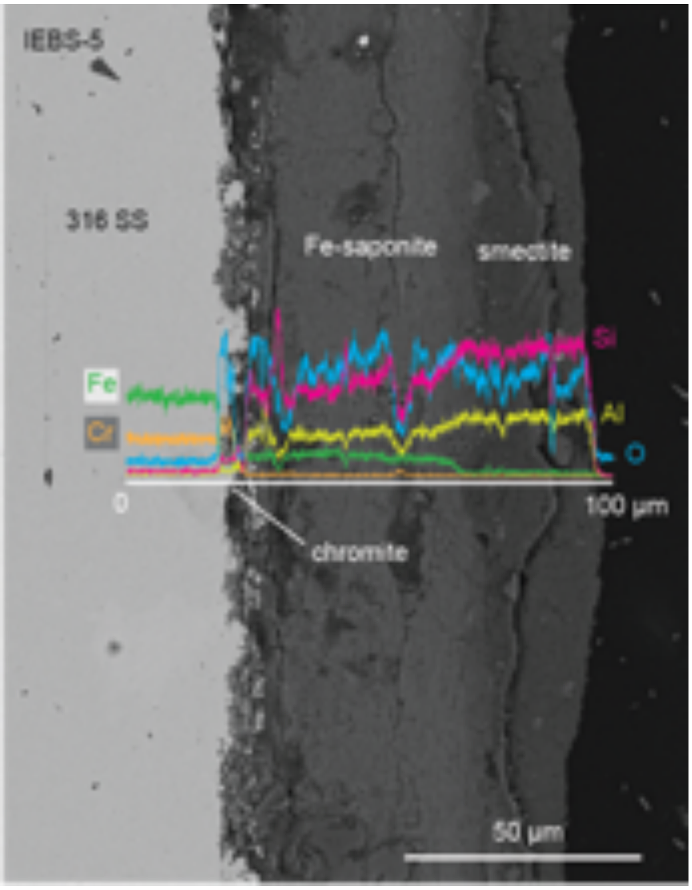

Figure 5-18. Energy dispersive X-ray spectroscopy (EDS) chemical results from a line scan (white line) across the steel-clay boundary. A layer of chromite followed by Fe-saponite is observed attached to the steel surface. A layer of unaltered smectite is observed outboard of the Fe-saponite layer.

The rate of alteration of the bentonite in proximity to the steel corrosion is dependent on the ability of the iron to migrate through the clay as Fe^{2+}. This is regulated by the rate of corrosion, the rate of formation of the Fe-oxide, which may reduce the Fe^{2+} released, and the system dynamics (Mosser-Ruck et al., 2010). The general reaction between the steel and bentonite is depicted in Figure 5-19. The stainless-steel interaction with bentonite via congruent dissolution/oxidation can be detailed by the reactions shown below.

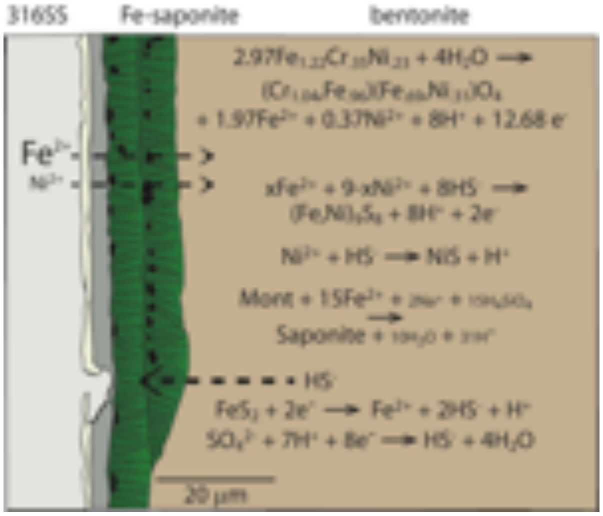

Figure 5-19. A stylized representation of phyllosilicate mineral growth at the steel interface. Of particular interest is the reaction Montmorillonite → Fe-saponite.

Synthetic Fe-saponites have been crystallized in dilute solutions and gels of silica, Fe-, Al-chlorides at temperatures up to 850°C and pH of 8.5 to 9.5 (Kloprogge et al., 1999). This is consistent with a partial dissolution of the steel plates contributing ferrous iron into a fluid phase with silica and aluminum, thereby facilitating Fe-saponite (smectite) crystallization with the steel surfaces acting as a growth substrate. Further, Fe-saponite alteration into chlorite has been suggested (Mosser-Ruck et al., 2010) in the presence of ferrous iron at temperatures approaching 300°C and near-neutral pH. This was confirmed by Mosser-Ruck et al (2016) through long duration experiments (up to 9 years). The authors were able to demonstrate that smectite is consumed by dissolution to produce chlorite (chamosite) by precipitation. Mosser-Ruck et al. (2016) depicts this reaction by:

$$3\text{ smectite} + 3\text{ Fe} + 4\text{ H}_2\text{O} \rightarrow 1\text{ chlorite} + 3\text{ quartz} + 2\text{ albite} + 3\text{ H}_2 + \text{zeolite} \qquad \textit{Equation 5-4}$$

The stainless steel interaction with bentonite via congruent dissolution/oxidation can be detailed by the following reactions (Cheshire et al., 2018).

Stainless Steel Dissolution

$$\text{Fe}_{1.22}\text{Cr}_{0.37}\text{Ni}_{0.22} \rightarrow 1.22\text{ Fe}^{2+} + 0.37\text{ Cr}^{3+} + 0.22\text{ Ni}^{2+} + 3.99\text{ e}^{-} \qquad \textit{Equation 5-5}$$

Formation of Fe-Saponite and Sulfides

$$\text{Fe}^{2+} + \text{Ni}^{2+} + \text{Cr}^{3+} + \text{H}_2\text{S}_{(aq)} + \underbrace{(\text{Na,K,Ca})_{0.33}(\text{Al}_{1.67},\text{Fe}^{3+}_{0.20},\text{Mg}_{0.13})\text{Si}_4\text{O}_{10}(\text{OH})_2}_{\text{smectite}} \rightarrow$$

$$\underbrace{(\text{Fe,Ni,Cr})_9\text{S}_8}_{\text{Pentlandite}} + \underbrace{(\text{Na, K, Ca})_{0.33}\,\text{Fe}_3(\text{Si}_{3.67},\text{Al}_{0.33})\text{O}_{10}(\text{OH})_2}_{\text{Fe-saponite}} \qquad \textit{Equation 5-6}$$

5.4.4.2 Steel Corrosion Summary

The results from the experiments discussed here indicate that the waste container will act as a substrate for mineral growth in response to steel corrosion. These surface-bound minerals likely formed via direct crystallization from the solution in their specific localized environment surrounding the metal plates. The iron in the newly precipitated mineral layers at the steel interface is sourced as the steel corrodes; however, the steel coupons from this study have yet to be evaluated for general versus localized (e.g., pitting) corrosion. Future work is needed to address the extent these mineral precipitants influence the engineered barrier performance or the repository system as a whole, and to whether these minerals (e.g., Fe-saponite) will act as a passive protecting layer against further corrosion of the waste containers.

5.5 Conclusions

This document summarizes the EBS Grimsel granodiorite wall rock hydrothermal experiments IEBS-1 through IEBS-6 that include combinations of Wyoming bentonite + Grimsel granodiorite + Grimsel granodiorite synthetic groundwater ± *stainless/low carbon steel* ± *cured OPC*. Results from experiments IEBS-1 through IEBS-6 are presented and include: 1) SEM images and EDS data, 2) QXRD data, 3) clay mineral XRD data, 4) EMP data for major mineral phases, and 5) aqueous geochemistry data.

Concepts developed so far include:

- Illitization of montmorillonite in Wyoming bentonite in a Grimsel granodiorite wall rock environment may be restricted due to the bulk chemistry of the overall system (i.e., low potassium) and/or kinetics
- Montmorillonite structural alterations were not observed in the Wyoming bentonite + Grimsel granodiorite + cured OPC experiment
- The inclusion of a cured Portland cement chip did not dramatically increase the solution pH but lead to the formation of diverse secondary mineral formation
- Analysis of clay mineral structural changes reveals that montmorillonite alteration did not occur
- Newly crystallized Fe-saponite forms at the steel-bentonite interface and grows perpendicular to the steel surface.
- Fe enrichment in the bentonite due to interaction with steel corrosion products does not migrate far from steel (<50 μm)
- C(A)SH minerals formed within the Wyoming bentonite-Grimsel granodiorite system
- Zeolite-forming reactions are not favored in the Wyoming bentonite-Grimsel system
- General steel corrosion is observed and thicknesses/rates of Fe-rich clay formation were measured

Research needs to be emphasized in the following areas for FY21:

- Continue to build a database of Grimsel granodiorite and EBS experiments
- Further work to understand formation of C(A)SH minerals at relatively low pH (<8.0)
- Complete characterization of the reaction products from the experiments with cement, including mineral reactions in the bentonite and within the cement chip
- Develop understanding of the role of secondary mineral formation in systems that include OPC
- Include low-pH cement formulations in EBS experiments
- Corrosion of steels/interface silicate mantling effects

- Detailed geochemical modelling of geochemical changes observed in the bentonite-granodiorite system
- Incorporate results into generic modeling codes

The database, along with summary conclusions, will be of use to other experimental teams in the DOE complex, system modeler, and the international repository science community in the development of concepts related to high-temperature crystalline repository environments.

5.6 Acknowledgements

We would like to thank Oana Marina and Rose Harris at LANL for water chemistry analyses and Katherine Telfeyan (LANL) for collecting the Zetasizer results. Scanning electron microscopy facilities were provided by Materials Science and Technology group at Los Alamos National Laboratory. Dr. Lindsey Hunt at the University of Oklahoma was instrumental in the obtaining of EMP analyses. QXRD analyses were performed by Dr. Steve Chipera at Chesapeake Energy. Funding was through the Department of Energy's Spent Fuel and Waste Science and Technology.

6. PROGRESS ON INVESTIGATING THE HIGH TEMPERATURE BEHAVIOR OF THE URANYL-CARBONATE COMPLEXES

6.1 Introduction

If a containment breach and subsequent infiltration of surrounding groundwater into a repository system occurs in the first 50 to 200 years of its lifetime (Hardin et al., 2013), there is a significant possibility that nuclear waste will interact with water at the peak thermal conditions of the repository. Although the aim in designing nuclear repositories is to maintain the surrounding near field environment at temperatures below the boiling point of water (primarily by employing an appropriate spatial distribution of hot canisters), temperatures of nuclear assemblies stored in the canisters, and, thus, the temperatures at which solutions interact with nuclear waste, can remain at 300°C (or higher) for a significant duration (Buscheck et al., 2002). Moreover, if the larger DPC concept is adopted, models suggest that not only the assembly itself, but even the surface of the canister could reach temperatures of ~300°C or higher (Greenburg and Wen, 2013), shifting the near-field environment to a much higher temperature range. Hence, understanding the solubility of U at elevated temperatures is critical. However, whereas the behavior of U has been studied in detail at ambient conditions, evaluation of the aqueous speciation of this element at elevated temperatures has been mostly done based on the theoretical extrapolation of available low-T stability constants: experimental high-T data are extremely sparse. Thus, the vast majority of proposed high-T models do not have any experimental support.

In general, uranium is most effectively transported by hydrothermal fluids when present in its hexavalent (U(VI)) oxidation state which, as the uranyl ion (UO_2^{2+}), forms stable complexes with a range of inorganic ligands, most commonly Cl^-, SO_4^{2-}, OH^- and CO_3^{2-} (Bastrakov et al., 2010; Guillaumont et al., 2003). In acidic fluids, uranyl complexes most readily with Cl^- and SO_4^{2-} (Bastrakov et al., 2010) but almost all groundwater systems and many uranium ore deposits are characterised by fluids with near-neutral pH ranges (Cuney, 2009; Hem, 1985; Ondrus et al., 2003).

Over such pH ranges uranium mobility is controlled by hydroxy and particularly carbonate complexes and current wisdom suggests that this holds true at both ambient and elevated temperatures (Bastrakov et al., 2010; Ewing, 2015; Ondrus et al., 2003). However, to date, there have been no experiments conducted on uranium carbonate complexes at elevated temperatures. This means that all inferences and models made for such conditions are solely based on extrapolations of room temperature data. Recent high-temperature experiments on other uranyl complexes have shown that such extrapolations are seldom accurate, potentially being off by orders of magnitude (Kalintsev et al., 2019; Migdisov et al., 2018). This casts doubt on the accuracy and relevance of any high-temperature models that indicate carbonate as a potent transport enabler of uranium. Given that these models are used to understand uranium transport in ore deposits and guide the designs of nuclear waste repositories this indicates that our knowledge of uranium transport in these systems is likely to be significantly flawed.

Considering the lack of high temperature experimentally-based data coupled with the great importance placed on uranyl-carbonate complexes as a transport enabler of uranium in hydrothermal systems the aim of the experiments documented in this report was to experimentally derive the thermodynamic constants of the uranyl carbonate complexes at elevated temperatures thus permitting accurate modeling of the aqueous mobilization of uranium (VI) by carbonate-bearing solutions in repository environments.

6.2 Experimental Overview and General Considerations

To determine the formation constants of the uranyl carbonate complexes at high temperature a number of experimental techniques were used, namely UV-VS, an autoclave solubility technique and Raman spectroscopy. In addition, to provide complementary structural data XAS experiments were also planned. To date, UV-VS, solubility and XAS experiments have been conducted though data collection and processing are still in progress, as such all data reported here are preliminary and interpretations based on them may change in the future. Raman experiments have not yet been conducted but will commence within the next month. It is worth mentioning that the purpose of these experiments is not to accurately replicate environmental conditions but rather to derive fundamental thermodynamic constants characterizing stability of uranyl-carbonate complexes at a range of temperatures. This task requires experimental operation with highly simplified systems, which can differ significantly from systems encountered in nature. Thermodynamic formalism suggests presentation of these fundamental values in a media-independent form (extrapolation to infinite dilution) to allow employment of these constants in modeling efforts applied to any kind of media that can be encountered in more complex real-world systems.

6.2.1 High Temperature Activity Model

Considering the above, experimental systems identified for investigation must be selected to be such that reliable extrapolation of experimentally derived quotients to infinite dilution is supported by experimentally proven models and calculation techniques. This requires the availability of accurate and experimentally proven activity models for chemical systems investigated in the experiments. Unlike at ambient temperatures, the selection of reliable activity models is extremely limited at the temperature range of interest (200°C–350°C). In fact, the best experimentally proven models at these temperatures are those developed for solutions predominated by a single 1:1 electrolyte, namely NaCl, KCl, NaOH, or KOH. These models are based on the extended Debye-Hückel model (Equation 6-1) (Helgeson et al., 1981; Oelkers and Helgeson, 1990, 1991) modified for 1:1 electrolyte-dominated solutions:

$$\log \gamma_{\mathrm{i}} = -\frac{\mathrm{A} \cdot [\mathrm{Z_i}]^2 \cdot \sqrt{\mathrm{I}}}{1 + \mathrm{B} \cdot \mathring{a} \cdot \sqrt{\mathrm{I}}} + \Gamma + \mathrm{b}_{\gamma}\mathrm{I} \qquad \textit{Equation 6-1}$$

where A and B are the Debye–Hückel parameters, γ_i, Z_i, Γ and $\dot{a}$ are the individual molal activity coefficients, the ionic charge, the molarity to molality conversion factor and the distance of closest approach of an ion i, respectively. The effective ionic strength calculated using the molal scale (moles per kilogram of water, abbreviated *m*) is I and b_γ is the extended-term parameter for the chosen 1:1 background electrolyte. Given the abovementioned modeling restrictions, to ensure the reliable extrapolation of the obtained data to infinite dilution, the experiments reported in this contribution were performed in solutions with a salt load predominated by NaCl. The concentrations of NaCl were chosen to be 1–2 *m*, while the concentrations of other solution components were at least two times lower than that of NaCl. One caveat of using NaCl-predominant solutions is that for such systems complexation of uranyl with chloride anions needs to be accounted for in the data interpretation. The stability constants of uranyl-chloride species required for this interpretation were recently obtained by our group for experimental conditions discussed in this report (Migdisov et al., 2018), and were used in the data interpretations discussed below.

6.3 UV-Visible Spectroscopy Experiments

6.3.1 UV-Visible Spectroscopy Method

In-situ UV-VS experiments were performed using the high-temperature flow-through spectroscopy cell available at Radiological Hydrothermal facility at LANL (EES-14; Figure 6-1). The cell comprises a main titanium body, sealing screws, gaskets, sapphire windows and titanium capillary heads—all constructed from commercial grade 2 titanium. Prior to experiments, all titanium cell components were passivated by heating them in air at 400°C for 12 hours thus promoting the formation of a dense, chemically inert surface coating of titanium oxide (TiO_2/rutile). Experimental solutions were introduced into the cell via titanium and polyether ether ketone (PEEK) capillaries. Titanium capillaries were used proximal to the main cell where the experimental solution was hot and PEEK capillaries were used where the solution was cool. Flow rate was controlled by a PEEK high-performance liquid chromatography (HPLC) pump and pressure was controlled using a PEEK back-pressure regulator. Together, the use of sapphire windows, Teflon O-rings, PEEK, and passivated titanium ensured that the solution was only ever in contact with chemically inert surroundings. Heating elements and a thermocouple were inserted into holes through the main cell body, allowing solution temperature to be controlled to within ± 0.5°C. This cell permits the in-situ measurement of the absorption patterns of heated solutions up to ~270°C (though potentially higher if gold O-rings are used instead of Teflon). Prior to experimental solution spectral measurements, the background absorbance of the sapphire windows was determined. This was done by measuring the spectrum of de-ionized water at each experimental temperature. The path length of the cell was calculated by comparing peak heights of several experimental solutions measured in our cell and a standard quartz cuvette with a known path length of 10 mm. The peak ratio was used to determine a path length of 9.5 mm.

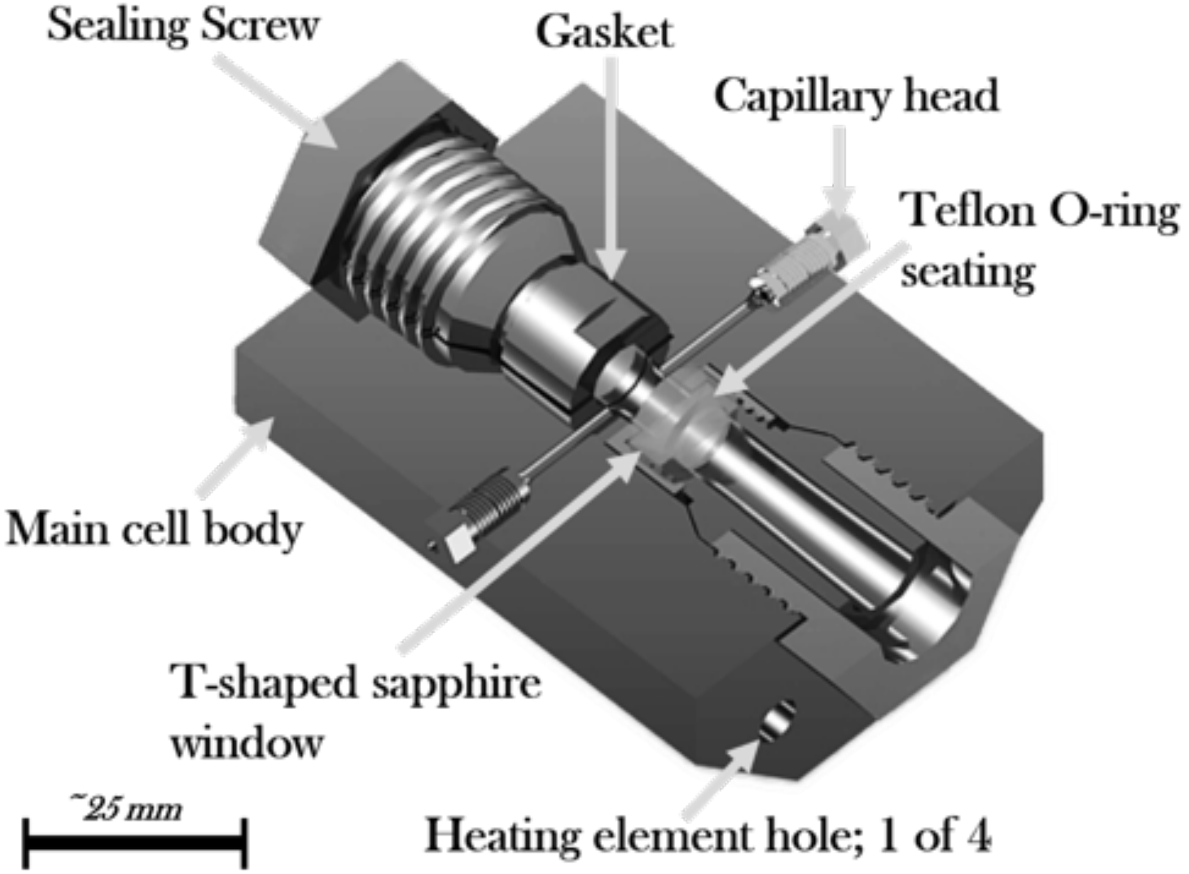

Source: Kalintsev et al. 2019.

Figure 6-1. Schematic diagram of the Hydrothermal UV-VS flow-through cell

Spectra were to be collected for a series of 25 homogeneous aqueous solutions with progressively increasing carbonate concentrations (0.05 to 0.525 Molar) and identical uranium concentrations (6 millimolar). For reasons discussed above all solutions additionally contained 1 Molar NaCl. Precise solution compositions are reported in Table 6-1. Isothermal spectral sets were to be measured at 25°C, 100°C, 150°C, 200°C and 250°C at a constant pressure of 100 bar using a Cary 5000 spectrophotometer across a wavelength range of 340–700 nm at 0.2 nm intervals. An amount of 6 mM of uranium was chosen to provide the best uranium signal without oversaturating the detector.

Spectra of experimental solutions were collected starting from that with the lowest ligand concentration. Initially, each solution was pumped through at a high flow rate to thoroughly flush out the cell of any remnant de-ionized water or prior solution thus ensuring that the cells contained only the experimental solution we intended to measure. The flow rate was then reduced and the solution was given time to equilibrate after which the solution's spectrum was recorded. This procedure was repeated until all solutions were measured for a single temperature then repeated for each experimental temperature.

Table 6-1. Table detailing the concentrations of $NaHCO_3$ present in the solutions presently investigated with solubility experiments. The concentration of uranium dissolved is also reported. Note that all solutions additionally contained ~1 *m* NaCl.

250°C Solution Compositions and Measured Concentrations of Dissolved Uranium			200°C Solution Compositions and Measured Concentrations of Dissolved Uranium		
Solution No.	$\text{Log}_m(\text{NaHCO}_3)$	$\text{Log}_m(\text{U})$	Solution No.	$\text{Log}_m(\text{NaHCO}_3)$	$\text{Log}_m(\text{U})$
10	−3	−5.9999834	45	−2.0190594	−4.5579765
11	−2.30103	−6.7858794	46	−2.0190594	−4.958251
12	−2	−6.8079575	47	−0.9983162	−5.2353915
13	−1	−7.0168159	49	−0.9983162	−5.3296375
14	−0.69897	−5.552255	50	−0.9983162	−4.5773973
15	−0.5228787	−5.6499304	52	−0.5214811	−4.7690914
16	−0.39794	−6.783065	54	−0.2213826	−4.850581
4	−2	−6.143808	55	−0.2213826	−5.2356274
5	−1.5228787	−5.4743085	56	−0.2213826	−5.326694
6	−1.30103	−5.7541698	—	—	—
7	−1.09691	−6.4865333	—	—	—
8	−1	−5.8988037	—	—	—

6.3.2 UV-Visible Spectroscopy Results

To date, UV-VS experiments have been performed at 100°C, 150°C, 200°C, and 250°C (experiments have been interrupted by the COVID-19 quarantine). The spectra collected are reported in Figure 6-2. At 150°C, 200°C, and 250°C (Figure 6-2A, B, and C respectively), spectra could only be collected from solutions with greater than 0.0875, 0.15 and 0.425 Molar total carbonate respectively. Solutions with concentrations lower than those mentioned above could not be measured at the respective temperatures because significant precipitation of an unidentified uranium phase was observed which lead to clogging of the flow-through system. Characterization of this precipitating phase was impossible as it re-dissolved upon cooling the cell and thus could not be isolated for XRD measurements. Nearly all spectra collected from subsequent solutions with higher carbonate concentrations showed no spectral shifts with increasing carbonate concentrations. Spectra were also collected at 100°C (Figure 6-2D) from solutions that were diluted by a factor of 3 relative to those measured at 150°C, 200°C and 250°C (thus containing ~2 mM instead of the original 6 mM uranium) in the hope of reducing precipitation effects; this allowed us to investigate lower carbonate concentrations however shifts in the spectra were still minimal despite carbonate concentrations changing by an order of magnitude over the whole solution series. It is evident from these observations that the stability of carbonate complexes is much lower than theoretically predicted. However, theoretical predictions (Figure 6-3) do suggest that over most carbonate concentration ranges when carbonate complexes are stable uranyl speciation appears to be dominated by a single complex, namely $UO_2(CO_3)_3^{4-}$, this is consistent with our observations of minimal spectral shifts observed at all temperatures. This lack of observed spectral shifts however makes it impossible to derive any thermodynamic data from the spectra we collected and suggests that any further UV-VS experiments may require a different approach. UV-VS experiments were interrupted by the COVID-19 quarantine. As laboratory work returns to normal, and in order to quantify changes in the stability of uranyl-carbonate complexes with temperature at low to moderate temperatures, we plan to conduct further UV-VS experiments at temperatures ranging from 25°C–120°C. These experiments will attempt to probe even lower carbonate concentrations in an effort to produce significant enough shifts that will in turn allow the derivation of thermodynamic data. These measurements will also complement planned Raman measurements that will be conducted at similar conditions.

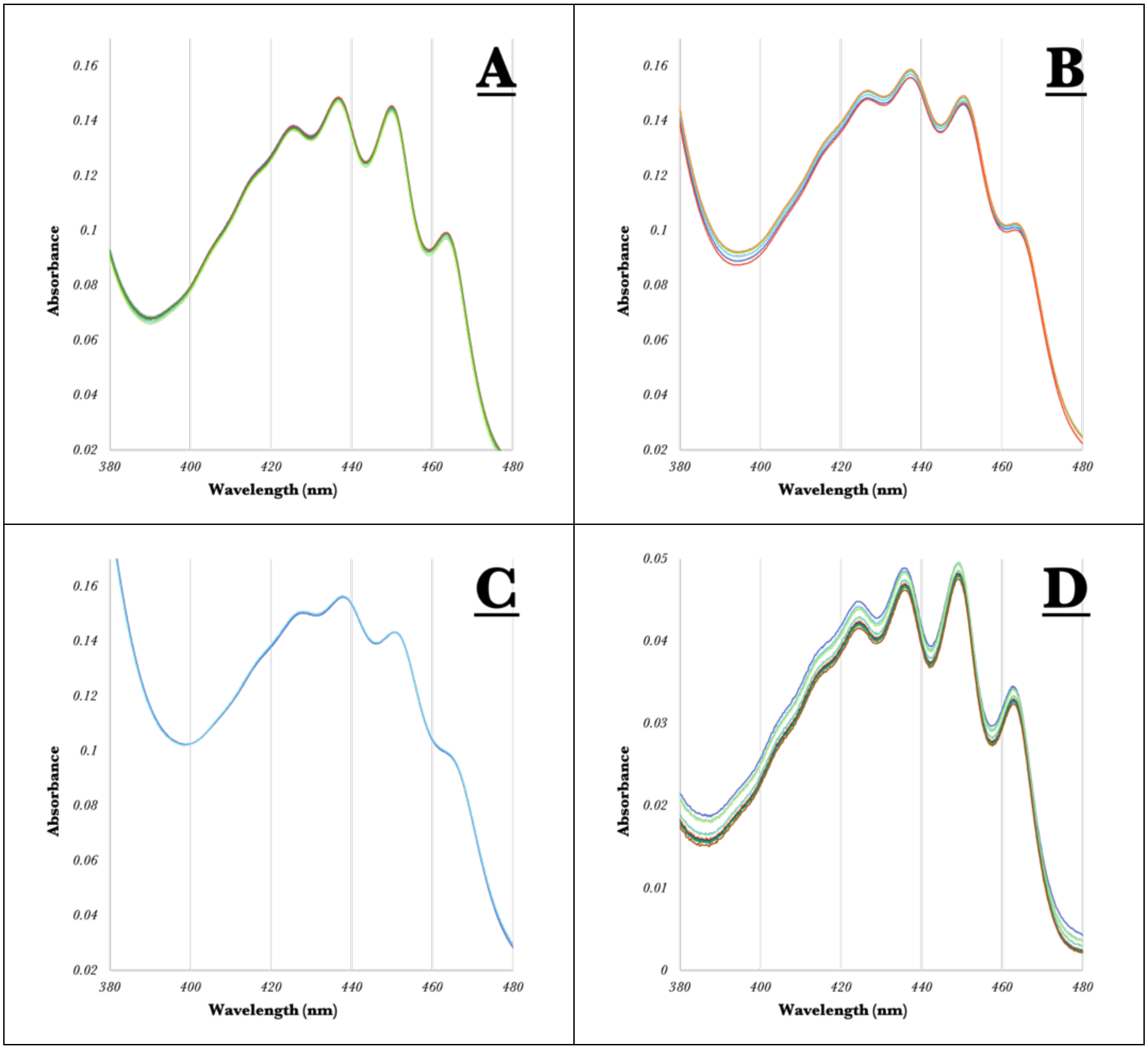

Figure 6-2. (A) UV-Visible spectra collected for 6mM uranyl carbonate solutions at 150°C (carbonate concentration from 0.0875 to 0.2 M), (B) at 200°C (concentration from 0.15 to 0.25 M), (C) at 250°C (concentrations of 0.425 and 0.525 M), and (D) at 100°C with solutions diluted to ~2 mM Uranium (1:6 from originals) and carbonate concentrations from 0.018 to 0.1 M.

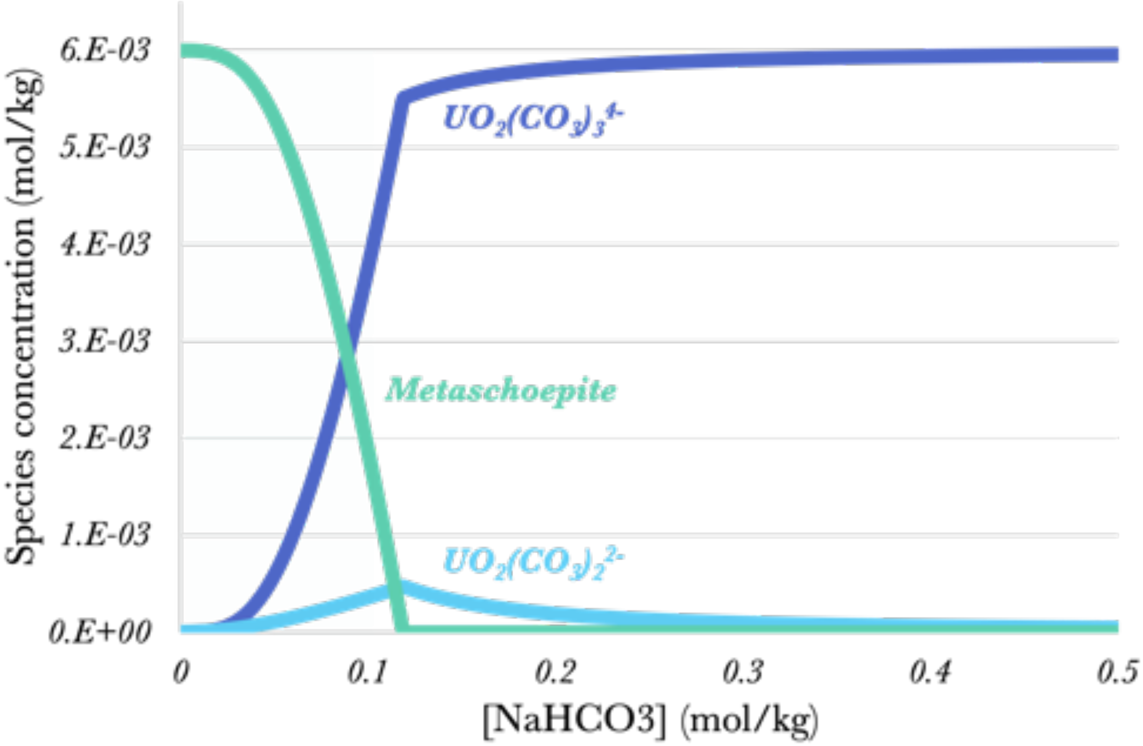

Figure 6-3. Theoretically calculated speciation of 6 mM uranium at 250°C relative to total carbonate concentration.

6.4 Solubility Experiments

6.4.1 Solubility Method

The purpose of our autoclave solubility experiments was/is to determine both the stoichiometry and formation constants of the uranyl-carbonate complex predominant over temperatures between 150°C–250°C. Experiments were performed in Teflon-lined, titanium (commercial grade 2, 30–40 cm^3) autoclaves containing 2 differently sized upright Teflon tubes (each sealed at one end) (Figure 6-4). UO_3 was used as a reference solid and a mix of Mn_2O_3 and Mn_3O_4 was used as an oxygen fugacity buffer to ensure that uranium was only present in its hexavalent oxidation state during the experiments. UO_3 was made to interact with experimental solutions containing varying concentrations of carbonate and a predominance of NaCl. To ensure that our experiments only recorded the results of equilibrium at the target temperature we took advantage of the volumetric expansion of our solutions with temperature. Solution expansion ratios were calculated using the SOWAT (SOdium chloride WATer) equations of state discussed in Driesner (2007) and Driesner and Heinrich (2007). These were then used to calculate precise volumes of experimental solution (~8 mL though this differed slightly between each autoclave) which at room temperature would be unable to fully submerge the reference solid tube but upon reaching the target temperature would expand sufficiently and 'spill over' and equilibrate with the reference solid (Figure 6-5). Autoclaves were heated to the experimental temperature in a ThermoFisher Scientific Thermolyne Largest Tabletop Muffle Furnace (±0.5°C). Pre-heating was first done at a "ramp" temperature lower than the desired experimental temperature, but high enough to overcome the slow kinetics of the solid-state redox buffer. Although the experimental solution undergoes thermal expansion at this stage, the volume of solution was calculated to ensure it was not sufficient to allow the solution to contact UO_3 at this temperature. The system re-equilibrated to the redox conditions set by the buffer for 2 days, after which the temperature was then ramped up to the desired experimental temperature, the solutions expanded further and contacted the UO_3 solid phase, initiating the dissolution/saturation processes. At the end of the experiments, autoclaves were removed and air-quenched to room temperature (~20 min). Quenching resulted in a quick contraction of the experimental solutions, which lost contact with the solid phase, precluding re-equilibration of the system at temperatures different from the experimental temperature. This approach ensured that the solubility determined in the experiments corresponded only to the experimental temperature and selected redox conditions, and was not affected by processes that may have occurred during heating/quenching of the autoclaves and due to redox impurities in the system. To ensure that any uranium that may have precipitated on the autoclave's walls during quenching was dissolved, 1–2 ml of concentrated nitric acid was added to each autoclave after cooling. Uranium concentrations in acidified solutions were then measured using Inductively Coupled Plasma – Mass Spectrometry (ICP-MS).

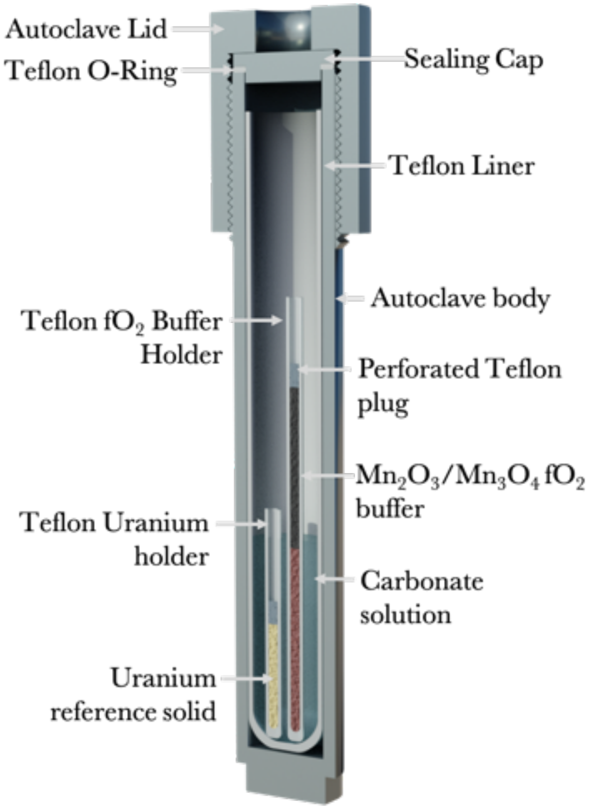

Figure 6-4. Schematic cross-section of the autoclave setup used in our solubility experiments. Note that this is representative of the experiment's state at ambient conditions. At the target temperature the experimental solution expands sufficiently to fully submerge the Teflon holder containing the uranium reference solid.

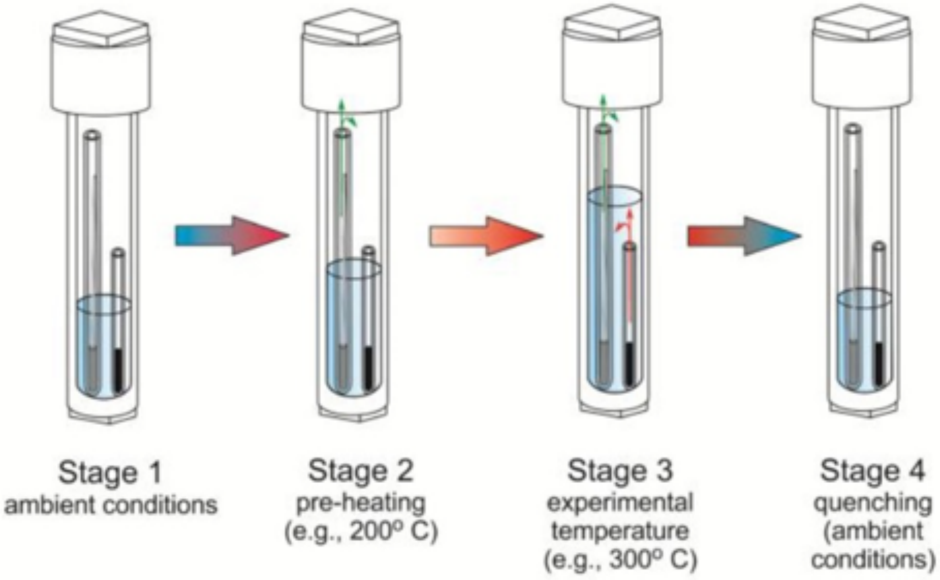

Figure 6-5. Illustration of heating procedure for autoclave solubility experiments. Note how the solution may only equilibrate with the solid at the target temperature.

Our experiments involve two series of solutions, one in which carbonate is introduced as $NaHCO_3$ (Fisher Chemical, Certified ACS) and the other as Na_2CO_3 (Anhydrous, Fisher Chemical, Certified ACS). The $NaHCO_3$ series is investigating carbonate concentrations ranging from 0–0.8 *m* whereas the Na_2CO_3 series is being conducted over a concentration range of 0–0.5 *m*. Solution pHs vary over temperature from 6.8 (25°C) – 7.5 (250°C) for the $NaHCO_3$ series and 12.1 (2°C) – 9.8 (250°C) for the Na_2CO_3 series. This allows us to determine whether uranyl-carbonate complexation behavior is affected by pH. All solutions used in these experiments also contained a predominance (1–2 *m*) of NaCl (for reasons discussed above). Based on high-temperature experimental data reported by Migdisov et al. (2018) predominance of uranyl-chloride species is not predicted for the pH ranges investigated.

In addition to the two experimental series described above a kinetic series was also conducted. This kinetic series was conducted in order to determine the length of time required to achieve equilibrium between the chosen reference solid and experimental solutions. In it, a number of identical solutions (each containing 0.2 Molar $NaHCO_3$) were heated to 200°C: then, single autoclaves were removed at regular intervals with the amount of uranium dissolved in each being measured. This allowed the plotting of total uranium dissolved as a function of time (Figure 6-6) thus revealing the time required for equilibration in our experimental systems. It was found that at 200°C the equilibrium/steady state was reached within 2 days. Thus, all experiments were maintained at the target temperature for 5 days to ensure without a doubt that equilibrium was reached.

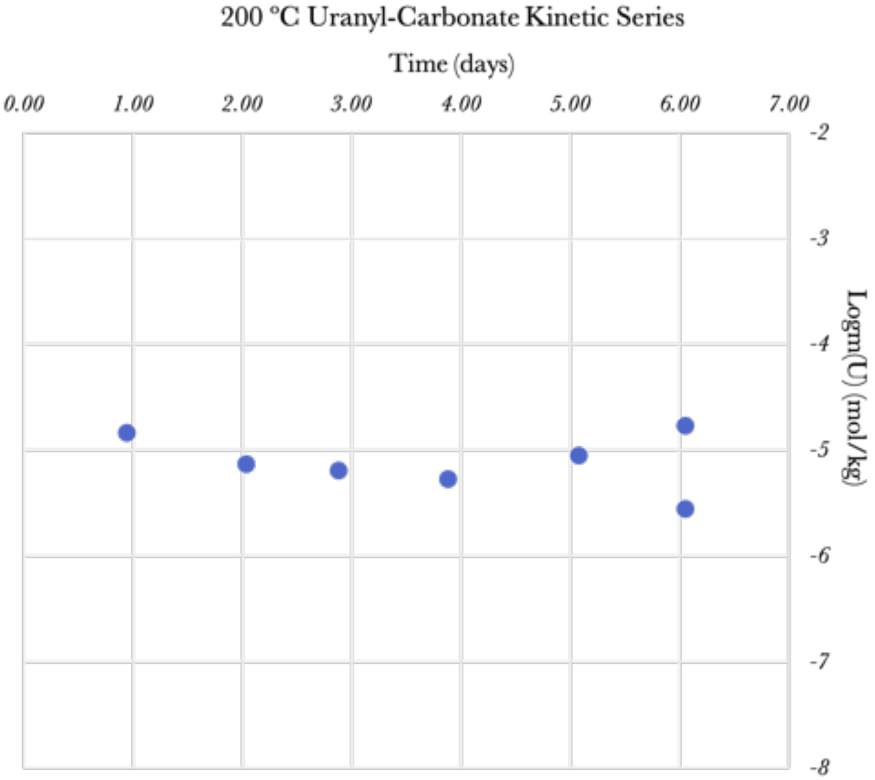

Figure 6-6. Results of kinetic series conducted at 200°C. These data suggest equilibrium is reached within 2 days of reaching the target temperature.

6.4.2 Solubility Experiment Results

To date, we have completed experiments from the $NaHCO_3$ series over concentrations ranging from 0.001 to 0.5 *m* and at 200°C and 250°C. The preliminary results from these initial experiments are reported in Figure 6-7. From these, we observed no dependence of uranium solubility on carbonate concentrations up to 0.5 *m*, and extremely low solubilities of uranium overall (~4 orders of magnitude less than theoretically predicted at 250°C with 0.5 *m* $NaHCO_3$). Solubility was higher by ~1 order of magnitude at 200°C than at 250°C. Together these data suggest that at least over the carbonate concentration range and temperatures investigated uranyl carbonate complexes are ineffective at solubilizing uranium confirming observations made during our UV-VS experiments. The lack of an observed dependence between dissolved uranium and carbonate concentration suggests that a different ligand is responsible for solubilizing uranium in high-temperature carbonate-bearing solutions. The solubility experiments discussed above will be continued in order to generate a more complete dataset. At 200°C and 250°C we plan to extend the range of investigated carbonate concentrations up to 0.8 *m*. Should a dependence of uranium concentration on carbonate be observed this will permit the derivation of the thermodynamic formation constants for the carbonate complex predominant at such conditions. Afterwards, solubility series will also be collected at 150°C for the $NaHCO_3$ series, and at 150°C, 200°C, and 250°C for the Na_2CO_3 series.

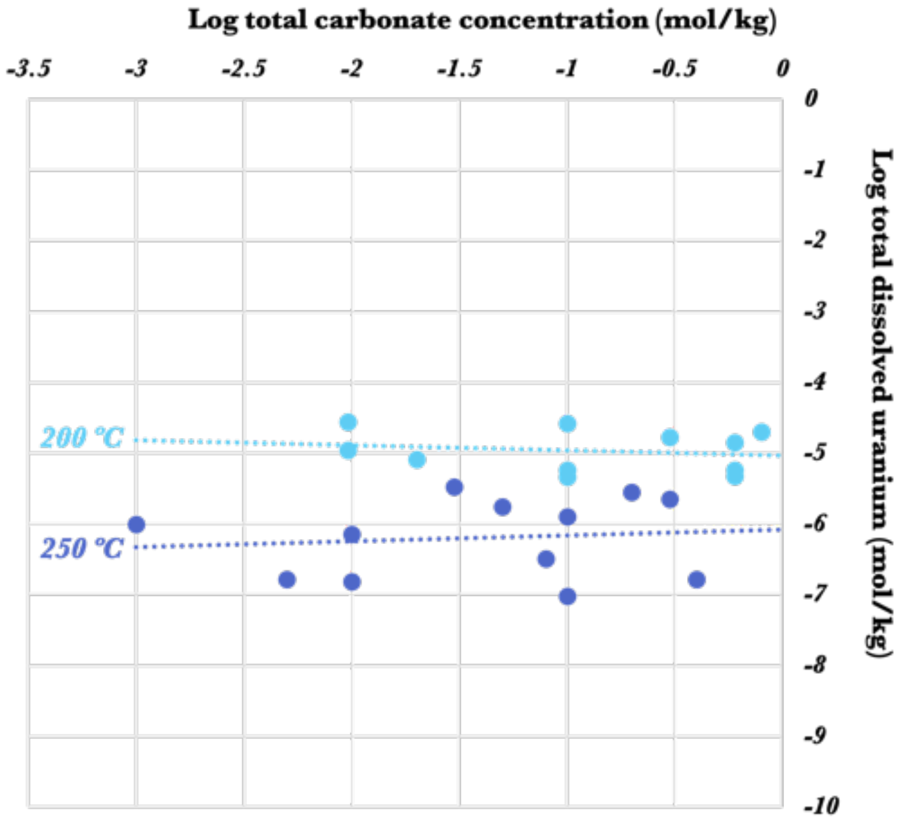

Figure 6-7. Preliminary autoclave solubility experiment results collected at 200°C and 250°C over carbonate concentrations of 0.001 to 0.5 *m*

6.5 X-Ray Absorption Spectroscopy

6.5.1 X-Ray Absorption Spectroscopy Method

To gain a molecular level understanding of the stoichiometry and structure of the uranyl carbonate complexes as well as to investigate the effect of pH on their behavior we conducted additional X-ray absorption spectroscopy (XAS) experiments.

6.5.1.1 Data Collection Procedure

XAS experiments were conducted at the Australian synchrotron at the XAS Beamline using the Australian Extreme SpecTROscopy (mAESTRO) cell system (Tian et al., 2010). The mAESTRO cell (Figure 6-8) consists of an external water-cooled high-pressure vessel equipped with beryllium windows enabling the collection of transmission and fluorescence X-ray signals. The sample is contained inside a glassy carbon tube with an internal diameter of 4 mm. Pressure is applied to the sample by two glassy carbon pistons, using helium as a pressure medium. The glassy carbon tube is placed inside a small cylindrical resistive heater; the heater and tube are then installed inside the high-pressure vessel. X-ray absorption near edge structure (XANES) and extended X-ray absorption fine structure (EXAFS) data were collected at the Uranium LIII-Edge (17,166 eV). Beam energy was calibrated with a Zr foil, such that the maximum of the first derivative was at 17,998 eV. A Si(111) double-crystal monochromator (DCM) was used providing an energy resolution $\Delta E/E$ of $\sim 1.5\times 10^{-4}$ eV. The full-width-at-half-maximum (FWHM) beam size at the sample was $750\times 140\ \mu m^2$. The incident and transmitted beam intensities were measured with ion chambers. All measurements were recorded with a 100×element Ge fluorescence detector (Canberra). Measurements were taken of 2 experimental solutions at a range of temperatures over ~25°C–250°C and a constant pressure of 600 bar.

The 2 solutions both contained 0.86 *m* $NaHCO_3$ with one also containing an additional 0.9 *m* NaOH to increase its pH to ~13°C at 25°C (~10°C at 250°C). Uranium concentration was ~20 mM for the solution without NaOH and ~10 mM for the solution with NaOH. One of the primary concerns raised by the initial observations from the UV-VS and solubility experiments was the remarkably low solubility of uranium at temperatures above 25°C even in solutions containing substantial concentrations of carbonate. 0.86 *m* $NaHCO_3$ was chosen to hopefully extend the potential range of temperatures we could investigate and to hopefully stabilize sufficient dissolved uranium to allow the collection of high quality EXAFS data. The solution containing 0.9 *m* NaOH was designed to observe the effect that pH had on the behavior of uranyl-carbonate complexes.

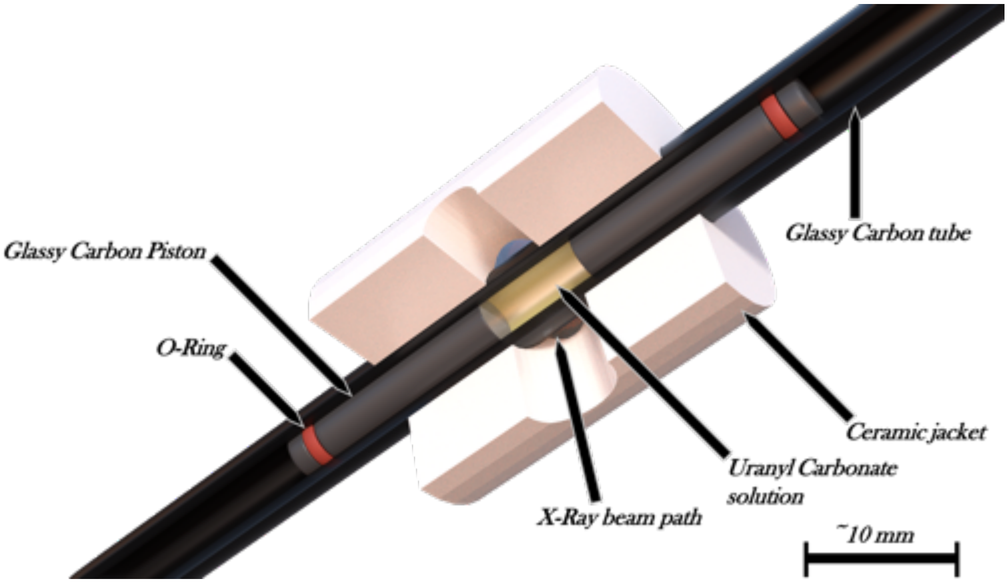

Figure 6-8. Schematic diagram of the mAESTRO cell system.

6.5.1.2 Data Deconvolution Procedure

All XAS data are currently being analyzed with the HORAE package (Ravel and Newville, 2005) using FEFF6 (Rehr et al., 1991). The amplitude reduction factor S_0^2 was set to 0.95 based on previous fits of uranyl in perchloric acid and was verified using the single-scattering axial oxygen peak at ~1.2 Å. E_0 was set at the peak of the white line. All parameter uncertainty ranges were calculated using Artemis (part of HORAE). The structure of Rutherfordine was used as the basis of the fits as it shares many geometrical features with the aqueous uranyl carbonate complexes. The cif file used was based on the work of Finch et al. (1999) and is available in the Crystallography Open Database (COD) as data entry #9004535.

6.5.2 X-Ray Absorption Spectroscopy Results

Raw normalized spectra for both solutions are reported in Figure 6-9, normalized and background corrected EXAFS spectra in Figure 6-10 and their Fourier transforms (FTs) in Figure 6-11. At room temperature the spectra recorded can be confidently attributed to the $UO_2(CO_3)_3^{4-}$ complex based both on solution composition calculations and the results of previous room temperature EXAFS studies (Allen et al., 1995; Ikeda et al., 2007). It is evident that these spectra change little as temperature increases, all features present at room temperature are present up to 247°C. General trends observed include an expected decrease in the amplitude of the ~1.8 Å peaks in the FTs associated with equatorial oxygens, a trend that has been previously reported by Brugger et al. (2016). The peak at ~2.6 Å is linked to single-scattering from the equatorial carbon atoms associated with the bonded carbonate ions and appears to subtly decrease (particularly in the NaOH free solution) in amplitude with increasing temperature suggesting a reduction in the number of bonded carbonate ions. However, preliminary fits have so far been unable to find any statistically significant difference between models that incorporate 2 versus 3 carbonate ions. FEFF calculations suggest that the two peaks at ~3 and 3.6 Å are likely associated with multiple scattering events between the equatorial carbon and oxygen atoms. Despite the preliminary nature of our reported fits, the bond distances derived from them (Table 6-2) closely match those reported in previous literature giving us confidence that these spectra are indeed representative of carbonate complexes present at elevated temperatures in solutions having extremely high carbonate concentrations.

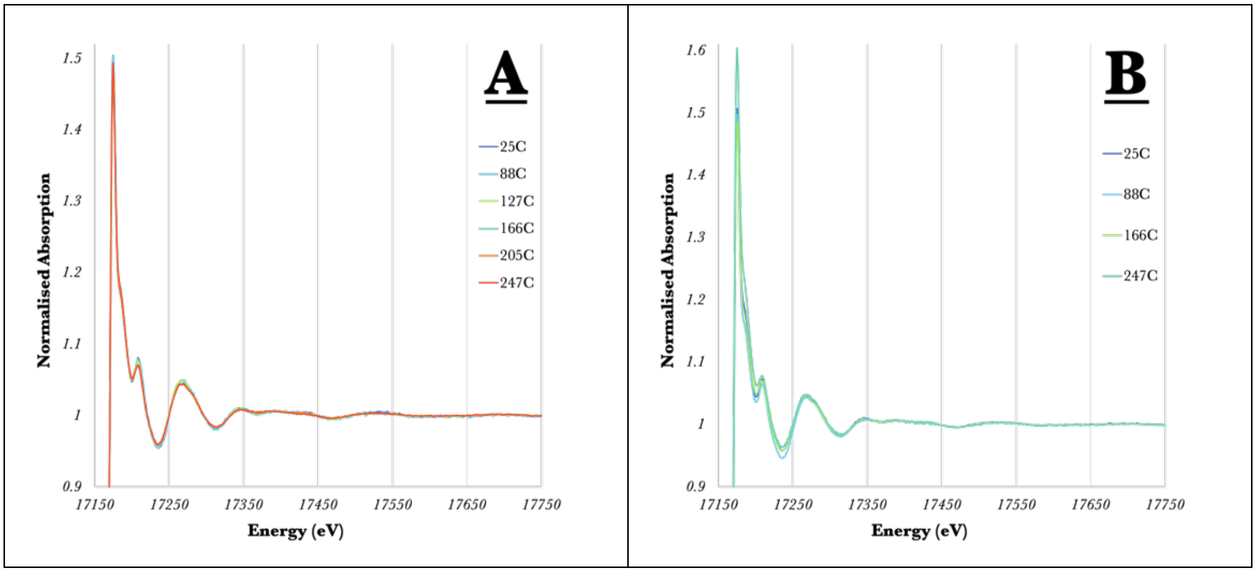

Figure 6-9. Normalized absorption spectra for the two experimental solutions. Spectra for the solution solely containing 0.86 *m* $NaHCO_3$ are shown in (A) while those for the solution containing an additional 0.9 *m* NaOH are shown in (B).

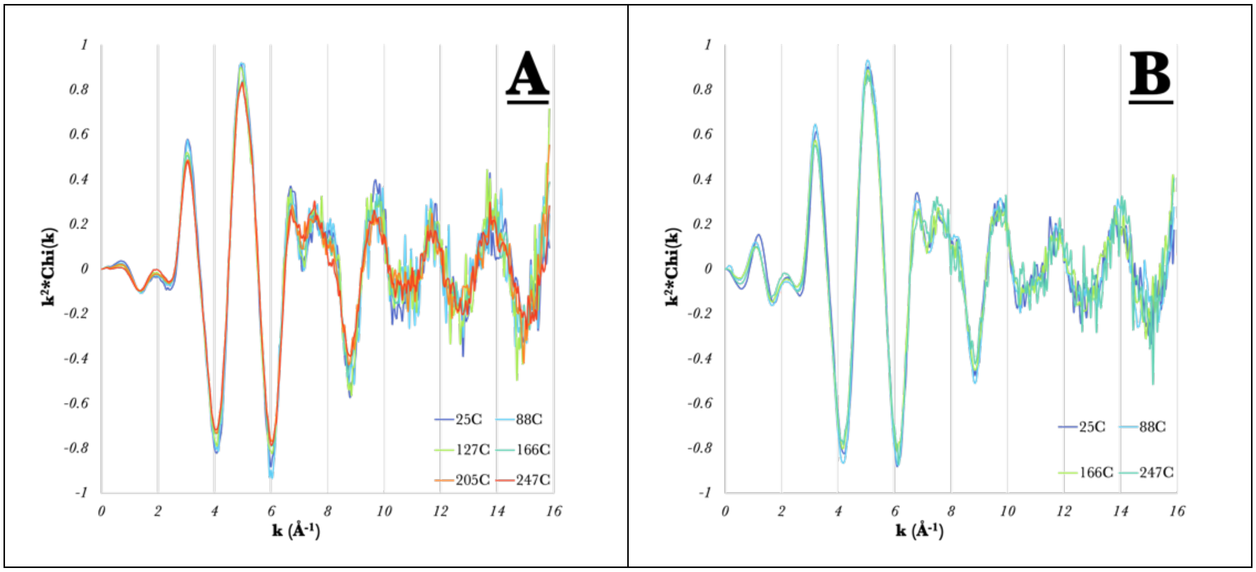

Figure 6-10. Normalized and background corrected EXAFS spectra in K-space for both measured solutions. Spectra for the solution solely containing 0.86 *m* $NaHCO_3$ are shown in (A) while those for the solution containing an additional 0.9 *m* NaOH are shown in (B).

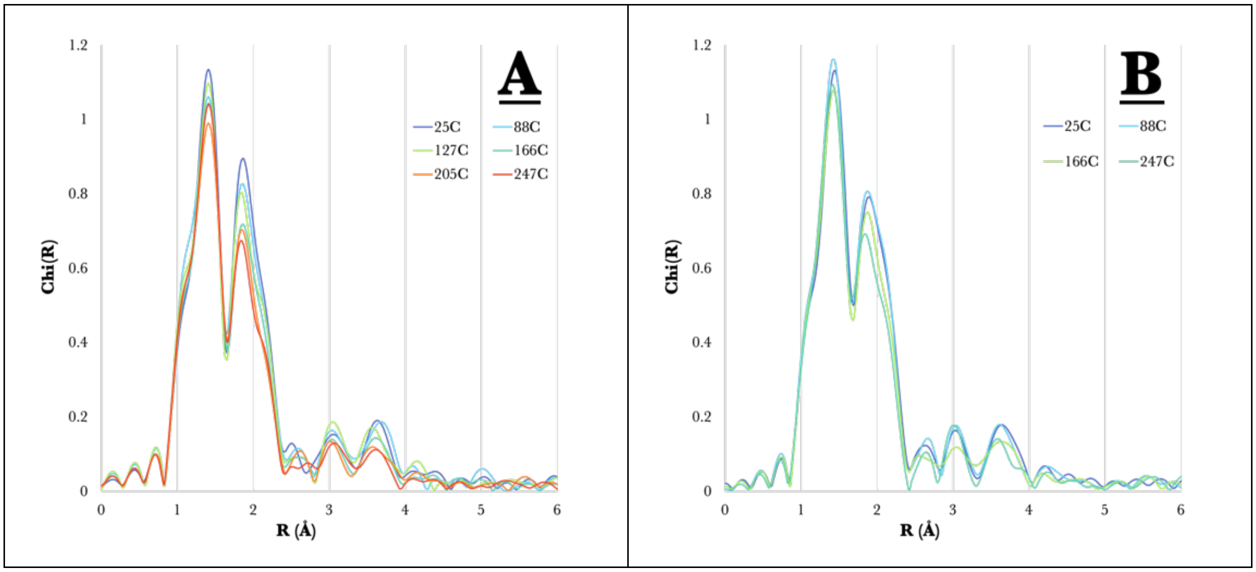

Figure 6-11. Nonphase corrected moduli of Fourier transforms of the spectra reported in Figure 6-10.

Table 6-2. Preliminary derivations of EXAFS parameters for 0.86 *m* $NaHCO_3$ (no NaOH) solution using data collected at 25°C and 205°C compared to values reported in Allen et al. (1995) and Ikeda et al. (2007)

Shell	Scattering Path	R (Å) (Ours)	R (Å) (Allen et al. 1995)	R (Å) (Ikeda et al. 2007)
$U\text{-}O_{ax}$	SS	1.82	1.79	1.81
$U\text{-}O_{eq}$	SS	2.43	2.42	2.44
U-C	SS	2.92	2.89	2.92
$U\text{-}O_{ax}\text{-}U$	MS	3.62	3.59	3.60
$U\text{-}C\text{-}O_{dist}\text{-}C\text{-}U$	MS	4.17	4.12	4.17

NOTE: SS = single scattering, MS = multiple scattering, ax = axial, eq = equatorial, dist = distal.

6.6 Discussion

The key observations we have made during the experiments we have conducted thus far are as follow:

- Currently available thermodynamic data for uranyl carbonate complexes are inadequate at predicting the stability of uranium in carbonate–bearing solutions. At worst (250°C, 0.5 *m* $NaHCO_3$) there appears to be a ~4 orders of magnitude discrepancy between room-temperature based extrapolations and our solubility measurements. This discrepancy increases with temperature and carbonate concentration with the converse being true as well.
- Our solubility experiments suggest that at 200°C and 250°C and at carbonate concentrations ranging from 0.001 to 0.5 *m* the solubility of uranium appears to be controlled by hydroxy complexes rather than carbonate complexes. Though we have yet to determine exactly which hydroxy complex is predominant in our solutions UO_2OH^+ and $UO_2OH_2^0$ are both likely candidates. More detailed investigations into their possible role will likely be a fruitful avenue for further research.
- Our Synchrotron experiments suggest that uranyl carbonate complexes can be identified at elevated temperatures though only in solutions containing extremely high carbonate concentrations. Due to the preliminary nature of our current fits we have yet to determine the exact stoichiometry of these complexes but it is likely that at lower temperatures $UO_2(CO_3)_3^{4-}$ is favored and that it gradually gives way to $UO_2(CO_3)_2^{2-}$ and possibly $UO_2CO_3^0$ as temperature increases. Such a trend would be consistent with an observed decrease in the amplitude of the U-C single-scattering peak visible in the Fourier transforms of our XAS data.
- Overall, it appears that uranyl carbonate complexes become less stable with temperature and that in order to stabilize them in solution significantly higher concentrations of carbonate are required than current predictions suggest. Additionally, it appears that over groundwater carbonate concentrations (Hem, 1985) relevant to geological nuclear waste repositories uranyl is more likely to be transported as uranyl-hydroxy complexes rather than carbonate complexes.
- To further bolster our understanding of uranyl-carbonate complexation we are also considering in-situ Raman spectroscopy experiments. We plan to mainly explore temperatures <150°C to cross-check the results of planned UV-VS studies. These lower temperatures are also advantageous for the fact that we will be able to explore the processes of replacement of uranyl-carbonate by likely uranyl-hydroxyl complexes with increasing temperature over more moderate carbonate concentrations.

6.7 Conclusion

To conclude, although we are still in the midst of the data collection phase of this project our preliminary data already suggest that currently available thermodynamic data for uranyl carbonate complexes are woefully inadequate at predicting their behavior at elevated temperatures. It appears that extrapolations of room temperature data greatly overestimate the stability of these complexes at elevated temperatures with the discrepancy between theory and reality evidently increasing with higher temperatures and carbonate concentrations (e.g. 4 orders of magnitude difference between reality and theory at 250°C and 0.5 *m* $NaHCO_3$). Initial solubility experiments failed to identify any carbonate complexation at 200°C and 250°C over carbonate concentrations of 0.001–0.5 *m*, where theory predicts they should be predominant. However, results from synchrotron experiments suggest that uranyl carbonate complexes are stable at these temperatures if the concentration of dissolved carbonate is ~0.9 *m*. To confirm this observation, we are currently in the process of conducting solubility experiments that cover a carbonate concentration range of 0.5–0.8 *m* thus bridging the reported experiments with our XAS observations. We also aim to commence Raman and new UV-VS experiments to investigate the behavior of uranyl carbonate complexes at relatively low (25°C–150°C) temperatures where issues of uranium insolubility are less prevalent.

7. IN-SITU AND ELECTROCHEMICAL WORK FOR MODEL VALIDATION

7.1 Introduction

The objective of this work is to develop in-situ testing cells for examining the corrosion rate of uranium oxide (UO_2) in the electron microscope, both SEM and transmission electron microscope (TEM) and obtaining experimental verification for the Fuel Matrix Mixed Potential Model. These cells could also be used for investigating the corrosion rate and/or radionuclide interaction behavior of other materials under in-situ conditions that are relevant to the EBS such as iron, boral, or bentonite backfill materials. An important advantage of the SALVI system is the small size of the samples required. This reduces the many challenges of handling hazardous radioactive materials in the laboratory environment.

7.1.1 The SALVI E-cell

The vacuum compatible microfluidic device, termed System for Analysis at the Liquid Vacuum Interface (SALVI) was developed at PNNL by Yu and co-workers (Yang et al., 2011; Y et al., 2011; Yu et al., 2013). The design details have been provided in many other papers and a version of SALVI is now available commercially as Wet Cell II Liquid Probe System marketed by Structure Probe, Inc. (West Chester, PA). The electrochemical version, or the SALVI E-cell was also developed to enable in operando analysis.

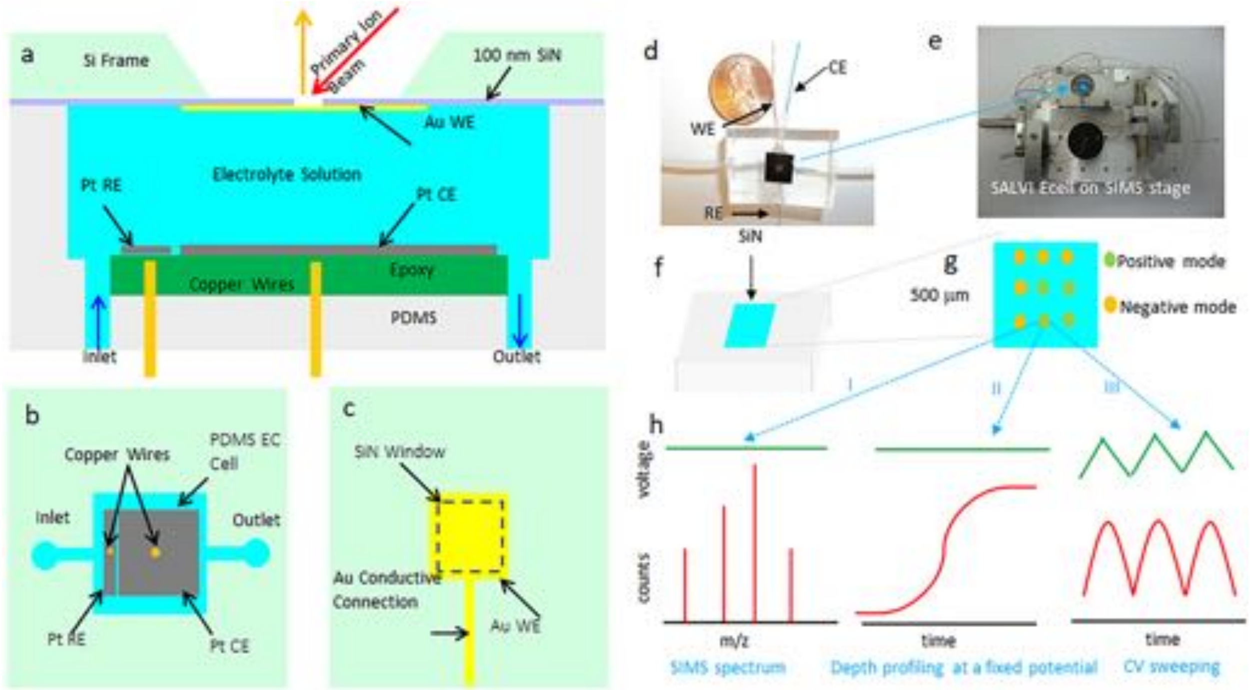

Source: (a) - (e) adapted from Yu (2020).

Figure 7-1. (a) Cross section of the SALVI E-cell design, (b) overview of the reference electrode (RE) and counter electrode (CE), (c) overview of the WE, (d) a finished E-cell, (e) the E-cell assembled on the ToF-SIMS stage, (f) the schematic of the detection SiN surface prior to dynamic depth profiling, (g) multiple holes drilled for positive and negative in operando ToF-SIMS, and (h) voltage and count profiles of the three operation modes

Figure 7-1a–e shows the schematic of the SALVI E-cell. More than one aperture can be drilled with the primary ion beam (e.g., Bi^+, Bi_3^+) in the positive or negative ion mode as seen in Figure 7-1g during in operando analysis, while maintaining a reasonably high vacuum ($< 5\times10^{-7}$ mbar) in the main chamber. Three operation modes are possible as depicted in Figure 7-1h, including (1) hold at a certain potential to collect secondary ion mass spectrometry (SIMS) spectra; (2) hold at a certain potential to do depth profiles; and (3) sweep potentials to acquire depth profiles dynamically. A well-known electrochemical system containing gold WE as well as platinum reference electrode (RE) and counter electrode (CE) is used to illustrate feasibility. A dilute electrolyte of potassium iodide (KI) with a concentration in the mM is used as the liquid electrolyte. In operando time-of-flight (ToF)-SIMS is effectively a 2D analysis offering electrochemical signals from an electrochemical station and mass to charge ratios (m/z) from the ToF-SIMS at the dynamic solid-liquid (s-l) interface simultaneously (Figure 7-1h). Since the iodine electrochemistry is reversible, cyclic voltammograms (CVs) are collected in this experiment.

The s-l interface is dynamic in this measurement. The information depth of static ToF-SIMS is known to be a few nanometers from published emission depth measurements (Yang et al., 2011; Wucher et al., 2004). The information depth of SEM is much bigger compared to SIMS. Generally, analysis depth of 1 μm is possible in SEM. Diffusion is an important factor for in-situ measurements, and the obtained SIMS spectra are expected to contain information from the electrode – electrolyte interface of a few nanometers thick and from the bulk electrolyte liquid of up to several micrometers (Yu, 2017). In the case of SEM, the analysis depth would allow imaging of particles suspended in the liquid and provide complementary information of particle changes.

We report electrode fabrication development and results to incorporate UO_2 particles into the SALVI E-cell in this milestone report. Several metal and metal oxide particles were used as model particles to optimize operation procedures and verify effectiveness before using UO_2.

7.2 Methods and Materials

We provide experimental and technical details of SALVI E-cell electrode fabrication, modification and characterization techniques in this section. First, we introduce several new approaches in WE fabrication. Second, we describe in-situ SEM analysis to verify electrode performance. Third, we use ToF-SIMS depth profiling to verify powder existence in the fabricated electrode. Lastly, we summarize electrochemical analysis results of various E-cell devices prepared using different methods including coating and stamping.

7.2.1 Microfluidic Electrochemical Cell Fabrication Methods

Our group recently developed a microfluidic device for multimodal spectroscopy and microscopy of liquids (Yu et al., 2016; Liu et al., 2014). This device is vacuum compatible named SALVI. The electrochemical SALVI or E-cell contains three electrodes and allows simultaneous electrochemical analysis coupled with *in operando* spectroscopy and microscopy of chemical imaging tools such as ToF-SIMS and SEM (Yang et al., 2011; Yu et al., 2011; Yu et al., 2013). This technology provides the potential to investigate the electrode reactions of precious and novel materials (Liu et al., 2014; Wang et al., 2017b; Yao et al., 2020). The basic configuration of SALVI E-cell was used to test and verify the novel nanoparticle fabrication methods to make WEs in this work.

Several methods to include powder materials as WEs were developed, tested, and verified in this effort. Specifically, two types of methods, namely (1) powder particles attachment using gold coating and (2) stamping will be described here. Experimental details are provided in this section.

7.2.1.1 Particle Attachment using Gold Coating Technique

First, we show results using gold coating to secure particles onto the silicon nitride (SiN) membrane to form the WE for a SALVI E-cell. This method uses a thin layer of gold coating to secure the attachment of the particles and prevent the particles from being washed away in the liquid electrolyte. In addition, gold is electrochemically inert, highly resistant to dissolution, and easy to be fabricated into many forms. The application of gold sputtering not only helps attachment of particles of interest onto the SiN detection window but also avoids using binding materials which may introduce interferences to the electrochemical microanalysis. Furthermore, this particle attachment can be applied to other flat substrates, e.g., silicon wafer, and thus this method is not limited to the use in SALVI E-cell.

Metal Particles and Electrolyte Preparation

Three types of metal particles were used for device modification and characterization analysis. Iron (III) oxide particle (<50 nm) was purchased from Sigma-Aldrich. Cerium oxide (CeO_2 10–15 nm) was purchased from U.S. Research Nanomaterials, Inc. CeO_2 was chosen as the surrogate material due to the fact that it has approximately the same density as various uranium oxides. Boehmite (γ-AlOOH) nanoparticles were synthesized at PNNL and their synthesis and characterization were reported in our recent publications (Yao et al., 2020; Yu et al., 2019). Particles were mixed in the deionized water (DI) and sonicated for 5 minutes to make a 0.1 M suspension, respectively. These particles were used before gold coating. 0.1 M KNO_3 electrolyte solution was prepared using 10 mL DI water and 101 mg KNO_3 (ACS grade, SIGMA ALDRICH).

Vacuum-Compatible SALVI E-cell Fabrication

The vacuum-compatible SALVI E-cell used in this work has three-electrodes, consisting of metal particles as the WE, and platinum wires as both the RE and CE. The core component of the new E-cell has a SiN membrane attached with metal particles as the WE. The WE is bonded to the polydimethylsiloxane (PDMS) reservoir ($2\times3\times1.5$ mm^3) as patented previously (Yang et al., 2011; Yu et al., 2011; Yu et al., 2013). The SiN membrane was first coated with 10 nm Ti and 30 nm Au using sputter coater (Cressington 208) to form a conductive path between the detection window (0.5×0.5 mm^2) and the edge of the SiN membrane. 10 μL of 0.1 M metal particles were deposited onto the center of the detection window and they were dried in the chemical fume hood (Figure 7-2). A 5 nm thick of gold layer (1×1 mm^2) were coated to cover the deposited dry particles. The gold-coated SiN membrane with particles was treated with oxygen plasma, then it was bonded to the PDMS reservoir that had been previously inserted with platinum CE and RE. The SALVI E-cell was assembled following the fabrication procedure reported previously (Yu et al., 2016; Liu et al., 2014).

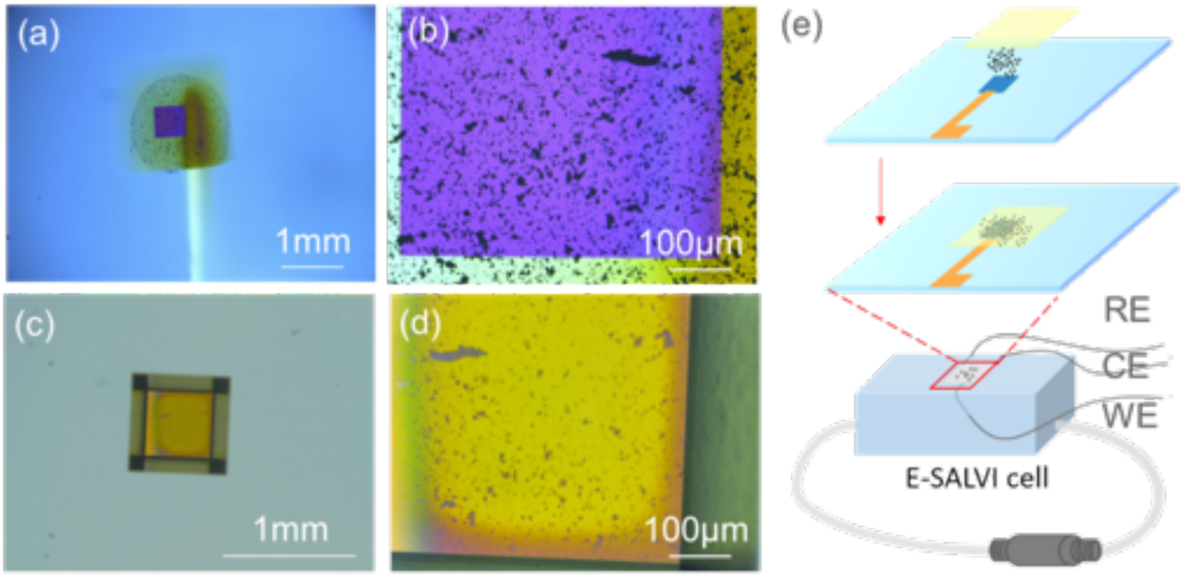

Figure 7-2. (a) Optical image of Fe_2O_3 particles on the inner side of Si_3N_4 membrane, (b) the same area showing particles attached underneath the Si_3N_4 membrane in higher magnification, (c) top view of the SiN membrane from the detector side, (d) the same area from the attached particle side in higher magnification, and (e) the schematic of EC cell fabrication. RE, CE and WE represent reference electrode, counter electrode and working electrode, respectively.

7.2.1.2 Stamping to Fabricate Powder Materials as WE

A number of electrochemical analysis methods are used to study a small quantity of powdery materials such as direct deposition on electrode surfaces consisting of polymer-film composite, graphite, and silver (Ag) (Doménech-Carbó et al., 2001; Ghosh and Bard, 1983; Hasse and Scholz, 2001; Valdés-Ramírez et al., 2011). The applied materials were covered with thick-film deposits or clay pastes in this approach. Earlier studies are limited due to fragile durability and poor reproducibility of the electrode as a result of low conductivity of the materials such as polymer composites, zeolites, and clays. Additionally, high current and resistance of the thick-film deposits can be problematic. Specifically, controlling the amount of the material deposited has been difficult when directly depositing on electrode (DDE) (Ghosh and Bard, 1983; Grygar et al., 2002).

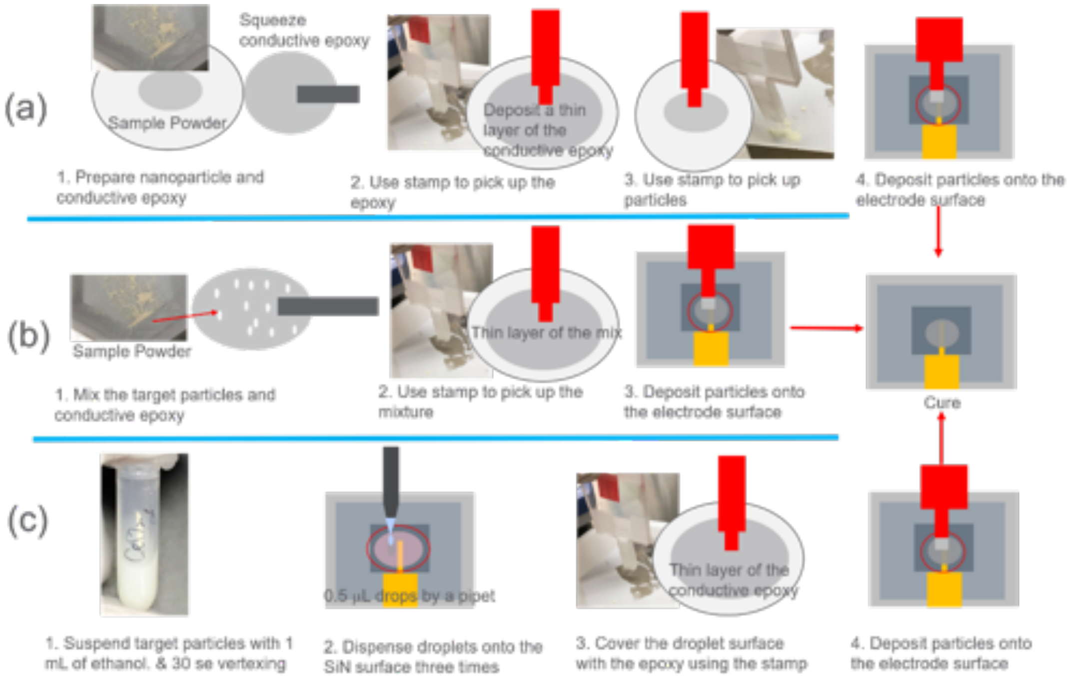

Figure 7-3. Overview of three different Ag conductive epoxy stamping methods for making nanoparticles onto the electrode: (a) sequence stamping, (b) mixing and stamping, and (c) droplet spraying and stamping method

To solve the known issues of DDE, we develop a new approach to incorporate nanoparticles onto the WE of the SALVI E-cell. The technique utilizes the silver conductive epoxy stamping method on the conductive layer to form an effective WE containing nanoparticles. Epoxy stamping has been used in electronic component packaging (Livelo and Rojas, 2002); however, stamping has not been used for making electrodes to the best of our knowledge. Three different methods to prepare electrodes containing nanoparticles are compared in this work, including sequence stamping, mix stamping, and droplet stamping as shown in Figure 7-3. All three methods use a stamped epoxy layer as a protection layer of nanoparticles from washing off by the electrolyte solution as the final step. The particle inclusion steps varied, and their effectiveness compared in this work. As proof-of-concept demonstration, two representative nanoparticles, namely, cerium oxide (CeO_2) and graphite, are selected to show the potential range of the new approach. Both materials have been widely used nano materials for energy storage system and sensor materials (Yao et al., 2011; Lim et al., 2012; Jeyanthi et al., 2014; Fan et al., 2011; Wei et al., 2016; Ku et al., 2013; Wang et al., 2017a; Zhang et al., 2012). Six types of SALVI E-cells were fabricated for CV analysis and device performance comparison. CV plots provide unique electrochemical current reaction profiles of each device fabricated using different nanoparticle stamping methods for CeO_2 and graphite, respectively. Additionally, an E-cell without any nanoparticle in the WE is used as a control. Atomic force microscopy (AFM) is used to characterize nanoparticle morphology on the WE surface. ToF-SIMS, a powerful imaging mass spectrometry for surface analysis, is used to acquire chemical mappings of the CeO_2 and graphite on the stamped WE surface to ascertain electrode fabrication effectiveness.

Particles and Electrolyte Preparation

In the stamping approach, two nanoparticles cerium oxide (CeO_2, US research materials Inc, 10 nm mean diameter) and graphite (Graphite NanoPlatelets, xGnP, 10–15 nm mean diameter) were used.

Nanoparticle Electrode Fabrication and SALVI E-cell Fabrication

The existing SALVI E-cell has a thin film Au WE sputter coated on the back side of the silicon nitride (SiN) window (Norcada, 0.5×0.5 mm on a 200 μm Si frame). Electrode deposition was done by the following steps: sputtering a layer of titanium of 10 nm as the adhesion layer followed with 40 nm gold forming the conductive layer on the SiN substrate. To apply nanoparticles onto the electrode surface, conductive epoxy (Silver conductive epoxy, Chemtronics) was used for stamping. Stamps were fabricated from 1.5 mm thick polymethyl methacrylate (PMMA) sheets and a CO_2 laser cutter. Ethanol was used as a carrier liquid for droplet spraying application. Because nanoparticles often exist as fine and light powders, particle handling were done in a ventilated nano enclosure (XPert Nano Enclosure, LABCONCO).

Figure 7-4 depicts the schematic of nanoparticle stamping. CeO_2 and graphite followed the same workflow. Nanoparticle samples will be applied directly on the boundary of electrode and SiN surface using stamping technique. Three stamping techniques are (1) sequence stamping, (2) mixing and stamping, (3) droplet spraying and stamping were developed and compared. After the making WE electrodes using stamping, the rest of SALVI device fabrication was conducted in the clean room to prevent particle contamination from the electrode surface. More details of the E-cell can be found in previous works (Yu et al., 2016; Liu et al., 2014). The use of SiN is not necessary in an E-cell fabrication. The main reason to use SiN is to make it compatible with other spectroscopy or microscopy tools. However, SiN is not a prerequisite as the substrate in stamping.

Sequence Stamping—A thin layer of Ag conductive epoxy was squeezed on a sample plate. A custom-made PMMA stamping tool (stamping surface 1.5 × 1.5 mm) was used to deposit a thin layer of 200 μm of the silver epoxy onto the gold conductive feature at the SiN surface. Next, ~ 0.3 mg nanoparticles were picked up by electrostatic force onto the Ag epoxy deposited stamping surface. Lastly, the epoxy layer with particles gently touched the gold conductive layer to leave the materials in position. Another thin layer of epoxy glue was used to protect the deposited particles.

Mixing and Stamping—The second method uses epoxy to mix and incorporate nanoparticles into the conductive glue before sequence stamping (Figure 7-3b). First, ~ 3 mg nanoparticles of graphite and 30 mg CeO_2 were spread gently on top of a thin layer of conductive epoxy, respectively, in a plastic plate. Additional epoxy could be added to make a consistent mixture. The mixture was smeared into a thin layer in a clean surface. Next, the nanoparticle containing epoxy layer was stamped by a custom-made PMMA stamp. The final step was gently smearing the stamp surface onto the gold conductive layer as in sequence stamping. The thin epoxy layer was applied to protect the particle containing WE surface.

Droplet Spraying and Stamping—The droplet spraying and stamping method utilizes ethanol droplets as a nanoparticle deposit agent onto the conductive layer and substrate (Figure 7-3c). The spraying liquids were prepared with 3 mg of graphite or 30 mg CeO_2 in 1 mL of ethanol in plastic tubes. Particles were suspended by 1 min. vertexing and 15 min. sonication. Then 3 μL of the liquid mixture was dropped on the substrate. Particles were deposited upon ethanol evaporation. The final step epoxy stamping to cover the electrode with a conductive epoxy glue layer as the other two methods.

7.2.2 Optical Microscopy of WE and AFM Characterization

An optical microscope (VHX500, Keyence) was used to image the surface of CeO_2 and graphite particles after being applied onto the substrate. Optical images were recorded with the built-in camera and magnification was 50× to 500×. Topographical analysis also was carried out using an MFP-3D Infinity AFM (Asylum, Oxford). Tapping mode measurements were performed using an Asylum RTESPA probe (40 N/m spring constant) with a set point of 0.8 V and a scan speed of 1 Hz. AFM images were leveled using the flat portion of the substrate which was used as a baseline to determine the height of individual particles. Samples for AFM imaging were prepared by suspending nanoparticles using 1.5 mL ethanol with a ratio of nanoparticles to ethanol of 1 to 5. Samples were sonicated for 3 hrs. 5 μL of the suspended nanoparticle sample was deposited on a clean mica surface (1.5 cm × 1.5 cm) and let dry for 20 min. The dried mica surface was blasted twice with nitrogen before analysis.

7.2.3 In-situ SEM Analysis of Particle-Attached WE

The SALVI E-cell with particle-attached WE by gold coating was introduced into a FEI Helios 660 NanoLab™ FEG SEM equipped with an Energy Dispersive X-ray Spectroscopy (EDS) (EDAX Inc., Mahwah, NJ) compositional analysis system. 100 µL KNO_3 was injected into the microfluidic E-cell before it was mounted onto the SEM stage and stabilized with the copper tape. The SE images and BSE images were acquired in the high vacuum mode before and after electrochemical analysis, as illustrated in Figure 7-4. The accelerating voltage and current were set at 10 keV and 0.11 nA, respectively. Images with high magnification were taken to show particle distribution and morphology before and after electrochemical reactions of the attached particles beneath the SiN detection window. The vacuum was kept at ~1×10^{-5} torr during measurement. The EDS was used to acquire elemental mapping of the electrode surface before and after applying potentials to the three-electrode SALVI E-cell, with the collecting time set to 100 seconds in both cases.

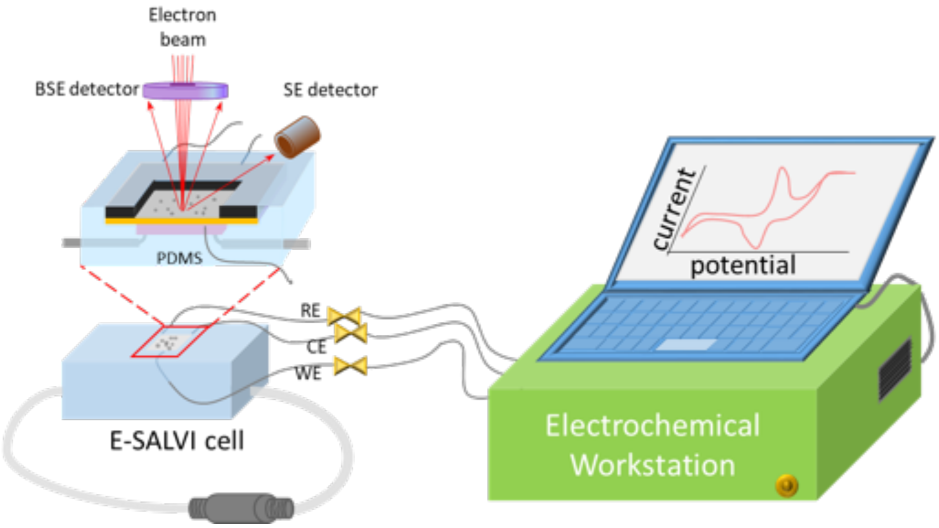

Figure 7-4. Schematic of in-situ SEM imaging of particle-attached SALVI E-cell before and after electrochemical analysis

7.2.4 ToF-SIMS Characterization of Fabricated Electrodes

7.2.4.1 SIMS Depth Profiling of the Particle-Attached Electrode

The E-cell consisting of the CeO_2-powder WE was characterized in a ToF-SIMS (ToF-SIMS V, IONTOF GmbH, Münster, Germany) to verify the presence of CeO_2 particles and validate their attachment. ToF-SIMS provided the microanalysis with chemically informative mass spectra and depth profiling. During depth profiling, the dual beam mode was used, namely, a 25 keV Bi^+ beam as the analysis beam and 2 keV Cs^+ beam as the sputter beam. The Cs^+ beam sputtered on a 150 µm × 150 µm surface and then Bi^+ rastered over 50 µm × 50 µm area in the center of the sputtered area. Noninterlaced technique was used to reduce the charging effect in addition to applying the 10 eV electron flood gun. The raster size was set to 128 × 128 pixels. Negative ions were collected for 20 scans. The negative mass spectra were calibrated using C^-, OH^-, and CN^-. Multiple locations on the SiN detection window were drilled through to confirm the measurement reproducibility of the particle-attached electrode. Mass spectra and depth profiling data were analyzed using the IONTOF SurfaceLab software (Version 7.0).

7.2.4.2 ToF-SIMS 2D Imaging and Spectral Analysis of Stamped Powder-Wes

Chemical mapping of the as fabricated WE surfaces using the stamping methods were collected using a ToF-SIMS (IONTOF GmbH, ToF-SIMS V, Münster, Germany). The pressure of the main chamber was maintained at 1×10^{-8} mbar during analysis. The primary ion beam was a 25 keV Bi_3^+ with 10 kHz pulse energy. The pulse width was 0.8 ns and the current was ~ 0.6 pA. SIMS 2D images were acquired by rastering over an area of 500×500 μm^2 for 100 scans. SIMS high resolution spectral data were acquired by rastering over an area of 500×500 μm^2 for 60 scans. ToF-SIMS data was processed using the IONTOF Surface Lab 7.0 software. Calibrated spectra data were exported to Origin Pro (OriginLab Corp., Northampton, MA, USA) for plotting.

7.2.5 Electrochemical Analysis

An electrochemical workstation (CH Instruments Model 600H) was used to characterize the electrochemical behavior of the particle-attached WE. Cyclic voltammetry (CV) analysis was performed by cycling the potential of the WE and measuring the resulting current. The applied voltage ranged from 1 V to −1 V to initiate the redox reaction. The CV scans were conducted at various scan rates ranging from 50 mV/s –100 mV/s for the particle-attached WEs with gold coatings.

As to the E-cell using the powder stamping methods, three types of devices were tested using CeO_2 and graphite particles, respectively, each representing different nanoparticle inclusion and stamping methods. Two control devices were prepared for comparison as well. One had only silver epoxy stamped layer as the WE and the other had no epoxy stamping at all. In total, eight devices were tested. An electrochemical station (CH instruments; 660 h) was used (Figure 7-5b). The following scan rates were used 10, 20, 40, 60, 80 and 100 mV/s, respectively, for each device. The sensitivity range was set at $1\times10^{-4} \sim 1\times10^{-5}$ A/V. The voltages sweeping polarity direction was from 1 V to −1 V then reverse back to 1 V. There were at least 20 sweeps at each scanning rate. The 2 mM potassium thiocyanate (KSCN) solution was used as the electrolyte (Nyasulu and Barlag, 2011). The KSCN solution was injected at the rate of 100 µL/min into the microfluidic device using a syringe pump (Cole Palmer) prior to analysis. 0.1 mL of electrolyte solution was injected within the E-cell system. Known CV procedures were followed (Elgrishi et al., 2017). Collected CV data were exported to Origin Pro (OriginLab Corp., Northampton, MA, USA) for plotting.

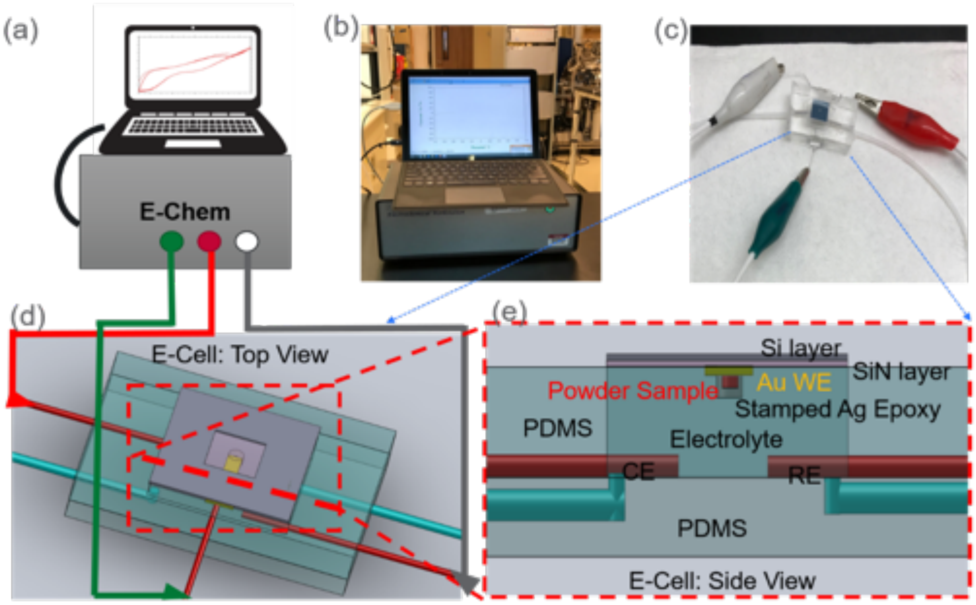

Figure 7-5. The overview of the electrochemical analysis setup: (a) electrochemical station with the control computer green port (WE), red port (CE), white port (RE); (b) picture of E-chem station; (c) close-up picture of the E-cell connected with alligator clips to the instrument; (d) 3D rendering image of the top view of the SALVI E-cell; and (e) cross-section view of the microfluidic cell

7.3 Results and Discussions

There are two sets of characterization and verification results in this section. First, we report results from the particle-attachment method followed with gold coating for protection. Second, we report results from three types of particle stamping methods. Before electrochemical performance validation experiments, various surface characterization tools were used to ensure that powder materials were securely deposited onto the substrate forming the foundation of a reliable WE.

7.3.1 UO_2-Electrode

7.3.1.1 Lift-Out Electrode

Initially electrochemical testing of the UO_2 electrode was produced by Ga ion milling using a FEI Helios 660 Focused Ion Beam (FIB) – SEM (see Figure 7-6). The UO_2 lift-out was imaged in the cell and an elemental map was obtained although because of the window and gold coating, it was not possible to detect the elements in the electrode easily (Figure 7-7). The ion beam welding process had to be performed extremely carefully as any damage to the window resulted in failures during the electrochemical testing in-situ in the microscope.

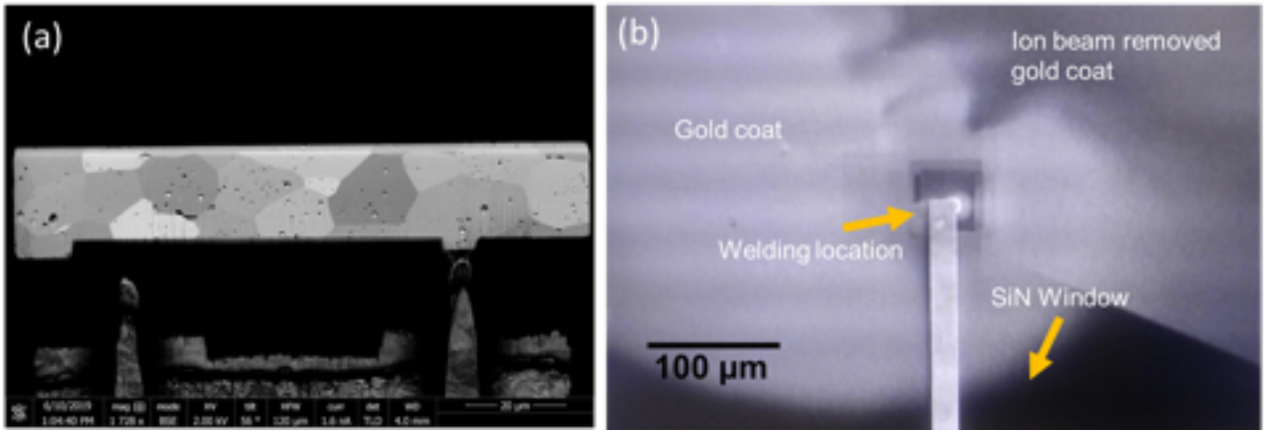

Figure 7-6. SEM images showing (a) the UO_2 lift-out preparation and (b) the welding process on the SiN window

The electrode was imaged in the SEM as depicted in Figure 7-6. SEM images showed grain boundary opening and oxidation along these boundaries as seen in the brighter contrast after the electrochemical corrosion experiments in the SALVI E-cell.

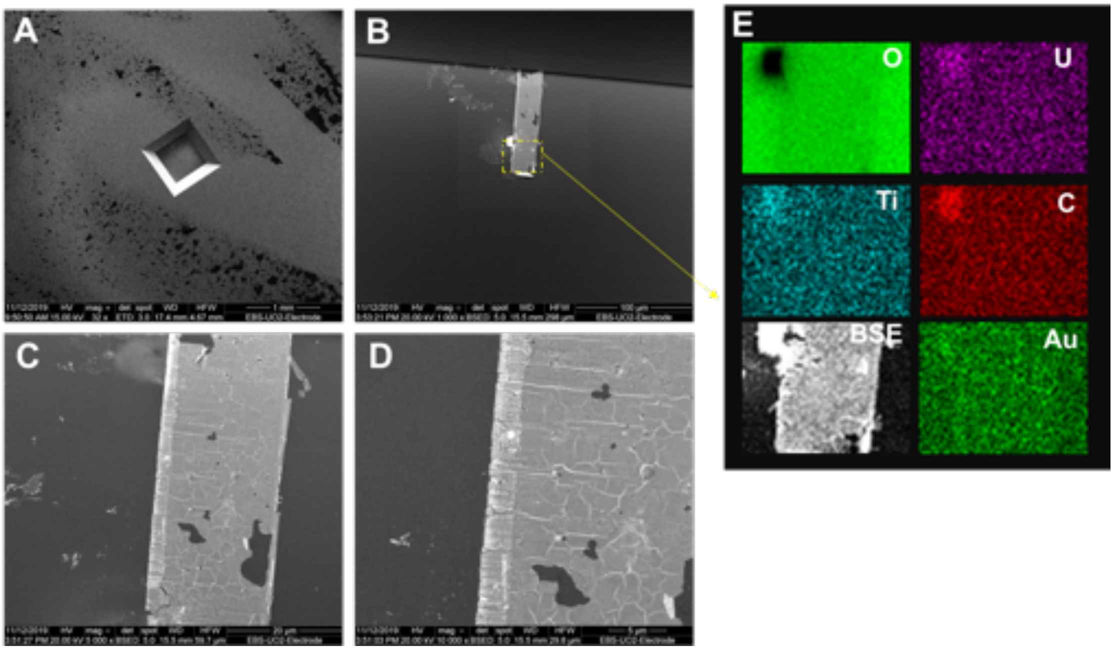

Figure 7-7. (a) In-situ liquid cell SEM image showing corroded FIB lift-out of UO_2 welded to the SiN window. The UO_2 electrode is visible in (b). (c-d) High magnification views of the UO_2 electrode showing a corrosion rind at one side and oxidized grain boundaries based on the BSE contrast in these regions. (e) Elemental x-ray energy dispersive spectroscopy (EDS) maps of the electrode.

7.3.1.2 UO_2 Particle Electrode

A single crystal UO_2 particle was milled to micrometer-sized particles. These UO_2 particles were prepared as the WE using the gold coating technique. The BSE images of UO_2 particles in high magnification 10,000× (Figure 7-8a) and low magnification 1,000× (Figure 7-8b) were acquired. Figure 7-8c depicts the binary image of Figure 7-8b processed using the ImageJ software. The particle size shown in Figure 7-8d was determined by fitting the binary image data using the lognormal distribution model in MATLAB (Mathworks Inc., Natick, MA, USA; Yao et al., 2020; Yang et al., 2012). The mean size of the UO_2 particles in Figure 7-8c is 7.56 μm, and the primary mode is approximately 4.5 μm.

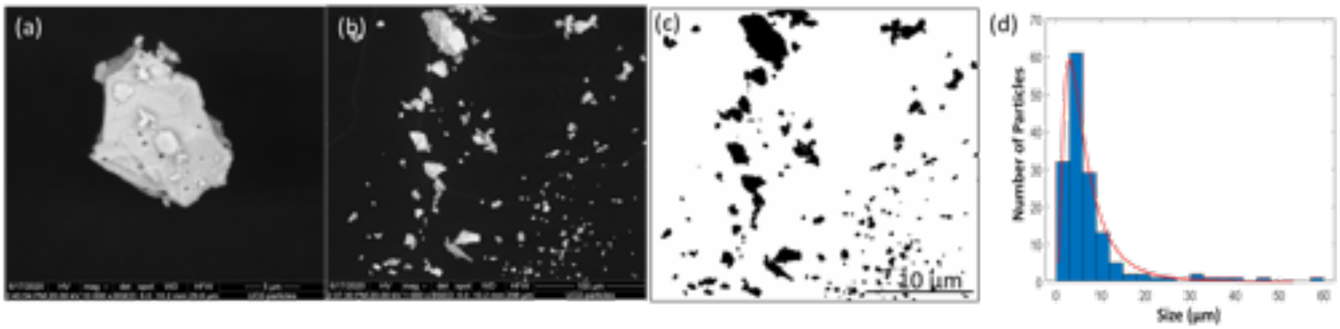

Figure 7-8. BSE images of UO_2 particles in (a) 10,000× and (b) 1,000× magnification, respectively; (c) the corresponding binary image, and (d) the lognormal particle size distribution.

7.3.2 In-situ Liquid SEM Analysis of Fe_2O_3-attached SALVI E-Cell

The SE images of the particle-attached SiN window prior to (Figure 7-9a,b) and after (Figure 7-9d,e) the electrochemical analysis were performed. Figure 7-9a and d show the entire SiN detection window that has attached Fe_2O_3 particles. There were no significant changes in the particle distribution between Figure 7-9a,d, indicating the effective attachment of particles before and after applying the cycling potential. Figure 7-9b shows the SE image of Fe_2O_3 particles with 10,000× magnification, revealing the morphology of nanometer-sized particles in the KNO_3 solution. The EDS mapping confirmed the chemical composition of particles on the SE images, as evidenced by the Fe peak in Figure 7-9c,f. The elemental signals of N and Si were from SiN; and O was from Fe_2O_3 particles and the electrolyte solution. The Au signal came from the gold coating that was used to stabilize the particles. Both in-situ SE images and EDS elemental spectra were acquired using the high vacuum mode in the SEM, enabled by the vacuum-compatible SALVI E-cell with particle-attached WE.

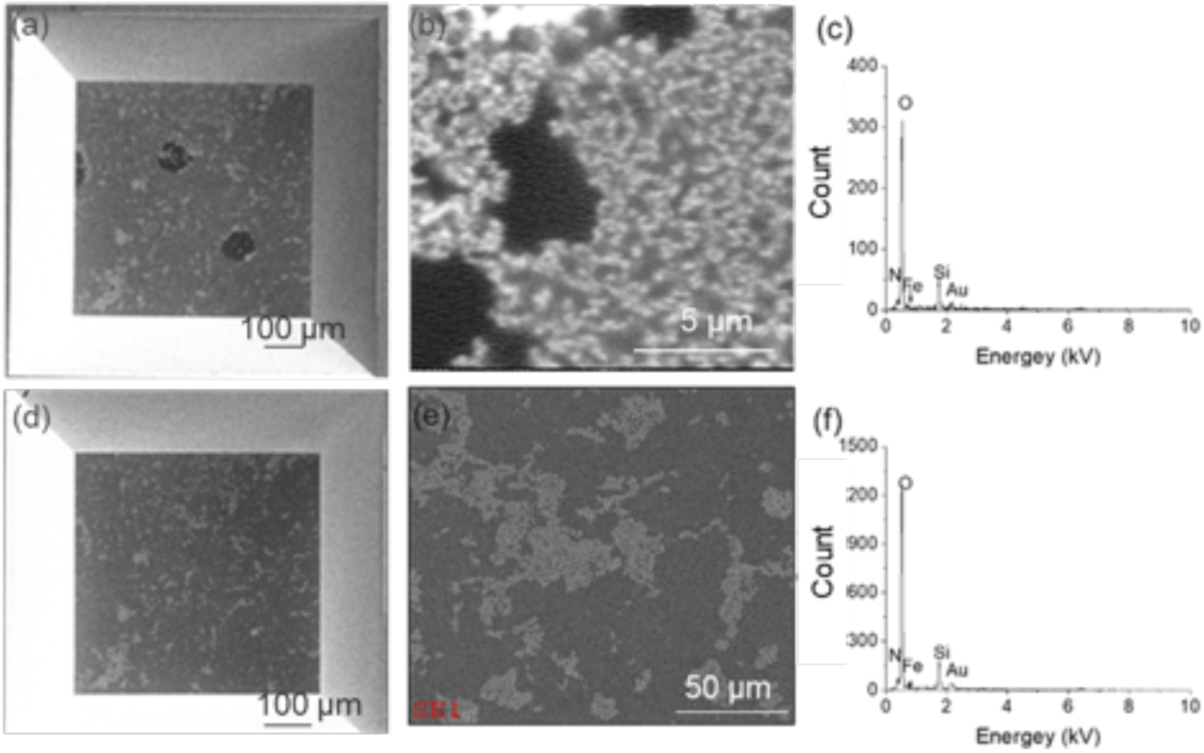

Figure 7-9. In-situ SE Images of particle-attached microfluidic EC liquid cell containing Fe_2O_3 ((a) and (b)) before and ((d) and (e)) after electrochemical analysis, and EDS spectra of the particle-attached area (c) before and (f) after electrochemical analysis

This result verified that the modified E-cell, i.e., attaching particles followed with gold coating, can be used to study the UO_2 particles using in-situ SEM and EDS techniques in the future. Since our original SALVI cells are compatible with SIMS and other vacuum techniques (Yu 2020), the SEM vacuum testing effectively verify that this modified E-cell can be integrated to other instrument platforms as well.

7.3.3 In-situ Liquid SEM Imaging of Boehmite Particles

Another type of non-radiological metal particle was tested as the WE to demonstrate the reliability and versatility of this particle-attached SALVI E-cell using in-situ SEM analysis. The same E-cell fabrication method was used to attach boehmite (γ-AlOOH) nanoparticles onto the SiN membrane. The γ-AlOOH-attached E-cell was imaged using in-situ SEM before and after the electrochemical analysis with KNO_3 electrolyte. The in-situ SEM results are shown in Figure 7-10.

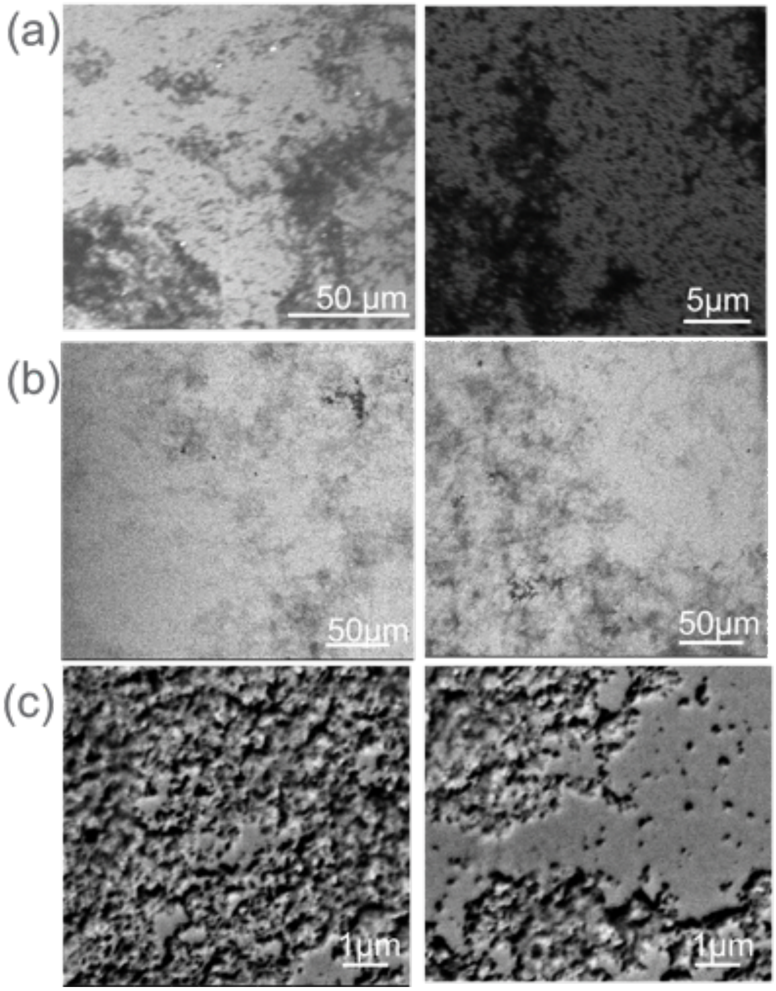

Figure 7-10. In-situ SE images of liquid EC cell of γ-AlOOH-attached WE (a) before and (b) after electrochemical analysis and (c) BSE images of γ-AlOOH particles after electrochemical analysis in higher magnification

The comparison between the SE images of synthesized γ-AlOOH nanoparticles prior to (Figure 7-10a) and after (Figure 7-10b) with potential applied shows the morphological changes of the boehmite particles. Particles appear less porous and rougher on the surface after electrochemical reactions. Figure 7-10c provides higher magnification (25,000×) BSE images at different regions of interest, giving more details of boehmite nanoparticles after electrochemical analysis.

In-situ SEM imaging of the $Fe_2O_3^-$ and γ-AlOOH-attached E-cells demonstrates the vacuum compatibility of the modified device, which allows the high magnification imaging to reveal the surface change of the particles before and after the redox reaction in vacuum. This fabrication technique will be applied to make UO_2 particles as WE and characterize the UO_2 corrosion potential. In operando electrochemical analysis and in-situ imaging with simultaneous electrochemical stimuli could provide more insights of the surface interaction and electron transfer of the spent fuel and its adjacent environment in liquid.

7.3.4 ToF-SIMS Analysis of the CeO_2-Attached E-cell

Additionally, ToF-SIMS depth profiling was used to characterize WE surface. CeO_2 nanoparticles were attached as the WE in the E-cell using the Au coating technique. ToF-SIMS depth profiling analyses in the negative ion mode were performed on the detection window with WE fabricated as described earlier

(50 µm × 50 µm). A representative SIMS depth profile and mass spectrum are shown in Figure 7-11. The signal characteristic of SiN membrane SiN^- m/z^- 42 was dominant in the first 40 s of the sputtering. However, this signal intensity dropped significantly after the SiN membrane was sputtered through (Figure 7-11a), demonstrating that the milling process removed the SiN membrane. This milling used the Cs^+ sputter gun and exposed the particle-attached WE to the primary Bi^+ beam for analysis. The detection of attached particles on the WE was illustrated by the increased counts of m/z^- 197 Au^-, 156 CeO^-, 172 CeO_2^- and 16 O^- during the sputter between 40–100 s, verifying the effective attachment of the particles onto the SiN window. The mass spectrum of the analyzed area is shown in Figure 7-11b, providing the molecular mapping in the z-direction from the SiN surface to the depth where the nanoparticles were attached to the substrate to form the WE.

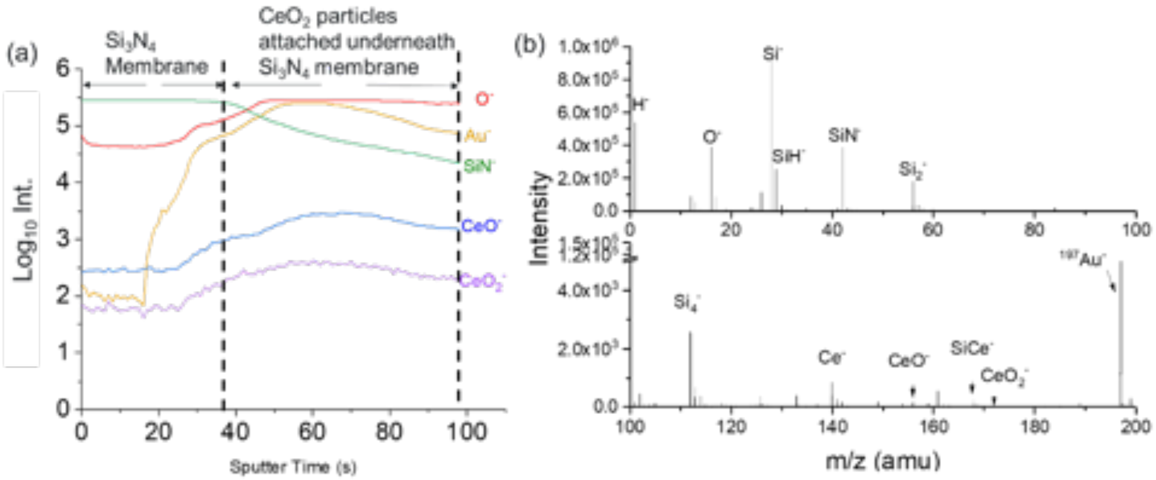

Figure 7-11. (a) ToF-SIMS depth profile and (b) mass spectrum in the m/z^- range of 1–200

ToF-SIMS depth profile and mass spectrum confirmed the attachment of CeO_2 particles and their distribution beneath the SiN membrane in the z-direction. With the use of vacuum-compatible E-cell, in-situ liquid ToF-SIMS was used to probe the electrode-electrolyte interface of the WE (Yu et al., 2016; Liu et al., 2014). The benefit of applying in operando liquid ToF-SIMS is to better understand the chemical species evolution on the WE during the electrochemical reaction. Future work will be conducted using in operando liquid ToF-SIMS coupled with real-time electrochemical analysis to characterize the UO_2 particle-attached WE, providing the important molecular information to enhance in-situ SEM/EDS analysis.

7.3.5 Optical Microscopy, AFM, and ToF-SIMS characterization of Stamped Electrodes

A series of experiments were conducted to verify the effectiveness of incorporating nanoparticles in the WE fabrication using stamping techniques. Optical and AFM images show nanoparticle distribution and as-deposited conditions on the substrate. ToF-SIMS 2D mapping and spectral data give evidence that the nanoparticles are present on the substrate surface. CV scans contain unique signatures of the redox peaks showing validity of the WE performance.

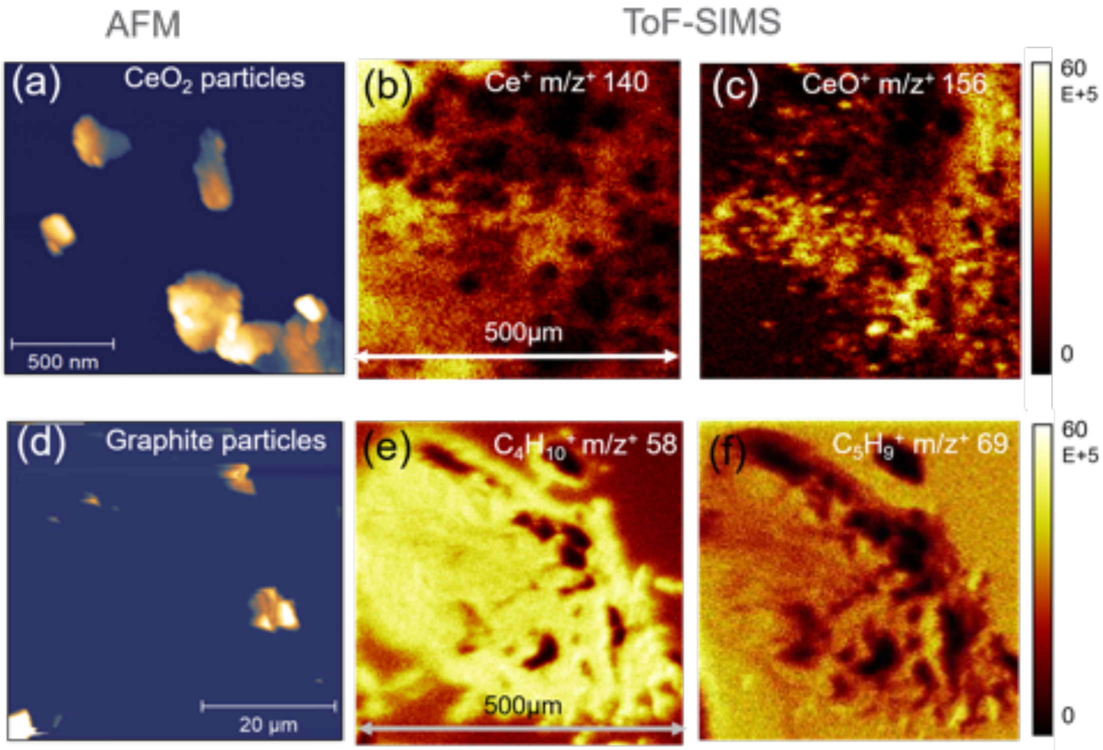

Figure 7-12. AFM and ToF-SIMS 2D mapping of nanoparticles: (a) AFM image of CeO_2; SIMS 2D mapping (b) Ce^+ ion and (c) CeO^+ ion on the as-made WE using CeO_2 sequence stamping; similarly (d) AFM image of graphite; SIMS 2D mapping of (e) $C_4H_{10}^+$ ion and (f) $C_5H_9^+$ ion of the as made WE using mixing and stamping of graphite nanoparticles

7.3.5.1 Optical Microscopy and AFM Characterization

AFM was used to image the as-made WE surfaces of the two types nanoparticles. The size of stamped electrode surface morphology was similar to that of PMMA stamping tool. However, images have some irregularity in the morphology profile. Figure 7-12a,d depict nanoparticles deposited on substrates using AFM imaging. Particles appear to coagulate, for instance, in the spraying and stamping approach. Figure 7-12a shows clusters of ~500 nm of CeO_2 nanoparticles. This is significantly bigger than the known 10 nm average size. Figure 7-12d also shows clusters of ~10 µm of graphite, which is significantly bigger than the original 10–15 nm particle size before fabrication.

7.3.5.2 ToF-SIMS 2D Mapping and Spectral Analysis

ToF-SIMS 2D mapping of the stamped electrode surfaces was also conducted. Figure 7-12b,c are 2D maps of the sequence stamped surface containing CeO_2. Strong Ce^+ m/z^+ 140 ion (Figure 7-12b) and CeO^+ m/z^+ 156 ion (Figure 7-12c) are observed. Additionally, these Ce^+ and CeO^+ peaks have high abundances in the ToF-SIMS spectra (not shown here). Both results support that CeO_2 particles are successfully included in the WE surface.

Similarly, Figure 7-12e,f are SIMS 2D maps of hydrocarbon fragment peaks $C_4H_{10}^+$ and $C_5H_9^+$ from graphite mixing and stamping WE surface. Identification of these fragments as graphite was reported previously (Deslandes et al., 2009; Smith et al., 2013). Additional SIMS spectral plots show dominant counts of these two peaks. Further, SIMS 2D mapping and spectral results the other four types of as-made WE surfaces were verified.

7.3.6 Electrochemical Characterization of Particle-Attached WEs

7.3.6.1 Cyclic Voltammogram of Gold Coating Assisted WE

In this section, we report CV results from the gold coating assisted particle attachment CV was applied to three aforementioned E-cells with different particle-attached WEs (i.e., CeO_2, γ–AlOOH, and Fe_2O_3) using the same electrolyte solution (0.1 M KNO_3). The same electrochemical analysis setting was used including sweeping range from1.0 V to −1.0 V with scanning rate of 100 mV/s. Figure 7-13 shows the CV, i.e., the applied potential versus resulting current. In the forward scan, the E-cells with CeO_2 WE, γ-AlOOH WE, and KNO_3 blank control (i.e., without particle attachment) share a similar cathodic peak potential at ~ −0.2 V marked by the dash line in Figure 7-13a. The additional peaks were explained by possible reduction reactions shown in Figure 7-13b–d. Further analyses are needed, for example, using different concentrations of electrolyte solutions and varying the scanning rate to characterize the properties of particle-attached WE.

The results of the CV of various particle-attached EC cells demonstrate that this technique can be applied to study the metal oxide particles and their electron transfer during the redox reaction. Future work will be performed on the liquid EC cell with UO_2-attached WE using in-situ SEM, in-situ ToF-SIMS, and in operando electrochemical analysis to gain more insights of the corrosion process of the spent fuel in the storage environment.

.

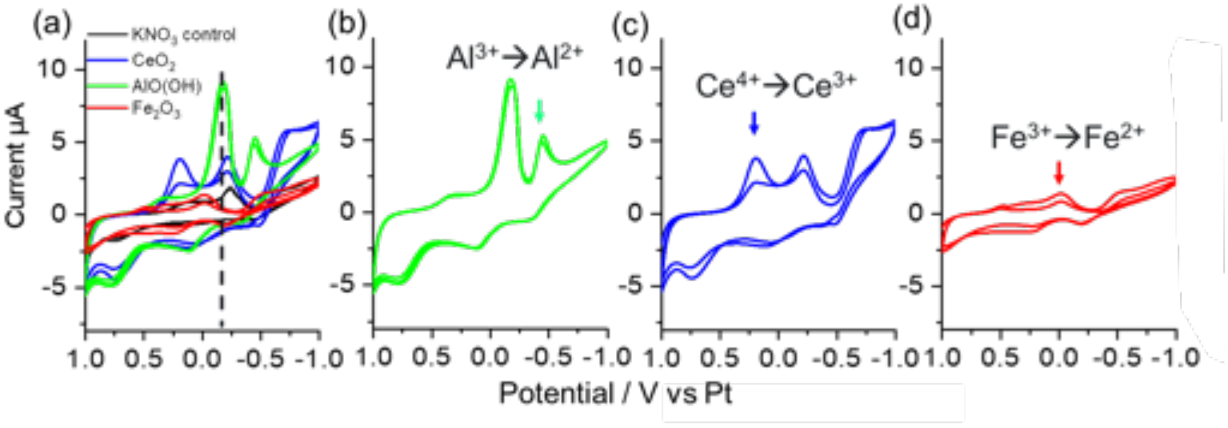

Figure 7-13. (a) Cyclic voltammograms SALVI E-cells with different particle-attached WEs and the E-cell without particle attachment; (b) CV of γ-AlOOH-attached WE; (c) CV of CeO_2-attached WE, and (d) CV of Fe_2O_3-attached WE in 0.1 M KNO_3 electrolyte

7.3.6.2 CV of Nanoparticle Stamped WE

In this section, we report CV results from the stamping approaches. Figure 7-14 and Figure 7-15 show CV comparisons among three different stamping methods (e.g., sequence stamping, mixing and stamping, droplet spraying and stamping) for CeO_2 and graphite nanoparticles as WEs, respectively. The CV results from the epoxy control device as a reference point was also included. For example, the blue cyclic voltammagrams represent the sequence stamping results, red mixing and stamping, green droplet spraying and stamping, and gray the silver epoxy control device. The scan rate was 100 mV/s. Additional CV results of control devices were acquired to ensure performance of all devices.

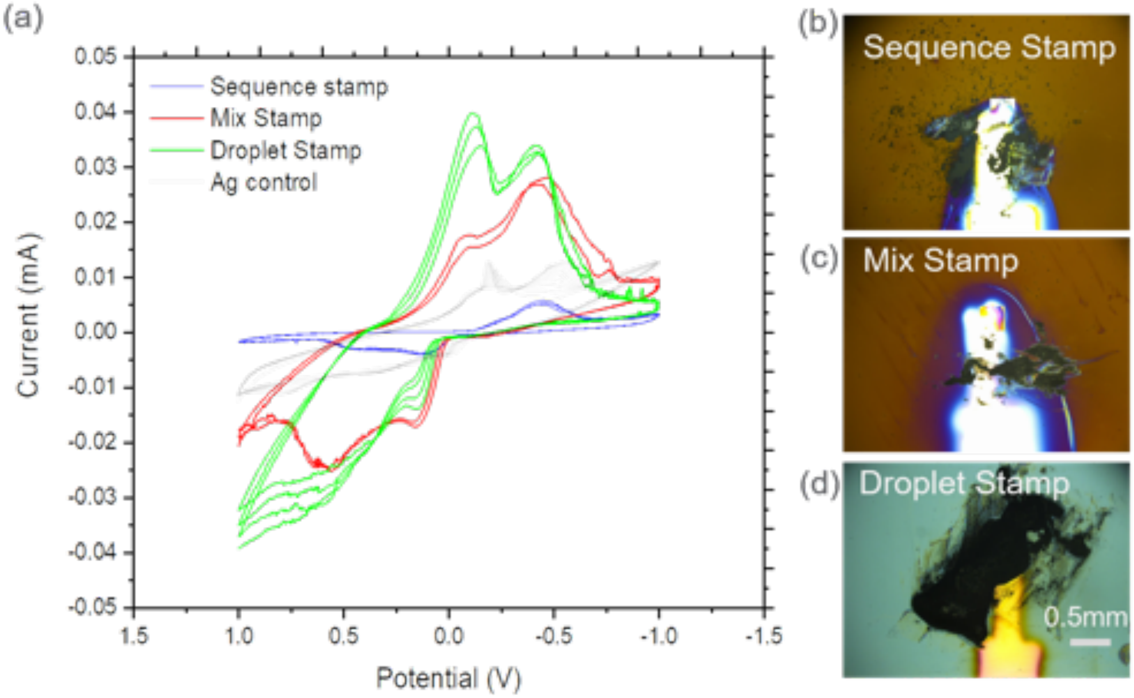

Figure 7-14. (a) CV comparisons of WEs containing CeO_2 nanoparticles using three stamping methods and the control device and optical microscope image of (b) sequence stamped surface, (c) mixing and stamping surface, and (d) droplet spraying and stamping surface. The shining finger-like feature in (B-D) is the Au conductive layer.

To interpret CV results from different CeO_2 devices, overlapped plots provide ease of comparison. During potential sweeping from 1 V to −1V, two peaks are observed in the mixing and stamping and spraying and stamping devices, both shifting toward 0 V in Figure 7-14a. In the mixing and stamping device, double peaks appeared at −0.05 V and −0.22 V. In the droplet spraying and stamping device, the double peaks appeared at −0.12 V and −0.42 V. The sequence stamping device has a peak at −0.4 V during the 1 V to −1 V sweep. During the reverse potential sweeping from −1 V to 1 V, peaks from mixing and stamping and droplet spraying and stamping devices appeared at 0.2 V and 0.55 V; while the Ag epoxy device had two peaks at ~0.03 V and ~0.3 V. Peaks from the sequence stamping device were 0.1 V and 0.45 V. The unique peaks observed here are related to CeO_2 reduction. The peaks at 0.1 V and 0.45 V were reported previously in CeO_2 electrochemical analysis (Uzunoglu, 2017). This agreement provides verification of the WE performance.

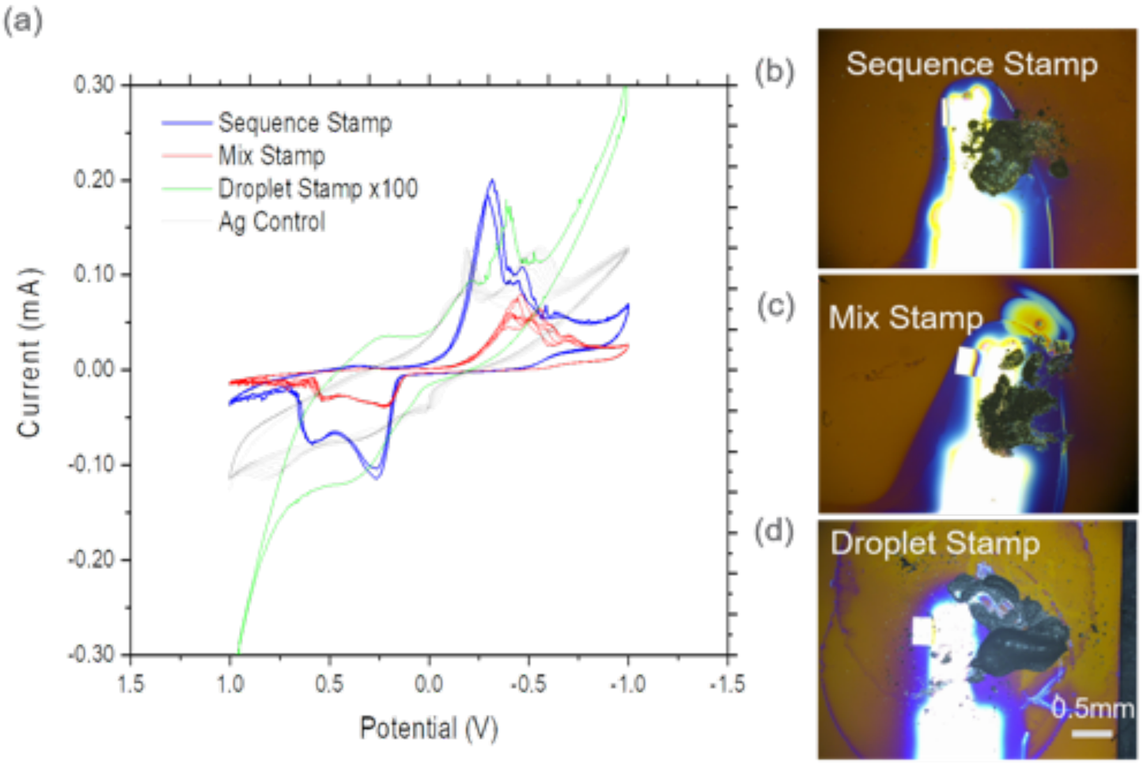

Figure 7-15. (a) CV comparisons of WEs containing graphite nanoparticles using three stamping methods and the control device and optical microscope image of (b) sequence stamped surface, (c) mixing and stamping surface; and (d) droplet spraying and stamping surface. The shining finger like feature in (b-d) is the Au conductive layer.

The graphite device comparisons are depicted in Figure 7-15a. During the potential sweep from 1 V to −1 V, a single major peak appeared between −0.3 V to −0.5 V; while double peaks appeared in the Ag epoxy control device. There was a major peak at −0.3 V and two minor peaks at 0.36 V and −0.46 V from the sequence stamping device. In the mixing and stamping device, two major peaks appeared at −0.42 V and −0.55 V and a minor peak at 0.3 V. In the droplet spraying and stamping device, there were a major peak at −0.42 V and a minor peak at 0.22 V. In the reverse direction potential sweep from −1 V to 1 V, two peaks appeared in the sequence stamping and mixing and stamping devices while the epoxy control had three minor peaks at −0.47 V, 0.78 V, and 0.017 V. During the reverse potential sweep, sequence stamping shows major peaks at 0.26 V and 0.6 V and a minor peak appeared at −0.5 V. Mixing and stamping showed a minor peak at −0.54 V and two major peaks at 0.22 V and 0.53 V. Droplet spraying and stamping had a minor peak at −0.42 V and a major peak at 0.35 V. Overall, characteristic peaks of graphite redox reaction appear in two stamping methods to prepare WEs, however, these peaks do not appear in the epoxy control device. The observed peaks from the graphite CV sweeps show similarities to a previously reported peak at 0.22 V in graphite electrochemical analysis (Ku et al., 2013; Mallesha et al., 2011).

ToF-SIMS 2D maps and spectral results verify that CeO_2 and graphite particles were deposited onto the substrate surface using all three methods involving stamping. The irregularity in the surface morphology of stamped surfaces shown in Figure 7-14b–d and Figure 7-15b–d were likely caused by the multiple smears of stamping layers. This process can be improved by using a single stroke stamping in the next phase of development. For example, the footprint size of single stroke stamping tool should be the same as the WE area. This will ensure more accurate electrode control. The particle coagulation that was observed may be caused by static force among nanoparticles. Static effect can be reduced by applying nanoparticles on the plasma treated SiN surface over longer exposure and assembling devices in the nano-enclosure. Additionally, hydrophobic treatment of the SiN membrane or other substrates for WE fabrication can be a solution to prevent air bubbles inside the E-cell chamber.

A new epoxy stamping technique has been developed to enable rapid electrochemical analysis of nanoparticles. To verify performance, two representative nanoparticles (e.g., CeO_2, graphite) are stamped directly onto the thin-film conductive electrode of an established microfluidic E-cell as the WE in a three-electrode system. Silver conductive epoxy acts as an adhesive agent for nanoparticles in the stamping method. Three different kinds of stamping methods sequence, mix, and droplet stamping are compared for WE performance in the SALVI E-cells. The particle distribution on the WE surface is verified using AFM and the particle chemical composition is characterization using ToF-SIMS to ascertain particle attachment. Cyclic voltammagrams of devices using the above stamping methods successfully demonstrate unique profiles of nanoparticles. Our results show that epoxy stamping can be a useful method for rapid analysis of nanoparticles and determine their electrochemical properties using microfluidic-like machines.

7.3.7 Liquid Cell Image of Uranium Buckyballs with TEM

We performed the first imaging of liquids containing particles on the JEOL 300F GrandARM scanning transmission electron microscope (STEM). The objective was to look at the liquid radiological material sandwiched between SIN chips using a Protochips holder. This experiment required extensive investment of additional capabilities, including a Plasma cleaner to clean the SiN chips prior to use, a pumping station to check the condition of the holder and to make sure there were no leaks in the system, and equipment for the loading station.

The uranium particles (or Buckyballs) were created by reacting a uranyl solution in H_2O_2 in the presence of a lithium salt. A diluted solution was pipetted onto the bottom SiN chip and then the device was sealed. It was then tested to make sure that it held vacuum. The particles were initially imaged in STEM-mode but this created too much radiolytic damage and therefore the particles were imaged in TEM mode. Figure 7-16 shows two Buckyball uranium particles in solution. This is the first time that such particles have been imaged in the electron microscope.

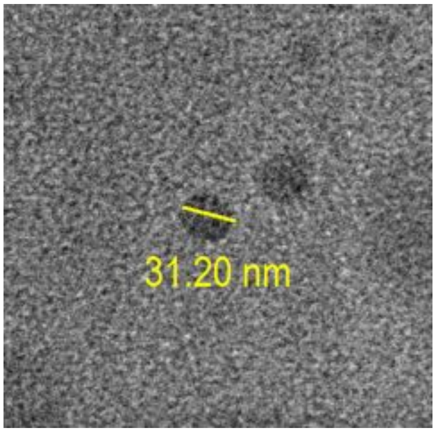

Figure 7-16. Direct Imaging of Uranium Buckyballs in Solution with TEM

Different morphologies are exhibited with various counter ions and we plan to run additional experiments looking at exchange with calcium, strontium, and potassium. Unfortunately, this specific holder is incompatible with EDS. This analysis was a test case for the eventual use of in-situ liquid methods with materials relevant to the Spent Fuel testing program.

7.4 Conclusion and Outlook

We developed two approaches to include UO_2 like particles onto the WE of the SALVI E-cells, namely particle attachment with gold coating and epoxy stamping. Multiple model particles were used to verify fabrication reliability. Surface characterization was used to verify particle attachment as WEs. Electrochemical analysis was performed on a variety of devices containing WEs fabricated using different particles and various techniques to illustrate feasibility. Our experimental results show that in operando and in-situ study of UO_2 particles using the modified SALVI E-cell platform is possible using one of the illustrated methods. These new approaches are easy to implement and cost effective, permitting UO_2 corrosion potential studies in a wide range of conditions. We plan to optimize and select the WE fabrication method and we will use the optimal option for UO_2 investigation in the near future.

7.5 Acknowledgements

We thank RPL Management for access to the Radiological Microscopy Suite (RMS) at PNNL and for the modification of existing instruments for conducting these experiments and access to the JEOL GrandARM STEM. The project team thanks Dr. Jennifer Lee for advice and consultation on intellectual property (IP) filing. Dr. Dallas Reilly is thanked for the SEM-FIB work, Dr. Bruce McNamara and Dr. Dev Chatterjee are thanked for providing uranium solutions and materials for testing, and Dr. Dongsheng Li thanked for assistance with handling in-situ liquid cells for TEM.

8. INVESTIGATION OF THE IMPACT OF HIGH TEMPERATURE ON EBS BENTONITE WITH THMC MODELING

8.1 Introduction

In the underground EBS, bentonite is expected to be used as a buffer material to isolate the disposed nuclear waste from the surrounding environment. Bentonite is characterized by swelling properties, absorption capabilities for radionuclides, and low permeability. The complexity of the underground multi-processes and the interaction between the bentonite buffer and the natural system (NS) makes it difficult to predict long-term evolution of bentonite buffer. This section is aimed at utilizing the coupled thermo-hydro-mechanical-chemical (THMC) model to evaluate the behavior of EBS bentonite and the NS clay formation.

Zheng et al. (2015) investigated the coupling between chemical and mechanical processes via an Extended Linear Swelling Model (ELSM) and the double structure BExM (Sánchez et al., 2005; Gens, 2010; Guimarães et al., 2013). However, the ELSM does not accurately describe the transient state of swelling, neglects the history of mechanical change, and is unable to account for the impact of cations exchange on the bentonite swelling. BExM linked mechanical process with chemistry, so the model could simultaneously incorporate the effects of exchangeable cations, ionic strength of pore water, and abundance of swelling clay on the swelling stress of bentonite. Two scenarios were presented: (1) a case in which the peak temperature in the bentonite near the waste canister is about 200°C and, (2) a case in which the temperature in the bentonite near the waste canister peaks at about 100°C. The comparison of these two cases delineates the impact of temperature on the coupled process in bentonite.

In FY20, we continued working on THMC modeling of bentonite and the transition to the new simulator, TReactMech. This section contains three parts: (1) the first part presents some new results using the dual-structure BExM model to conduct a parametric study on pre-consolidation pressure; (2) TReactMech (Sonnenthal et al., 2015; 2018) with new libraries, which modified the coupling strategy from iterative two-way coupling to a sequential coupling method, and used it to simulate the high temperature cases in nuclear waste disposal; (3) in the third part, we summarize the studies on using reduced order models for investigations of new constitutive laws for bentonite.

8.2 Generic Model Development with BExM

Because the model used in this report is similar to that described in previous report (Liu et al., 2013; Zheng et al., 2014; Zheng et al., 2015a; Zheng et al., 2016; Zheng et al., 2017), we only briefly describe each element of the THMC model here, focusing on the parametric study conducted in FY20.

8.2.1 Double Structure Model

The dual structure model, BExM, considers the elasto-plasticity at the macrostructure, and incorporates a microstructure into the model to form a dual structure, which enables simulating the behavior of expansive soils, such as the dependency of swelling strains and swelling pressure on the initial stress state and on the stress path, strain accumulation upon suction cycles and secondary swelling. In the model design, the microstructure can swell to invade the macro-porosity, depending on the mechanical confinement and the load level. This is relevant when considering permeability changes during the soil swelling, because fluid flow takes place mostly through the macro-porosity, which is not proportional to the total strain and deformation of the expansive soil. Details regarding concept and equations to describe the mechanical behavior of micro-structural and macro-structural levels and the interaction between structural levels are given there, but they can be found in Zheng et al. (2019a). A one-way coupling approach, in which chemical changes affect mechanical behaviors of bentonite through the evolution of volume fraction of smectite, exchangeable cation concentration, and ionic strength (via osmotic suction), is taken into account through BExM.

8.2.2 Simulator

In this study, the numerical simulations are conducted with TOUGHREACT-FLAC3D (FLAC stands for Fast Lagrangian Analysis of Continua), which sequentially couples the multiphase fluid flow and reactive transport simulator, TOUGHREACT (Xu et al., 2011), with the finite-difference geomechanical code FLAC3D (Itasca, 2009). The coupling of TOUGHREACT and FLAC3D was initially developed in the work by Zheng et al. (2012) to provide the necessary numerical framework for modeling fully coupled THMC processes. Recently, the numerical code was expanded with multiple constitutive models, such as the dual structural BExM and Extended Linear Swelling Model (ELSM).

8.2.3 Modeling Scenarios

The model is applied to a hypothetical bentonite-backfilled nuclear waste repository, which involves a horizontal nuclear waste emplacement tunnel at 500 m depth in Opalinus clay (Figure 8-1). The case is a pseudo 2D model with the y-axis aligned parallel to the tunnel, with a 1 m thickness in the y-direction. The z-axis is vertical, and the horizontal x-axis is orthogonal to the tunnel direction. Note that while the canister is modeled as a heat source with mechanical properties of steel, the THC changes in the canister and its interactions with the EBS bentonite are not considered for the sake of simplicity.

An initial stress field is imposed by the self-weight of the rock mass. Zero normal displacements are prescribed on the lateral boundaries of the model. Zero stress is applied to the top, and vertical displacements are prevented at the bottom. Liquid pressure is constantly constrained at the top and bottom, and the model domain is in a hydrostatic state. The initial temperature of 11°C was assigned at the top, and of 38°C at the bottom, with a thermal gradient of 27°C/km along the depth (i.e., the z-axis). The model simulations were conducted in a non-isothermal mode with a time-dependent heat power input. The power curve in Figure 8-1 was scaled from representative heating data from the U.S. DOE’s SFWD campaign for pressurized water reactor (PWR) used fuel for the current “high T” case. This heat load is then scaled in the 2D model to represent an equivalent line load, which depends on the assumed spacing between individual waste packages along an emplacement tunnel. The heat load corresponds to an initial thermal power of 520 W/m along the length of the heater. The EBS bentonite has an initial water saturation of 65% and the argillite (Opalinus clay) is fully saturated. From time zero, the EBS bentonite undergoes simultaneously re-saturation, heating, chemical alteration, and stress changes.

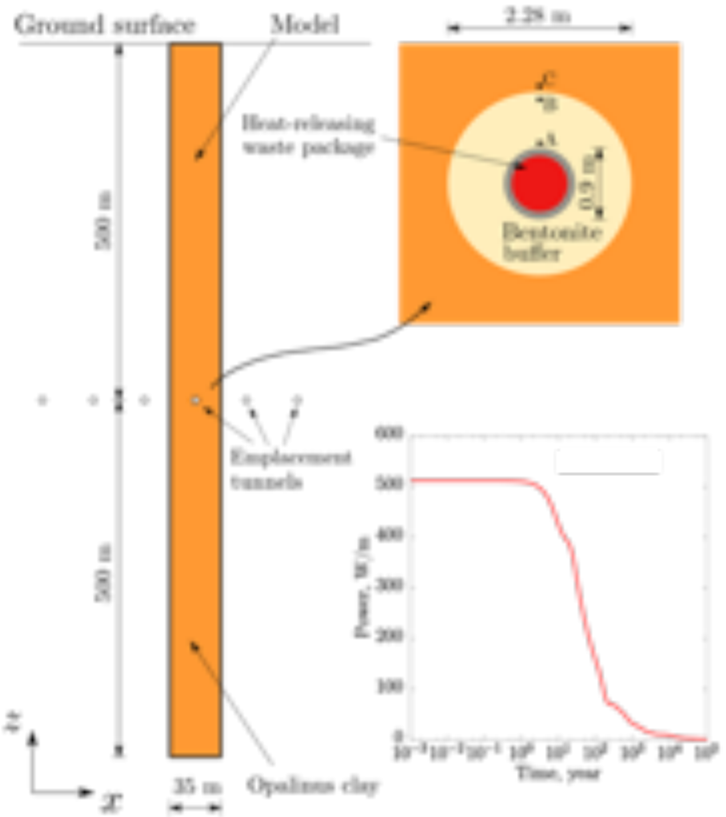

Source: Rutqvist et al., 2014.

Figure 8-1. Domain for the test example of a bentonite back-filled horizontal emplacement drift at 500 m. Modeling monitoring points: A is in the bentonite near the canister, B is in the bentonite near the EBS-NS interface, and C is in the Opalinus clay near the EBS-NS interface. Power curves used in simulations to generate a 200°C peak temperature in the buffer.

8.2.4 Model Results on Pre-consolidation Pressure, p_0^*

With BExM, we conducted several simulations with different pre-consolidation pressure, p_0^*, to investigate the variety of bentonite response under THMC processes. In BExM, p_o is the yield/pre-consolidation pressure at the current suction, while p_o^* is the associated yield stress at full saturation. These two variables are two points on the locus of loading-collapse (LC) curve defined in BExM, and the locus with respect to the suction forms the range of the elastic domain. If the stress path of p reaches the locus, the macrostructural plasticity will occur. The value of p_0^* ranges from 5 to 12 MPa based on the reported values in several published papers (Sánchez et al., 2005, 2008c; Guimarães et al., 2013; Lloret et al., 2003) using BExM. To study the effect of this parameter on the elasto-plastic behavior, we computed three cases, $p_0^* = 4$ MPa, 6.5 MPa and 8 MPa (noted as cases 1, 2 and 3, respectively). Figure 8-2 displays the stress path at Points A and B on p-s_m plane for these 3 cases. Figure 8-2a shows that no intersections or overlapping between p and p_0 are found in all 3 cases, indicating that Point A in all cases remains inside the elastic domain, and the LC curve path of p_0 in the space evolve quite similar in three cases. Figure 8-2b shows that p at Point B in Case 1 intersects with the path of p_0 at around 2.5 MPa when the bentonite is just fully saturated, indicating the yield threshold was reached. Stress collapse will happen at Point B in Case 1, and the material will consequently lose some swelling capacity.

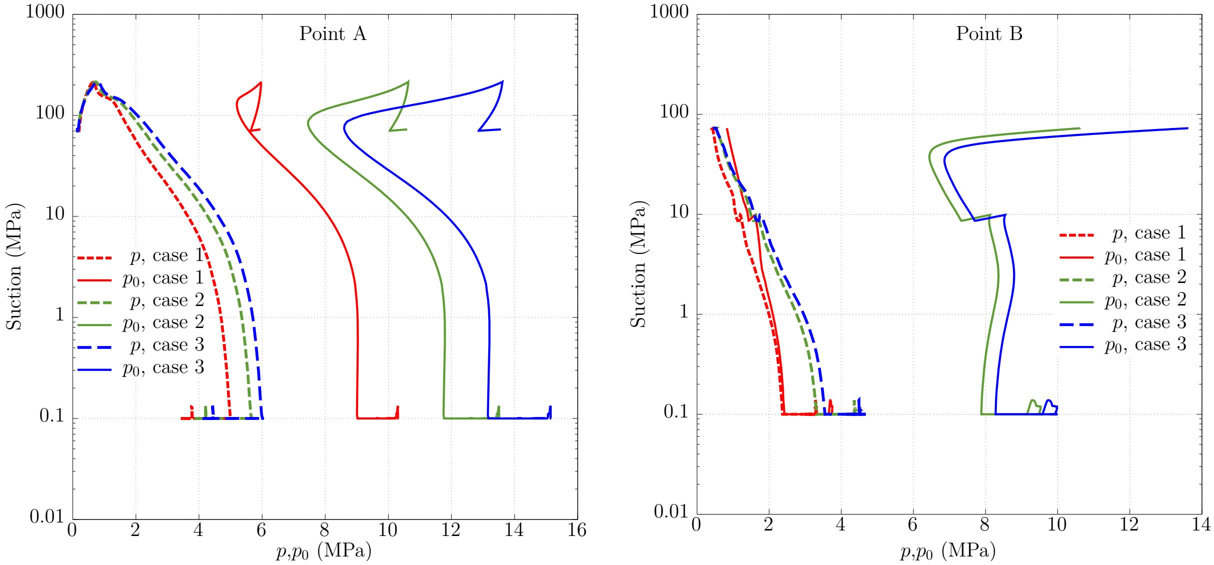

(a) Stress path of Point A on p-s_m plane (b) Stress path of Point B on p-s_m plane

Figure 8-2. Simulation results of stress at Points A and B with different initial p_0^*

As these 3 cases illustrate, initial p_0^* affects the behavior of the material. However, the value p_o varies depending on the historical stress path and the sample preparation process. Although the sample was carefully compacted, the heterogeneity of material's density induced distinct internal stress paths.

8.3 Transition to a New Simulator and Platform

8.3.1 Introduction

In FY19, as a part of the GDSA framework, we started to move our work to the Linux platform with a new numerical simulator, TReactMech, which has been recently developed at LBNL. However, the convergence in mechanical calculations was likely not well achieved, especially when the PETSc (an acronym for Portable, Extensible Toolkit for Scientific Computation) library was used for parallel computing, and the iterative two-way coupling induced very tiny time increments, resulting in extremely long computational time in our high T case. In FY20, we used the deal.II library to reconstruct the mechanical module. The deal.II library is an open source Finite Element library written in C++, which supports a broad variety of partial differential equations for different types of problems, such as mechanics, fluid flow, heat transfer, etc. (Bangerth, 2019; Arndt et al., 2019). It also provides interfaces to numerous programs and libraries, such as PETSc and Trillions for parallel computing, GPU (an acronym for Graphics Processing Unit) support via CUDA (an acronym for Compute Unified Device Architecture), HDF5 (the Hierarchical Data Format version 5) for data structures, etc. (Bangerth et al., 2007). Figure 8-3 shows one example developed with the deal.II library for parallel computing. The deal.II is initially programmed for adaptive mesh refinement (Bangerth et al., 2007; 2012), so it supports multiple mesh formats or result formats both for input and output. Although the built-in C++ classes in deal.II are not easily understandable and implemented, after getting familiar with them, it's more easily to modify partial differential equations for any specific scenario. Moreover, the C++ class in deal.II is optimized for better memory access following the hierarchical structure of the memory and cache.

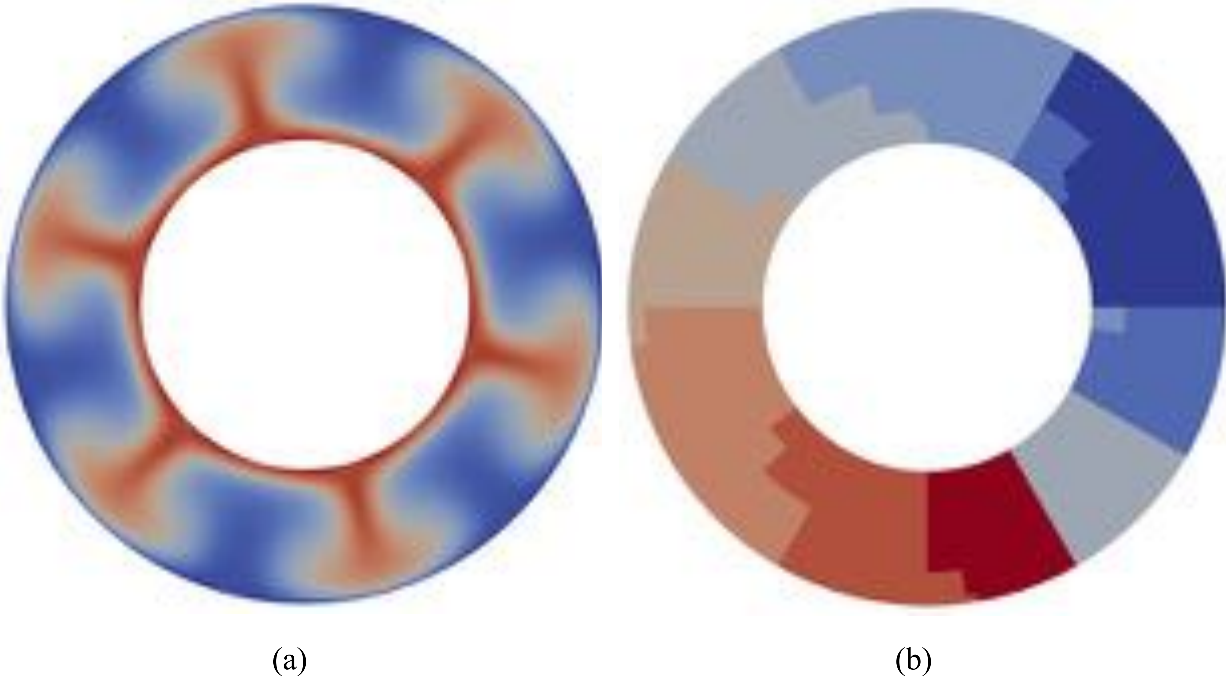

NOTE: ASPECT = Advanced Solver for Problems in Earth's ConvecTion
CPU = central processing unit

Source: The results are based on the work by Kronbichler et al. (2012).

Figure 8-3. Numerical simulation results of TH processes in the Earth's mantle with an open source code ASPECT developed with the deal.II library: (a) temperature results, and (b) partition of the whole domain with 8 CPUs

For the flow part in the simulator, we modified the code slightly to transfer from Intel FORTRAN compiler to GNU (recursive acronym meaning "GNU is not Unix") compiler. The reason to the change is that because the Intel compiler uses stack for many variables in the program, it is faster but may cause stack overflow and segmentation fault errors. On Linux, users need to increase the stack limit when compiling the source code and running the program. The GNU compiler uses heap for variables, which is a little slower than the stack, but safer. Another advantage of using the GNU compiler is that we can use more open source tools to diagnose the source code or to link with our program.

The current code only combines mechanics with Thermo-Hydraulic module, since some bugs related to OpenMP were found in the chemical part. After we diagnose and fix more code bugs, we will attach the chemical part back to the simulator. The coupling strategy includes the application of the sequential coupling method developed by Kim et al. (2012), which is widely used in the DEvelopment of COupled Models and their VAlidation against Experiments (DECOVALEX)-2019 project (Xu et al., 2020). This coupling method is performing, and the convergence is better than that in the previous version of two-way coupling in TReactMech, which induced a very tiny time increment. Now, the code uses mixed-languages compiling, C++ for mechanics, and FORTRAN for TH processes. Some variables used in both parts, like pore pressure, are declared as global variables stored in the memory, which can be accessed by any function in C++ and FORTRAN. A a result, no more files output and reading are required.

8.3.2 3D THM Modeling Verification

In this section we used the same benchmark case (Zheng et al., 2019a), a consolidation case of a homogeneous saturated porous medium around a constant point heat input power, to verify the implementation of the new coupling method. For simplicity, we don't present all details, but rather only present a comparison between the numerical results and analytical solutions (Booker and Savvidou, 1985; Smith and Booker, 1993). The only change is the domain size, which is a cube of 20 × 20 × 20 m, the heat power (only 17.5 W), and output points. Temperature, pressure, stresses and displacements evolution up to 100,000 hours are printed at the monitoring points as listed in Table 8-1.

Table 8-1. Points for numerical results for the 3D THM benchmark.

Points	(x, y, z) Coordinates	Quantity
P1	(0.275, 0, 0)	Temperature, pressure
P2	(0.35, 0, 0)	Temperature, pressure
P3	(0.45, 0, 0)	Temperature, pressure
P4	(0.275, 0.35, 0.45)	Temperature, pressure, stress
P5	(0.3, 0.4, 0.5)	Displacement

The results of 3D THM numerical modeling and analytical calculations of temperature are plotted in Figure 8-4. Figure 8-4a,b display the temperature changes at Points P1, P2, P3 and P4; Figure 8-4c presents the displacement changes at Point P5; and Figure 8-4d,e show the normal stress and shear stress changes at Point P4.

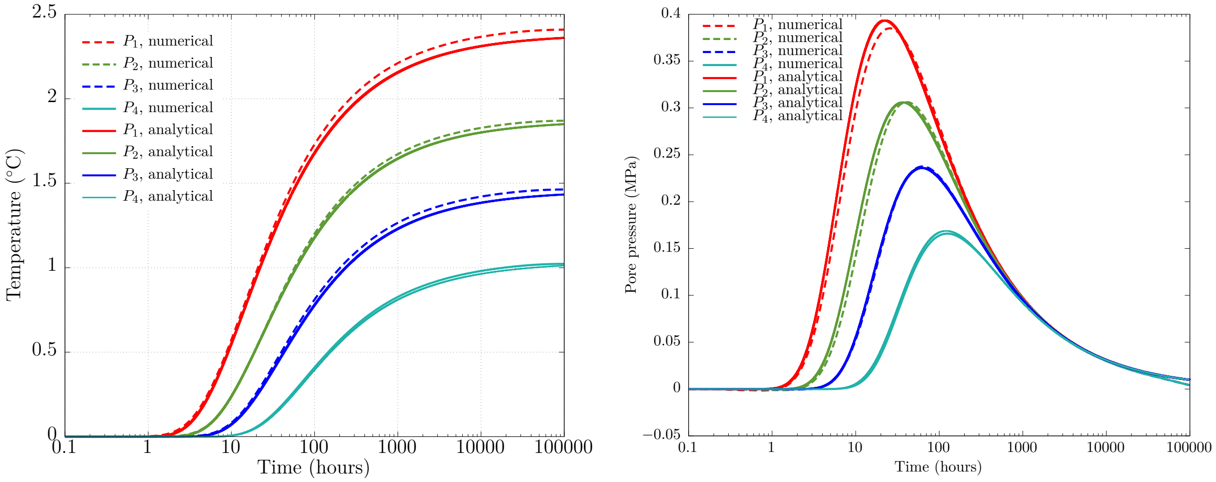

(a) (b)

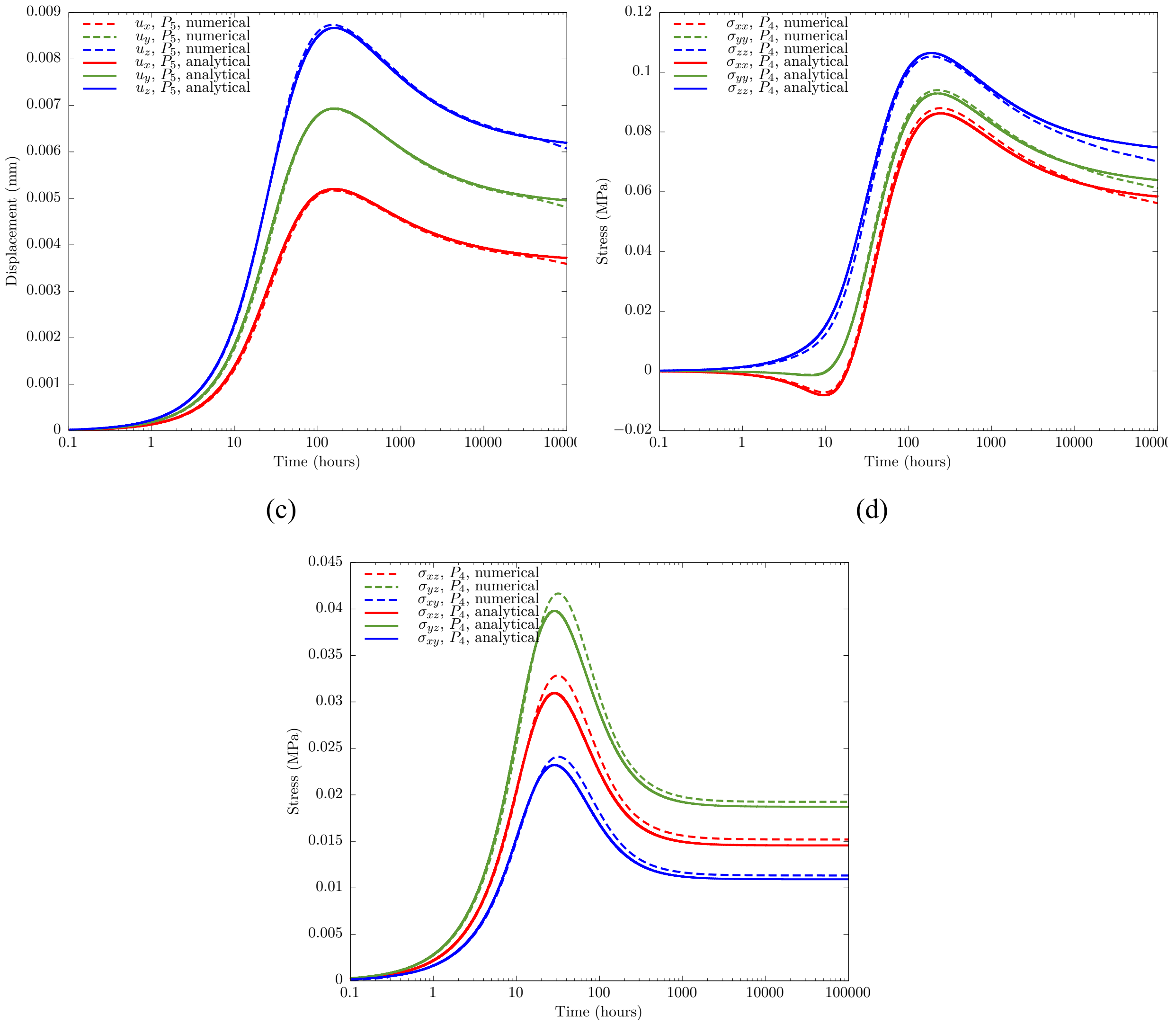

(c) (d)

(e)

Figure 8-4. Simulation results of 3D THM modeling: (a) temperature evolution at P1, P2, P3 and P4; (b) pore pressure evolution at P1, P2, P3 and P4; (c) displacement changes at P5; (d) normal stress changes at P4; and (e) shear stress changes at P4.

A good agreement between numerical simulations and analytical solutions is obtained, which verifies the correctness of the THM models' computation using the new simulator.

We used the uftrace, a profiling tool for C/C++ program developed by a group of Korean computer engineers (Kim, 2020), to analyze the code performance. Its functionality is similar as gcov and valgrind, but provides more interfaces to other tools, such as Chrome and Flame Graph (Gregg, 2019), to visualize the function calling. Because the model comprises of over than 20,000 elements, the debug mode of the program generates a large amount of profiling data. Because Chrome is used more frequently for web applications and has a limitation on the data size, we used Flame Graph tool to show the function calling.

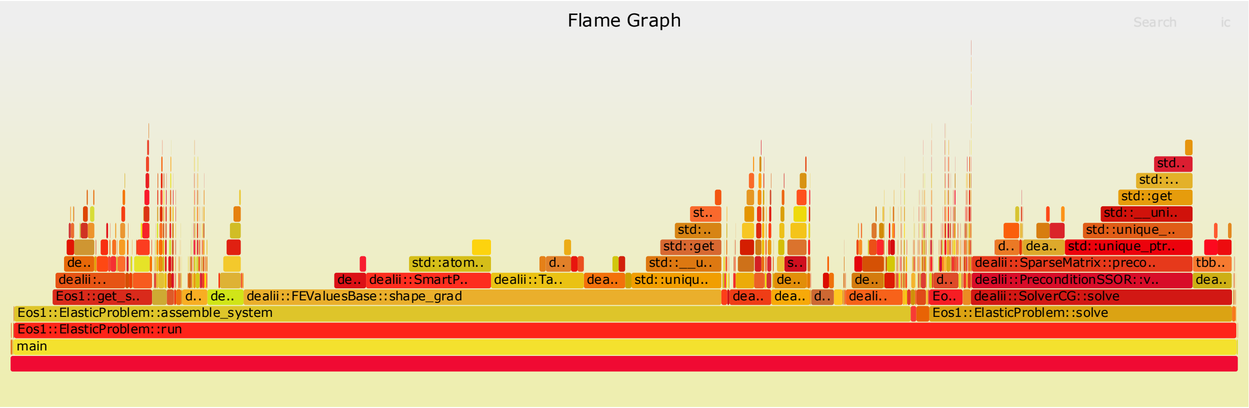

Figure 8-5. CPU time flame graph of the mechanical calculation in one time step.

Figure 8-5 shows the graph of central processing unit (CPU) running time of each function, and the horizontal length illustrates that the time length is proportional to the main function. This hierarchical graph shows the function calling relation during just one time increment in mechanical calculations. The parent function is at the lower level, and the child function called by this parent function is placed on top of the parent function. For example, main function creates the Eos1 object, and calls its public member function Eos1::ElasticProblem::run to start the problem. Then, Eos1::ElasticProblem::run calls the private member function Eos1::ElasticProblem::assemble_system to assemble the linear system, and so on. Usually, in the graph, the sharper the function is and closer the time of the child function is to its parent function, the more efficient the code is. From Figure 8-5, the most expensive and inefficient function is dealii::FEValuesBase::shape_grad, which calculates the gradients of the shape function to form the A matrix in the linear equation system $Ax = b$. Since the element number is not small, this function needs to be called numerously, and it's inevitable for the calculation. But if the material is linear elastic and a small deformation is assumed, it is only called in the first-time increment, which saves a lot of time for later computation in this specific case.

8.3.3 THMC Modeling of Bentonite in Nuclear Waste Disposal

In this section, we present the results of simulations of a generic case similar to that described in Section 8.3.3. We generated a similar model following the same geological formation and used the same material of the EBS, such as steel cell at the center surrounded by FEBEX bentonite and Opalinus clay, shown in Figure 8-6. In this model, the depth of the same domain is 1,000 m. For the canister and bentonite, the mesh was refined with 0.05 × 0.05 m elements to capture the detailed THM evolution. During the heating period, the unsaturated bentonite is placed in the tunnel, but the surrounding clay is assumed being fully saturated. The material properties were kept the same as in the previous case.

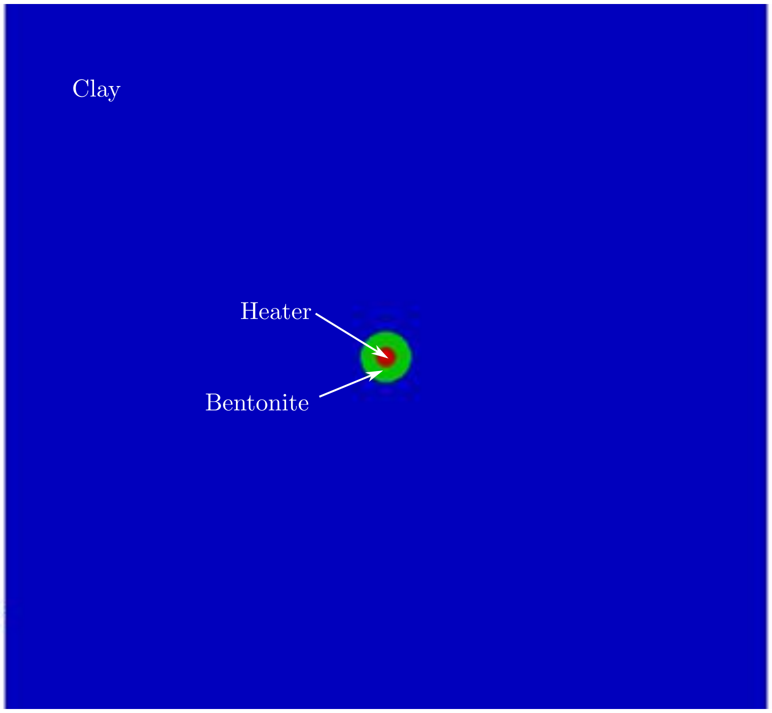

Figure 8-6. Simulation domain of the new “high T” case.

In this case, we didn’t simulate the excavation process before the heating phase. Figure 8-8 and Figure 8-9 demonstrate the simulated results of temperature and liquid saturation at Points A and B. But, unfortunately, there was a convergence issue in the flow computation. The simulation crashed around about 7 years before the planed temperature peak was reached. Figure 8-7 display the temperature distribution at the crash time point. As this figure shows, the temperature at the canister already reached 200°C. Figure 8-9 displays that the liquid saturation at point B gradually increased to close to fully saturation, while the liquid saturation at A increased slower, which is different from our previous simulation with TOUGHREACT-FLAC.

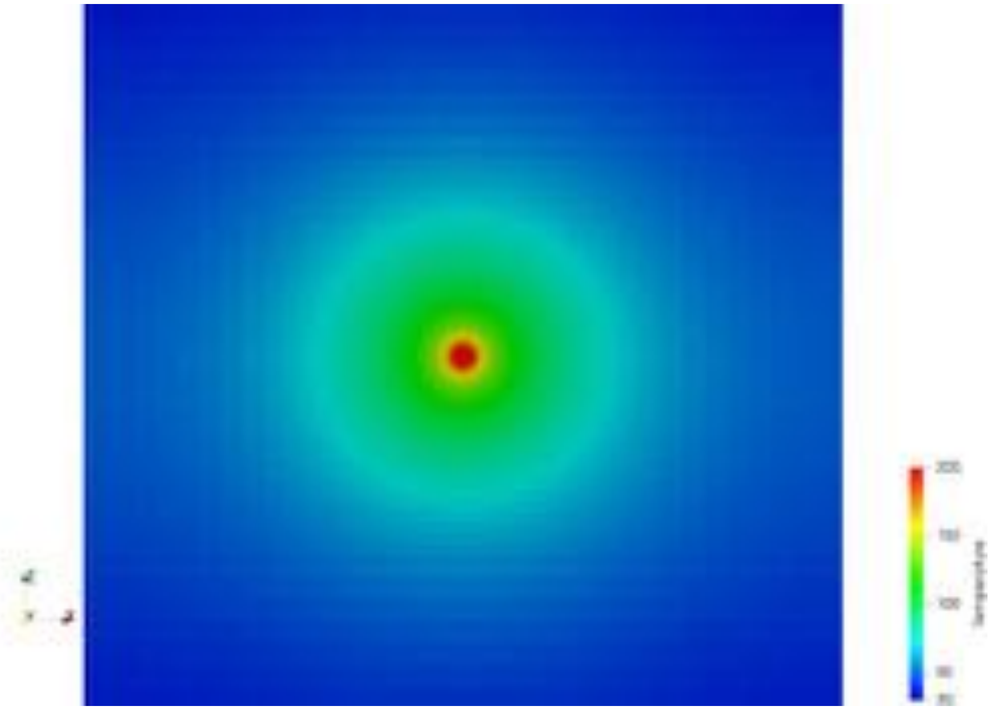

Figure 8-7. Simulation results of temperature at around 7 years.

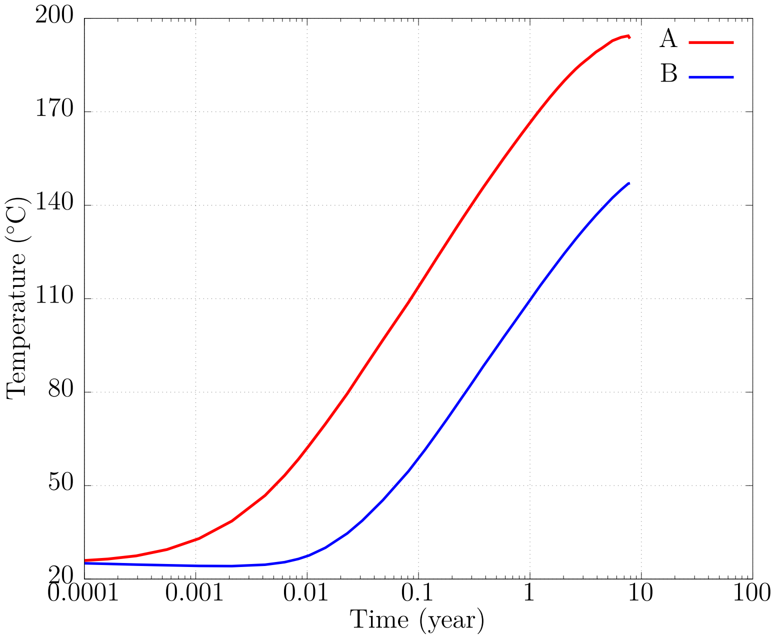

Figure 8-8. Simulation results of temperature, at Points A and B in “high T” scenario.

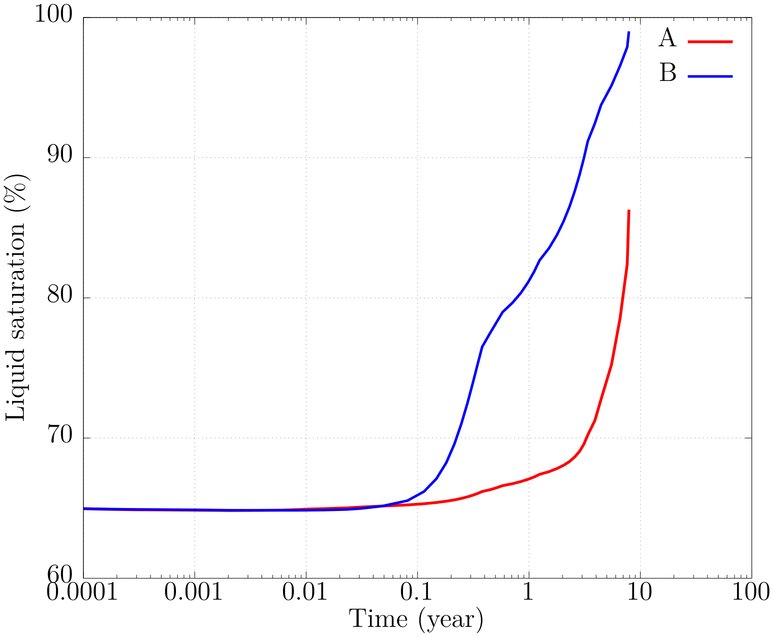

Figure 8-9. Simulation results of liquid saturation, at Points A and B in “high T” scenario.

Based on these results, the simulation ran well until the temperature peak was close, then the computation crashed in the flow part due to the oscillation between two-phase and a single-phase transition in bentonite. The hardiness of this transition is because the flow part uses different primary variables, for example, pore pressure (p) and temperature (T) are the state variables of a single phase, while gas pressure (p_g) and gas saturation (s_g) are the state variables of the two-phase system. Thus, during the two-phase calculation, the A matrix and the b vector in the linear equation system $Ax = b$ are related to p_g and s_g. Then, in the next time step for single phase, A and b are related to p and T. Since it’s a nonlinear problem, we used an iterative solver—Conjugate Gradient (CG) solver—instead of the default direct solver. The CG solver is dependent on its preconditioner, which needs to be modified based on the A matrix and organization of sparse matrix in A. Also note that if a larger size of elements is used, the convergence will become better. For example, in the DECOVALEX project, we also considered the unsaturated bentonite buffer in the tunnels, but the elements sizes were about 1 m, so the convergence was not severe. But with a coarse mesh, we are losing detailed information for bentonite at different locations. The deal.II library has considered much about CG solver and its preconditioner, since the code developers did much works on that problem in the past years. We will investigate this issue and try to improve the robustness of the simulator with the help of the deal.II library. More work to improve the simulation is undergoing.

8.4 Summary and Future Work

In the past few years, we have dedicated our efforts to developing a series of coupled THMC models to evaluate the chemical alteration and associated mechanical changes in a generic repository and to consider the interaction between EBS bentonite and the NS clay formation. In FY20, we tested the BExM with a parametric study, improved the simulator TReactMech, and modified it with a new coupling strategy. The achievements we have reached are as follow:

- We conducted a parametric study on pre-consolidation pressure in BExM for bentonite buffer under THMC processes. With this study, a distinct elasto-plastic behavior of bentonite was obtained, revealing that the spatial heterogeneity of the sample may induce uneven performance inside the material.

- We have improved the simulator on Linux platform with the deal.II library, and modified the coupling strategy to a sequential coupling method. A good agreement between numerical simulations and analytical solutions is obtained, but in the THM simulation of high T case, the hydrological calculation failed to converge due to phase changes.

To further improve the coupled THMC model on the Windows platform to obtain a better understanding of the coupled processes contributing to chemical and mechanical alteration in EBS bentonites and NS argillite formations and to answer questions regarding the thermal limit of EBS bentonite in clay repository, we are planning the following:

- To improve the convergence of hydrological part in the simulator with the deal.II library, and recalculate the high T case. Use this new library to conduct parallel computation and modify the chemical reaction part and link with the THM part. To investigate chemical-induced deformation in solid skeleton related to the change of solution compositions and to derive an improved coupling model for compacted clays following the framework of poromechanics.
- To derive reduced order model that can be integrated into the performance assessment model in GDSA. The importance of bentonite alteration and its impact on mechanical behavior needs to be integrated to performance assessment model to assess their relevance to the safety of a repository. Specifically, we will first implement of bentonite swelling models such as linear swelling, state surface, Barcelona Basic Model (BBM), and BExM into a parallel THMC simulator and then reduced order model will be developed based on the large number of THMC simulations.
- To use a physics-constrained data-driven computational framework to develop a constitutive function with the Long-Short Term Memory (LSTM) method-based strain-stress data search for simulation of clay behavior under thermal and hydration processes.
- To implement more constitutive models into the new simulator for better representation of different geomaterials, and continue working on coupled THMC modeling about different materials with the new simulator.

9. SORPTION AND DIFFUSION EXPERIMENTS ON BENTONITE

9.1 Introduction

In order for nuclear energy to be viable, a long-term nuclear waste disposal repository capable of isolating high-level and low-level radioactive waste ((HLW and LLW respectively) over the time scales necessary for the decay of long-lived radioactive isotopes (> 10^6 years) must be created. Most disposal options currently under investigation use clay media (i.e., bentonite or shale) as engineered barriers or as the host rock for geologic storage (Altmann, 2008; Altmann et al., 2012; Delay et al., 2007; Guyonnet et al., 2009; SKB, 2011; Tournassat et al., 2015). Clays are good barriers for HLW due to their low hydraulic conductivity, which restricts contaminant mobility to slow diffusion-based transport, and their high adsorption capacity for radionuclides, which slows transport even further. Montmorillonite ($M^+_{0.33}(Al_{1.67}Mg_{0.33})Si_4O_{10}(OH)_2$) is the dominant clay mineral found in bentonite. It has a 2:1 layer-type phyllosilicate structure, with a large specific surface area (~750 m^2/g) and cation exchange capacity (~1 mol/kg), and strongly sorbing surface complexation sites on clay edge surfaces.

In compacted clay, solute transport is controlled by diffusion, and adsorption of solutes to the clay can significantly retard transport. Uranium is the primary constituent of spent nuclear fuel, and the long half-lives of ^{238}U and ^{235}U (4.5×10^9 and 7.0×10^8 years, respectively) and high toxicity of U underscore the importance of understanding the transport of U through engineered barriers. U(VI) K_d (distribution coefficient) values for adsorption onto montmorillonite can vary over 4 orders of magnitude depending on aqueous chemical conditions, such as pH, partial pressure of CO_2, ionic strength, and Ca concentration (Tournassat et al., 2018). A limited number of studies have examined U(VI) diffusion through bentonite (García-Gutiérrez et al., 2003; Idemitsu et al., 1995; Joseph et al., 2017; Joseph et al., 2013; Ramebäck et al., 1998; Torstenfelt and Allard, 1986; Wang et al., 2005) and montmorillonite (Glaus and Van Loon, 2012; Tinnacher et al., 2016b). Most of these experiments have been conducted under conditions where U(VI) K_d values were relatively low (1–50 L/kg), with only a few studies performed at moderate U(VI) K_d values (93–310 L/kg, (Torstenfelt and Allard, 1986; Wang et al., 2005). This is likely due in part to the extremely long-time scales necessary for diffusion of strongly sorbing solutes. Joseph et al., (2017) found that the U(VI) had migrated only about 2 mm into the clay after 6 years of diffusion under relatively low U(VI) sorption conditions (K_d = 2.6–5.8 L/kg). Diffusion experiments with natural bentonite are complicated by changes in porewater chemistry during experiments due to processes such as dissolution of carbonates (e.g., calcite) and cation exchange. This can lead to variable and unknown pH values and Ca and bicarbonate concentrations in the porewater during diffusion experiments, which in turn leads to dynamic changes in U(VI) aqueous speciation and adsorption during the experiments. Without a full understanding of the mechanistic factors underpinning U(VI) diffusion it is difficult to accurately predict the mobility of U(VI) in a waste disposal scenario.

While present at lower total amounts than U, ^{79}Se is a major driver of the safety case for nuclear waste disposal due to its long half-life (3.3×10^5 yr) and presence as relatively mobile anionic species under a range of chemical conditions (e.g., HSe^-, SeO_3^{2-}, SeO_4^{2-}). Se redox chemistry is complex, with oxidation states ranging from −II to +VI over environmentally relevant conditions. While Se(−II) and Se(0) are relatively immobile due to the formation of low solubility precipitates, Se(IV) and Se(VI) exist as the oxyanions selenite (SeO_3^{2-}) and selenate (SeO_4^{2-}) and are highly mobile in water due to their high solubility. Se adsorption to clay minerals is quite low compared to other important radionuclides such as U. K_d values for selenite adsorption to smectite are in the range of 1–10 L/kg (Missana et al., 2009; Montavon et al., 2009) compared to values up to 10^4 for U(VI) (Tournassat et al., 2018). Selenite and selenate adsorption to the clay minerals kaolinite and Ca-montmorillonite were studied by Bar-Yosef and Meek (1987) over the pH range 4–8. Both selenite and selenate adsorption decreased with increasing pH, with very low or negligible adsorption above pH 8 and selenate adsorption to kaolinite was lower than selenite adsorption (Bar-Yosef and Meek, 1987). Similar trends of lower selenate vs selenite adsorption and decreasing adsorption with increasing pH are observed on iron oxides and oxyhydroxides (Balistrieri and Chao, 1987, 1990).

Selenite diffusion through bentonite has been investigated in several studies (García-Gutiérrez et al., 2001; Idemitsu et al., 2016; Wang et al., 2016; Wu et al., 2017). Idemitsu et al. (2016) measured apparent diffusion coefficient (D_a) values of 2.5×10^{-11} to 1.9×10^{-13} m^2/s over a range of dry bulk densities (0.8–1.6 kg/L), ionic strengths (0.01–1.0 M NaCl), and temperatures (10°C−55°C) for purified bentonite consisting of 99% montmorillonite. Measured D_a values for bulk bentonite (i.e., with lower smectite content) under similar conditions are 1−2 orders of magnitude higher (Sato et al., 1995; Wu et al., 2014). Under anaerobic conditions, it is possible for Se(IV) to become reduced to Se(0) or Se(−II) (Charlet et al., 2012; Charlet et al., 2007; Ma et al., 2019). Due to the lower adsorption of selenate compared to selenite, selenate diffusion may be even higher than observed for selenite, although we could find no studies on selenate diffusion through bentonite in the literature.

Storage of HLW can result in transient high temperatures near the waste canisters resulting from radioactive decay. The effects of elevated temperature on the engineered barrier must be taken into account when designing a nuclear waste repository. The duration of the transient elevated temperature and temperature profiles in the engineered barrier can vary widely depending on the repository design and site-specific (e.g., host rock) factors, however most HLW repository concepts impose a temperature limit of 100°C−200°C in the bentonite buffer, with elevated temperatures persisting for on the order of thousands of years (Johnson et al., 2002; Wersin et al., 2007; Zheng et al., 2015b). Temperature effects on the bentonite barrier may include changes to the clay's hydrological and mechanical properties, changes to pore water chemical compositions, and changes to the clay and accessory mineral composition (Cuadros and Linares, 1996; Wersin et al., 2007; Zheng et al., 2015). In a previous study, we found that U(VI) adsorption to lab-heated (300°C, 7 weeks) and field-heated (95°C, 18 years) bentonite was lower compared to non-heated bentonite in batch experiments, with K_d values decreasing by approximately 50% and 30%, respectively (Fox et al., 2019). While some of the lower U(VI) adsorption could be explained by changes in aqueous U(VI) speciation, changes to the clay minerals was also considered to be important in the lower U(VI) adsorption.

In this section, we focus on the diffusion of ^3H, U, and Se through compacted smectite. In Section 9.2, we present the results from ^3H and U diffusion experiments from field-heated (95°C, 18 years) and cold-zone (20°C) FEBEX bentonite under different chemical conditions. In Section 9.3, we present plans for studying Se(VI) diffusion through compacted montmorillonite under different background electrolyte compositions. We note that experimental work was interrupted/delayed due to the shelter in place orders associated with COVID-19 pandemic. In Section 9.3, we also present plans for modeling the diffusion experiments.

9.2 FEBEX Diffusion Experiments

9.2.1 Materials and Methods

9.2.1.1 Bentonite Samples

Bentonite samples were obtained from the second dismantling of the FEBEX in-situ heater test in 2015, after 18 years of heating. Detailed information on the heater test can be found elsewhere (Huertas et al., 2000). Briefly, bentonite was compacted into blocks ("bentonite rock") at 1650 kg/m^3 dry density, placed in a radial arrangement around two underground heaters and heated to a maximum of 100°C. The original FEBEX bentonite contained primarily smectite (92%), with minor amounts of quartz (2%), plagioclase (2%), cristobalite (2%), and traces of potassium feldspar, calcite, and trydimite (Fernández et al., 2004). The smectite is made up of a mixed layer illite-montmorillonite with approximately 11% of illite layers (Fernández et al., 2004). Based on results from adsorption experiments, we chose to focus on bentonite samples from two locations; one location in the heater test zone (BD-48) at a radial distance of 50 cm from the center axis and one location from a control non-heated zone (BD-59) at 50 cm. The section layout during dismantling is described by Detzner and Kober (2015). Three replicate blocks, measuring approximately 10 × 12 × 14 cm, were used from each location. The blocks were split open and approximately 200 g of bentonite was removed from the center of each block and dried in an oven at 60°C for 1 week. The dried bentonite was then crushed by hand using a porcelain mortar and pestle, and sieved through a 0.063 mm sieve in order to remove sand particles and reduce sample heterogeneity. Equivalent weights of each replicate block were mixed together to form composite samples for the three locations. Average water contents were approximately 18% and 25% and historical in-situ temperatures were approximately 95°C and 20°C for the 50-cm heater-zone and 50-cm cold-zone samples, respectively (Villar et al., 2018a; Villar et al., 2018b).

Composite FEBEX bentonite samples were purified in order to produce a purified clay sample (i.e., without carbonate and other accessory mineral impurities) for U(VI) diffusion experiments. The purification procedure was adapted from Tinnacher et al. (2016a). The procedure included the following major steps: (1) dialysis against sodium acetate at pH 5 for carbonate mineral removal, (2) dialysis against NaCl to remove acetate and complete Na-saturation, (3) dialysis against water to remove excess salts, and (4) centrifugation to remove particles greater than 2 μm. Composite clay samples (20 g) were suspended in 200 mL of 1 M sodium acetate solution buffered at pH 5 with acetic acid, placed into pre-rinsed dialysis tubing (SpectraPor7, 8 kDa), and dialyzed against acetate buffer for 1 week, changing dialysis solution daily. The acetate buffer dialysis solution was then replaced with 1 M NaCl (dialyzed for one week), then with MilliQ water (dialyzed for two weeks), again changing dialysis solution daily. The clay suspensions were then transferred into plastic bottles and diluted and dispersed in MilliQ water to reach a clay concentration of approximately 15 g/L, and centrifuged at 1000 × *g* for 7 minutes. This centrifugation speed and time was deemed sufficient to remove all particles > 2 μm as calculated from Stoke’s Law. The replicate < 2 μm clay fractions were then combined into a glass beaker, dried at 45°C and ground in ball mill with tungsten carbide balls.

9.2.1.2 Pre-equilibration of Clay

In order to ensure that aqueous porewater chemical concentrations are constant during the diffusion experiments, purified clay samples were pre-equilibrated with the appropriate background electrolyte prior to packing in diffusion cells. 2 g of purified clay was suspended in 20 mL of electrolyte solution and the clay suspension was transferred to pre-rinsed dialysis tubing (SpectrPor7, 8 kDa). Clay samples were dialyzed against 1 L of background electrolyte for 2 weeks, changing dialysis solution at least 3 times and manually adjusting pH daily. After dialysis was complete, the clay suspension was transferred to 40 mL polycarbonate centrifuge tubes and centrifuged at 39,000 × *g* for 20 minutes. The supernatant was removed and the clay was dried at 45°C and ground in ball mill with tungsten carbide balls and stored at room temperature prior to packing the cells. At the time of packing, a subsample of each clay was dried at 150°C to determine the moisture content.

9.2.1.3 Diffusion Experiments

Diffusion experiments were conducted with purified, pre-equilibrated FEBEX clay at a dry bulk density (ρ_d) of approximately 1.25 kg/L using the diffusion cell design shown in Figure 9-1. The diffusion cells used for experiments were machined in-house at Lawrence Berkeley National Laboratory and are based on the design of Van Loon et al. (2003), with dimensions adjusted to accommodate smaller samples. Preliminary experiments with stainless steel filters showed evidence of corrosion, therefore PEEK filters with a polychlorotrifluoroethylene (PCTFE) O-ring were used instead (IDEX # OC-815, overall D = 0.95 cm, filter D = 0.74 cm, thickness = 0.16 cm, pore size = 5 μm).

Experiments were performed at room temperature in the presence of 0.1 M NaCl, 0.1 or 2.0 mM Ca, and pH 7.0 in equilibrium with atmospheric CO_2. The pre-equilibrated dry clay samples were carefully weighed into PEEK diffusion cells and compacted using a custom PEEK packing rod. Three phases of the diffusion experiment were conducted: (1) saturation, (2) tritiated water (^3H) diffusion, and (3) U(VI) diffusion. The clay was saturated by circulating 200 mL of background electrolyte at both ends of the cell at approximately 1 mL/min using a peristaltic pump for 18–35 days. The background electrolyte solution was monitored for pH and dissolved Ca concentrations during saturation. After the saturation period, the ^{3}H through-diffusion phase was started by replacing the background electrolyte solutions with a high ^{3}H reservoir containing background electrolyte spiked with 30 nCi/mL ^{3}H (200 mL) at one end and a low ^{3}H reservoir containing only background electrolyte (20 mL) at the other end. The high concentration reservoir was sampled at the beginning and the end of the ^{3}H diffusion experiment and did not change significantly over that time period. The low ^{3}H reservoir was changed at time intervals of 2–48 hr, and the ^{3}H concentration was measured in the low reservoir samples by liquid scintillation counting. The concentration in the low reservoir never exceeded 2% of the concentration in the high reservoir. The ^{3}H diffusion was continued for 13–15 days. After this period, one end of the diffusion cell was plugged (low ^{3}H side) and the high ^{3}H reservoir at the other end was replaced with 20 mL of electrolyte solution spiked with 1×10^{-6} M U(VI), marking the start of the U(VI) in-diffusion experiment. Subsamples of the U(VI) solution reservoir were collected periodically for dissolved U(VI) and other metal measurement by ICP-MS and pH was measured directly in the U(VI) solution reservoir. U(VI) diffusion was continued for 31 days. U(VI) controls consisting of U(VI)-spiked electrolyte solution recirculating through the peristaltic pump (i.e., without the diffusion cell) were performed in parallel. The U(VI) control reservoirs were monitored and sampled in the same manner as the U(VI) diffusion experiment reservoirs in order to check for U(VI) adsorption to tubing and reservoir containers. Note that the U(VI) diffusion experiment was completed for the two samples in the presence of 2 mM Ca; the U(VI) diffusion for the 0.1 mM Ca sample was interrupted.

At the end of the U(VI) diffusion period, the diffusion cells were disassembled and the clay plug was extruded using the PEEK packing rod and sliced into thin slices. The thickness of the clay slices was measured using a digital caliper with a precision of 0.1 mm. The clay slices were placed into 20 mL glass scintillation vials, dried at 150°C for 24 hours, and weighed to determine the exact dry clay weight for each slice. The PEEK filters were removed from each end of the clay plug, suspended in 10 mL of MilliQ water in a glass scintillation vial and shaken vigorously to dislodge any clay that was stuck to the filter. The filter was then transferred to a new vial and 10 mL of 0.15 M nitric acid was added to the filter to dissolve any adsorbed U(VI). The clay slices were extracted with 10 mL of 0.15 M ultrex grade nitric acid for 24 hours, then centrifuged at 39,000 × *g* for 20 min and filtered through a 0.45 µm PVDF syringe filter. Metal concentrations were measured in the nitric acid extracts by ICPMS. The small amount of clay which was removed from the filters with MilliQ water was dried at 150°C, weighed, and extracted in the same manner as the clay slices. Both the dry bulk density (ρ_d) and U concentrations in the clay plug are expressed in terms of the 150°C oven dry weight of clay. At room temperature, the clays had a water content of approximately 11%.

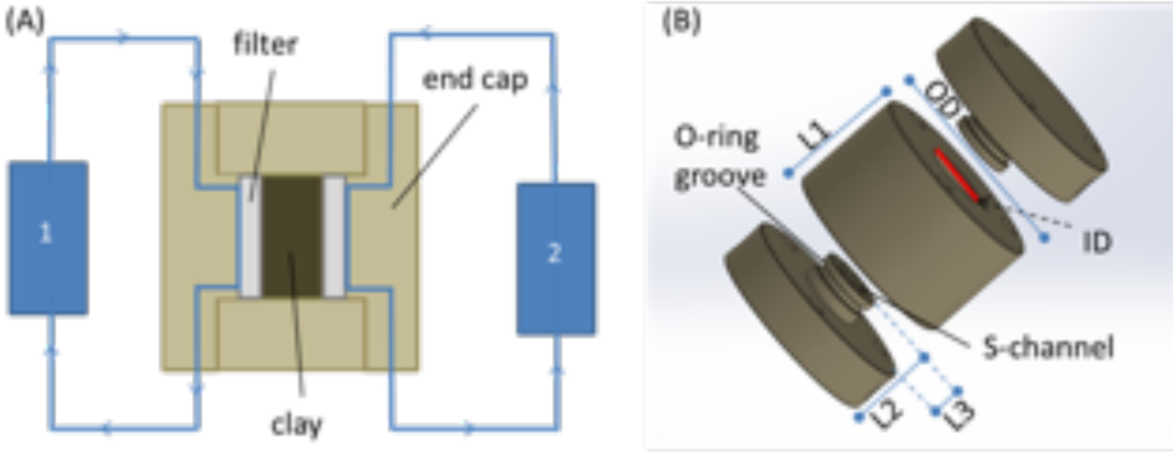

Figure 9-1. Schematic of diffusion cells machined in house. (A) Cross-sectional view of the diffusion cell showing the clay plug, filters and two solution reservoirs. During saturation and ^{3}H diffusion, both reservoirs are used, and during U(VI) in-diffusion, reservoir 2 is removed and the cell is plugged at that end. (B) Detailed schematic of the cell design, with grooves for the o-rings and an S-shaped channel, which allows the solution to distribute evenly over the entire filter of the diffusion cell. The dimensions for the cell are as follows: OD=30 mm, ID=9.5 mm, L1=17.8 mm, L2=12.2 mm, L3=4.9 mm. O-rings measure 7.5 mm ID and 9.5 mm OD.

9.2.1.4 Analytical Techniques

Samples were analyzed for metal concentrations (U, Ca, Mg, Al, Si, and Fe) by ICP-MS (Perkin-Elmer Elan DRC II) after acidification and dilution with ultrapure (ultrex grade) 0.15 M nitric acid and internal standard addition. Samples were analyzed for ^{3}H using liquid scintillation counting (Perkin-Elmer Liquid Scintillation Analyzer Tri-Carb 2900TR) by mixing 4 mL of sample with 18 mL of Ultima Gold XR liquid scintillation cocktail.

9.2.2 Results and Discussion

9.2.2.1 Tritium (^{3}H) Diffusion

Normalized mass flux (J_N, in m/day) reaching the low concentration reservoir was calculated using Equation 9-1:

$$J_N = \frac{C_{low} V_{low}}{C_{high} A \cdot \Delta t} \qquad \text{Equation 9-1}$$

where C_{low} is the concentration in the low concentration reservoir, C_{high} is the concentration in the high concentration reservoir, V_{low} is the volume of the low concentration reservoir (approximately 20 mL), A is the cross-sectional area of the diffusion cell (0.709 cm^2), and Δt is the time interval since the previous sampling event.

The normalized flux of ^{3}H is shown in Figure 9-2 for the purified FEBEX samples from the heated and cold ones. Diffusive flux increased over the first 48 hr, reaching steady state thereafter for both samples. Note that the first sampling point for the heated-zone sample shows a higher apparent flux than subsequent points. This is due to the fact that the tubing for the low-concentration reservoir was mistakenly dipped in the high-concentration reservoir prior to starting the flow. The contaminated tubing was rinsed with MilliQ water, however a small amount residual ^{3}H contamination remained. The average normalized flux at steady state (≥50 hr) ranged from 1.38 ± 0.13 × 10^{-3} m/day (cold-zone, 2 mM Ca) to 1.73 ± 0.17 × 10^{-3} m/day (heated-zone sample, 0.1 mM Ca) as shown in Table 9-1. Small differences in the normalized measured ^{3}H flux may result from small differences in cell packing, which can in turn affect porosity or pore structure (i.e., pore constrictivity or tortuosity). However, it should be noted that the observed normalized fluxes are not significantly different from one another. Total porosity (ε) depends on bulk density, and can be calculated using Equation 9-2:

$$\varepsilon = 1 - \frac{\rho_d}{\rho_g} \qquad \textit{Equation 9-2}$$

where ρ_g is the crystal density of clay mineral layers (i.e., grain density). For montmorillonite, ρ_g is approximately 2.84 kg/L (Bourg et al., 2006; Tournassat and Appelo, 2011). There is no measurable difference in the calculated bulk density or total porosity of the two samples (Table 9-1).

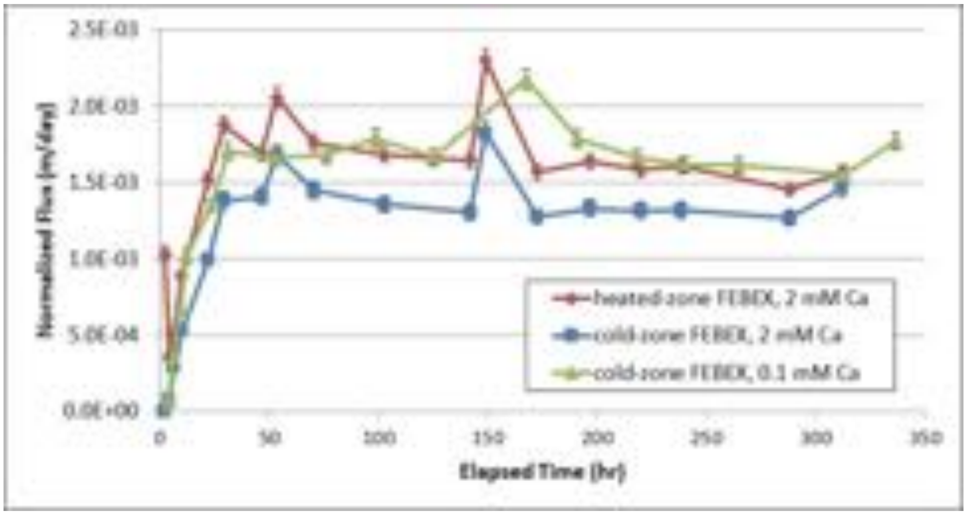

Figure 9-2. Tritium diffusion through heated-zone and cold-zone purified FEBEX bentonite at pH 7 in the presence of 2 mM or 0.1 mM Ca and 0.1 M NaCl. Diffusion is expressed as normalized mass flux as a function of time. Error bars represent the analytical error (standard deviation).

Table 9-1. Summary of diffusion cell properties

Sample	ρ_d (kg/L)	ε	Ca (mM)	^{3}H Avg J_N (m/day)[a]	U(VI) K_d (L/kg)[b]
FEBEX, 95°C heated-zone	1.25	0.56	2.0	1.66 ± 0.16 × 10^{-3}	9,333
FEBEX, 20°C cold-zone	1.24	0.56	2.0	1.38 ± 0.13 × 10^{-3}	16,982
FEBEX, 20°C cold-zone	1.25	0.56	0.1	1.73 ± 0.17 × 10^{-3}	19,055

NOTE: [a] The average normalized mass flux for ^{3}H during steady state (≥50 hr).

[b] U(VI) K_d values determined from batch adsorption experiments (Fox et al., 2019).

9.2.2.2 U(VI) Diffusion

Dissolved U(VI) concentrations in the U(VI) reservoirs during the U(VI) diffusion experiments are shown in Figure 9-3. Dissolved U(VI) concentrations decreased over time for both samples and the control experiment. The decrease in U(VI) concentration in the control reservoir indicates that U(VI) adsorption onto tubing and container walls likely occurred. However, U(VI) concentrations in the sample reservoirs were lower than in the control reservoir, therefore the difference between the control and sample reservoirs represents the diffusive loss of U(VI). Tests with different types of tubing will be performed in order to minimize U(VI) adsorptive loss in future experiments. The two clay samples tested exhibited nearly identical U(VI) loss under these conditions. Interpretation of the U(VI) diffusion data is confounded by the small differences observed in ^{3}H diffusion and modeling will be required to separate the effects of pore structural differences (if significant) and U(VI) adsorption on the U(VI) diffusion. Figure 9-4 and Figure 9-5 show the Ca concentrations and pH observed in the U(VI) reservoir solution during the experiment. Changes in Ca concentration were very small, while pH values varied within 0.2 pH units (6.8–7.2) over the course of the experiment.

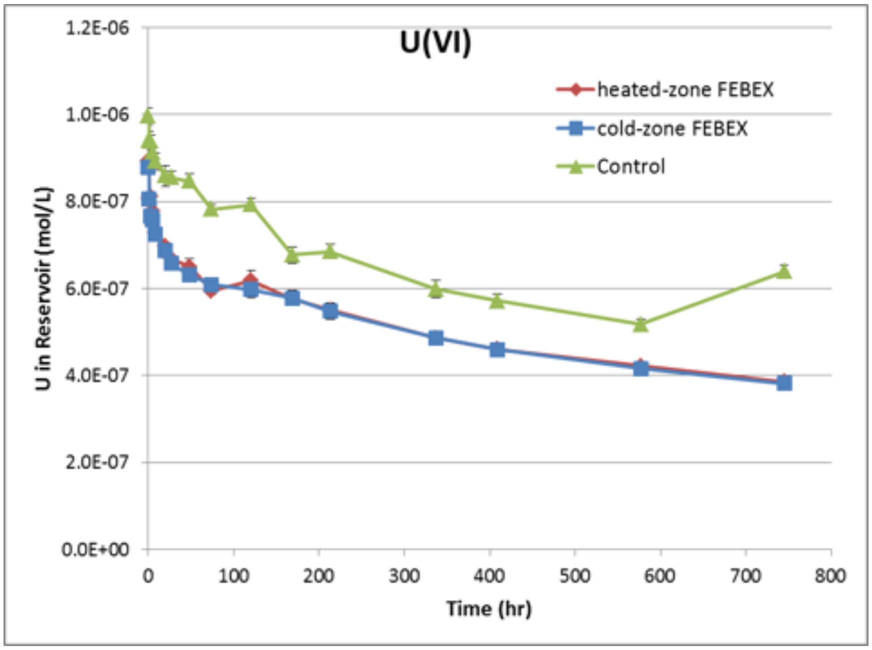

Figure 9-3. Dissolved U(VI) in reservoir during U(VI) diffusion experiments with purified heated-zone and cold-zone FEBEX clay. Concentrations are also shown for a control reservoir containing U(VI)-spiked background electrolyte that was recirculated through the peristaltic pump. Error bars represent analytical error.

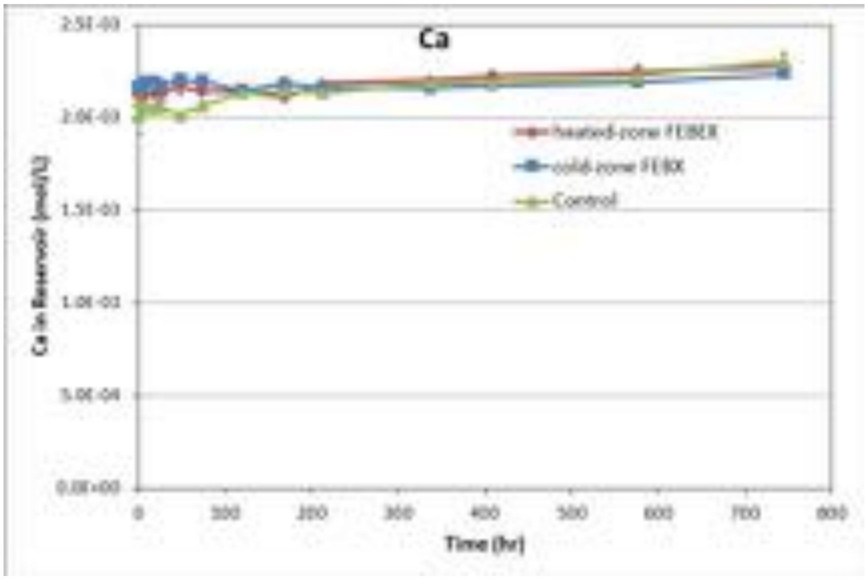

Figure 9-4. Dissolved Ca in reservoir during U(VI) diffusion experiments with purified heated-zone and cold-zone FEBEX clay. Concentrations are also shown for a control reservoir containing U(VI)-spiked background electrolyte that was recirculated through the peristaltic pump. Error bars represent analytical error.

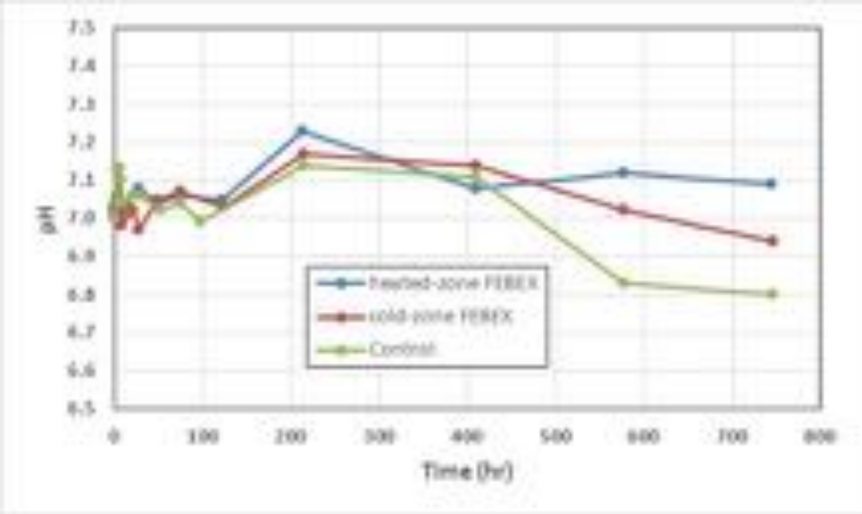

Figure 9-5. Measured pH in reservoir during U(VI) diffusion experiments with purified heated-zone and cold-zone FEBEX clay. pH values are also shown for a control reservoir containing U(VI)-spiked background electrolyte that was recirculated through the peristaltic pump.

9.2.2.3 Clay Slicing

In order to determine the U(VI) diffusion profile in the clay, the clay plugs were sliced at the end of each experiment and total U and other metal concentrations were measured in the clay. The results for U and Ca are shown in Figure 9-6. Background metal concentrations extracted from the FEBEX clays which had been pre-equilibrated with 0.1 M NaCl and 2 mM Ca at pH 7.0 are shown in Table 9-2. U accumulated only in the first two slices of clay (<1 mm). No evidence for changes in concentrations of other elements from background concentrations was observed. The net U recovered on the clay (after subtracting out the background U) was $2.6 \pm 0.04 \times 10^{-9}$ mol U and $2.3 \pm 0.03 \times 10^{-9}$ mol U for the heated and cold-zone samples, respectively. This agreed well with the $2.7 \pm 0.3 \times 10^{-9}$ mol net U lost from the reservoir for both samples (corrected for U lost to sorption to tubing and reservoir walls using concentrations in the control reservoir).

Table 9-2. Background metal concentrations in purified FEBEX clay, which was pre-equilibrated with 0.1 M NaCl, 2 mM Ca, at pH 7.0 measured by nitric acid extraction

Metal	Extracted Concentration (mol/g)	
	Heated Zone	Cold Zone
Mg	$8.81 \pm 0.38 \times 10^{-06}$	$7.65 \pm 0.44 \times 10^{-06}$
Al	$1.48 \pm 0.04 \times 10^{-04}$	$1.23 \pm 0.04 \times 10^{-04}$
K	$1.84 \pm 0.03 \times 10^{-05}$	$2.24 \pm 0.04 \times 10^{-05}$
Si	$6.75 \pm 0.28 \times 10^{-04}$	$6.70 \pm 0.06 \times 10^{-04}$
Mn	$5.43 \pm 0.10 \times 10^{-07}$	$5.08 \pm 0.15 \times 10^{-07}$
Ca	$2.21 \pm 0.03 \times 10^{-04}$	$2.25 \pm 0.02 \times 10^{-04}$
Fe	$1.43 \pm 0.02 \times 10^{-05}$	$1.19 \pm 0.02 \times 10^{-05}$
U	$1.14 \pm 0.03 \times 10^{-09}$	$9.25 \pm 0.22 \times 10^{-10}$
Sr	$4.55 \pm 0.13 \times 10^{-08}$	$4.73 \pm 0.13 \times 10^{-08}$

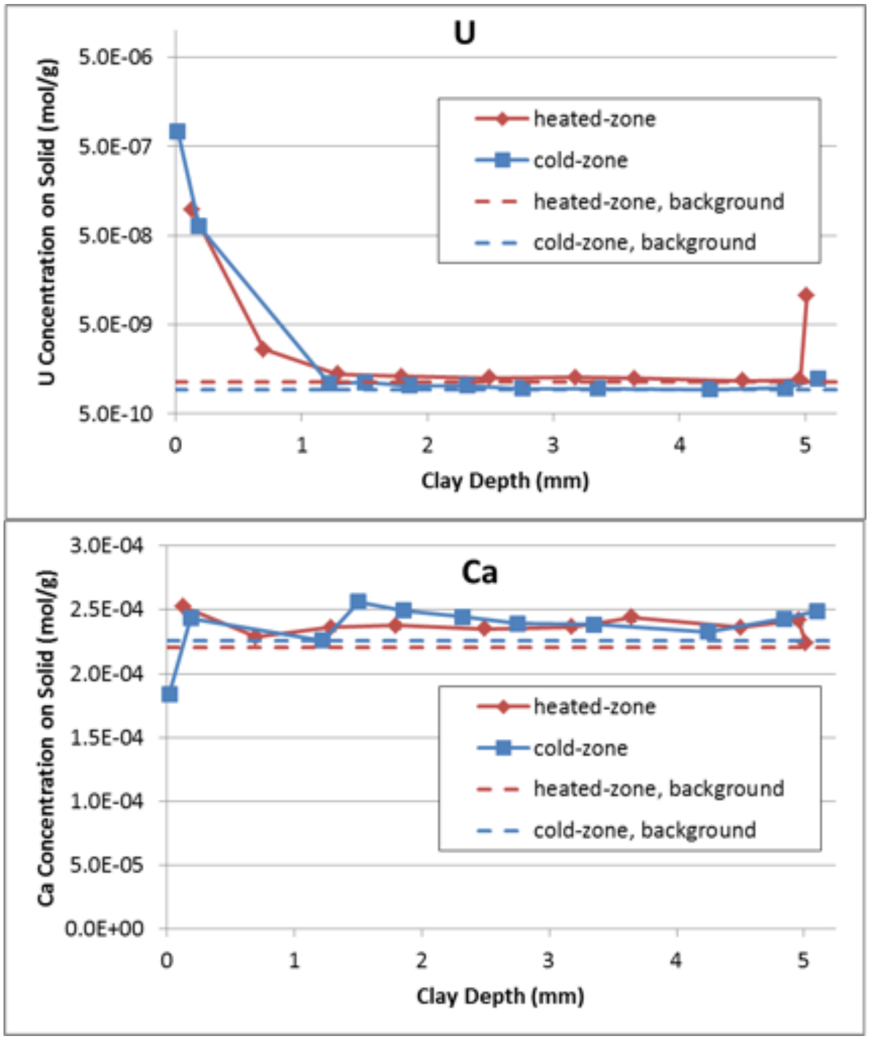

Figure 9-6. Top: U diffusion profile in clay at the end of the experiment for FEBEX clay equilibrated with 2 mM Ca. U is expressed as the total U concentration (note log scale of y-axis). The U(VI) inlet end of the cell is at a clay depth of 0.0 mm and the outlet end (plugged) is at 5.0 mm. Bottom: Ca profiles in the clay, expressed as total Ca concentration. Concentrations of U and Ca in the original pre-equilibrated clay are shown for reference. The data points are shown at the end of the clay depth, i.e., the data point at 0.13 mm represents the clay slice from 0–0.13 mm, then point at 0.70 mm represents the clay slice from 0.13–0.70 mm, and so on.

9.3 Summary and Future Work

In FY20, diffusion experiments were conducted with 95°C heated and 20°C cold-zone purified FEBEX bentonite at a bulk density of 1.25 kg/L. The experiments were conducted at a constant ionic strength (0.1 M NaCl) at pH 7 in the presence of 0.1 mM Ca or 2 mM Ca. The average normalized ^3H flux at steady state (≥50 hr) for ^3H through-diffusion was not significantly different across samples, with values ranging from $1.38 \pm 0.13 \times 10^{-3}$ m/day to $1.73 \pm 0.17 \times 10^{-3}$ m/day. U(VI) in-diffusion experiments conducted in the presence of 2 mM Ca showed the diffusive loss of U(VI) from the high concentration reservoir was indistinguishable for the heated and cold-zone bentonite and U(VI) traveled less than 1 mm into the clay over the 30-day diffusion period. While lower U(VI) adsorption was previously measured on the heated-zone FEBEX bentonite compared to the cold-zone bentonite, it is possible that differences in U(VI) diffusion due to differences in adsorption may only become apparent over much longer time periods than can be realistically tested in the laboratory. Reactive transport modeling of these results using CrunchClay is currently underway and will provide further insight into the geochemical conditions and time periods in which differences in U(VI) diffusion as a result of heating may be observed.

Future work will focus on the diffusion and redox transformations of Se through compacted montmorillonite. Experiments will be conducted under a single ionic strength (0.1 M) and three different electrolyte compositions: 0.1 M NaCl, 0.033 M $CaCl_2$, and 0.085 M NaCl + 0.005 M $CaCl_2$, representing pure Na, pure Ca, and a Na-Ca mixture, respectively. We hypothesize that Se(VI) diffusion will be different under these different electrolyte compositions due to both differences in aqueous Se speciation and differences in the clay swelling in the presence of Na and Ca. These experiments will also be modeled using CrunchClay.

A detailed understanding of selenium diffusion through and transformation within bentonite is critical for the successful design and implementation of the EBS due to the long half-life (3.3×10^5 yr) and high mobility of ^{79}Se. Se redox chemistry is complex, with oxidation states ranging from −II to +VI over environmental conditions relevant for deep geologic disposal, and each species has different mobility due to differences in adsorption, solubility, and charge. Over the next year, we plan to begin a detailed investigation of Se diffusion and reactivity in bentonite in order to better our understanding of its behavior in engineered barriers. This work will be done in close coordination with a modeling effort described in Section 9.3. Our primary goal is to evaluate Se(VI) diffusion through compacted montmorillonite over a range of electrolyte compositions although future work will expand into important Se redox transformations driven by reactions with reduced constituents present in the EBS.

Se(VI) diffusion experiments will be conducted using a well-characterized, purified montmorillonite source clay (SWy-2). Through-diffusion experiments will be conducted using the same diffusion cells described in Section 9.2.1.3 at a dry bulk density of 1.25 kg/L. Experiments will be conducted under a single ionic strength (0.1 M) and three different electrolyte compositions: 0.1 M NaCl, 0.033 M $CaCl_2$, and 0.085 M NaCl + 0.005 M $CaCl_2$, representing pure Na, pure Ca, and a Na-Ca mixture, respectively. We hypothesize that Se(VI) diffusion will be different under these different electrolyte compositions due to both differences in aqueous Se speciation and differences in the clay swelling in the presence of Na and Ca. Se(VI) aqueous speciation over the pH range of 5–8 is shown in Figure 9-7, where three major Se(VI) species with different charge dominate: SeO_4^{2-}, $HSeO_4^-$, and $CaSeO_4^0{}_{(aq)}$.

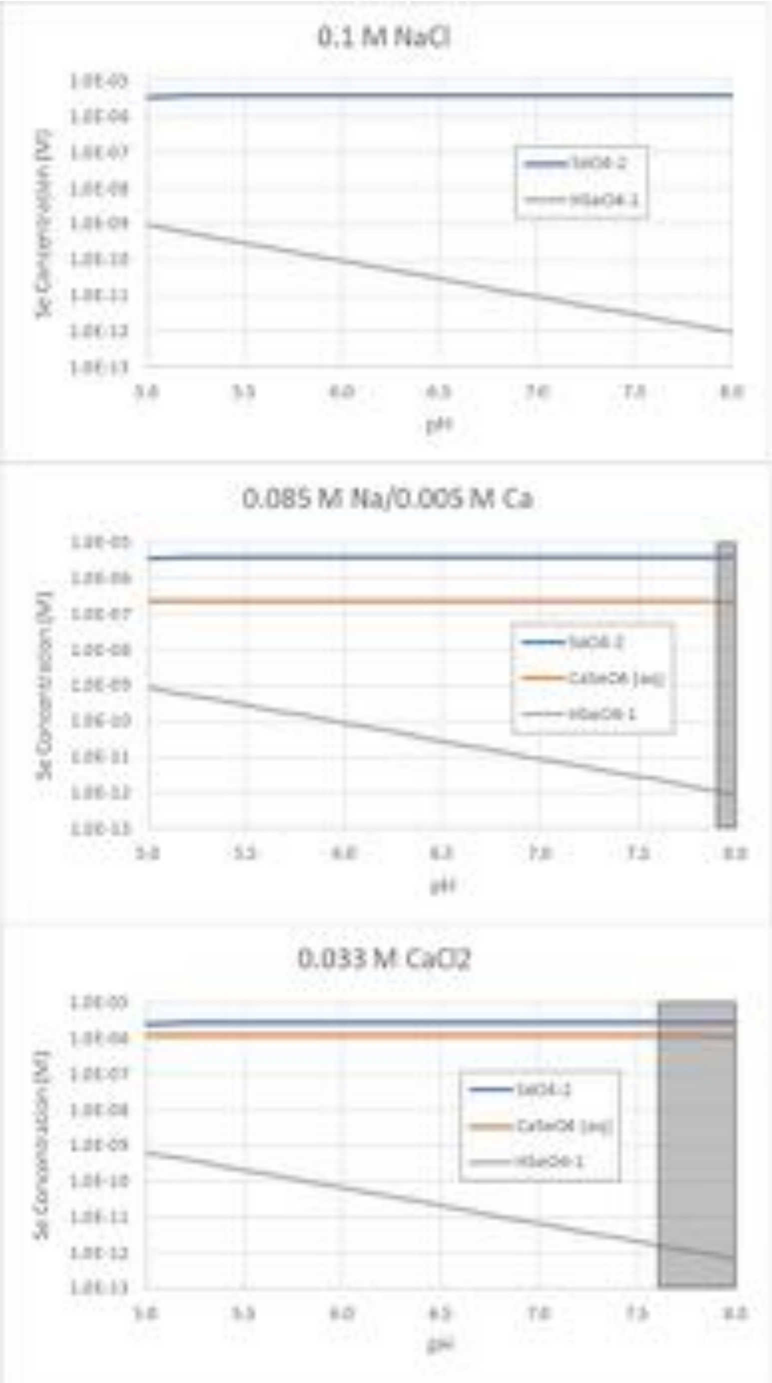

Figure 9-7. Aqueous speciation of Se(VI) as a function of pH in equilibrium with atmospheric CO_2 (380 ppm) for three different electrolyte compositions. Total Se(VI) concentration is 4 μM. The area shaded in grey represents conditions which are oversaturated with respect to calcite.

Modeling of diffusion experiments will be carried out using CrunchClay (Steefel et al., 2015; Tournassat and Steefel, 2019a) taking full advantage of the capabilities of this reactive transport code developed at LBL. CrunchClay is currently one of only two codes that can handle diffusion processes in the diffuse layer, in which the solution is not electroneutral, and for which coupled interdiffusion processes must be taken into account to model diffusion properties with a mechanistic approach (Tournassat and Steefel, 2019b). CrunchClay has the ability to treat both electrical double layer and bulk porosity with differing anion and cation diffusivities, which makes it possible to simulate the diffusion of a range of tracers with different charges in a single run, and with the same input parameters. CrunchClay also has surface complexation and cation exchange modeling capabilities, thus making it possible to couple mechanistic adsorption models with diffusion models in clay media. Our goal is to derive consistent diffusion and adsorption parameters for Se, ^{3}H and other trace elements as a function of ionic strength and electrolyte composition, which will be probed experimentally in this project.

10. CHEMICAL CONTROLS ON MONTMORILLONITE STRUCTURE AND SWELLING PRESSURE

10.1 Introduction

Despite many decades of study, quantitatively predictive models for diffusion-driven mass transport through clay rich geomaterials remain elusive. Predicting mass transport through clays is difficult, because the material is largely nanoporous, and interactions between charged clay layers and nanopore fluid give rise to structural and dynamical fluid properties that cannot be quantified with existing continuum models. Our research focuses on montmorillonite, which is the dominant smectite clay mineral that makes up bentonite, which is expected to be widely used as a barrier material. Under confinement and under certain aqueous solution conditions, montmorillonite clays adopt crystalline swelling states, with defined water contents (Norrish, 1954; Smith et al., 2006; Rotenberg et al., 2009; Holmboe and Bourg, 2013). Multiple swelling states typically coexist at equilibrium (Bérend et al., 1995; Homboe et al., 2012), but there are no models available that can predict the distribution of swelling states as a function of solution composition, particularly in mixed electrolyte solutions. Moreover, perturbations to stress state or fluid chemistry will result in shifts to the equilibrium swelling state, leading to what is known as chemical-mechanical coupling. The central aim of this research is to develop an equilibrium model to predict clay swelling states in mixed-electrolyte solutions under varying stress states.

A molecular-level understanding of the interlayer and inter-tactoid forces causing swelling/collapse, influenced by the chemical composition and mobility of water and ions in the interlayers and pores, can provide valuable upscaling strategies to inform macroscopic models. Numerous physical and chemical variables have been shown to have a major influence on clay swelling—clay layer charge, water activity, electrolyte ion composition, and confining pressure being the dominant controlling variables (Sun et al., 2015; Teich-McGoldrick et al., 2015). Other factors, such as the crystalline alignment of individual clay layers, have been shown to depend on ion composition and are, therefore, likely to influence swelling (Whittaker et al., 2019). Traditional models implementing the DLVO and the Modified Guoy-Chapman (MGC) theory can reasonably predict osmotic swelling (in the case of symmetric monovalent, low ionic-strength electrolyte) provided molecular-level information (e.g. distance of closest approach) is available; however, these continuum model predictions break down for hydrates with basal spacing ~ 10–12 $\AA$ (1-2 water layers) where water molecules need to be treated as discrete.

In this report, we present the progress on an integrated set of experiments, molecular simulations, and thermodynamic modeling to develop a predictive understanding of ion exchange-driven swelling and collapse of montmorillonite clay. In our previous reports (Zheng et al., 2019a,b), we focused on developing modeling and simulation approaches to understanding clay thermodynamics. Accomplishments from the prior funding period include development of molecular simulations approaches (Subramanian et al., 2020) that inform a new thermodynamic model for ion exchange driven clay swelling and collapse (outlined in Whittaker et al., 2019). Our FY 2020 efforts focus on transferring this knowledge to compacted clay systems accounting for non-zero effective normal stress. We report on the development of an X-ray transparent micro-oedometer system for the measurement of montmorillonite swelling pressure as a function of dry bulk density and aqueous solution composition. Initial work focuses on pure homoionic NaCl and KCl solutions as well as NaCl+KCl mixtures. Preliminary data are presented from in-situ X-ray scattering experiments conducted at the Advanced Photon Source (APS), Argonne National Laboratory. To develop a theoretical understanding of microstructural evolution, we applied our newly published structural model for cis-vacant smectite clay (Subramanian et al., 2020) to simulate the free energy of mixing crystalline layer states and find that highly unfavorable mixing energetics can drive phase separation in mixed layer state systems. Ongoing simulations of swelling free energy are being conducted using a PMF calculation method. Finally, these results are integrated into a thermodynamic model, previously developed (Zheng et al., 2019a,b;

Whittaker et al., 2019), to predict swelling pressure as a function of pore fluid composition in compacted bentonite.

10.2 Experimental Studies of Swelling Pressure and Microstructure in Compacted Montmorillonite

In early FY 2020, we set up a new X-Ray transparent micro oedometer system (Figure 10-1). This system is designed to measure the evolution of swelling pressure as a function of time during equilibration of a clay sample of fixed bulk density with an aqueous solution or with pure water. The swelling pressure is a key property of bentonite barriers for EBS. Swelling of the clay minerals causes closing of part of the pore space or preferential flow pathways (formed, for example, due to shrinkage), reducing permeability of the clay barrier. Macroscopic swelling pressure is a measure of the excess pressure required to obtain a defined water content and is equivalent to disjoining pressure for an infinite clay tactoid. Pressure in excess of the hydrostatic stress arises in clay interlayers from the sum of several forces, including electrostatic interactions, van der Waals dispersion forces, and especially the clay interlayer cation hydration energy. The latter quantity arises due to the relatively strong interaction between clay interlayer cations with their waters of hydration (cf. Norrish, 1954; Teppen and Miller, 2005). Together these forces promote water uptake and volumetric increase in clays at fixed pressure, and conversely pressure increase in clays with volumetric constraints.

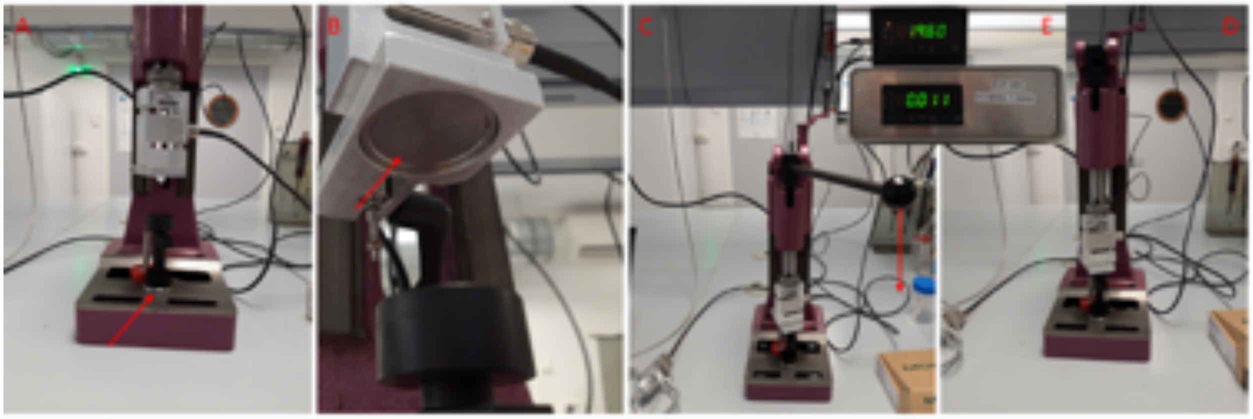

Figure 10-1. Photographs of the custom micro-oedometer showing (a) the position of the black PEEK cell on the holder, (b) the top contact with the force sensor, (c) the whole cell and holder illustrating the emplacement of the force sensor on the cell, (d) the cell configured for a measurement, and (e) the force (top) and displacement (bottom) sensors logging data.

Measurements of swelling pressures are typically made to obtain a swelling pressure curve, which gives swelling pressure as a function of clay dry bulk density for a given aqueous solution composition (Pusch, 1982; Liu et al., 2013). These measurements can be obtained using an oedometer, which measures the force on a stiff spring applied by a swelling material confined to a fixed volume. Briefly, clay is packed into a small cylinder bounded on either side by permeable filters and frits. The clay is confined by a displaceable piston. Miniscule displacements on the piston generate a force measurement, which is subsequently converted to pressure based on the geometry of the cell.

In this section, we detail the Oedometer configuration and provide some preliminary swelling pressure data for our study clay, Wyoming Montmorillonite SWy-3 obtained from the Source Clay Minerals Repository.

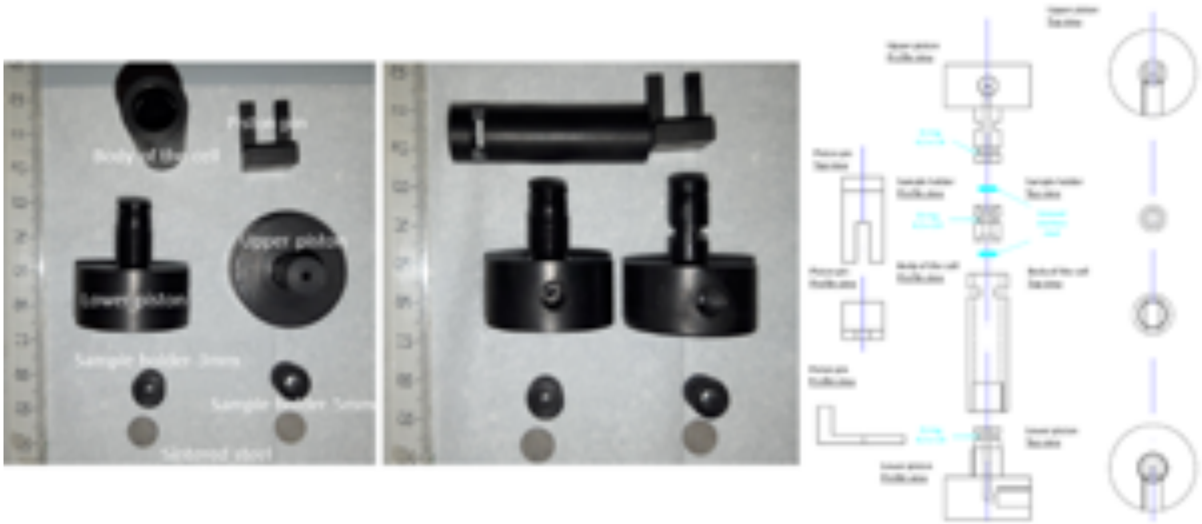

Figure 10-2. Close-up photographs of a micro-oedometer cell displaying the components and highlighting the fluid ports for equilibration of the clay with aqueous solutions. Assembly of the cell yields an internal cylindrical volume into which the clay is packed to obtain the desired dry bulk density.

10.2.1 Micro-Oedometer Cell Design

Custom micro-oedometer cells were developed for simultaneous measurement of basal spacings and overall microstructure by small-, mid-, and wide-angle X-ray scattering (SAXS/MAXS/WAXS) performed on beamline 5-ID at the APS (described in the following section). These oedometer cells were designed to allow for aqueous solution to flow across the top and bottom of the clay sample, facilitating water and ion exchange. The micro-oedometer cells shown in Figure 10-2 consist of three primary components: upper and lower pistons and the cylindrical cell body. A pin is machined to align with a notch in the cell body to constrain the volume of the cell when it is removed from the oedometer, allowing for intermittent measurements. The top and bottom cell pistons were machined to allow for internal flow in a T-configuration, with influent and effluent ports in both pistons. This allows for flow of aqueous solution across the permeable steel frit that holds the clay in place, removing stagnant fluid and facilitating equilibration of the clay with the aqueous solution. Six identical cells were machined on-site at LBNL in January 2020, so many experiments can now be setup and equilibrated simultaneously.

For each cell, three internal geometries are possible. All three geometries have approximately identical internal heights (9 mm) but inserts provide variable diameter configurations (3 mm, 5 mm, and 9 mm; Figure 10-2). All cells are constructed with relatively X-ray transparent PEEK material (TECAPEEK CF30, Ensinger Plastics), which is more transparent to X-rays than hydrated clay. The different diameters were made to optimize for different critical measurements: The 3 mm cell is best suited to in-situ X-ray scattering measurements, while the largest 9 mm cell gives the most sensitive measurement of swelling pressure. Thus, every set of swelling experiments conducted in the 3 mm cell at the APS will be reproduced in the 9 mm cell on the benchtop at LBNL.

10.2.2 Oedometer Swelling Pressure Measurements

Our collaborators at the French Geologic Survey (BRGM) were contracted to construct a custom oedoemeter apparatus of sufficiently small size to transport and install on the X-ray synchrotron beamline at the APS. The oedometer (Figure 10-3) measures force and displacement on the oedometer cell piston with two digital displays tied into a datalogging Excel macro for continuous time-resolved swelling pressure measurements. The minimum force on the piston measurable by the apparatus is 10–20 N, which equates to a minimum accessible swelling pressure measurement of 160 kPa in the 9 mm cell and 1,400 kPa on the 3 mm cell. These sensitivity values equate to a minimum bulk density of ~1,200 kg/m^3 for the 3 mm cell and ~800 kg/m^3 for the 9 mm cell for swelling pressure measurement of Na-MMT (Na-montmorillonite) in contact with pure water. These calculations illustrate the tradeoff between X-ray sensitivity and the ability to obtain swelling pressure measurements.

To prepare a sample, the bottom piston is fitted to the body of the cell, and a steel frit and filter paper are inserted into the cell to contain the clay. If smaller internal diameter cell configurations are desired, the appropriate insert is added at this time. Dried clay is precisely weighed to obtain the appropriate bulk density and then carefully packed into the cell. During packing we attempted to ensure an even density of clay throughout the column, although the manual nature of the packing means some variability will occur. A second filter paper and steel frit were placed on top of the clay, and then the top piston was inserted. Once the cell was assembled, the pin was put in place, and the cell was placed in the oedometer. The clay pack was then evacuated, and fluid of a known composition was introduced to the bottom (and optionally top) pistons. Fluid was allowed to flow continuously to ensure constant composition boundary conditions in the cell. Once flow was established, the pin was removed, and pressure logging began.

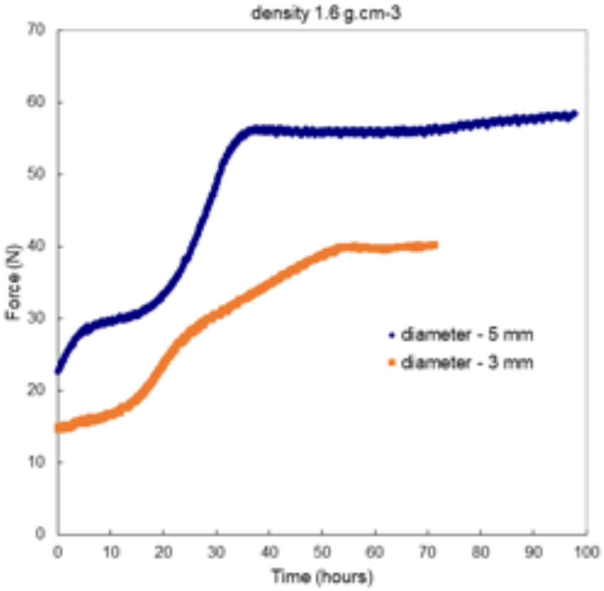

Figure 10-3. Force curves for montmorillonite swelling experiments in contact with pure water in the micro-oedometer (BRGM, *pers. comm.*).

10.2.3 Preliminary Swelling Pressure Results

Time resolved measurements of swelling pressure in montmorillonite clay displays interesting and unexpected behavior (Figure 10-3). Starting with an initially dry clay packed in the oedometer, early wetting by pure water led to a rapid increase in force. The force rise subsided at intermediate times, followed by a second pressurizing event. Final equilibration was achieved after ~30 and ~55 hours on the 5 mm and 3 mm cells, respectively. Final swelling pressures for these two experiments equal to 3.0 MPa for the 5 mm cell and 5.6 MPa for the 3 mm cell. The time required to obtain an equilibrium swelling pressure was variable and dependent on the initial dry bulk density and the cell geometry. Variation in equilibration times were also observed for identically packed clays, indicating a dependence on the heterogeneity and density of the clay pack: clays packed more densely and with more force were slower to achieve the equilibrium swelling pressure.

One successful measurement of a swelling curve was obtained at LBNL prior to the lab-wide shut down in March 2020. This measurement was made on raw, untreated SWy-3 equilibrated with the pure MiliQ water packed to a dry bulk density of approximately 1.9 g/cm^3 in the 3 mm sample holder. The final force of 32.4 N corresponds to a swelling pressure of 4.6 MPa, which places the clay on a relatively low-pressure swelling curve compared to comparable Na-montmorillonite clays (Liu et al., 2013).

10.2.4 Planned Oedometer Measurements for Remainder of FY 2020

When on-site work is permitted to resume at LBNL, we have planned a systematic series of swelling experiments to prepare for anticipated beamtime at the APS. Briefly, we will generate a swelling curve by measuring equilibrium swelling pressure as a function of dry bulk density for the Na-treated SWy-3 montmorillonite clay in contact with pure MiliQ water in both the 3 mm and 9 mm sample holders. We will generate swelling pressure data for equilibration of the clay with aqueous solutions at a total 1 M concentration [KCl] + [NaCl] with variable K/Na ratios to generate swelling pressure data concurrent with the X-Ray scattering experiments reported in Whittaker et al. (2019). Finally, in FY20 we plan to perform a series of mixed-electrolyte swelling pressure measurements for NaCl + $CaCl_2$ mixtures more closely resembling fluids in contact with EBS bentonite barriers.

10.3 In-situ Microstructure by X-ray Scattering at the Advanced Photon Source, Argonne, IL

The microstructure of clay, in particular the distribution of pore sizes and basal spacings, dictates the macroscopic transport properties of clay materials. We applied X-ray scattering to investigate the crystalline hydrate layer state distribution as a function of aqueous solution chemistry, using the micro-oedometer cell described in the previous section. X-ray scattering was performed at beamline 5ID-D of the APS at Argonne National Laboratory. Simultaneous SAXS, MAXS, and WAXS were collected on three Rayonix charge-coupled device detectors with sample-detector distances of 8505.0, 1012.1, and 199.5 mm, respectively. The wavelength of radiation was set to 1.2398 Å (10 keV), resulting in a continuous range of scattering vector, $q = 0.0017–4.2$ Å^{-1}, corresponding to real space distances between 370-1.5 nm.

Reflections from (020) and (110) planes of montmorillonite layers in the WAXS region ($q = 1–4.5$ Å^{-1}) confirmed the presence of montmorillonite and was used as an internal calibration standard. Constant (020) + (110) peak intensities throughout the experiment confirm that the volume and average orientation distribution of the layers did not change during the course of the experiment.

In the SAXS region ($q < 0.1$ Å^{-1}) a Porod slope of ~3 was the dominant feature. Fitting in the SAXS region was performed using a modified Guinier-Porod model (Moore et al., 1997) for thin platelets where the scattering intensity I at scattering vector $q = 4\pi sin(\theta)/\lambda$), takes the form

$$I(q << 1) = Ae^{-\frac{R_g^2}{3}} q^{-p} \qquad \textit{Equation 10-1}$$

where A is a pre-exponential intensity factor for the particle radius of gyration R_g and P is the Porod slope. The radius of gyration, R_g, defined as $R_g^2=3/2R^2$, was fixed at 560 Å based on the average particle radius calculated from AFM measurements of the particle size distribution. A Porod slope of $P = -2.85$ for Na-MMT and -2.93 for K-MMT low q is characteristic of lamellar structures separated by interlayer water, with K-MMT slightly denser, as expected for a smaller basal spacing.

The MAXS region ($1.5 > q > 0.1$ Å^{-1}) was characterized by the presence of a strong diffraction peak at $q_{001} = 0.331$ Å^{-1} (19.0 Å) for Na-MMT and $q_{001} = 0.398$ Å^{-1} (15.9 Å) for K-MMT, characteristic of 3- or

2-water layer crystalline hydrates, respectively. Non-negligible peak asymmetry to the low-q side of the basal spacing peak has been frequently observed (Segad et al., 2012; Tester et al., 2016), but has been attributed primarily to Scherrer-type broadening. We use a recently described empirical peak profile function to fit the basal spacing peaks and higher order reflections. This function was necessary to fit the very broad tails of the peak profiles of both K- and Na-MMT and low-q asymmetry due to defective stacking motifs measured in cryo-TEM. The diffraction intensity, I, in the vicinity of a diffraction peak at q_d is given by

$$I(q) = C\left[1 + \frac{(q-\mu)^2}{\sigma\left(\frac{2\gamma}{1+e^{\alpha(q+\mu)}}\right)^2}\right]^{-\sigma} \qquad \textit{Equation 10-2}$$

were μ is the peak position, σ determines the extent of the tails, γ is a shape parameter, α defines the degree of asymmetry, and C is a constant proportional to the total intensity. This function yields higher-quality fits than Gaussian, Lorentzian, Pseudo-Voigt, Skewed-Gaussian, or combinations thereof.

Ion exchange between Na-MMT in 1 M NaCl and 1 M KCl were performed by flowing KCl solution over both the inlet of the oedometer cell. X-ray scattering patterns were collected at regular time intervals over the course of approximately 7 hours while simultaneously recording the swelling pressure. Profiles of the clay plug at intervals of 0.5 mm (approximately the height of the beam) were recorded at each timepoint to track the position of the exchange front.

Structural changes were observed over multiple length scales as a result of K^+ exchange for Na^+ (Figure 10-4). Clay mesostructure at the largest length scales remained relatively unimpacted by ion exchange (Figure 10-4a). Only subtle changes in the Porod slope ($q < 0.25$ Å^{-1}, >2 nm) that corresponded to densification upon the expulsion of interlayer water were observed. Importantly, this indicates that there is no appreciable change in mesoscale porosity (i.e., osmotic hydrates) during ion exchange at the high clay volume fractions employed in this study. Changes in porosity were confined to the nanoscale, with the collapse of the basal spacing from three water layers ($q = 0.33$ Å^{-1}, 1.9 nm) to two ($q = 0.39$ Å^{-1}, 1.6 nm). Collapse was also accompanied by a restructuring of the interlayer cations, which manifest as changes in scattering intensity at smaller scales ($q > 0.5$ Å^{-1}). The three-water-layer state in Na-MMT exhibited a second order harmonic peak at $2q = 0.66$ Å^{-1}, which is indicative of bilateral symmetry. This confirms that the interlayer cations predominantly reside in a symmetric configuration about the interlayer midplane. However, the $2q$ harmonic peak for the two-water-layer state, which would be expected to occur at 0.78 Å^{-1}, is absent. This indicates that the cations in this state are in an asymmetric configuration relative to the interlayer midplane.

Using the change Porod slope, collapse of the basal spacing peak, and reconfiguration of interlayer cations as indications of the exchange front, the evolution of ion exchange was tracked along the 10 mm height of the clay plug over the course of 7 hours. Two important conclusions can be drawn from these experiments: (1) exchange of K^+ for Na^+ is slow on the experimental timescale, and (2) the exchange front is sharp. The exchange front traveled less than 0.5 mm in 7 hours (Figure 10-4b). Predominantly two-water layer hydrate coexisted with a small fraction of three-water-layer hydrate within the first 0.5 mm. Between 0.5 mm and 1 mm there was only a minor fraction of two-water-layer hydrate, and the rest of the clay plug remained unchanged.

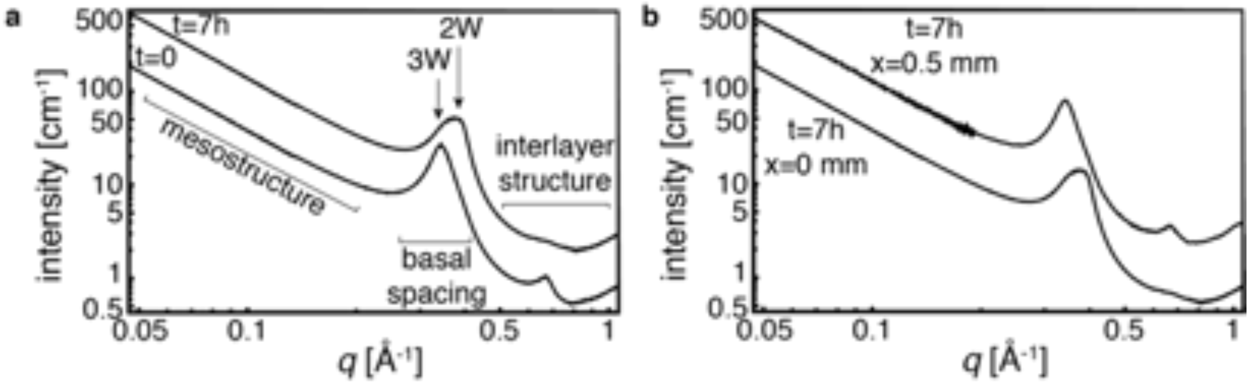

Figure 10-4. Ion exchange between Na-MMT and 1 M KCl tracked via X-ray scattering. Patterns collected at *t* = 0 and *t* = 7 hours following the start of aqueous KCl flow. Curves are offset for clarity.

10.4 Molecular Simulations of Ion Exchange and Swelling Thermodynamics for cis-vacant Montmorillonite

10.4.1 Problem Statement

Decades of study has shown that crystalline swelling states in montmorillonite often coexist, and their relative proportions vary as a function of water activity (Bérend, 1995; Ferrage, 2005; Holmboe et al., 2012). A mixture of coexisting swelling states was generally thought to yield an 'interstratified' structure with multiple distinct basal spacings (swelling states) within a montmorillonite particle. However, recent cryo-TEM and X-ray scattering data indicate the presence of coexisting but physically separated montmorillonite particles with proportions of the discrete swelling states that depend on the NaCl/KCl electrolyte composition (Whittaker et al., 2019). A clear understanding of swelling state distribution and its effect on the structure of montmorillonite at the aggregate scale is critical to predict swelling pressure and transport properties as a function of solution composition and confinement.

To investigate the energetics of swelling and layer state mixtures, we performed molecular dynamics (MD) simulations of montmorillonite hydrates in homoionic bulk solution. Classical molecular simulations serve as powerful tools to investigate the structure and energetics of equilibrium hydration states and the microstructures arising from phase coexistence of montmorillonite. Several atomistic models have simulated the diffusion (Holmboe and Bourg, 2013), kinetics (Tournassat et al., 2016) and free energies of cation exchange (Rotenberg 2009; Teppen 2006; Lammers et al., 2017), and swelling thermodynamics (Hsiao and Hedström, 2017; Svoboda et al., 2018; Whitley and Smith, 2004) in various clay minerals. However, a quantitative evaluation of phase coexistence through the explicit modeling of mixed phases is missing in literature. Here, we employed the recently developed molecular structure for cis-vacant montmorillonite (Subramanian et al., 2020) to investigate the energetic underpinnings of phase transition and coexistence in homoionic electrolytes. In particular, these simulations allow us to calculate the free energies of transition between swelling states and the excess free energies of mixing of mixed swelling states, in order to relax the assumption of ideal mixing.

10.4.2 Swelling Energetics

A phase transition corresponds to the adsorption or desorption of water molecules in the montmorillonite interlayer to switch between swelling states. The calculation of free energy difference between stable hydrates yields the swelling free energy at a given solution composition. Significant focus has been dedicated to the estimation of swelling free energies using molecular modeling (Whitley and Smith, 2004;

Smith et al., 2006, Honorio et al., 2017; Svoboda et al., 2018; Underwood and Bourg, 2020). These studies have calculated the swelling free energy for trans-vacant montmorillonite, which has a centrosymmetric molecular structure. Available experimental data unambiguously show that Wyoming montmorillonite has a cis-vacant structure. Our recent study of water adsorption on cis-vacant montmorillonite revealed that interlayer water is more structured and 'ice-like' due to a stronger hydrogen bonding network at the mineral/water interface. We believe that this could have an impact on the energetics of swelling/collapse mechanisms under various conditions (electrolyte type and concentration, pressure, temperature, etc.). Therefore, we computed the PMF between two montmorillonite layers as a function of their basal spacing.

Each clay layer in our model contains 175 units cells of cis-vacant montmorillonite, where structural hydroxyls occupy adjacent positions relative to the octahedral vacancy sites. The edges of clay layers perpendicular to the *x*-*z* plane were made unreactive with OH, OH_2 terminations that result in neutral edge charge. Isomorphic substitutions of Mg^{2+} for octahedral Al^{3+} were also randomly introduced to yield a structural charge of $-0.57e$ per $O_{20}(OH)_4$ of clay. It must be noted that in cis-vacant montmorillonite we did not impose a constraint preventing two adjacent Mg^{2+} substitutions. The two clay layers (9.35 × 9.05 nm) were immersed in bulk solution of 1M NaCl as shown in Figure 10-5. Although the electrolyte concentration is relatively high compared to solutions in the EBS context, it was chosen to be close in concentration to the phase transition boundary between the 2- and 3-water layer hydrates of Na-MMT. Interatomic interaction terms that represent the van der Waals and electrostatic forces are obtained from ClayFF (Cygan et al., 2004) for the mineral atoms and ions, and water interaction parameters use the SPC/E (extended simple point charge) model (Berendsen et al., 1981). The pairwise Lennard Jones energy is calculated using the Lennard-Jones potential given by

$$E_{pair,ij} = 4\varepsilon_{ij}\left[\left(\frac{\sigma_{ij}}{r_{ij}}\right)^{12} - \left(\frac{\sigma_{ij}}{r_{ij}}\right)^{6}\right] \qquad \textit{Equation 10-3}$$

where r is the distance between two particles, and ε and σ are the maximum depth of the potential energy well and the distance of zero potential, respectively. The pairwise interaction terms between dissimilar atoms are calculated via Lorentz-Berthelot mixing rules – $\varepsilon_{ij} = \sqrt{\varepsilon_{ii}\varepsilon_{jj}}\ and\ \sigma_{ij} = (\sigma_{ii} + \sigma_{jj})/2$. Coulombic interactions are calculated using $E_{coul,ij} = \frac{q_i q_j}{4\epsilon_0 r_{ij}}$ where q is the partial charge and ϵ_0 is the permittivity in vacuum. A cutoff distance of 15 Å is used to calculate short-range interactions and the Particle-Mesh Ewald's summation method with an accuracy of 99.99% is used to compute long range electrostatics. The system was equilibrated in the NPT ensemble (i.e., constant number, pressure, and temperature—in this case $T = 298$ K) for 1 ns, following which, a steered molecular dynamics (SMD) simulation was performed over 3 ns in the NPT ($P = 1$ atm, $T = 298$ K) ensemble. During the equilibration, the clay layers were held tethered to their initial positions. This is because the initial state of the simulation corresponds to an unstable dry state (0.25 H_2O molecules per unit cell of clay) and the electrostatic repulsive forces between the layers cause the layers to deform.

In the SMD run, the bottom montmorillonite layer was tethered while the top montmorillonite layer was translated along the *z*-direction with a constant velocity of 2 Å/ns by a harmonic stiff spring (Park and Schulten, 2004). The layers were allowed to be flexible during the translation. We then segmented the entire SMD run into trajectory windows of 1 Å change in basal spacing and used the initial step of each window as input to perform umbrella sampling. The umbrella sampling, which was implemented using the Collective Variables (COLVARS) library in LAMMPS (an acronym for Large-scale Atomic/Molecular Massively Parallel Simulator) (Fiorin et al., 2013), spanned 40 stages per window, and each stage sampled the distance between the layers and the harmonic potential of the spring for a translation of 0.025 Å. The small size of umbrella windows ensured that there was sufficient sampling of the entire reaction coordinate (here, the reaction coordinate is the basal spacing) and overlap among the umbrella windows. Since the umbrella sampling approach imposes a biasing potential (here, the biasing potential is the harmonic potential of the stiff spring), we need an unbiasing algorithm to compute the PMF. We used the Weighted Histogram Analysis Method (WHAM) code (Grossfield) to extract the PMF profile from the umbrella sampling results. Ho et al. (2019) showed that the ClayFF parameter set does not predict the dry to one-water layer (0W–1W) hydration process well. The authors of the study modified ClayFF to capture the dry to hydrated state transition. Since we used the traditional ClayFF parameters and because we are interested in the swelling states applicable to engineered barriers, our focus is restricted to the 2W to 3W transition.

We observed the 2W and 3W minima at basal spacings of 16.11Å and 18.89Å, respectively, from the PMF profile in Figure 4.6. It appears that the global minimum for the chosen electrolyte concentration corresponds to a 2W hydrate. Contrary to our experimental data, which suggest that Na-MMT occurred as a stable 3W hydrate in dilute suspensions and 1M NaCl, the simulations showed that the most energetically favorable hydrate at this concentration was a 2W state. Additional simulations will be performed to identify the transition concentration where 2W clay becomes favorable. The water activity and the clay dry bulk density play a critical role in determining the stable montmorillonite hydrate for a given solution. For clay layers in suspension, the water activity in solution was ~0.98; therefore, it was surprising that the 2W was clearly favored over the 3W state. This discrepancy might have been an artifact of the selected force-field potential model; however, there is plenty of evidence in literature for Na-MMT commonly occurring in the 2W state. Svoboda et al. (2018) computed the PMF profiles for Na-MMT suspended in pure water and 2.8 M salt solution, and concluded that the 3W state has the lowest free energy in pure water, whereas a lower hydration state (2W) was favored in the salt solution. XRD studies (Cases et al., 1992; Morodome and Kawamura, 2009) showed that the 3W hydrate occurs in significant proportions only at relative humidity (RH) of 0.93 or above. A model developed based on fitting XRD data (Holmboe et al., 2012) also validated this finding, and the fraction of 3W was small even at RH values higher than 0.96. Whitley and Smith (2004) found that at room temperature with RH = 1, Na-MMT may exist as 2W, 3W, or even osmotic hydrates depending on preparation and clay dry density.

Further investigations are needed with pure water (0M NaCl) and higher electrolyte concentrations (perhaps 2M NaCl) to understand how the global minimum shifts as a function of ionic strength. From the PMF profile, we calculated the swelling free energy (2W–3W) to be ~7 kJ/mol, which is consistent with reported literature (1–3kT). In comparison to reported values of swelling free energy for trans-vacant clay layers, we find that the swelling free energy for our cis-vacant structure is slightly higher.

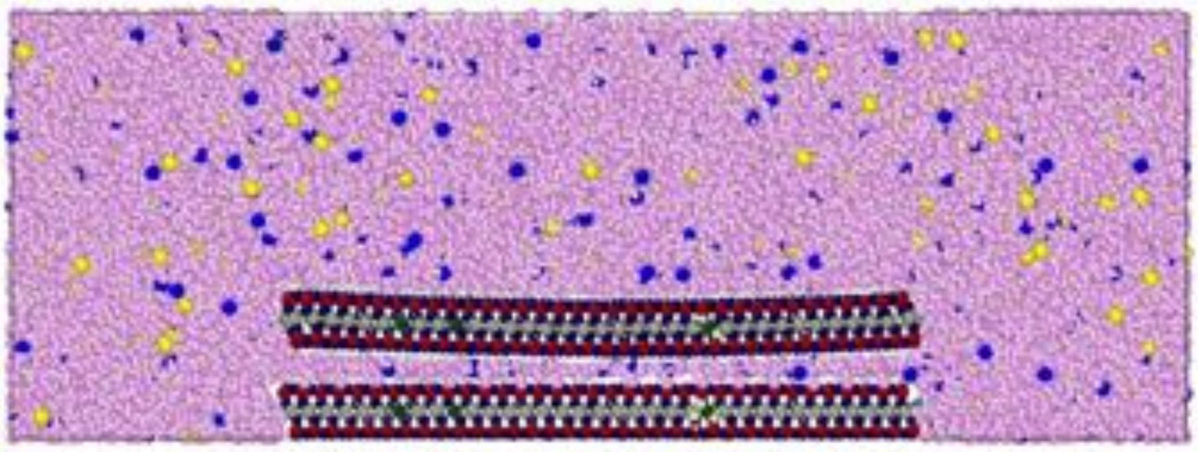

Figure 10-5. Montmorillonite layers immersed in bulk solution of 1M NaCl. Al atoms in the octahedral sheet are in gray, Mg substitutions in dark green, Si atoms in the tetrahedral sheet are in dark red, clay oxygen atoms in dark blue, terminal edge oxygen atoms in violet, water oxygen atoms are in pink, water and clay hydrogen in white, sodium ions in blue, and chloride ions are in yellow.

10.4.3 Layer State Mixing Energetics

We explicitly modeled interstratified mixed layer states to probe the energy penalties (if any) for the mixing of swelling states. The molecular models consist of four layers of montmorillonite suspended in a bulk electrolyte solution of 1 M NaCl. The simulation volume was designed to be large enough to facilitate diffusion and exchange of interlayer water and ions with the bulk solution. The clay layers were placed at the center of a box (16.5 nm × 9.05 nm × *Z*), where *Z* was determined by the equilibrium basal spacing of the layer states. Periodic boundary conditions were imposed to the volume along all three dimensions, thus rendering the clay tactoid infinite in the *y* and *z* dimensions and finite along the *x* direction. The large *x* dimension of the box also ensured that we were able to extract bulk solution properties away from the clay mineral edges and that the particles do not interact across periodic boundaries. With 2W and 3W states as pure end-members, we generated mixed layer states by changing the proportions of these states in the tactoid. Figure 10-6 shows an interstratified clay particle with equal proportions of 2W and 3W phases. The starting point of the current model was the near-optimal values of hydration stoichiometry (~5 and ~4.8 H_2O molecules per $O_{20}(OH)_4$ per water layer for 2W and 3W, respectively) and equilibrium basal spacings (16 Å and 18.9 Å, respectively) we determined for 2W and 3W cis-vacant Na-MMT from previous Grand Canonical Monte Carlo (GCMC) and μVT simulations (Subramanian et al., 2020), which were also validated by the results of the PMF profiles and corresponding swelling thermodynamics.

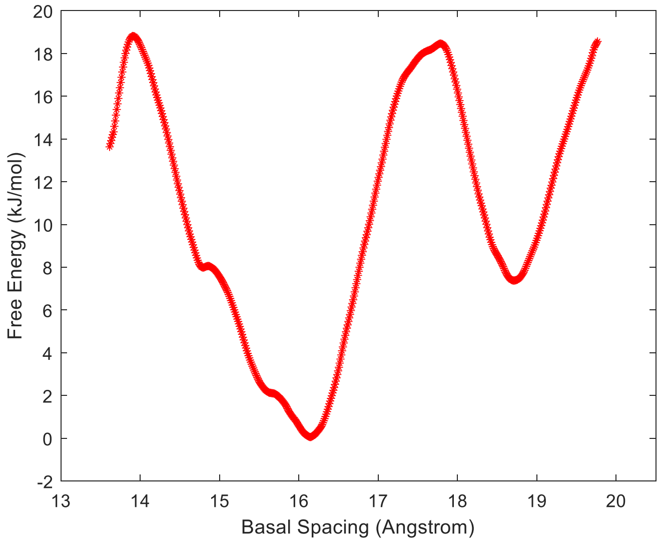

Figure 10-6. Potential of mean force profile of Na-MMT swelling free energy in 1M NaCl.

The structures were equilibrated for 1 ns in the NVT ensemble (i.e., constant number, volume, and temperature—in this case $T = 298$ K) and 5 ns in the NPT (P = 1 atm, T = 298 K) with a Nose-Hoover thermostat and barostat. The equations of motion for the particles were solved using the Verlet algorithm with a 1 fs timestep. Production simulations were carried out in the same isothermal-isobaric ensemble for 3 ns over the course of which data was sampled.

The atoms of the clay particle, with the exception of the hydroxyls (including those in edge terminations), were held rigid during the equilibration. The pure end-member components equilibrated well under these conditions and resulted in uniform basal spacings. Based on the newly obtained basal spacings for 2W and 3W states in equilibrium with 1M NaCl solution, the mixed layer states were tethered in the *z* direction with a spring force of 5 eV/Å^2. We observed that without the tethering, the mixed states yielded non-uniform basal spacings (with 2W and 3W in the same interlayer) indicating that the interstratified configuration was energetically unfavorable.

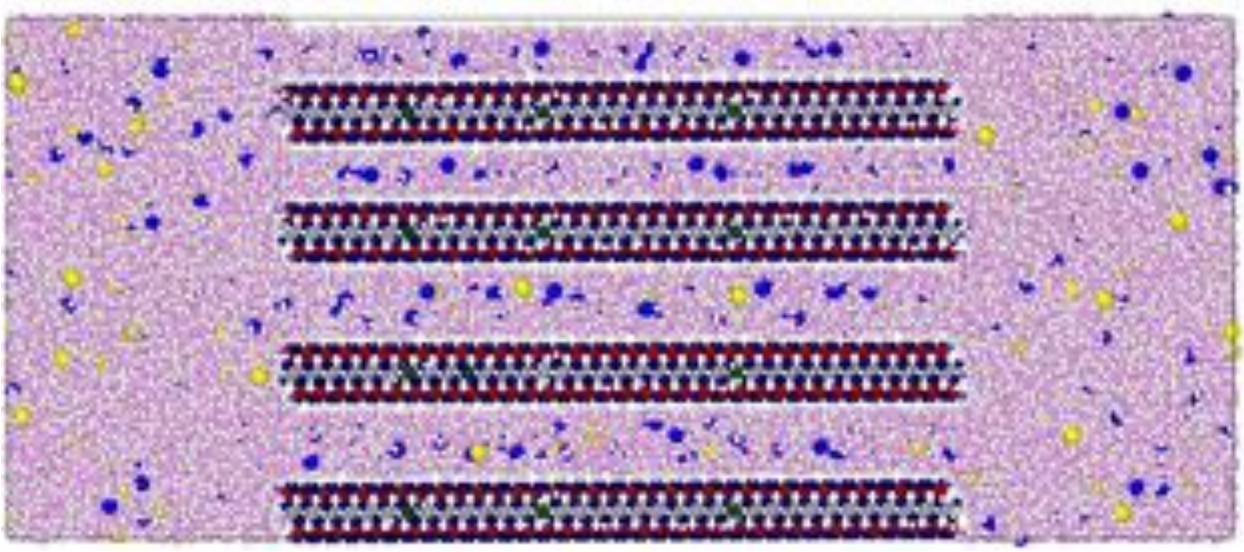

Figure 10-7. Simulation volume containing an interstratified clay particle with 50% 3W and 50% 2W fractions in 1M NaCl solution.

An analysis of the resulting average basal spacing in each mixed layer state (Table 10-1) shows that there are minor deviations from the equilibrium d_{001} values despite the applied spring force. The observed strains become generally larger as the relative proportion of the phase decreases in the mixture (16.01 Å for the 2W phase in 25%–75% mixture is the exception). Simulations of mixed layer states that did not impose a spring force (untethered configuration) confirmed that 2W interlayers displayed a tendency to expand whereas the 3W interlayers tended to collapse (see Figure 10-8). The applied spring force adds to the total enthalpy of the tethered system, but helps retain the solid solution in a physically meaningful configuration with uniform basal spacings.

Table 10-1. Calculated basal spacings of hydrates from simulations

Configuration	Bulk NaCl concentration (mol/dm^3)	d_{001} $(MMT2, MMT3)$ (Å)
100% MMT2	0.99	$(15.91 \pm 0.095, N/A)$
75% MMT2 – 25% MMT3	0.98	$(15.84 \pm 0.002, 18.27 \pm 0.005)$
50% MMT2 – 50% MMT3	1.01	$(15.37 \pm 0.001, 18.67 \pm 0.001)$
25% MMT2 – 75% MMT3	1.00	$(16.01 \pm 0.005; 18.83 \pm 0.009)$
100% MMT3	0.97	$(N/A, 18.94 \pm 0.03)$

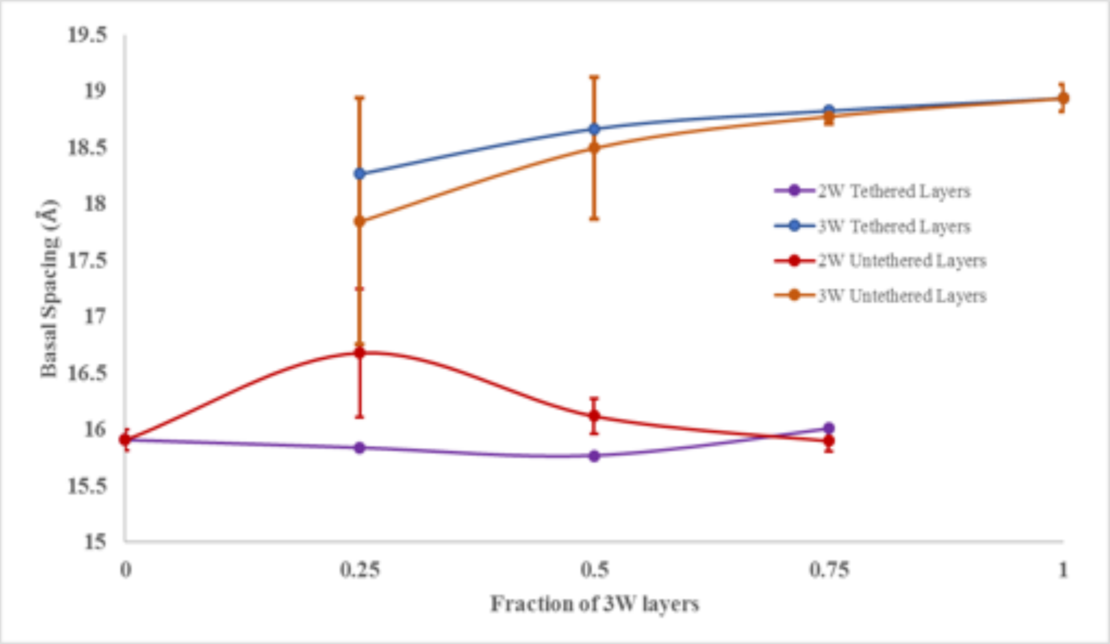

Figure 10-8. Average basal spacings in pure and mixed layer states with tethered and untethered (rigid) configurations. Fluctuations of layers in unstable states lead to large error bars in some cases.

We then calculated the enthalpies of formation of the pure and mixed layer states. The total internal energy output of the system (U_{total}) can be broken down into contributions from the clay hydrate and the bulk solution. Since the concentration of bulk solution (and therefore, water activity) was kept constant in simulations, we expect the internal energy per mole of solution ($\underline{U}_{soln}$) to be constant. This was verified by energy output from the bulk region of the simulation volume normalized by the number of moles of solution (n_{soln}) as shown in Table 10-2. Based on Equation 10-1, we calculated the total internal energy from the clay hydrate ($n_{clay}\underline{U}_{clay}$) in each of the pure and mixed layer states from the equation given by

$$U_{total} = n_{clay}\underline{U}_{clay} + n_{soln}\underline{U}_{soln} \qquad \text{Equation 10-4}$$

Table 10-2. Solution concentration and total internal energy per mole of solution calculated after equilibration

Configuration	Bulk NaCl concentration (mol/dm^3)	$\underline{U}_{soln}(\frac{kJ}{mol})$
100% MMT2	0.99	-48.13
75% MMT2 – 25% MMT3	0.98	-47.67
50% MMT2 – 50% MMT3	1.01	-47.91
25% MMT2 – 75% MMT3	1.00	-47.69
100% MMT3	0.97	-47.17

Including the pressure-volume work done on the mixed layer hydrate to the total internal energy yields the mixing enthalpies (expressed in per molar quantities). Although the magnitude of bulk pressure ($P_{z,bulk}$) is significant, the change in basal spacing from the corresponding equilibrium values is small. Thus, the contribution of the pressure-volume work term to the enthalpy of mixing is small, and was calculated from equations given by

$$\Delta \underline{H}_{mix} = \Delta \underline{U}_{mix} + \underline{PdV}_{mix} \qquad \textit{Equation 10-5}$$

$$\Delta \underline{H}_{mix} = \left[\underline{U}_{mixed,clay} - (x_{2W}\underline{U}_{clay,2W} + (1 - x_{2W})\underline{U}_{clay,3W})\right] + \frac{1}{n_{clay}}\left[(P_{z,bulk)} \times l_x l_y \times \Delta d_{001}\right] \qquad \textit{Equation 10-6}$$

The computed enthalpies of mixing from the molecular simulations indicate non-ideal mixing between the 2W and 3W phases, with the excess free energy of mixing being symmetric, thus exhibiting near-perfect regular solid solution behavior (see Figure 10-9). In the regular solution model, we calculated the excess free energies of mixing with ideal entropic components for each mixed layer state as described by the following equations:

$$\Delta \underline{G}_{mix} = \Delta \underline{H}_{mix} - T\Delta \underline{S}_{mix} \qquad \textit{Equation 10-7}$$

$$\Delta \underline{S}_{mix,ideal} = -R(x_{2W} ln x_{2W} + (1 - x_{2W}) ln\,(1 - x_{2W})\,) \qquad \textit{Equation 10-8}$$

Here, we find that the excess free energy of mixing of the 2W and 3W states is significantly higher than the free energy difference between them (swelling free energy determined in the previous section). The proximity in the free energy between the 2W and 3W hydrates will likely allow these phases to switch among each other completely as opposed to existing in mixed layer states. These calculations provide a thermodynamic basis for the absence of montmorillonite layer state coexistence in NaCl solutions.

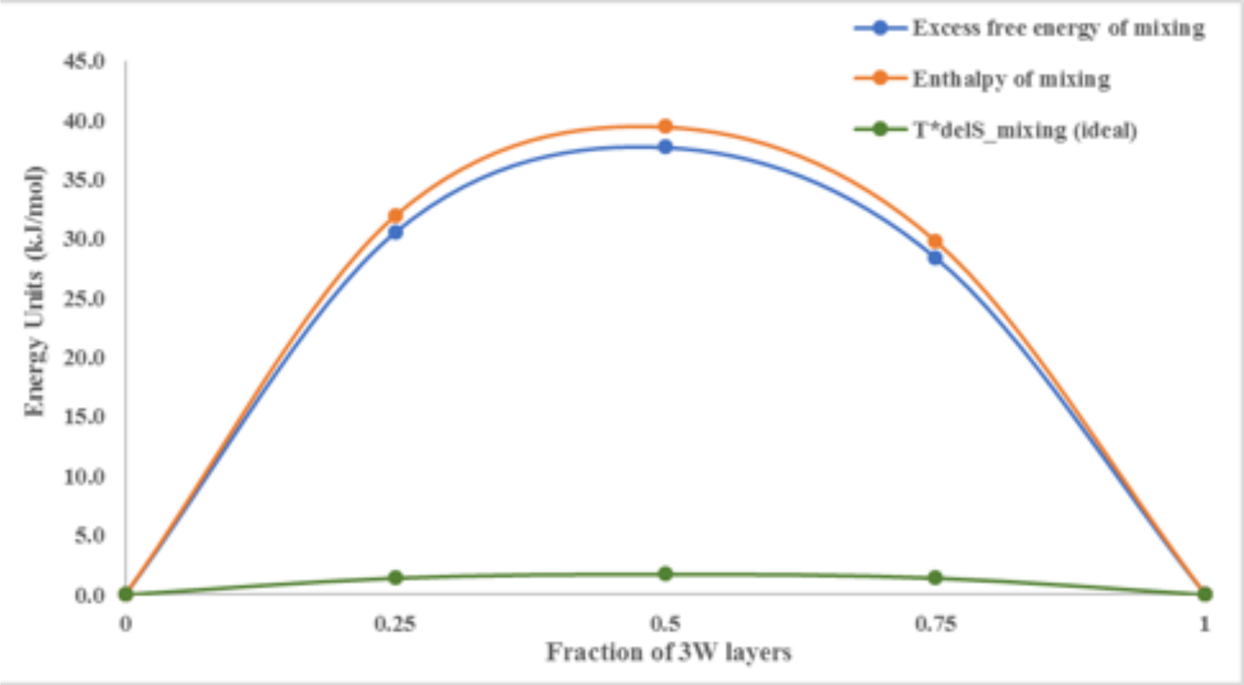

Figure 10-9. Excess free energy of mixing as a function of mole fractions of 3W hydrate in the solid solution

10.4.4 Ion Exchange Thermodynamics

Research has shown that swell/shrink reactions and ion exchange processes in smectites are tightly coupled. X-ray scattering data acquired recently (Whittaker et al., 2019) indicates a selectivity of the hydration states to ion adsorption. For example, during an exchange reaction of Na+ for K+, it was observed that the 3W particles were Na+ rich whereas the 2W montmorillonite particles were K+ rich. The exchange of Na+ for K+ was found to drive the collapse of 3W montmorillonite layers to 2W states. To better understand the coupling between hydration reactions and ion exchange reactions, we set up molecular simulations of layer states in a mixed electrolyte solution. These simulations will allow us to quantify the selectivity of layer states for ion adsorption.

Thermodynamic integration calculations were performed to calculate the free energies of ion exchange reactions between Na and K in the bulk aqueous solution. We start with one of the equilibrated end-member hydrate (2W) states in 1 M NaCl from the previous section. Then, 25% of Na ions in solution were randomly selected and progressively transformed into K ions by changing their pairwise interaction potentials in a series of 10 steps, using a coupling parameter $\lambda \in [0,1]$, with 0 representing Na, and 1 representing K, using equations given by:

$$\sigma(\lambda) = \sigma_{Na} + \lambda(\sigma_{Na} - \sigma_K) \qquad \textit{Equation 10-9}$$

$$\varepsilon(\lambda) = \varepsilon_{Na} + \lambda(\varepsilon_{Na} - \varepsilon_K) \qquad \textit{Equation 10-10}$$

At each step, an NPT equilibration for 3 ns follows the change in the Lennard Jones interaction parameters. The result at the end of the transformation yields a 2W hydrate in a mixed electrolyte solution containing 0.75M NaCl and 0.25M KCl. This series of progressive transformation steps will be carried out until we arrive at 2W hydrates with 0.5M, 0.75M, and 1M KCl (with decreasing NaCl concentration accordingly). The variation in the Hamiltonian of the system (the total energy of the system in our case) during the transformation as a function of the coupling parameter λ gives us the free energy for the exchange reaction. Along with the change in bulk electrolyte and the free energy associated with the exchange, we can also compute the selectivity of the 2W hydrate for ion adsorption as a function of aqueous composition.

10.5 Summary and Future Work

In FY20 we have conducted a comprehensive set of experiments and simulations, which provided deep insights into the thermodynamics of clay swelling in mixed electrolyte solutions. Experimental procedures are in place to generate a comprehensive swelling pressure data set in multicomponent electrolyte solutions as soon as laboratory work is resumed in FY20 and extended into FY21. The swelling pressure data will be compared against model expectations based on the thermodynamic approach described in Zheng et al. (2019a) and Whittaker et al. (2019), with subsequent model refinements based on experimental outcomes. Additional X-ray scattering beamtime will be sought toward the end of FY20 to obtain additional microstructural data constraints, including the evolution of montmorillonite microstructure, upon ion exchange in mixed electrolyte solutions including calcium. Additional simulations will be completed to determine swelling free energies for mixed electrolytes, but a different simulation technique is required to quantify interlayer ion exchange thermodynamics. These will be investigated further in FY21, using the thermodynamic integration technique described above.

11. MICROSCOPIC ORIGINS OF COUPLED TRANSPORT PROCESSES IN BENTONITE

11.1 Background and Proposal Goals

Thermal processes play a major role in controlling the fate of nuclear waste disposed in geological repositories through coupled effects on hydration, mechanical and chemical (THMC) properties of the barrier/backfill material. Heat conduction away from the nuclear waste cannister has a significant impact on the design, construction and operation of any disposal system, and the ability to predict the thermal properties of a barrier/backfill is of high importance to the safety case for any design concept. Reducing the peak temperature of the barrier/backfill near the cannister, and thermal gradients between the cannister and host rock, will significantly improve the ability to predict the outcomes of specific nuclear waste disposal designs. However, the thermal conductivity of bentonite is a strong function the hydration state, which changes considerably with temperature (Lee et al., 2016; Tang et al., 2007), especially under irradiation (Gu et al., 2001).

Initial work in this area focused on extending a model of the intermolecular forces that govern montmorillonite structures and energetics (in preparation) to high mineral volume fractions where the properties of bentonite are strongly influenced by the details of the interfacial hydration structure (Subramanian et al., 2020; Zarzycki and Gilbert, 2016) and the coupling between hydration and ion distributions at mineral interfaces are highly temperature dependent.

We propose to develop and validate a microscopic model of coupled transport processes in bentonite and to use this model to determine cost effective augmentation strategies to increase the bulk thermal conductivity of hydrated bentonite. Results of preliminary work through FY19–20 will serve as a foundation for a larger scale effort in FY20–21 to stably increase the thermal conductivity of bentonite above 2 W/(m·K) at temperatures relevant to modern nuclear waste storage design concepts.

11.2 Proposed Work

11.2.1 Model Development

Here, we outline the model that has been developed during FY19–20, which will serve as a foundation for an upscaled effort in FY20–21. This model incorporates a range of experimental results on the properties of water and ions in the confinement of clay interlayers that collectively point to persistent non-equilibrium behavior in hydrated bentonite at elevated temperatures. We will show that non-equilibrium dynamics are the result of tightly coupled mobility of ions and water in the confinement of clay interlayers and their ability to mechanically deform the layers, which results in fluctuations that generate, and conduct, heat. We aim to determine the exact microscopic origins of thermal fluctuations and investigate the effects of chemical or structural alterations designed to enhance the thermal conductivity of bentonite by amplifying these fluctuations.

Bentonite backfill can be considered to be a three-component composite material: mineral phases (predominantly montmorillonite), water, and electrolyte (Bourg and Ajo-Franklin, 2017). Thermal and ionic transport properties of montmorillonite depend on the relative contributions from the mineral layers, the interlayer cations, water and the coupling between them. Pyrophyllite and mica are structural analogs of montmorillonite that have thermal conductivities of 0.81 and 0.21 W/(m·K), respectively (Horai, 1971). Both minerals are highly electrically insulating and thermal transport is phonon-mediated. The lower conductivity of mica suggests that the presence of interlayer cations (i.e., K+) decreases the phonon mean free path, likely due to the low areal density of these cations relative to the tetrahedral and octahedral sheets. From this perspective, montmorillonite structural charge that is intermediate to pyrophyllite and mica would be expected to result in intermediate thermal conductivity. However, the thermal conductivity of fully dense, anhydrous montmorillonite exceeds that of pyrophyllite (1.0 W/(m·K)) and may increase by a factor of two when fully saturated (Lee et al., 2016; Tang et al., 2007). The thermal conductivity of bulk water is 0.6 W/(m·K), and therefore understanding the anomalous thermal conductivity of montmorillonite and its amplification when hydrated is imperative for improving the thermal properties of barrier materials.

Measurements of bentonite electrical conductivity reveal distinct mechanisms of diffusive ion transport at various temperatures and levels of hydration that elucidate the atomic-scale phenomena underlying thermal conduction in the absence of applied electric fields. The direct current (DC) electrical conductivity of anhydrous montmorillonite is extremely low ($\sim 10^{-13}\ \Omega^{-1}\text{cm}^{-1}$ at 80°C) and has a high activation energy of approximately 1 eV/ion for Na^+ ions (Balme et al., 2010; Kharroubi et al., 2012). Electrical conductivity of anhydrous montmorillonite increases with temperature with Arrhenius kinetics, suggesting that ionic mobility is limited by individual hopping events between charge sites (Belarbi et al., 1997). Each hop is highly unfavorable due to the high repulsive electrostatic potential from neighboring charges that originate over a relatively large region of the mineral.

Even small quantities of water increase the DC electrical conductivity of montmorillonite by 10 orders of magnitude ($\sim 10^{-3}\ \Omega^{-1}\text{cm}^{-1}$ at 20°C) (Balme et al., 2010), and activation energies decrease rapidly with water content. For example, the activation energy for diffusion of Na-MMT with two layers of interlayer water is approximately 0.25 eV. This dramatic increase in ionic mobility relative to dry montmorillonite is due to the effective screening of the long-range electrostatic potential by the relatively high dielectric permittivity of water $\varepsilon_{\text{water}}$. Bulk water has $\varepsilon_{\text{water}} = 80$, and therefore $\varepsilon_{\text{water}} \cong 10\varepsilon_{\text{MMT}}$. In the limit of full hydration, the length scale over which Coulombic interactions contribute appreciably to the forces felt by an ion is reduced by approximately a factor of 10. This reduction is anisotropic, occurring preferentially within the interlayer where water can penetrate. Therefore, water has a strong and chemistry dependent, but spatially anisotropic, effect on intermolecular interactions in bentonite.

In addition to decreasing the activation energy for diffusion, the presence of water also gives rise to super-Arrhenian temperature dependence of the ionic conductivity, which is indicative of nonequilibrium conditions. The bulk thermal conductivity of bentonite (Lee et al., 2016; Tang et al., 2007) has been shown to have a similar, non-Arrhenian, dependence on temperature. The activation energy for water diffusion in hydrated montmorillonite is 0.12-20 eV (Sánchez et al., 2008a; 2008b), lower than that of the ions, and displays Arrhenian temperature dependence above 0°C. Thus, ionic mobility is strongly influenced by the presence of water, but is decoupled from water diffusion and proceeds via a distinct mechanism. This suggests that the overall thermal conductivity of bentonite is largely controlled by the mobility of ions. However, ionic mobilities are highly dependent on the hydration state and strongly coupled to the structure of the charged mineral layers, and thus understanding the thermal conductivity of bentonite requires explicit elucidation of these microscopic couplings.

Below 0°C, water within clay interlayers becomes supercooled and exhibits super-Arrhenian temperature dependence approaching a glass transition at ~120 K (Sánchez et al., 2008). While these temperatures are not directly relevant to nuclear waste storage, this behavior is a well-studied example of non-equilibrium dynamics exhibited by the same system that are analogous in many ways to the behavior observed for interlayer cations at elevated temperatures. In both cases, super-Arrhenian diffusivities exhibit a 'glass-transition' temperature, below which dynamics are quenched and above which dynamics are activated, but starkly contrast the 'hopping' type ion diffusion that occurs in anhydrous clays, or for water above 0°C.

Glassy, supercooled water in between clay layers results from the geometrical inability to form a critical nucleus of crystalline ice. We propose that hydrated clay minerals are supercooled liquid crystals resulting from the geometrical inability of neighboring layers to find a local energy minimum that also satisfies global charge neutrality. Disordered structural charge on either side of an interlayer cannot be compensated by the same number of cations in each interlayer, on average (Figure 11-1). We hypothesize that the anomalous thermal conduction of hydrated bentonite arises from a transition between interactions dominated by long-range electrostatics observed in pyrophyllite, mica, and anhydrous bentonite to local, hydration-mediated interactions that reduce the local system energy but globally unfavorable configurations. We propose to apply an Ising model for the charge, hydration, and structural state of a mineral layer (Figure 11-1) (Chamberlin, 1999) based on supercooled liquids that describes how the structure of bentonite responds to different chemical, hydration, and thermal conditions.

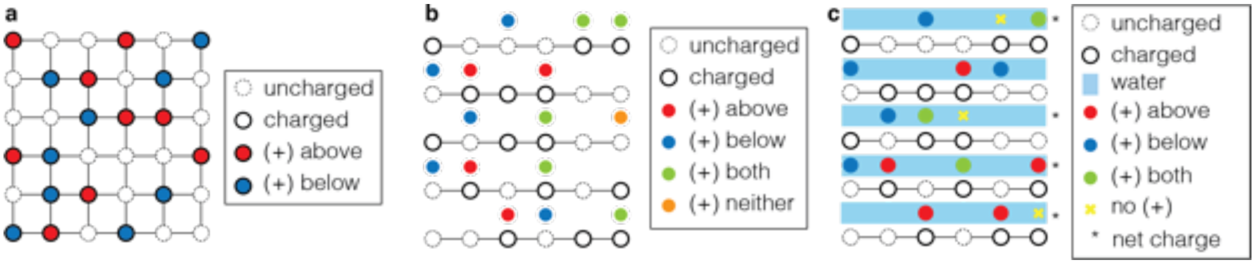

Figure 11-1. Using model for microscopic transport in clay minerals: (a) Face-on view of clay layer with x = 0.5 (solid circles). For a single layer, charge neutrality is maintained when half of the interlayer cations (red, blue) are located on each side of a layer. (b) Charges become dissociated from structural charge sites when anhydrous layers are stacked, but because electrostatic forces are long-range, the charge distribution finds a minimum energy state. (c) Interactions become highly anisotropic and local when water is introduced because it screens charge laterally, leading to net charge states within interlayers.

11.2.2 Model Validation

Microscopic model validation relies primarily on cryo-electron tomography (CET) to determine the 3D structure of hydrated bentonites (Whittaker et al., 2020) with near atomic resolution (Whittaker et al., 2019), and dielectric relaxation spectroscopy (DRS) to probe the behavior of water in the confinement of clay interlayers and at elevated temperatures. These techniques are complimentary because water is effectively transparent in CET, while it dominates the signal of DRS. We have recently shown that Na^+ and K^+ ions in montmorillonite tactoids reside in distinct sites within the interlayer, either partially dehydrated and directly bound to the clay mineral surface or fully hydrated and approximately 0.3 nm (approximate molecular diameter of water) away from the mineral surface. The relative proportions of these binding configurations are chemistry-specific and control the swelling state of the clay (Figure 11-2). Thus, we expect these distinct structures to exhibit vastly different DRS spectra that will reveal important information about the ability of water to modulate the interactions between ions and clay that control heat transport.

Bulk thermal conductivity measurements will be performed over a range of chemical, hydration, and temperature conditions using custom designed therm-oedometer cells. Cell concepts are based on the sorption and diffusion cells described in the Section 9 (Sorption and Diffusion Experiments on Bentonite) and the X-ray transparent oedometer pressure cells described in Section 10 (Chemical Controls on Montmorillonite Structure and Swelling Pressure). Therm-oedometer cells will be modified with a plane-source thermoelectric heating element and sheet temperature sensor at opposite ends of the bentonite plug for in-situ application of temperature gradients and measurements of thermal conductivity. These multifunctional cells will have the capacity to facilitate simultaneous chemical, uniaxial pressure, and thermal stimuli with real time measurements of swelling pressure, uniaxial temperature gradient, and X-ray scattering or tomography. Initial cell designs will be completed in the remainder of FY19–20 and early FY20–21, with fabrication and testing to following.

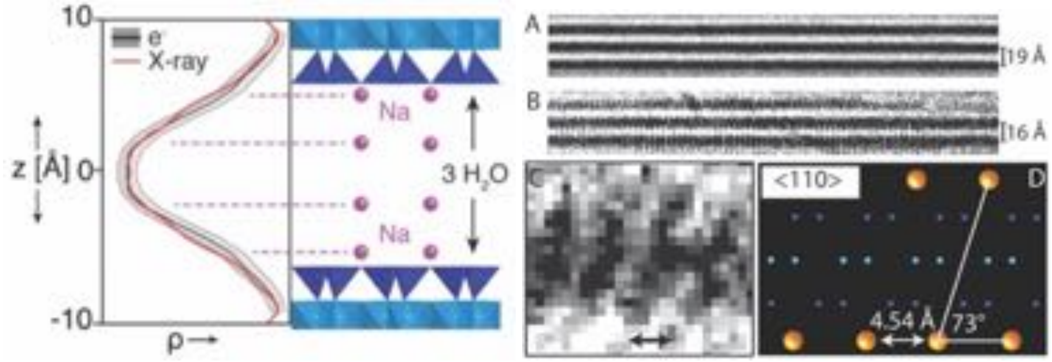

Source: Whittaker et al., 2019.

Figure 11-2. Ion binding sites in montmorillonite tactoids. (Left) Electron density (ρ) profile determined by X-ray scattering and cryo-transmission electron microscopy (cryo-TEM) of Na-MMT, showing two types of binding sites within a three-water-layer hydrate. (A) Na-MMT in 1 M NaCl, with 19 Å spacing corresponding to a three-water-layer hydrate. (B) K-MMT in 1 M KCl with 16 Å corresponding to two-water-layer hydrate. (C) Enlarged region of (B), showing atomic contrast adjacent to the mineral interface consistent with bound K ions. (D) Atomic model of cations in a clay layer, showing spacing and geometry reflected in (C).

11.3 Expected Outcomes

Our model predicts two important consequences for the thermal conductivity of bentonite. The first is that a local equilibrium is not possible without macroscopic rearrangement of mineral layers, and therefore microscopic gradients of ions and water are pervasive in bentonite unless or until the mineral is chemically altered to redistribute structural charge. The second is that a ‘turbostratic’ rearrangement of layers, as is observed in natural bentonites, may minimize the free energy of a given local arrangement, but that any structural fluctuations away from this arrangement will alter the energetic landscape and drive ion and water fluxes. These phenomena represent two important couplings between the chemistry and mechanical deformation of mineral layers in bentonite whose ultimate consequence is to create microscopic fluxes that generate entropy, and therefore, heat. We anticipate that this model can be used to quantify the specific interactions/fluctuations through which heat is transferred and make predictions about deliberate chemical or structural alteration that may augment heat conduction.

With further development in FY20-21, we expect to be able to identify and test bulk chemical modifications to bentonite that enhance the thermal conductivity beyond 2 W/(m·K). For example, fluorine functionalization of the montmorillonite octahedral sheet reduces hydrophilicity and may significantly alter the dielectric properties of confined water to more effectively screen interlayer charge and sustain dynamic fluctuations that drive thermal transport. Alternatively, mixing bentonite with aromatic hydrocarbons, such as chemical precursors to graphite, may facilitate the in-situ formation of thermally conductive carbon nanomaterials that enhance the thermal conductivity of bentonite.

12. UNDERSTANDING THE THMC EVOLUTION OF BENTONITE IN FEBEX-DP—COUPLED THMC MODELING

12.1 Introduction

The safety functions of EBS bentonite include limiting transport in the near field; damping the shear movement of the host rock; preventing the sinking of canisters (if emplaced in the center of the tunnel), limiting pressure on the canister and rock, and reducing microbial activity. To assess whether EBS bentonite can maintain these favorable features when undergoing heating from the waste package and hydration from the host rock, we need a thorough understanding of the thermal, hydrological, mechanical, and chemical evolution of bentonite under disposal conditions. Despite of numerous laboratory, field, and numerical studies, there is a lack of studies on coupled THMC processes. As part of SFWST program, a series of coupled THMC models have recently been developed for a design of a generic disposal system in clayey host rock with the EBS bentonite (Liu et al., 2013; Zheng et al., 2014; Zheng et al., 2015b; 2016; 2017;2018; 2019a). However, model validation was difficult due to the lack of THMC data from long-term, large-scale experiments. The FEBEX in-situ test (Huertas et al., 2000), which has been operated for 18 years, provides a unique opportunity of validating coupled THMC models.

The FEBEX-DP project is comprised of extensive THMC and biological characterization tests of bentonite, along with the development of numerical models. In the FEBEX in-situ test, two heaters surrounded by bentonite blocks about 0.7 m thick were emplaced in a tunnel excavated in granite. The heaters were switched on in 1997. Heaters #1 and #2 were dismantled in 2002 and 2015, respectively. LBNL/DOE joined the FEBEX-DP project in FY15. The ultimate goal is to use THMC data from FEBEX-DP project to validate THMC models, and, therefore, enhance our understanding of coupled THMC process. From 2015 to 2017, extensive THMC characterization of bentonite samples, collected during the dismantling of Heater #2, was carried by partners of FEBEX-DP. Ion concentrations in the pore-water of bentonite were obtained via an indirect method, aqueous extract, and these concentrations were used to initially constrain the chemical model. In FY18, the geochemical models were used to infer the “true” ion concentrations in pore-water from aqueous extract data for one of the sections, and the developed coupled THMC model reasonably explained all the THM data and the trend of the chloride concentration in the pore-water of bentonite. In FY19 (Zheng et a., 2019a), the “true” ion concentrations in pore-water from aqueous extract data for another section were inferred by geochemical modeling; key processes that control the hydration of bentonite were re-evaluated, especially regarding the necessity of including thermal osmosis in the flow model to explain the relative humidity and water content data (Zheng et al., 2019b); chemical models were refined and used to explain the sulfate time series data. From FY16 to FY19, extensive model calibrations were conducted, and finally in FY19, the THCM model provided a coherent explanation of THMC data collected at the FEBEX in-situ test. In FY20, the modeling work is, therefore, aimed at using the THMC to explore the long-term alteration of bentonite. The first question we are now trying to address is the necessity of using the THMC model (as apposed to THC model) for studying long-term alteration of bentonite, especially geochemical alteration. THMC model is computationally expensive and numerically more unstable than THC model, while upgrading of THMC code using parallel computing and a better solver can alleviate the issue. Using the THC model could be beneficial in terms of a computation time and simulation stability, given that the performance assessment is most likely a THC simulation, not THMC simulation.

12.2 A Brief Description of FEBEX Experiments

The FEBEX in-situ test was conducted at the Grimsel URL from 1997 to 2015 (Huertas et al., 2000). It consisted of five basic components: the drift, the heating system, the bentonite barrier, the instrumentation, and the monitoring and control system. The main elements of the heating system are two heaters (#1 and #2), 1 m apart. Heaters were placed inside a cylindrical steel liner. Heaters were at a constant-temperature control mode to maintain a maximum temperature of 100°C at the steel liner/bentonite interface 20 days after the heating started. The bentonite barrier is made of blocks of highly compacted bentonite. The average values of the initial dry density and the gravimetric water content of compacted bentonite blocks were 1.7 g/cm^3 and 14.4%, respectively.

The in-situ test began on February 27, 1997, and went through two dismantling events. Table 8-1 presents the operation timeline. Comprehensive post-mortem bentonite sampling and analysis program was performed during both dismantling events (Bárcena et al., 2003; Garcia-Sineriz et al., 2016). After Heater #2 was switched off and a short cool-off time period, dismantling was carried out from the shotcrete toward the bentonite section by sections, and the types of monitoring and sampling are shown in Figure 8-1 (Garcia-Sineriz et al., 2016).

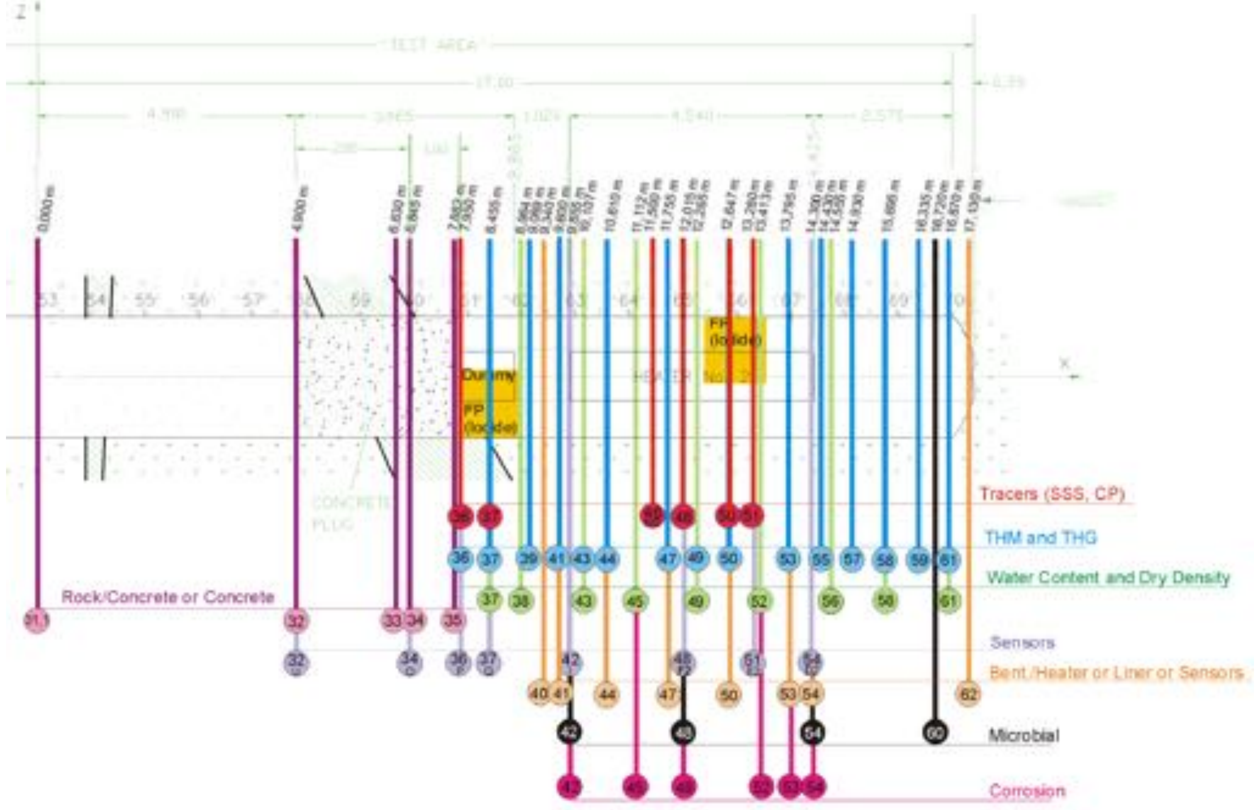

Source: Detzner and Kober, 2015.

Figure 12-1. Section layout during the dismantling operation of Heater #2, showing the types of monitoring and sampling

The sensors installed in the bentonite blocks were used to measure temperature, relative humidity and stress. The bentonite samples that were taken after dismantling of test sections were used to determine the water content and dry density. The dismantling of Heater #1 in 2002 and Heater #2 in 2015 (Table 8-1) provides two snapshots of measured water content, dry density, and ion concentrations in pore water of bentonite, which are important for understanding the temporal evolution of the key THM processes. More detailed description of the FEBEX in-situ test and available THM data were given in Zheng et al. (2018).

Table 12-1. Timeline of the FEBEX in-situ test.

Event	Date Start	Time (days)	Time (years)
Commencement of heating by Heater #1	2/27/1997	0	0.0
Shutdown of Heater #1	2/2/2002	1827	5.0
Sampling after Heater #1 was dismantled	5/2/2002	1930	5.3
Shutdown of Heater #2	4/24/2015	6630	18.2
Sampling after Heater #2 was dismantled	7/3/2015	6700	18.3

Zheng et al. (2018) described in detail the types of chemical data available in the FEBEX in-situ test. Ion concentration in the pore-water of granite was collected and measured in the two boreholes parallel to the in-situ test tunnel, which can be used to evaluate the diffusion of water from bentonite into granite. However, the chemical data for the solid phase are too scattered to be used to determine the spatial trend; data for exchangeable cations are problematic, but could be used with caution; the concentration data were not directly measured and geochemical modeling was involved to infer the ion concentration in pore water from data obtained by aqueous extract. Ion concentrations in pore water of bentonite still the primary data to validate model.

13. MODELING IN SUPPORT OF HOTBENT, AN EXPERIMENT STUDYING THE EFFECTS OF HIGH TEMPERATURES ON CLAY BUFFERS/NEAR-FIELD

13.1 Introduction

Several international disposal programs have recently initiated investigations of whether clay-based barriers can withstand temperature higher than the 100°C threshold for bentonite that is usually considered in mined repository designs. For example, the SFWST campaign has been investigating the feasibility of direct geological disposal of large spent nuclear fuel canisters, currently in dry storage (Hardin et al., 2014), which are expected to result in much higher emplacement temperature. Even for small canisters with 2 or 4 PWR, allowing a thermal limit go higher can significantly decrease a footprint of the repository, and, therefore, reduce the cost of the repository. The performance of bentonite barriers in the <100°C temperature range is underpinned by a broad knowledge based on laboratory and large-scale in-situ experiments. Bentonite characterization at above 100°C is less common, although for temperature up to about 150°C no significant changes in safety-relevant properties were determined (e.g. Cheshire et al., 2014). At temperature above 150°C, it is possible that a potentially detrimental temperature-driven physical-chemical response of materials (cementation, illitization) may occur, the characteristics of which are highly dependent on, and coupled with, the complex moisture transport processes induced by strong thermal gradients. The impact of such complex processes on the performance of a repository cannot be realistically reproduced and properly (nonconservatively) assessed at a small laboratory scale. Such an assessment needs to be conducted by large-scale in-situ experiments at URLs, where the most relevant features of future emplacement conditions can be adequately reproduced.

Potential options for a targeted high-temperature experiment (150°C to 200°C) in a crystalline rock environment are currently being considered under the leadership of NAGRA with several international partners. The proposed HotBENT experiment will be conducted in the well-characterized FEBEX drift at the Grimsel Test Site. The benefit of such a large-scale test, accompanied by a systematic laboratory program and modeling effort, is that the temperature effects can be evaluated under realistic conditions of strong thermal, hydraulic and density gradients, which cannot be reproduced in the laboratory. This will lead to the development of improved mechanistic models for the prediction of temperature-induced processes, including chemical alteration and mechanical changes, which can then be used for the performance assessment analysis of high-temperature scenarios. The key question is whether higher repository temperature would trigger mechanisms that compromise the various barrier functions of the engineered components and the host rock. If the barrier function is (at least partially) compromised, the performance assessment analysis can evaluate whether a reduced performance of a sub-barrier (or parts thereof) would still provide an adequate performance.

HotBENT partners include NAGRA (Switzerland), U.S. DOE (USA), SURAO (Czech Republic), NUMO (Japan), RWM (UK), BGR (Germany), ENRESA (Spain), Obayashi (Japan). Participation in the HotBENT testing would be beneficial for DOE. Substantial cost savings would be achieved in the design of a repository, if HotBENT demonstrates that the maximum temperature of bentonite backfill can be raised without drastic performance implications.

LBNL/DOE was part of the HotBENT project since the very beginning, including the initiation of the idea of large-scale high temperature field test (Vomvoris, et al., 2015) and using numerical models to support the design of the experiment. For example, Zheng et al. (2018) developed the models of a simple geometric setup, both 1D or 2D, with consideration of coupled thermal, hydrological, mechanical and chemical (THMC) processes. Zheng et al. (2019a) developed a 3D THM model to further understand the evolution of all the design components. However, these simulations were conducted based on bentonite parameters that are similar to those of the FEBEX bentonite in the in-situ test (Huertas et al., 2000). In April 2020 (Kober et al., 2020), the design for HotBENT was finalized. In this report, we provide the results of THC modeling to predict the evolution of Wyoming bentonite that will be used in the HotBENT.

13.2 Status of HotBENT

The final design of HotBENT is shown in Figure 13-1. In this design, the test is composed of 4 modules that differ in heating temperature, bentonite parameters, time length and with or without concrete liner. Module H4 locates closest to the instrumentation area. A 2 m long heater will be emplaced on top of bentonite pedestals and then surrounded with granular bentonite mixture (GBM). Pedestals are bentonite blocks. Bentonite used in module H4 is the BCV bentonite, a type bentonite from Czech Republic. Module H4 targets a heater at temperature of 175°C, and is planned to run for 5 years. Module H3 is similar to module H4, except the bentonite is Wyoming bentonite. Module H2 is identical to module H3 in design, except it will run for longer time. One lesion learnt from modeling the FEBEX in-situ test (Zheng et al., 2018) is that multiple temporal snapshots of spatial distribution of key THMC results are critical for finding the “right” model and enhance the predictability of modeling. Modules H2 and H3 will provide two snapshots of THMC evolution of Wyoming bentonite. Module H1 has similar design to module H2, but with two differences: first, temperature will be 200 ºC for the heater rather than 175°C for the heater in module H2, and second, a concrete liner will be installed to the rock wall of the test tunnel.

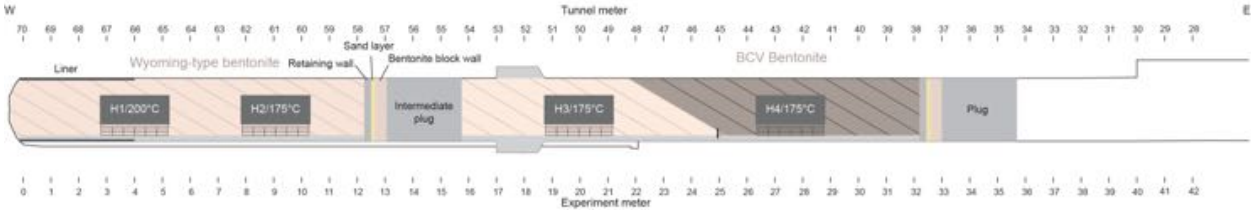

Source: Kober et al, 2020.

Figure 13-1. Design of modules for HotBENT.

Bentonite blocks will be used to build a pedestal below the heater and the rest of space will be filled with GBM (Figure 13-2). The target dry density for bentonite blocks is 1.78 g/cm^3 and for GBM is 1.5 g/cm^3. The Wyoming type Na bentonite is Laviobent_GN0318, formerly known as MX-80.

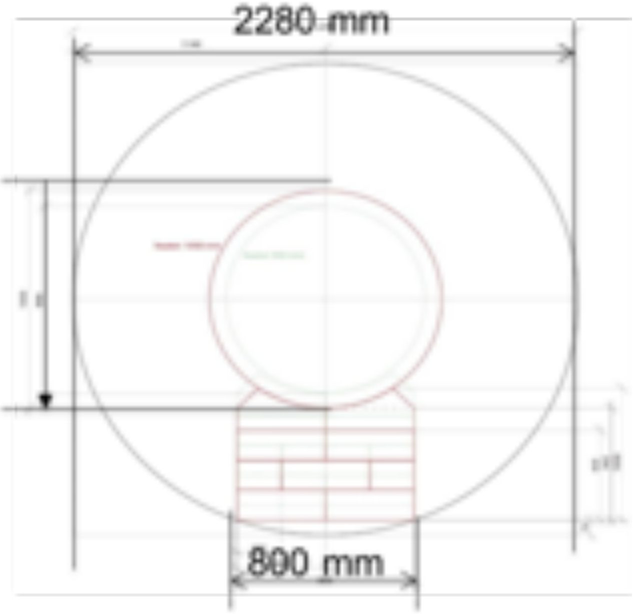

Source: Kober et al., 2020.

Figure 13-2. Cross section of HotBENT experiment at areas with heaters

The time schedule for the HotBENT experiment is given in Figure 13-3, but adjustment might be expected as the experiment enters into construction.

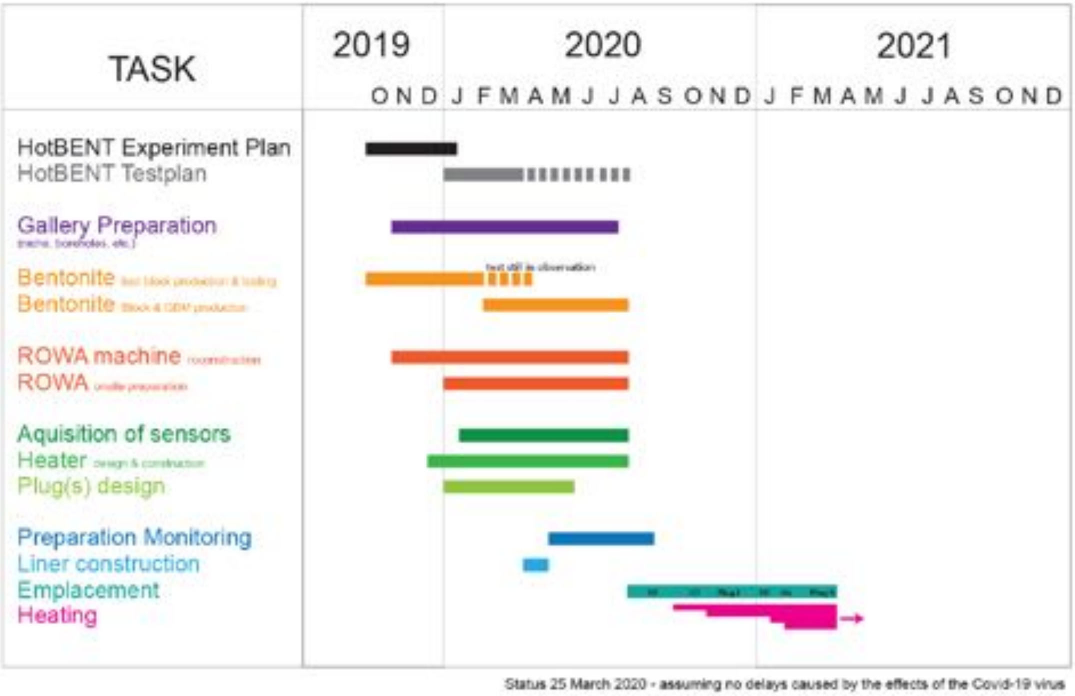

Source: Kober et al., 2020.

Figure 13-3. Time-schedule for the HotBENT experiment

13.3 Predicative Model for HotBENT

13.3.1 Introduction

While working with the NAGRA and HotBENT partners to finalize the design of the HotBENT test and an instrumentation plan, LBNL also conducted simulations to further understand what's expected in the HotBENT test. Zheng et al. (2017; 2018; 2019a) conducted 1D axi-symmetrical simulations based on the THMC model for FEBEX in-situ test and 2D THC modeling assuming the FEBEX bentonite. Finsterle et al. (2017) developed a 3D TH model for varioius scenarios to facilitate the design of the field test. As in the final design, two types of bentontie are going to be used: MX-80 and BCV bentonites. In this report, we developed a 1D axi-symmetric THC model to study the geochemical changes of MX-80 bentontie in HotBENT.

13.3.2 Model Development

The model was developed based on the THMC model for the FEBEX in-situ test (see Chapter 6), with two major differences: the bentonite is Wyoming bentonite (MX-80) instead of FEBEX bentonite, and the hydraulic pressure in granite is 2 MPa instead of 0.7 MPa. The natural hydraulic pressure surrounding the FEBEX tunnel is around 7 bars (Huertas et al., 2000). In order to ensure a speedy hydration of bentonite in HotBENT, artificial hydration by pressurizing the granite around the tunnel will be used and the target pressure would be 2 MPa.

13.3.3 Simulator

The numerical simulations in Zheng et al. (2016; 2017) were conducted with TOUGHREACT-FLAC3D, which sequentially couples the multiphase fluid flow and reactive transport simulator, TOUGHREACT V2 (Xu et al., 2011), with the finite-difference geomechanical code FLAC3D (Itasca, 2009). The coupling of TOUGHREACT and FLAC was initially developed by Zheng et al. (2012) to provide the necessary numerical framework for modeling fully coupled THMC processes. It was equipped with a linear elastic swelling model (Zheng et al., 2012; Rutqvist et al., 2014) to account for swelling as a result of changes in saturation and pore-water composition and the abundance of swelling clay (Zheng et al., 2014). In FY18, the code went through a major upgrade by replacing TOUGHREACT V2 (Xu et al., 2011) with TOUGHREACT V3.0-OMP (Xu et al., 2014). In comparison with TOUGHREACT V2 (Xu et al., 2011), TOUGHREACT V3.0-OMP (Xu et al., 2014) has the several major improvements (see http://esd1.lbl.gov/research/projects/tough/software/toughreact.html), one of the them is the OpenMP parallelization of chemical routines on multi-core shared memory computers, which significantly decreases the computation time.

13.3.4 Modeling Setup

Unlike the FEBEX in-situ test, in which pre-fabricated blocks were used everywhere, in HotBENT, bentonite blocks will be used to build a pedestal below the heater, and the rest of space will be filled with granulated bentonite mixture (GBM) (Figure 13-3). However, to take advantage of existing model and use it as a precursor for the 2D cross-sectional model, we still use an axi-symmetrical mesh (Figure 13-4), despite of knowing that the hydration won't be totally axi-symmetrical, because of the pedestal bentonite blocks have different properties from GBM. Such practice saves computation time, so that we can focus on the key coupling processes. Because the geochemical alteration will mostly be triggered by the interaction between granite water and bentonite, and geochemical interaction between pedestal and GBM is only limited to the near vicinity of their interface (Zheng et al., 2018), current modeling results are expected be valid for areas far away from the pedestal.

The model considers two material zones: one is for the bentonite, and the other is for the granite. The first two nodes (1 and 2) are located on the external wall of the heater (r = 0.45-0.46 m). Bentonite is located within 0.45 m < r < 1.135 m. The remaining domain up to 50 m is used to simulate the granite. The simulation is conducted for 10 years.

The initial temperature of 12°C is uniformly distributed. A constant temperature of 200 ºC is prescribed at the heater/bentonite interface (r = 0.45 m), while the temperature is assumed to remain constant at its initial value of 12°C at the external boundary (r = 50 m), because the thermal perturbation induced by the heaters over the time frame of the experiment does not extend to this boundary.

The initial a gravimetric water content of bentonite is 14%, which corresponds to a saturation degree of 55% and a suction of 1.11×10^5 kPa. The boundary conditions for flow include: (1) no flow at r = 0.45 m, and (2) a liquid pressure of 2 MPa at r = 50 m, as the area surrounding the tunnel will be pressurized by constantly injecting Grimsel groundwater with a target pressure of 2 MPa through 4 boreholes locating roughly 2 m away from the tunnel wall (Kober et al., 2020) .

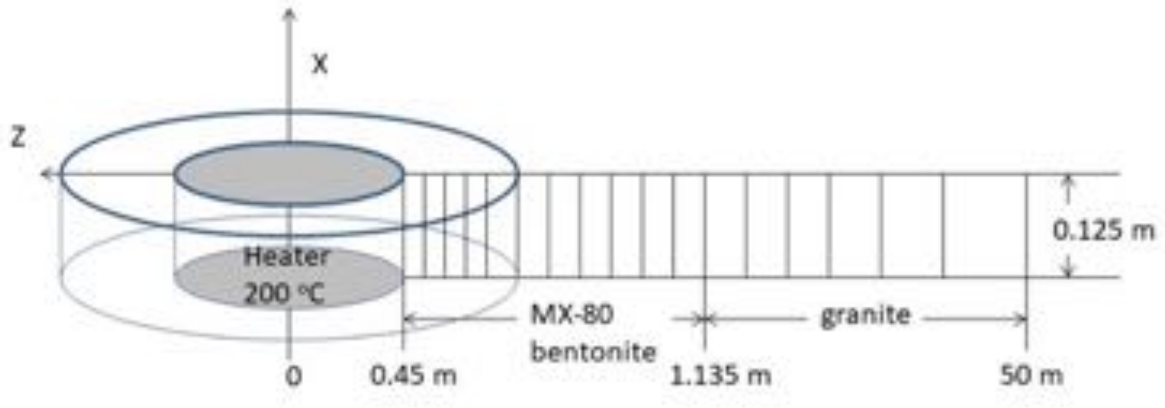

Figure 13-4. Mesh used for the model, shown not to the scale.

13.3.5 The TH Model

The model considers non-isothermal two-phase (air and water) flow, with each phase fluxes given by a multiphase version of Darcy's law. For the vapor flow in the air phase, in addition to Darcy flow, mass transport can also occur by diffusion and dispersion according to Fick's law. In the current model, both conductive (Fourier's law) and convective heat flux are considered in the model, and thermal conductivity is the key parameter. Thermal behavior is relatively well understood because it is less affected by coupled processes in comparison with hydrological and chemical processes, and the relevant parameters can be reliably measured.

The thermal conductivity of bentonites is affected by the degree of compaction (dry density) and water saturation. Figure 13-5 shows the measured thermal conductivity for MX-80 at different dry density. In the current design, the granulated bentonite mixture has a target dry density of ~1.45 g/cm^3. We use a linear relationship implemented in TOUGH2 (Pruess et al., 1999) to represent the thermal conductivity and water saturation relationship:

$$K_{th} = K_{wet} + S_l(K_{wet} - K_{dry}) \qquad \textit{Equation 13-1}$$

where K_{wet} is the thermal conductivity under fully saturated conditions, K_{dry} is the thermal conductivity under dry conditions, and S_l is the liquid saturation degree. K_{wet} and K_{dry} are given in Table 13-1.

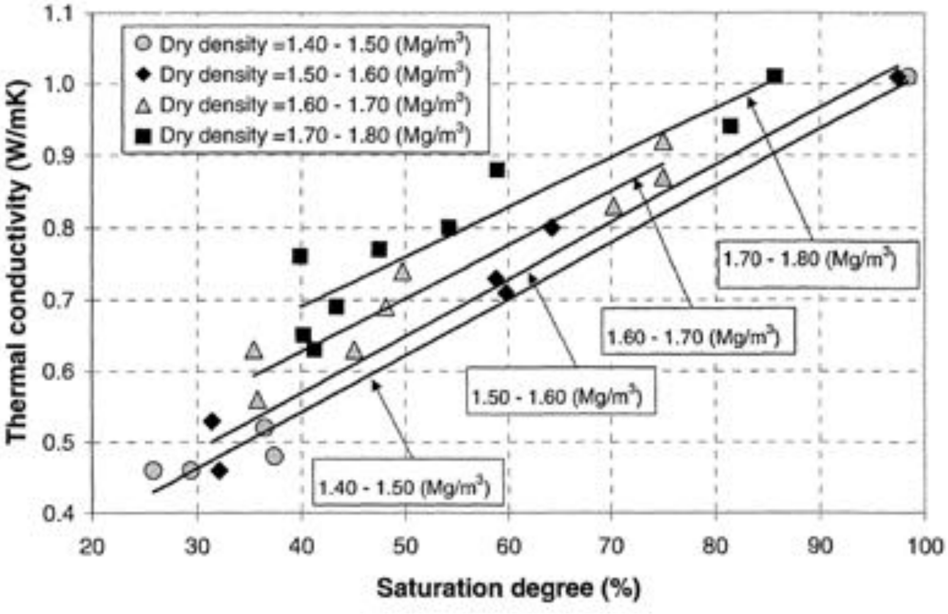

Source: Tang and Cui, 2006.

Figure 13-5. Thermal conductivity vs saturation degree for different dry density

According to the sensitivity analysis, based on the THMC model for the FEBEX in-situ test, the key parameters affecting the hydration of bentonite are permeability of granite, relative permeability, retention curves of bentonite, the vapor diffusion coefficient and permeability of bentonite. Granite is fractured media and should be represented by fractures and matrix. Just as previous models for in-situ tests (Samper et al., 2008; Sánchez et al., 2012), the current model also assumes that granite is a homogeneous porous medium, which can be simulated based on a model of an equivalent permeability. Based on the total water flow from the tunnel wall at the entire length of the test zone (Huertas et al., 2000), permeability of fractured granite is estimated to range from 5×10^{-18} to 8×10^{-18} m^2. Huertas et al. (2000) also reports that the most frequent permeability is 1×10^{-18} m^2, but it seems be more representative of the rock matrix. Zheng et al. (2011) used 8×10^{-18} m^2, Kuhlman and Gaus (2014) estimated permeability of 6.8×10^{-19} m^2, and Sánchez et al. (2012) used a surprisingly small value of 8.18×10^{-21} m^2. Based on the published values, it seems that a permeability value between 7×10^{-19} to 8×10^{-18} m^2 is plausible. Based on the evaluation in Zheng et al. (2015a), a permeability of 2×10^{-18} m^2 is used (Table 13-1).

The capillary pressure (retention curve) is calculated by the van Genuchten function as:

$$P_{cap} = -\frac{1}{\alpha}\left(\left[S^*\right]^{-1/m} - 1\right)^{1-m} \qquad \textit{Equation 13-2}$$

where P_{cap} is the capillary pressure (Pa), $S^* = (S_l - S_{lr})/(1 - S_{lr})$ and S_l is the water saturation, S_{lr} is the residual water saturation. S_{lr} is 0.1 for bentonite and 0.01 for granite. The values of α and m for the FEBEX bentonite are given in Table 13-1 (Zheng et al., 2019a).

Table 13-1. Thermal and hydrodynamic parameters.

Parameter	Granite	Bentonite
Grain density (kg/m^3)	2,700	2,780
Porosity ϕ	0.01	0.46
Saturated permeability (m^2)	2.0×10^{-18}	3.69×10^{-20}
Relative permeability, k_{rl}	$k_{rl} = S$	$k_{rl} = S^3$
Van Genuchten $1/\alpha$ (1/Pa)	4.76×10^{-4}	1.1×10^{-8}
Van Genuchten m	0.7	0.45
Compressibility, β (1/Pa)	3.2×10^{-9}	5.0×10^{-8}
Thermal expansion coeff. (1/°C)	1.0×10^{-5}	1.5×10^{-4}
Dry specific heat (J/(kg·°C))	793	1091
Thermal conductivity (W/(m·°C)) dry/wet	3.2/3.3	0.4/1.0
Effective vapor diffusion coefficient (m^2/s)	1.03×10^{-4}	1.03×10^{-4}

NOTE: In the relative permeability function, S is water saturation.

The effective permeability of bentonite plays a critical role in determining the hydration of bentonite. It is the product of intrinsic permeability (k) (or saturated permeability, absolute permeability) and relative permeability (k_r). Relative permeability, $k_r=S_l^3$ (where S_l is water saturation degree), has been consistently used by different models (Zheng et al., 2011; Sánchez et al., 2012; Kuhlman and Gaus, 2014) for FEBEX bentonite, and we use the same function for MX-80 here.

The stress-dependence of permeability for low-permeability sedimentary rock is fairly well known (e.g., Ghabezloo et al., 2009; Kwon et al., 2001). Many empirical relationships have been put forward to describe the permeability changes with effective stress. Villar (2005) derived an empirical relationship by fitting the permeability-dry density data as:

$$\log k = -2.94\rho_d - 8.17 \qquad \textit{Equation 13-3}$$

where ρ_d is dry density. Equation 13-3 give an initial permeability of 3.69×10^{-20} m^2 for GBM.

Kiverant et al. (2018) reported that the grain density of Wyoming bentonite varied between 2.773 and 2.806 g/cm^3, with an average of 2.78 g/cm^3. Karnland (2010) reported a slightly lower grain density of the bentonite MX-80 than Kiverant et al. (2018), which ranged from 2.75 to 2.78 g/cm^3, and a value of 2.75 g/cm^3 was used in their Buffer Production report. In this report, we used a grain density of 2.78 g/cm^3. With a target dry density of bentonite of 1.5 g/cm^3, we calculated a porosity of 0.46.

Taking into account coupled transport phenomena, thermal, hydraulic and chemical gradients all have effects on the heat, liquid and solute fluxes. Thermal osmosis is a coupled process that can produce a fluid flux. Zhou et al. (1999) showed that additional coupled flow terms due to a temperature gradient had a significant effect on the distribution of capillary pressure and saturation in a THM model of a thick cylinder heating test. The flux of fluid caused by thermal osmosis v_{to} can be written as (Dirksen, 1969):

$$v_{to} = -k_T \nabla T \qquad \text{Equation 13-4}$$

where T is temperature and k_T is the thermo-osmotic permeability ($m^2/(K{\cdot}s)$). Liquid flux caused by thermal osmosis term can be added to Darcian terms (Ghassemi and Diek, 2002; Zhou et al., 1999). In current model, k_T of 1.2×10^{-12} $m^2/(K{\cdot}s)$ is used.

13.3.6 Chemical Model

The establishment of the chemical model requires first the knowledge of initial chemical conditions in bentonite and granite, i.e., the initial mineralogical and pore water compositions. In this report, the mineralogical composition for MX-80 bentonite were taken from Karnland (2010). Table 13-2 shows the mass fraction and Table 13-3 shows the volume fraction (ratio of the volume for a mineral to the total volume of medium) using a porosity of 0.46 (see Table 13-2). Because tridymite, a polymorph of silica, was not found in the database, in the model we assumed that tridymite thermodynamically is the same as quartz. Note the minerals assigned the zero initial volume fraction are the secondary minerals that could be formed.

Table 13-2. Mass fraction of mineral measured from the XRD analysis of five consignments of the Wyoming MX-80 material (Karnland, 2010). Column under "Wym" are the average.

Phase	WySt	WyL1	WyL2	WyR1	WyR1m	WyR2	Wym	Plus	Minus
Montmorillonite	82.5	79.5	79.8	82.7	83.9	80	81.4	2.5	1.9
Illite	0.7	0.8	0.7	0.8	0.8	0.7	0.8	0.1	0.1
Calcite	1.3	0	0	0.1	0	0	0.2	1.1	0.2
Cristobalite	0.2	1.4	2.5	0.6	0.7	0	0.9	1.6	0.9
Gypsum	1.4	0.7	0.9	0.7	0.8	1.1	0.9	0.5	0.2
Muscovite	2.4	5.1	2.6	3.5	4.4	2.5	3.4	1.7	1
Plagioclase	4.6	2.4	4	3.2	2.3	4.7	3.5	1.2	1.2
Pyrite	0.8	0.6	0.6	0.6	0.3	0.9	0.6	0.3	0.3
Quartz	2.6	2.5	3.8	3	2.8	3.2	3	0.8	0.5
Tridymite	1.7	5	3.8	3.9	3.1	5.1	3.8	1.3	2.1

Table 13-3. Mineral volume fraction (dimensionless, ratio of the volume for a mineral to the total volume of medium) MX-80 bentonite (Karnland, 2010) and granite (Zheng et al., 2011).

Mineral	MX-80 Bentonite	Granite
Calcite	0.00108	0
Smectite	0.439	0
Gypsum	0.00486	0
Quartz	0.0162	0.37
Cristobalite	0.0367	0.00
K-Feldspar	0.000	0.35
Plagioclase	0.0189	0.27
Dolomite	0.0	0
Illite	0.00432	0
Kaolinite	0.0	0
Siderite	0.0	0
Ankerite	0.0	0
Anhydrite	0.0	0
Chlorite	0.0	0
Muscovite	0.01836	0
Pyrite	0.00324	0

The initial pore water composition in MX-80 varies with dry density and water content (Bradbury and Baeyens, 2003). Because the target dry density of bentonite in granulated bentonite mixture is 1.5 g/cm^3, we take the values reported in Bradbury and Baeyens (2003), shown in Table 13-4). The pore water composition for granite (Table 13-4) is taken from Zheng et al. (2011).

Table 13-4. Pore-water composition (mol/kg water except for pH) of MX-80 bentonite (Bradbury and Baeyens, 2002; Bradbury and Baeyens, 2003) and granite (Zheng et al., 2011).

	MX-80 Bentonite	Granite
pH	8	8.35
Cl	6.75E-02	1.31E-05
SO_4^{-2}	1.04E-01	7.86E-05
HCO_3^-	8.8E-04	3.97E-04
Ca^{+2}	9.47E-03	1.81E-04
Mg^{+2}	7.06E-03	1.32E-06
Na^+	2.43E-01	3.76E-04
K^+	1.23E-03	7.80E-06
Fe^{+2}	2.06E-08	2.06E-08
SiO_2(aq)	1.1E-04	6.07E-04
AlO_2^-	1.91E-09	3.89E-08

In the chemical model, we consider aqueous complexation, cation exchange, surface complexation, and mineral dissolution/precipitation. Details of aqueous complexes and their disassociation constants for reactions, solubility and reaction rate for minerals are given in Zheng et al. (2018)

13.4 Model Results

13.4.1 TH Results

With constant heating at 200°C at the heater, a point 3 cm away from the heater is quickly heated to 190°C (Figure 13-6), in the middle of the bentonite barrier the temperature is about 128ºC, and the temperature in bentonite 6 cm away from granite is about 97°C (Figure 13-6). The temperature at the bentonite/granite interface is 87°C (not shown in the figure). The temperature in granite decreases to 75°C at about 1.6 m away from the heater, and to 40°C at 4 m away from the heater (Figure 13-6). At a 10 m depth in the granite (*R*=11 m), the temperature is about 20°C. Thermal disturbance penetrates about 25 m into the granite.

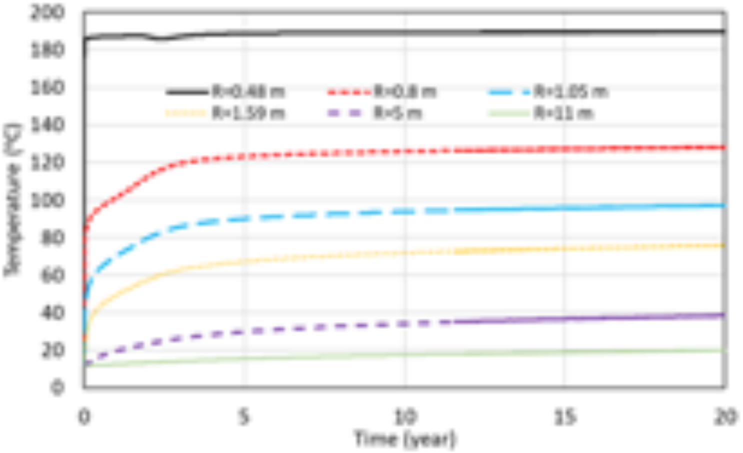

Figure 13-6. Temporal evolution of temperature at several radial distances. Note that bentonite/granite interface locates at *R* = 1.13 m.

Typically, bentonite near the heater goes through desaturation/re-saturation cycling: evaporation due to high heat dries the bentonite, and re-saturation occurs once the hydraulic pressure overcomes the vapor pressure. However, the time span of such a cycle depends on the temperature, permeability of bentonite, and hydraulic pressure in granite. Model results showed that re-saturation for HotBENT is much faster than the FEBEX in-situ test (Zheng et al., 2019b), because permeability of bentonite is higher and hydraulic pressure in granite is higher, despite of higher temperature.

Figure 13-7 shows the evolution of liquid saturation at several radial distances, and Figure 13-8 shows the radial profiles for several times. Most parts of bentonite become fully saturation in about 3 years, but an area about 3 cm away from the heater remains slightly unsaturated (95% to 98% liquid saturation) until the end of simulation, because hydraulic pressure cannot exceed the high gas pressure (Figure 13-9) at this area. Note that pore pressure, shown in Figure 13-9, is the gas pressure for unsaturated condition, and liquid pressure for full saturation. Another indicator that a small area near the heater remans unsaturated is that the relative humidity of 92% at *R*=0.48 m remains stable until the end of simulation after bentonite goes through a desaturation (decrease in relative humidity) and re-saturation.

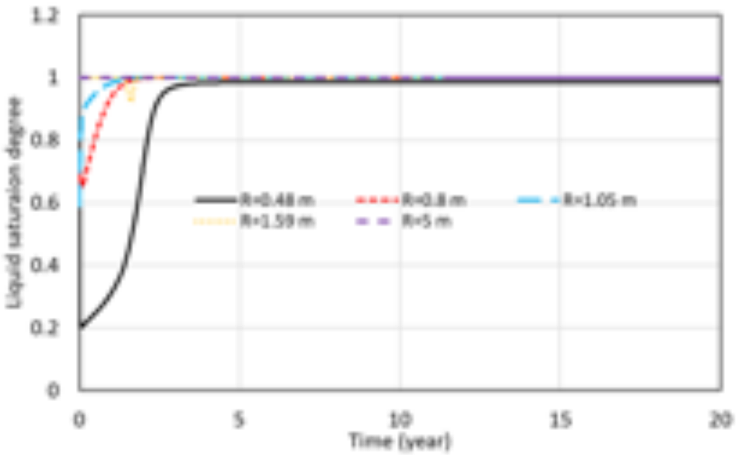

Figure 13-7. Temporal evolution of liquid saturation at several radial distances. Note that points at *R*= 0.48, 0.8, and 1.05 m are located within the bentonite barrier, and the rest of the points are located in granite.

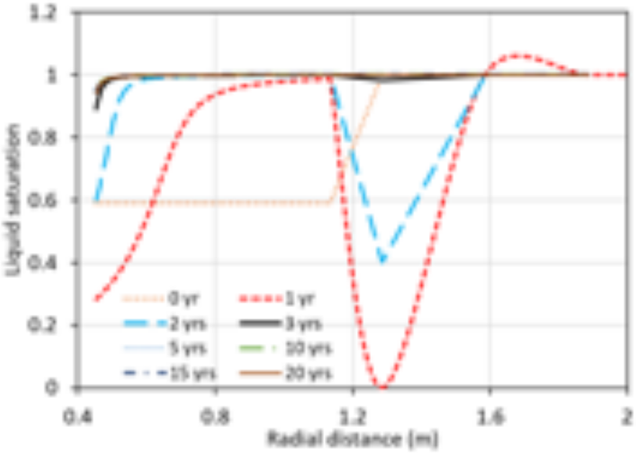

Figure 13-8. Spatial profiles of liquid saturation at several times. Note that the bentonite/granite interface is located at *R* = 1.13 m.

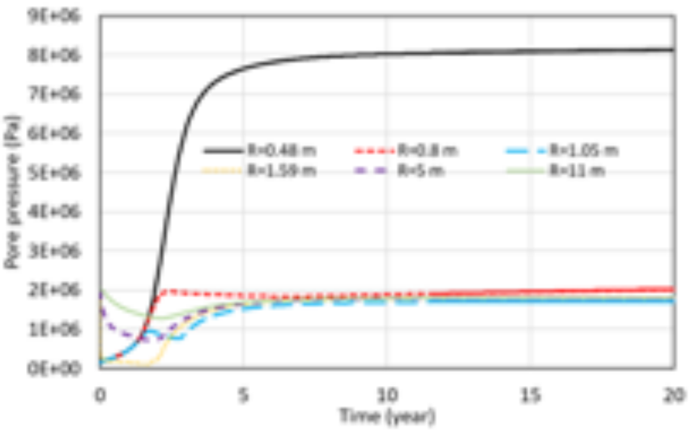

Figure 13-9. Temporal evolution of pore pressure at several radial distances. Note that points at *R*= 0.48, 0.8, and 1.05 m are located within bentonite barrier, and the rest of points are located in granite.

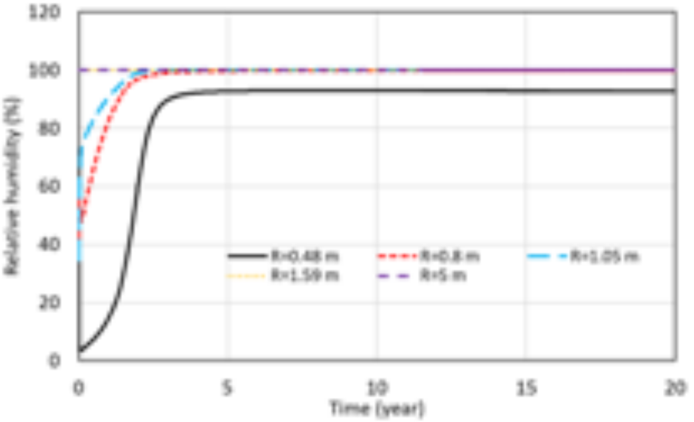

Figure 13-10. Temporal evolution of relative humidity at several radial distance. Note that points at *R*= 0.48, 0.8 and 1.05 m are located within bentonite barrier, and the rest of points are located in granite.

13.4.2 Chemical Results

The evolution of conservative chemical species, i.e., Cl, as shown in Figure 13-11, is controlled by three major processes: water displacement, diffusion, and evaporation/condensation. As granite water infiltrates into the bentonite, it displaces bentonite pore water and pushes the bentonite pore water towards the heater. Evaporation caused by heating generates vapor and vapor move outwards to the relatively cooler area and condenses. The evaporation leads to an increase in concentration, whereas condensation results in a decrease in concentration. Because of the concentration difference between bentonite pore water and granite water, diffusion also occurs with ions moving from bentonite to granite for most species. As a result of the combination of these processes, the Cl profile can be divided into three areas: from radial distance of 0.45 m to 0.48 m, a narrow area (referred as "evaporation zone") with a high concentration due to continuous evaporation, and from radial distance of 0.48 m to 0.8 m, a condensation area (referred as "condensation zone") that is characterized by a gradually decreasing concentration. Because of the continuous condensation, the concentration in the "condensation zone" can be lower than in the granite water; from the radial distance of 0.8 m to the bentonite/granite interface, an area is featured with a concentration gradient decreasing from bentonite to granite due to diffusion, which is referred as "diffusion zone." Please note the subdivision onto three zone is rather descriptive, and the temporal and spatial distribution of these zones changes with time.

Despite of other chemical reactions are involved in the transport of sulfate, its radial and temporal distributions (Figure 13-12) are similar to those of chloride, which is consistent with findings from the THMC model for the FEBEX in-situ test (Zheng et al., 2018). The MX-80 bentonite contains a small amount of gypsum that quickly dissolves uniformly along the entire bentonite barrier (Figure 13-13), leading to a uniform rise of the sulfate concentration shortly after the simulation starts, but later it behaves just like chloride, and the spatial distribution is dominated by transport processes including displacement by penetration of granite water, evaporation/condensation, and diffusion.

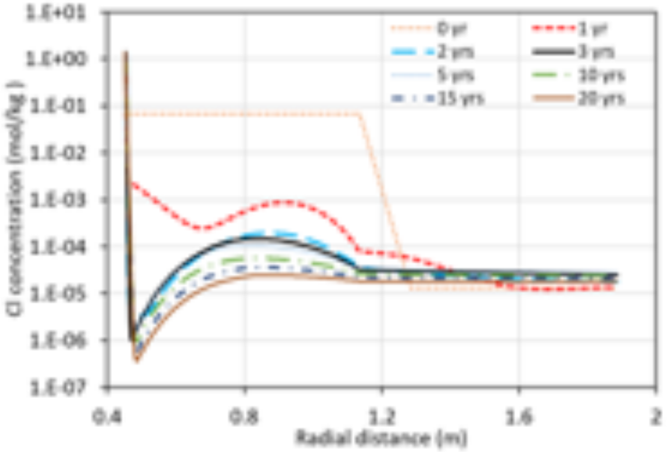

Figure 13-11. Radial profiles of Cl concentrations at several times. Note that bentonite/granite interface is located at *R* = 1.13 m.

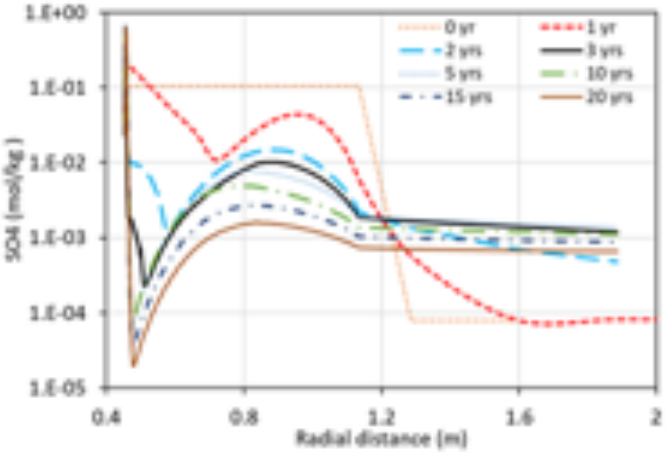

Figure 13-12. Radial profiles of SO_4 concentrations at several times. Note that bentonite/granite interface is located at *R* = 1.13 m.

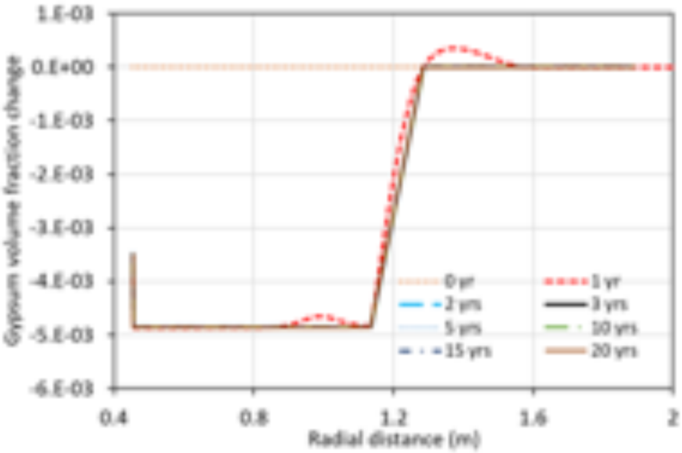

Figure 13-13. Radial profiles of gypsum volume fraction change at several times. Negative values mean dissolution, and positive values indicate precipitation.

Calcium is involved in many chemical reactions including calcite and gypsum dissolution/precipitation, cation exchange, which regulate the calcium concentration level, but the radial trend of calcium (Figure 13-14) follows that of chloride: an "evaporation zone" that is characterized by high concentration, an "condensation zone" that features low concentration and a "diffusion zone" that shows the decreasing concentration from bentonite to granite. Calcite dissolution/precipitation and precipitation of the anhydrite are the major reactions that affect the concentration of calcium. Evolution of calcite roughly follows the three zones, but changes spatially and temporally. Model shows precipitation in the "diffusion zone." In the "condensation zone," dissolution dominates, but precipitation appears at the boundary between the "diffusion zone" and the "condensation zone." There is re-precipitation in the "evaporation zone," i.e. calcite dissolves in the first 5 years and then re-precipitates, although the volume fraction therein is still lower than the initial value (negative value in Figure 13-15). Precipitation of the anhydrite is also observed in the model (Figure 13-16). Both gypsum and anhydrite are calcium sulfate minerals, but gypsum is the hydrous form, with two water molecules in the chemical formula. Anhydrite is more stable, when the temperature is higher than 43°C (Zheng et al., 2011), which is why precipitation of anhydrite is usually expected under the conditions of HotBENT.

Like calcium, magnesium (Figure 13-17) follows the spatial trend of chloride, and can roughly be divided into three zones. The chemical reaction that changes the concentration of magnesium is cations exchange, which will be discussed later in the section.

The radial profile of sodium (Figure 13-18) similar to that of chloride, showing very high concentration up to 3 mol/kg near the heater at the "evaporation zone." But they are also affected by the dissolution of plagioclase (Figure 13-19) and cation exchange.

Potassium concentrations (Figure 13-20) are similar to other major cations. Dissolution/precipitation of illite and muscovite interplay with the aqueous potassium that is strongly affected by transport processes, and display similar spatial patterns as aqueous potassium. In the "diffusion zone," illite dissolves and muscovite precipitates; in the area between "diffusion zone" and "condensation zone," illite precipitates and muscovite dissolves, but in the "condensation zone," close to the "evaporation zone," illite dissolves and muscovite precipitates; and in the "evaporation zone," illite precipitates and muscovite dissolves.

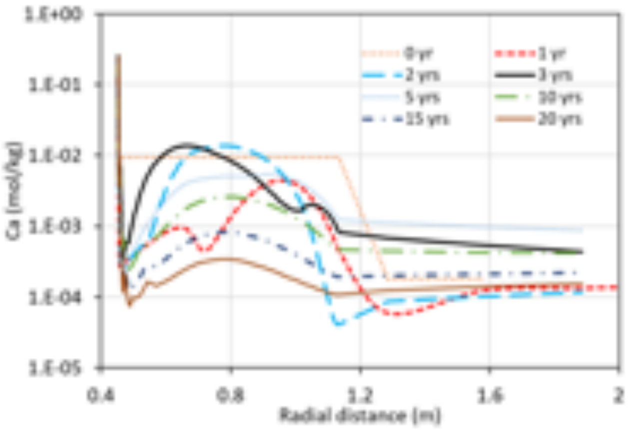

Figure 13-14. Spatial profiles of Ca concentration at several times. Note that bentonite/granite interface locates at *R* = 1.13 m.

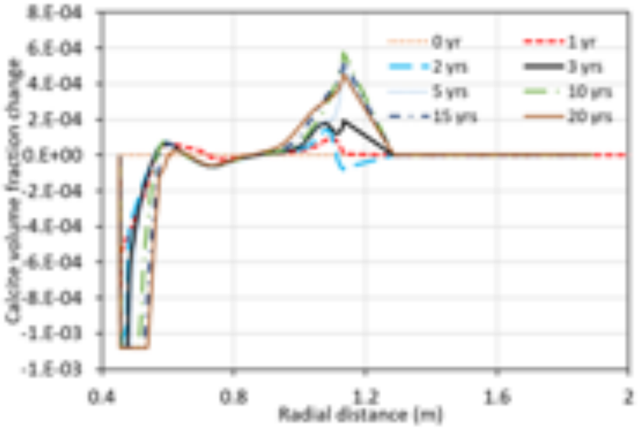

Figure 13-15. Radial profiles of calcite volume fraction change at several times. Negative values mean dissolution and positive values indicate precipitation.

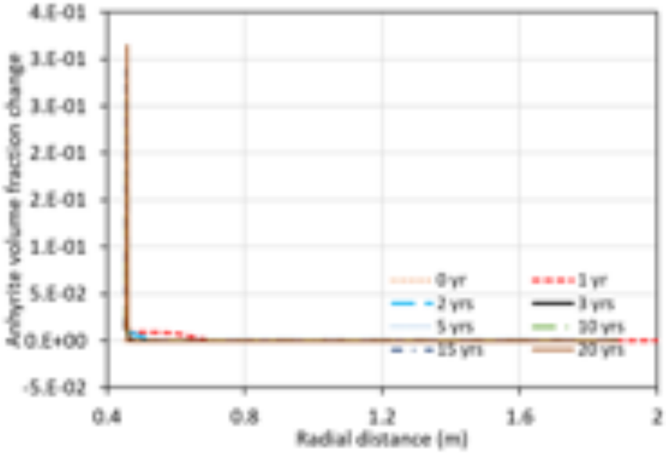

Figure 13-16. Radial profiles of anhydrite volume fraction change at several times. Negative values mean dissolution and positive values indicate precipitation.

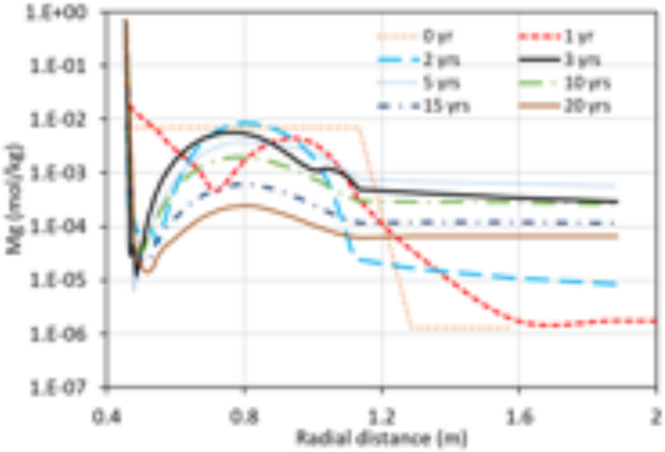

Figure 13-17. Radial profiles of Mg concentration at several times. Note that bentonite/granite interface is located at *R* = 1.13 m.

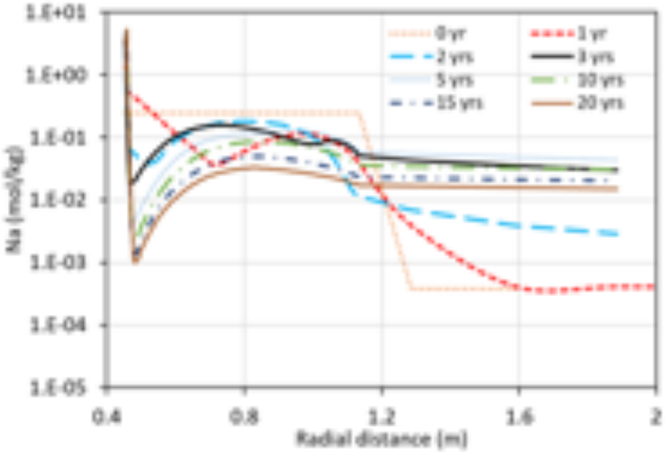

Figure 13-18. Radial profiles of Na concentration at several times. Note that bentonite/granite interface is located at *R* = 1.13 m.

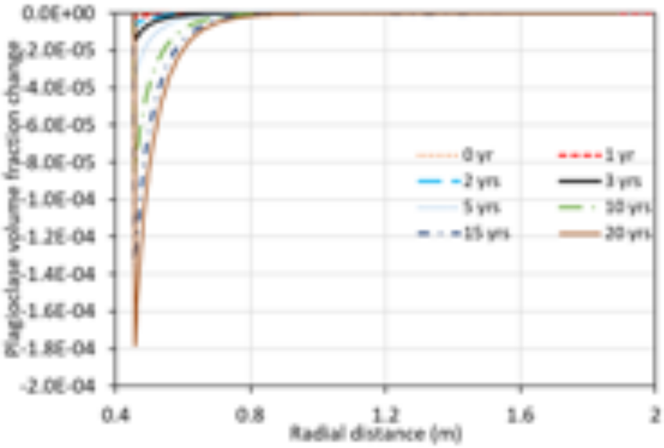

Figure 13-19. Radial profiles of plagioclase volume fraction change at several times. Negative values mean dissolution and positive values indicate precipitation.

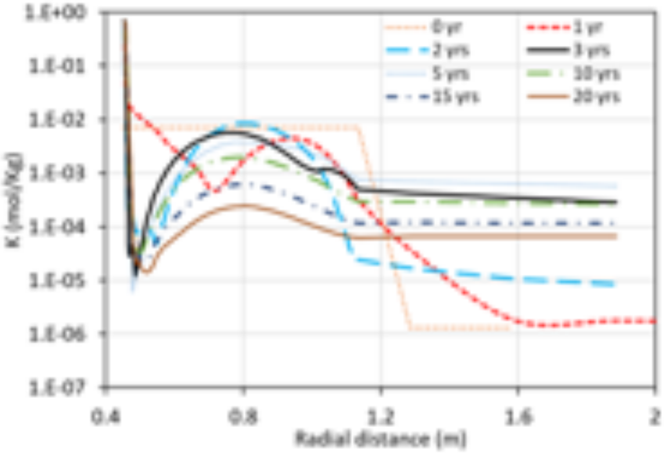

Figure 13-20. Radial profiles of K concentration at several times. Note that bentonite/granite interface locates at *R* = 1.13 m.

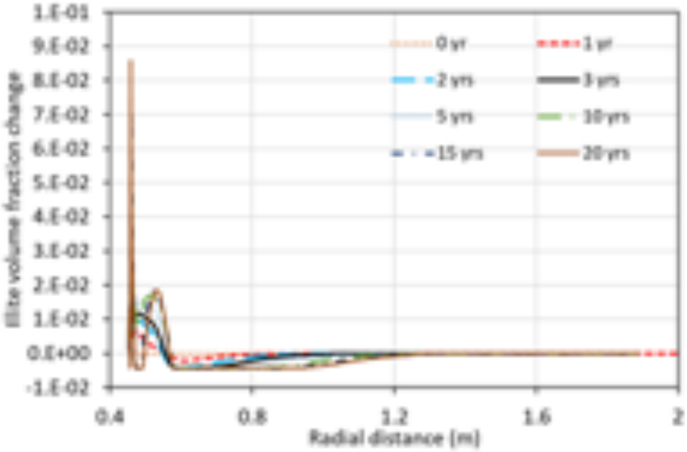

Figure 13-21. Radial profiles of illite volume fraction change at several times. Negative values mean dissolution and positive values indicate precipitation.

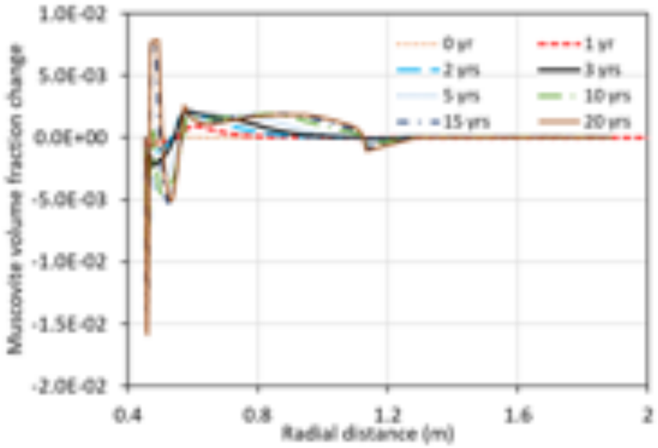

Figure 13-22. Radial profiles of muscovite volume fraction change at several times. Negative values mean dissolution and positive values indicate precipitation.

Simulations using the THMC model of FEBEX in-situ test (Zheng et al., 2018) showed that pH and bicarbonate behave differently compared to other reactive species (i.e., sulfate, Ca, Mg, Na, K), and they do not follow the spatial pattern of conservative species (e.g., Cl), indicating chemical reactions, rather than transport processes dominating the evolution of pH and bicarbonate. The current predictive model for HotBENT shows the same. In most areas, pH is buffered by the surface protonation, but in the "condensation zone," right next to the evaporation zone in a very narrow area, continuous condensation and mineral dissolution drive the pH to 3. The dissolution of muscovite, smectite, and precipitation tends to decrease the pH, whereas the dissolution of calcite leads to an increase in pH, but the combined effect is that pH drops significantly. The rise of pH at areas near the granite in early time (1 year) is likely caused by the interaction between the bentonite pore water and granite water.

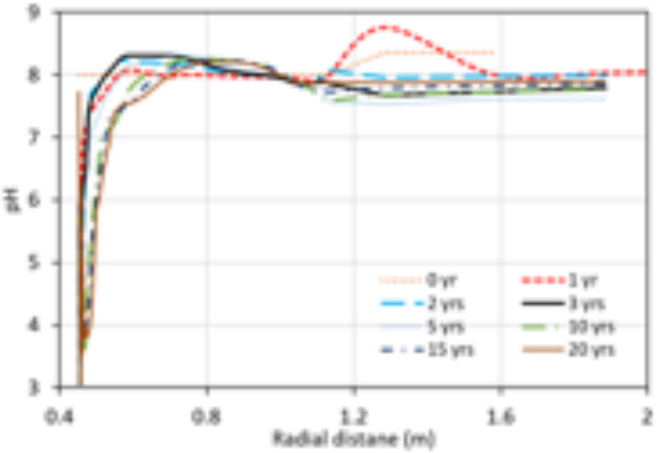

Figure 13-23. Radial profiles of pH at several times. Note that bentonite/granite interface is located at *R* = 1.13 m.

The spatial distribution of bicarbonate is controlled dominantly by reactions rather than by transport processes. The evolution of CO_2 gas trapped in the bentonite pore water and dissolution/precipitation of calcite are major reactions that are responsible for the changes in bicarbonate concentration.

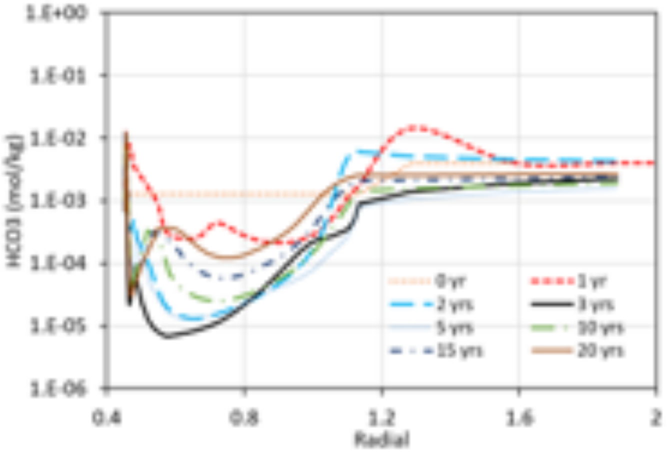

Figure 13-24. Radia profiles of bicarbonate concentration at several times. Note that bentonite/granite interface locates at R = 1.13 m.

The key mineral in bentonite that is a major concern for the long-term stability of bentonite barrier is smectite (Zheng et al., 2015a). Based on the results of the FEBEX in-situ test (Zheng et al., 2018), comparison of smectite mass fraction in bentonite samples that were collected after 18-years of heating, and hydration with reference bentonite (reserved, represent the state of bentonite before the test) did not show a clear difference, because the data were too scattered. But the model for FEBEX in-situ test (Zheng et al., 2018) showed bentonite in the narrow area close to heater loss about 1% smectite. The current model predicts a significant dissolution of smectite (Figure 13-25) in an area about 3 cm thick next to the heater because of strong and continuous evaporation near the heater, meanwhile illite precipitated at the same area (Figure 13-22).

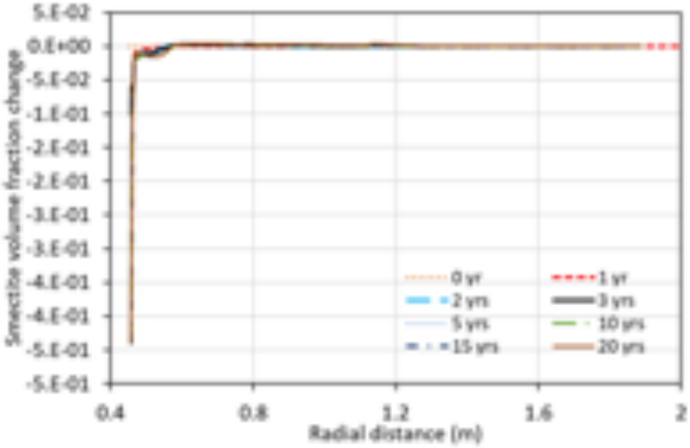

Figure 13-25. Radial profiles of smectite volume fraction change at several times. Note that bentonite/granite interface is located at *R* = 1.13 m.

In general, based on the results of modeling, changes in minerals phases occurred mostly in areas close to the heater by the end of the planned prediction time of 20 years. In an area very next to the heater, about 3 cm thick with radial distance from 0.45 m to 0.48 m, model showed the dissolution of smectite (Figure 13-25), precipitation of illite (Figure 13-22) and anhydrite (Figure 13-16), quartz (Figure 13-26) and cristobalite (Figure 13-27). Calcite, muscovite, and plagioclase dissolved initially, but started to precipitate at a later time, although the volume fractions of these minerals at the 20 years are still lower than their perspective initial values. Changes of siderite, ankerite, albite, and anorthite have not been shown by the model.

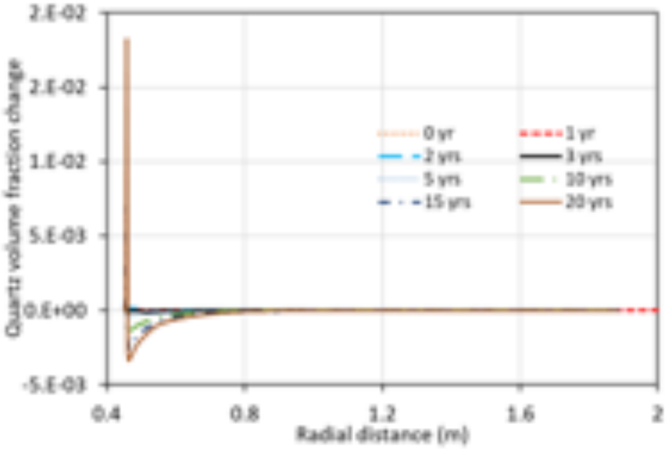

Figure 13-26. Radial profiles of quartz volume fraction change at several times. Note that bentonite/granite interface is located at *R* = 1.13 m.

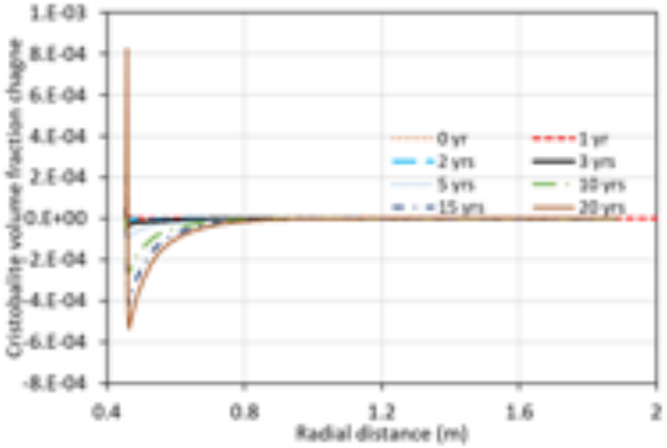

Figure 13-27. Radial profiles of cristobalite volume fraction change at several times. Note that bentonite/granite interface is located at *R* = 1.13 m.

The spatial distribution of exchangeable cations is the result of the interplay between exchangeable cations with their aqueous counterparts and competition between different exchangeable cations for the exchange sites. In most areas in the bentonite barrier, exchangeable Ca (Figure 13-32) and K (Figure 13-29) are loaded to the exchangeable sites, whereas exchangeable Na (Figure 13-28) and Mg (Figure 13-33) are released from exchangeable sites. But the model showed an opposite trend in the area close to the heater: exchangeable Ca (Figure 13-32) and K (Figure 13-29) are released from the exchangeable sites, whereas exchangeable Na (Figure 13-28) and Mg (Figure 13-33) are loaded to exchangeable sites.

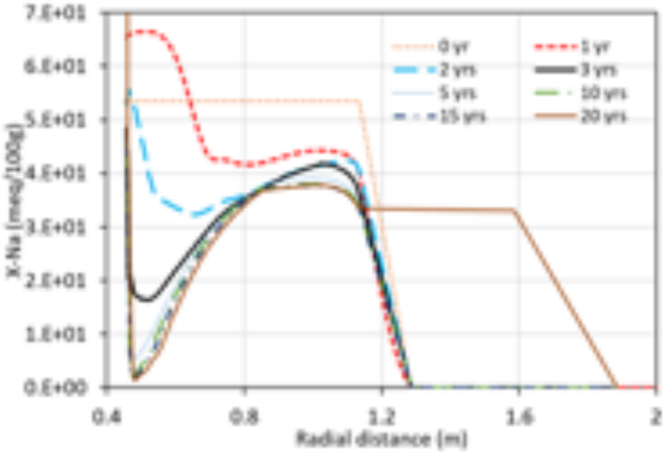

Figure 13-28. Radial profiles of exchangeable Na at different times. Note that bentonite/granite interface is locates at *R* = 1.13 m.

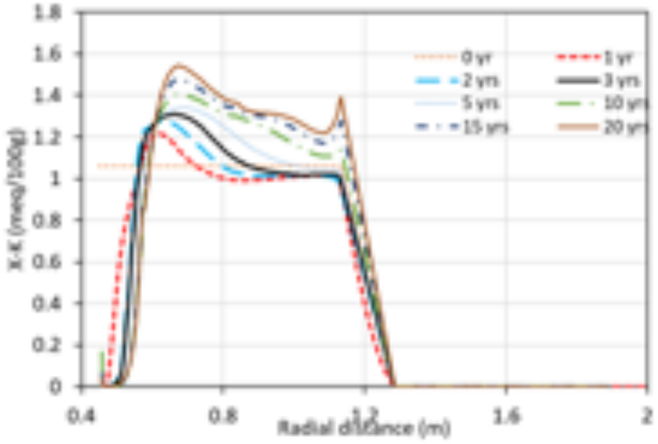

Figure 13-29. Radial profiles of exchangeable K at several times. Note that bentonite/granite interface locates at *R* = 1.13 m.

13.4.3 Sensitivity of Simulations of Chloride Concentration to Heater Temperature

Accumulation of high ions in the close vicinity of the heater had been observed in the FEBEX in-situ test and the corresponding interpretative models (Zheng et al., 2018), and also is shown in the current model as the “evaporation zone.” The “condensation zone” with a low concentration that is located a bit further away from the heater than the “evaporation zone” was also observed in FEBEX in-situ test. The concentration level in the “condensation zone” in the current model, however, is much lower than that having ever been observed in the FEBEX in-situ test, and for some species, the concentration is even lower than that in the granite water. Considering that the heater was 100°C in FEBEX in-situ test, a sensitivity run, assuming the heater has a temperature of 100°C, was conducted. Chloride concentration profiles shown in Figure 13-32 are similar to the chloride concentration profile in the FEBEX in-situ test (Figure 13-33). In HotBENT, because of 200°C heater temperature, evaporation in the close vicinity of the heater is much stronger and condensation in the area further away from the heater is also stronger than that in the case with 100°C heater temperature. Note that permeability of the bentonite barrier in HotBENT is about 17 times higher than that in FEBEX in-situ test, which may have also caused the difference in the concentration profiles.

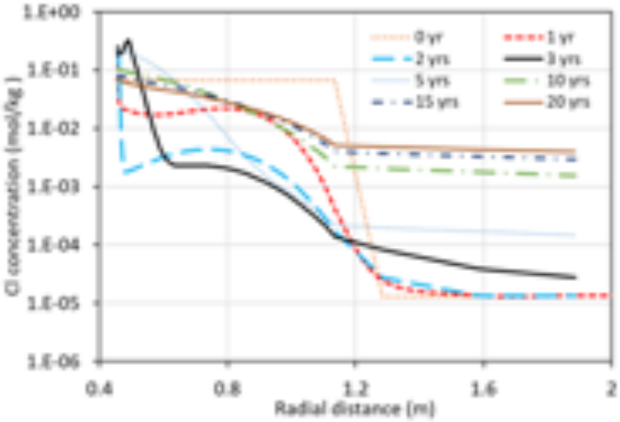

Figure 13-30. Radial profiles of Cl concentration at several times. Note that bentonite/granite interface is located at *R* = 1.13 m.

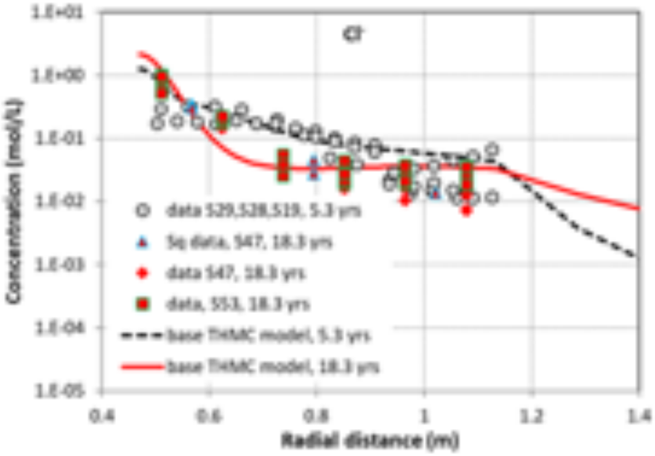

Figure 13-31. Calibrated chloride concentration data at 5.3 years from aqueous extract test for Sections 29, 28, and 19 (Zheng et al., 2011), calibrated chloride concentration data at 18.3 years from aqueous extract test for Section 47 ("data S47, 18.3 yrs") and Section 53 ("data S53, 18.3 yrs"), chloride concentration data from squeezing test for Section 47 ("Sq data, S47, 18.3 yrs"), and model results from the THMC model, modified from Zheng et al. (2018).

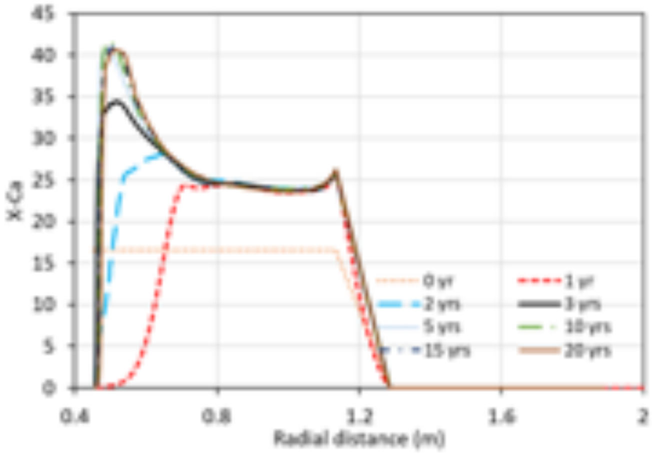

Figure 13-32. Radial profiles of exchangeable Ca at several times. Note that bentonite/granite interface is located at *R* = 1.13 m.

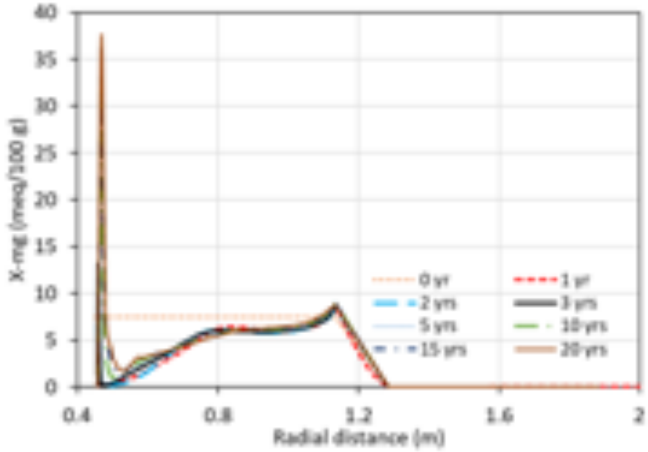

Figure 13-33. Radial profiles of exchangeable Mg at several times. Note that bentonite/granite interface is located at *R* = 1.13 m.

13.5 Summary and Future Work

In this report, we, therefore, developed a THC model to predict the evolution of Wyoming bentonite (MX-80) that will be used in the HotBENT. Modeling of coupled THC processes affected by high temperature, relatively high permeability and high hydraulic pressure, combined with the effect of artificial hydration, generated the results that have not been observed in FEBEX in-situ test (Zheng et al., 2018). Modeling results can be summarized as follows.

With a heater temperature of 200°C, temperature at the bentonite/granite interface is expected to reach 87°C. In about 3 years, most of bentonite would become fully saturated, but a narrow zone about 3 cm thick in the close vicinity of heater would remain unsaturated with a water saturation degree from 95% to 98% until 20 years.

The narrow unsaturated zone is where the most remarkable chemical changes are expected to occur, because of the continuous strong evaporation (referred as "evaporation zone" in this report). Ion concentrations are expected to increase up to 2–3 mol/kg due to the dissolution of smectite, precipitation of illite, anhydrite, quartz and cristobalite, very high exchange Na and Mg and very low exchange of Ca and K at the cation exchangeable sites. Modeling showed the development a chemically active area a little further away from the heater and right next to the narrow unsaturated zone. It is referred to as the "condensation zone," in which chemical changes are induced by continuous condensation of vapor that is generated in the "evaporation" zone. In this area, model showed a significant dilution of the bentonite pore water, dissolution of most aluminum-silicate minerals, except muscovite, very high exchange of Ca and K, and very low exchangeable Na and Mg at the cation exchangeable sites.

Measurements of chemical concentrations in bentonite in a narrow zone close to the heaters may become a challenging problem, when modules H3 and H4 in HotBENT are dismantled after 5 years of operation.

The 1D model sheds light on the potential chemical changes in MX-80 bentonite in HotBENT, but the hydraulic calculation is not entirely faithful to the condition of HotBENT, because of the existence of pedestal underneath the heater. Currently, a 2D cross-section model (Figure 7-34) is under development.

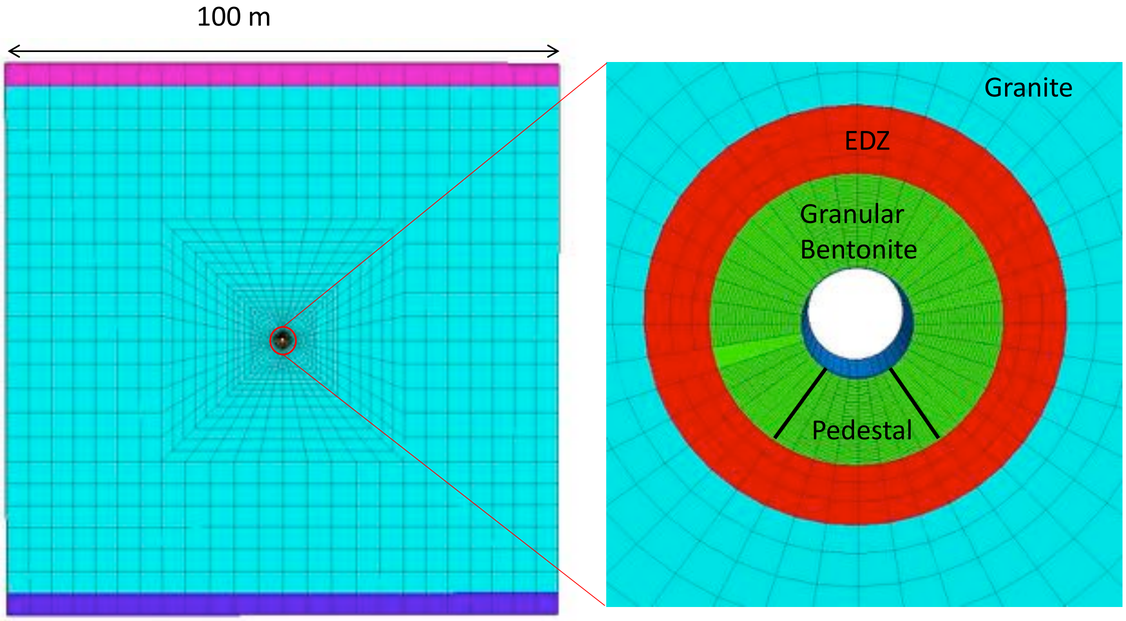

Figure 13-34. 2D cross-sectional mesh for the THC model.

In the remaining time of FY20 and FY21, we will continue making model predictions for the HotBENT, to help design a monitoring protocol and guide future measuring plan. Specifically, we will

- Develop a 1D THC model for BCV bentonite
- Extend the 1D axi-symmetrical THC model for MX-80 to THMC model
- Develop a 2D THMC model for MX-80 and BCV bentonites

14. HEATING AND HYDRATION COLUMN TEST ON BENTONITE

14.1 Introduction

This Chapter of the report details of laboratory-scale experimental results in support of the HotBENT field-scale experiment, which is designed to study THMC behavior during long-term heating of clay to 200°C. This effort is built upon previous efforts of long-term laboratory-scale clay heating experiments conducted at lower temperatures (Fernández and Villar, 2010; Gómez-Espina and Villar, 2010; Villar et al., 2008). This benchtop-scale laboratory experiment, HotBENT-Lab, provides a laboratory analog of the HotBENT field experiment to obtain a comprehensive set of characterization data and monitoring measurements, which are difficult to conduct at the field scale. The primary goal of this laboratory experiment is to obtain well-characterized datasets to (1) improve understanding of bentonite THMC processes under heating and hydration for model parameterization and benchmarking, (2) compare the HotBENT-Lab data with HotBENT field-scale test results, and (3) develop a prototype of an experimentation platform for future studies of bentonite under conditions of high temperature.

In support of this effort, and as described in the FY18–19 report, the HotBENT-Lab experiment a cylindrical pressure column was constructed to reproduce realistic heating and hydration conditions of the field-scale experiment. The design of the experimental apparatus and monitoring tools are based on estimated ranges of temperature and pressure, ability to accommodate characterization methods, i.e., X-ray CT and ERT, and safety. In order to better separate the effects of heating and hydration, two identical test columns are used, with the control column undergoing only hydration, and the experiment column experiencing both heating and hydration.

14.2 HotBENT-Lab Design

14.2.1 Column Design

A schematic diagram of the column design is shown in Figure 8-1, and was described in detail in the FY18–19 progress report. To review, clay was packed in an Aluminum 7071 pressure column designed to withstand a maximum working pressure of 1,000 psi (~6.9 MPa) at 200°C. The inner diameter (ID) of the column is 6.5 in., an outer diameter (OD) is 7.5 in., and a height is 18 in. A cartridge heater of 12 in. long and 0.25 in. OD is housed in a titanium shaft of 3/8 in. OD penetrating through the center of the column. Using MX-80 bentonite (Cetco), we packed two columns at an initial gravimetric water content of 15%, and a bulk dry and wet density of ~1.2 and 1.5 g/cm^3. A 0.25 in. thick layer of sand pack (12/20 mesh grain size) was installed between the clay column and the column wall as a high-permeability boundary. Hydration was achieved by flowing a synthetic brine (Table 14-1) continuously through the sand layer via a flow port at each of the end caps (Figure 14-2) via a syringe pump (ISCO pumps, 500 ml capacity).

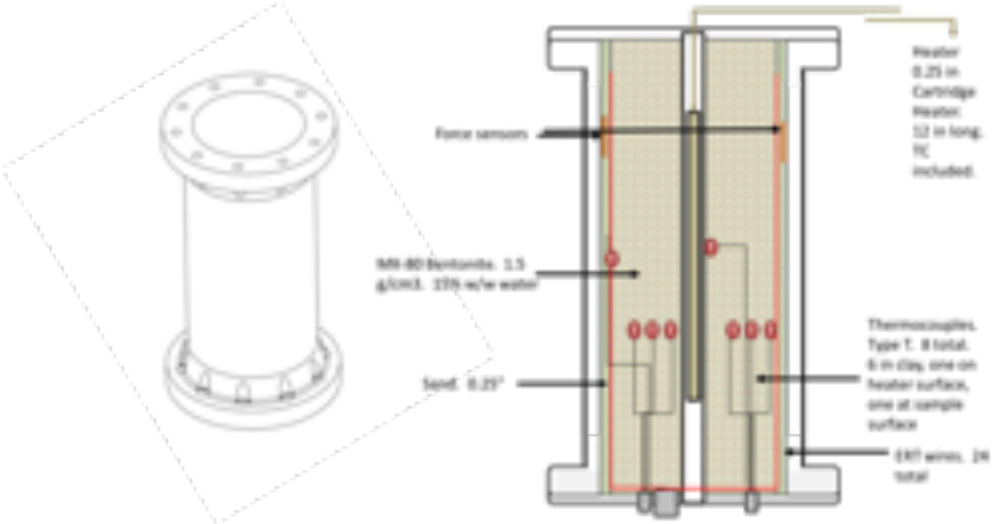

Figure 14-1. Schematic diagram of the column design for HotBENT-Lab experiment. Left: 3D rendering of the column exterior; right: interior design of the bentonite column, showing locations of sensors and the heater. The 1.5 g/cm^3 in the figure represents the bulk wet density of packed clay.

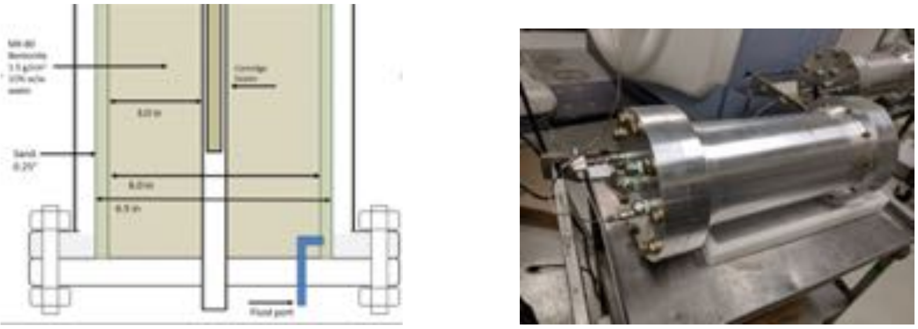

Figure 14-2. Schematic diagram showing the geometry of the different components of the test column (left) and an image of the completed column (right).

Table 14-1. Chemical composition of the artificial groundwater used to saturate the column.

Compound	Molarity (mM)	Ion	Molarity (mM)
$NaHCO_3$	0.798	Na	243
Na_2SO_4	104	C	0.881
NaCl	34.2	SO_4	104
KCl	1.23	Cl	68.3
$CaCl_2*2H_2O$	9.35	K	1.23
$MgCl_2*6H_2O$	7.06	Ca	9.46
CaF_2	0.109	Mg	7.06
$SrCl_2$	0.0831	F	0.218
Si	0.183	Si	0.183
—	—	Sr	0.0831

Source: Bradbury and Baeyens, 2003.

14.2.2 Characterization and Monitoring

To characterize the sample during the heating process, the techniques below were employed.

X-ray CT Imaging—X-ray CT images were collected to provide a 3D visualization of the density distribution in the column, which can be used to visualize density changes due to water saturation, clay swelling or structural deformation during the experiments. A GE Lightspeed 16 medical CT scanner was used to scan the experimental columns periodically throughout the experiment. Based on the column dimensions, the spatial resolution of the CT images is 400 × 400 × 625 µm. Because of the large weight of the experimental columns (~55 lbs), a cart/lift is used to move the columns onto and off the CT scanner table. Alignment of the scans is achieved via markings on the CT table and on the outside of the column, as well as key features in the CT images (high and low-density anomalies) inside the column during post processing. The post processing and analysis of the obtained CT scan images are conducted using self-developed codes in ImageJ software (Rasband, 1997–2020).

Continuous Temperature Monitoring—Temperature monitoring was conducted using thermocouples (type T) installed in the column. A total of 8 thermocouples were installed in each column between the heater shaft and the column wall. The distances of other thermocouples from the heater shaft were 0 (on the heater), 0.5, 1, 1.5 2, 2.5, 3, and 3.5 inches (the latter was on inside of the column wall). These feedthrough-coupled thermocouples, with an accuracy of 0.1°C, were acquired from Conax Technologies. The temperature readings from the thermocouples were recorded at 30s intervals with a data logger (Keithley 2701) throughout the experiment. In addition to the thermocouples inside the columns, additional temperature measurements were taken on the outside wall of the column.

Time Lapse ERT Monitoring—The ERT data acquisition is conducted using a DAS-1 ERT system (Multi-phase Technologies), combining electrodes used to send electrical current or measure electrical potential. Measurements were conducted using a pre-defined monitoring schedule (Figure 14-3). A total of ~2,600 data points were collected for a single resistivity survey in each column, which takes ~ 40 minutes. The voltage used for ERT data acquisition was targeted at < 50 V, but it varied depending on the resistivity of the tested clay and its hydration status during the experiment. Both the heated and unheated columns were configured to allow for sequential data collection during the same data acquisition event. Tri-hourly data collection is designed for the initial stage of the experiment, and this frequency was adjusted based on the observed rate of changes during the experiment and was was reduced for the longer term experiment. Data collection was autonomously carried out via a control software. Analysis of the post-experiment collected datasets included data quality assessment, inversion and visualization. The open software BERT (boundless ERT; Günther and Rücker, 2012) and Paraview (Kitware, NY) were used for data inversion and visualization.

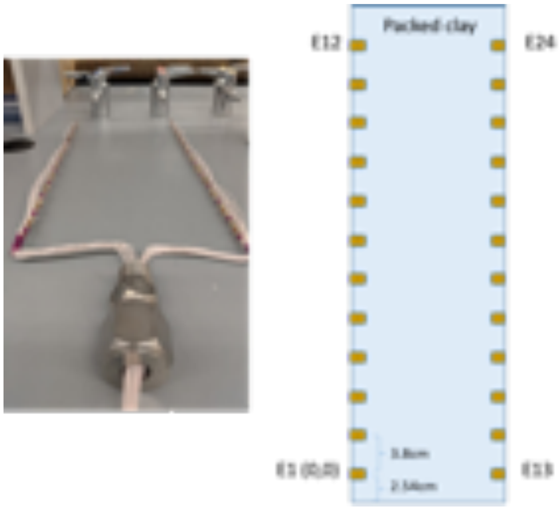

Figure 14-3. ERT monitoring design and a geometric layout of the column.

Influent and Effluent Fluid Geochemical Analysis—The fluid (Table 14-1) used to hydrate the bentonite was sampled and analyzed to monitor geochemical changes in the bentonite system. Changes in water chemistry are being used to understand the geochemical processes in the column due to evaporation, dilution, diffusion and other transformations. Samples collected from the experiments were filtered, acidified, when necessary, prepared and analyzed using the standard ion chromatography (IC) and inductively coupled plasmas – mass spectrometry (ICP-MS) protocols.

Pre- and Postexperiment Clay Analysis following a Gradient from the Heater—The post-experiment clay analysis data will be compared with those from the pre-experiment clay samples to understand changes in physical, chemical and hydrological characteristics of bentonite due to hydration and heating, including gravimetric water content analysis and mineralogical analysis with X-ray Diffractometry (XRD). Preliminary measurements have been made on the pre-experiment clay and more extensive tests are planned when the experiment is dismantled.

Lab Petrophysical Studies—In addition to the heating and hydration experiments conducted in the pressure column, parallel experiments with non-pressurized and smaller columns were set up for petrophysical model studies. The main goal of such studies is to determine petrophysical correlations that can be used to link indirect geophysical measurements to parameters of interests. For instance, resistivity-moisture content correlations can be determined from the results of such studies, so the electrical resistivity map acquired from the pressure columns can be translated into a moisture distribution map. Such studies can also be used to acquire water content-density calibration datasets for CT images as well as for porosity- permeability correlation studies.

14.3 Experimental Operation

Packing and startup of the system occurred in June 2019, and hydration and heating have been continuous since inception. Two columns have been continuously operated, a heated and unheated column. After the baseline scan and testing other components, hydration and heating were started. A schematic diagram of the experimental setup with the column and supporting components is shown in Figure 14-4.

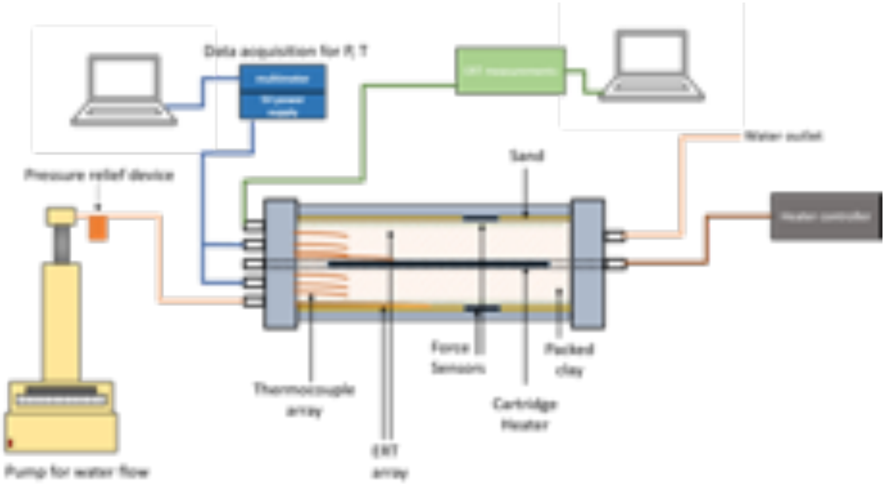

Figure 14-4. Schematic diagram of the entire experimental setup including the column, flow control, and sensors. The ID of the column is 6.5 in., the OD is 7.5 in., and the height is 18 in.

14.4 Preliminary Results

14.4.1 X-ray CT

14.4.1.1 Baseline CT

The baseline CT image provides information on the clay and sand packing, and the layout the column sensors. The cross-sectional CT images of the Column 1 (C1), which was used for the heating and a hydration experiment, is shown in Figure 14-5. The color scale in the images is CT numbers that are proportional to the bulk density. In general, the higher numbers (i.e., brighter color) represent higher density. As shown on the image, the bright yellow color on the column perimeter represents the Al pressure column. The white shining spots are either the copper electrodes, the copper wires connecting the electrodes, or the metal in the pressure sensors. Blue color represents low-density features, which include the interior open space of the heater shaft, penetrating through the middle of the bentonite column, and some lower density features created during packing. The brownish color between the column and the clay pack represents the sand layer packed into the column with the purpose to evenly saturate the bentonite. Visible strikes running horizontally across the column are resulting from the dry packing process. Overall, the density variability as the artifact of packing is generally very small. We selected a representative 2D image (marked by the yellow dotted line in Figure 14-5) to discuss the clay hydration subject to heating in Section 14.4.2.

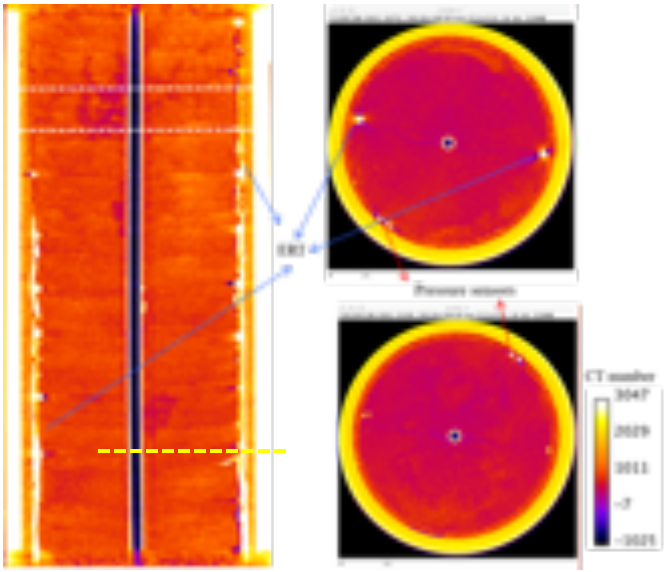

Figure 14-5. Cross sectional CT images of Column 1 that is used for a heating and hydration experiment. The two circular cross sections are from locations marked with the dashed lines on the vertical cross section image on the left. The yellow dashed line indicates locations of the 2D image selected in Figure 14-11.

The cross-sectional CT images of Column 2 (C2), which was subject to hydration only, are shown in Figure 14-6, which show similar density features in this column, but some visible variances can be observed as well. Noticeably, some local low-density features on the top of the column are visible resulting from uneven packing. In addition, a seemingly slightly larger lateral heterogeneity exists, which is also related to packing. In Section 14.4.2, we will discuss two representative 2D images (marked by the yellow dotted line in Figure 14-6) of the clay that was subject to hydration only.

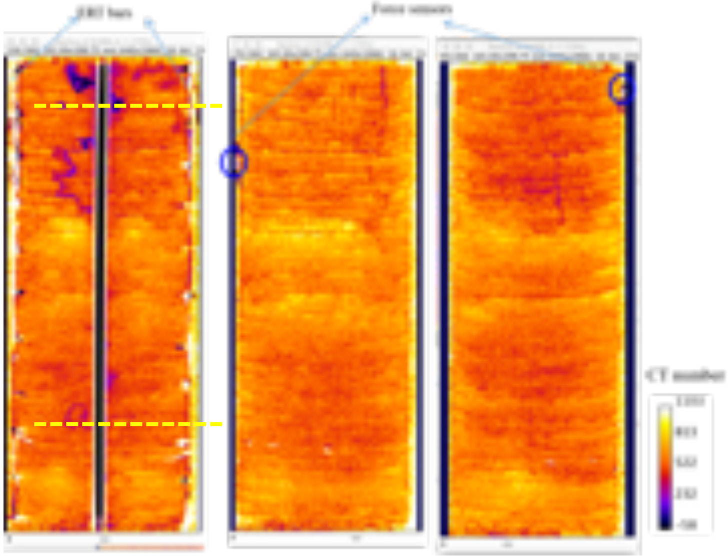

Figure 14-6. Cross sectional CT images of Column 2 that are used for hydration only experiment as the control. The three different cross sections represent different slices at different depths in the axis-normal direction. The two yellow dotted lines indicate locations of the two 2D image selected for the time series presentation in Figure 14-10.

A 3D rendering of C1 is shown in Figure 14-7, and a similar image for C2 is shown in Figure 14-8, with marked key features.

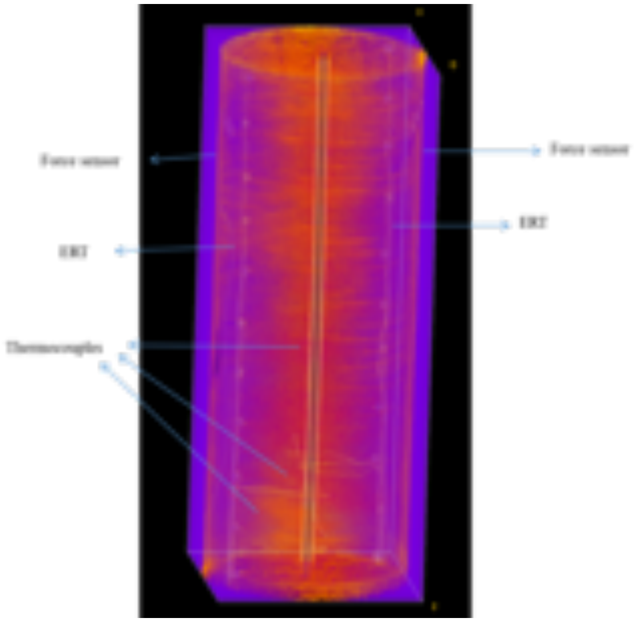

Figure 14-7. 3D CT image of C1 with key instrumentation: thermocouples, ERT and force sensors, and sensor wires.

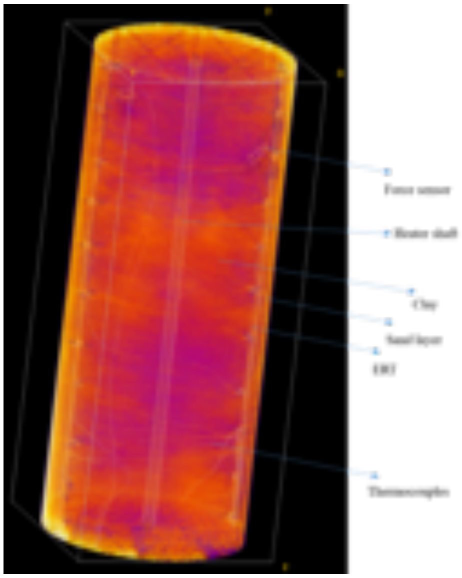

Figure 14-8. 3D CT image of C2 with key features indicated.

Overall, the CT images provide well-defined visualization of the column density structure. This can be used to determine precise locations of the sensors and boundaries in the sample column, which are needed for interpreting and modeling the behavior of the system as experimental data are being collected. Additionally, the images can be used to understand changes in density and structure during clay hydration and heating. We built the relationship between CT number vs. density by scanning columns compacted with bentonite clay of different bulk wet density. Figure 14-9 represents calibration curve, which was used to interpret the correlation between the CT number and the clay density for both of the heated and non-heated columns. It should be also noted that the clay density is dependent on the bulk dry density and water content, i.e., the value increases with increasing water content and clay dry density. Also noted that no hysteretic or dynamic wetting-drying processes were considered in Figure 14-9 as it was built on static conditions with pre-packed columns.

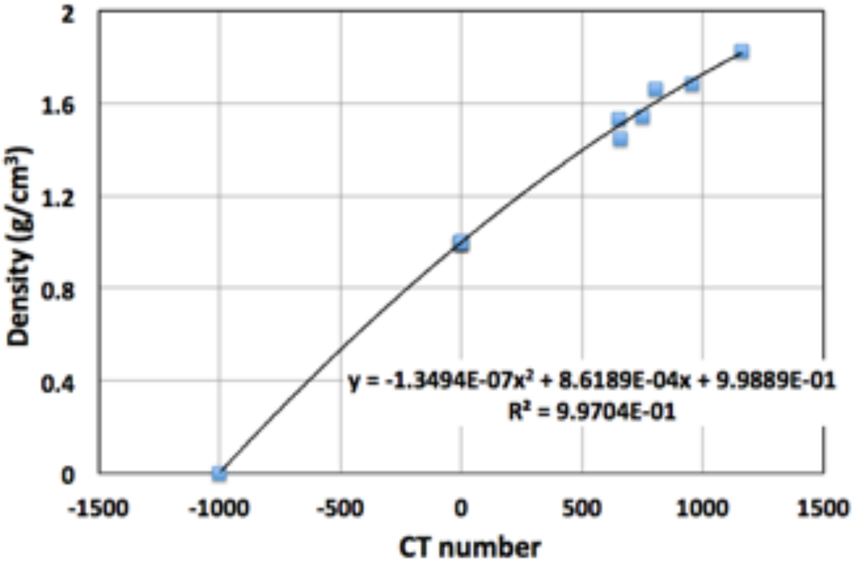

Figure 14-9. The calibration curve used to interpret the correlation between the CT value and density.

We have kept running the experiments and monitoring the density distributions and temporal changes in both columns through frequent CT scans for 255 days. In the following sections, we will present the 3D density map of Column 2 subject to hydration, and column 1 subject to both hydration and heating. Comparison will focus on (1) the temporal changes of 2D and 3D clay density distributions due to water intrusion, swelling and structural deformation during hydration in the non-heated column, and hydration and heating in the heated column, (2) the swelling and deformation of clay subject to hydration and heating by image-tracking the transit movement of the thermocouple sensors, and (3) the density averaged over the entire clay column and its changes as a function of time.

14.4.1.2 2D Hydration

Figure 14-10 depicts examples of 2D images of CT density map during the first 8 days, when Column 2 was subjected to hydration. The sub-image at T = 0 day shows the initial density map when bentonite clay was packed with a CT density of 1.43 g/cm^3, close to the wet density of 1.46 g/cm^3 measured from the wet clay mass and column volume. The peripheral sand layer has a higher density of 1.67 g/cm^3, presenting a clear boundary (marked by the black dotted line) to the packed clay. The two bright spots of high CT density are the ERT arrays near the sand-clay boundary, while the one in the center indicates the stainless-steel shaft with the heater inserted. We also observe a fracture with a low apparent density (see the blue arrow) due to the uneven packing.

At T=1 day, we first injected gas CO_2 into both columns, followed by brine injection to fully saturate the sand layer. After that, brine injection was kept constant at a rate of 0.11 mL/min under 120 psi. From the 2D CT images, once brine was introduced into the column at T=1 day, the density of the sand layer increased to 1.85 g/cm^3. From T=1 day to 2 days, there exists a density segmentation between the top and bottom portions of the sand due to gravity. After that, we were able to keep a constant density boundary (i.e., a constant water saturation boundary) in the sand layer via maintaining a constant water injection rate (see the density distribution at T=4 and 8 days). The fluid pressure was also maintained constant and monitored by pressure transducers at the inlet and outlet ends. The white arrows in Figure 14-10(A) and (B) indicate the brine intrusion front, based on the CT density difference. Figure 14-10(C) shows the corresponding changes in the average density vs. radial distance from the center shaft as a function of time. At T = 1 and 2 days, we observe the increase in CT density near the clay-sand boundary due to brine intrusion. At T = 4 days, a peak CT density occurred 54 mm away from the center shaft (see Figure 14-10(A)), with a continuous density reduction at locations towards the shaft and the clay-sand boundary. The peak density propagates further into the clay, and at T = 8 days, it reaches 41 mm away from the shaft. The density reduction near the clay-sand boundary may be attributed to clay swelling subject to hydration. At this point (T=8 days), CT density was affected by both water content and solid migration/displacement. This clay swelling may also compact the interior clay and contribute to the density increase to the peak value in addition to water intrusion. The average clay density, shown in this 2D image, increased from 1.43 g/cm^3 at T=0 day to 1.61 g/cm^3 at T=8 days due to hydration.

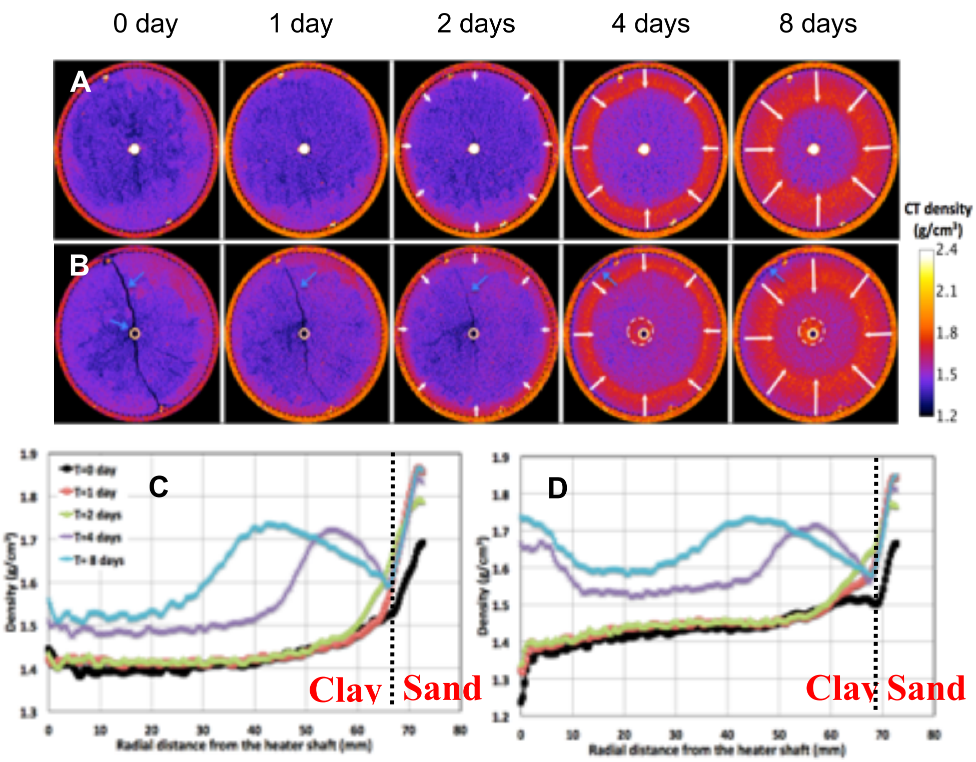

Figure 14-10. (A) 2D images showing the typical hydration process in the nonheated column. (B) 2D images showing the impact of an initial fracture on brine hydration in the non-heated column. (C) and (D) are corresponding average density vs. radial distance from the heater shaft for (A) and (B). The black dotted lines represent the clay-sand boundaries, the white dashed lines indicate the density increase around the heater shaft. The white and blue arrows show the hydration direction and sealing of fracture and boundary gaps due to clay swelling. The 2D images represent locations marked by the yellow dashed lines in Figure 14-6.

Figure 14-10(B) and (D) also demonstrate the impact of initial clay fracture on the 2D hydration process. After brine was injected into the sand layer at T=1 day, the fracture across the center shaft gradually self-sealed due to clay swelling. The fracture cannot be observed at T=4 days at the CT resolution. We also observe in the figure that clay swells at the sand-clay boundary and fills the low-density gap (see the blue arrow at T=4 and 8 days). After that, the sand density remains constant at 1.84 g/cm^3. The graph of the average density vs. distance to the heater shaft in Figure 14-10(D) indicates a density increase close to the shaft at T=4 and 8 days, after the fracture is sealed. More detailed images and a discussion will be presented in Section 14.4.1.4. In this case, the average density increased from 1.43 g/cm^3 at T=0 day to 1.65 g/cm^3 at T=8 days, higher than the average density increase in the non-fractured case.

14.4.1.3 2D Heating and Hydration

After we injected brine in the sand layer at T= 1 day, we turned on the heater in Column 1 at T= 2 days. Figure 14-11(A) shows the CT density at T= 2 days after heating, when the temperature of clay on the heater shaft (monitored by a pre-emplaced thermocouple) was increased to 150°C. The temperature was then gradually increased to 175°C and 200°C at T=4 and 8 days, and kept constant afterward. Similar closure of fracture in the clay column and gap at the clay-sand boundary (see the blue arrows) indicate the swelling of clay subject to hydration. After increasing the heater temperature at T=2 days, a sharp drop of density occurred around the heater shaft shown in Figure 14-11(A) and (B). Meanwhile, the clay density increased near the clay-sand boundary due to hydration. Figure 14-11(C) shows the density reduction close to the sand-clay boundary at T=4 days, as well as the density peak at 45.5 mm from the heater shaft, indicating the swelling of clay occurred after hydration initiated from the sand-clay boundary. Comparing the peak density locations shown in the non-heated column (Figure 14-10(B) and (D)), we may infer a faster hydration process in clay subject to heating from the center. At T=4 and 8 days, the clay density around to the heater shaft (<15 mm) rebounded quickly to ~1.40 g/cm^3, similar to the density at initial conditions at T=0 day, i.e., prior to hydration and heating. It should be noted that this density rebound occurred before the hydration front arrived. Additional interpretation and analysis of the results of investigations will be given in Section 14.4.1.6.

Figure 14-11(C) presents the average CT density of clay over the 2D image in the three cases (Figure 14-10(A),(B) and Figure 14-11(A)), and their changes as a function of time. The overall density values increased with time after hydration. Comparison of the three cases indicates the highest CT density near the fracture, while heating (up to 200°C) led to the lowest density. A better understanding of the preferential brine flow path and heating hydration processes needs a detailed analysis of 3D images showing the dynamic and spatial CT density changes.

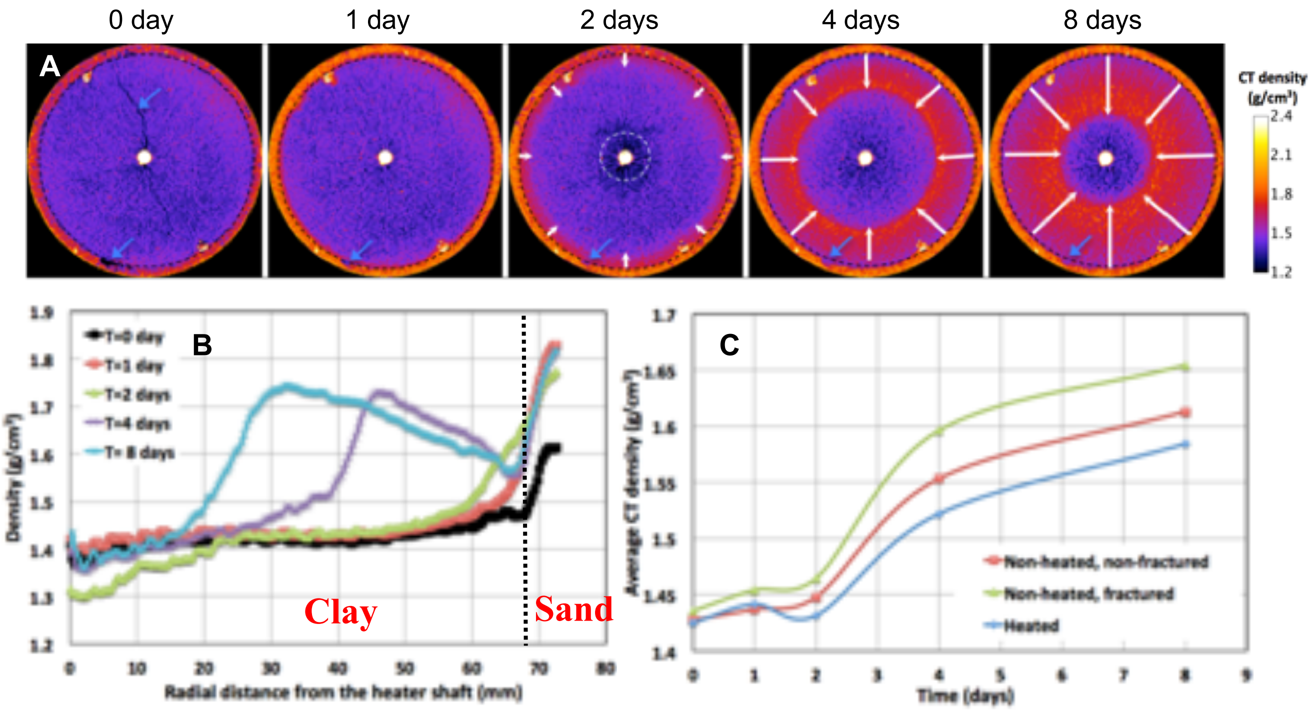

Figure 14-11. (A) 2D images showing the typical processes of heating and hydration in Column 1. (B) the corresponding average density vs. radial distance from the heater shaft. (C) The average density vs. time for the three cases. The black dotted lines represent the clay-sand boundaries. The white and blue arrows show the hydration direction and sealing of fracture due to clay swelling.

14.4.1.4 3D Hydration

Figure 14-12 depicts the 3D orthogonal view of CT density distribution and temporal changes in the non-heated column. The color bar bounds density changes from 1.2 to 2.4 g/cm^3, and a brighter color indicates a higher density. The image at T = 0 day shows the initial conditions and density distribution after packing, including the heater and heater shaft in the center (white color), the sand layer surrounding the clay (orange color), the ERT bars emplaced at the sand-clay boundary (white line in the top slice, the other ERT bar was emplaced in the opposite position that cannot be directly seen in the figure), and clay packed between the sand layer and the central shaft (blue to orange color). The density variations, bedding layers and the dark fracture patches (bounded by the white dotted lines) close to one end of the column are attributed to uneven packing. The uneven packing, especially the fracture patches, affect the hydration process and induce preferential brine flow pathway. The CT density of clay averaged over the entire column is 1.46 g/cm^3, similar to the measured value of 1.44 g/cm^3 by weighing the clay mass used for packing and the column volume.

At T = 1 day, we saturated the sand layer with brine and kept flowing at 0.11 mL/min under 120 psi. Hydration was then initiated and indicated by the changes of clay density. At T = 8 days in Figure 14-12, the increase of CT density in the column indicates the considerable hydration. The density distribution, however, is not uniform. As shown in the figure, the high-density front represents the hydration front, which has advanced halfway towards the center shaft. We also observe great density reduction at the sand-clay boundary relative to the hydration front. This can be attributed to the more considerable reduction in clay dry density by swelling after hydration. The clay swelling initiated at the sand-clay boundary may push and compact the interior clay, and contribute to the high-density hydration front. We also show at T = 8 days the seal of the fracture patches by swelling, which hinders the propagation of hydration along the center shaft (see the magnified image, Figure 14-12). The clay swelling meanwhile smoothens the density variations and impedes preferential flow of brine from the surround sand layer. All these are in favor of retardation of radionuclide and securing the spent nuclear fuel and waste disposal. At T = 255 days, the overall density distribution become more uniform.

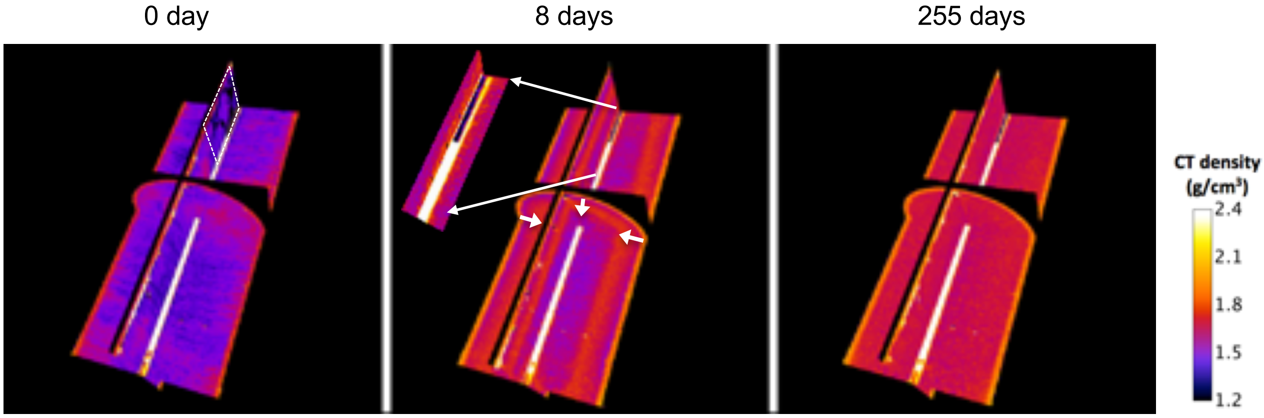

Figure 14-12. The 3D clay density maps showing the spatial and temporal variations of clay density in the non-heated column. The sub-image at T = 0 day shows the initial condition after packing, with the uneven-packing induced fracture marked by the white dotted box. The white arrows at T = 8 days depict the continuous hydration from the surrounding sand layer, while the magnified image at T = 8 days presents the preferential water intrusion along the center shaft at early time.

The 3D images indicate radial symmetry of hydration distribution from the sand layer to the center shaft. We thus applied the radially averaged images to show the 3D hydration process. For each CT scan, the obtained CT image stack was first orthogonally reconstructed by rotating a line at 360° around the center shaft. Then, an image was obtained by averaging over the 360° radially reconstructed images, and the CT number was converted into the density using the calibration curve shown by Figure 14-13.

Figure 14-13 shows the time-lapse images of the non-heated column subject to clay hydration from the sand layer up to 255 days. Note that each sub-image was radially averaged, and the density profile along a single line (e.g., the white dotted line at *t*=255 days) represents the average density vs. radial distance from the heater shaft, as shown in Figure 14-13(B). Figure 14-13(A) clearly shows that the hydration was initiated from the peripheral sand layer and the top and bottom boundaries, where brine invaded the clay column from gaps between the column end caps. The hydration along the center shaft, however, stopped at T=8 days, because of clay swelling and sealing of the gaps after hydration (also see the 3D images in Figure 14-12). The continuous propagation of hydration occurred from the peripheral sand layer, as indicated by the temporal changes of the peak density in Figure 14-13(B). At T=33 days, the hydration front approached the center shaft. After that, the clay density increased at a location close to the shaft, along with the density reduction in the middle part (~40 cm from the shaft), resulting in a more uniform density distribution in the entire column.

The clay swelling and density reduction along the sand-clay boundary can also be observed at early times (T=4 and 8 days) in Figure 14-13(A) and (B). The swelling of clay at the boundary may compact the interior clay, resulting in the sharp density increase ahead of the hydration front. For example, in Figure 14-13(B) and at T=4 days, at the distance of <40 mm from the center shaft, the density of clay increased by ~0.05 g/cm^3, when compared to the density at T=2 days. At T=8 days, the density increased another 0.03 g/cm^3 ahead of the hydration front (<20 mm from the center shaft). As hydration continued and propagated to the center, the compaction weakened, the density at the sand-clay boundary gradually rebounded, along with the density reduction in the middle part. These induced flattening of the density profile along the white dotted line perpendicular to the center shaft, and the uniform density distribution in the entire column. The magnified CT image shown in Figure 14-13(A) depicts a relatively uniform density distribution close to the center shaft, with thermocouple sensors attached on the shaft shown in bright spots. The frequent X-ray CT images and changes in clay density represent the spatial and temporal dependent processes of increasing saturation and clay swelling due to hydration. At T=255 days, the column averaged clay density was stable at 1.68 g/cm^3, 0.21g/cm^3 higher than the initial value before hydration.

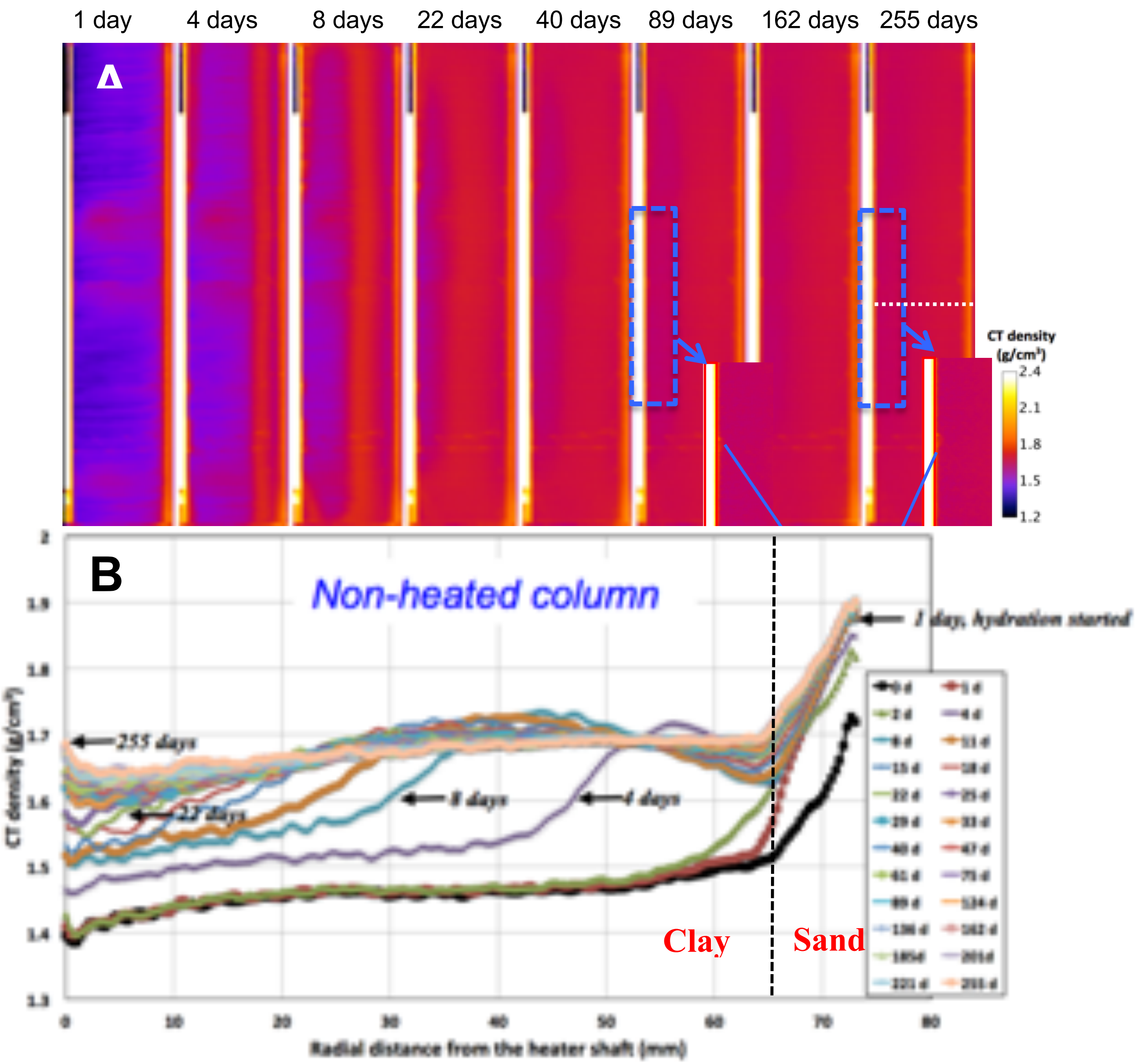

Figure 14-13. (A) The radially averaged density map and changes with time for the non-heated column subject to hydration only. (B) The average density vs. radial distance from the heater shaft along the white dotted line in (A). The magnified image in (A) (bounded by the blue dotted box) showing the density distribution close to the center shaft at T=89 and 255 days. The blue arrows in (A) mark the bright spot of thermocouple sensors.

14.4.1.5 3D Heating Hydration

In the heated column at T=1 day, we also saturated the surrounding sand layer with brine and kept it flowing at 0.11 mL/min under 120 psi. At T=2 days, we turned on the heater and kept the temperature of clay on the heater shaft constant at 200°C since T=8 days. Figure 14-14 depicts the 3D density distribution and changes with time in the heated column, while Figure 14-15 shows the radially averaged density map (A) and the average density profile vs. radial distance from the heater shaft (B). Image at

T=0 day presents an initial condition similar to that in the non-heated column. The column averaged CT density was 1.44 g/cm^3, close to the measured value of 1.41 g/cm^3 by weighting the packed clay mass. The image also presents the patterned layers and density variations, as well as the fracture close to one end of the column. At T=8 days, we observe similar (1) swelling of clay and sealing of the fracture after hydration, (2) density reduction at the sand-clay boundary due to clay swelling, and (3) clay density increase ahead of the hydration due to compaction.

Differing from the non-heated column, however, Figure 14-14 and Figure 14-15(A) at T=8 days present a dry-out zone of a lower density close to the heater shaft. Because of heating, the average density within this dry-out zone was 1.32, 1.38, and 1.40 g/cm^3 at T=2, 4, and 8 days, respectively, lower than the values of 1.43, 1.52 and 1.56 g/cm^3 within the same region of the non-heated column. The heating, thus, induced a larger density gradient (thus, larger gradient of water content) and vapor outward transport (from the innermost heating zone) and condensation in the middle part as temperature decreased (also see Figure 14-15(B)). The hydration front approached the location 5 mm away from the middle shaft at T=25 days, after that a dry-out zone sustained. At T=255 days, the dry-out zone was confined in location <5mm away from the heater shaft, while the overall density distribution in the column became more uniform.

Within the dry-out zone, we observe bright, high-density deposition on the heater shaft, as shown by the magnified image in Figure 14-14 at T=255 days. More frequent CT images (Figure 14-15(A) and (B)) indicate the deposition initiated at T=75 days (the sharp increase in the CT density in the dry-out zone in Figure 14-15(B)), followed by the quick increase to 1.83 g/cm^3 until T=124 days. After that, the density increased slowly and stabilized at 1.89 g/cm^3 at T=255 days. The deposition also occurred along the heater shaft, as shown in Figure 14-15(A). We assume the high-density deposition was caused by mineral precipitation as water vaporization in the dry-out zone and continuous transport of dissolved mineral species with hydration to the dry-out zone. We will dismantle the column and collect the pore fluid and clay samples for more detailed chemical analysis.

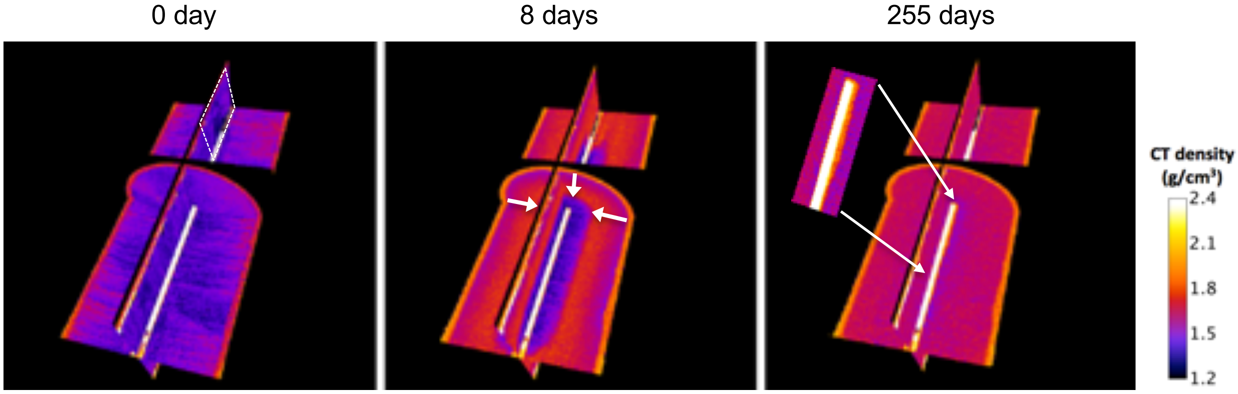

Figure 14-14. The 3D clay density map and temporal variations in the heated column. The sub-image at T=0 day shows the initial condition after packing, with the uneven-packing induced fracture marked by the white dotted box. The white arrows at T=8 days depict the continuous hydration from the surrounding sand layer. The magnified image at T=255 days presents the bright high-density deposition on the heater shaft subject to heating and water vaporization.

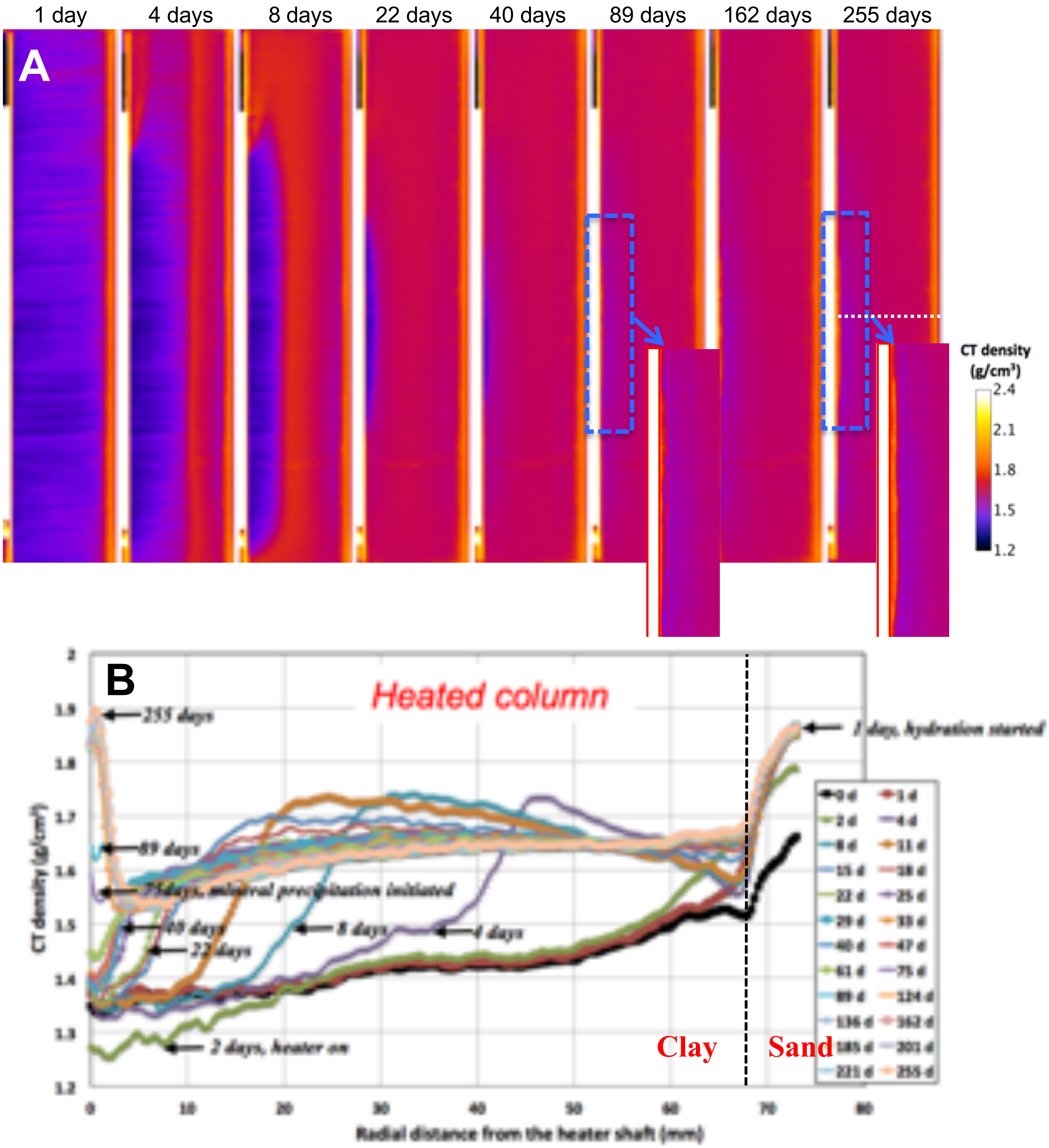

Figure 14-15. (A) The radially averaged density map and changes with time for the heated column subject to heating and hydration. (B) is the average density profile vs. radial distance from the heater shaft along the white dotted line in (A). The magnified image (bounded by the blue dotted box in (A)) shows the density distribution and bright high-density deposition on the heater shaft at T=89 and 255 days.

14.4.1.6 Deformation Subject to Hydration

We have shown in previous images potential clay swelling and compaction subject to hydration and heating through the dynamic changes of clay CT density. The clay swelling and compaction subject to hydration were further investigated by the transit movement of the thermocouple sensors (induced by the deformation of surrounding clay) through frequent CT images. We selected 2D CT images that present the bright spots representing thermocouple sensors, and tracked their distance to the central shaft and monitor the changes as a function of time. Figure 14-16(A) depicts the 2D CT image selected from the non-heated column at different times. The white arrows mark the initial position of the exterior thermocouple before hydration, which was 48 mm away from the center shaft. The T=1day image shows the surrounding sand layer saturated with brine (orange color), the packed clay (purple color), and the brightly white shaft at the center, as well as the ERT bars emplaced at the sand-clay boundary.

As shown in Figure 14-16(A), as the high-density hydration front propagated into the clay column at T=4 days, the considerable clay swelling at the sand-clay boundary induced a significant density reduction. Meanwhile, the thermocouple was pushed towards the center shaft along with the compaction of surrounding clay (see the offset of the bright spot relative to the white arrow). At T= 8 days, the offset reached maximum as the hydration front approached the thermocouple. After that, as the hydration continued and the front passed the thermocouple, the thermocouple was pushed back slowly to its original location, as indicated by the reduced offsets between the bright spot and the white arrow (see the images at T=8 days and 255 days).

To better illustrate the process, we measured the distance between the center shaft and the thermocouple, and plotted in Figure 14-16(B) the changes as a function of time (marked by the red dotted line). The displacement was calculated by subtracting the initial distance between the thermocouple sensor and the center shaft (thus the displacement at T=0 day was normalized as 0). We define the negative displacement when the thermocouple was pushed toward the center shaft, and positive displacement when the thermocouple was pushed away from the center shaft relative to its initial position. Figure 14-16(B) also present the changes in the clay CT density around the thermocouple (the blue curve), with the density peak representing the hydration front. As shown in the figure, before the hydration front arrived at T= 8 days, the displacement continuously decreased from 0 mm to the minimum value at −2.3 mm. Most clay is compacted by the strong hydration and swelling along the sand-clay boundary. After the hydration front arrived, the deformation gradually rebounded back along with the clay swelling at the surrounding clay and more interior locations closer to the center shaft. This might have also caused the slow decrease in the clay CT density around the thermocouple. At T=255 days, the CT density and displacement were relatively stable at 1.68 g/cm^3 and −0.9 mm. These indicate the coupled processes of hydration and clay swelling, as well as their spatial and temporal dependent behaviors.

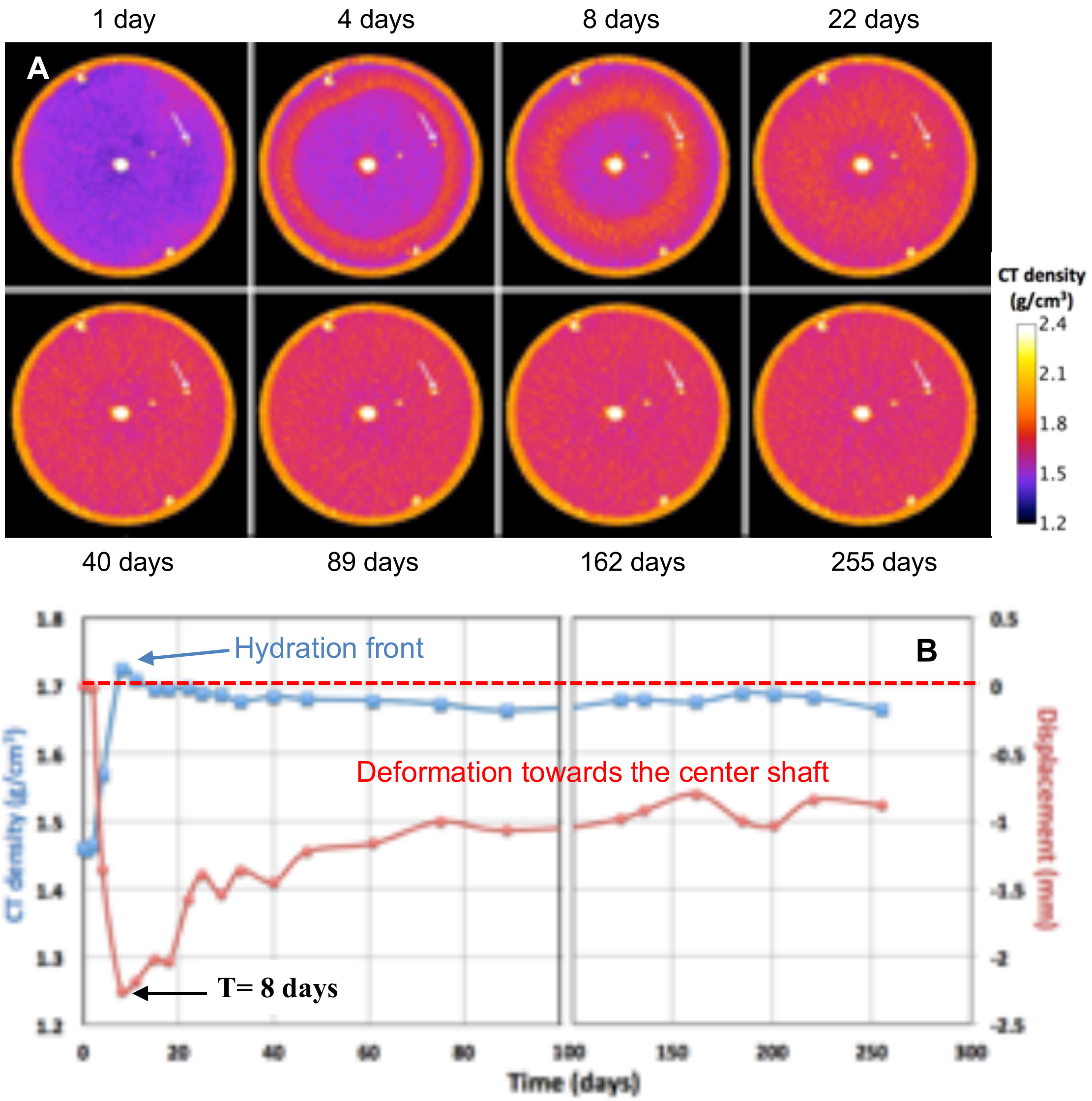

Figure 14-16. (A) The time-lapse 2D CT images showing the transit movement of the thermocouple sensor along with the dynamic CT density changes of clay in the non-heated column. (B) Comparison of the displacement of the thermocouple sensor vs. surrounding clay CT density. The white arrows in (A) mark the initial position of the thermocouple sensor.

14.4.1.7 Deformation Subject to Heating and Hydration

Figure 14-17(A) presents the 2D time-lapse CT images and transit movement of the thermocouple (originally 11 mm from the heater shaft) in the heated column. We turned the heater on at T=2 days and maintained the temperature on the heater shaft constant at 200°C since T=8 days. Differing from the observations in the non-heated column, the inward movement of the thermocouple at early time (1–8 days) was followed by the backward movement to its original location at T=22 days. After that, the thermocouple sensor continuously moved outward to the sand-clay boundary and maintained a constant offset at T=255 days. The deformation and clay density around the thermocouple further quantify the coupled processes subject to heating and hydration. In Figure 14-17(B), as we turned the heater on at T=2 days, the local clay density sharply reduced from the initial value of 1.40 g/cm^3 to 1.32 g/cm^3 due to water vaporization, followed by a quick rebound to 1.41 g/cm^3 at T=4 days. The continuous reduction in the displacement also confirms that most of the interior clay is dominated by compaction after the hydration, and clay swelling initiate at the sand-clay boundary. At T= 8 days, the deformation reached minimum values at −1.1 mm toward the heater shaft. It should be noted that, compared to that in the non-heated column, the local clay subject to heating and compaction is higher in its bulk dry density, thus obtained higher swelling potential once in contact with brine. When the hydration front arrived, the local and more interior clay swelled, and continuously pushed the thermocouple sensor back to its initial position at T=22 days. After that, the initially drier and tighter clay continued to swell and moved the thermocouple further away from its initial position by 1 mm at T=255 days. Note the temperature of the thermocouple increased with time and kept constant at 140°C after T=89 days, lower than the water boiling temperature of 175°C under 120 psi. This enabled the hydration and swelling of clay to occur. The clay subject to heating and hydration shows a more considerable and complex process of deformation.

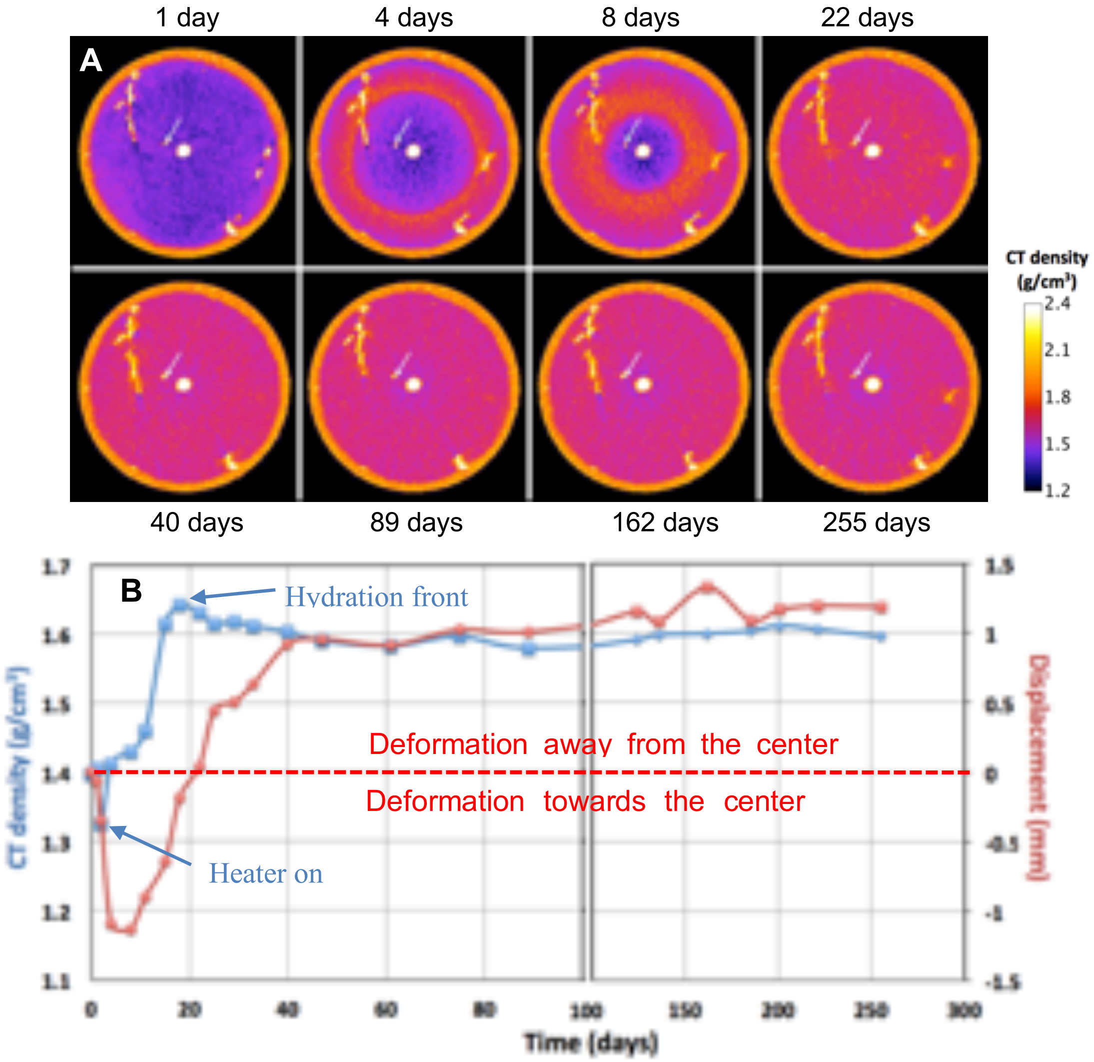

Figure 14-17. (A) The time-lapse 2D CT images showing the transit movement of the thermocouple sensor along with the dynamic CT density changes of clay in the heated column. (B) Comparison of the displacement of the thermocouple sensor vs. surrounding clay CT density. The white arrows in (A) mark the initial position of the thermocouple sensor.

14.4.1.8 Deformation at Different Locations

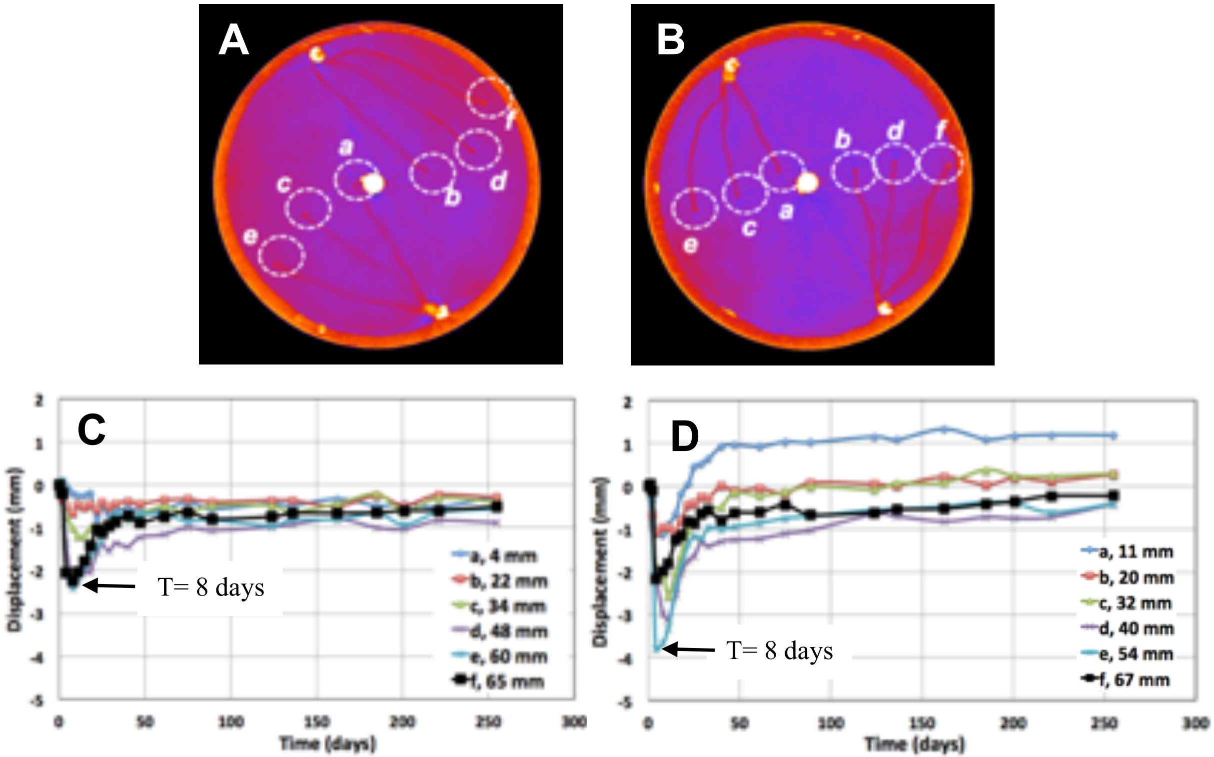

Figure 14-18. The six thermocouple sensors that are used for tracking clay deformation at different locations in the non-heated (A) and heated (B). (C) and (D) present the displacement changes relative to their original positions vs. time for the six thermocouple sensors. The legend marks the initial position of each thermocouple relative to the center shaft.

We investigated the spatially variable deformations of clay by tracking all six thermocouple sensors emplaced in both of the non-heated and heated columns. Figure 14-18(A) and (B) present the locations of each thermocouple sensor in the non-heated (A) and heated (B) columns. Figure 14-18(C) and (D) depict their displacements and variations as a function of time up to 255 days. In both columns, thermocouple *a* was closest to the center shaft, while thermocouple *f* was closest to the sand-clay boundary. Thermocouples *b, c, d, e* located 20 to 60 mm away from the center shaft. In the non-heated column, as shown in Figure 14-18(A) and (C), all six thermocouples showed similar trending of displacement variations vs. time. For instance, at early time (1–8 days), all thermocouples along with their surrounding clay were compacted toward the center shaft with continuous decrease in displacement. Spatially, the displacement decreased from exterior to interior clay, where deformation was confined by the rigid boundary at the center. After that, as hydration propagates to the center, all the thermocouples were pushed backward to their initial positions. The displacements for all the thermocouples thus gradually rebounded and kept constant at −0.4 to −0.9 mm relative to their initial positions.

Figure 14-18(B) and (D) show the initial locations of the six thermocouple sensors in the heated column, and their displacement changes vs. time. Comparing to the non-heated column in Figure 14-18(C), the clay presents more considerable deformation subject to heating and hydration. The deformation could be both inward (negative displacement values) and outward (positive displacement values), depending on the location and time. At early times (1–8 days), all thermocouples along with their surrounding clay were similarly compacted toward the heater shaft by swelling at the sand-clay boundary. The displacement values, however, ranged from −1.0 to −3.8 mm, showing larger compaction than that in the non-heated column at −0.2 to −2.4 mm. This indicates larger compaction induced by hydration and clay swelling at the sand-clay boundary when heating at the center. Note the clay CT density (1.58 g/cm^3) at the clay-sand boundary (marked by the black dotted line) at T=8 days in the heated column is lower than that in the non-heated column (1.63 g/cm^3). While more water was sucked into the column by larger water saturation gradient, the reduced clay CT density indicates larger reduction in clay dry density after more considerable swelling. It should be also noted that for thermocouple *f*, the compaction and displacement were limited by the clay available for swelling as its location was too close to the clay-sand boundary.

Thermocouple *a* was discussed in details in the previous section. While the other thermocouples more or less recovered to their initial positions, the displacement of thermocouple *a* was affected by larger heating-induced swelling, as it was closest to the clay dry-out zone. It can be inferred that more interior clay would be drier as temperature increases beyond water boiling point. More considerable clay swelling at some locations (e.g., around the thermocouple *a*) of favorable temperature and water content (i.e., the local temperature is high enough to vaporize pore brine but still below water boiling temperature so that the subsequent hydration is allowed) may hinder fracture development at the shaft-clay interface by heating, thus is in favor of securing the spent nuclear fuel and waste disposal.

14.4.1.9 Average Density Change of the Clay Columns

Through the frequent X-ray CT imaging, we are able to calculate the average CT clay density over the entire clay column, and show in Figure 14-19 the density increase after hydration in Column 2 (the non-heated column) and in Column 1 (the heated column) subject to heating and hydration. In the non-heated column, the clay density increased quickly once hydration started and at T= 22 days, the average density was 1.68 g/cm^3, increased by 0.21 g/cm^3, when compared to the initial condition. After that, the value kept relatively constant until T=255 days. By comparison and in the heated column, the density increased faster and at T= 15 days, the density increase reached the peak value of 0.21 g/cm^3. After that, clay density decreased slowly, but was 0.2 g/cm^3 higher than the initial one, and finally stabilized at 1.64 g/cm^3 at T= 255 days. Overall, Figure 14-19 presents a faster hydration of clay and density increase subject to heating and hydration, followed by a slow density reduction and finally stabilized. The observed bright deposition on the heater shaft after 75 days in the heated column indicates potential mineral precipitations and chemical interactions (e.g., indicated by Section 14.4.2), and coupled THMC processes of bentonite clay subject to heating and hydrations. As we discussed earlier, these processes are spatial and temporal dependent. We will dismantle both columns and collecte clay and pore water samples for detailed mineralogical and chemical analysis. These will help in understanding the complex processes and provide a complete dataset for modeling the behavior of bentonite based EBS system, which is key to the evaluation and prediction of its performance in the long term.

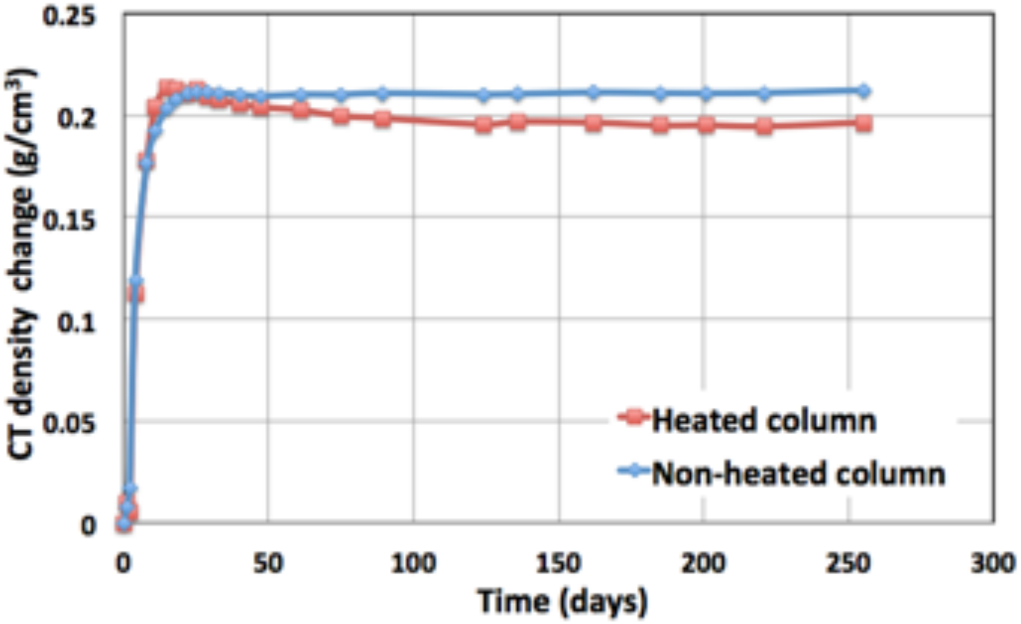

Figure 14-19. The CT density changes in the heated Column 1 and non-heated Column 2.

14.4.2 Geochemistry

Effluent water was collected, weighed and sampled from the influent mixture (see Table 14-1) and from the effluent of both columns (Figure 14-20). In the heated column, the effluent showed the sulfur reduction (also identified observed through the smell of sulfide), excess of silicon and potassium, and calcium, magnesium retention.

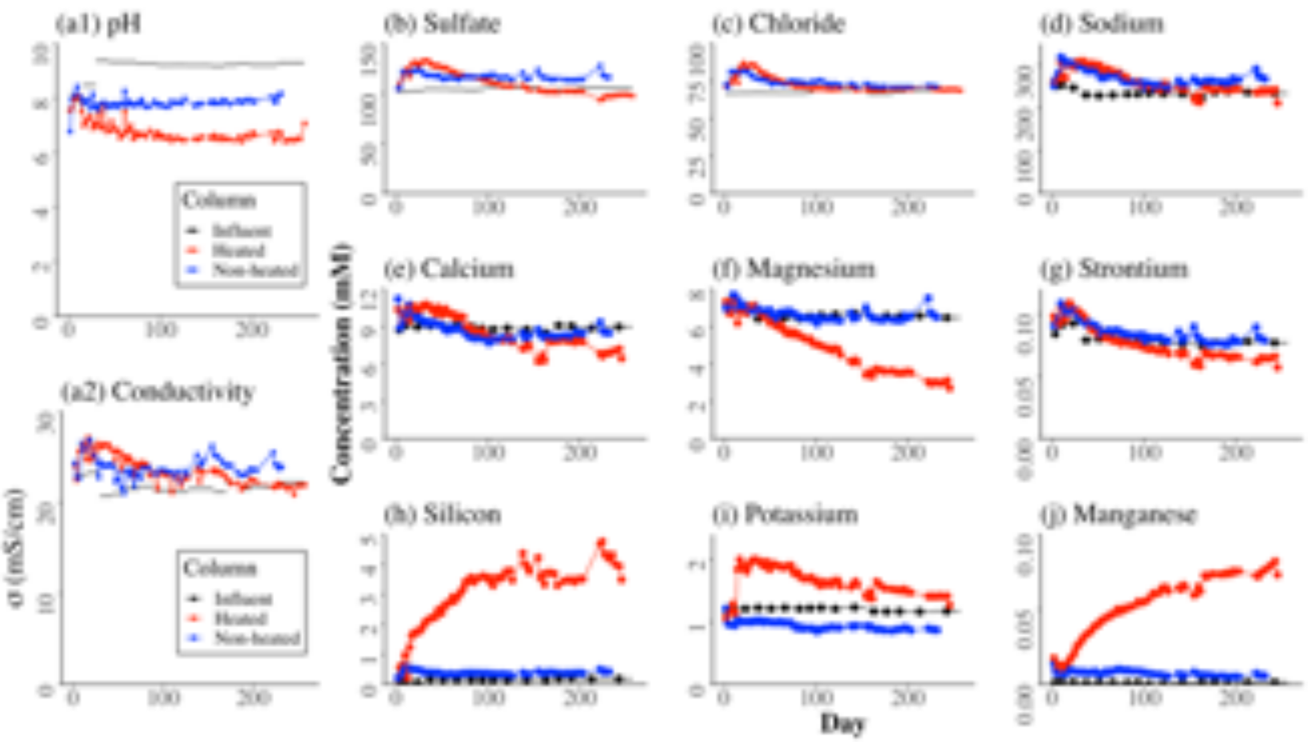

Figure 14-20. Influent and effluent geochemistry results: (a) pH and conductivity, (b-d) anions and (e-j) cations concentration in mM.

14.4.3 Electrical Resistivity Tomography

In HotBent-Lab experiment, we evaluated the potential of using the ERT as a long-term field monitoring technique for the bentonite barrier system. Under heating and hydration, the clay enfolds much of the information in its electrical resistivity, and water content is one of the dominant parameters of interest. Temporal variation and spatial distribution of moisture in the barrier system are crucial for evaluating bentonite sealing properties and for THMC modelling, while obtaining spatial water content data at the field scale is challenging due to site accessibility and sensor availability under the thermal and geochemical conditions of the operation. With the electrodes embedded into the clay as part of the packing processes, time lapse ERT would be able to provide continuous and dynamic visualization of the changes in the bentonite. In this section, we would be discussing (1) ERT data acquisition, processing and visualization, (2) calibration between resistivity and water content using physics-based model and laboratory data (including CT, temperature, effluent chemistry) from lab petrophysical experiments and in-situ measurements in the columns, and (3) the application of the calibration for the ERT time lapse imaging to generate temporal water content distribution maps. The limitations of current setups and improvements that could be made would also be addressed.

14.4.3.1 ERT Data Acquisition, Processing and Visualization

Our current ERT setup included (1) an electrical impedance tomography system (MPT DAS-1) and (2) 24 square copper electrodes (0.5 by 0.5 cm) evenly spaced on a pair of fiberglass rods (12 electrodes on each rod, inter-electrode distance was 3.8 cm) (Figure 14-1 and Figure 14-3). The rods were positioned at the sand-clay boundary opposite at each other from the central shaft, with the electrodes embedded inside the clay. The wires were soldered onto the copper, wrapped along the rods, exited through a feed-through port on the end-cap and connected back to the system. The materials of the rods and the wires were chosen to withstand the operation temperature and saline conditions, and the aluminum column and the titanium heater shaft were painted with electrically-insulated silicone gel to minimize current conduction from the metals.

During an ERT data acquisition, electrical potential was applied through two selected electrodes, and the potential difference was measured between multiple combinations of the other electrodes in pair. The electrical potential was applied in the frequency domain at 1 Hz with a target voltage at 10 V. The measurement sequence followed dipole-dipole electrode configurations (a combination of skip-0, 1, 2, 4, 6, 11 arrays) with 3 stacks, summing up to 1326 lines of data in one acquisition. Our current setup allowed for automatic and simultaneous imaging of both columns with a specifiable time interval (on a tri-hourly basis), and the data were remotely retrieved, thus offering the opportunity to provide spatially and temporally dense datasets. A python-based algorithm BERT (Günther and Rücker, 2012) was used for ERT data simulations and for generating a 3D electrical resistivity distribution in the clay. Figure 14-21 shows the numerical mesh used to perform forward and inverse simulations. The inversion results can be opened in software such as paraview that allows for inspecting the internal structures at desirable cross-sections and performing spatial analyses.

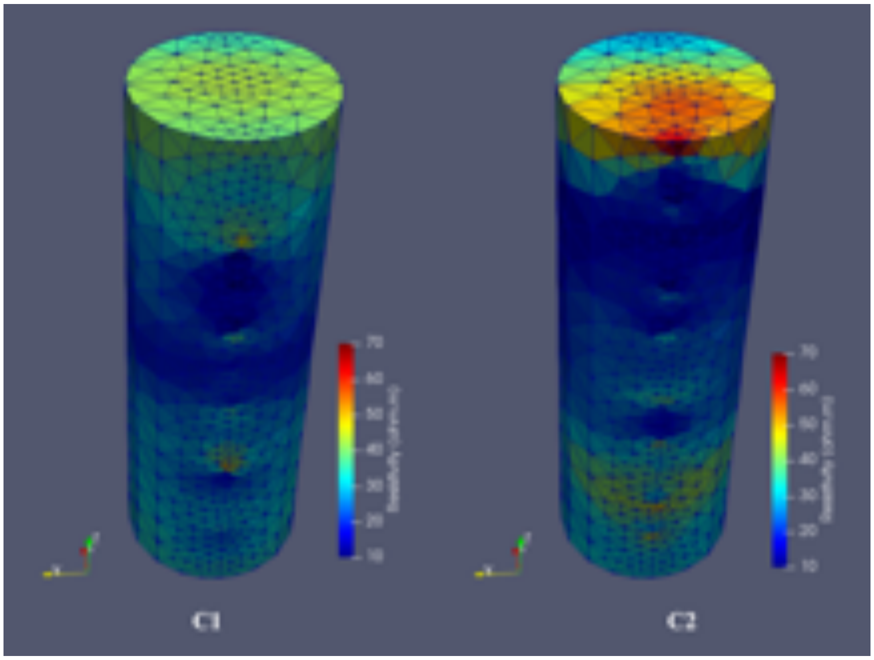

Figure 14-21. Numerical mesh used for ERT inversion and 3D visualization of the electrical resistivity structure of the columns after packing (T=0 day). C1 is the heated column, and C2 is the non-heated.

As was shown in the CT analysis, heating and water infiltration could be described as radial processes. Therefore, radial-averaged resistivity along the column depths was calculated as part of the post inversion data processing. Since the electrode rods were planted at two ends of the *x*-axis, the major electrical current flow paths were along the rod or in a cross-well manner, therefore giving higher data coverage of the ERT inversion model near the *x*-axis (Figure 14-22(A)). As the distance to the electrode rods increased, the data coverage decreased, generating bigger and sparser cells in the numerical mesh. In this analysis, we only included the data inside the high coverage cuboid bounded by the red lines (Figure 14-22(A)). When calculating the radial-averaged resistivity, a 1 cm (radius) by 1 cm (depth) mesh grid was adopted for interpolation, using the inverse distance weighing with 2 cm (chosen as the electrode half space) moving window (Figure 14-22(C)). Figure 14-22(C) also shows three column depths, which would later be used to compare with CT: (1) thermocouple depth z = 11cm, (2) mid-heater depth z = 21 cm, and (3) midcolumn range with depths between z = 11 and 31 cm.

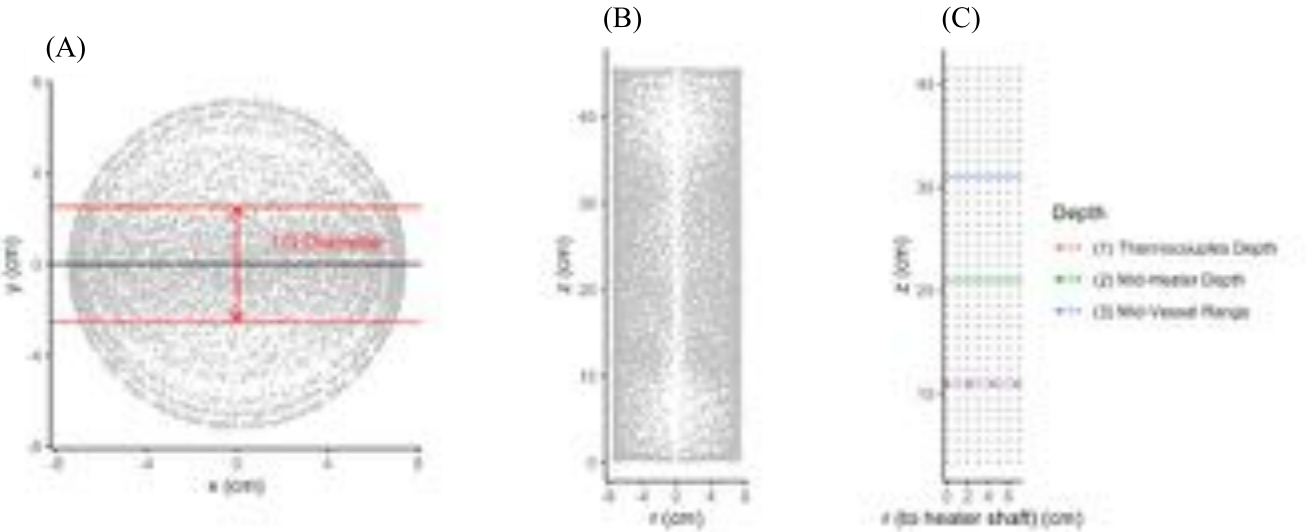

Figure 14-22. Radial data coverage of the ERT inversion model in (A) cross-sectional and (B) bird’s-eye view. Each point is the center of a cell from the numerical mesh (Figure 14-21) and carried a resistivity value. (C) Mesh grid for radial-averaged resistivity and selected depths for joint analyses with CT.

The resistivity of the clay depends heavily on its saturation degree. On the dry end, Figure 14-21 shows generally similar resistivity structures of both columns packed for 21% (v/v) volumetric water content and 1.2 g/cm^3 dry bulk density. At this water content, more than 95% of the resistivity values fell in the range of 15−40 Ωm, with a noticeably higher anomaly approaching 70 Ωm at the top of non-heated column (C2). Due to the dryness of the material, contact resistance between the electrodes and the clay was relatively high (>10 kΩ) during the pre-flow acquisition. High contact resistance reduces signal to noise ratio, thus the data quality. Since the flow started, contact resistance of most electrodes has significantly decreased (<10^3 Ω), and mean resistivity value already dropped down to 5 Ωm on day 1. However, a small magnitude of anomaly (~2 Ωm) persisted at the top-center of the non-heated column (Figure 14-23). Based on CT images, this region did not remain particularly dry and could have initially undergone faster fluid saturation due to the fractures near the end-caps. Because the ERT data coverage in this region was short (Figure 14-22(B)), and the contact resistance of few (1 or 2) electrodes remained high (~10 kΩ), the resistivity in this zone could have been overestimated.

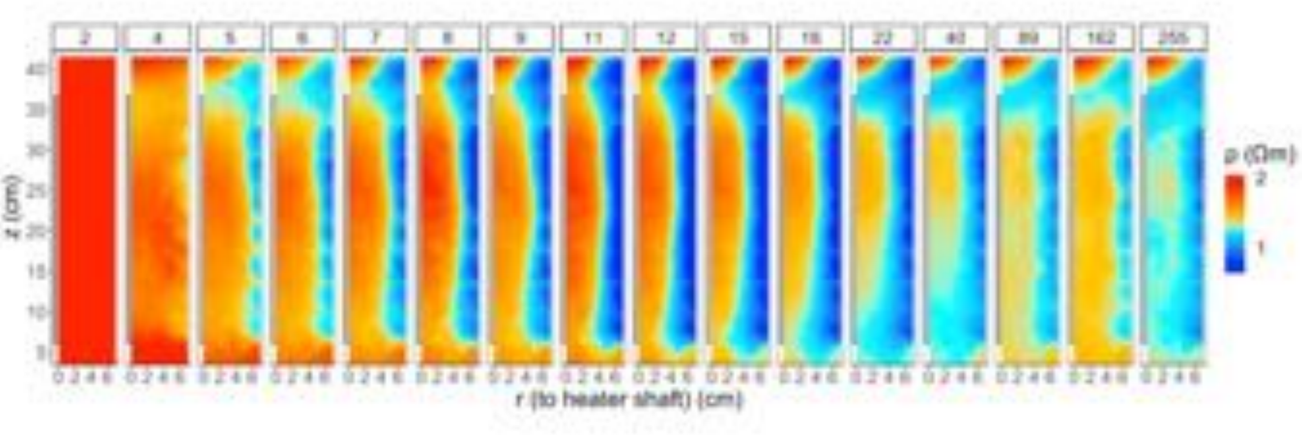

Figure 14-23. Radial resistivity map of the non-heated column (C2) after flow started (day 2 to 255). Flow was along the positive *z* direction. Color bar is log-scaled from 0.8 to 2.0 Ωm.

Time-lapse ERT of the non-heated column captures the sprawl of a low resistivity zone that matched with the CT images both spatially and temporally. From CT images (Figure 14-13), we to see (1) an overall increase in CT density on day 4 due to clay water uptake, with the high-density front reaching half of the radial distance by day 8, (2) a vertical low-density zone started to develop along the sand-clay boundary on day 4 due to clay swelling, and which slowly faded after day 22, and (3) low clay density remained in only the mid-center zone after day 22, while the top and bottom of the central shaft had higher density due to saturation through end-caps. Figure 14-23 shows similar development in terms of resistivity: (1) starting from day 4, low resistivity spots emerged near the sand-clay boundary and progressively migrated inward between day 5 and 22, (2) a highly conductive region (deep blue) developed near the sand-clay boundary and gradually dialed down after day 22, and (3) if we exclude the resistivity anomaly near the top-center, the mid-center zone remained the most resistive, and the top and bottom of the heater shaft seemed to have lower resistivity. Comparing the two datasets, the increase in CT density was found to be well aligned with the decrease in resistivity. Until the clay started to swell, CT density decreased because locally water displaced high density minerals, while the resistivity continued dropping following the increasing water content trend. This one-way relationship between higher water content and lower resistivity makes interpreting time lapse ERT straight forward in the non-heated column.

On the other hand, the ERT of the heated column was coated with the temperature effect in addition to the changes in water content. As the temperature rises (below the boiling point of saturation fluid, around 175°C at the applied pressure of 120 psi), the resistivity of the clay drops due to more vigorous movements of ions in the pore water and on the clay surfaces. Between day 4 and 12, Figure 14-24 captures a low resistivity zone moving inward due to water saturation. Compared to CT, the drying near the heat source was less pronounced, because the increase in temperature competed with the decrease in water content in terms of resistivity trend. After day 15, the distribution of resistivity over the entire column became homogeneous. On day 12 and 13, we improved the exterior insulation, thereby the clay temperature increased significantly. Between day 15 and 89, the clay gradually warmed up (Figure 14-25), which visually masked the effect of water content on resistivity. As the temperature of the clay reached stability in the range of 100°C–140°C around day 120, low resistivity zones were spotted both near the sand-clay boundary due to high water content and near the heater due to high temperature. In order to decouple the temperature from the water content variation, our lab setting provided great opportunities for ERT-CT joint analysis to relate time lapse ERT to moisture dynamics, structural change, and the diffusion processes.

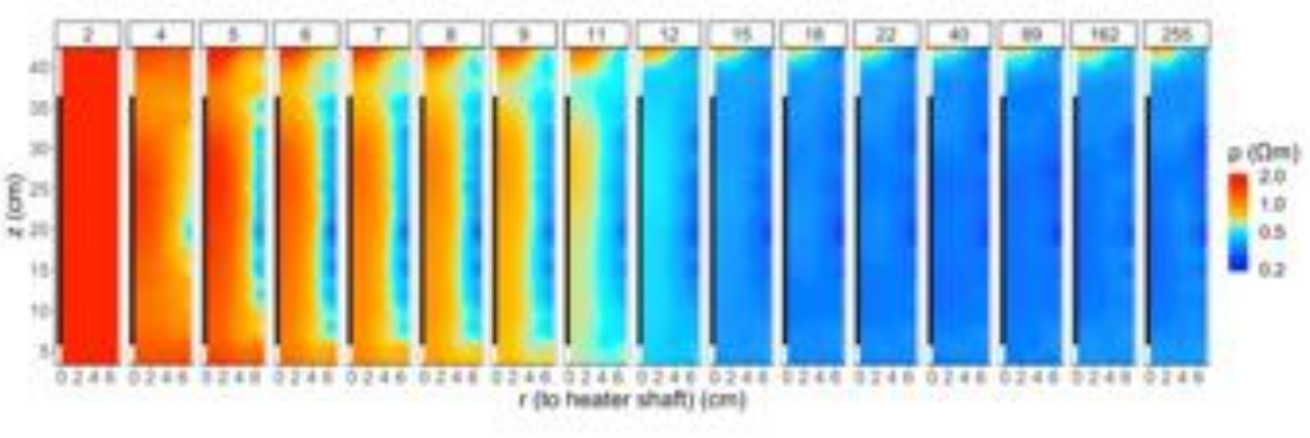

Figure 14-24. Radial resistivity map of the heated column (C1) after flow started (day 2 to 255). The black rectangle at the center (r < 0 cm) is the location of the heater. Color bar is log-scaled from 0.2 to 2.0 Ωm.

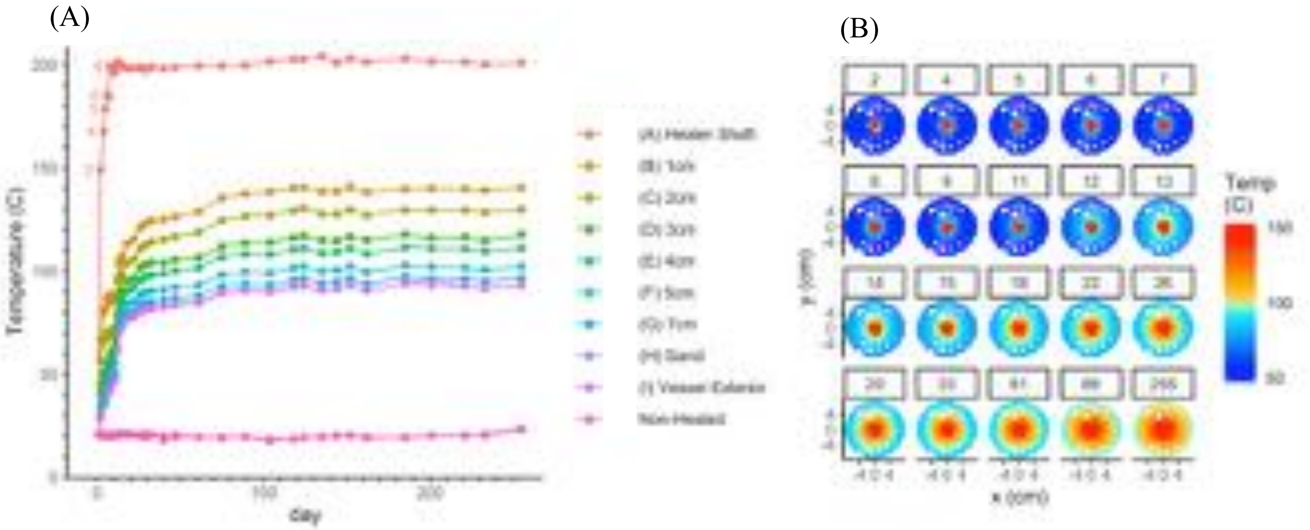

Figure 14-25. (A) Temporal temperature trend measured with the thermocouples in heated (A through I) and non-heated columns. (B) Radially-interpolated temperature distribution in heated column on selected days (days 2 to 255). Color bar is scaled from 50°C to 150°C.

Calibration between Resistivity and Water Content

One of the main objectives of HotBent-Lab is to establish, improve and validate a material-specific relationship between resistivity and water content. As discussed above, high water content increases the electrical current flow paths through pore fluid connectivity, and high temperature enhanced the movement of the electrolytes in pore fluid and cations on clay surfaces. In addition, chemical diffusion affects the electrical conductivity of the pore fluid, and mechanical compaction (and swelling) affects the porosity and the pore structure (Figure 14-28). A typical petrophysical relationship between resistivity and the four factors mentioned above for rocks and porous media can be described by Archie's Law:

$$\rho = \Phi^{-m} S^{-n} \sigma_f^{-1} \qquad \text{Equation 14-1}$$

where **ρ** is the resistivity of the media (Ωm), **Φ** porosity (m^3/m^3), **m** (-) cementation factor (typically lies between 1.5 and 4.0 and increases with cementation), **S** degree of saturation (m^3/m^3), **n** (-) saturation factor (typically ~ 2), **σ_f** conductivity of pore fluid (S/m).

Since montmorillonite, the main mineral component of the MX-80 bentonite, has high surface conductance, resistivity is expected to decrease with the increasing amount of clay mineral present. The Waxman-Smits Model (8-2), a modified version of Archie's Law, incorporates an additional surface conductance term, **bQv**, and is more suitable for clay application. Table 8-2 summarizes the parameters used in the WS model.

$$\rho = \Phi^{-m} S^{-n} \left(\sigma_f + \frac{bQ_v}{S} \right)^{-1} \qquad \text{Equation 14-2}$$

$$Q_v = cec * D_{grain} * \frac{1 - \Phi}{\Phi} \qquad \text{Equation 14-3}$$

where b is the equivalent ionic conductance of clay exchange cations (S/m cm^3/meq) as a function of σf and temperature T, and Q_v is the cation exchange capacity per unit pore volume (meq/cm^3) as a function of porosity, cec cation exchange capability (meq/g), and D_{grain} grain density (g/cm^3). The value of cec was held constant at 0.75 meq/g, and D_{grain} = 2.75 g/cm^3 was based on the SKB TR-10-60 technical report (Karland, 2010) for MX-80 bentonite.

Table 14-2. Waxman-Smits Model Parameters

Processes	Parameters in WS Model	Function of	Formulae
Mechanical	Porosity (Φ)	Dry bulk density (BD_{clay})	$\Phi = 1 - BD_{clay}/D_{mineral}$
	Cementation exponent (m)	Pore network connectivity	Fitting Parameter
Hydrological	Saturation (S)	Dry bulk density, water content (θ)	$S = \theta/\Phi$
	Saturation exponent (*n*)	Continuity of pore network when unsaturated	Fitting Parameter
Thermal and Chemical	Pore fluid conductivity (σf)	Temperature (T), Effluent Conductivity measured at 20C (σ_{20})	$\sigma_f = \sigma_{20}(1 - (20 - T) * 0.02)$
	Clay cation conductance (*b*)		$b = \left(1 - 0.83e^{-e^{\sigma f\left(-2.38 + \frac{42.17}{T}\right)}}\right) * (-3.16 + 1.59\ln(T))^2$ (Dacy and Martin, 2006)

The calibration was provided in two trials: (1) initial fit of WS model parameters (*m* and *n*) using separately packed calibration columns, and (2) second fit using in-situ ERT and CT observations

(Figure 14-26(A)). The final goal is to correlate the time lapse ERT with column-level porosity, effluent fluid conductivity and spatial temperature data, and apply the WS model to obtain the water content distribution maps (Figure 14-26(B)).

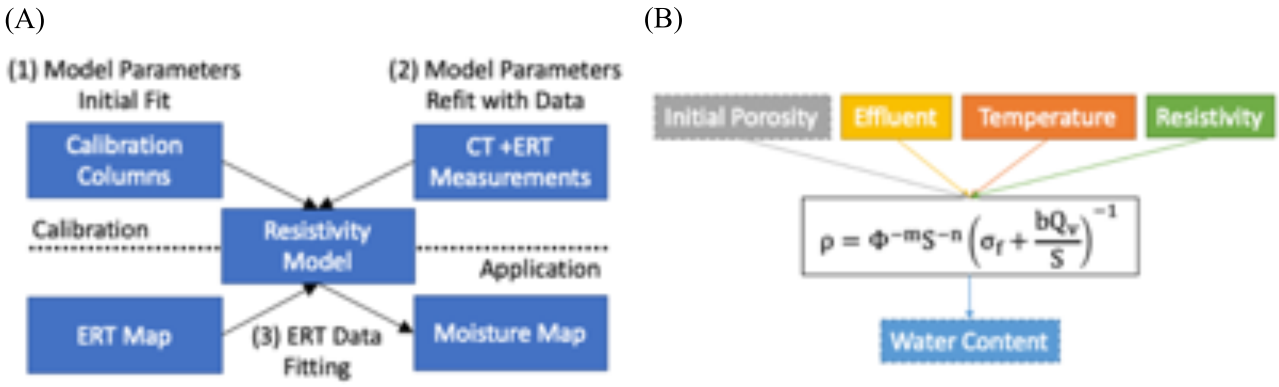

Figure 14-26. (A) Schematic flowchart of petrophysical and *in-situ* calibration (1, 2) and ERT-water content fitting (3). (B) The Waxman-Smits Model as the resistivity model and the desirable model inputs and deliverable.

In parallel to the main columns, we prepared several bentonite clay columns of various water content and dry density with the fluid of the same composition ($\sigma 20 \sim 2$ S/m, Figure 14-20(A2)) (Table 14-3). For each column, an averaged CT value from the CT scan plus resistivity at a range of temperatures were measured. Resistance was measured with PSIP instrument (Ontash & Ermac) at 1 Hz frequency, which is consistent with the ERT data acquisition, and resistivity was calculated with geometric factor pre-determined with fluid of known conductivity. Because the columns were not pressurized, the maximum measurement temperature was more or less confined to the water boiling point at the ambient pressure. The water content and dry density of each column were determined after oven-dried at 160°C for at least 48 hours. The calibration of CT number and CT density has been shown in Figure 14-9. The parameters for Waxman-Smits Model were fitted: cementation exponent $m = -3.8$ and saturation exponent $n = -3.0$.

Table 14-3. Properties of the petrophysical calibration columns used for CT and ERT calibration.

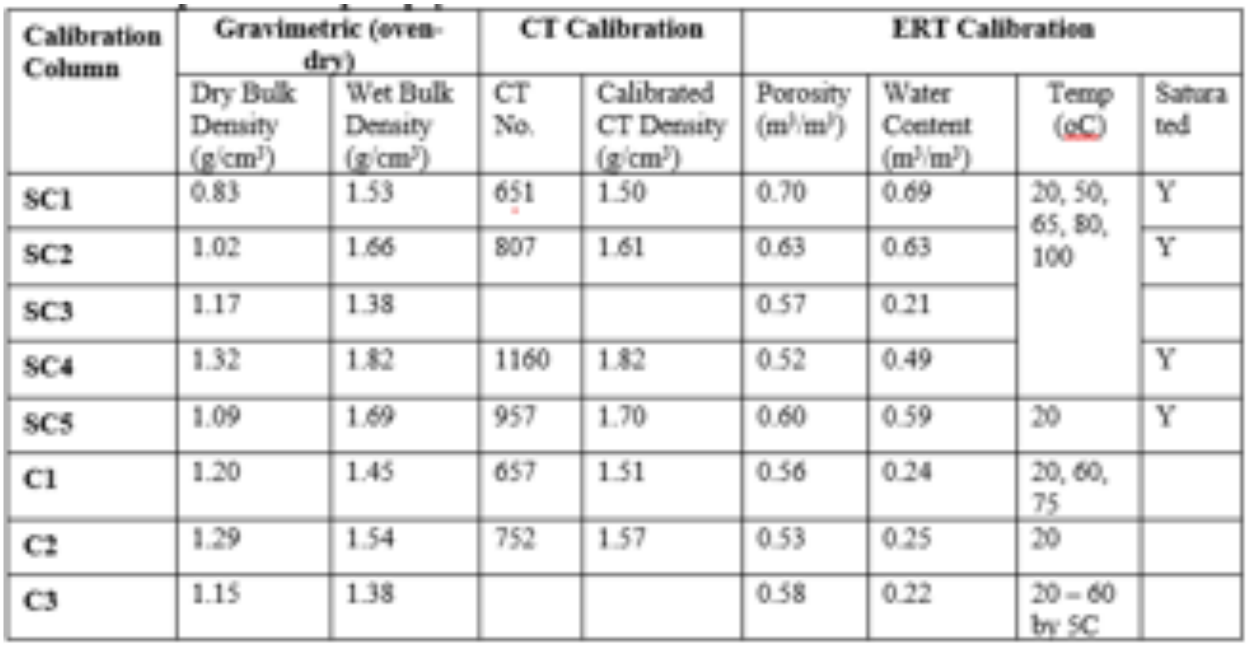

Calibration Column	Gravimetric (oven-dry)		CT Calibration		ERT Calibration			
	Dry Bulk Density (g/cm^3)	Wet Bulk Density (g/cm^3)	CT No.	Calibrated CT Density (g/cm^3)	Porosity (m^3/m^3)	Water Content (m^3/m^3)	Temp (oC)	Saturated
SC1	0.83	1.53	651	1.50	0.70	0.69	20, 50, 65, 80, 100	Y
SC2	1.02	1.66	807	1.61	0.63	0.63		Y
SC3	1.17	1.38			0.57	0.21		
SC4	1.32	1.82	1160	1.82	0.52	0.49		Y
SC5	1.09	1.69	957	1.70	0.60	0.59	20	Y
C1	1.20	1.45	657	1.51	0.56	0.24	20, 60, 75	
C2	1.29	1.54	752	1.57	0.53	0.25	20	
C3	1.15	1.38			0.58	0.22	20 – 60 by SC	

To evaluate how the fitted parameters (*m* and *n*) can be used with the datasets from the pressured cells, we selected ERT and CT data at two vertical depths (thermocouples at z = 11 cm and the mid-heater at z = 21 cm) and registered them at six radial distances as the training/testing dataset (Figure 14-27). Here, we jointly addressed the observations previously made in CT and ERT sections: for the heated column, the resistivity itself showed no radial discrimination because of the competing thermal and hydration processes, whereas CT retained the radial density difference created by the central heat source. For the non-heated column, the outer region had lower resistivity, in agreement with higher CT density closer to the sand layer. At the thermocouple depths, CT values were radially similar due to early water infiltration through the heater shaft, and the radial resistivity difference was also slightly smaller comparing to the mid-heater depth. Initial swelling created high water content near the sand layer, creating dips of CT value (locally replacing minerals with water) and resistivity.

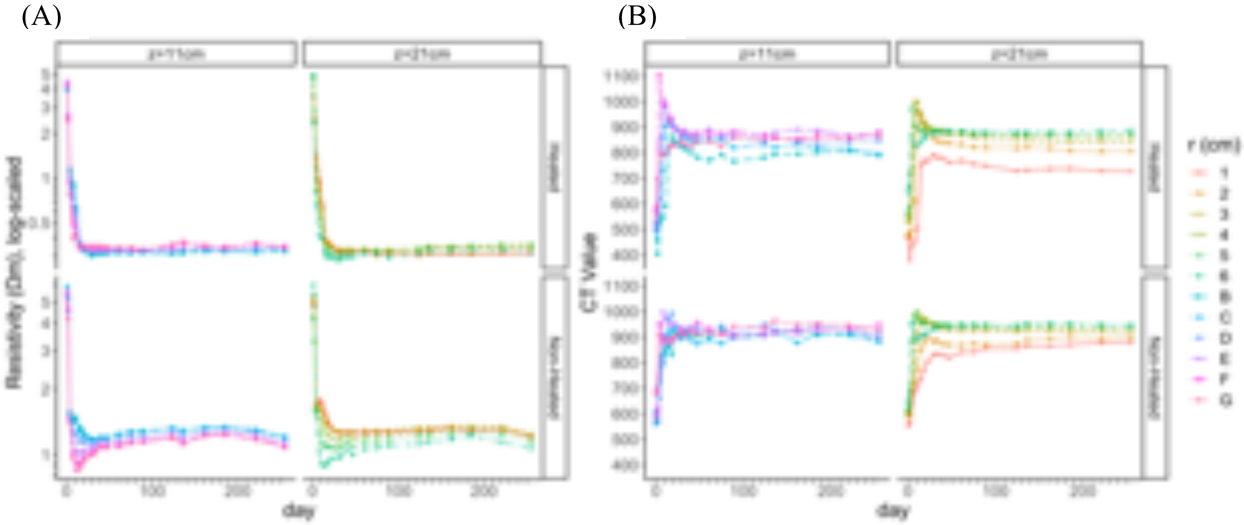

Figure 14-27. Temporal (A) resistivity (after day 1) and (B) CT trend of heated (top) and non-heated (bottom) columns at two selected depths. Data in the left panel were sampled adjacent to the thermocouples labeled as B-G, where B was closer to the heater and G to the sand-clay boundary. Data in the right panel were sampled at 6 radial distances (1 to 6 cm) from the heater shaft at the mid-heater depth (*z*=21cm).

Figure 14-28(A) shows where the testing data from the non-heated column fall on the WS model. Non-heated column was chosen for visualization because the temperature was homogeneous, and the results could be easily displayed on a 2D surface. The background is the WS model fitting results with the parameters from the calibration columns ($m = -3.8$, $n = -3.0$), temperature of 20°C, and effluent conductivity of 2.5 S/m, and it is colored-coded by water content: the higher water content corresponds to the lower resistivity. A single water content crosses through multiple CT values because of different dry density, which could be due to different packing targets or local clay swelling or compaction. The firm line crosses through our dry bulk density at 1.2 g/cm^3, and the dashed line crosses through the saturated conditions. Due to its high swelling capacity, bentonite could be saturated at highly variable water content depending on the local dry density. From the fitting, the horizontally parallel trend indicates that the WS resistivity model is more sensitive to water than to the clay content and its surface conductance. The testing dataset from the CT and ERT measurements is plotted as data points in Figure 14-27.

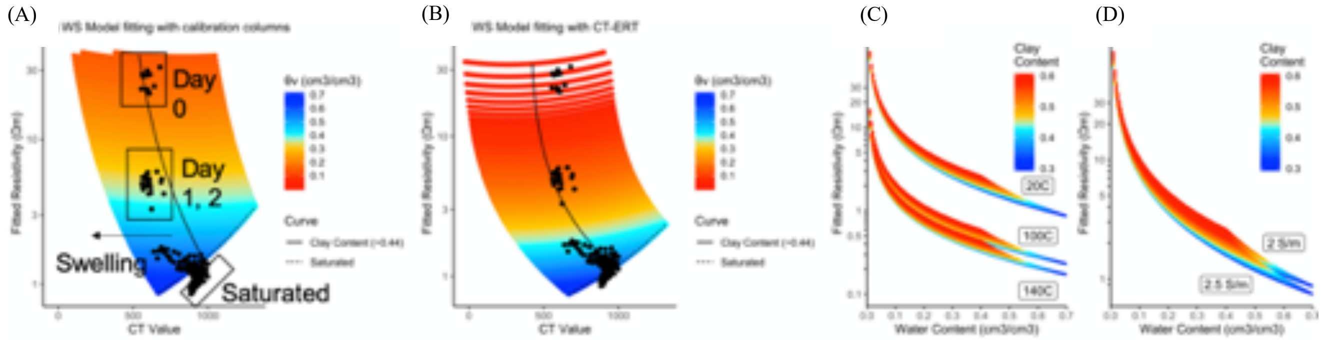

Figure 14-28. Model fitting results based on (A) calibration columns, and (B) column ERT plus CT data, demonstrating the effects of dry density (clay content), (C) temperature, and (D) fluid conductivity on the resistivity.

Two types of mis-fits are shown in Figure 14-28(A). The model overestimated the saturated resistivity, because many data points fell beneath the model fitting space, which would have led to overestimation of water content without CT constraints. Also, the model overestimated the unsaturated resistivity. Based on this fitting, the water content was 0.2 on day 0 and 0.3 to 0.4 on day 1 and 2. However, CT profile showed that CT density did not change much ($r < 6$ cm) between days 0 and 2, except for the center zone of the heated column (Figure 14-10 and Figure 14-11). Therefore, the resistivity difference between day 0 and days 1 and 2 was less likely from the water content, but from the suboptimal contact between dry clay and electrodes on day 0. The four unsaturated calibration columns used in this fitting were also packed at a similar water content (0.21 to 0.25), but without flow. Therefore, the contact resistance remained high and could decrease data quality of data interpretation.

This overestimation indicates the need for an adjustment of the WS model parameters based on the actual data collected from the pressured columns. The cementation exponent (m) was refitted with the saturated data from the training dataset ($r > 6$ cm), and the saturation exponent (n) was refitted with the unsaturated data from day 1 and 2, assuming a homogeneous 21% initial water content based on oven-drying tests. The reason for only using data from days 1 and 2 in this refit was that clay displacement became more significant after day 4 (Figure 14-16 to Figure 14-18). Movement of clay particles could change the local saturation, but was not easily distinguishable from CT data, as the water content was also simultaneously increasing. The following new WS model parameters were fitted as $m = -3.4$ and $n = -1.9$, with the saturation exponent approaching the common value of ~2 (Figure 14-28(B)). With constraint from the CT value, this adjusted WS model was applied to the rest of the testing dataset to fit the water content. Figure 14-29 shows both the drying and wetting of the clay in the heated column, extracting the water content information from the resistivity data based on the model fitting.

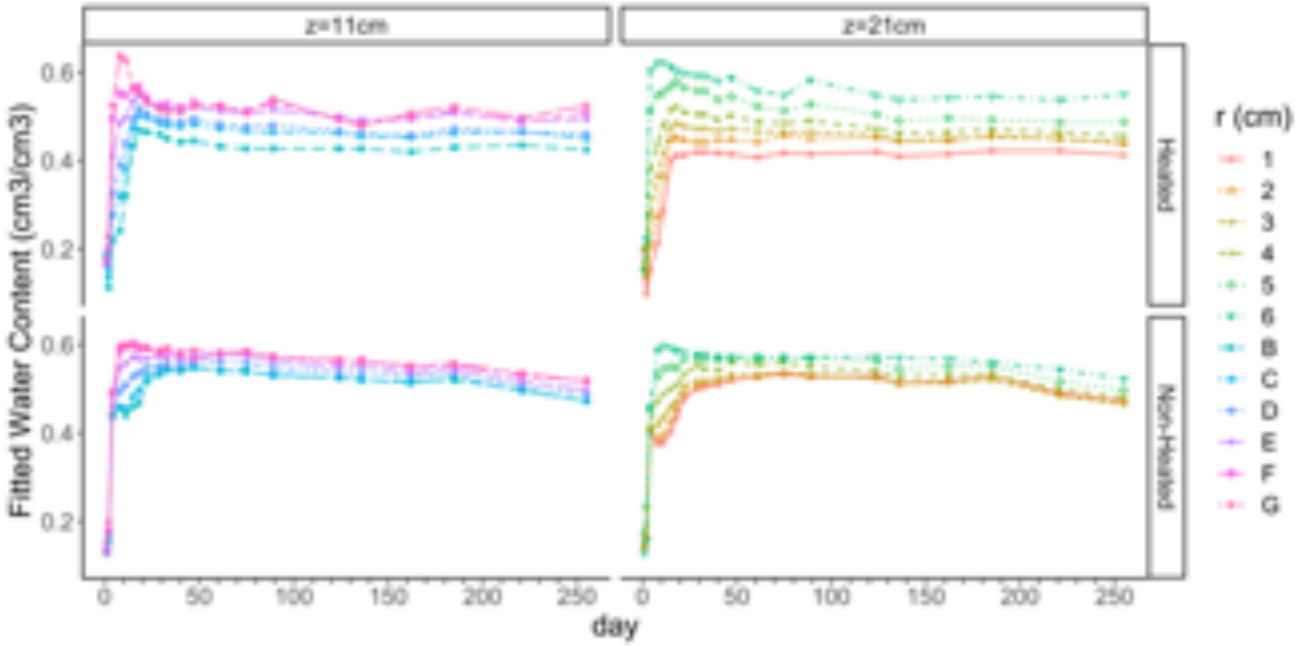

Figure 14-29. Temporal water content trend of heated (top) and non-heated (bottom) columns at thermocouple depth (z = 11cm) and mid-heater depth (z = 21cm) after day 2. Thermocouple (B) was closer to the heater, and (G) was closer to the sand-clay boundary.

From ERT Time Lapse to Water Content Maps

With the calibration between resistivity and water content being established and improved, we wanted to validate if ERT alone could be sensitive enough to distinguish local water content variation given such a small observation range of resistivity (0.2–2 Ωm). The fitting included inputs of resistivity, temperature, fluid conductivity and initial porosity estimation, while without the direct constraints from CT (Figure 14-26(B)). The ERT and temperature (from the thermocouples) were taken as the radial averaged data. Effluent fluid conductivity was used as the best approximation of fluid conductivity at the moment. Initial porosity was estimated as 0.56 based on 1.2 g/cm^3 dry density. The model would try to stay close to this porosity, which is generally acceptable especially with higher dry density and confined volume. While acknowledging that approximating local pore fluid and porosity with column level measurements would introduce errors in the fitting, it would be a good starting point because these datasets could be the most available if not only ones from the field depending on the sensor types and geochemical measurements routine. The fitting results are displayed in Figure 14-30 and Figure 14-31.

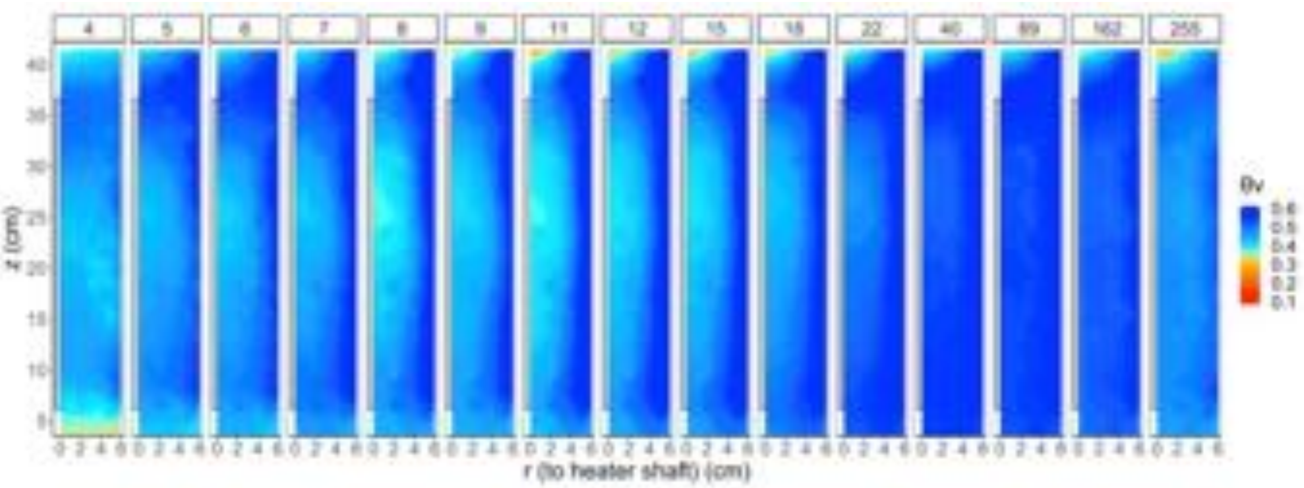

Figure 14-30. Radial water content map of the non-heated column (C2) on selected days (day 4-255). Color bar is volumetric water content (cm^3/cm^3) scaled from 0.1 to 0.6.

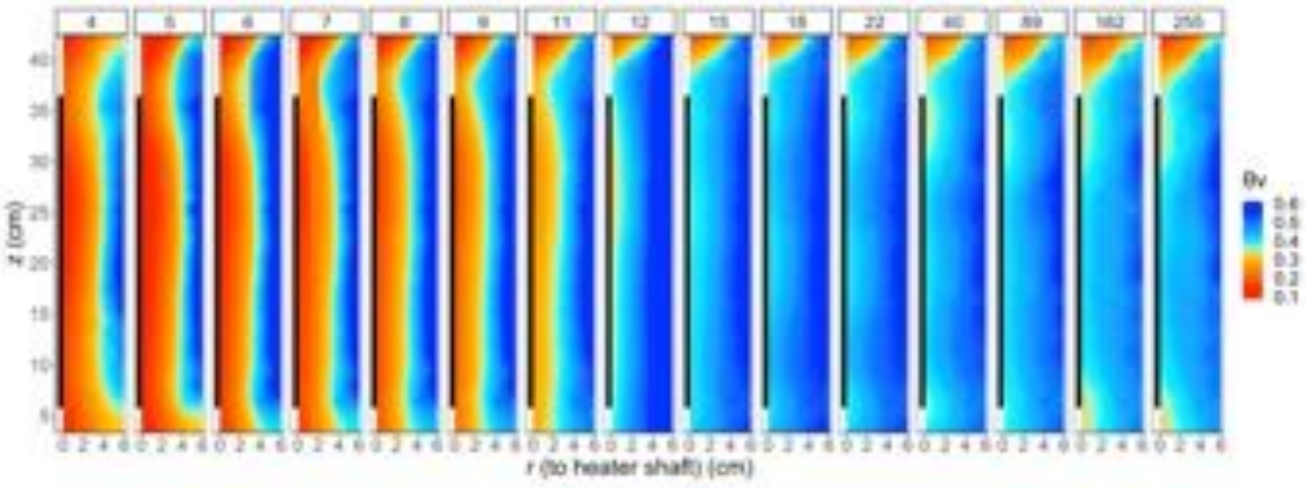

Figure 14-31. Radial water content map of the heated column (C1) on selected days (day 4-255). Color bar is volumetric water content (cm3/cm3) scaled from 0.1 to 0.6.

The movement of the water can generally be matched with the changes in CT images. Note that for the heated column, the temperature input for the ERT-water content fitting was radially interpolated among the readings from the thermocouples, which were located in the heated zone (z ~ 11 cm). Therefore, the temperature near the cold zones (indicated by the white gaps inside the heater shaft, z 0 to 6 cm and z > 36 cm) was overestimated, which would lead to an underestimation of water content in these regions. Also from the thermocouple readings, a small region (few millimeters) around the heater is also expected to have temperature higher than the boiling point at 175°C (given the columns were pressurized at 120 psi), at which the water is in the vapor form and the calibration wouldn't be applicable. The radial average water content was also calculated across the mid-column depths ($z = 11$ to 31 cm) (Figure 14-32(A)). THM processes such as (1) initial drying near the heat source, (2) water saturation starting from the sand-clay boundary, and (3) swelling and clay content redistribution were captured.

At the column level, the water content derived from ERT fitting was compared against the water content estimated from mass balance. The ERT-fitted water content was averaged from all the radial values in the mid-column depths ($z = 11$ to 31 cm, to avoid cold zones), and the mass balance was calculated from how much of the injected fluid was retained inside the column, namely the mass difference between influx and efflux. The influx was continuously tracked with the inlet pump flow rate, and the effluent fluid was collected and measured gravimetrically routinely. Figure 14-32(B) shows that, for non-heated column, the fitting generated pretty similar averaged water content comparing to the mass balance water content, and both of them approached the estimated porosity of 56%. The water content of the heated column derived from the ERT fitting was also found to lower than that of the non-heated column, which was expected due to the heat source at the center. However, the mass balance water content of the heated column still needs to be corrected for potential instrument drift in the pumps.

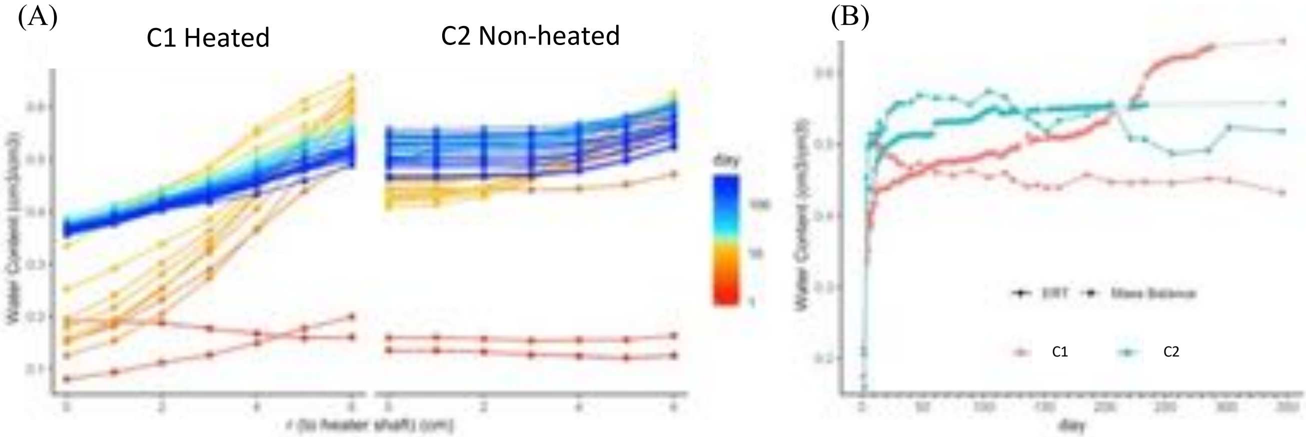

Figure 14-32. (A) Radial averaged water content from the mid-column depths (z = 11 cm to 31 cm). The days are log-scaled for visualization. (B) Mass balance water content versus averaged water content from the mid-column depths derived from ERT.

The fitting results show the capability of ERT in capturing local moisture variation given simple inputs such as temperature, effluent chemistry and porosity estimation. The model applicability will also be tested and improved in the next rounds of experiments. Based on the ERT data we have collected, the data quality could be improved by (1) ensuring good contact between electrodes and the clay, possibly with minimal local wetting and increasing the contact area by varying the sizes and shapes of the electrodes, (2) application of additional electrodes and electrode rods to provide a more detailed spatial coverage. Such efforts could increase data quality and reduce the needs for data smoothing during the inversion simulation, thereby capturing more of the radial differences in the early days where radial differences have been shown to be more announced from the CT images. For the water content calibration, a temperature distribution model throughout the columns and chemical diffusion analysis would be necessary for more accurate calibration and estimation of water content, and increasing the training datasets could also improve the calibration.

14.5 Summary and Future Work

During FY18–19 pressure columns were designed, built, and instrumented for the HotBENT-lab experiment. Starting in June 2019, hydration was started in both columns, and heating was applied to one column. In FY19–20, columns were monitored continuously for hydration, temperature distribution, effluent chemistry, and density changes. Detailed in this report are results that show steady state hydration for both columns, with some density, hydration and chemistry differences between the heated and non-heated condition.

Major observations shown by the data collected in the column test are the following:

- Clay hydration monitored by CT imaging and ERT was able to clearly show the hydration front moving radially inward. Density measurements from CT images were also able to observe clay swelling occurring with hydration, which caused localized compaction, closed fast flow paths created from column packing heterogeneities, and swelling along the clay/sand interface.
- In the center of the heated column, the clay showed lower hydration but increase in density due to mineral precipitation.

- Effluent chemistry showed differences between the heated and non-heated columns, specifically with the heated column demonstrating sulfate, calcium, potassium and magnesium reduction and silicon and potassium production.

For the remainder of FY20, we will complete this hydration testing, followed by a detailed dismantling of both heated and non-heated clays. The clays will be carefully removed and measured for water content, mineralogy changes, and chemistry of pore water, following techniques outlined by previous work on heated clays (Cuevas et al., 1997; Järvinen et al., 2016). Following the dismantling, we will repack the columns, focusing on the correspondence mineral density and the water chemistry to such characteristics determined the HotBENT field site.

15. CONCLUSIONS

This report documents progress made during FY20 on the EBS R&D Work Package in the SFWST Campaign. The R&D activities were designed to improve the understanding of EBS component evolution and interactions, as well as interactions between the host media and the EBS. A primary goal of this work is to advance the development of process models that include certain distinct processes that can be incorporated into a performance assessment or can provide critical information for implementing better constraints on barrier performance. The plan is to either directly implement the models within the GDSA platform or use the models for confidence building and/or to provide insight into the underlying processes. The R&D team consisted of individuals from Sandia, LBNL, LANL, PNNL, Vanderbilt University, the Nuclear Research Center of the Negev, and the Nuclear Research and Consultancy Group (NRG) The Netherlands.

The FY20 EBS activities involved modeling and analysis work as well as experimental work. The following subsections summarize the progress made in the different research areas.

15.1 EBS Task Force: Task 9/FEBEX Modeling Final Report: Thermo-Hydrological Modeling with PFLOTRAN (Section 2)

The research team used the HPC facilities at Sandia to conduct TH modeling of the Stage 1 and Stage 2 FEBEX in-situ experiment with the massively parallel reactive transport code PFLOTRAN. Because the modeling only included TH processes, shrink/swell aspects were neglected as were other structural deformational aspects of the bentonite barrier. Nonetheless the simulation results show good agreement with some FEBEX measurements, while some disagreement with some others. The overall modeling results show the following:

- Good agreement with temperature measurements near Heater 1, while slightly underpredicting temperatures measured near Heater 2 for Stage 1.
- Good agreement with measured liquid saturations after the first dismantling.
- Good agreement with measured temperatures during Stage 2 (Heater 2).
- Underprediction of liquid saturations at the end of Stage 2.

In general, the modeling under-calculated humidity measurements, which may have been a consequence of the spatially constant initial conditions for bentonite wetting assumed in the modeling.

15.2 Preliminary Sensitivity Analysis for the FEBEX In-situ Heater Test (Section 3)

Section 3 presented preliminary modeling work on sensitivity and uncertainty analysis applied to Stage 1 of the Full-scale Engineered Barriers Experiment in Crystalline Host Rock (FEBEX) in-situ test for the EBS Task Force, Task 9, which was discussed in Section 2. The goal of this analysis is to determine parameters important to defining the TH condition in the bentonite buffer and the host rock.

The sensitivity and uncertainty analysis was conducted by wrapping PFLOTRAN with an uncertainty quantification and optimization code (DAKOTA). A total of 25 realizations were run with the DAKOTA-PFLOTRAN coupled codes. In general, the experimental temperature fell in the middle of the distribution of predicted temperatures on a plot of temperature versus time, though there is still a need to improve predictions at early time. Matching relative humidity is not as straightforward as matching temperature because of the nonlinear relations involved. Predictions of relative humidity at one location are close to the experimental data while at another location most of the predictions are lower than the experimental data.

The preliminary analysis examined the data for an indication of (1) how sensitive Heater 1 temperature is to Heater 1 power, buffer dry thermal conductivity, buffer saturated thermal conductivity and granite thermal conductivity and (2) how sensitive relative humidity at Point 1 on Section E1 is to air entry pressure (Po) and buffer van Genuchten parameter λ. The stronger correlations are between Heater 1 temperature and Heater 1 power, and between relative humidity and buffer van Genuchten parameters. The strong correlation between Heater temperature and Heater power is expected as the power directly controls the temperature. The correlation between relative humidity and van Genuchten parameters is also consistent with the matching exercise described in Section 3.2. Matching of relative humidity is very sensitive to the values of the reciprocal of the air entry pressure and the parameter λ. Further analysis will be needed to obtain a complete interpretation of the results.

15.3 Cement-Carbonate Rock Interaction under Saturated Conditions: From Laboratory to Modeling (Section 4)

The work in Section 4 demonstrates how the integration of laboratory characterization methods with reactive transport simulations (LXO) facilitates evaluation over long time periods of the behavior of interfaces between two materials with chemical and physical gradients. This set of tools can be used for performance assessment of carbonate rocks and OPC paste interfaces. The simulation results indicated the likely key parameters for optimizing cement integrity when in contact with carbonate rocks. The porosity to tortuosity ratio ($\emptyset/\boldsymbol{\tau}^2$) was found to control the thickness of the carbonated cement layers, as the thickness of carbonated layers after a given time interval were proportional to $\emptyset/\boldsymbol{\tau}^2$ ratio between the two rocks. When choosing a geological formation for geological disposal site, it is recommended to choose a target formation with the lowest $\emptyset/\boldsymbol{\tau}^2$ available. However, macro-scale features in the rock, such as fractures and karst were not considered, and when they exist in the host rock, they potentially can dominate bicarbonate and other constituent fluxes from the rock to cement and vice versa.

The simulation results show the change in the carbonation front location with time. Preliminary estimates of carbonation depth for OPC paste were estimated for 100 and 1000 years when in contact with limestone and marl. After 1000 years, the carbonation depth for marl/OPC cement is about an order of magnitude deeper than for limestone/OPC paste interface.

The findings of this work are not limited to engineered barriers used in geological waste disposal sites but may also be useful for assessing the long-term performance of cements used in wellbores for oil/gas and geological carbon sequestration. The results may help in designing appropriate wellbore cements as well as in choosing subsurface geological formations that have a minimal degradation effect on sealing cements.

Future work on simulations will be used for long-term behavior estimates. Simulations will include (1) interfaces of other typical carbonate rocks such as chalk, oil shale, and phosphorite with OPC paste cement and low pH cement; (2) the geochemical speciation and transport of radionuclide simulants; (3) the effect of organic material content on interface integrity and the partitioning and transport of radionuclide simulants; and (4) unsaturated reaction, moisture transport, and temperature variations.

In parallel with simulations, interface experiments of carbonate rocks with cements are being carried out in the laboratory. Samples from these experiments are in early stages of chemical and physical characterization. Characterization methods include (1) interface characterization using LA-ICP-MS, SEM EDS, and micro-CT and (2) nano indentation to measure changes in material mechanical properties as a result of interface reactions.

15.4 Hydrothermal Experiments (Section 5)

Section 5 summarizes the EBS Grimsel granodiorite wall rock hydrothermal experiments IEBS-1 through IEBS-6 that include combinations of Wyoming bentonite + Grimsel granodiorite + Grimsel granodiorite synthetic *groundwater ± stainless/low carbon steel ± cured OPC*. Results from experiments IEBS-1 through IEBS-6 are include: (1) SEM images and EDS data, (2) QXRD data, (3) clay mineral XRD data, (4) EMP data for major mineral phases, and (5) aqueous geochemistry data.

Concepts developed so far include the following:

- Illitization of montmorillonite in Wyoming bentonite in a Grimsel granodiorite wall rock environment may be restricted due to the bulk chemistry of the overall system (i.e., low potassium) and/or kinetics.
- Montmorillonite structural alterations were not observed in the Wyoming bentonite + Grimsel granodiorite + cured OPC experiment.
- The inclusion of a cured Portland cement chip did not dramatically increase the solution pH but lead to the formation of diverse secondary mineral formation.
- Analysis of clay mineral structural changes reveals that montmorillonite alteration did not occur.
- Newly crystallized Fe-saponite forms at the steel-bentonite interface and grows perpendicular to the steel surface.
- Fe enrichment in the bentonite due to interaction with steel corrosion products does not migrate far from steel (<50 μm).
- C(A)SH minerals formed within the Wyoming bentonite-Grimsel granodiorite system.
- Zeolite-forming reactions are not favored in the Wyoming bentonite-Grimsel system.
- General steel corrosion is observed and thicknesses/rates of Fe-rich clay formation were measured.

Research needs to be emphasized in the following areas for FY21:

- Continue to build a database of Grimsel granodiorite and EBS experiments
- Further work to understand formation of C(A)SH minerals at relatively low pH (<8.0)
- Complete characterization of the reaction products from the experiments with cement, including mineral reactions in the bentonite and within the cement chip
- Develop understanding of the role of secondary mineral formation in systems that include OPC
- Include low-pH cement formulations in EBS experiments
- Corrosion of steels/interface silicate mantling effects
- Detailed geochemical modelling of geochemical changes observed in the bentonite-granodiorite system
- Incorporate results into generic modeling codes

The database, along with summary conclusions, will be of use to other experimental teams in the DOE complex, system modelers, and the international repository science community in the development of concepts related to high-temperature crystalline repository environments.

15.5 Progress on Investigating the High Temperature Behavior of the Uranyl-Carbonate Complexes (Section 6)

The investigation of the high temperature behavior of the uranyl-carbonate complexes is still in the midst of the data collection phase. Preliminary data suggest that currently available thermodynamic data for uranyl carbonate complexes are inadequate for predicting behavior at elevated temperatures. It appears that extrapolations of room temperature data greatly overestimate the stability of these complexes at elevated temperatures with the discrepancy between theory and reality evidently increasing with higher temperatures and carbonate concentrations (e.g. 4 orders of magnitude difference between reality and theory at 250°C and 0.5 *m* $NaHCO_3$). Initial solubility experiments failed to identify any carbonate complexation at 200°C and 250°C over carbonate concentrations of 0.001–0.5 *m*, where theory predicts they should be predominant. However, results from synchrotron experiments suggest that uranyl carbonate complexes are stable at these temperatures if the concentration of dissolved carbonate is ~0.9 *m*. To confirm this observation, we are currently in the process of conducting solubility experiments that cover a carbonate concentration range of 0.5–0.8 *m* thus bridging the reported experiments with our XAS observations. We also aim to commence Raman and new UV-VS experiments to investigate the behavior of uranyl carbonate complexes at relatively low (25°C–150°C) temperatures where issues of uranium insolubility are less prevalent.

15.6 In-situ and Electrochemical Work for Model Validation (Section 7)

Two approaches were developed to include UO_2 like particles onto the WE of the SALVI E-cells, namely particle attachment with gold coating and epoxy stamping. Multiple model particles were used to verify fabrication reliability. Surface characterization was used to verify particle attachment as WEs. Electrochemical analysis was performed on a variety of devices containing WEs fabricated using different particles and various techniques to illustrate feasibility. The experimental results show that in operando and in-situ study of UO_2 particles using the modified SALVI E-cell platform is possible using one of the illustrated methods. These new approaches are easy to implement and cost effective, permitting UO_2 corrosion potential studies in a wide range of conditions. There are plans to optimize and select the WE fabrication method and to use the optimal option for UO_2 investigation in the near future.

15.7 Investigation of the Impact of High Temperature on EBS Bentonite with THMC Modeling (Section 8)

Over the past few years, significant progress has been made on the development of a series of coupled THMC models to evaluate the chemical alteration and associated mechanical changes in a generic repository and to consider the interaction between EBS bentonite and the NS clay formation. Activities during FY20 include the following:

- A parametric study was conducted to examine the pre-consolidation pressure in BExM for bentonite buffer under THMC processes. With this study, a distinct elasto-plastic behavior of bentonite was obtained, revealing that the spatial heterogeneity of the sample may induce uneven performance inside the material.
- The simulator on Linux platform has been improved with the deal.II library, and modified the coupling strategy to a sequential coupling method. A good agreement between numerical simulations and analytical solutions is obtained, but in the THM simulation of high T case, the hydrological calculation failed to converge due to phase changes.

To further improve the coupled THMC model on the Windows platform to obtain a better understanding of the coupled processes contributing to chemical and mechanical alteration in EBS bentonites and NS argillite formations and to answer questions regarding the thermal limit of EBS bentonite in clay repository, we are planning the following:

- To improve the convergence of hydrological part in the simulator with the deal.II library, and recalculate the high T case. Use this new library to conduct parallel computation and modify the chemical reaction part and link with the THM part. To investigate chemical-induced deformation in solid skeleton related to the change of solution compositions and to derive an improved coupling model for compacted clays following the framework of poromechanics.

- To derive reduced order model that can be integrated into the performance assessment model in GDSA. The importance of bentonite alteration and its impact on mechanical behavior needs to be integrated to performance assessment model to assess their relevance to the safety of a repository. Specifically, we will first implement of bentonite swelling models such as linear swelling, state surface, BBM, and BExM into a parallel THMC simulator and then reduced order model will be developed based on the large number of THMC simulations.
- To use a physics-constrained data-driven computational framework to develop a constitutive function with the LSTM method-based strain-stress data search for simulation of clay behavior under thermal and hydration processes.
- To implement more constitutive models into the new simulator for better representation of different geomaterials, and continue working on coupled THMC modeling about different materials with the new simulator.

15.8 Sorption and Diffusion Experiments on Bentonite (Section 9)

In FY20, diffusion experiments were conducted with 95°C heated- and 20°C cold-zone purified FEBEX bentonite at a bulk density of 1.25 kg/L. The experiments were conducted at a constant ionic strength (0.1 M NaCl) at pH 7 in the presence of 0.1 mM Ca or 2 mM Ca. The average normalized 3H flux at steady state (≥50-hr) for 3H through-diffusion was not significantly different across samples, with values ranging from $1.38 \pm 0.13 \times 10^{-3}$ m/day to $1.73 \pm 0.17 \times 10^{-3}$ m/day. U(VI) in-diffusion experiments conducted in the presence of 2 mM Ca showed the diffusive loss of U(VI) from the high concentration reservoir was indistinguishable for the heated and cold-zone bentonite, and U(VI) traveled less than 1 mm into the clay over the 30-day diffusion period. While lower U(VI) adsorption was previously measured on the heated-zone FEBEX bentonite compared to the cold-zone bentonite, it is possible that differences in U(VI) diffusion due to differences in adsorption may only become apparent over much longer time periods than can be realistically tested in the laboratory. Reactive transport modeling of these results using CrunchClay is currently underway and will provide further insight into the geochemical conditions and time periods in which differences in U(VI) diffusion as a result of heating may be observed.

In the remaining time of FY20 and FY21 our work will focus on the diffusion and redox transformations of Se through compacted montmorillonite. Experiments will be conducted under a single ionic strength (0.1 M) and three different electrolyte compositions: 0.1 M NaCl, 0.033 M $CaCl_2$, and 0.085 M NaCl + 0.005 M $CaCl_2$, representing pure Na, pure Ca, and a Na-Ca mixture, respectively. We hypothesize that Se(VI) diffusion will be different under these different electrolyte compositions due to both differences in aqueous Se speciation and differences in the clay swelling in the presence of Na and Ca. These experiments will also be modeled using CrunchClay.

15.9 Studying Chemical Controls on Montmorillonite Structure and Swelling Pressure (Section 10)

In FY20 we have conducted a comprehensive set of experiments and simulations, which provided deep insights into the thermodynamics of clay swelling in mixed electrolyte solutions. Accomplishments from the prior funding period include development of molecular simulations approaches (Subramanian et al., 2020) that inform a new thermodynamic model for ion exchange driven clay swelling and collapse (Whittaker et al., 2019). Our FY 2020 efforts focus on transferring this knowledge to compacted clay systems accounting for non-zero effective normal stress. We report on the development of an X-Ray transparent micro-oedometer system for the measurement of montmorillonite swelling pressure as a function of dry bulk density and aqueous solution composition. Initial work focused on pure homoionic NaCl and KCl solutions as well as NaCl+KCl mixtures. Preliminary data are presented from in-situ X-Ray scattering experiments conducted at the APS, Argonne National Laboratory. To develop a theoretical understanding of microstructural evolution, we applied a structural model for cis-vacant smectite clay (Subramanian et al., 2020) to simulate the free energy of mixing crystalline layer states and found that highly unfavorable mixing energetics could drive phase separation in mixed layer state systems. Ongoing simulations of swelling free energy are being conducted using a PMF calculation method. Finally, these results are integrated into a thermodynamic model to predict swelling pressure as a function of pore fluid composition in compacted bentonite.

In the future, as soon as laboratory work is resumed in FY20 and extended into FY21, we are going to perform experiments to generate a comprehensive swelling pressure data set in multicomponent electrolyte solutions. The swelling pressure data will be compared against model expectations based on the thermodynamic approach described in Zheng et al. (2019a) and Whittaker et al. (2019), with subsequent model refinements based on experimental outcomes. Additional X-ray scattering beamtime will be sought toward the end of FY20 to obtain additional microstructural data constraints, including the evolution of montmorillonite microstructure, upon ion exchange in mixed electrolyte solutions including calcium. Additional simulations will be completed to determine swelling free energies for mixed electrolytes, but a different simulation technique is required to quantify interlayer ion exchange thermodynamics. These will be investigated further in FY21, using the thermodynamic integration technique described above.

15.10 Microscopic Origins of Coupled Transport Processes in Bentonite (Section 11)

In this section we present a research plan for a newly added research activity on the development and validation of a microscopic model of coupled transport processes in bentonite and using this model to determine cost effective augmentation strategies to increase the bulk thermal conductivity of hydrated bentonite. Because this activity was added in March 2020, we only report a research plan and some preliminary results, which will serve as a foundation for a larger scale effort in FY20–21 to stably increase the thermal conductivity of bentonite above 2 W/(m·K) at temperature relevant to modern nuclear waste storage design concepts.

Our model predicts two important consequences for the thermal conductivity of bentonite. The first is that a local equilibrium is not possible without macroscopic rearrangement of mineral layers, and therefore microscopic gradients of ions and water are pervasive in bentonite unless or until the mineral is chemically altered to redistribute structural charge. The second is that a ‘turbostratic’ rearrangement of layers, as is observed in natural bentonites, may minimize the free energy of a given local arrangement, but that any structural fluctuations away from this arrangement will alter the energetic landscape and drive ion and water fluxes. These phenomena represent two important couplings between the chemistry and mechanical deformation of mineral layers in bentonite whose ultimate consequence is to create microscopic fluxes that generate entropy, and therefore, heat. We anticipate that this model can be used to quantify the specific interactions/fluctuations through which heat is transferred and make predictions about deliberate chemical or structural alteration that may augment heat conduction.

With further development in FY20–21, we expect to be able to identify and test bulk chemical modifications to bentonite that enhance the thermal conductivity beyond 2 W/(m·K). For example, fluorine functionalization of the montmorillonite octahedral sheet reduces hydrophilicity and may significantly alter the dielectric properties of confined water to more effectively screen interlayer charge and sustain dynamic fluctuations that drive thermal transport. Alternatively, mixing bentonite with aromatic hydrocarbons, such as chemical precursors to graphite, may facilitate the in-situ formation of thermally conductive carbon nanomaterials that enhance the thermal conductivity of bentonite.

15.11 Understanding the THMC Evolution of Bentonite in FEBEX-DP—Coupled THMC Modeling (Section 12)

The FEBEX in-situ test, which lasted more than 18 years, is extremely valuable for validating the coupled THMC model and improving our understanding of the evolution of the bentonite barrier throughout heating and hydration. The ultimate goal is to use THMC data from FEBEX-DP to validate the THMC models, and therefore enhance our understanding of coupled THMC processes in bentonite.

From FY16 to FY19, extensive model calibrations were conducted, and finally, in FY19, the THCM model provided a coherent explanation of THMC data collected at the FEBEX in-situ test. In FY20, the modeling work included using the THMC model to explore the long-term alteration of bentonite. The first question we are trying to address is the necessity of using the THMC model for studying long-term alteration of bentonite, especially the geochemical alteration. The use of the THMC model is computationally expensive and numerically more unstable than the THC model, while up-gradation of the THMC code, using parallel computing and the better solver, can alleviate this issue. Using the THC model could be beneficial in terms of the computation time and simulation stability, knowing that the performance assessment is most likely based on THC simulations, not THMC simulations. The following results of simulations were obtained:

- In terms of the hydrological behavior, the THMC and THC modeling results are similar for the period of 50 years despite of a remarkable difference for the first 30 years.
- The evolution of conservative chemical species (e.g., chloride) based on the results of THMC and THC modeling is similar.
- The evolution of reactive species (e.g., potassium) based on the results of THMC and THC modeling is different, indicating that the reaction history in THMC and THC models in the early time (<30 years) have a long-term effect.
- Bentonite will become fully saturated in 30-40 years based on the model with a heat decay function, and the bentonite barrier is expected to homogenize in most areas.
- High chemical concentrations in bentonite near the heater, which were observed in the field test, are predicted to disappear after bentonite becomes fully saturated.
- Illitization will continue for 50 years, but won’t proceed. However, the THC model shows more illitization in area near the heater compared to the THMC model.

In the remaining time of FY20 and FY21, we will continue improving the stability and numerical efficiency of TOUGHREACT-FLAC and finish the long-term THMC simulations. In addition, a reactive transport model will be developed to study the geochemical changes at the interfacial areas, including the bentonite/concrete interface and the bentonite/steel interface.

15.12 Modeling in Support of HotBENT, an Experiment Studying the Effects of High Temperatures on Clay Buffers/Near-field (Section 13)

We developed a THC model to predict the evolution of Wyoming bentonite (MX-80) to be used in the HotBENT field test. Modeling of coupled THC processes affected by high temperature, relatively high permeability and high hydraulic pressure, combined with the effect of artificial hydration, generated the results that have not been observed in FEBEX in-situ test (Zheng et al., 2018). Modeling results can be summarized as follows.

- With a heater temperature of 200°C, the temperature at the bentonite/granite interface is expected to reach 87°C. In about 3 years, most of bentonite would become fully saturated, but a narrow zone about 3 cm thick in the close vicinity of heater would remain unsaturated with a water saturation degree from 95% to 98% until 20 years.
- The most remarkable chemical changes are expected to occur in a narrow unsaturated zone, because of the continuous strong evaporation (referred as "evaporation zone" in this report). Ion concentrations are expected to increase up to 2–3 mol/kg due to the dissolution of smectite, precipitation of illite, anhydrite, quartz and cristobalite, very high exchange Na and Mg and very low exchange of Ca and K at the cation exchangeable sites. Modeling showed the development a chemically active area a little further away from the heater and right next to the narrow unsaturated zone. It is referred to as the "condensation zone," in which chemical changes are induced by continuous condensation of vapor that is generated in the "evaporation" zone. In this area, model showed a significant dilution of the bentonite pore water, dissolution of most aluminum-silicate minerals, except muscovite, very high exchange of Ca and K, and very low exchangeable Na and Mg at the cation exchangeable sites.
- It will be a challenging problem of measurements of chemical concentrations in bentonite in a narrow zone close to the heaters, when modules H3 and H4 in HotBENT are dismantled after 5 years operation.

The 1D model sheds light on the potential chemical changes in MX-80 bentonite in HotBENT, but the hydraulic calculation is not entirely faithful to the condition of HotBENT, because of the existence of pedestal underneath the heater. In the remaining time of FY20 and FY21, we will continue making model predictions for the HotBENT, to help design a monitoring protocol and guide the development of a future measurements plan. Specifically, we will

- Develop a 1D THC model for BCV bentonite,
- Extend the 1D axi-symmetrical THC model to the THMC model for the MX-80 bentonite, and
- Develop a 2D THMC model for MX-80 and BCV bentonites.

15.13 High Temperature Heating and Hydration Column Test on Bentonite (Section 14)

During FY18–19, two pressure columns were designed, built, and instrumented for the HotBENT-lab experiment. In June 2019, hydration was started in both columns, and heating was applied to one column. In FY19–20, columns were monitored continuously for hydration, temperature distribution, effluent chemistry, and density changes. Detailed in this report are results that show steady state hydration for both columns, with some density, hydration and chemistry differences between the heated and non-heated conditions. Major results of observations in the column tests are the following:

- CT imaging and ERT of clay hydration clearly showed the hydration front moving radially inward. Density measurements from CT images indicated that hydration caused clay swelling, which, in turn, caused localized compaction, closed flow paths created from column packing heterogeneities, and swelling along the clay/sand interface.
- In the center of the heated column, the clay hydration was lower, but the density increased due to mineral precipitation.
- Effluent chemistry showed differences between the heated and non-heated columns, specifically, sulfate, calcium, potassium and magnesium reduction and silicon and potassium production occurred in the heated column.

In the remainder of FY20, we will complete the hydration testing, followed by a detailed dismantling of both heated and non-heated columns. The clays will be carefully removed and measured for water content, mineralogy changes, and chemistry of pore water, using the techniques outlined by previous work on heated clays (Cuevas et al., 1997; Järvinen et al., 2016). Following the dismantling, we will repack the columns, resembling their mineral density and the water chemistry to such characteristics determined at the HotBENT field site.

16. REFERENCES

Adams, B.M., Ebeida, M.S., Eldred, M.S., Geraci, G., Jakeman, J.D., Maupin, K.A., Monschke, J.A., Stephens, J.A., Swiler, L.P., Vigil, D.M., Wildey, T.M., Bohnhoff, W.J., Dalbey, K.R., Eddy, J.P., Frye, J.R., Hooper, R.W., Hu, K.T., Hough, P.D., Khalil, M., Ridgway, E.M., Rushdi, A. 2019. *Dakota, A Multilevel Parallel Object-Oriented Framework for Design Optimization, Parameter Estimation, Uncertainty Quantification, and Sensitivity Analysis: Version 6.10 User's Manual*. SAND2014-4633, Updated May 15, 2019. Sandia National Laboratories, Albuquerque, NM.

Allen, P.G., Bucher, J.J., Clark, D.L., Edelstein, N.M., Ekberg, S.A., Gohdes, J.W., Hudson, E.A., Kaltsoyannis, N., Lukens, W.W., Neu, M.P., Palmer, P.D., Reich, T., Shuh, D.K., Tait, C.D. and Zwick, B.D. 1995. Multinuclear NMR, Raman, EXAFS, and X-ray diffraction studies of uranyl carbonate complexes in near-neutral aqueous solution. X-ray structure of [C(NH2)3]6[(UO2)3(CO3)6].cntdot.6.5H2O. *Inorg. Chem.* 34:4797–4807.

Alonso, M.C., Calvo, J.L.G., Cuevas, J., Turrero, M.J., Fernández, R., Torres, E., and Ruiz, A.I. 2017. Interaction processes at the concrete-bentonite interface after 13 years of FEBEX-Plug operation. Part I: Concrete alteration. *Physics and Chemistry of the Earth, Parts A/B/C* 99:38–48.

Altmann, S. 2008. 'Geochemical research: A key building block for nuclear waste disposal safety cases. *Journal of Contaminant Hydrology* 102:174-179.

Altmann, S., Tournassat, C., Goutelard, F., Parneix, J.-C., Gimmi, T., and Maes, N. 2012. Diffusion-driven transport in clayrock formations. *Applied Geochemistry* 27:463–478.

Álvarez, M. G., Lapitz, P. and Ruzzante, J. 2008. AE response of type 304 stainless steel during stress corrosion crack propagation. *Corrosion Science* 50 (12): 3382–3388.

AMBERG. 2019. *HotBENT: Experiment Plan* (Draft 20190927 v2.docx). Distributors: Florian Kober (NAGRA) and Stratis Vomvoris (NAGRA).

Andersson, J., Skagius, K., Winberg, A., Lindborg, T., and Ström, A. 2013. Site descriptive modeling for a final repository for spent nuclear fuel in Sweden. *Environ Earth Sci* 69(3): 1045–1060.doi:10.1007/s12665-013-2226-1.

Arndt, D., Bangerth, W., Clevenger, T.C., Davydov, D., Fehling, M., Garcia-Sanchez, D., Harper, G., Heister, H., Heltai, L., Kronbichler, M., Maguire Kynch, R., Maier, M., Pelteret J.-P., Turcksin, B., and Wells, D. 2019. The deal.II library, Version 9.1. *Journal of Numerical Mathematics* 27(4): 203–213.

Arnold, J., Duddu, R., Brown, K. and Kosson, D.S. 2017. Influence of multi-species solute transport on modeling of hydrated Portland cement leaching in strong nitrate solutions. *Cement and Concrete Research* 100:227–244.

ASTM International. 2010. ASTM D4404-10, *Standard Test Method for Determination of Pore Volume and Pore Volume Distribution of Soil and Rock by Mercury Intrusion Porosimetry*. West Conshohocken, PA.

Balistrieri, L.S., and Chao, T.T. 1987. Selenium Adsorption by Goethite. *Soil Science Society of America Journal* 51:1145–1151.

Balistrieri, L.S., and Chao, T.T. 1990. Adsorption of selenium by amorphous iron oxyhydroxide and manganese dioxide. *Geochimica et Cosmochimica Acta* 54:739–751.

Balme, S., Kharroubi, M., Haouzi, A., and Henn, F. 2010. Non-Arrhenian Ionic dc Conductivity of Homoionic Alkali Exchanged Montmorillonites with Low Water Loadings. *Journal of Physical Chemistry C* 114:9431–9438.

Bangerth, W. 2019. *deal.II — an open source finite element library*. https://www.dealii.org/.

Bangerth, W., Burstedde, C., Heister, T., and Kronbichler, M. 2012. Algorithms and Data Structures for Massively Parallel Generic Adaptive Finite Element Codes. *ACM Transactions on Mathematical Software* 38(2): Article 14.

Bangerth, W., Hartmann, R., and Kanschat, G. 2007. deal.II—A general-purpose object-oriented finite element library. *ACM Transactions on Mathematical Software* 33(4): Article 24.

Bárcena, I., Fuentes-Cantillana, J.L. and García-Siñeriz, J.L. 2003. *Dismantling of the Heater 1 at the FEBEX "“in situ”" test. Description of operations.* ENRESA Technical Report 9/2003.

Bar-Yosef, B., and Meek, D. 1987. Selenium Sorption by Kaolinite and Montmorillonite. *Soil Science* 144:11–19.

Bastrakov, E., Jaireth, S. and Mernagh, T. 2010. “Solubility of uranium in hydrothermal fluids at 25˚C to 300˚C. Implications for the formation of uranium deposits.” in: *Australia*, G. (Ed.), Canberra, p. 91.

Belarbi, H., Haouzi, A., Guintini, J.C., Zanchetta, J.V., Niezette, J., and Vanderschueren, J. 1997. Interpretation of orientation polarization in dry montmorillonite. *Clay Minerals* 32:13–20.

Bérend, I.; Cases, J.-M.; François, M.; Uriot, J.-P.; Michot, L.; Masion, A.; Thomas, F. 1995. Mechanism of Adsorption and Desorption of Water Vapor by Homoionic Montmorillonites: 2. The Li Na , K , Rb and Cs -Exchanged Forms. *Clays Clay Miner*. 43 (3): 324–336.

Berendsen, H.J.C., Postma, J.P., van Gunsteren, W.F. and Hermans, J. 1981. “Interaction models for water in relation to protein hydration.” In *Intermolecular Forces* (ed. B. Pullmann).Reidel, Dordrecht, pp. 331–342.

Biscaye, P.E. 1965. Mineralogy and Sedimentation of Recent Deep-Sea Clay in the Atlantic Ocean and Adjacent Seas and Oceans. *GSA Bulletin* 76:803–832.

Booker, J.R. and Savvidou, C. 1985. Consolidation around a point heat source. *International Journal for Numerical and Analytical Methods in Geomechanics* 9:173–184.

Börjesson, L., Gunnarsson, D., Johannesson, L-E., and Jonsson, E. 2010. *Design, production and initial state of the buffer*. Svensk Kärnbränslehantering Technical Report, TR-10-15, 89.

Bourdelle, F., Mosser-Ruck, R., Truche, L., Lorgeoux, C., Pignatelli, I., and Michau, N. 2017. A new view on iron-claystone interactions under hydrothermal conditions (90° C) by monitoring in situ pH evolution and H2 generation. *Chemical Geology* 466:600–607.

Bourdelle, F., Truche, L., Pignatelli, I., Mosser-Ruck, R., Lorgeoux, C., Roszypal, C., and Michau, N. 2014. Iron–clay interactions under hydrothermal conditions: Impact of specific surface area of metallic iron on reaction pathway. *Chemical Geology* 381:194–205.

Bourg, I.C., and Ajo-Franklin, J.B. 2017. Clay, Water, and Salt: Controls on the Permeability of Fine-Grained Sedimentary Rocks. *Acc Chem Res* 50(9): 2067–2074, doi:10.1021/acs.accounts.7b00261.

Bourg, I.C., Sposito, G., and Bourg, A.C.M. 2006. Tracer diffusion in compacted, water-saturated bentonite. *Clays and Clay Minerals* 54:363–374.

Boving, T.B. and Grathwohl, P. 2001. Tracer diffusion coefficients in sedimentary rocks: correlation to porosity and hydraulic conductivity. *Journal of Contaminant Hydrology* 53:85–100.

Bradbury, M.H. and Baeyens, B. 2003. Porewater chemistry in compacted re-saturated MX-80 bentonite. *Journal of Contaminant Hydrology* 61(1–4): 329–338.

Bradbury, M.H., Berner, U., Curti, E., Hummel, W., Kosakowski, G., and Thoenen, T. 2014. *The long term geochemical evolution of the nearfield of the HLW repository.* No. NTB--12-01. Paul Scherrer Institute (PSI).

Branch, J.L. 2018. *Impact of Aging in the Presence of Reactive Gases on Cementitious Waste Forms and Barriers, Environmental Engineering*. Vanderbilt University, Nashville, Tennessee, p. 197.

Brugger, J., Liu, W., Etschmann, B., Mei, Y., Sherman, D.M. and Testemale, D. 2016 A review of the coordination chemistry of hydrothermal systems, or do coordination changes make ore deposits? *Chem. Geol*. 447:219–253.

Buscheck, T., Rosenberg, N., Gansemer, J. and Sun, Y. 2002 Thermohydrologic behavior at an underground nuclear waste repository. *Water Resour. Res*. 38: 10-11-10-19.

Calvo, J.G., Hidalgo, A., Alonso, C. and Luco, L.F. 2010. Development of low-pH cementitious materials for HLRW repositories: Resistance against ground waters aggression. *Cement and Concrete Research* 40(8): 1290–1297.

Calvo, R., Klein-BenDavid, O., Peer, G., MacKinnon, R., Freeze, G. and Sassani, D. 2019. *Borehole Disposal of Radioactive Waste in the Vadose Zone of the Yamin Plain, Negev, Israel.*

Caporuscio, F.A., Migdissov, A., Rock, M.J., Sauer, K.B., and van Hartesveldt, N.F. 2019. *Engineered Barrier System R&D and International Collaborations–LANL (FY19)* (No. LA-UR-19-24222). Los Alamos National Lab (LANL), Los Alamos, NM (United States).

Caporuscio, F.A., Sauer, K.B., Rock, M.J., and Houser, L.M. 2018. *Engineered System R&D and International Collaborations – Los Alamos National Laboratory (FY18).* Deliverable SF&WD R&D Work package # SF18LA01030801/SF-18LA01030805, LA-UR-18-27601.

Cardoso, R. and Alonso, E.E. 2009. Degradation of Compacted Marls: A Microstructural Investigation. *Soils and Foundations* 49:315–327.

Cases, J.M., Berend, I., Besson, G., Francois, M., Uriot, J.P., Thomas, F., Poirier, J.E. 1992. Mechanism of adsorption and desorption of water vapor by homoionic montmorillonite. 1. The sodium-exchanged form. *Langmuir* 8 (11): 2730–2739.

Cathelineau, M., Guillaume, D., Mosser-Ruck, R., Dubessy, J., Charpentier, D., Villiéras, F., Michau, N., 2005. "Dissolution–crystallization processes affecting di-octahedral smectite in presence of iron metal: implication on mineral distribution in clay barriers." *Clays in Natural and Engineered Barriers for Radioactive Waste Confinement*. ANDRA, France, p. 35.

Charlet, L., Kang, M., Bardelli, F., Kirsch, R., Géhin, A., Grenèche, J.-M., Chen, F. 2012. Nanocomposite Pyrite–Greigite Reactivity toward Se(IV)/Se(VI). *Environmental Science & Technology* 46:4869–4876.

Charlet, L., Scheinost, A.C., Tournassat, C., Greneche, J.M., Géhin, A., Fernández-Martı´nez, A., Coudert, S., Tisserand, D., and Brendle, J. 2007. Electron transfer at the mineral/water interface: Selenium reduction by ferrous iron sorbed on clay. *Geochimica et Cosmochimica Acta* 71:5731–5749.

Chermak, J.A. 1992. Low temperature experimental investigation of the effect of high pH NaOH solutions on the opalinus shale, Switzerland. *Clays and Clay Minerals* 40:650–658.

Cheshire, M.C., Caporuscio, F.A., Jove Colón, C. and McCarney, M.K. 2014. Bentonite Clay evolution at elevated pressures and temperatures: An experimental study for generic nuclear repositories. *American Mineralogist* 99:1662–1675.

Cheshire, M.C., Caporuscio, F.A., Jove Colón, C.F., Norskog, K.E. 2018. Fe-saponite growth on low-carbon and stainless steel in hydrothermal-bentonite experiments. *Journal of Nuclear Materials* 511:353–366.

Chipera, S.J. and Bish, D.L. 2002. FULLPAT: a full-pattern quantitative analysis program for X-ray powder diffraction using measured and calculated patterns. *Journal of Applied Crystallography* 35:744–749.

Chung, F.H. 1974. Quantitative interpretations of X-ray diffraction patterns of mixtures. I. Matrix flushing method for quantitative multicomponent analysis. *Journal of Applied Crystallography* 7:519–525.

Crerar, D.A., Susak, N.J., Borcsik, M., and Schwartz, S. 1978. Solubility of the buffer assemblage pyrite + pyrrhotite + magnetite in NaCl solution from 200 to 350 °C. *Geochimica et Cosmochimica Acta* 42:1427–1437.

Crossland, I. 2017. "Surface, subsurface, intermediate depth and borehole disposal." in: *Apted, M.J.*, Ahn, J. (Eds.), second edition ed. Woodhead Publishing, UK, pp. 57–88.

Cuadros, J., and Linares, J. 1996. Experimental kinetic study of the smectite-to-illite transformation. *Geochimica et Cosmochimica Acta* 60:439–453.

Cuevas, J., De La Villa, R. V., Ramírez, S., Sánchez, L., Fernández, R. and Leguey, S. 2006 The alkaline reaction of FEBEX bentonite: a contribution to the study of the performance of bentonite/concrete engineered barrier systems. *Journal of Iberian Geology* 32(2): 151–174

Cuevas, J., Villar, M. V., Fernández, A. M., Gómez, P., and Martín, P. L. 1997. Pore waters extracted from compacted bentonite subjected to simultaneous heating and hydration. *Applied Geochemistry* 12(4): 473–481. doi:https://doi.org/10.1016/S0883-2927(97)00024-3

Cui, L. and Cahyadi, J.H. 2001. Permeability and pore structure of OPC paste. *Cement and Concrete Research* 31:277–282.

Cuney, M. 2009. The extreme diversity of uranium deposits. *Miner. Depos.* 44:3–9.

Cygan, R.T.; Liang, J.-J.; and Kalinichev, A.G. 2004. Molecular Models of Hydroxide, Oxyhydroxide, and Clay Phases and the Development of a General Force Field. *J. Phys. Chem. B* 108 (4): 1255–1266. https://doi.org/10.1021/jp0363287.

Dacy, J., and Martin, P. 2006. *Practical advances in core-based water saturation analysis of shaly tight gas sands*. SCA2006-29.

Delay, J., Vinsot, A., Krieguer, J.-M., Rebours, H., and Armand, G. 2007. Making of the underground scientific experimental programme at the Meuse/Haute-Marne underground research laboratory, North Eastern France. *Physics and Chemistry of the Earth, Parts A/B/C* 32:2–18.

Deslandes, A.; Jasieniak, M.; Ionescu, M.; Shapter, J.G.; Fairman, C.; Gooding, J.J.; Hibbert, D.B.; Quinton, J.S. 2009. ToF-SIMS characterisation of methane- and hydrogen-plasma-modified graphite using principal component analysis. *Surface and Interface Analysis* 41 (3): 216–224.

Detzner, K. and Kober, F. 2015. *FEBEX-DP drilling and sampling report sections 32-34.* Internal report, AN15-714, NAGRA.

Dirksen, D. 1969 Thermo-osmosis through compacted saturated clay membranes. *Soil Sci. Soc. Am. Proc*. 33(6): 821–826.

Dittrich, T.M., Boukhalfa, H., Ware, S.D., and Reimus, P.W. 2015. Laboratory investigation of the role of desorption kinetics on americium transport associated with bentonite colloids. *Journal of environmental radioactivity* 148:170–182.

Doménech-Carbó, A.; Doménech-Carbó, M.T.; Gimeno-Adelantado, J.V.; Bosch-Reig, F.; Saurí-Peris, M.C.; Casas-Catalán, M.J. 2001. Electrochemical analysis of the alterations in copper pigments using charge transfer coefficient/peak potential diagrams. Application to microsamples of baroque wall paintings attached to polymer film electrodes. *Fresenius J Anal Chem* 369:6.

Driesner, T. 2007. The System H2O–NaCl. II. Correlations for molar volume, enthalpy, and isobaric heat capacity from 0 to 1000 °C, 1 to 5000 bar, and 0 to 1 XNaCl. *Geochim. Cosmochim. Acta* 71:4902–4919.

Driesner, T. and Heinrich, C.A. 2007. The System H2O–NaCl. I. Correlation Formulae for Phase Relations in Temperature–Pressure-Composition Space from 0 to 1000°C, 0 to 5000 bar, and 0 to 1 XNaCl. *Geochim. Cosmochim. Acta* 71:4880–4901.

Eberl, D. 1978. Reaction series for dioctahedral smectites. *Clays and Clay Minerals* 26:327–340.

Eberl, D. and Hower, J. 1977. The hydrothermal transformation of sodium and potassium smectite into mixed-layer clay. *Clays and Clay Minerals* 25:215–227.

Eberl, D.D., Velde, B., and McCormick, T. 1993. Synthesis of illite-smecite from smectite at Earth surface temperatures and high pH. *Clay Minerals* 28:49–60.

ECN. 2019. *LeachXS User's Guide: LeachXS Pro Version 3.0.10*. Energy Research Centre of The Netherlands, Petten, The Netherlands,.

Elgrishi, N., Rountree, K.J., McCarthy, B.D., Rountree, E.S.; Eisenhart, T.T.; Dempsey, J.L. 2017. A Practical Beginner's Guide to Cyclic Voltammetry. *Journal of Chemical Education* 95 (2): 197–206.

Ewing, R.C. 2015. Long-term storage of spent nuclear fuel. *Nature Materials* 14:252–257.

Ewing, R.C., Whittleston, R.A., and Yardley, B.W.D. 2016. Geological Disposal of Nuclear Waste: a Primer. *Elements* 12:233–237.

Fan, X.; Lu, Y.; Xu, H.; Kong, X.; Wang, J. 2011. Reversible redox reaction on the oxygen-containing functional groups of an electrochemically modified graphite electrode for the pseudo-capacitance. *Journal of Materials Chemistry* 21 (46).

Fernández, A.M., and Villar, M. V. 2010. Geochemical behaviour of a bentonite barrier in the laboratory after up to 8years of heating and hydration. *Applied Geochemistry* 25(6): 809–824. doi:https://doi.org/10.1016/j.apgeochem.2010.03.001

Fernández, A.M., Baeyens, B., Bradbury, M., and Rivas, P. 2004. Analysis of the porewater chemical composition of a Spanish compacted bentonite used in an engineered barrier. *Physics and Chemistry of the Earth, Parts A/B/C* 29:105–118.

Fernández, A.M., Kaufhold, S., Sánchez-Ledesma, D.M., Rey, J.J., Melón, A., Robredo, L.M., Fernandez, S., Labajo, M.A., and Clavero, M.A. 2018. Evolution of the THC conditions in the FEBEX in situ test after 18 years of experiment: Smectite crystallochemical modifications after interactions of the bentonite with a C-steel heater at 100° C. *Applied Geochemistry* 98:152–171.

Fernández, R., Cuevas, J., and Mäder, U.K. 2009. Modelling concrete interaction with a bentonite barrier. *European Journal of Mineralogy* 21(1): 177–191.

Fernández, R., Cuevas, J., Sánchez, L., de la Villa, R.V. and Leguey, S. 2006 Reactivity of the cement–bentonite interface with alkaline solutions using transport cells. *Applied Geochemistry* 21:977–992.

Fernández, R., Torres, E., Ruiz, A.I., Cuevas, J., Alonso, M.C., Calvo, J.L. G., ... and Turrero, M.J. 2017. Interaction processes at the concrete-bentonite interface after 13 years of FEBEX-Plug operation. Part II: Bentonite contact. *Physics and Chemistry of the Earth, Parts A/B/C* 99:49–63.

Ferrage, E. 2005. Investigation of Smectite Hydration Properties by Modeling Experimental X-Ray Diffraction Patterns: Part I. Montmorillonite Hydration Properties. *Am. Mineral.* 90 (8–9): 1358–1374. https://doi.org/10.2138/am.2005.1776.

Figueiredo, B., Tsang, C.F., Niemi, A., and Lindgren, G. 2016. The state-of-art of sparse channel models and their applicability to performance assessment of radioactive waste repositories in fractured crystalline formations. *Hydrogeology Journal* 24(7): 1607–1622.

Finch, R.J., Cooper, M.A., Hawthorne, F.C. and Ewing, R.C. 1999. Refinement of the crystal structure of rutherfordine. *Can. Mineral*. 37:929–938.

Finsterle, S., Kowalsky M., Kober F., and Vomvoris, S. 2017. *HotBENT – Preliminary Design Study of Phenomenological Aspects*. NAB 17-30.

Fiorin, G.; Klein, M. L.; Hénin, J. 2013. Using Collective Variables to Drive Molecular Dynamics Simulations. *Mol. Phys.* 111 (22–23): 3345–3362. https://doi.org/10.1080/00268976.2013.813594.

Fox, P.M., Tinnacher, R.M., Cheshire, M.C., Caporuscio, F., Carrero, S., Nico, P.S. 2019. Effects of bentonite heating on U(VI) adsorption. *Applied Geochemistry* 109:104392.

Gaboreau, S., Prêt, D., Tinseau, E., Claret, F., Pellegrini, D. and Stammose, D. 2011. 15 years of in situ cement–argillite interaction from Tournemire URL: Characterisation of the multi-scale spatial heterogeneities of pore space evolution. *Applied Geochemistry* 26:2159–2171.

Garcia-Garcia, S., Wold, S., and Jonsson, M. 2009. Effects of temperature on the stability of colloidal montmorillonite particles at different pH and ionic strength. *Applied Clay Science* 43(1): 21–26.

García-Gutiérrez, M., Cormenzana, J.L., Missana, T., Mingarro, M., and Alonso, U. 2003. "Analysis of Uranium Diffusion Coefficients in Compacted FEBEX Bentonite." *MRS Proceedings* 807:603.

García-Gutiérrez, M., Missana, T., Mingarro, M., Samper, J., Dai, Z., Molinero, J. 2001. Solute transport properties of compacted Ca-bentonite used in FEBEX project. *Journal of Contaminant Hydrology* 47:127–137.

Garcia-Sineriz, J.L., Abós, H., Martínez, V., De la Rosa, C., Mäder, U. and Kober, F. 2016. *FEBEX-DP Dismantling of the heater 2 at the FEBEX "in situ" test.* Nagra Arbeitsbericht NAB 16-011. p. 92.

Garrabrants, A., Kosson, D., Stefanski, L., DeLapp, R., Seignette, P., Van der Sloot, H., Kariher, P., and Baldwin, M. 2012. *Interlaboratory validation of the leaching environmental assessment framework (LEAF) method 1313 and method 1316*.

Garrabrants, A.C., Kosson, D.S., van der Sloot, H.A., Sanchez, F., and Hjelmar, O. 2010. *Background information for the Leaching Enviornmental Assessment Framework (LEAF) Test Methods.* U.S. Environmental Protection Agency.

Gaucher, E.C., and Blanc, P. 2006. Cement/clay interactions – A review: Experiments, natural analogues, and modeling. *Waste Management* 26:776–788.

Gaudin, A., Bartier, D., Truche, L., Tinseau, E., Foct, F., Dyja, V., Maillet, A. and Beaufort, D. 2013. First corrosion stages in Tournemire claystone/steel interaction: In situ experiment and modelling approach. *Applied clay science* 83:457–468.

Gens, A. 2010. Soil environment interactions in geotechnical engineering. *Géotechnique* 60:3–74.

Gens, A., Sanchez, M., Guimaraes, L. Do N., Alonso, E.E., Lloret, A., Olivella, S., Villar, M.V., and Huertas, F. 2009. A full-scale in situ heating test for high-level nuclear waste disposal: Observations, analysis and interpretation. *Geotechnique* 59(4): 377–399.

Ghabezloo, S, Sulem, J, Guédon, S, Martineau, F. 2009. Effective stress law for the permeability of a limestone. *Int. J. Rock Mech. Min. Sci.*46:297–306.

Ghassemi, A. and Diek, A. (2002) Porothermoelasticity for swelling shales. Journal of Petroleum Science and Engineering, 34: 123-125.

Ghosh, P.K.; Bard, A.J. 1983. Clay-Modified Electrodes. *Journal of the American Chemical Society* 105:3.

Glaus, M.A., and Van Loon, L.R. 2012. "Diffusive behavior of charged metal ion complexes in compacted montmorillonite, Clays in natural and engineered barriers for radioactive waste confinement – 5." *International meeting Book of abstracts*. France, p. 923.

Gómez-Espina, R., and Villar, M.V. 2010. Geochemical and mineralogical changes in compacted MX-80 bentonite submitted to heat and water gradients. *Applied Clay Science* 47(3): 400–408. doi:https://doi.org/10.1016/j.clay.2009.12.004

Grambow, B. 2016. Geological Disposal of Radioactive Waste in Clay. *Elements* 12:239–245.

Greenburg, H. and Wen, J. 2013. *Repository layout and host rock thermal gradient trade study for large waste packages in clay/shale: Using the DSEF thermal analytical model*. p. 38.

Gregg, B. 2019. *Flame Graphs*. http://www.brendangregg.com/flamegraphs.html.

Grygar, T.; Marken, F.; Schröder, U.; Scholz, F. 2002. Electrochemical Analysis of Solids. A Review. *Collection of Czechoslovak Chemical Communications* 67 (2): 163–208.

Gu, B.X., Wang, L.M., Minc, L.D., and Ewing, R.C. 2001. Temperature effects on the radiation stability and ion exchange capacity of smectites. *Journal of Nuclear Materials* 297:345–354.

Gueven, N., and Huang, W.L. 1990. *Effects of Mg2+ and Fe3+ substitutions on the crystallization of discrete illite and illite/smectite mixed layers*. Int. rep. Dept. Geosciences Texas Tech University, Exxon Production research Co, Houston, Texas.

Guillaume, D., Neaman, A., Cathelineau, M., Mosser-Ruck, R., Peiffert, C., Abdelmoula, M., Dubessy, J., Villieras, F., and Michau, N. 2004. Experimental study of the transformation of smectite at 80 to 300°C in the presence of Fe oxides. *Clay Minerals* 39:17–34.

Guillaumont, R., Fanghanel, T., Fuger, J., Grenthe, I., Neck, V., Palmer, D.A. and Rand, M.A. 2003. *Update on the Chemical Thermodynamics of Uranium, Neptunium, Plutonium, Americium and Technetium*.

Guimarães, L.D.N., Gens, A., Sánchez, M., and Olivella, S. 2013. A chemo-mechanical constitutive model accounting for cation exchange in expansive clays. *Géotechnique* 63:221–234.

Günther, T., and Rücker, C. 2012. *Boundless Electrical Resistivity Tomography (BERT) v. 2.0 - Open Access Software for Advanced and Flexible Imaging*. presented January 2012 at Schlumberger Symposium - 100 years of electrical imaging, Paris.

Guyonnet, D., Touze-Foltz, N., Norotte, V., Pothier, C., Didier, G., Gailhanou, H., Blanc, P., and Warmont, F. 2009. Performance-based indicators for controlling geosynthetic clay liners in landfill applications. Geotextiles and Geomembranes 27:321–331.

Hadgu, T., Dewers, T., Matteo, E., Gomez, S., and Matteo, E. 2020. *EBS Task Force: Task 9/FEBEX Modeling Final Report: Thermo-Hydrologic Modeling with PFLOTRAN*, Sandia National Laboratories, Albuquerque, NM, SAND2020-4195 R.

Hadi, J., Wersin, P., Serneels, V., and Greneche, J.M. 2019. Eighteen years of steel–bentonite interaction in the FEBEX in situ test at the Grimsel Test Site in Switzerland. *Clays and Clay Minerals* 67(2): 111–131.

Hammond, G.E., Lichtner, P.C., and Mills, R.T. 2014. Evaluating the Performance of Parallel Subsurface Simulators: An Illustrative Example with PFLOTRAN. *Water Resources Research* 50. doi:10.1002/2012WR013483.

Hangx, S.J.T., Linden, A.v.d., Marcelis, F. and Liteanu, E. 2016. Defining the Brittle Failure Envelopes of Individual Reaction Zones Observed in CO2-Exposed Wellbore Cement. *Environmental Science & Technology* 50:1031–1038.

Hardin, E., Bryan, C., Ilgen, A., Kalinina, E., Teich-Goldrick, S., Banerjee, K., Clarity, J., Howard, R., Jubin, R., Scaglione, J., Perry, F., Zheng, L., Rutqvist, J., Birkholzer, J.T., Greenberg, H., Carter, J., and Severynse, T. 2014. *Investigation of Dual-Purpose Canister Direct Disposal Feasibility*. FCRD-UFD-2014-000069 REV 1. Sandia National Laboratories, Albuquerque, NM:

Hardin, E., Clayton, D., Howard, R., Scaglione, J., Pierce, E., Banerjee, K., Voegele, M., Greenberg, H., Wen, J. and Buscheck, T. 2013. *Preliminary Report on Dual-Purpose Canister Disposal Alternatives (FY13)*. US Department of Energy, Used Fuel Disposition Campaign.

Hardin, E., Hadgu, T., and Clayton, D.J. 2015. *Cavern/Vault Disposal Concepts and Thermal Calculations for Direct Disposal of 37-PWR Size DPCs*. United States: N. Web. doi:10.2172/1172177.

Hasse, U., and F. Scholz. 2001. In situ atomic force microscopy of the reduction of lead oxide nanocrystals immobilised on an electrode surface. *Electrochemistry Communications* 3:6.

Hedin, A. and Olsson, O. 2016. Crystalline Rock as a Repository for Swedish Spent Nuclear Fuel. *Elements* 12:247–252.

Helgeson, H.C., Kirkham, D.H. and Flowers, G.C. 1981. Theoretical prediction of the thermodynamic behaviour of aqueous electrolytes at high pressures and temperatures IV. Calculation of activity coefficients , osmotic coefficients, and apparent molal and standard and relative partial molal properties to 600°C and 5KB. *Am. J. Sci*. 281:1249–1516.

Hem, J.D. 1985. “Study and Interpretation of the Chemical Characteristics of Natural Water,” in: *USGS* (Ed.). United States Government Printing Office.

Ho, T.A.; Criscenti, L.J.; and Greathouse, J.A. 2019. Revealing Transition States during the Hydration of Clay Minerals. *J. Phys. Chem. Lett.* 10 (13): 3704–3709. https://doi.org/10.1021/acs.jpclett.9b01565.

Holmboe, M., and Bourg, I.C. 2013. Molecular dynamics simulations of water and sodium diffusion in smectite interlayer nanopores as a function of pore size and temperature. *The Journal of Physical Chemistry C* 118 (2): 1001–1013.

Holmboe, M.; Wold, S.; Jonsson, and M. 2012. Porosity Investigation of Compacted Bentonite Using XRD Profile Modeling. *J. Contam. Hydrol.* 128 (1–4): 19–32. https://doi.org/10.1016/j.jconhyd.2011.10.005.

Honorio, T., Brochard, L., and Vandamme, M. 2017. Hydration phase diagram of clay particles from molecular simulations. *Langmuir* 33 (44): 12766–12776.

Horai, K.-I. 1971. Thermal conductivity of rock-forming minerals., *Journal of Geophysical Research* 76 (5): 1278.

Hsiao, Y., and Hedström, M. 2017. Swelling pressure in systems with na-montmorillonite and neutral surfaces: A molecular dynamics study. *The Journal of Physical Chemistry C* 121 (47): 26414–26423.

Huertas, F., Fuentes-Cantillana, J., Jullien, F., Rivas, P., Linares, J., Fariña, P., Ghoreychi, M., Jockwer, N., Kickmaier, W., Martínez, M. 2000. *Full-scale engineered barriers experiment for a deep geological repository for high-level radioactive waste in crystalline host rock (FEBEX project).* EUR(Luxembourg).

Idemitsu, K., Kozaki, H., Yuhara, M., Arima, T., and Inagaki, Y. 2016. Diffusion behavior of selenite in purified bentonite. *Progress in Nuclear Energy* 92:279–285.

Idemitsu, K., Tachi, Y., Furuya, H., Inagaki, Y., and Arima, T. 1995. "Diffusion of uranium in compacted bentonites in the reducing condition with corrosion products of iron." *MRS Online Proceedings Library Archive* 412.

Ikeda, A., Hennig, C., Tsushima, S., Takao, K., Ikeda, Y., Scheinost, A.C. and Bernhard, G. 2007. Comparative study of uranyl(VI) and -(V) carbonato complexes in an aqueous solution. *Inorg. Chem.* 46:4212–4219.

Ingraffea, A.R., Wells, M.T., Santoro, R.L. and Shonkoff, S.B.C. 2014. "Assessment and risk analysis of casing and cement impairment in oil and gas wells in Pennsylvania, 2000–2012." *Proceedings of the National Academy of Sciences* 111, 10955.

Ishikawa, H., Umeki, H. and Miyahara, K. 2005. "Research and development challenges for repository design and implementation." *Proceedings of an International Conference High Level Radioactive Waste Management,* 167-176.

Itasca. 2009. *FLAC3D, Fast Lagrangian Analysis of Continua in 3 Dimensions, Version 4.0*. Minneapolis, Minnesota, Itasca Consulting Group.

Jackson, R.B. 2014. "The integrity of oil and gas wells." *Proceedings of the National Academy of Sciences* 111, 10902.

Järvinen, J., Matusewicz, M., and Itälä, A. 2016. Methodology for studying the composition of non-interlamellar pore water in compacted bentonite. *Clay Minerals* 51:173–187. doi:10.1180/claymin.2016.051.2.05

Jenni, A., Mäder, U., Lerouge, C., Gaboreau, S. and Schwyn, B. 2014. In situ interaction between different concretes and Opalinus Clay. *Physics and Chemistry of the Earth, Parts A/B/C* 70-71:71-83.

Jeyanthi, C.E.; Siddheswaran, R.; Medlín, R.; Karl Chinnu, M.; Jayavel, R.; Rajarajan, K. 2014. Electrochemical and structural analysis of the RE3+:CeO2 nanopowders from combustion synthesis. *Journal of Alloys and Compounds* 614:118–125.

Johannesson, L. E., Börgesson, L., Goudarzi, R., Sandén, T., Gunnarsson, D. and Svemar, C. 2007. Prototype repository: A full scale experiment at Äspö HRL. *Physics and Chemistry of the Earth, Parts A/B/C* 32:58–76. https://doi.org/10.1016/j.pce.2006.04.027. 1252

Johnson, L., Niemeyer, M., Klubertanz, G., Siegel, P., and Gribi, P. 2002. *Calculations of the temperature evolution of a repository for spent fuel, vitrified high-level waste and intermediate level waste in Opalinus Clay.* National Cooperative for the Disposal of Radioactive Waste.

Joseph, C., Mibus, J., Trepte, P., Müller, C., Brendler, V., Park, D.M., Jiao, Y., Kersting, A.B., and Zavarin, M. 2017. Long-term diffusion of U(VI) in bentonite: Dependence on density. *Science of the Total Environment* 575:207–218.

Joseph, C., Van Loon, L.R., Jakob, A., Steudtner, R., Schmeide, K., Sachs, S., and Bernhard, G. 2013. Diffusion of U(VI) in Opalinus Clay: Influence of temperature and humic acid. *Geochimica et Cosmochimica Acta* 109:74–89.

Jové Colon, C.F., Caporuscio, F.A, Sauer, K., and Cheshire, M.C. 2019. *Engineered barrier material interactions at elevated temperatures: Bentonite-metal interactions under elevated temperature conditions*. Sandia National Laboratories: SAND2019-0714C. https://www.osti.gov/servlets/purl/1595898.

Jove Colón, C.F., Caporuscio, F.A., Levy, S.S., Sutton, M., Blink, J., Greenberg, H.R., Fratoni, M., Halsey, W.G., Wolery, T.J., Rutqvist, J., et al. 2011. *Disposal systems evaluations and tool development - Engineered Barrier System (EBS) Evaluation (Fuel Cycle Research and Development)*. Sandia National Laboratory, (FCRD-USED-2011-000132), 1-192.

Kalintsev, A., Migdisov, A.A., Xu, H., Roback, R. and Brugger, J. 2019. Uranyl speciation in sulfate-bearing hydrothermal solutions up to 250 °C. *Geochim. Cosmochim. Acta* In press.

Karnland O. 2010. *Chemical and mineralogical characterization of the bentonite buffer for the acceptance control procedure in a KBS-3 repository.* SKB Technical Report TR-10-60.

Karnland, O. 1997. *Cement/bentonite interaction. Results from 16 month laboratory tests.* No. SKB-TR--97-32. Swedish Nuclear Fuel and Waste Management Co.

Kaufhold, S., Hassel, A. W., Sanders, D., and Dohrmann, R. 2015. Corrosion of high-level radioactive waste iron-canisters in contact with bentonite. *Journal of Hazardous Materials* 285:464–473.

Kersting, A., Zavarin, M., Zhao, P., Dai, Z., Carroll, S., Wang, Y., Miller, A., James, S., Reimus, P., Zheng, L., Li, L., Rutqvist, J., Liu, H., and Birkholzer, J. 2012. *Radionuclide Interaction and Transport in Representative Geologic Media.* Lawerence-Livermore National Lab: FCRD-UFD-2012-000154. https://www.energy.gov/sites/prod/files/2013/06/f1/FY12%20Radionuclide%20Interaction%20and%20Transport%20in%20Representative%20Geologic%20Media.pdf

Kharroubi, M., Balme, S., Haouzi, A., Belarbi, H., Sekou, D., and Henn, F. 2012. Interlayer Cation–Water Thermodynamics and Dynamics in Homoionic Alkali and Alkaline-Earth Exchanged Montmorillonites with Low Water Loadings. *The Journal of Physical Chemistry C* 116 (28): 14970–14978, doi:10.1021/jp303963r.

Kim, J., Sonnenthal, E.L., and Rutqvist, J. 2012. Formulation and sequential numerical algorithms of coupled fluid/heat flow and geomechanics for multiple porosity materials. *International Journal for Numerical Methods in Engineering* 92 (5): 425–456.

Kim, N. 2020. Uftrace. https://github.com/namhyung/uftrace.

Kiverant, L., Kumpulainen, S., Pintado, X., Karttnen, P., Schatz, T. 2018. *Characterization of Bentonite and Clay minerals 2012-2015*. POSIVA working report 2016-05

Klein-BenDavid, O., Harlavan, Y., Levkov, I., Teutsch, N., Brown, K.G., Gruber, C. and Ganor, J. 2019. Interaction between spent fuel components and carbonate rocks. *Science of the Total Environment* 689:469–480.

Kloprogge, J.T., Komarneni, S. and Amonette, J.E. 1999. Synthesis of smectite clay minerals: a critical review. *Clays and Clay Minerals* 47:529–554.

Kober F., Schneeberger, R., Manukyan, E., Stasiek, L., Müller, H., and Vomvoris S. 2020. *HotBENT : Experiment Plan*. NAB19-43.

Kober, F., et al. 2017. FEBEX-DP. *Metal Corrosion and Iron-Bentonite Interaction Studies*. Nagra Arbeitsbericht, NAB 16–16, Nagra, Wettingen, Switzerland, 300 pp.

Kong, L. and Du, Y. 2015. Interfacial interaction of aggregate-cement paste in concrete. *Journal of Wuhan University of Technology-Mater. Sci.* 30:117–121.

Kosakowski, G. and Berner, U. 2013. The evolution of clay rock/cement interfaces in a cementitious repository for low- and intermediate level radioactive waste. *Physics and Chemistry of the Earth, Parts A/B/C* 64:65–86.

Kronbichler, M., Heister, T., and Bangerth, W. 2012. High accuracy mantle convection simulation through modern numerical methods. *Geophysical Journal International* 191:12–29.

Ku, S.; Palanisamy, S.; Chen, S.-M. 2013. Highly selective dopamine electrochemical sensor based on electrochemically pretreated graphite and nafion composite modified screen printed carbon electrode. *J Colloid Interface Sci* 411:182–186.

Kuhlman, U., and Gaus, I. 2014. *THM Model validation modelling of selected WP2 experiments: Inverse Modelling of the FEBEX in situ test using iTOUGH2*. Deliverable-N°: D3.3-1.

Kurosawa, S., James, S. C., Yui, M., and Ibaraki, M. 2006. Model analysis of the colloid and radionuclide retardation experiment at the Grimsel Test Site. *Journal of Colloid and Interface Science* 298 (1): 467–475.

Kursten, B., Cornelis, B., Labat, S. and Van Iseghem, P. 1996. *Geological Disposal of Conditioned High-Level and Long Lived Radioactive Waste. In situ experiments*. Report R-3121, SCK•CEN (Mol, Belgium).

Kursten, B., Cornelis, B., Labat, S. and Van Iseghem, P. 1997. *Completion of the Corrosion Programme in Boom Clay – in situ experiments*. Report EUR-17105, SCK•CEN (Mol, Belgium).

Kursten, B., Smailos, E., Azkarate, I., Werme, L., Smart, N.R. and Santarini, G. 2004. COBECOMA. *State of the art document on the Corrosion Behaviour of Container Materials*.

Kwon O., Kronenberg A.K., Gangi A.F., and Johnson B. 2001. Permeability of Wilcox shale and its effective pressure law. *J. Geophys. Res.-Sol. Ea.* 106:19339–53.

Lammers, L.N., Bourg, I.C., Okumura, M., Kolluri, K., Sposito, G., and Machida, M. 2017. Molecular dynamics simulations of cesium adsorption on illite nanoparticles. *Journal of colloid and interface science* 490:608–620.

Lantenois, S. 2003. *Réactivité fer métal/smectites en milieu hydraté à 80°C*. Doctoral dissertation.

Lantenois, S., Lanson, B., Muller, F., Bauer, A., Jullien, M., and Plançon, A. 2005. Experimental study of smectite interaction with metal Fe at low temperature: 1. Smectite destabilization. *Clays and Clay Minerals* 53 (6): 597–612.

Lee, J.O., Choi, H., and Lee, J.Y. 2016. Thermal conductivity of compacted Bentonite as a buffer material for a high level waste repository. *Annals of Nuclear Energy* 94:848–855.

Li, Y.-X., Chen, Y.-M., Wei, J.-X., He, X.-Y., Zhang, H.-T. and Zhang, W.-S. 2006. A study on the relationship between porosity of the cement paste with mineral additives and compressive strength of mortar based on this paste. *Cement and Concrete Research* 36:1740–1743.

Lichtner, P.C., Pabalan, R.T. and Steefel, C.I. 1997. "Model Calculations of Porosity Reduction Resulting From Cement-Tuff Diffusive Interaction." *MRS Proceedings* 506:709.

Lim, T.S.; Ryu, H.S.; Hong, S.-H. 2012. Electrochemical corrosion properties of CeO2-containing coatings on AZ31 magnesium alloys prepared by plasma electrolytic oxidation. *Corrosion Science* 62:104–111.

Liu, B.; Yu, X.-Y.; Zhu, Z.; Hua, X.; Yang, L.; Wang, Z. 2014. In situ chemical probing of the electrode–electrolyte interface by ToF-SIMS. *Lab on a Chip* 14 (5): 855–859.

Liu, H.H., Houseworth, J., Rutqvist, J., Zheng, L., Asahina, D., Li, L., Vilarrasa, V., Chen, F., Nakagawa, S., Finsterle, S., Doughty, C., Kneafsey, T. and Birkholzer, J. 2013. *Report on THMC modeling of the near field evolution of a generic clay repository: Model validation and demonstration*. Lawrence Berkeley National Laboratory, August, 2013, FCRD-UFD-2013-0000244.

Livelo, E.; Rojas, R. 2009. Microdot Epoxy Stamping Process Qualification for Substrate-Based Optocoupler BGA Packaging. *ECS Transactions* 18 (1): 10.

Lloret, A., Villar, M.V., Sánchez, M., Gens, A., Pintado, X., and Alonso, E.E. (2003) Mechanical behaviour of heavily compacted bentonite under high suction changes. *Géotechnique* 53 (1): 27–40.

Lorek, A., Labus, M. and Bujok, P. 2016. Wellbore cement degradation in contact zone with formation rock. *Environmental Earth Sciences* 75:499.`

Lothenbach, B., Kulik, D.A., Matschei, T., Balonis, M., Baquerizo, L., Dilnesa, B., Miron, G.D. and Myers, R.J. 2019. Cemdata18: A chemical thermodynamic database for hydrated Portland cements and alkali-activated materials. *Cement and Concrete Research* 115:472–506.

Lothenbach, B., Scrivener, K. and Hooton, R.D. 2011. Supplementary cementitious materials. *Cement and Concrete Research* 41 (12): 1244–1256.

Ma, B., Charlet, L., Fernandez-Martinez, A., Kang, M., and Madé, B. 2019. A review of the retention mechanisms of redox-sensitive radionuclides in multi-barrier systems. *Applied Geochemistry* 100: 414–431.

Mackin, J.E. and Aller, R.C. 1983. The infinite dilution diffusion coefficient for A1(OH)4− at 25°C. *Geochimica et Cosmochimica Acta* 47:959–961.

Mallesha, M., Manjunatha, R., Nethravathi, C., Suresh, G.S., Rajamathi, M., Melo, J.S., Venkatesha, T.V. 2011. Functionalized-graphene modified graphite electrode for the selective determination of dopamine in presence of uric acid and ascorbic acid. *Bioelectrochemistry* 81 (2): 104–8.

Mariner, P.E., Lee, J.H., Hardin, E.L., Hansen, F.D., Freeze, G.A., Lord, A.S., ... and Price, R.H. 2011. *Granite disposal of US high-level radioactive waste*. SAND2011-6203, Sandia, Albuquerque, NM.

Martin, P.L., Barcala, J.M., and Huertas, F. 2006. Large-scale and long-term coupled thermo-hydro-mechanic experiments with bentonite: the FEBEX mock-up test. *Journal of Iberian Geology*. 32:259–282.

Martinez, M.J. and Stone, C.M. 2008. *Considerations for developing models of multiphase flow in deformable porous media*. Sandia National Laboratories SAND Report, SAND2008-5887, Albuquerque New Mexico, USA, 24p.

Martinez, V., Abós, H. and García-Siñeriz, J.L. 2016. *FEBEXe: Final Sensor Data Report (FEBEX "in situ" Experiment) – Arbeitsbericht*. NAB 16-19, National Cooperative for the Disposal of Radioactive Waste (NAGRA), Wettingen, Switzerland.

Matteo, E., Hardin, E., Hadgu T., Park, H., Rigali, M., and Jove-Colon, C.F. 2016. *Status of Progress Made Toward Preliminary Design Concepts for the Inventory in Select Media for DOE-Managed HLW/SNF*. SAND2016-9823 R; FCRD-UFD-2016-000081. Sandia National Laboratories, Albuquerque, NM.

Meeussen, J.C.L. 2003. ORCHESTRA: An Object-Oriented Framework for Implementing Chemical Equilibrium Models. *Environmental Science & Technology* 37:1175–1182.

Meeussen, J.C.L. and Brown, K.G. 2018. "ORCHESTRA manual and documentation." in: *NRG* (Ed.)Petten, The Netherlands.

Migdisov, A.A., Boukhalfa, H., Timofeev, A., Runde, W., Roback, R. and Williams-Jones, A.E. 2018. A spectroscopic study of uranyl speciation in chloride-bearing solutions at temperatures up to 250 ºC. *Geochim. Cosmochim. Acta* 222:130–145.

Miglio, B., Richardson, D., Yates, T., and West, D. 2000. "Assessment of the Durability of Porous Limestones: Specification and Interpretation of Test Data in UK Practice," in *Dimension Stone Cladding:*

Design, Construction, Evaluation, and Repair, ed. K. Hoigard (West Conshohocken, PA: ASTM International, 57-70. https://doi.org/10.1520/STP13539S.

Mills, R. 1973 Self-diffusion in normal and heavy water in the range 1-45 deg. *The Journal of Physical Chemistry* 77:685–688.

Missana, T., Alonso, U., and García-Gutiérrez, M. 2009. Experimental study and modelling of selenite sorption onto illite and smectite clays. *Journal of Colloid and Interface Science* 334,:132–138.

Missana, T., Alonso, Ú., and Turrero, M.J. 2003. Generation and stability of bentonite colloids at the bentonite/granite interface of a deep geological radioactive waste repository. *Journal of Contaminant Hydrology* 61 (1-4): 17–31.

Missana, T., Alonso, U., García-Gutiérrez, M., and Mingarro, M. 2008. Role of bentonite colloids on europium and plutonium migration in a granite fracture. *Applied Geochemistry* 23 (6): 1484–1497.

Missana, T., and Geckeis, H. 2006. *Grimsel Test Site–Investigation Phase V*. The CRR Final Project Report Series II: Supporting Laboratory Experiments with Radionuclides and Bentonite Colloids. NAGRA Technical Report Series NTB, 03-02.

Montavon, G., Guo, Z., Lützenkirchen, J., Alhajji, E., Kedziorek, M.A.M., Bourg, A.C.M., Grambow, B. 2009. Interaction of selenite with MX-80 bentonite: Effect of minor phases, pH, selenite loading, solution composition and compaction. *Colloids and Surfaces A: Physicochemical and Engineering Aspects* 332:71–77.

Monteiro, P.J.M. and Mehta, P.K. 1986. Interaction between carbonate rock and cement paste. *Cement and Concrete Research* 16:127–134.

Moore, D. M.; Robert C. and Reynolds, J. 1997. *Xray diffraction and the identification and analysis of clay minerals*. 2 ed.; Oxford University Press: New York, New York, 1997.

Möri, H., Müller, A.H., and Klee, J.E. 2003. Intelligent colloidal hybrids via reversible pH-induced complexation of polyelectrolyte and silica nanoparticles. *Journal of the American Chemical Society* 125 (13): 3712–3713.

Morodome, S., and Kawamura, K. 2009. Swelling behavior of Na-and Ca-montmorillonite up to 150 C by in situ X-ray diffraction experiments. *Clays and Clay Minerals* 57 (2): 150–160.

Moshier, S.O. 1989. Microporosity in micritic limestones: a review. *Sedimentary Geology* 63:191–213.

Mosser-Ruck, R., Cathelineau, M., Guillaume, D., Charpentier, D., Rousset, D., Barres, O., and Michau, N. 2010. Effects of temperature, pH, and iron/clay and liquid/clay ratios on experimental conversion of dioctahedral smectite to berthierine, chlorite, vermiculite, or saponite. *Clays and Clay Minerals* 58:280–291.

Mosser-Ruck, R., Pignatelli, I., Bourdelle, F., Abdelmoula, M., Odile Barres, O., Guillaume, D., Charpentier, D., Rousset, D., · Cathelineau, M., and Michau, N. 2016. Contribution of long-term hydrothermal experiments for understanding the smectite-to-chlorite conversion in geological environments. Contributions to *Mineralogy and Petrology* 171: 97–118.

Nguyen-Thanh, L., Hoang-Minh, T., Kasbohm, J., Herbert, H.J., Thuy, D.N., and Le Thi, L. 2014. Characterization of Fe-smectites and their alteration potential in relation to engineered barriers for HLW repositories: The Nui Nua clay, Thanh Hoa province, Vietnam. *Applied Clay Science* 101:168–176.

Norrish, K. 1954. The swelling of montmorillonite. *Discussions of the Faraday Society* 18:120–134.

Nutt, M. Voegele, M., Jove Colón, C.F., Wang, Y., Howard, R., Blink, J., Liu, H.H., Hardin, E., and Jenni, K. 2011. *Used fuel disposition campaign disposal research and development road map (Fuel cycle research and development)*. FCRD-USED-2011-000065. Sandia National Laboratory, 1–121.

Nyasulu, F.; Barlag, R. 2011. Colorimetric Determination of the Iron(III)-Thiocyanate Reaction Equilibrium Constant with Calibration and Equilibrium Solutions Prepared in a Cuvette by Sequential Additions of One Reagent to the Other. *Journal of Chemical Education* 88 (3): 2.

Oelkers, E.H. and Helgeson, H.C. 1990 Triple-ion anions and polynuclear complexing in supercritical electrolyte solutions. *Geochim. Cosmochim. Acta* 54:727–738.

Oelkers, E.H. and Helgeson, H.C. 1991. Calculation of activity coefficients and degrees of formation of neutral ion pairs in supercritical electrolyte solutions. *Geochim. Cosmochim. Acta* 55:1235–1251.

Ohmoto, H., Hayashi, K-I, and Kajisa, Y. 1994. Experimental study of the solubilities of pyrite in NaCl-bearing aqueous solutions at 250-350°C. *Geochimica et Cosmochimica Acta* 58:2169–2185.

Ondrus, P., Veselovsky, F., Gabasova, A., Drabek, M., Dobes, P., Maly, K., Hlousek, J. and Sejkora, J. 2003. Ore-forming processes and mineral parageneses of the Jachymov ore district. *Journal of the Czech Geological Society* 48:157–192.

Papadakis, V.G., Vayenas, C.G. and Fardis, M.N. 1989. A reaction engineering approach to the problem of concrete carbonation. *AIChE Journal* 35:1639–1650.

Park, S., and Schulten, K. 2004. Calculating Potentials of Mean Force from Steered Molecular Dynamics Simulations. *J. Chem. Phys.* 120 (13): 5946–5961. https://doi.org/10.1063/1.1651473.

Parkhurst, D.L. and Appelo, C.A.J. 2013. *Description of input and examples for PHREEQC version 3: a computer program for speciation, batch-reaction, one-dimensional transport, and inverse geochemical calculations, Techniques and Methods.* Reston, VA, p. 519.

Perronnet, M. 2004. *Réactivité des matériaux argileux dans un contexte de corrosion métallique: application au stockage des déchets radioactifs en site argileux*. Doctoral dissertation.

Philip, J.R. and de Vries, D.A. 1957. Moisture movement in porous materials under temperature gradients. *EOS Transactions of the Amer. Geophys. Union* 38:222–232.

Pignatelli, I., Bourdelle, F., Bartier, D., Mosser-Ruck, R., Truche, L., Mugnaioli, E., and Michau, N. 2014. Iron–clay interactions: Detailed study of the mineralogical transformation of claystone with emphasis on the formation of iron-rich T–O phyllosilicates in a step-by-step cooling experiment from 90° C to 40° C. *Chemical Geology* 387:1–11.

Pignatelli, I., Mugnaioli, E., Hybler, J., Mosser-Ruck, R., Cathelineau, M., and Michau, N. 2013. A multi-technique characterization of cronstedtite synthesized by iron-clay interaction in a step-by-step cooling procedure. *Clays and Clay Minerals* 61 (4): 277–289.

Pintado, X., Ledesma, A., and Lloret, A. 2002. Back analysis of thermohydraulic bentonite properties from laboratory tests. *Eng, Geol.* 64:91–115.

Pruess, K., Oldenburg, C., Moridis, G. 1999. *TOUGH2 User's Guide*, Version 2.0. LBL-43134. Lawrence Berkeley National Laboratory, Berkeley, CA.

Pusch, R. 1982. Mineral–water interactions and their influence on the physical behavior of highly compacted Na bentonite. *Canadian Geotechnical Journal* 19:381–387.

Pusch, R. and Madsen, F.T. 1995. Aspects on the illitization of the Kinnekulle bentonites. *Clays and Clay Minerals* 43 (3): 261–270.

Pusch, R., Kasbohm, J., Knutsson, S., Yang, T., and Nguyen-Thanh, L. 2015. The role of smectite clay barriers for isolating high-level radioactive waste (HLW) in shallow and deep repositories. *Procedia Earth and Planetary Science* 15:680–687.

Pusch, R., Prikryl, R., Weishauptová, Z., Xiaodong, L., and Knutsson, S. 2012. Role of clay microstructure in expandable buffer clay. *Journal of Purity, Utility Reaction and Environment* 1 (6): 267–292.

Ramebäck, H., Skälberg, M., Eklund, U., Kjellberg, L., and Werme, L. 1998. Mobility of U, Np, Pu, Am and Cm from spent nuclear fuel into bentonite clay. *Radiochimica Acta* 82:167–172.

Rasband, W.S. 1997–2020. *Image J.* U. S. National Institutes of Health, Bethesda, Maryland, USA. https://imagej.nih.gov/ij/,.

Ravel, B. and Newville, M. 2005. ATHENA, ARTEMIS, HEPHAESTUS: data analysis for X-ray absorption spectroscopy using IFEFFIT. *Journal of Synchrotron Radiation* 12:537–541.

Rehr, J., Mustre de Leon, J., Zabinsky, S. and Albers, R. 1991. Theoretical X-ray absorption fine structure standards. *J. Am. Chem. Soc*. 113:5135–5140.

Reimus, P.W. 2012. *Preliminary Interpretation of a Radionuclide and Colloid Tracer Test in a Granodiorite Shear Zone at the Grimsel Test Site, Switzerland*. LA-UR-12-24411. Los Alamos National Lab.(LANL), Los Alamos, NM (United States).

Rotenberg, B., Morel, J., Marry, V., Turq, P., and Morel-Desrosiers, N. 2009. On the driving force of cation exchange in clays: Insights from combined microcalorimetry experiments and molecular simulation. *Geochimica Et Cosmochimica Acta* 73 (14): 4034–4044.

Rutqvist, J., Zheng, L., Chen, F., Liu, H.-H. and Birkholzer, J. 2014. Modeling of Coupled Thermo-Hydro-Mechanical Processes with Links to Geochemistry Associated with Bentonite-Backfilled Repository Tunnels in Clay Formations. *Rock Mechanics and Rock Engineering* 47:167–186.

Samper, J., Mon, A., and Montenegro, L. 2018. A revisited thermal, hydrodynamic, chemical and mechanical model of compacted bentonite for the entire duration of the FEBEX in situ test. *Applied Clay Science* 160:58–70.

Samper, J., Zheng, L., Fernández, A.M., and Montenegro, L. 2008. Inverse modeling of multicomponent reactive transport through single and dual porosity media. *Journal of Contaminant Hydrology* 98 (3–4): 115–127.

Samson, E., Lemaire, G., Marchand, J. and Beaudoin, J.J. 1999. Modeling chemical activity effects in strong ionic solutions. *Computational Materials Science* 15:285–294.

Sánchez, F.G., Jurányi, F., Gimmi, T., Van Loon, L., Seydel, T., and Unruh, T. 2008a. Dynamics of supercooled water in highly compacted clays studied by neutron scattering. *Journal of Physics: Condensed Matter* 20 (41). doi:10.1088/0953-8984/20/41/415102.

Sánchez, F.G., Van Loon, L.R., Gimmi, T., Jakob, A., Glaus, M.A., and Diamond, L.W. 2008b. Self-diffusion of water and its dependence on temperature and ionic strength in highly compacted montmorillonite, illite and kaolinite. *Applied Geochemistry* 23:3840–3851. doi:10.1016/j.apgeochem.2008.08.008.

Sánchez, M., Gens, A., and Olivella, S. 2010. Effect of thermo-coupled processes on the behavior of a clay barrier submitted to heating and hydration. *An. Acad. Bras. Cienc*. 82 (1): 153–168.

Sánchez, M., Gens, A., and Olivella, S. 2012. THM analysis of a large-scale heating test incorporating material fabric changes. *International Journal for Numerical and Analytical Methods in Geomechanics* 36 (4): 391–421.

Sánchez, M., Gens, A., Guimarães, L., and Olivella, S. 2008c. Implementation algorithm of a generalised plasticity model for swelling clays. *Computers and Geotechnics* 35 (6): 860–871.

Sánchez, M., Gens, A., Guimarães, L.D.N., and Olivella, S. 2005. A double structure generalized plasticity model for expansive materials. *International Journal for Numerical and Analytical Methods in Geomechanics* 29:751–787.

Sauer K., Caporuscio, F., Rock, M., Cheshire, M. and Jove Colon, C. 2020. Hydrothermal interactions of Wyoming bentonite and Opalinus clay. *Clay and Clay Minerals*.

Savage, D. 1997. *Review of the potential effects of alkaline plume migration from a cementitious repository for radioactive waste.* Research & Development Technical Report P60, UK Environment Agency, Bristol, UK.

Savage, D., Benbow, S., Watson, C., Takase, H., Ono, K., Oda, C., and Honda, A. 2010. Natural systems evidence for the alteration of clay under alkaline conditions: an example from Searles Lake, California. *Applied Clay Science* 47 (1–2): 72–81.

Savage, D., Noy, D., and Mihara, M. 2002. Modelling the interaction of bentonite with hyperalkaline fluids. *Applied Geochemistry* 17 (3): 207–223.

Savage, D., Walker, C., Arthur, R., Rochelle, C., Oda, C., and Takase, H. 2007. Alteration of bentonite by hyperalkaline fluids: A review of the role of secondary minerals. *Physics and Chemistry of the Earth, Parts A/B/C* 32 (1–7): 287–297.

Schaefer, C.E., Arands, R.R., van der Sloot, H.A. and Kosson, D.S. 1995. Prediction and experimental validation of liquid-phase diffusion resistance in unsaturated soils. *Journal of Contaminant Hydrology* 20:145–166.

Segad, M., Hanski, S., Olsson, U., Ruokolainen, J., Åkesson, T., and Jönsson, B. 2012. Microstructural and Swelling Properties of Ca and Na Montmorillonite: (In Situ) Observations with Cryo-TEM and SAXS. *The Journal of Physical Chemistry C* 116 (13): 7596–7601.

Seyfried, J.R., Janecky, D.R., and Berndt, M.E. 1987. "Rocking autoclaves for hydrothermal experiments: II. The flexible reaction-cell system." *Hydrothermal Experimental Techniques*, eds. Ulmer, G.C. and Barnes, H.L. John Wiley & Sons, pp. 216–239.

SKB. 2011. *Long-term safety for the final repository for spent nuclear fuel at Forsmark. Main report of the SR-Site project*. Swedish Nuclear Fuel and Waste Management Co.

Smailos, E., Cuñado, M. A., Azkarate, I., Kursten, B. and Marx, G. 2002. *Long-Term Performance of Candidate Materials for HLW/Spent Fuel Disposal Containers*. Report FZKA 6706, FZK.INE (Karlsruhe, Germany).

Smart, N.R., et al. 2004. *The anaerobic corrosion of carbon and stainless steels in simulated cementitious repository environments: A summary review of NIREX research*. Harwell, England, AEA Technology.

Smith, D.E., Wang, Y., Chaturvedi, A., and Whitley, H.D. 2006. Molecular Simulations of the Pressure, Temperature, and Chemical Potential Dependencies of Clay Swelling. J. *Phys. Chem. B* 110 (40) 20046–20054. https://doi.org/10.1021/jp062235o.

Smith, D.W., and Booker, J.R. 1993. Green's functions for a fully coupled thermoporoelastic material. *International Journal for Numerical and Analytical Methods in Geomechanics* 17:139–163.

Smith, T.E.; McCrory, S.; Dunzik-Gougar, M.L. 2013. Limited Oxidation of Irradiated Graphite Waste to Remove Surface Carbon-14. *Nuclear Engineering and Technology* 45 (2): 211–218.

Somerton, W.H., El-Shaarani, A.H., and Mobarak, S.M. 1974. "High temperature behavior of rocks associated with geothermal-type reservoirs." Paper SPE-4897. *Proceedings of the 44th Annual California Regional Meeting of the Society of Petroleum Engineers*. Richardson, TX: Society of Petroleum Engineers.

Sonnenthal, E., Pettitt, W., Smith T., Riahi, A., Siler D., Kennedy, M., Majer, E., Dobson, P., Ayling, B., Damjanac, B., and Blankenship D. 2018. Continuum Thermal-Hydrological-Mechanical Modeling of the Fallon FORGE Site. *GRC Transactions,* Vol. 42.

Sonnenthal, E.L., Smith, J.T., Cladouhos, T., Kim, J., and Yang L. 2015. "Thermal-Hydrological-Mechanical-Chemical Modeling of the 2014 EGS Stimulation Experiment at Newberry Volcano, Oregon." *Proceedings, 40th Workshop on Geothermal Reservoir Engineering.* Stanford University, Stanford, California, January 26–28.

Środoń, J. 1980. Precise identification of illite-smectite interstratifications by X-ray powder diffraction. *Clays and Clay Minerals* 28:401–411.

Steefel, C.I. and Maher, K. 2009. Fluid-Rock Interaction: A Reactive Transport Approach. *Reviews in Mineralogy and Geochemistry* 70:485–532.

Steefel, C.I., Appelo, C.A.J., Arora, B., Jacques, D., Kalbacher, T., Kolditz, O., Lagneau, V., Lichtner, P.C., Mayer, K.U., Meeussen, J.C.L., Molins, S., Moulton, D., Shao, H., Šimůnek, J., Spycher, N., Yabusaki, S.B., and Yeh, G.T. 2015. Reactive transport codes for subsurface environmental simulation. *Computational Geosciences* 19:445–478.

Ström, A., Andersson, J., Skagius, K. and Winberg, A. 2008. Site descriptive modelling during characterization for a geological repository for nuclear waste in Sweden. *Applied Geochemistry* 23:1747–1760.

Subramanian, N., Whittaker, M.L., Ophus, C., and Lammers, L.N. 2020. Structural Implications of Interfacial Hydrogen Bonding in Hydrated Wyoming-Montmorillonite Clay. *J. Phys. Chem. C*. acs.jpcc.9b11339. https://doi.org/10.1021/acs.jpcc.9b11339.

Sun, L., Hirvi, J.T., Schatz, T., Kasa, S., and Pakkanen, T.A. 2015. Estimation of montmorillonite swelling pressure: A molecular dynamics approach. *The Journal of Physical Chemistry C* 119 (34): 19863–19868.

Svemar, C., 2005. *Cluster Repository Project (CROP)*. Final Report of European Commission Contract FIR1-CT-2000-2003, Brussels, Belgium.

Svoboda, M., Moučka, F., and Lísal, M. 2018. Saturated Aqueous NaCl Solution and Pure Water in Na-Montmorillonite Clay at Thermodynamic Conditions of Hydraulic Fracturing: Thermodynamics, Structure and Diffusion from Molecular Simulations. *J. Mol. Liq*. 271:490–500. https://doi.org/10.1016/j.molliq.2018.08.144.

Swift, P.N. and Bonano, E.J. 2016. Geological Disposal of Nuclear Waste in Tuff: Yucca Mountain (USA). *Elements* 12:263–268.

Tang, A.-M., and Cui, Y. 2006. Determining the Thermal Conductivity of Compacted MX80 Clay. *Unsaturated Soil* 1695–1706.

Tang, A.-M., Cui, Y.-J., and Le, T.-T. 2007. A study of the thermal conductivity of compacted Bentonites. *Applied Clay Science* 41:181–189.

Teich-McGoldrick, S.L., Greathouse, J.A., Jove-Colon, C.F., and Cygan, R.T. 2015. Swelling properties of montmorillonite and beidellite clay minerals from molecular simulation: Comparison of temperature, interlayer cation, and charge location effects. *The Journal of Physical Chemistry C* 119 (36): 20880–20891.

Telfeyan, K., Reimus, P.W., Boukhalfa, H., and Ware, S.D. 2020. Aging effects on Cesium-137 (137Cs) sorption and transport in association with clay colloids. *Journal of Colloid and Interface Science* 566:316–326.

Teppen, B.J.; and Miller, D.M. 2006. Hydration Energy Determines Isovalent Cation Exchange Selectivity by Clay Minerals. *Soil Sci. Soc. Am. J.* 70 (1): 31–40. https://doi.org/10.2136/sssaj2004.0212.

Tester, C.C., Aloni, S., Gilbert, B., and Banfield, J.F. 2016. Short- and Long-Range Attractive Forces That Influence the Structure of Montmorillonite Osmotic Hydrates. *Langmuir* 32 (46): 12039–12046.

Tian, Y., Brugger, J., Liu, W., Borg, S., Etschmann, B., O'Neill, B., Testemale, D., Hazemann, J.-L., Glover, C. and Ngothai, Y. 2010. “High-temperature and pressure spectroscopic cell for in-situ XAS study of supercritical fluids at the Australian Synchrotron.” *Chemeca 2010: Engineering at the Edge*, 26-29 September 2010, Hilton Adelaide, South Australia, 3425.

Tinnacher, R.M., Holmboe, M., Tournassat, C., Bourg, I.C., and Davis, J.A. 2016a. Ion adsorption and diffusion in smectite: Molecular, pore, and continuum scale views. *Geochimica et Cosmochimica Acta* 177:130–149.

Tinnacher, R.M., Tournassat, C., and Davis, J.A. 2016b. *Laboratory Experiments on Bentonite Samples: FY16 Progress*. U.S. Department of Energy, Used Fuel Disposition Campaign.

Torstenfelt, B., and Allard, B. 1986. *Migration of fission products and actinides in compacted bentonite.* KBS Report 86, 14.

Tournassat, C., and Appelo, C.A.J. 2011. Modelling approaches for anion-exclusion in compacted Na-bentonite. *Geochimica et Cosmochimica Acta* 75:3698–3710.

Tournassat, C., and Steefel, C.I. 2019a. Modeling diffusion processes in the presence of a diffuse layer at charged mineral surfaces: a benchmark exercise. *Computational Geosciences*.

Tournassat, C., and Steefel, C.I. 2019b. Reactive Transport Modeling of Coupled Processes in Nanoporous Media. *Reviews in Mineralogy and Geochemistry* 85:75–109.

Tournassat, C., Bourg, I.C., Holmboe, M., Sposito, G., and Steefel, C.I. 2016. Molecular dynamics simulations of anion exclusion in clay interlayer nanopores. *Clays and Clay Minerals* 64 (4): 374–388.

Tournassat, C., Steefel, C.I., Bourg, I.C., and Bergaya, F. 2015. *Natural and engineered clay barriers.* Elsevier.

Tournassat, C., Tinnacher, R.M., Grangeon, S., and Davis, J.A. 2018. Modeling uranium(VI) adsorption onto montmorillonite under varying carbonate concentrations: A surface complexation model accounting for the spillover effect on surface potential. *Geochimica et Cosmochimica Acta* 220:291–308.

Trotignon, L., Devallois, V., Peycelon, H., Tiffreau, C. and Bourbon, X. 2007. Predicting the long term durability of concrete engineered barriers in a geological repository for radioactive waste. *Physics and Chemistry of the Earth, Parts A/B/C* 32:259–274.

U.S. Congress. 1996. Public Law 102-579. *Waste Isolation Pilot Plant Land Withdrawal Act of 1992*, as Amended by Public Law 104-201.

U.S. Environmental Protection Agency. 1998. *MINTEQA2/PRODEFA2, A geochemical assessment model for environmental systems--User manual supplement for version 4.0*. Revised September 1999 ed. National Exposure Research Laboratory, Ecosystems Research Division, Athens, Georgia, p. 76.

U.S. EPA. 2004. *Method 6060A, rev. 1-Total Organic Carbon*. Washington, D.C.

U.S. EPA. 2017a. *Method 1313, Liquid-solid partitioning as a function of extract pH using a parallel batch extraction procedure*.

U.S. EPA. 2017b. *SW-846 Test Method 1315: Mass Transfer Rates of Constituents in Monolithic or Compacted Granular Materials Using a Semi-Dynamic Tank Leaching Procedure*. Washington, D.C.

U.S. EPA. 2018. *Method 6010D (SW-846): Inductively Coupled Plasma-Atomic Emission Spectrometry*, Revision 5 ed, Washington, DC. .

Underwood, T.R., and Bourg, I.C. 2020. Large-Scale Molecular Dynamics Simulation of the Dehydration of a Suspension of Smectite Clay Nanoparticles. *J. Phys. Chem. C* 124 (6): 3702–3714. https://doi.org/10.1021/acs.jpcc.9b11197.

Uzunoglu, A. 2017. The Use of CeO2-TiO2 Nanocomposites as Enzyme Immobilization Platforms in Electrochemical Sensors. *Journal of the Turkish Chemical Society, Section A: Chemistry* 855–868.

Valdés-Ramírez, G., Ramírez-Silva, M.T., Palomar-Pardavé, M., Romero-Romo, M., Álvarez-Romero, G.A., Hernández-Rodríguez, P.R. Marty, J.L., Juárez-García, J.M. 2011. Design and Construction of Solid State Ag/AgCl Reference Electrodes Through Electrochemical Deposition of Ag and AgCl Onto a Graphite/Epoxy Resin-Based Composite. Parte 1: Electrochemical Deposition of Ag Onto a Graphite/Epoxy ResinBased Composite. *International Journal Electrochem Science* 6:16.

Van der Sloot, H., Seignette., P., Meeussen, J., Hjelmar, O. and Kosson, D. 2008. “A database, speciation modelling and decision support tool for soil, sludge, sediments, wastes and construction products: LeachXS™-Orchestra.” *Second international symposium on energy from biomass and waste, Venice*.

Van Loon, L.R., Soler, J.M., and Bradbury, M.H. 2003. Diffusion of HTO, 36Cl− and 125I− in Opalinus Clay samples from Mont Terri: Effect of confining pressure. *Journal of Contaminant Hydrology* 61:73–83.

Vany´sek, P. 2018. “Ionic Conductivity and Diffusion at Infinite Dilution in: Rumble.” J.R. (Ed*.), CRC Handbook of Chemistry and Physics*, 98th Edition ed. CRC Press/Taylor & Francis, Boca Raton, FL.

Villar M.V. 2005. *MX-80 Bentonite Thermo-Hydro-Mechanical Characterisation Performed at CIEMAT in the Context of the Prototype Project*. Informes Técnicos Ciemat 1053 Febrero, 2005

Villar, M.V., and Lloret, A. 2004. Influence of temperature on the hydro-mechanical behavior of a compacted bentonite. *Applied Clay Sci.* 26:337–350.

Villar, M.V., Fernandez, A.M., Martin, P.L., Barcala, J.M., Gomez-Espina, R., and Rivas, P. 2008. *Effect of Heating/hydration on Compacted Bentonite: tests in 60-cm Long Cells*. Spain: Editorial CIEMAT.

Villar, M.V., Iglesias, R.J., and García-Siñeriz, J.L. 2018a. State of the in situ Febex test (GTS, Switzerland) after 18 years: a heterogeneous bentonite barrier. *Environmental Geotechnics* 1–13.

Villar, M.V., Iglesias, R.J., Gutiérrez-Álvarez, C., and Carbonell, B. 2018b. Hydraulic and mechanical properties of compacted bentonite after 18years in barrier conditions. *Applied Clay Science* 160:49–57.

Vomvoris, S., Birkholzer, J., Zheng, L., Gaus, I., and Blechschmidt, I. 2015. *THMC behavior of clay-based barriers under high temperature- from laboratory to URL scale.* 678–687.

von Berlepsch, T. and Haverkamp, B. 2016. Salt as a Host Rock for the Geological Repository for Nuclear Waste. *Elements* 12:257–262.

Wang, R.; Li, X.; Wang, Z.; Zhang, H. 2017a. Electrochemical analysis graphite/electrolyte interface in lithium-ion batteries: p-Toluenesulfonyl isocyanate as electrolyte additive. *Nano Energy* 34:131–140.

Wang, X., Chen, C., Zhou, X., Tan, X., and Hu, W. 2005. Diffusion and sorption of U (VI) in compacted bentonite studied by a capillary method. *Radiochimica Acta* 93:273–278.

Wang, Y., Dewers, T., Hadgu, T., Jove-Colon, C.F., Sun, A.C. and McNeish, J., 2010. *Enhanced Performance Assessment System (EPAS) for Carbon Sequestration*. SAND2010-6173. Sandia National Laboratories, Albuquerque, New Mexico.

Wang, Z., Wang, H., Li, Q., Xu, M., Guo, Y., Li, J., and Wu, T. 2016. pH effect on Re(VII) and Se(IV) diffusion in compacted GMZ bentonite. *Applied Geochemistry* 73:1–7.

Wang, Z.; Zhang, Y.; Liu, B.; Wu, K.; Thevuthasan, S.; Baer, D. R.; Zhu, Z.; Yu, X.-Y.; Wang, F. 2017b. In Situ Mass Spectrometric Monitoring of the Dynamic Electrochemical Process at the Electrode–Electrolyte Interface: a SIMS Approach. *Anal. Chem.* 89 (1): 960–965.

Watson, C., Hane, K., Savage, D., Benbow, S., Cuevas, J. and Fernandez, R. 2009. Reaction and diffusion of cementitious water in bentonite: results of 'blind' modelling. *Applied Clay Science* 45 (1–2): 54–69.

Watson, C., Savage, D., Wilson, J., Benbow, S., Walker, C. and Norris, S. 2013. The Tournemire industrial analogue: reactive-transport modelling of a cement–clay interface. *Clay Minerals* 48:167–184.

Watson, C., Wilson, J., Savage, D. Norris, S. 2018. Coupled reactive transport modelling of the international Long-Term Cement Studies project experiment and implications for radioactive waste disposal. *Applied Geochemistry* 97:134–146.

Wei, Y.; Li, Y.; Li, N.; Zhang, Y.; Yan, T.; Ma, H.; Wei, Q. 2016. Sandwich-type electrochemical immunosensor for the detection of AFP based on Pd octahedral and APTES-M-CeO(2)-GS as signal labels. *Biosens Bioelectron* 79:482–7.

Wersin, P., Birgersson, M., Olsson, S., Karnland, O. and Snellman, M. 2008. *Impact of corrosion-derived iron on the bentonite buffer within the KBS-3H disposal concept*. *The Olkiluoto site as case study*. No. SKB-R--08-34. Swedish Nuclear Fuel and Waste Management Co.

Wersin, P., Johnson, L.H., and McKinley, I.G. 2007. Performance of the bentonite barrier at temperatures beyond 100°C: A critical review. *Physics and Chemistry of the Earth, Parts A/B/C* 32:780–788.

Whitley, H.D., and Smith, D.E. 2004. Free Energy, Energy, and Entropy of Swelling in Cs–, Na–, and Sr–Montmorillonite Clays. *J. Chem. Phys.* 120 (11): 5387–5395. https://doi.org/10.1063/1.1648013.

Whittaker, M.L., Comolli, L.R., Gilbert, B., and Banfield, J.F. 2020. Layer size polydispersity in hydrated montmorillonite creates multiscale porosity networks. *Applied Clay Science* 1.

Whittaker, M.L., Lammers, L.N., Carrero, S., Gilbert, B., and Banfield, J.F. 2019. "Ion exchange selectivity in clay is controlled by nanoscale chemical–mechanical coupling." *Proceedings of the National Academy of Sciences*. doi:10.1073/pnas.1908086116.

Wilson, J., Cressey, G., Cressey, B., Cuadros, J., Ragnarsdottir, K.V., Savage, D., and Shibata, M. 2006b. The effect of iron on montmorillonite stability.(II) Experimental investigation. *Geochimica et Cosmochimica Acta* 70 (2): 323–336.

Wilson, J., Savage, D., Cuadros, J., Shibata, M., and Ragnarsdottir, K.V. 2006a. The effect of iron on montmorillonite stability.(I) Background and thermodynamic considerations. *Geochimica et Cosmochimica Acta*, 70 (2): 306–322.

Wu, T., Wang, Z., Wang, H., Zhang, Z., and Van Loon, L.R. 2017. Salt effects on Re(VII) and Se(IV) diffusion in bentonite. *Applied Clay Science* 141:104–110.

Wucher, A.; Sun, S.; Szakal, C.; Winograd, N. 2004. Molecular Depth Profiling of Histamine in Ice Using a Buckminsterfullerene Probe. *Anal. Chem.*76 (24): 7234–7242.

Xu, H. Rutqvist, J., Plua, C., Armand, G., and Birkholzer, J. (2020) Modeling of Thermal Pressurization in Tight Claystone using Sequential THM Coupling: Benchmarking and Validation against In-situ Heating Experiments in COx Claystone. Tunnelling and Underground Space Technology, http://doi.org/10.1016/j.tust.2020.103428.

Xu, T., Sonnenthal, E., Spycher, N., and Zheng, L. 2014. *TOUGHREACT V3. 0-OMP reference manual: a parallel simulation program for non-isothermal multiphase geochemical reactive transport*. University of California, Berkeley.

Xu, T., Spycher, N., Sonnenthal, E., Zhang, G., Zheng, L. and Pruess, K. 2011. TOUGHREACT Version 2.0: A simulator for subsurface reactive transport under non-isothermal multiphase flow conditions. *Computers & Geosciences* 37 (6): 763–774.

Yang, L., Yu, X.-Y., Zhu, Z.H., Thevuthasan, T., Cowin, J.P. 2011. Making a hybrid microfluidic platform compatible for in situ imaging by vacuum-based techniques. *J. Vac. Sci. Technol. A* 29 (6): article no. 061101.

Yang, X.; Lee, J.; Barker, D. E.; Wang, X.; Zhang, Y. 2012. Comparison of six particle size distribution models on the goodness-of-fit to particulate matter sampled from animal buildings. *J. Air Waste Manage. Assoc.* 62 (6): 725–735.

Yao, J., Ossana, A., Chun, J., Yu, X.-Y. 2020. In situ liquid SEM imaging analysis revealing particle dispersity in aqueous solutions. *Journal of Microscopy* 279 (2): 79–84.

Yao, J., Wu, F., Qiu, X., Li, N., Su, Y. 2011. Effect of CeO2-coating on the electrochemical performances of LiFePO4/C cathode material. *Electrochimica Acta* 56 (16): 5587–5592.

Yu, J., Zhou, Y., Hua, X., Liu, S., Zhu, Z., Yu, X.-Y. 2016. Capturing the transient species at the electrode-electrolyte interface by in situ dynamic molecular imaging. *Chemical Communications* 52 (73): 10952–10955.

Yu, X.-Y. 2017. Imaging mass spectrometry tackles interfacial challenges in electrochemistry. *Current Opinion in Electrochemistry* 6 (1): 53–59.

Yu, X.-Y. 2020. In situ, in vivo, and in operando imaging and spectroscopy of liquids using microfluidics in vacuum. *Journal of Vacuum Science & Technology A* 38 (4): 040804.

Yu, X.-Y., Liu, B., Yang, L. 2013. Imaging liquids using microfluidic cells. *Microfluid Nanofluid* 15 (6): 725–744.

Yu, X.-Y., Yang, L., Cowin, J., Iedema, M., Zhu, Z. 2011. *Systems and methods for analyzing liquids under vacuum*. 8,555,710, Filed on March 14, 2011 Pub. Date: Sep. 20, 2012, 2011.

Yu, X.-Y.; Arey, B.W.; Chatterjee, S. D.; Chun, J. 2019. In situ liquid SEM imaging of particles. *Surface and Interface Analysis* submitted.

Zarzycki, P., and Gilbert, B. 2016. Long-Range Interactions Restrict Water Transport in Pyrophyllite Interlayers. *Sci Rep*, 6:25278. doi:10.1038/srep25278.

Zhang, Y.; Sun, J.; Hu, Y.; Li, S.; Xu, Q. 2012. Bio-cathode materials evaluation in microbial fuel cells: A comparison of graphite felt, carbon paper and stainless steel mesh materials. *International Journal of Hydrogen Energy* 37 (22): 16935–16942.

Zheng L., Rutqvist J. Kim, K. and Houseworth, J. 2015a. *Investigation of Coupled Processes and Impact of High Temperature Limits in Argillite Rock*. FCRD-UFD-2015-000362; LBNL-187644.

Zheng, L. Rutqvist, J., Steefel, C., Kim, K., Chen, F., Vilarrasa, V., Nakagawa, S., Zheng, J., Houseworth, J., and Birkholzer, J. 2014. *Investigation of Coupled Processes and Impact of High Temperature Limits in Argillite Rock.* FCRD-UFD-2014-000493, LBNL-6719E.

Zheng, L., Fox, P., Zarzycki, P., Sonnenthal, E., Borglin, S., Chang, C., Chou, C., Wu, Y., Xu, H., Nico, P., Gilbert, B., Kneafsey, T., Cheng, Y., and Birkholzer, J. 2019a. *Engineered Barrier System Research Activities at LBNL Via International Collaboration: FY19 Progress Report*. LBNL-2001210. Lawrence Berkeley National Laboratory.

Zheng, L., Kim, K., Xu, H., and Rutqvist, J. 2016. *DR Argillite Disposal R&D at LBNL*. FCRD-UFD-2016-000437, LBNL-1006013, Lawrence Berkeley National Laboratory.

Zheng, L., Li, L., Rutqvist, J., Liu, H. and Birkholzer, J.T. 2012. *Modeling Radionuclide Transport in Clays*. FCRD-URD-2012-000128.Lawrence Berkeley National Laboratory.

Zheng, L., Rutqvist, J., Birkholzer, J.T., and Liu, H.-H. 2015b. On the impact of temperatures up to 200 °C in clay repositories with bentonite engineer barrier systems: A study with coupled thermal, hydrological, chemical, and mechanical modeling. *Engineering Geology* 197: 278–295.

Zheng, L., Rutqvist, J., Xu, H., Kim, K., Voltolini, M., and Cao, X. 2017. *Investigation of Coupled Processes and Impact of High Temperature Limits in Argillite Rock*. SFWD-SFWST-2017-000040, LBNL-2001014. Lawrence Berkeley National Laboratory.

Zheng, L., Samper, J., and Montenegro, L. 2011.) A coupled THC model of the FEBEX "in situ" test with bentonite swelling and chemical and thermal osmosis. *Journal of Contaminant Hydrology* 126 (1–2): 45–60.

Zheng, L., Xu, H., Fox, P., Nico, P., and Birkholzer, J. 2018. *Engineered Barrier System Research Activities at LBNL: FY18 Progress Report*. SFWD-SFWST-2018-000040, LBNL-200117. Lawrence Berkeley National Laboratory.

Zheng, L., Xu, H., Rutqvist, J., Reagan, M., Birkholzer, J., Villar, M.V., and Fernández, A.M. 2019b. The hydration of bentonite buffer material revealed by modeling analysis of a long-term in situ test. *Applied Clay Science* 105360.

Zhou, Y., Rajapakse, R.K.N.D., and Graham, J. 1999. Coupled Field in a deformable unsaturated medium. *International Journal of Solid and Structures* 36:4841–4868.

APPENDIX A

Methods and Mineral Characterization

This page is intentionally left blank.

A-1. Experimental Setup

The Wyoming bentonite used in this experimental work was mined from a reducing horizon in Colony, Wyoming. The bentonite was pulverized and sieved to <3 mm and used with a free moisture content of ~15.5 wt.%. The groundwater solution was prepared using reagent grade materials dissolved in double deionized water. NaOH and HCl were added to adjust the initial solution pH. This solution was then filtered through a 0.45 μm filter and sparged with He before each experiment. Initial components for wall rock experiments are summarized in Table 1 in Chapter 1.

Experiments were performed to examine bentonite mineral stability in a hydrothermal system with host rock inclusion. The host rock used in these experiments was Grimsel granodiorite from the Grimsel Test Site URL, which is located in Switzerland near Grimsel Pass. A portion of the Grimsel granodiorite was crushed and sieved with 10 mesh (~2 mm). Grimsel granodiorite to be used in experiments was reconstituted at 80 wt.% −10 mesh and 20 wt.% +10 mesh. Synthetic groundwater was chosen to replicate the groundwater composition that represents borehole fluid compositions at the Grimsel Test Site (Table 5-2; Kersting et al., 2012). The synthetic groundwater was added at ~8 to 13:1 by mass water:rock ratio.

The redox conditions for each system were buffered using a 1:1 mixture (by mass) of Fe_3O_4 and Fe° added at 0.07 wt.% of the bentonite mass. Approximately 7 wt.% (of total solids mass) 304 stainless steel (NIST SRM 101 g), 316 stainless steel (NIST SRM 160b), or low carbon steel, (provided by Sandia National Laboratory) were added to the experiments to mimic the presence of a waste canister.

Reactants were loaded into a flexible gold reaction cell and fixed to a 500 mL Gasket Confined Closure reactor (Seyfried et al., 1987). Experiments were pressurized to 150 to 160 bar and were heated isothermally at 250°C for either 6 or 8 weeks. Reaction liquids were extracted during the experiments and analyzed to investigate the aqueous geochemical evolution in relationship to mineralogical alterations. The sampled reaction liquids were split three-ways producing aliquots for unfiltered anion, unfiltered cation, and filtered (0.45 μm syringe filter) cation determination. All aliquots were stored in a refrigerator at 1°C until analysis.

A-2. X-ray Diffraction Mineral Characterization

A-2.1 Chesapeake Energy Laboratory QXRD

QXRD analyses of experimental materials determined relative mineral abundances in the starting materials and reaction products. Each sample was ground with 20 wt.% corundum (Al_2O_3) for QXRD analysis of the bulk rock (Chung, 1974). XRD measurements were conducted with a Siemens D500 diffractometer using Cu-Kα radiation. Data were collected from 2 to 70 °2θ with a 0.02 °2θ step-size and count times of 8 to 12 seconds per step. Quantitative phase analysis (QXRD) was performed using FULLPAT (Chipera and Bish, 2002).

A-2.2 Los Alamos National Laboratory Clay Mineral XRD

XRD at Los Alamos National Laboratory were conducted on a Bruker D8 Discover using Cu-Kα radiation. To better analyze the non-clay and clay fractions, the < 2 μm particles were separated via sedimentation in DI H_2O. An aliquot of the < 2 μm suspension was dropped on a zero-background quartz plate and dried. This oriented mount was X-rayed from 2 to 40°2θ at 8 to 12 s per step. The oriented mount was then saturated with ethylene glycol in a 60°C oven for 24 hours and XRD analysis was repeated. A portion of the > 2 μm particles was ground with a mortar/pestle, deposited on a zero-background quartz plate, and X-rayed under the same parameters as the bulk powder material. The remaining > 2 μm portion was used for electron microscopy. Mineral identification and unit-cell parameters analysis was performed using Jade© 9.5 X-ray data evaluation program with ICDD PDF-4 database. Illite-smectite composition of higher-ordered (R1-3) illite-smectites were modeled via ClayStrat+ (developed by Hongji Yuan and David Bish). Expandable component abundances for the disordered illite-smectites were calculated via the Δ°2Θ method (Środoń, 1980; Eberl et al., 1993; Moore and Reynolds, 1997). A regression from calculated data were used to calculate the % expandable (%Exp) component in each untreated and reacted bentonite. The equation is

$$\%Exp = 973.76 - 323.45\Delta + 38.43\Delta^2 - 1.62\Delta^3$$

(Eberl et al., 1993, Eq. 3, R^2=0.99)

Equation A-1

with Δ corresponding to Δ°2Θ between the 002 and 003 peak positions for the oriented, ethylene glycol saturated samples.

A-3. Scanning Electron Microscopy

Analytical electron microscopy was performed using a FEI™ Inspect F SEM at Los Alamos National Laboratory. All samples were Au/Pd-coated prior to SEM analysis. Imaging with the SEM was performed using a 5.0 kV accelerating voltage and 1.5 spot size. Energy dispersive X-ray spectroscopy (EDS) was performed at 30 kV and a 3.0 spot size.

A-4. Aqueous Geochemical Analyses

Major cations and trace metals were analyzed via inductively coupled plasma-optical emission spectrometry (Perkin Elmer Optima 2100 DV) and inductively coupled plasma-mass spectrometry (Elan 6100) utilizing EPA methods 200.7 and 200.8. Ultra-high purity nitric acid was used in sample and calibration preparation prior to sample analysis. Internal standards (Sc, Ge, Bi, and In) were added to samples and standards to correct for matrix effects. Standard Reference Material (SRM) 1643e Trace Elements in Water was used to check the accuracy of the multi-element calibrations. Inorganic anion samples were analyzed by IC following EPA method 300 on a Dionex DX-600 system.

APPENDIX B

Electron Microprobe Data: TEBS-1 to -5

This page is intentionally left blank.

B-1. Electron Microprobe Data: TEBS-1 to -5

Table B-1. EMP standards and oxide detection limits for silicate analyses

Element	**Standard Material**	**Minimum Detection Limit[a]**
Mg	Synthetic Phlogopite	0.02
F	Synthetic Phlogopite	0.11
Na	Albite (Amelia, NC, U.S.A, Rutherford Mine)	0.02
Al	Labradorite (Chihuahua, Mexico)	0.02
Si	Labradorite (Chihuahua, Mexico)	0.02
Ca	Labradorite (Chihuahua, Mexico)	0.01
Cl	Tugtupite (Greenland)	0.01
K	Adularia (St. Gotthard, Switzerland)	0.01
Ti	Titanite glass (Penn State)	0.02
Cr	Synthetic Magnesio-chromite	0.04
Mn	Rhodonite (unknown locality)	0.02
Fe	Augite (unknown locality)	0.02
Ni	Synthetic Liebenbergite	0.06
Zn	Gahnite	0.05

NOTE: [a] Minimum Detection Limit (MDL) values for oxides of respective elements.

IEBS-1															
Clinoptilolite	**SiO_2**	**TiO_2**	**Al_2O_3**	**Cr_2O_3**	**FeO**	**NiO**	**MnO**	**MgO**	**CaO**	**Na_2O**	**K_2O**	**Cl**	**F**	**O=F&Cl**	**TOTAL**
IEBS-1 Area 1 Shard	70.70	0.01	11.28	0.00	0.10	0.00	0.01	0.10	1.98	1.89	0.39	0.01	0.02	-0.01	86.47
IEBS-1 Area 3 Shard	62.94	0.01	12.29	0.00	0.09	0.00	0.01	0.13	1.83	3.07	0.45	0.00	0.03	-0.01	80.83
IEBS-1 Area 3 Shard	70.38	0.01	11.82	0.00	0.08	0.01	0.03	0.10	1.88	2.17	0.40	0.00	0.05	-0.02	86.87
IEBS-1 Area 3 Shard	64.94	0.00	11.35	0.00	0.11	0.00	0.04	0.13	1.77	3.34	0.29	0.00	0.02	-0.01	81.96
IEBS-1 Area 4 shard	61.11	0.00	12.28	0.00	0.10	0.00	0.02	0.11	2.03	2.29	0.48	0.00	0.00	0.00	78.42
AVERAGE	**66.02**	**0.00**	**11.80**	**0.00**	**0.10**	**0.00**	**0.02**	**0.11**	**1.90**	**2.55**	**0.40**	**0.00**	**0.03**	**-0.01**	**82.91**
Std. Dev.	**4.35**	**0.00**	**0.48**	**0.00**	**0.01**	**0.01**	**0.01**	**0.01**	**0.11**	**0.62**	**0.08**	**0.00**	**0.02**	**0.01**	**3.66**
	18 oxygen atoms per formula unit (sum excludes F & Cl)														
	Si	**Ti**	**Al**	**Cr**	**Fe**	**Ni**	**Mn**	**Mg**	**Ca**	**Na**	**K**	**Cl**	**F**		**Sum**
IEBS-1 Area 1 Shard	7.676	0.001	1.443	0.000	0.009	0.000	0.000	0.016	0.231	0.397	0.054	0.001	0.008		9.827
IEBS-1 Area 3 Shard	7.399	0.000	1.703	0.000	0.009	0.000	0.001	0.023	0.231	0.700	0.068	0.000	0.012		10.133
IEBS-1 Area 3 Shard	7.619	0.001	1.508	0.000	0.007	0.001	0.002	0.016	0.218	0.455	0.055	0.000	0.018		9.882
IEBS-1 Area 3 Shard	7.513	0.000	1.548	0.000	0.010	0.000	0.004	0.022	0.219	0.748	0.042	0.000	0.009		10.108
IEBS-1 Area 4 shard	7.388	0.000	1.749	0.000	0.010	0.000	0.002	0.019	0.263	0.538	0.074	0.001	0.000		10.043
AVERAGE	**7.52**	**0.00**	**1.59**	**0.00**	**0.01**	**0.00**	**0.00**	**0.02**	**0.23**	**0.57**	**0.06**	**0.00**	**0.01**		**10.00**
Std. Dev.	**0.13**	**0.00**	**0.13**	**0.00**	**0.00**	**0.00**	**0.00**	**0.00**	**0.02**	**0.15**	**0.01**	**0.00**	**0.01**		**0.14**
Chlorite	**SiO_2**	**TiO_2**	**Al_2O_3**	**Cr_2O_3**	**FeO**	**NiO**	**MnO**	**MgO**	**CaO**	**Na_2O**	**K_2O**	**Cl**	**F**	**O=F&Cl**	**TOTAL**
IEBS-1 Area 1 Chlorite	34.60	1.58	16.65	0.00	22.61	0.00	0.60	7.11	0.01	0.16	9.24	0.09	0.72	-0.32	92.64
IEBS-1 Area 3 chlorite	36.26	1.86	16.32	0.00	22.18	0.00	0.57	8.04	0.00	0.17	9.53	0.07	0.80	-0.35	95.00
IEBS-1 Area 4 chlorite	34.40	4.52	14.13	0.00	24.58	0.00	0.28	7.82	0.00	0.41	8.85	0.22	0.54	-0.28	95.21
AVERAGE	**35.09**	**2.65**	**15.70**	**0.00**	**23.12**	**0.00**	**0.48**	**7.66**	**0.01**	**0.25**	**9.21**	**0.13**	**0.69**	**-0.32**	**94.29**
Std. Dev.	**1.02**	**1.62**	**1.37**	**0.00**	**1.28**	**0.00**	**0.18**	**0.49**	**0.00**	**0.14**	**0.34**	**0.08**	**0.14**	**0.04**	**1.43**
	11 oxygen atoms per formula unit (sum excludes F & Cl)														
	Si	**Ti**	**Al**	**Cr**	**Fe**	**Ni**	**Mn**	**Mg**	**Ca**	**Na**	**K**	**Cl**	**F**		**Sum**
IEBS-1 Area 1 Chlorite	2.777	0.095	1.575	0.000	1.517	0.000	0.040	0.850	0.001	0.025	0.946	0.012	0.182		7.826
IEBS-1 Area 3 chlorite	2.768	0.107	1.469	0.000	1.416	0.000	0.037	0.915	0.000	0.025	0.928	0.009	0.193		7.665
IEBS-1 Area 4 chlorite	2.721	0.269	1.317	0.000	1.626	0.000	0.019	0.922	0.000	0.063	0.893	0.029	0.135		7.830
AVERAGE	**2.76**	**0.16**	**1.45**	**0.00**	**1.52**	**0.00**	**0.03**	**0.90**	**0.00**	**0.04**	**0.92**	**0.02**	**0.17**		**7.77**
Std. Dev.	**0.03**	**0.10**	**0.13**	**0.00**	**0.10**	**0.00**	**0.01**	**0.04**	**0.00**	**0.02**	**0.03**	**0.01**	**0.03**		**0.09**
Unknown zeolite pseudomorph	**SiO_2**	**TiO_2**	**Al_2O_3**	**Cr_2O_3**	**FeO**	**NiO**	**MnO**	**MgO**	**CaO**	**Na_2O**	**K_2O**	**Cl**	**F**	**O=F&Cl**	**TOTAL**
IEBS-1 Area 2 Analcime?	46.76	0.13	13.44	0.00	18.93	0.00	0.14	5.24	0.70	2.98	0.22	0.03	0.12	-0.06	88.58
IEBS-1 Area 6 analcime?	42.38	0.09	11.97	0.00	26.47	0.08	0.20	5.83	1.27	6.03	0.26	0.02	0.00	0.00	94.58

AVERAGE	**44.57**	**0.11**	**12.71**	**0.00**	**22.70**	**0.04**	**0.17**	**5.53**	**0.99**	**4.50**	**0.24**	**0.02**	**0.06**	**-0.03**	**91.58**
Std. Dev.	**3.10**	**0.03**	**1.04**	**0.00**	**5.33**	**0.05**	**0.04**	**0.42**	**0.40**	**2.15**	**0.03**	**0.01**	**0.08**	**0.04**	**4.25**
	6 oxygen atoms per formula unit (sum excludes F & Cl)														
	Si	**Ti**	**Al**	**Cr**	**Fe**	**Ni**	**Mn**	**Mg**	**Ca**	**Na**	**K**	**Cl**	**F**		**Sum**
IEBS-1 Area 2 Analcime?	1.935	0.004	0.655	0.000	0.655	0.000	0.005	0.323	0.031	0.239	0.011	0.002	0.015		3.859
IEBS-1 Area 6 analcime?	1.760	0.003	0.586	0.000	0.919	0.003	0.007	0.361	0.057	0.485	0.014	0.001	0.000		4.194
AVERAGE	**1.85**	**0.00**	**0.62**	**0.00**	**0.79**	**0.00**	**0.01**	**0.34**	**0.04**	**0.36**	**0.01**	**0.00**	**0.01**		**4.03**
Std. Dev.	**0.12**	**0.00**	**0.05**	**0.00**	**0.19**	**0.00**	**0.00**	**0.03**	**0.02**	**0.17**	**0.00**	**0.00**	**0.01**		**0.24**
Clay Matrix	**SiO_2**	**TiO_2**	**Al_2O_3**	**Cr_2O_3**	**FeO**	**NiO**	**MnO**	**MgO**	**CaO**	**Na_2O**	**K_2O**	**Cl**	**F**	**O=F&Cl**	**TOTAL**
IEBS-1 Area 4 Matrix	61.55	0.11	21.61	0.00	3.99	0.00	0.01	1.91	0.54	1.11	0.28	0.02	0.20	-0.09	91.14
IEBS-1 Area 4 matrix	59.35	0.12	22.31	0.00	4.17	0.01	0.01	1.90	0.14	0.99	0.27	0.02	0.28	-0.12	89.29
IEBS-1 Area 1 Matrix	59.55	0.12	22.16	0.00	3.93	0.01	0.02	2.08	0.42	1.15	0.27	0.02	0.21	-0.09	89.74
AVERAGE	**60.15**	**0.12**	**22.03**	**0.00**	**4.03**	**0.01**	**0.01**	**1.97**	**0.37**	**1.08**	**0.27**	**0.02**	**0.23**	**-0.10**	**90.06**
Std. Dev.	**1.22**	**0.01**	**0.37**	**0.00**	**0.13**	**0.01**	**0.00**	**0.10**	**0.20**	**0.09**	**0.01**	**0.00**	**0.05**	**0.02**	**0.96**
	12 oxygen atoms per formula unit (sum excludes F & Cl)														
	Si	**Ti**	**Al**	**Cr**	**Fe**	**Ni**	**Mn**	**Mg**	**Ca**	**Na**	**K**	**Cl**	**F**		**Sum**
IEBS-1 Area 4 Matrix	4.341	0.006	1.796	0	0.235	0	6E-04	0.201	0.041	0.152	0.025	0.002	0.045		6.80
IEBS-1 Area 4 matrix	4.268	0.006	1.891	0	0.251	6E-04	6E-04	0.204	0.011	0.138	0.025	0.002	0.064		6.80
IEBS-1 Area 1 Matrix	4.271	0.006	1.873	0	0.236	6E-04	0.001	0.222	0.032	0.16	0.025	0.002	0.048		6.83
AVERAGE	**4.29**	**0.01**	**1.85**	**0.00**	**0.24**	**0.00**	**0.00**	**0.21**	**0.03**	**0.15**	**0.02**	**0.00**	**0.05**		**6.81**
Std. Dev.	**0.04**	**0.00**	**0.05**	**0.00**	**0.01**	**0.00**	**0.00**	**0.01**	**0.02**	**0.01**	**0.00**	**0.00**	**0.01**		**0.02**
Stilpnomelane	**SiO_2**	**TiO_2**	**Al_2O_3**	**Cr_2O_3**	**FeO**	**NiO**	**MnO**	**MgO**	**CaO**	**Na_2O**	**K_2O**	**Cl**	**F**	**O=F&Cl**	**TOTAL**
IEBS-1 Area 5 stil?	33.81	0.02	12.03	0.00	24.99	0.01	0.11	1.31	0.58	1.84	0.08	0.13	0.00	-0.03	74.90
IEBS-1 Area 5 stil?	32.93	0.01	12.39	0.00	25.73	0.02	0.12	1.23	0.75	1.96	0.06	0.09	0.02	-0.03	75.29
IEBS-1 Area 5 stil?	31.76	0.03	11.14	0.01	21.30	0.00	0.11	1.28	0.34	2.02	0.08	0.16	0.05	-0.05	68.21
IEBS-1 Area 5 stil?	43.61	0.09	15.21	0.01	25.60	0.00	0.11	2.00	1.09	2.45	0.15	0.01	0.16	-0.07	90.32
IEBS-1 Area 6 stil?	34.02	0.01	11.09	0.01	24.29	0.00	0.10	2.12	0.48	1.59	0.02	0.10	0.00	-0.02	73.85
IEBS-1 Area 6 stil?	35.03	0.02	12.55	0.00	26.48	0.00	0.10	1.94	0.46	1.78	0.03	0.09	0.05	-0.04	78.49
IEBS-1 Area 6 stil?	32.95	0.02	11.79	0.01	26.36	0.02	0.10	1.59	0.44	1.57	0.04	0.14	0.01	-0.03	75.02
IEBS-1 Area 6 stil?	45.21	0.06	17.01	0.01	22.68	0.00	0.10	1.84	0.96	4.45	0.30	0.02	0.07	-0.03	92.64
AVERAGE	**36.17**	**0.03**	**12.90**	**0.01**	**24.68**	**0.01**	**0.11**	**1.66**	**0.64**	**2.21**	**0.10**	**0.09**	**0.04**	**-0.04**	**78.59**
Std. Dev.	**5.20**	**0.03**	**2.10**	**0.00**	**1.84**	**0.01**	**0.01**	**0.36**	**0.27**	**0.95**	**0.09**	**0.05**	**0.05**	**0.02**	**8.47**

	28 oxygen atoms per formula unit (sum excludes F & Cl)														
	Si	**Ti**	**Al**	**Cr**	**Fe**	**Ni**	**Mn**	**Mg**	**Ca**	**Na**	**K**	**Cl**	**F**		**Sum**
IEBS-1 Area 5 stil?	8.281	0.003	3.472	0.000	5.120	0.002	0.022	0.478	0.151	0.875	0.026	0.052	0.000		18.431
IEBS-1 Area 5 stil?	8.089	0.002	3.586	0.000	5.286	0.004	0.025	0.451	0.196	0.935	0.019	0.036	0.018		18.593
IEBS-1 Area 5 stil?	8.434	0.005	3.486	0.001	4.730	0.000	0.024	0.506	0.096	1.042	0.026	0.070	0.038		18.351
IEBS-1 Area 5 stil?	8.577	0.013	3.526	0.001	4.211	0.000	0.018	0.586	0.229	0.934	0.037	0.005	0.098		18.131
IEBS-1 Area 6 stil?	8.406	0.002	3.230	0.002	5.020	0.000	0.022	0.781	0.128	0.762	0.008	0.042	0.000		18.361
IEBS-1 Area 6 stil?	8.198	0.003	3.462	0.000	5.183	0.001	0.019	0.677	0.114	0.809	0.010	0.037	0.040		18.477
IEBS-1 Area 6 stil?	8.141	0.004	3.434	0.002	5.448	0.003	0.021	0.586	0.116	0.754	0.012	0.059	0.005		18.520
IEBS-1 Area 6 stil?	8.558	0.009	3.794	0.001	3.591	0.000	0.016	0.518	0.194	1.632	0.073	0.007	0.039		18.388
AVERAGE	**8.34**	**0.01**	**3.50**	**0.00**	**4.82**	**0.00**	**0.02**	**0.57**	**0.15**	**0.97**	**0.03**	**0.04**	**0.03**		**18.41**
Std. Dev.	**0.19**	**0.00**	**0.16**	**0.00**	**0.63**	**0.00**	**0.00**	**0.11**	**0.05**	**0.29**	**0.02**	**0.02**	**0.03**		**0.14**

IEBS-2															
C(A)SH (Zeophyllite, tobermorite?)	**SiO_2**	**TiO_2**	**Al_2O_3**	**Cr_2O_3**	**FeO**	**NiO**	**MnO**	**MgO**	**CaO**	**Na_2O**	**K_2O**	**Cl**	**F**	**O=F&Cl**	**TOTAL**
IEBS-2 Area 1 zeolite?	12.11	0.01	1.65	0.00	0.76	0.00	0.06	0.08	46.27	0.28	0.03	0.03	0.69	-0.30	61.28
IEBS-2 Area 1 zeolite?	9.79	0.01	1.88	0.00	0.82	0.00	0.06	0.09	48.20	0.31	0.02	0.02	0.54	-0.23	61.20
IEBS-2 Area 1 zeolite?	7.45	0.01	1.07	0.00	0.66	0.00	0.07	0.08	41.74	0.55	0.02	0.02	0.22	-0.10	51.66
IEBS-2 Area 1 zeolite?	7.27	0.01	1.74	0.00	0.64	0.00	0.08	0.06	42.03	0.38	0.02	0.03	0.57	-0.25	52.26
IEBS-2 Area 1-2 zeolite?	10.13	0.00	1.80	0.00	0.70	0.01	0.04	0.13	48.64	0.43	0.02	0.03	0.94	-0.40	61.93
IEBS-2 Area 1-2 zeolite?	9.33	0.00	1.25	0.00	0.58	0.01	0.05	0.08	48.25	0.49	0.03	0.03	1.24	-0.53	60.11
IEBS-2 Area 1-2 zeolite?	10.45	0.00	3.37	0.00	0.66	0.00	0.03	0.12	43.09	0.74	0.04	0.04	0.80	-0.35	58.52
AVERAGE	**9.50**	**0.01**	**1.82**	**0.00**	**0.69**	**0.00**	**0.05**	**0.09**	**45.46**	**0.45**	**0.03**	**0.03**	**0.71**	**-0.31**	**58.14**
Std. Dev.	**1.70**	**0.00**	**0.74**	**0.00**	**0.08**	**0.00**	**0.02**	**0.02**	**3.09**	**0.16**	**0.01**	**0.01**	**0.32**	**0.14**	**4.36**
	12 oxygen atoms per formula unit (sum excludes F & Cl)														
	Si	**Ti**	**Al**	**Cr**	**Fe**	**Ni**	**Mn**	**Mg**	**Ca**	**Na**	**K**	**Cl**	**F**		**Sum**
IEBS-2 Area 1 zeolite?	1.815	0.001	0.291	0.000	0.095	0.000	0.008	0.018	7.431	0.081	0.006	0.008	0.327		9.747
IEBS-2 Area 1 zeolite?	1.516	0.001	0.343	0.000	0.106	0.000	0.008	0.021	7.998	0.093	0.004	0.005	0.264		10.090
IEBS-2 Area 1 zeolite?	1.407	0.001	0.238	0.000	0.104	0.000	0.011	0.023	8.447	0.201	0.005	0.006	0.131		10.438
IEBS-2 Area 1 zeolite?	1.330	0.001	0.375	0.000	0.098	0.000	0.012	0.016	8.239	0.135	0.005	0.009	0.330		10.212
IEBS-2 Area 1-2 zeolite?	1.523	0.000	0.319	0.000	0.088	0.001	0.005	0.029	7.834	0.125	0.004	0.008	0.447		9.928
IEBS-2 Area 1-2 zeolite?	1.441	0.000	0.228	0.000	0.075	0.001	0.007	0.018	7.985	0.147	0.006	0.008	0.606		9.908
IEBS-2 Area 1-2 zeolite?	1.626	0.000	0.618	0.000	0.086	0.000	0.004	0.028	7.184	0.223	0.008	0.011	0.394		9.776
AVERAGE	**1.52**	**0.00**	**0.34**	**0.00**	**0.09**	**0.00**	**0.01**	**0.02**	**7.87**	**0.14**	**0.01**	**0.01**	**0.36**		**10.01**
Std. Dev.	**0.16**	**0.00**	**0.13**	**0.00**	**0.01**	**0.00**	**0.00**	**0.00**	**0.44**	**0.05**	**0.00**	**0.00**	**0.15**		**0.25**
Plagioclase	**SiO_2**	**TiO_2**	**Al_2O_3**	**Cr_2O_3**	**FeO**	**NiO**	**MnO**	**MgO**	**CaO**	**Na_2O**	**K_2O**	**Cl**	**F**	**O=F&Cl**	**TOTAL**
IEBS-2 Area 1 feldspar	62.07	0.00	22.72	0.00	0.24	0.02	0.00	0.00	4.91	7.69	0.91	0.00	0.02	-0.01	98.57
	8 oxygen atoms per formula unit (sum excludes F & Cl)														
	Si	**Ti**	**Al**	**Cr**	**Fe**	**Ni**	**Mn**	**Mg**	**Ca**	**Na**	**K**	**Cl**	**F**		**Sum**
IEBS-2 Area 1 feldspar	2.792	0.000	1.205	0.000	0.009	0.001	0.000	0.000	0.237	0.671	0.052	0.000	0.003		4.967
Clay Matrix	**SiO_2**	**TiO_2**	**Al_2O_3**	**Cr_2O_3**	**FeO**	**NiO**	**MnO**	**MgO**	**CaO**	**Na_2O**	**K_2O**	**Cl**	**F**	**O=F&Cl**	**TOTAL**
IEBS-2 Area 1 matrix	58.94	0.14	21.33	0.00	6.81	0.00	0.04	2.23	0.24	1.56	0.26	0.01	0.21	-0.09	91.56
IEBS-2 Area 3 matrix	59.02	0.12	21.19	0.00	5.06	0.01	0.01	1.75	0.32	1.04	0.29	0.01	0.23	-0.10	88.85
IEBS-2 Area 1-2 matrix	58.13	0.12	21.06	0.00	4.10	0.00	0.01	1.94	0.18	1.19	0.34	0.01	0.24	-0.10	87.10
IEBS-2 Area 4 matrix	60.06	0.11	22.16	0.00	4.60	0.00	0.01	1.82	0.29	0.93	0.26	0.01	0.19	-0.08	90.27
AVERAGE	**59.04**	**0.13**	**21.43**	**0.00**	**5.14**	**0.00**	**0.02**	**1.94**	**0.26**	**1.18**	**0.29**	**0.01**	**0.22**	**-0.09**	**89.44**

Std. Dev.	**0.79**	**0.01**	**0.50**	**0.00**	**1.17**	**0.01**	**0.02**	**0.21**	**0.06**	**0.27**	**0.04**	**0.00**	**0.02**	**0.01**	**1.92**
	12 oxygen atoms per formula unit (sum excludes F & Cl)														
	Si	**Ti**	**Al**	**Cr**	**Fe**	**Ni**	**Mn**	**Mg**	**Ca**	**Na**	**K**	**Cl**	**F**		**Sum**
IEBS-2 Area 1 matrix	4.223	0.008	1.801	0.000	0.408	0.000	0.002	0.238	0.018	0.217	0.024	0.001	0.048		6.940
IEBS-2 Area 3 matrix	4.297	0.007	1.818	0.000	0.308	0.001	0.001	0.190	0.025	0.147	0.027	0.001	0.053		6.820
IEBS-2 Area 1-2 matrix	4.297	0.007	1.835	0.000	0.253	0.000	0.001	0.214	0.014	0.171	0.032	0.001	0.056		6.823
IEBS-2 Area 4 matrix	4.289	0.006	1.865	0.000	0.275	0.000	0.001	0.194	0.022	0.129	0.024	0.001	0.043		6.804
AVERAGE	**4.28**	**0.01**	**1.83**	**0.00**	**0.31**	**0.00**	**0.00**	**0.21**	**0.02**	**0.17**	**0.03**	**0.00**	**0.05**		**6.85**
Std. Dev.	**0.04**	**0.00**	**0.03**	**0.00**	**0.07**	**0.00**	**0.00**	**0.02**	**0.00**	**0.04**	**0.00**	**0.00**	**0.01**		**0.06**
Shard (Clinoptilolite?)	**SiO_2**	**TiO_2**	**Al_2O_3**	**Cr_2O_3**	**FeO**	**NiO**	**MnO**	**MgO**	**CaO**	**Na_2O**	**K_2O**	**Cl**	**F**	**O=F&Cl**	**TOTAL**
IEBS-2 Area 1-2 shard	71.66	0.01	12.01	0.00	0.20	0.01	0.04	0.13	2.33	1.60	0.10	0.00	0.00	0.00	88.08
IEBS-2 Area 1-2 shard	71.59	0.00	11.64	0.00	0.18	0.01	0.04	0.15	1.53	2.27	0.24	0.00	0.00	0.00	87.64
IEBS-2 Area 1-2 shard	69.62	0.00	11.55	0.00	0.22	0.00	0.03	0.13	1.85	1.40	0.11	0.00	0.02	-0.01	84.92
IEBS-2 Area 1 shard	68.13	0.00	10.28	0.00	0.15	0.00	0.02	0.07	2.22	1.88	0.17	0.00	0.00	0.00	82.92
IEBS-2 Area 1-2- shard	59.92	0.00	9.27	0.00	0.24	0.00	0.01	0.12	1.20	1.91	0.17	0.11	0.01	-0.03	72.97
IEBS-2 Area 3 shard	61.68	0.00	9.37	0.00	0.23	0.00	0.02	0.15	2.49	1.67	0.07	0.00	0.09	-0.04	75.69
IEBS-2 Area 4 shard	64.31	0.00	7.16	0.00	0.15	0.00	0.02	0.15	1.69	1.90	0.13	0.00	0.00	0.00	75.52
AVERAGE	**66.70**	**0.00**	**10.18**	**0.00**	**0.20**	**0.00**	**0.03**	**0.13**	**1.90**	**1.80**	**0.14**	**0.02**	**0.02**	**-0.01**	**81.10**
Std. Dev.	**4.76**	**0.00**	**1.73**	**0.00**	**0.04**	**0.00**	**0.01**	**0.03**	**0.47**	**0.28**	**0.06**	**0.04**	**0.03**	**0.02**	**6.27**
	18 oxygen atoms per formula unit (sum excludes F & Cl)														
	Si	**Ti**	**Al**	**Cr**	**Fe**	**Ni**	**Mn**	**Mg**	**Ca**	**Na**	**K**	**Cl**	**F**		**Sum**
IEBS-2 Area 1-2 shard	7.629	0.001	1.507	0.000	0.018	0.000	0.003	0.021	0.266	0.329	0.013	0.000	0.000		9.788
IEBS-2 Area 1-2 shard	7.663	0.000	1.469	0.000	0.016	0.000	0.003	0.023	0.175	0.471	0.032	0.001	0.000		9.854
IEBS-2 Area 1-2 shard	7.666	0.000	1.498	0.000	0.021	0.000	0.003	0.022	0.218	0.299	0.016	0.001	0.007		9.742
IEBS-2 Area 1 shard	7.713	0.000	1.371	0.000	0.015	0.000	0.002	0.012	0.269	0.412	0.025	0.001	0.000		9.820
IEBS-2 Area 1-2- shard	7.711	0.000	1.406	0.000	0.026	0.000	0.001	0.023	0.166	0.475	0.029	0.025	0.004		9.838
IEBS-2 Area 3 shard	7.673	0.000	1.373	0.000	0.023	0.000	0.003	0.028	0.332	0.402	0.012	0.000	0.035		9.847
IEBS-2 Area 4 shard	7.962	0.000	1.045	0.000	0.015	0.000	0.003	0.027	0.224	0.457	0.020	0.000	0.002		9.754
AVERAGE	**7.72**	**0.00**	**1.38**	**0.00**	**0.02**	**0.00**	**0.00**	**0.02**	**0.24**	**0.41**	**0.02**	**0.00**	**0.01**		**9.81**
Std. Dev.	**0.11**	**0.00**	**0.16**	**0.00**	**0.00**	**0.00**	**0.00**	**0.01**	**0.06**	**0.07**	**0.01**	**0.01**	**0.01**		**0.05**
Stilpnomelane	**SiO_2**	**TiO_2**	**Al_2O_3**	**Cr_2O_3**	**FeO**	**NiO**	**MnO**	**MgO**	**CaO**	**Na_2O**	**K_2O**	**Cl**	**F**	**O=F&Cl**	**TOTAL**
IEBS-2 Area 2 Stilp?	34.60	0.00	11.14	0.00	31.40	0.01	0.09	1.27	5.85	2.51	0.03	0.15	0.06	-0.06	87.05
IEBS-2 Area 3 stilp?	41.95	0.05	16.08	0.01	29.64	0.02	0.14	1.68	0.76	2.98	0.14	0.07	0.00	-0.02	93.53

IEBS-2 Area 3 stilp?	36.58	0.02	15.09	0.01	27.74	0.02	0.13	1.73	0.59	2.41	0.16	0.09	0.01	-0.03	84.56
IEBS-2 Area 3 stilp?	38.07	0.02	15.82	0.00	30.21	0.01	0.15	1.54	0.78	3.57	0.15	0.06	0.11	-0.06	90.38
AVERAGE	**37.80**	**0.02**	**14.53**	**0.01**	**29.75**	**0.02**	**0.13**	**1.55**	**1.99**	**2.87**	**0.12**	**0.09**	**0.04**	**-0.04**	**88.88**
Std. Dev.	**3.11**	**0.02**	**2.30**	**0.01**	**1.53**	**0.01**	**0.03**	**0.21**	**2.57**	**0.53**	**0.06**	**0.04**	**0.05**	**0.02**	**3.91**
	18 oxygen atoms per formula unit (sum excludes F & Cl)														
	Si	**Ti**	**Al**	**Cr**	**Fe**	**Ni**	**Mn**	**Mg**	**Ca**	**Na**	**K**	**Cl**	**F**		**Sum**
IEBS-2 Area 2 Stilp?	7.671	0.000	2.911	0.000	5.822	0.002	0.017	0.420	1.390	1.079	0.008	0.056	0.042		19.38
IEBS-2 Area 3 stilp?	8.171	0.007	3.691	0.002	4.828	0.003	0.023	0.488	0.159	1.125	0.035	0.023	0.000		18.56
IEBS-2 Area 3 stilp?	7.938	0.003	3.859	0.002	5.034	0.003	0.024	0.560	0.137	1.014	0.044	0.033	0.007		18.65
IEBS-2 Area 3 stilp?	7.799	0.003	3.820	0.000	5.176	0.002	0.026	0.470	0.171	1.418	0.039	0.021	0.071		18.95
AVERAGE	**7.89**	**0.00**	**3.57**	**0.00**	**5.21**	**0.00**	**0.02**	**0.48**	**0.46**	**1.16**	**0.03**	**0.03**	**0.03**		**18.88**
Std. Dev.	**0.21**	**0.00**	**0.45**	**0.00**	**0.43**	**0.00**	**0.00**	**0.06**	**0.62**	**0.18**	**0.02**	**0.02**	**0.03**		**0.37**

IEBS-2 Steel															
Fe-saponite	**SiO_2**	**TiO_2**	**Al_2O_3**	**Cr_2O_3**	**FeO**	**NiO**	**MnO**	**MgO**	**CaO**	**Na_2O**	**K_2O**	**Cl**	**F**	**O=F&Cl**	**TOTAL**
IEBS-2 Steel Area 1 Fe sap	41.79	0.03	16.85	0.17	29.86	0.24	0.29	1.52	0.89	3.86	0.06	0.01	0.01	-0.01	95.58
IEBS-2 Steel Area 1 Fe sap	43.70	0.06	16.35	0.15	27.16	0.23	0.25	1.57	0.92	3.24	0.07	0.02	0.00	-0.01	93.73
IEBS-2 Steel Area 1 Fe sap	41.41	0.04	17.17	0.18	29.27	0.23	0.24	1.50	0.85	3.60	0.08	0.02	0.00	0.00	94.60
IEBS-2 Steel Area 1 Fe sap	35.41	0.02	15.74	0.33	34.11	0.29	0.33	1.20	0.45	2.58	0.08	0.01	0.03	-0.02	90.57
IEBS-2 Steel Area 4 Fe sap	41.10	0.03	16.11	0.23	27.33	0.40	0.22	1.58	0.14	4.19	0.17	0.08	0.08	-0.05	91.59
IEBS-2 Steel Area 4 Fe sap	33.77	0.03	15.05	0.22	25.55	0.25	0.26	1.46	0.08	5.65	0.10	0.09	0.06	-0.04	82.52
AVERAGE	**39.53**	**0.04**	**16.21**	**0.21**	**28.88**	**0.27**	**0.27**	**1.47**	**0.56**	**3.86**	**0.09**	**0.04**	**0.03**	**-0.02**	**91.43**
Std. Dev.	**3.97**	**0.01**	**0.77**	**0.07**	**3.00**	**0.07**	**0.04**	**0.14**	**0.39**	**1.04**	**0.04**	**0.04**	**0.03**	**0.02**	**4.75**
	12 oxygen atoms per formula unit (sum excludes F & Cl)														
	Si	**Ti**	**Al**	**Cr**	**Fe**	**Ni**	**Mn**	**Mg**	**Ca**	**Na**	**K**	**Cl**	**F**		**Sum**
IEBS-2 Steel Area 1 Fe sap	3.434	0.002	1.632	0.011	2.052	0.016	0.020	0.186	0.079	0.614	0.006	0.002	0.002		8.053
IEBS-2 Steel Area 1 Fe sap	3.587	0.004	1.581	0.010	1.864	0.015	0.018	0.192	0.081	0.516	0.008	0.002	0.001		7.876
IEBS-2 Steel Area 1 Fe sap	3.426	0.003	1.675	0.012	2.025	0.015	0.017	0.186	0.075	0.578	0.008	0.002	0.000		8.021
IEBS-2 Steel Area 1 Fe sap	3.196	0.001	1.674	0.024	2.575	0.021	0.025	0.162	0.044	0.452	0.010	0.001	0.009		8.185
IEBS-2 Steel Area 4 Fe sap	3.497	0.002	1.615	0.015	1.945	0.027	0.016	0.200	0.013	0.691	0.019	0.012	0.020		8.041
IEBS-2 Steel Area 4 Fe sap	3.267	0.002	1.716	0.017	2.067	0.019	0.021	0.210	0.008	1.060	0.012	0.015	0.018		8.401
AVERAGE	**3.40**	**0.00**	**1.65**	**0.01**	**2.09**	**0.02**	**0.02**	**0.19**	**0.05**	**0.65**	**0.01**	**0.01**	**0.01**		**8.10**
Std. Dev.	**0.15**	**0.00**	**0.05**	**0.01**	**0.25**	**0.00**	**0.00**	**0.02**	**0.03**	**0.22**	**0.00**	**0.01**	**0.01**		**0.18**
Chlorite?	**SiO_2**	**TiO_2**	**Al_2O_3**	**Cr_2O_3**	**FeO**	**NiO**	**MnO**	**MgO**	**CaO**	**Na_2O**	**K_2O**	**Cl**	**F**	**O=F&Cl**	**TOTAL**
IEBS-2 Steel Area 3 chl?	46.02	0.10	21.84	0.12	5.98	0.10	0.06	1.57	0.19	2.29	0.35	0.01	0.23	-0.10	78.63
IEBS-2 Steel Area 3 chl?	62.39	0.12	21.12	0.07	6.69	0.11	0.01	1.97	0.22	1.42	0.43	0.01	0.17	-0.08	94.58
AVERAGE	**54.20**	**0.11**	**21.48**	**0.09**	**6.33**	**0.11**	**0.04**	**1.77**	**0.21**	**1.85**	**0.39**	**0.01**	**0.20**	**-0.09**	**86.60**
Std. Dev.	**11.58**	**0.01**	**0.51**	**0.03**	**0.51**	**0.01**	**0.04**	**0.28**	**0.03**	**0.62**	**0.06**	**0.00**	**0.04**	**0.02**	**11.27**
	11 oxygen atoms per formula unit (sum excludes F & Cl)														
	Si	**Ti**	**Al**	**Cr**	**Fe**	**Ni**	**Mn**	**Mg**	**Ca**	**Na**	**K**	**Cl**	**F**		**Sum**
IEBS-2 Steel Area 3 chl?	3.570	0.006	1.997	0.007	0.388	0.006	0.004	0.182	0.016	0.344	0.035	0.001	0.056		6.56
IEBS-2 Steel Area 3 chl?	3.957	0.006	1.579	0.004	0.355	0.006	0.001	0.186	0.015	0.175	0.035	0.001	0.034		6.32
AVERAGE	**3.76**	**0.01**	**1.79**	**0.01**	**0.37**	**0.01**	**0.00**	**0.18**	**0.02**	**0.26**	**0.03**	**0.00**	**0.05**		**6.44**
Std. Dev.	**0.27**	**0.00**	**0.30**	**0.00**	**0.02**	**0.00**	**0.00**	**0.00**	**0.00**	**0.12**	**0.00**	**0.00**	**0.02**		**0.17**

IEBS-3														
Clay	**SiO_2**	**TiO_2**	**Al_2O_3**	**Cr_2O_3**	**FeO**	**NiO**	**MnO**	**MgO**	**CaO**	**Na_2O**	**K_2O**	**Cl**	**F**	**O=F&Cl**	**TOTAL**
IEBS 3 Area 1 clay	63.83	0.12	24.30	0.00	3.18	0.01	0.00	2.42	0.27	2.07	0.25	0.01	0.19	-0.08	96.47
IEBS 3 Area 1 clay	64.50	0.11	24.62	0.00	3.41	0.00	0.02	2.21	0.29	2.08	0.21	0.01	0.21	-0.09	97.46
IEBS 3 Area 2 clay	61.90	0.11	23.46	0.00	3.94	0.00	0.02	1.97	0.29	1.61	0.21	0.01	0.17	-0.07	93.54
IEBS 3 Area 2 clay	58.95	0.09	23.73	0.00	2.83	0.00	0.02	2.18	0.24	2.09	0.17	0.01	0.39	-0.17	90.32
IEBS 3 Area 2 clay	63.00	0.09	23.47	0.00	3.93	0.00	0.03	1.83	0.28	1.65	0.18	0.01	0.21	-0.09	94.47
IEBS 3 Area 3 clay	65.86	0.13	24.07	0.00	4.20	0.00	0.01	1.86	0.36	1.24	0.28	0.01	0.12	-0.05	98.03
IEBS 3 Area 3 clay	63.61	0.09	27.09	0.00	3.84	0.00	0.02	1.54	0.31	1.29	0.17	0.01	0.02	-0.01	97.96
IEBS 3 Area 3 clay	63.55	0.10	26.52	0.00	3.60	0.00	0.01	1.52	0.36	2.18	0.19	0.01	0.04	-0.02	98.04
AVERAGE	**63.150**	**0.107**	**24.657**	**0.001**	**3.616**	**0.002**	**0.016**	**1.942**	**0.301**	**1.776**	**0.209**	**0.008**	**0.169**	**-0.073**	**95.787**
Std. Dev.	**1.911**	**0.015**	**1.301**	**0.001**	**0.425**	**0.005**	**0.008**	**0.299**	**0.039**	**0.355**	**0.035**	**0.002**	**0.108**	**0.045**	**2.617**
	12 oxygen atoms per formula unit (sum excludes F & Cl)														
	Si	**Ti**	**Al**	**Cr**	**Fe**	**Ni**	**Mn**	**Mg**	**Ca**	**Na**	**K**	**Cl**	**F**		**Sum**
IEBS 3 Area 1 clay	4.267	0.006	1.914	0.000	0.178	0.001	0.000	0.241	0.019	0.269	0.021	0.001	0.040		6.915
IEBS 3 Area 1 clay	4.269	0.005	1.920	0.000	0.189	0.000	0.001	0.218	0.021	0.267	0.017	0.001	0.045		6.908
IEBS 3 Area 2 clay	4.276	0.006	1.910	0.000	0.228	0.000	0.001	0.203	0.022	0.216	0.019	0.001	0.036		6.880
IEBS 3 Area 2 clay	4.210	0.005	1.998	0.000	0.169	0.000	0.001	0.232	0.019	0.289	0.016	0.001	0.088		6.939
IEBS 3 Area 2 clay	4.303	0.005	1.890	0.000	0.224	0.000	0.001	0.187	0.020	0.218	0.016	0.001	0.045		6.864
IEBS 3 Area 3 clay	4.329	0.007	1.865	0.000	0.231	0.000	0.000	0.183	0.025	0.158	0.024	0.001	0.025		6.822
IEBS 3 Area 3 clay	4.184	0.005	2.100	0.000	0.211	0.000	0.001	0.151	0.022	0.164	0.015	0.001	0.005		6.851
IEBS 3 Area 3 clay	4.189	0.005	2.060	0.000	0.198	0.000	0.001	0.149	0.026	0.278	0.016	0.001	0.009		6.923
AVERAGE	**4.253**	**0.005**	**1.957**	**0.000**	**0.204**	**0.000**	**0.001**	**0.195**	**0.022**	**0.232**	**0.018**	**0.001**	**0.037**		**6.888**
Std. Dev.	**0.050**	**0.001**	**0.080**	**0.000**	**0.022**	**0.000**	**0.000**	**0.032**	**0.002**	**0.048**	**0.003**	**0.000**	**0.024**		**0.037**
K-feldspar	**SiO_2**	**TiO_2**	**Al_2O_3**	**Cr_2O_3**	**FeO**	**NiO**	**MnO**	**MgO**	**CaO**	**Na_2O**	**K_2O**	**Cl**	**F**	**O=F&Cl**	**TOTAL**
IEBS 3 Area 1 feldspar	64.90	0.01	20.07	0.00	0.18	0.00	0.01	0.00	0.14	3.50	10.50	0.00	0.00	0.00	99.30
IEBS 3 Area 1 feldspar	64.86	0.00	20.47	0.00	0.18	0.00	0.01	0.00	0.17	3.16	10.79	0.00	0.00	0.00	99.66
IEBS 3 Area 1 feldspar	64.92	0.01	20.14	0.00	0.15	0.01	0.00	0.00	0.18	3.05	10.20	0.00	0.00	0.00	98.67
IEBS 3 Area 3 feldspar	64.84	0.00	20.11	0.00	0.15	0.02	0.02	0.00	0.18	3.38	10.86	0.00	0.04	-0.02	99.55
IEBS 3 Area 3 feldspar	64.21	0.01	20.72	0.00	0.15	0.00	0.00	0.02	0.18	3.09	10.50	0.00	0.00	0.00	98.88
IEBS 3 Area 3 feldspar	64.89	0.01	20.28	0.00	0.13	0.00	0.00	0.00	0.20	3.33	10.48	0.00	0.00	0.00	99.31
IEBS 3 Area 3 feldspar	64.99	0.01	20.10	0.00	0.17	0.00	0.00	0.00	0.18	3.26	11.05	0.00	0.00	0.00	99.77
AVERAGE	**64.802**	**0.006**	**20.270**	**0.000**	**0.160**	**0.004**	**0.005**	**0.003**	**0.175**	**3.253**	**10.625**	**0.001**	**0.005**	**-0.002**	**99.307**
Std. Dev.	**0.245**	**0.003**	**0.225**	**0.000**	**0.017**	**0.006**	**0.006**	**0.007**	**0.018**	**0.152**	**0.265**	**0.001**	**0.013**	**0.006**	**0.376**

	8 oxygen atoms per formula unit (sum excludes F & Cl)													
	Si	**Ti**	**Al**	**Cr**	**Fe**	**Ni**	**Mn**	**Mg**	**Ca**	**Na**	**K**	**Cl**	**F**		**Sum**
IEBS 3 Area 1 feldspar	2.943	0.000	1.089	0.000	0.007	0.000	0.000	0.000	0.007	0.313	0.617	0.000	0.000		4.977
IEBS 3 Area 1 feldspar	2.945	0.000	1.095	0.000	0.007	0.000	0.000	0.000	0.008	0.278	0.625	0.000	0.000		4.959
IEBS 3 Area 1 feldspar	2.929	0.000	1.120	0.000	0.006	0.000	0.000	0.000	0.009	0.279	0.614	0.000	0.000		4.957
IEBS 3 Area 3 feldspar	2.951	0.000	1.079	0.000	0.006	0.001	0.001	0.000	0.009	0.299	0.630	0.000	0.005		4.974
IEBS 3 Area 3 feldspar	2.926	0.000	1.111	0.000	0.006	0.000	0.000	0.001	0.009	0.286	0.640	0.000	0.000		4.981
IEBS 3 Area 3 feldspar	2.939	0.000	1.100	0.000	0.005	0.000	0.000	0.000	0.010	0.297	0.615	0.000	0.000		4.966
IEBS 3 Area 3 feldspar	2.953	0.000	1.076	0.000	0.007	0.000	0.000	0.000	0.009	0.287	0.640	0.000	0.000		4.972
AVERAGE	**2.941**	**0.000**	**1.096**	**0.000**	**0.006**	**0.000**	**0.000**	**0.000**	**0.009**	**0.291**	**0.626**	**0.000**	**0.001**		**4.970**
Std. Dev.	**0.009**	**0.000**	**0.015**	**0.000**	**0.001**	**0.000**	**0.000**	**0.001**	**0.001**	**0.011**	**0.011**	**0.000**	**0.002**		**0.008**

Plagioclase	**SiO_2**	**TiO_2**	**Al_2O_3**	**Cr_2O_3**	**FeO**	**NiO**	**MnO**	**MgO**	**CaO**	**Na_2O**	**K_2O**	**Cl**	**F**	**O=F&Cl**	**TOTAL**
IEBS 3 Area 1 feldspar	61.82	0.01	25.28	0.00	0.27	0.00	0.00	0.01	4.75	7.57	1.08	0.00	0.05	-0.02	100.79
IEBS 3 Area 1 feldspar	57.98	0.01	28.38	0.00	0.22	0.00	0.01	0.01	6.99	6.58	0.51	0.00	0.00	0.00	100.68
IEBS 3 Area 3 feldspar	49.06	0.00	33.91	0.00	0.44	0.00	0.01	0.02	13.87	2.41	0.11	0.01	0.00	0.00	99.86
IEBS 3 Area 3 feldspar	60.12	0.01	25.02	0.00	0.28	0.01	0.00	0.01	5.04	7.79	0.79	0.00	0.00	0.00	99.06
AVERAGE	**57.246**	**0.007**	**28.147**	**0.000**	**0.301**	**0.002**	**0.006**	**0.010**	**7.660**	**6.087**	**0.623**	**0.002**	**0.012**	**-0.006**	**100.096**
Std. Dev.	**4.916**	**0.004**	**3.580**	**0.001**	**0.086**	**0.003**	**0.004**	**0.004**	**3.689**	**2.172**	**0.358**	**0.003**	**0.021**	**0.009**	**0.697**

	8 oxygen atoms per formula unit (sum excludes F & Cl)														
	Si	**Ti**	**Al**	**Cr**	**Fe**	**Ni**	**Mn**	**Mg**	**Ca**	**Na**	**K**	**Cl**	**F**		**Sum**
IEBS 3 Area 1 feldspar	2.722	0.000	1.312	0.000	0.010	0.000	0.000	0.000	0.224	0.646	0.061	0.000	0.007		4.975
IEBS 3 Area 1 feldspar	2.569	0.000	1.482	0.000	0.008	0.000	0.000	0.001	0.332	0.565	0.029	0.000	0.000		4.986
IEBS 3 Area 3 feldspar	2.233	0.000	1.819	0.000	0.017	0.000	0.000	0.001	0.677	0.213	0.006	0.001	0.000		4.967
IEBS 3 Area 3 feldspar	2.742	0.000	1.281	0.000	0.010	0.000	0.000	0.001	0.234	0.656	0.044	0.000	0.000		4.968
AVERAGE	**2.567**	**0.000**	**1.473**	**0.000**	**0.011**	**0.000**	**0.000**	**0.001**	**0.367**	**0.520**	**0.035**	**0.000**	**0.002**		**4.974**
Std. Dev.	**0.204**	**0.000**	**0.214**	**0.000**	**0.003**	**0.000**	**0.000**	**0.000**	**0.184**	**0.181**	**0.020**	**0.000**	**0.003**		**0.008**

Sericite	**SiO_2**	**TiO_2**	**Al_2O_3**	**Cr_2O_3**	**FeO**	**NiO**	**MnO**	**MgO**	**CaO**	**Na_2O**	**K_2O**	**Cl**	**F**	**O=F&Cl**	**TOTAL**
IEBS 3 Area 1 feldspar	76.68	0.00	14.74	0.00	0.22	0.00	0.02	0.15	1.91	2.24	0.03	0.00	0.00	0.00	95.99

	8 oxygen atoms per formula unit (sum excludes F & Cl)														
	Si	**Ti**	**Al**	**Cr**	**Fe**	**Ni**	**Mn**	**Mg**	**Ca**	**Na**	**K**	**Cl**	**F**		**Sum**
IEBS 3 Area 1 feldspar	3.332	0.000	0.755	0.000	0.008	0.000	0.001	0.010	0.089	0.189	0.001	0.000	0.000		4.385

Clinoptilolite	**SiO_2**	**TiO_2**	**Al_2O_3**	**Cr_2O_3**	**FeO**	**NiO**	**MnO**	**MgO**	**CaO**	**Na_2O**	**K_2O**	**Cl**	**F**	**O=F&Cl**	**TOTAL**
IEBS 3 Area 1 feldspar	73.12	0.00	14.34	0.00	0.16	0.00	0.02	0.11	1.72	2.95	0.01	0.00	0.00	0.00	92.43
IEBS 3 Area 1 feldspar	69.54	0.00	12.67	0.00	0.15	0.00	0.01	0.11	1.53	3.44	0.01	0.00	0.08	-0.03	87.47
IEBS 3 Area 1 feldspar	64.19	0.00	13.15	0.00	0.18	0.00	0.00	0.11	1.61	2.20	0.01	0.00	0.05	-0.02	81.46
IEBS 3 Area 3 zeolite-glass	67.70	0.00	13.39	0.00	0.18	0.02	0.02	0.09	2.02	0.99	0.02	0.01	0.02	-0.01	84.43
IEBS 3 Area 3 zeolite-glass	70.11	0.00	12.79	0.00	0.15	0.00	0.01	0.12	2.53	1.88	0.01	0.00	0.00	0.00	87.60
AVERAGE	**68.933**	**0.002**	**13.268**	**0.000**	**0.161**	**0.003**	**0.013**	**0.107**	**1.884**	**2.291**	**0.011**	**0.002**	**0.030**	**-0.013**	**86.677**
Std. Dev.	**2.942**	**0.002**	**0.594**	**0.000**	**0.014**	**0.007**	**0.006**	**0.012**	**0.365**	**0.852**	**0.004**	**0.003**	**0.031**	**0.013**	**3.655**

12 oxygen atoms per formula unit (sum excludes F & Cl)

	Si	**Ti**	**Al**	**Cr**	**Fe**	**Ni**	**Mn**	**Mg**	**Ca**	**Na**	**K**	**Cl**	**F**		**Sum**
IEBS 3 Area 1 feldspar	4.968	0.000	1.148	0.000	0.009	0.000	0.001	0.011	0.126	0.388	0.001	0.000	0.000		6.652
IEBS 3 Area 1 feldspar	5.004	0.000	1.075	0.000	0.009	0.000	0.001	0.012	0.118	0.480	0.000	0.000	0.018		6.699
IEBS 3 Area 1 feldspar	4.944	0.000	1.194	0.000	0.011	0.000	0.000	0.013	0.133	0.328	0.001	0.000	0.012		6.624
IEBS 3 Area 3 zeolite-glass	4.999	0.000	1.165	0.000	0.011	0.001	0.001	0.009	0.160	0.141	0.002	0.001	0.004		6.490
IEBS 3 Area 3 zeolite-glass	5.018	0.000	1.078	0.000	0.009	0.000	0.001	0.013	0.194	0.261	0.001	0.000	0.000		6.574
AVERAGE	**4.986**	**0.000**	**1.132**	**0.000**	**0.010**	**0.000**	**0.001**	**0.012**	**0.146**	**0.320**	**0.001**	**0.000**	**0.007**		**6.608**
Std. Dev.	**0.027**	**0.000**	**0.048**	**0.000**	**0.001**	**0.000**	**0.000**	**0.001**	**0.028**	**0.115**	**0.000**	**0.000**	**0.007**		**0.072**

IEBS-3 Steel															
Fe-saponite	**SiO_2**	**TiO_2**	**Al_2O_3**	**Cr_2O_3**	**FeO**	**NiO**	**MnO**	**MgO**	**CaO**	**Na_2O**	**K_2O**	**Cl**	**F**	**O=F&Cl**	**TOTAL**
IEBS 3 Steel Area 1 saponite	40.39	0.06	17.12	0.11	19.28	0.13	0.11	1.52	0.63	2.79	0.27	0.08	0.08	-0.05	82.49
IEBS 3 Steel Area 4 saponite	49.23	0.08	17.30	0.05	15.98	0.11	0.08	1.58	1.55	2.63	0.24	0.04	0.14	-0.07	88.88
IEBS 3 Steel Area 1 spot 2	40.63	0.04	17.76	0.10	26.40	0.17	0.15	1.62	0.84	2.35	0.16	0.01	0.00	0.00	90.25
IEBS 3 Steel Area 4 saponite	45.73	0.07	18.00	0.04	22.93	0.20	0.15	1.74	0.82	2.62	0.09	0.03	0.01	-0.01	92.43
IEBS 3 Steel Area 2 saponite	41.37	0.04	17.91	0.09	27.09	0.19	0.15	1.80	0.83	3.03	0.11	0.01	0.04	-0.02	92.63
IEBS 3 Steel Area 5 saponite	37.26	0.00	15.04	0.49	34.68	0.17	0.24	1.31	1.11	2.68	0.09	0.01	0.03	-0.02	93.09
IEBS 3 Steel Area 3 saponite	45.75	0.21	16.68	0.06	24.19	0.18	0.15	2.38	0.84	2.52	0.16	0.02	0.07	-0.03	93.14
IEBS 3 Steel Area 3 saponite	43.88	0.04	18.14	0.08	26.00	0.17	0.15	2.13	0.82	3.20	0.06	0.01	0.00	0.00	94.69
IEBS 3 Steel Area 3 saponite	44.19	0.04	18.27	0.09	25.77	0.18	0.15	2.19	0.77	3.03	0.07	0.01	0.10	-0.04	94.78
IEBS 3 Steel Area 2 saponite	43.63	0.05	18.86	0.15	26.83	0.22	0.17	1.85	0.77	3.27	0.22	0.02	0.08	-0.04	96.05
IEBS 3 Steel Area 2 saponite	44.33	0.05	19.20	0.11	25.99	0.20	0.16	1.86	0.73	3.31	0.26	0.01	0.05	-0.02	96.21
AVERAGE	**43.307**	**0.061**	**17.662**	**0.124**	**25.013**	**0.175**	**0.151**	**1.818**	**0.883**	**2.856**	**0.157**	**0.022**	**0.055**	**-0.028**	**92.240**
Std. Dev.	**3.091**	**0.050**	**1.080**	**0.120**	**4.522**	**0.030**	**0.038**	**0.302**	**0.239**	**0.312**	**0.074**	**0.019**	**0.043**	**0.020**	**3.752**
	12 oxygen atoms per formula unit (sum excludes F & Cl)														
	Si	**Ti**	**Al**	**Cr**	**Fe**	**Ni**	**Mn**	**Mg**	**Ca**	**Na**	**K**	**Cl**	**F**		**Sum**
IEBS 3 Steel Area 1 saponite	3.634	0.004	1.815	0.008	1.450	0.010	0.008	0.204	0.061	0.486	0.031	0.012	0.023		7.710
IEBS 3 Steel Area 4 saponite	3.952	0.005	1.637	0.003	1.073	0.007	0.005	0.189	0.134	0.409	0.024	0.005	0.037		7.440
IEBS 3 Steel Area 1 spot 2	3.461	0.002	1.783	0.007	1.880	0.011	0.011	0.206	0.077	0.388	0.018	0.001	0.000		7.845
IEBS 3 Steel Area 4 saponite	3.684	0.004	1.709	0.002	1.545	0.013	0.010	0.209	0.071	0.409	0.010	0.004	0.004		7.666
IEBS 3 Steel Area 2 saponite	3.445	0.003	1.758	0.006	1.887	0.013	0.011	0.224	0.074	0.489	0.012	0.002	0.010		7.921
IEBS 3 Steel Area 5 saponite	3.268	0.000	1.555	0.034	2.543	0.012	0.018	0.171	0.104	0.456	0.010	0.002	0.008		8.171
IEBS 3 Steel Area 3 saponite	3.688	0.013	1.585	0.004	1.631	0.011	0.011	0.286	0.073	0.394	0.016	0.002	0.017		7.711
IEBS 3 Steel Area 3 saponite	3.529	0.003	1.719	0.005	1.749	0.011	0.010	0.256	0.071	0.499	0.006	0.001	0.000		7.859
IEBS 3 Steel Area 3 saponite	3.541	0.003	1.725	0.006	1.727	0.012	0.010	0.262	0.066	0.470	0.007	0.002	0.025		7.830
IEBS 3 Steel Area 2 saponite	3.478	0.003	1.772	0.010	1.789	0.014	0.012	0.220	0.066	0.506	0.022	0.003	0.020		7.892
IEBS 3 Steel Area 2 saponite	3.505	0.003	1.790	0.007	1.719	0.013	0.011	0.219	0.061	0.507	0.026	0.001	0.012		7.861
AVERAGE	**3.562**	**0.004**	**1.713**	**0.008**	**1.727**	**0.012**	**0.011**	**0.222**	**0.078**	**0.456**	**0.017**	**0.003**	**0.014**		**7.809**
Std. Dev.	**0.168**	**0.003**	**0.082**	**0.008**	**0.339**	**0.002**	**0.003**	**0.032**	**0.021**	**0.045**	**0.008**	**0.003**	**0.011**		**0.174**
Outer Clay	**SiO_2**	**TiO_2**	**Al_2O_3**	**Cr_2O_3**	**FeO**	**NiO**	**MnO**	**MgO**	**CaO**	**Na_2O**	**K_2O**	**Cl**	**F**	**O=F&Cl**	**TOTAL**
IEBS 3 Steel Area 3 saponite	58.15	0.10	23.81	0.03	3.96	0.04	0.02	1.69	0.47	1.08	0.12	0.01	0.10	-0.05	89.46
IEBS 3 Steel Area 3 saponite	57.57	0.13	24.98	0.03	3.85	0.07	0.02	1.54	0.47	1.14	0.16	0.01	0.12	-0.05	89.98
AVERAGE	**57.860**	**0.115**	**24.394**	**0.029**	**3.903**	**0.053**	**0.022**	**1.612**	**0.466**	**1.109**	**0.138**	**0.011**	**0.110**	**-0.049**	**89.720**
Std. Dev.	**0.288**	**0.019**	**0.585**	**0.000**	**0.054**	**0.015**	**0.001**	**0.077**	**0.001**	**0.027**	**0.020**	**0.002**	**0.006**	**0.003**	**0.256**

12 oxygen atoms per formula unit (sum excludes F & Cl)															
	Si	**Ti**	**Al**	**Cr**	**Fe**	**Ni**	**Mn**	**Mg**	**Ca**	**Na**	**K**	**Cl**	**F**		**Sum**
IEBS 3 Steel Area 3 saponite	4.202	0.005	2.028	0.002	0.239	0.002	0.001	0.182	0.036	0.152	0.011	0.001	0.024		6.860
IEBS 3 Steel Area 3 saponite	4.141	0.007	2.118	0.002	0.232	0.004	0.001	0.165	0.036	0.159	0.014	0.002	0.026		6.879
AVERAGE	**4.171**	**0.006**	**2.073**	**0.002**	**0.235**	**0.003**	**0.001**	**0.173**	**0.036**	**0.155**	**0.013**	**0.001**	**0.025**		**6.869**
Std. Dev.	**0.030**	**0.001**	**0.045**	**0.000**	**0.004**	**0.001**	**0.000**	**0.009**	**0.000**	**0.003**	**0.002**	**0.000**	**0.001**		**0.009**

IEBS-4

Clay	**SiO_2**	**TiO_2**	**Al_2O_3**	**Cr_2O_3**	**FeO**	**NiO**	**MnO**	**MgO**	**CaO**	**Na_2O**	**K_2O**	**Cl**	**F**	**O=F&Cl**	**TOTAL**
IEBS 4 Area 1 clay	61.70	0.11	23.88	0.00	5.04	0.00	0.01	1.79	0.50	1.50	0.20	0.00	0.23	-0.10	94.73
IEBS 4 Area 1 clay	63.39	0.10	24.10	0.00	5.46	0.00	0.02	1.70	0.49	1.65	0.26	0.00	0.12	-0.05	97.18
IEBS 4 Area 1 clay	61.85	0.12	24.64	0.00	4.16	0.00	0.02	1.82	0.55	1.34	0.18	0.00	0.02	-0.01	94.70
AVERAGE	**62.317**	**0.110**	**24.203**	**0.000**	**4.888**	**0.000**	**0.016**	**1.769**	**0.514**	**1.497**	**0.211**	**0.003**	**0.123**	**-0.053**	**95.54**
Std. Dev.	**25.719**	**0.047**	**10.227**	**0.000**	**2.162**	**0.003**	**0.007**	**0.762**	**0.069**	**0.300**	**0.094**	**0.001**	**0.083**	**0.042**	**1.01**

	12 oxygen atoms per formula unit (sum excludes F & Cl)														
	Si	**Ti**	**Al**	**Cr**	**Fe**	**Ni**	**Mn**	**Mg**	**Ca**	**Na**	**K**	**Cl**	**F**		**Sum**
IEBS 4 Area 1 clay	4.236	0.006	1.932	0.000	0.290	0.000	0.000	0.183	0.037	0.199	0.017	0.000	0.050		6.900
IEBS 4 Area 1 clay	4.251	0.005	1.904	0.000	0.306	0.000	0.001	0.170	0.035	0.215	0.022	0.000	0.025		6.910
IEBS 4 Area 1 clay	4.225	0.006	1.984	0.000	0.238	0.000	0.001	0.185	0.041	0.178	0.015	0.000	0.005		6.873
AVERAGE	**4.238**	**0.006**	**1.940**	**0.000**	**0.278**	**0.000**	**0.001**	**0.179**	**0.037**	**0.197**	**0.018**	**0.000**	**0.027**		**6.895**
Std. Dev.	**1.823**	**0.002**	**0.820**	**0.000**	**0.122**	**0.000**	**0.000**	**0.077**	**0.005**	**0.038**	**0.008**	**0.000**	**0.018**		**0.014**

K-feldspar	**SiO_2**	**TiO_2**	**Al_2O_3**	**Cr_2O_3**	**FeO**	**NiO**	**MnO**	**MgO**	**CaO**	**Na_2O**	**K_2O**	**Cl**	**F**	**O=F&Cl**	**TOTAL**
IEBS 4 Area 1 feldspar	64.77	0.01	20.13	0.00	0.19	0.00	0.02	0.01	0.18	3.15	10.73	0.00	0.00	0.00	99.19
IEBS 4 Area 1 feldspar	64.77	0.01	20.87	0.00	0.18	0.00	0.00	0.00	0.16	3.26	9.48	0.00	0.11	-0.04	98.78
IEBS 4 Area 1 feldspar	64.62	0.00	20.25	0.00	0.14	0.01	0.01	0.00	0.16	3.01	10.55	0.00	0.01	-0.01	98.75
IEBS 4 Area 1 feldspar	64.88	0.01	20.23	0.00	0.27	0.00	0.01	0.00	0.32	3.29	10.31	0.00	0.03	-0.01	99.34
IEBS 4 Area 1 feldspar	64.79	0.02	19.91	0.00	0.18	0.00	0.00	0.00	0.17	3.01	11.39	0.00	0.00	0.00	99.47
AVERAGE	**64.767**	**0.009**	**20.279**	**0.000**	**0.195**	**0.002**	**0.009**	**0.003**	**0.197**	**3.144**	**10.491**	**0.002**	**0.030**	**-0.013**	**99.106**
Std. Dev.	**0.085**	**0.005**	**0.319**	**0.000**	**0.043**	**0.004**	**0.006**	**0.004**	**0.063**	**0.122**	**0.620**	**0.002**	**0.040**	**0.016**	**0.292**

8 oxygen atoms per formula unit (sum excludes F & Cl)															
	Si	**Ti**	**Al**	**Cr**	**Fe**	**Ni**	**Mn**	**Mg**	**Ca**	**Na**	**K**	**Cl**	**F**		**TOTAL**
IEBS 4 Area 1 feldspar	2.891	0.000	1.147	0.000	0.008	0.000	0.001	0.001	0.009	0.295	0.662	0.000	0.000		5.014
IEBS 4 Area 1 feldspar	2.917	0.000	1.123	0.000	0.008	0.000	0.000	0.000	0.009	0.320	0.611	0.000	0.017		4.987
IEBS 4 Area 1 feldspar	2.922	0.000	1.112	0.000	0.006	0.000	0.000	0.000	0.008	0.286	0.660	0.000	0.002		4.994
IEBS 4 Area 1 feldspar	2.901	0.000	1.136	0.000	0.011	0.000	0.000	0.000	0.016	0.304	0.627	0.000	0.005		4.996
IEBS 4 Area 1 feldspar	2.932	0.001	1.096	0.000	0.007	0.000	0.000	0.000	0.008	0.272	0.678	0.000	0.000		4.995
AVERAGE	**2.912**	**0.000**	**1.123**	**0.000**	**0.008**	**0.000**	**0.000**	**0.000**	**0.010**	**0.295**	**0.647**	**0.000**	**0.005**		**4.997**
Std. Dev.	**0.015**	**0.000**	**0.018**	**0.000**	**0.002**	**0.000**	**0.000**	**0.000**	**0.003**	**0.016**	**0.025**	**0.000**	**0.006**		**0.009**

Tobermorite	**SiO_2**	**TiO_2**	**Al_2O_3**	**Cr_2O_3**	**FeO**	**NiO**	**MnO**	**MgO**	**CaO**	**Na_2O**	**K_2O**	**Cl**	**F**	**O=F&Cl**	**TOTAL**
IEBS 4 Area 1 tobermorite	9.82	0.02	3.71	0.00	0.97	0.01	0.13	0.24	45.84	0.44	0.02	0.01	0.50	-0.21	61.22

IEBS 4 Area 1 tobermorite	9.80	0.02	3.85	0.00	0.92	0.00	0.10	0.31	45.07	0.52	0.02	0.01	0.76	-0.32	60.64
IEBS 4 Area 1 tobermorite	10.88	0.01	4.11	0.01	1.15	0.00	0.13	0.27	45.32	0.45	0.02	0.01	0.65	-0.28	62.35
IEBS 4 Area 2 tobermorite	9.71	0.03	3.63	0.00	0.84	0.00	0.24	0.21	47.06	0.38	0.02	0.01	0.50	-0.21	62.13
IEBS 4 Area 2 tobermorite	9.90	0.03	3.91	0.00	0.96	0.00	0.17	0.25	45.61	0.48	0.02	0.01	0.56	-0.24	61.34
IEBS 4 Area 2 tobermorite	14.99	0.02	5.26	0.00	1.77	0.00	0.17	0.22	41.18	0.51	0.02	0.01	0.76	-0.32	64.15
IEBS 4 Area 2 tobermorite	**9.18**	**0.01**	**3.63**	**0.00**	**0.91**	**0.00**	**0.15**	**0.26**	**43.19**	**0.50**	**0.03**	**0.01**	**0.52**	**-0.22**	**57.86**
AVERAGE	**10.611**	**0.020**	**4.014**	**0.002**	**1.073**	**0.002**	**0.156**	**0.252**	**44.754**	**0.468**	**0.022**	**0.010**	**0.607**	**-0.258**	**61.385**
Std. Dev.															
18 oxygen atoms per formula unit (sum excludes F & Cl)															
	Si	**Ti**	**Al**	**Cr**	**Fe**	**Ni**	**Mn**	**Mg**	**Ca**	**Na**	**K**	**Cl**	**F**		**TOTAL**
IEBS 4 Area 1 tobermorite	2.294	0.003	1.021	0.000	0.189	0.003	0.025	0.083	11.472	0.200	0.005	0.006	0.370		15.295
IEBS 4 Area 1 tobermorite	2.304	0.004	1.067	0.000	0.180	0.000	0.020	0.110	11.350	0.239	0.006	0.006	0.565		15.281
IEBS 4 Area 1 tobermorite	2.461	0.002	1.097	0.001	0.218	0.000	0.025	0.091	10.991	0.196	0.005	0.003	0.465		15.088
IEBS 4 Area 2 tobermorite	2.244	0.005	0.989	0.000	0.162	0.000	0.046	0.073	11.650	0.168	0.007	0.002	0.369		15.345
IEBS 4 Area 2 tobermorite	2.301	0.006	1.070	0.000	0.186	0.000	0.033	0.087	11.362	0.218	0.007	0.003	0.413		15.270
IEBS 4 Area 2 tobermorite	3.141	0.003	1.298	0.001	0.311	0.000	0.030	0.069	9.248	0.208	0.005	0.003	0.502		14.313
IEBS 4 Area 2 tobermorite	2.268	0.001	1.057	0.000	0.187	0.000	0.032	0.095	11.437	0.238	0.009	0.005	0.403		15.325
AVERAGE	**2.431**	**0.003**	**1.086**	**0.000**	**0.205**	**0.000**	**0.030**	**0.087**	**11.073**	**0.209**	**0.006**	**0.004**	**0.441**		**15.131**
Std. Dev.	**0.297**	**0.001**	**0.093**	**0.000**	**0.046**	**0.001**	**0.008**	**0.013**	**0.767**	**0.023**	**0.001**	**0.001**	**0.068**		**0.343**
Clinoptilolite	**SiO_2**	**TiO_2**	**Al_2O_3**	**Cr_2O_3**	**FeO**	**NiO**	**MnO**	**MgO**	**CaO**	**Na_2O**	**K_2O**	**Cl**	**F**	**O=F&Cl**	**TOTAL**
IEBS 4 Area 2 zeolite-glass	73.98	0.00	12.92	0.00	0.18	0.01	0.02	0.11	2.49	2.17	0.04	0.00	0.00	0.00	91.95
IEBS 4 Area 2 zeolite-glass	70.12	0.00	12.39	0.00	0.22	0.01	0.01	0.15	2.54	2.11	0.07	0.00	0.00	0.00	87.63
IEBS 4 Area 2 zeolite-glass	71.17	0.01	14.06	0.00	0.21	0.00	0.01	0.17	2.55	2.29	0.10	0.00	0.00	0.00	90.57
IEBS 4 Area 2 zeolite-glass	75.17	0.00	13.99	0.00	0.17	0.00	0.03	0.09	2.15	2.02	0.06	0.00	0.06	-0.03	93.68
AVERAGE	**72.610**	**0.004**	**13.339**	**0.000**	**0.197**	**0.005**	**0.018**	**0.130**	**2.430**	**2.148**	**0.067**	**0.003**	**0.016**	**-0.007**	**90.956**
Std. Dev.	**2.044**	**0.004**	**0.711**	**0.000**	**0.021**	**0.005**	**0.007**	**0.031**	**0.164**	**0.098**	**0.022**	**0.002**	**0.027**	**0.012**	**2.216**
12 oxygen atoms per formula unit (sum excludes F & Cl)															
	Si	**Ti**	**Al**	**Cr**	**Fe**	**Ni**	**Mn**	**Mg**	**Ca**	**Na**	**K**	**Cl**	**F**		**TOTAL**
IEBS 4 Area 2 zeolite-glass	5.046	0.000	1.039	0.000	0.010	0.000	0.001	0.011	0.182	0.286	0.003	0.000	0.000		6.580
IEBS 4 Area 2 zeolite-glass	5.027	0.000	1.047	0.000	0.013	0.001	0.001	0.017	0.195	0.293	0.006	0.000	0.000		6.599
IEBS 4 Area 2 zeolite-glass	4.947	0.001	1.151	0.000	0.012	0.000	0.001	0.017	0.190	0.309	0.009	0.000	0.000		6.636
AVERAGE	**5.020**	**0.000**	**1.101**	**0.000**	**0.010**	**0.000**	**0.002**	**0.009**	**0.154**	**0.262**	**0.005**	**0.000**	**0.013**		**6.562**
Std. Dev.	**5.010**	**0.000**	**1.084**	**0.000**	**0.011**	**0.000**	**0.001**	**0.013**	**0.180**	**0.288**	**0.006**	**0.000**	**0.003**		**6.594**

IEBS-4 Steel															
Inner Saponite	**SiO_2**	**TiO_2**	**Al_2O_3**	**Cr_2O_3**	**FeO**	**NiO**	**MnO**	**MgO**	**CaO**	**Na_2O**	**K_2O**	**Cl**	**F**	**O=F&Cl**	**TOTAL**
IEBS 4 Steel Saponite A1	29.31	0.01	15.70	0.00	39.38	0.03	0.19	0.76	0.69	0.66	0.02	0.02	0.06	-0.03	86.77
IEBS 4 Steel Saponite A1	30.19	0.03	17.15	0.00	38.23	0.01	0.19	0.85	0.61	0.45	0.01	0.03	0.00	-0.01	87.73
AVERAGE	**29.746**	**0.020**	**16.423**	**0.000**	**38.802**	**0.022**	**0.190**	**0.804**	**0.649**	**0.556**	**0.013**	**0.026**	**0.032**	**-0.019**	**87.25**
Std. Dev.	**0.440**	**0.009**	**0.727**	**0.000**	**0.575**	**0.012**	**0.002**	**0.043**	**0.040**	**0.103**	**0.005**	**0.001**	**0.032**	**0.013**	**0.483**
	12 oxygen atoms per formula unit (sum excludes F Cl)														
	Si	**Ti**	**Al**	**Cr**	**Fe**	**Ni**	**Mn**	**Mg**	**Ca**	**Na**	**K**	**Cl**	**F**		**Sum**
IEBS 4 Steel Saponite A1	2.882	0.001	1.819	0.000	3.239	0.003	0.016	0.112	0.073	0.126	0.002	0.004	0.020		8.272
IEBS 4 Steel Saponite A1	2.893	0.002	1.937	0.000	3.063	0.001	0.015	0.121	0.063	0.084	0.001	0.004	0.000		8.180
AVERAGE	**2.887**	**0.001**	**1.878**	**0.000**	**3.151**	**0.002**	**0.016**	**0.116**	**0.068**	**0.105**	**0.002**	**0.004**	**0.010**		**8.226**
Std. Dev.	**0.005**	**0.001**	**0.059**	**0.000**	**0.088**	**0.001**	**0.000**	**0.005**	**0.005**	**0.021**	**0.001**	**0.000**	**0.010**		**0.046**
Outer Saponite	**SiO_2**	**TiO_2**	**Al_2O_3**	**Cr_2O_3**	**FeO**	**NiO**	**MnO**	**MgO**	**CaO**	**Na_2O**	**K_2O**	**Cl**	**F**	**O=F&Cl**	**TOTAL**
IEBS 4 Steel Saponite A2	32.22	0.01	10.89	0.00	27.08	0.01	0.09	1.35	0.15	1.07	0.08	0.19	0.00	-0.04	73.14
IEBS 4 Steel Saponite A3	35.93	0.02	11.58	0.00	27.16	0.01	0.06	1.69	0.05	2.11	0.12	0.11	0.00	-0.03	78.86
IEBS 4 Steel Saponite A3	41.05	0.02	12.57	0.00	30.91	0.01	0.07	1.81	0.05	3.24	0.22	0.03	0.00	-0.01	89.97
IEBS 4 Steel Saponite A2	39.66	0.02	13.45	0.00	32.48	0.00	0.08	1.71	0.29	2.62	0.18	0.03	0.00	-0.01	90.55
AVERAGE	**37.216**	**0.016**	**12.122**	**0.002**	**29.407**	**0.006**	**0.072**	**1.641**	**0.135**	**2.261**	**0.149**	**0.092**	**0.000**	**-0.021**	**83.130**
Std. Dev.	**3.439**	**0.005**	**0.971**	**0.002**	**2.351**	**0.003**	**0.009**	**0.173**	**0.099**	**0.794**	**0.056**	**0.066**	**0.000**	**0.015**	**7.416**
12 oxygen atoms per formula unit (sum excludes F Cl)															
	Si	**Ti**	**Al**	**Cr**	**Fe**	**Ni**	**Mn**	**Mg**	**Ca**	**Na**	**K**	**Cl**	**F**		**TOTAL**
IEBS 4 Steel Saponite A2	3.524	0.001	1.405	0.000	2.477	0.001	0.008	0.221	0.018	0.227	0.011	0.035	0.000		7.892
IEBS 4 Steel Saponite A3	3.598	0.001	1.366	0.000	2.275	0.001	0.005	0.252	0.005	0.410	0.015	0.019	0.000		7.930
IEBS 4 Steel Saponite A3	3.614	0.001	1.304	0.000	2.276	0.000	0.005	0.238	0.004	0.552	0.025	0.005	0.000		8.021
IEBS 4 Steel Saponite A2	3.502	0.001	1.400	0.000	2.399	0.000	0.006	0.225	0.027	0.449	0.020	0.004	0.000		8.032
AVERAGE	**3.560**	**0.001**	**1.369**	**0.000**	**2.357**	**0.001**	**0.006**	**0.234**	**0.014**	**0.410**	**0.018**	**0.016**	**0.000**		**7.969**
Std. Dev.	**0.048**	**0.000**	**0.040**	**0.000**	**0.086**	**0.000**	**0.001**	**0.012**	**0.009**	**0.118**	**0.005**	**0.013**	**0.000**		**0.059**

IEBS-5

Clay	SiO_2	TiO_2	Al_2O_3	Cr_2O_3	FeO	NiO	MnO	MgO	CaO	Na_2O	K_2O	Cl	F	O=F&Cl	TOTAL
IEBS 5 clay A1	65.56	0.13	23.56	0.01	4.98	0.01	0.03	1.82	0.40	1.21	0.18	0.01	0.26	-0.11	97.92
IEBS 5 clay A1	64.12	0.12	24.70	0.01	3.74	0.01	0.01	1.71	0.89	1.76	0.28	0.00	0.22	-0.09	97.35
IEBS 5 clay A1	67.18	0.12	25.24	0.01	4.30	0.00	0.01	1.71	0.47	1.19	0.24	0.01	0.15	-0.06	100.49
IEBS 5 clay A2	64.67	0.11	24.93	0.01	3.79	0.03	0.03	1.65	0.50	1.41	0.28	0.01	0.34	-0.14	97.42
IEBS 5 clay A2	65.08	0.13	25.51	0.01	3.90	0.00	0.00	1.50	0.60	1.23	0.20	0.01	0.08	-0.04	98.20
IEBS 5 clay A2	64.84	0.11	24.87	0.00	3.68	0.00	0.01	1.67	0.63	1.38	0.20	0.01	0.00	0.00	97.41
AVERAGE	**65.242**	**0.121**	**24.800**	**0.007**	**4.065**	**0.008**	**0.016**	**1.676**	**0.582**	**1.364**	**0.232**	**0.007**	**0.175**	**-0.075**	**98.132**
Std. Dev.	**0.969**	**0.009**	**0.614**	**0.003**	**0.456**	**0.011**	**0.011**	**0.094**	**0.159**	**0.198**	**0.038**	**0.002**	**0.112**	**0.047**	**1.099**

	12 oxygen atoms per formula unit (sum excludes F Cl)														
	Si	**Ti**	**Al**	**Cr**	**Fe**	**Ni**	**Mn**	**Mg**	**Ca**	**Na**	**K**	**Cl**	**F**		**Sum**
IEBS 5 clay A1	4.332	0.006	1.835	0.000	0.275	0.001	0.002	0.179	0.029	0.155	0.016	0.001	0.055		6.830
IEBS 5 clay A1	4.260	0.006	1.934	0.000	0.208	0.000	0.001	0.169	0.064	0.227	0.024	0.000	0.046		6.892
IEBS 5 clay A1	4.308	0.006	1.907	0.000	0.231	0.000	0.001	0.164	0.032	0.148	0.020	0.001	0.030		6.816
IEBS 5 clay A2	4.279	0.005	1.944	0.000	0.210	0.002	0.002	0.162	0.035	0.181	0.024	0.001	0.070		6.845
IEBS 5 clay A2	4.269	0.007	1.972	0.000	0.214	0.000	0.000	0.147	0.042	0.157	0.017	0.001	0.017		6.826
IEBS 5 clay A2	4.286	0.006	1.937	0.000	0.204	0.000	0.001	0.165	0.045	0.176	0.017	0.001	0.000		6.836
AVERAGE	**4.289**	**0.006**	**1.922**	**0.000**	**0.223**	**0.000**	**0.001**	**0.164**	**0.041**	**0.174**	**0.019**	**0.001**	**0.036**		**6.841**
Std. Dev.	**0.024**	**0.000**	**0.043**	**0.000**	**0.025**	**0.001**	**0.001**	**0.010**	**0.012**	**0.027**	**0.003**	**0.000**	**0.024**		**0.025**

Tobermorite	SiO_2	TiO_2	Al_2O_3	Cr_2O_3	FeO	NiO	MnO	MgO	CaO	Na_2O	K_2O	Cl	F	O=F&Cl	TOTAL
IEBS 5 tobermorite A1	7.10	0.01	2.55	0.00	0.75	0.00	0.04	0.16	47.15	0.30	0.01	0.01	0.20	-0.09	58.08
IEBS 5 tobermorite A1	5.46	0.00	2.19	0.00	0.50	0.02	0.02	0.14	47.83	0.28	0.01	0.00	0.36	-0.15	56.46
IEBS 5 tobermorite A2	7.69	0.01	2.09	0.00	0.58	0.03	0.00	0.12	48.19	0.35	0.02	0.01	0.38	-0.16	59.07
IEBS5 tob A2+clay?	45.45	0.08	18.74	0.00	2.86	0.00	0.00	1.73	14.53	1.01	0.19	0.01	0.17	-0.07	84.62
IEBS 5 tobermorite A2	7.33	0.01	2.21	0.00	0.51	0.00	0.03	0.19	48.35	0.33	0.01	0.01	0.44	-0.19	58.99
AVERAGE	**14.606**	**0.022**	**5.555**	**0.001**	**1.040**	**0.009**	**0.019**	**0.467**	**41.211**	**0.454**	**0.046**	**0.009**	**0.311**	**-0.133**	**63.444**
Std. Dev.	**15.439**	**0.029**	**6.594**	**0.001**	**0.913**	**0.010**	**0.017**	**0.633**	**13.345**	**0.278**	**0.072**	**0.003**	**0.105**	**0.044**	**10.632**

12 oxygen atoms per formula unit (sum excludes F & Cl)															
	Si	**Ti**	**Al**	**Cr**	**Fe**	**Ni**	**Mn**	**Mg**	**Ca**	**Na**	**K**	**Cl**	**F**		**Sum**
IEBS 5 tobermorite A1	1.210	0.001	0.512	0.000	0.107	0.000	0.006	0.040	8.606	0.099	0.001	0.002	0.110		10.583
IEBS 5 tobermorite A1	0.978	0.000	0.463	0.001	0.075	0.002	0.003	0.038	9.180	0.096	0.001	0.001	0.201		10.838
IEBS 5 tobermorite A2	1.286	0.001	0.411	0.000	0.081	0.003	0.000	0.029	8.636	0.114	0.004	0.003	0.203		10.566
IEBS5 tob A2+clay?	3.741	0.005	1.818	0.000	0.197	0.000	0.000	0.213	1.282	0.161	0.020	0.002	0.044		7.436
IEBS 5 tobermorite A2	1.231	0.002	0.437	0.000	0.072	0.000	0.004	0.047	8.701	0.108	0.002	0.003	0.233		10.604

AVERAGE	**1.689**	**0.002**	**0.728**	**0.000**	**0.106**	**0.001**	**0.003**	**0.073**	**7.281**	**0.116**	**0.006**	**0.002**	**0.158**		**10.006**
Std. Dev.	**1.031**	**0.002**	**0.546**	**0.000**	**0.047**	**0.001**	**0.002**	**0.070**	**3.007**	**0.023**	**0.007**	**0.001**	**0.070**		**1.288**
Tobermorite	**SiO_2**	**TiO_2**	**Al_2O_3**	**Cr_2O_3**	**FeO**	**NiO**	**MnO**	**MgO**	**CaO**	**Na_2O**	**K_2O**	**Cl**	**F**	**O=F&Cl**	**TOTAL**
IEBS 5 glass-zeolite A2	70.17	0.01	12.97	0.00	0.14	0.00	0.01	0.12	2.12	2.64	0.02	0.00	0.00	0.00	88.21
IEBS 5 glass-zeolite A1	70.34	0.00	13.42	0.00	0.18	0.00	0.02	0.12	2.35	2.09	0.01	0.00	0.00	0.00	88.54
IEBS 5 glass-zeolite A1	73.30	0.00	13.26	0.00	0.19	0.02	0.02	0.11	2.13	2.06	0.01	0.00	0.06	-0.02	91.11
IEBS 5 glass-zeolite A2	73.38	0.00	13.89	0.00	0.20	0.01	0.01	0.12	2.18	2.10	0.06	0.00	0.11	-0.04	91.95
IEBS 5 glass-zeolite A2	76.50	0.00	12.89	0.00	0.16	0.00	0.00	0.10	2.34	2.14	0.03	0.00	0.01	-0.01	94.17
AVERAGE	**72.738**	**0.001**	**13.288**	**0.000**	**0.174**	**0.006**	**0.013**	**0.113**	**2.224**	**2.206**	**0.028**	**0.000**	**0.035**	**-0.015**	**90.794**
Std. Dev.	**2.336**	**0.002**	**0.358**	**0.000**	**0.021**	**0.008**	**0.008**	**0.009**	**0.099**	**0.219**	**0.017**	**0.000**	**0.041**	**0.017**	**2.218**
12 oxygen atoms per formula unit (sum excludes F & Cl)															
	Si	**Ti**	**Al**	**Cr**	**Fe**	**Ni**	**Mn**	**Mg**	**Ca**	**Na**	**K**	**Cl**	**F**		**Sum**
IEBS 5 glass-zeolite A2	4.999	0.000	1.089	0.000	0.008	0.000	0.001	0.013	0.162	0.365	0.002	0.000	0.000		6.640
IEBS 5 glass-zeolite A1	4.985	0.000	1.121	0.000	0.011	0.000	0.001	0.013	0.178	0.287	0.001	0.000	0.000		6.598
IEBS 5 glass-zeolite A1	5.035	0.000	1.073	0.000	0.011	0.001	0.001	0.011	0.157	0.275	0.001	0.000	0.012		6.566
IEBS 5 glass-zeolite A2	5.001	0.000	1.116	0.000	0.011	0.001	0.001	0.012	0.159	0.277	0.005	0.000	0.023		6.583
IEBS 5 glass-zeolite A2	5.081	0.000	1.009	0.000	0.009	0.000	0.000	0.010	0.166	0.275	0.003	0.000	0.003		6.553
AVERAGE	**5.020**	**0.000**	**1.082**	**0.000**	**0.010**	**0.000**	**0.001**	**0.012**	**0.165**	**0.296**	**0.002**	**0.000**	**0.008**		**6.588**
Std. Dev.	**0.035**	**0.000**	**0.040**	**0.000**	**0.001**	**0.000**	**0.000**	**0.001**	**0.008**	**0.035**	**0.001**	**0.000**	**0.009**		**0.030**
Feldspars with a wide range of compositions	**SiO_2**	**TiO_2**	**Al_2O_3**	**Cr_2O_3**	**FeO**	**NiO**	**MnO**	**MgO**	**CaO**	**Na_2O**	**K_2O**	**Cl**	**F**	**O=F&Cl**	**TOTAL**
IEBS 5 feldspars A1 (K-spar)	63.52	0.00	20.44	0.00	0.17	0.01	0.02	0.00	0.16	3.33	11.72	0.00	0.00	0.00	99.40
IEBS 5 feldspars A1 (K-spar)	63.61	0.01	18.98	0.00	0.13	0.00	0.01	0.00	0.00	0.62	15.78	0.00	0.00	0.00	99.17
IEBS 5 feldspars A2 (K-spar)	64.20	0.02	20.08	0.00	0.17	0.00	0.01	0.00	0.20	3.07	11.12	0.00	0.02	-0.01	98.89
IEBS 5 feldspars A1 (plag)	61.24	0.01	23.99	0.00	0.28	0.00	0.00	0.01	4.94	7.37	1.10	0.00	0.00	0.00	98.95
IEBS 5 feldspars A1 (plag)	67.71	0.00	21.08	0.00	0.14	0.00	0.00	0.00	1.41	9.97	0.07	0.01	0.00	0.00	100.39
IEBS 5 feldspars A2 (plag)	52.66	0.01	30.09	0.01	0.36	0.00	0.00	0.03	10.41	5.03	0.41	0.00	0.00	0.00	99.02
IEBS 5 feldspars A1 (plag)	59.21	0.00	26.62	0.00	0.29	0.01	0.00	0.00	7.43	6.59	0.69	0.00	0.00	0.00	100.84
IEBS 5 feldspars A2 (plag)	58.47	0.01	27.37	0.00	0.28	0.00	0.02	0.01	7.01	6.45	0.83	0.00	0.00	0.00	100.49

12 oxygen atoms per formula unit (sum excludes F & Cl)														
	Si	**Ti**	**Al**	**Cr**	**Fe**	**Ni**	**Mn**	**Mg**	**Ca**	**Na**	**K**	**Cl**	**F**		**Sum**
IEBS 5 feldspars A1 (K-spar)	4.420	0.000	1.594	0.000	0.010	0.001	0.001	0.000	0.012	0.450	1.040	0.000	0.000		7.528
IEBS 5 feldspars A1 (K-spar)	4.449	0.001	1.564	0.000	0.007	0.000	0.000	0.000	0.000	0.084	1.408	0.001	0.000		7.515
IEBS 5 feldspars A2 (K-spar)	4.342	0.001	1.707	0.000	0.010	0.000	0.001	0.000	0.015	0.429	1.024	0.000	0.006		7.530
IEBS 5 feldspars A1 (plag)	4.121	0.001	1.903	0.000	0.016	0.000	0.000	0.001	0.356	0.962	0.095	0.000	0.000		7.455
IEBS 5 feldspars A1 (plag)	4.415	0.000	1.620	0.000	0.008	0.000	0.000	0.000	0.099	1.261	0.006	0.001	0.000		7.408
IEBS 5 feldspars A2 (plag)	3.607	0.001	2.429	0.000	0.021	0.000	0.000	0.003	0.764	0.668	0.036	0.000	0.000		7.529
IEBS 5 feldspars A1 (plag)	3.936	0.000	2.086	0.000	0.016	0.000	0.000	0.000	0.529	0.849	0.058	0.000	0.000		7.475
IEBS 5 feldspars A2 (plag)	3.900	0.001	2.151	0.000	0.016	0.000	0.001	0.001	0.501	0.834	0.070	0.000	0.000		7.476

IEBS-5 Steel														
Inner Saponite	SiO_2	TiO_2	Al_2O_3	Cr_2O_3	FeO	NiO	MnO	MgO	CaO	Na_2O	K_2O	Cl	F	O=F&Cl	TOTAL
IEBS 5 Steel saponite A3	47.47	0.07	19.81	0.14	18.90	0.16	0.12	1.59	0.68	2.32	0.13	0.01	0.01	-0.01	91.40
IEBS 5 Steel saponite A3	39.65	0.02	17.91	0.35	29.42	0.26	0.19	1.88	0.79	1.97	0.09	0.01	0.11	-0.05	92.55
IEBS 5 Steel saponite A3	43.21	0.05	19.27	0.19	25.70	0.18	0.16	1.56	0.61	2.88	0.10	0.01	0.00	0.00	93.93
IEBS 5 Steel saponite A3	40.77	0.03	17.19	0.58	28.97	0.38	0.20	2.00	0.86	3.18	0.06	0.02	0.07	-0.04	94.24
IEBS 5 Steel saponite A3	43.92	0.05	18.40	0.18	25.08	0.17	0.20	1.79	0.64	4.00	0.12	0.02	0.00	0.00	94.57
IEBS 5 Steel saponite A2	44.23	0.05	17.36	0.12	25.98	0.19	0.20	2.46	1.27	2.66	0.11	0.06	0.03	-0.03	94.68
IEBS 5 Steel saponite A3	42.51	0.05	18.16	0.32	28.19	0.29	0.20	1.79	0.83	3.36	0.07	0.01	0.07	-0.03	95.79
IEBS 5 Steel saponite A3	45.56	0.04	20.03	0.24	28.44	0.27	0.21	1.86	0.73	3.30	0.12	0.01	0.08	-0.04	100.81
IEBS 5 Steel saponite A1	50.37	0.09	19.69	0.02	19.04	0.07	0.14	2.06	0.52	2.81	0.13	0.02	0.15	-0.07	94.96
AVERAGE	**44.187**	**0.051**	**18.647**	**0.238**	**25.524**	**0.219**	**0.179**	**1.888**	**0.770**	**2.942**	**0.104**	**0.021**	**0.059**	**-0.030**	**94.771**
Std. Dev.	**3.109**	**0.020**	**1.022**	**0.153**	**3.788**	**0.084**	**0.031**	**0.255**	**0.204**	**0.569**	**0.023**	**0.016**	**0.050**	**0.021**	**2.469**

	12 oxygen atoms per formula unit (sum excludes F Cl)													
	Si	**Ti**	**Al**	**Cr**	**Fe**	**Ni**	**Mn**	**Mg**	**Ca**	**Na**	**K**	**Cl**	**F**		**Sum**
IEBS 5 Steel saponite A3	3.755	0.004	1.847	0.009	1.250	0.010	0.008	0.188	0.057	0.356	0.013	0.002	0.003		7.497
IEBS 5 Steel saponite A3	3.351	0.001	1.784	0.023	2.079	0.018	0.013	0.237	0.072	0.323	0.010	0.002	0.030		7.911
IEBS 5 Steel saponite A3	3.493	0.003	1.837	0.012	1.738	0.012	0.011	0.189	0.053	0.451	0.010	0.001	0.000		7.809
IEBS 5 Steel saponite A3	3.388	0.002	1.684	0.038	2.014	0.025	0.014	0.248	0.076	0.513	0.007	0.003	0.019		8.009
IEBS 5 Steel saponite A3	3.531	0.003	1.744	0.011	1.687	0.011	0.013	0.215	0.055	0.623	0.012	0.003	0.000		7.906
IEBS 5 Steel saponite A2	3.560	0.003	1.647	0.008	1.749	0.012	0.013	0.295	0.109	0.415	0.012	0.009	0.008		7.823
IEBS 5 Steel saponite A3	3.437	0.003	1.730	0.021	1.906	0.019	0.014	0.215	0.072	0.526	0.007	0.002	0.019		7.951
IEBS 5 Steel saponite A3	3.463	0.003	1.794	0.014	1.808	0.016	0.013	0.210	0.059	0.487	0.012	0.002	0.019		7.880
IEBS 5 Steel saponite A1	3.819	0.005	1.760	0.001	1.207	0.004	0.009	0.233	0.042	0.413	0.013	0.002	0.036		7.507
AVERAGE	**3.533**	**0.003**	**1.758**	**0.015**	**1.715**	**0.014**	**0.012**	**0.226**	**0.066**	**0.456**	**0.011**	**0.003**	**0.015**		**7.810**
Std. Dev.	**0.150**	**0.001**	**0.062**	**0.010**	**0.287**	**0.006**	**0.002**	**0.031**	**0.018**	**0.087**	**0.002**	**0.002**	**0.012**		**0.174**

Outer Saponite	SiO_2	TiO_2	Al_2O_3	Cr_2O_3	FeO	NiO	MnO	MgO	CaO	Na_2O	K_2O	Cl	F	O=F&Cl	TOTAL
IEBS 5 Steel saponite A2	54.16	0.10	19.39	0.02	4.40	0.03	0.01	1.56	0.37	0.64	0.13	0.06	0.19	-0.09	80.87
IEBS 5 Steel saponite A3	56.74	0.11	20.53	0.04	4.03	0.04	0.01	1.42	0.40	0.88	0.13	0.06	0.12	-0.07	84.39
IEBS 5 Steel saponite A2	55.27	0.12	22.66	0.03	5.05	0.06	0.01	1.65	0.44	0.95	0.15	0.06	0.05	-0.03	86.45
AVERAGE	**55.393**	**0.112**	**20.859**	**0.029**	**4.491**	**0.045**	**0.008**	**1.541**	**0.401**	**0.822**	**0.136**	**0.063**	**0.118**	**-0.064**	**83.904**
Std. Dev.	**1.056**	**0.008**	**1.354**	**0.010**	**0.424**	**0.010**	**0.001**	**0.096**	**0.027**	**0.135**	**0.011**	**0.001**	**0.057**	**0.024**	**2.306**

	12 oxygen atoms per formula unit (sum excludes F Cl)														
	Si	**Ti**	**Al**	**Cr**	**Fe**	**Ni**	**Mn**	**Mg**	**Ca**	**Na**	**K**	**Cl**	**F**		**TOTAL**
IEBS 5 Steel saponite A2	4.336	0.006	1.829	0.001	0.294	0.002	0.001	0.186	0.032	0.099	0.013	0.009	0.047		6.799

IEBS 5 Steel saponite A3	4.340	0.006	1.851	0.002	0.258	0.003	0.000	0.162	0.033	0.131	0.012	0.008	0.030		6.798
IEBS 5 Steel saponite A2	4.170	0.007	2.015	0.002	0.319	0.004	0.001	0.186	0.035	0.139	0.015	0.008	0.011		6.891
AVERAGE	**4.282**	**0.007**	**1.898**	**0.002**	**0.290**	**0.003**	**0.001**	**0.178**	**0.033**	**0.123**	**0.013**	**0.008**	**0.029**		**6.829**
Std. Dev.	**0.079**	**0.000**	**0.083**	**0.001**	**0.025**	**0.001**	**0.000**	**0.011**	**0.001**	**0.017**	**0.001**	**0.000**	**0.015**		**0.044**

APPENDIX C

SEM Images: IEBS-1 to -6

This page is intentionally left blank.

C-1. IEBS-1

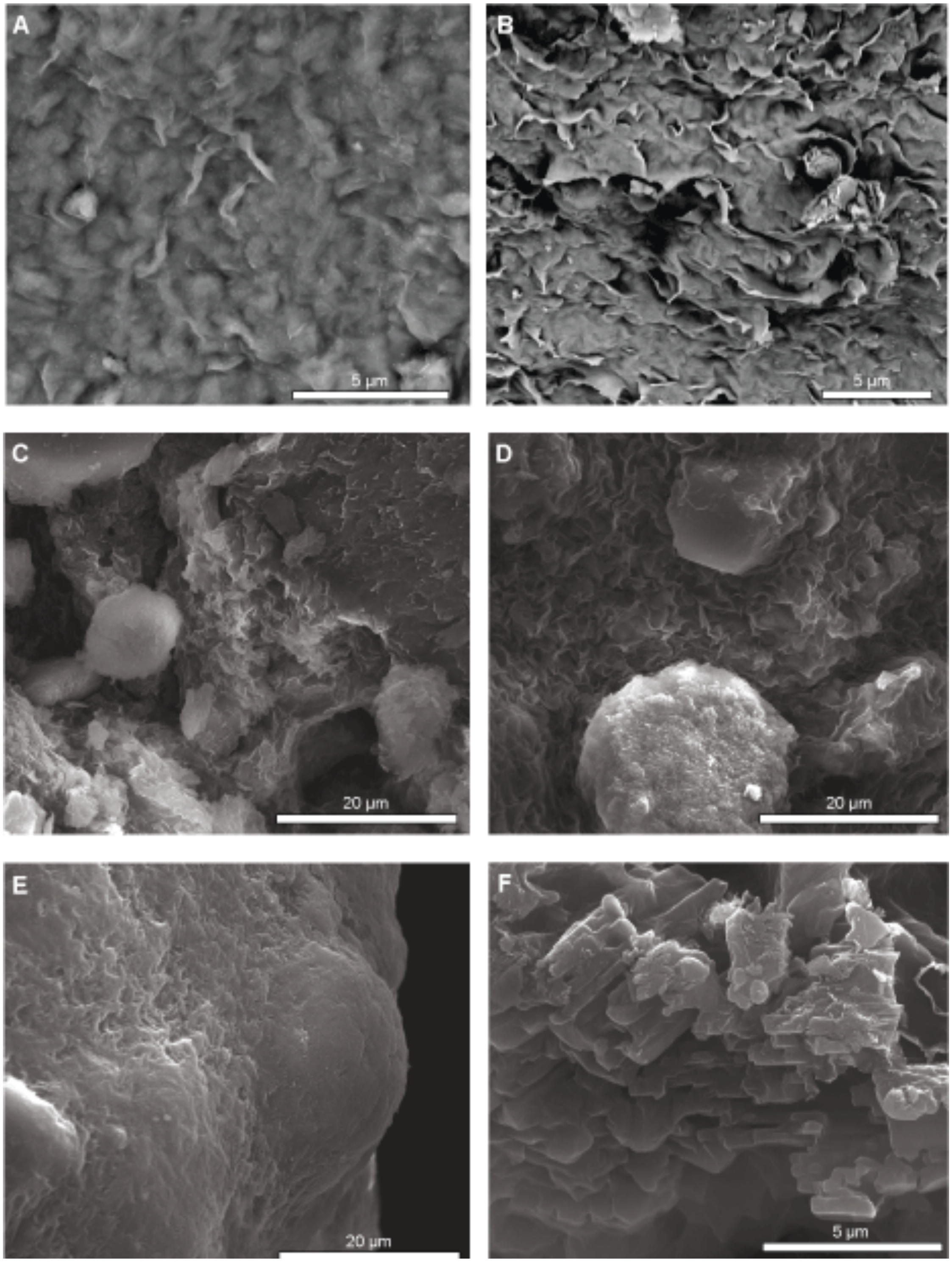

Figure C-1. SE images of the reaction products from IEBS-1. [A, B] Montmorillonite groundmass with a foily texture. [C, D, E] Rounded C(A)SH minerals embedded in the foily montmorillonite groundmass. [F] Albite crystals derived from precursor Grimsel granodiorite material showing dissolution textures.

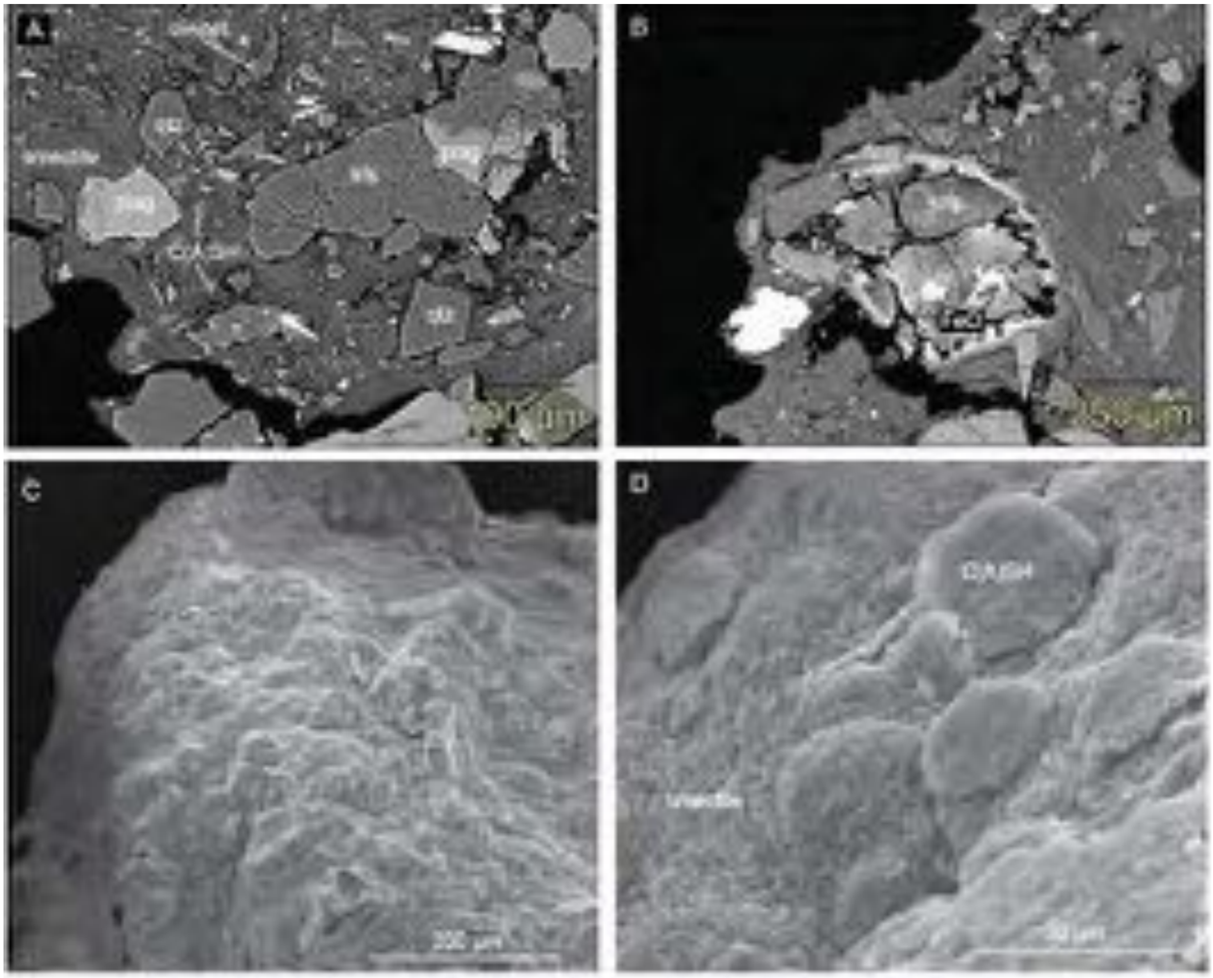

Figure C-2. [A] Backscattered electron image of an IEBS-1 thin section showing feldspar (kfs, K- feldspar; plag, plagioclase feldspar), quartz (qtz), calcium (aluminum) silicate hydrate (C(A)SH) minerals, and clinoptilolite replacing glass shards in a smectite matrix. [B] Stilpnomelane (stilp.) growth around a grain of FeO (buffer material) in the smectite matrix. [C] SE image showing distribution of C(A)SH mineral (rounded crystals) growth in smectite (fine-grain matrix. [D] SE image showing rounded, platey C(A)SH mineral embedded in foily-textured smectite.

C-2. IEBS-2

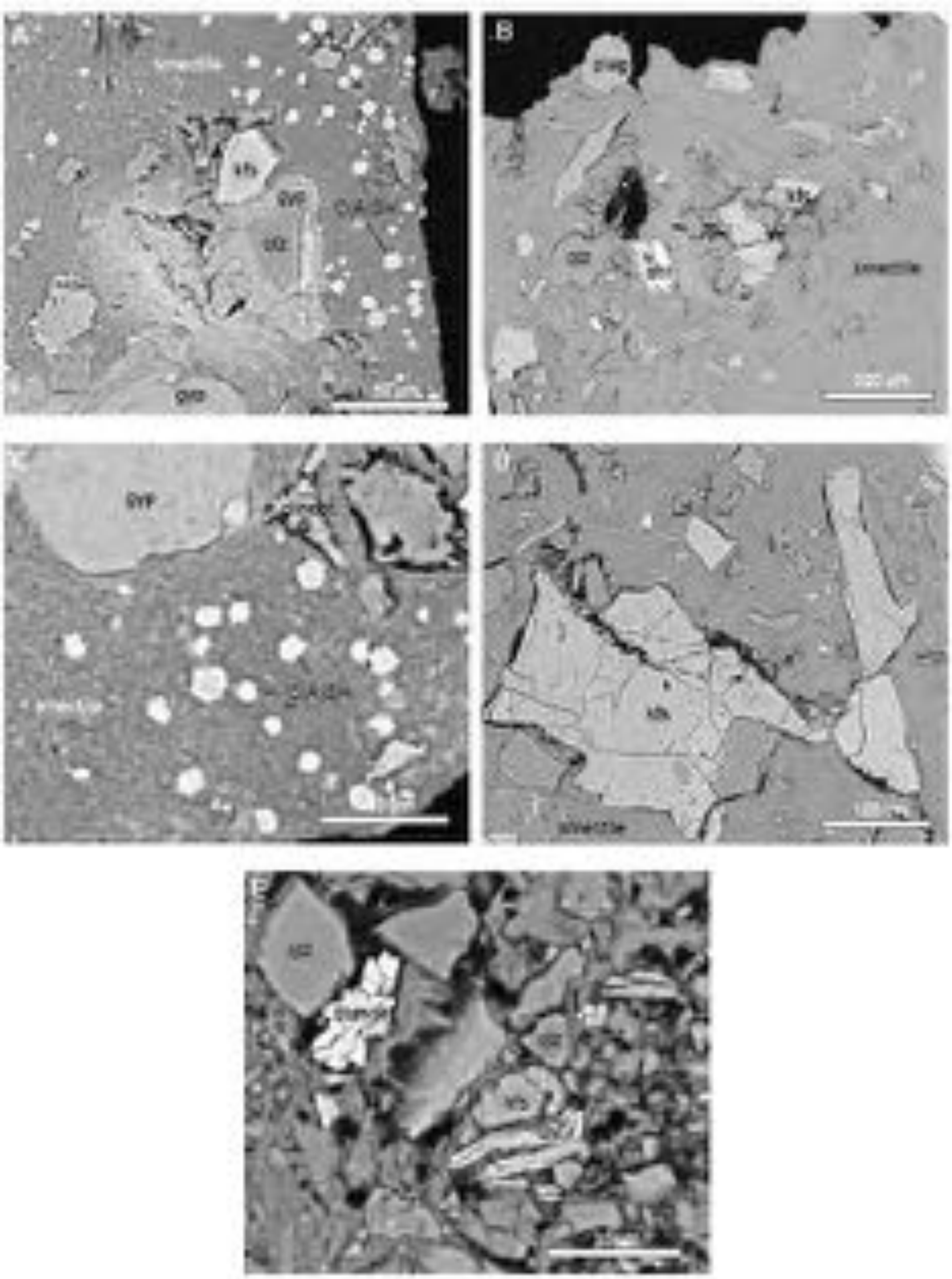

Figure C-3. Backscattered electron images from IEBS-2 (thin section). Labelled minerals were identified with EDS. [A-D] Feldspar, quartz, and gypsum in the fine-grained clay matrix. Note the lack of alteration to the feldspar grains. [A, C] White spherical minerals are C(A)SH minerals. [E] Grimsel granodiorite fragment composed of feldspars, quartz, chlorite, and accessory minerals (e.g., titanite). Note the void spaces between grains which may be related to partial dissolution of feldspar grains. Abbreviations: C(A)SH, calcium (aluminum) silicate hydrate; chl, chlorite; clinopt., clinoptilolite; gyp, gypsum; kfs, K- feldspar; plag, plagioclase; qtz, quartz.

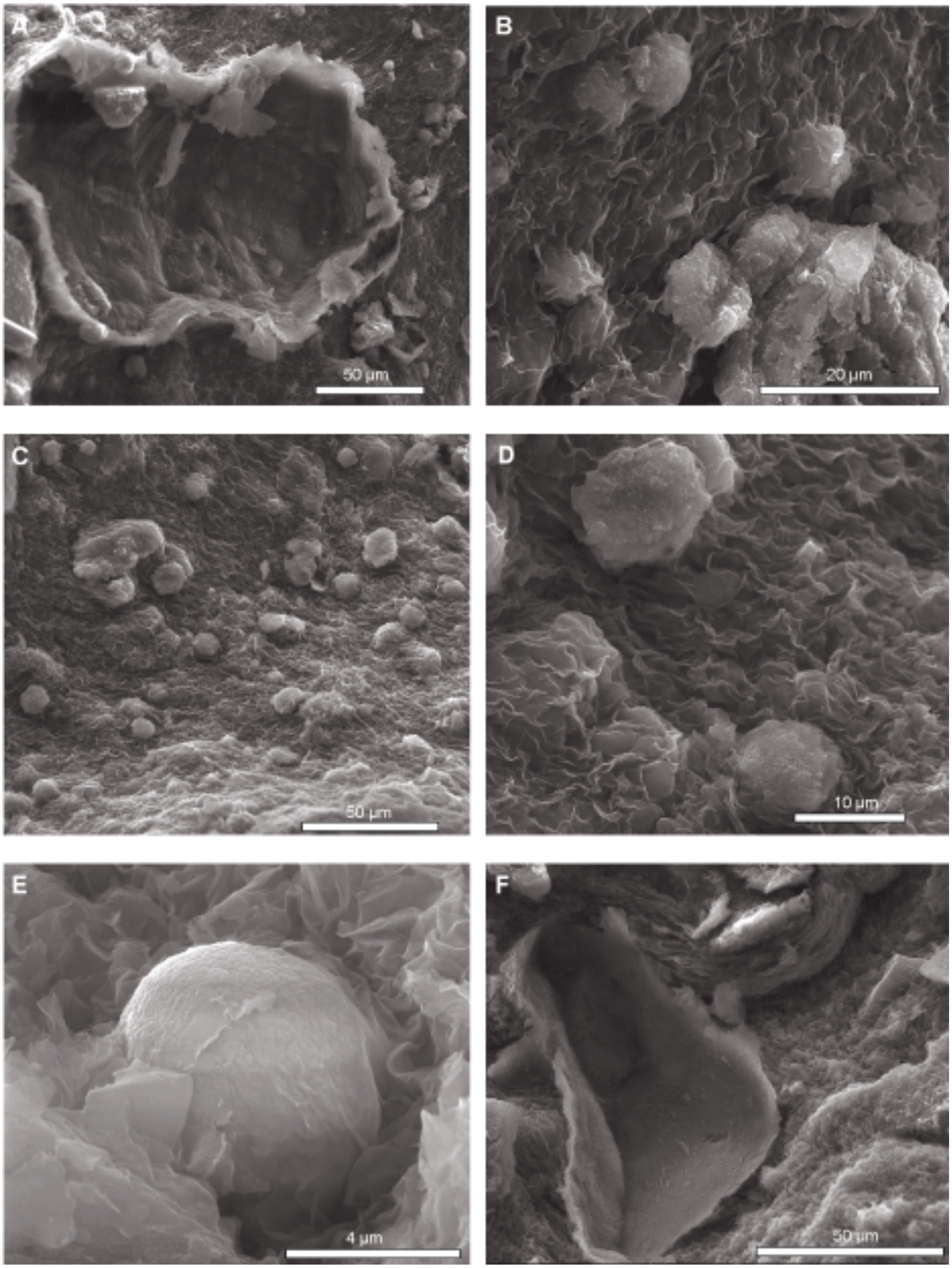

Figure C-4. IEBS-2 SE images. [A] Chlorite fragment from original host granodiorite. [B, C, D, E] C(A)SH crystals embedded in a foily smectite matrix. [F] Chlorite grain derived from the Grimsel granodiorite.

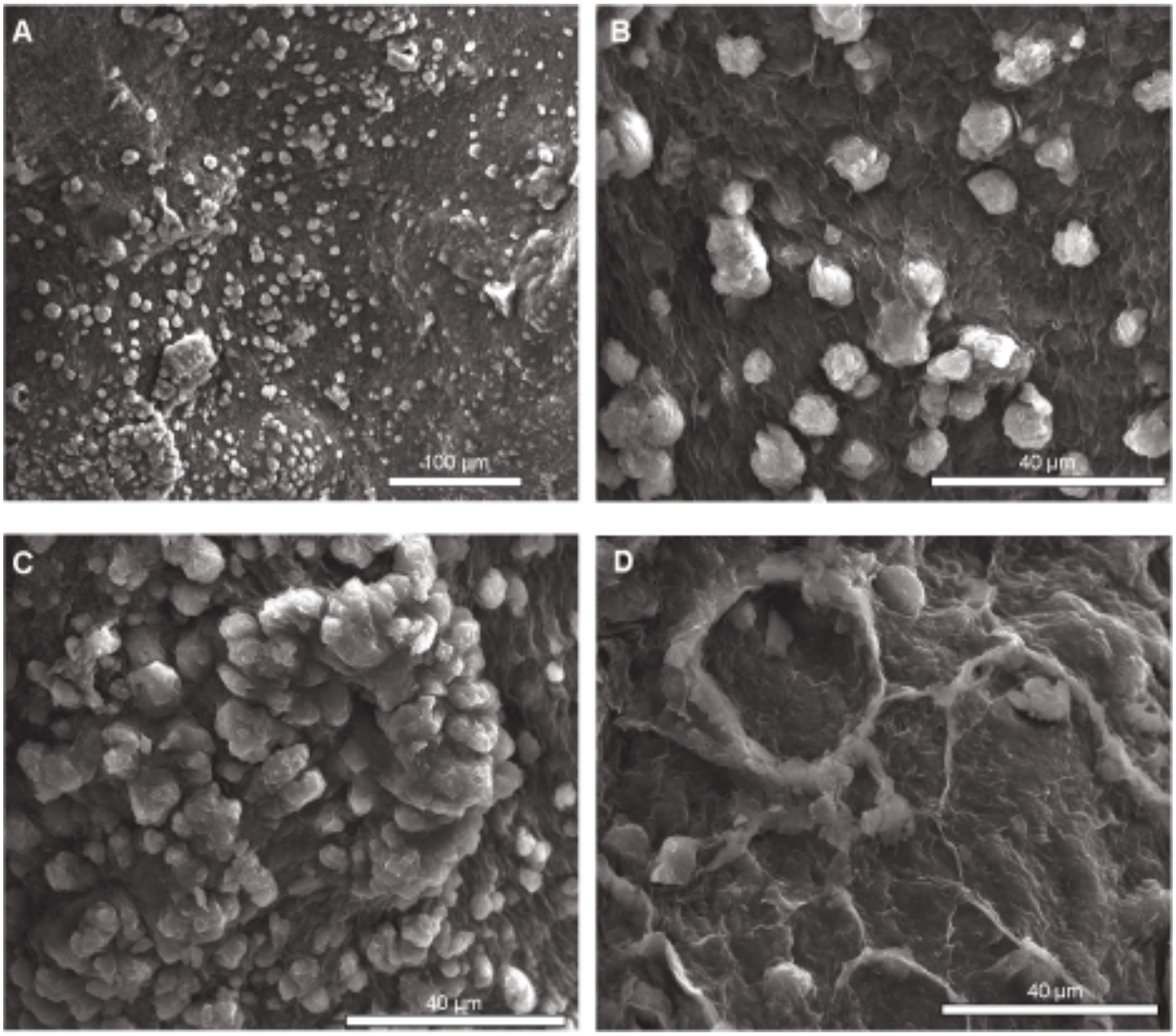

Figure C-5. IEBS-2 SE images. [A, B, C] different contexts of gypsum crystals embedded in smectite matrix. [A, B] Small gypsum crystals (white) in smectite. [C] Cluster of gypsum. [D] Ridged smectite with platey CSH minerals.

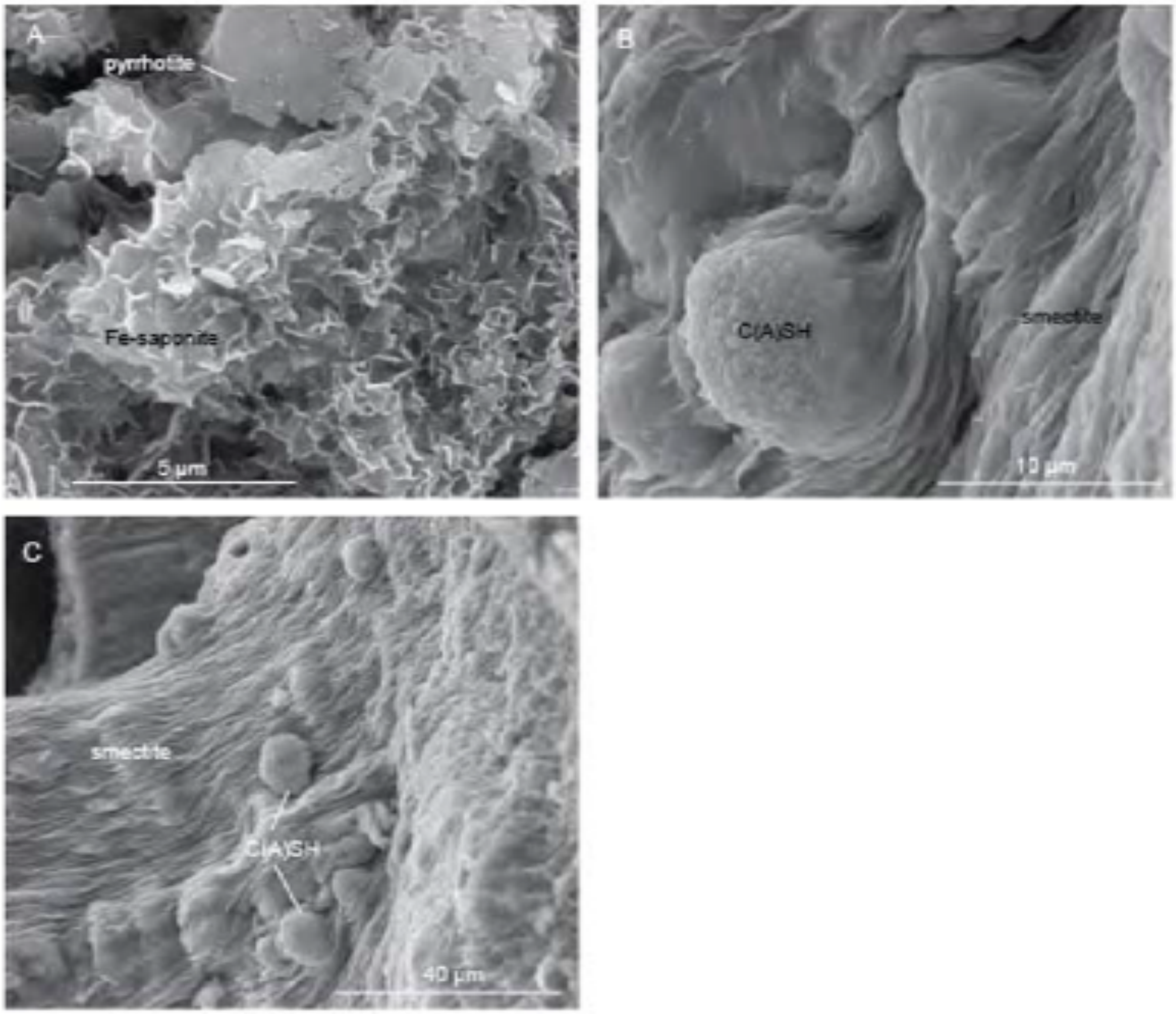

Figure C-6. SE images of IEBS-2 reaction products. [A] Fe-saponite and pyrrhotite that likely formed at the interface of the 316 SS and the Wyoming bentonite. [B, C] C(A)SH minerals embedded in smectite.

C-3. IEBS-3

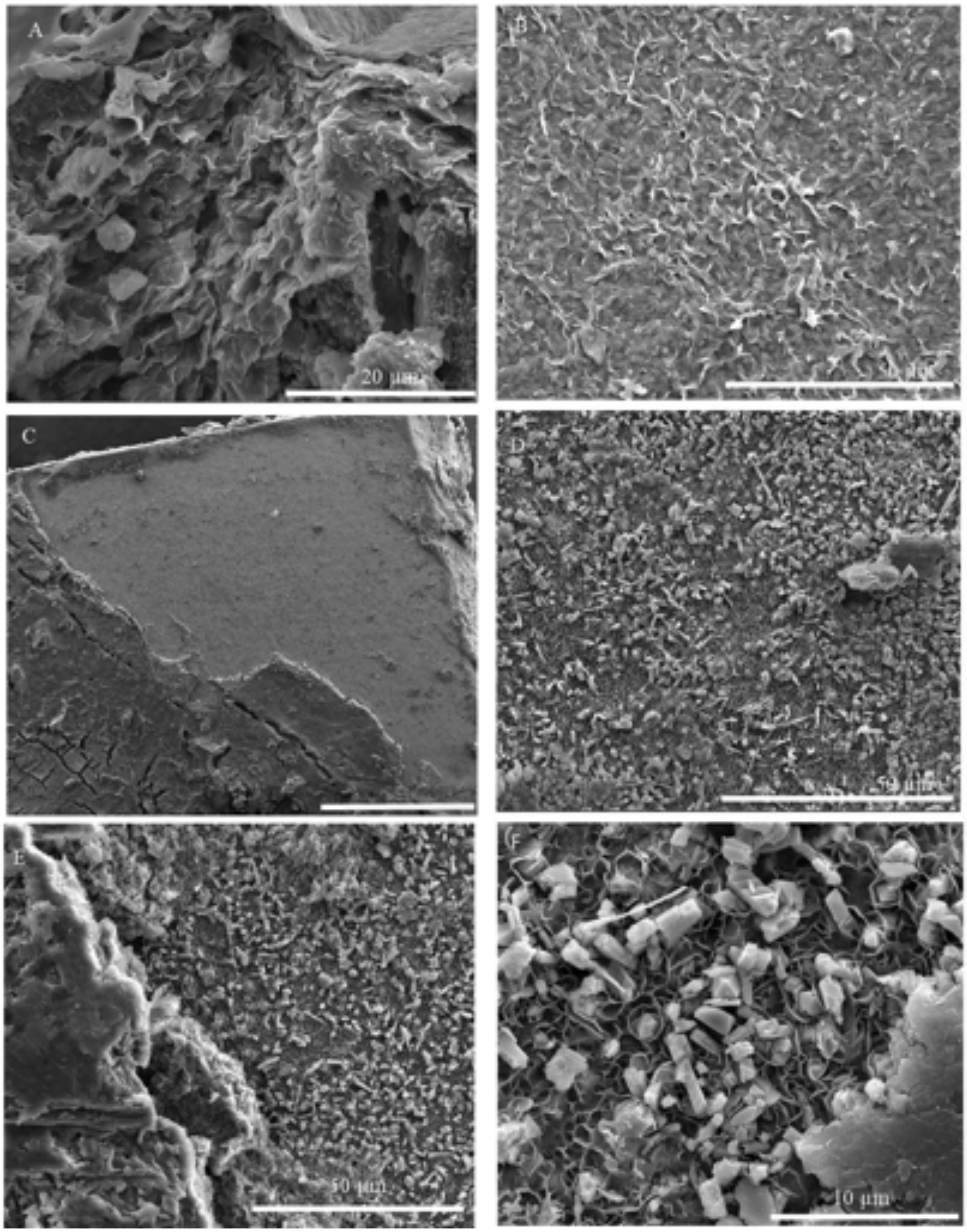

Figure C-7. SE images of IEBS-3 reaction products. [A] Foily-textured smectite with rounded C(A)SH minerals. [B] Smectite. [C] Plan view of the surface of the reacted 304SS coupon showing smectite (dark gray) attached to an underlying layer of Fe-rich reaction products (lighter gray). [D] Fe- Saponite mat with embedded Fe-rich accessory minerals (sulfides and oxides) on the reacted steel surface. [E] Smectite (left side) over Fe-saponite. [F] Fe-saponite (honeycomb texture) with embedded Fe,Ni,Cr- sulfide minerals (light gray crystals) on the reacted steel surface.

C-4. IEBS-4

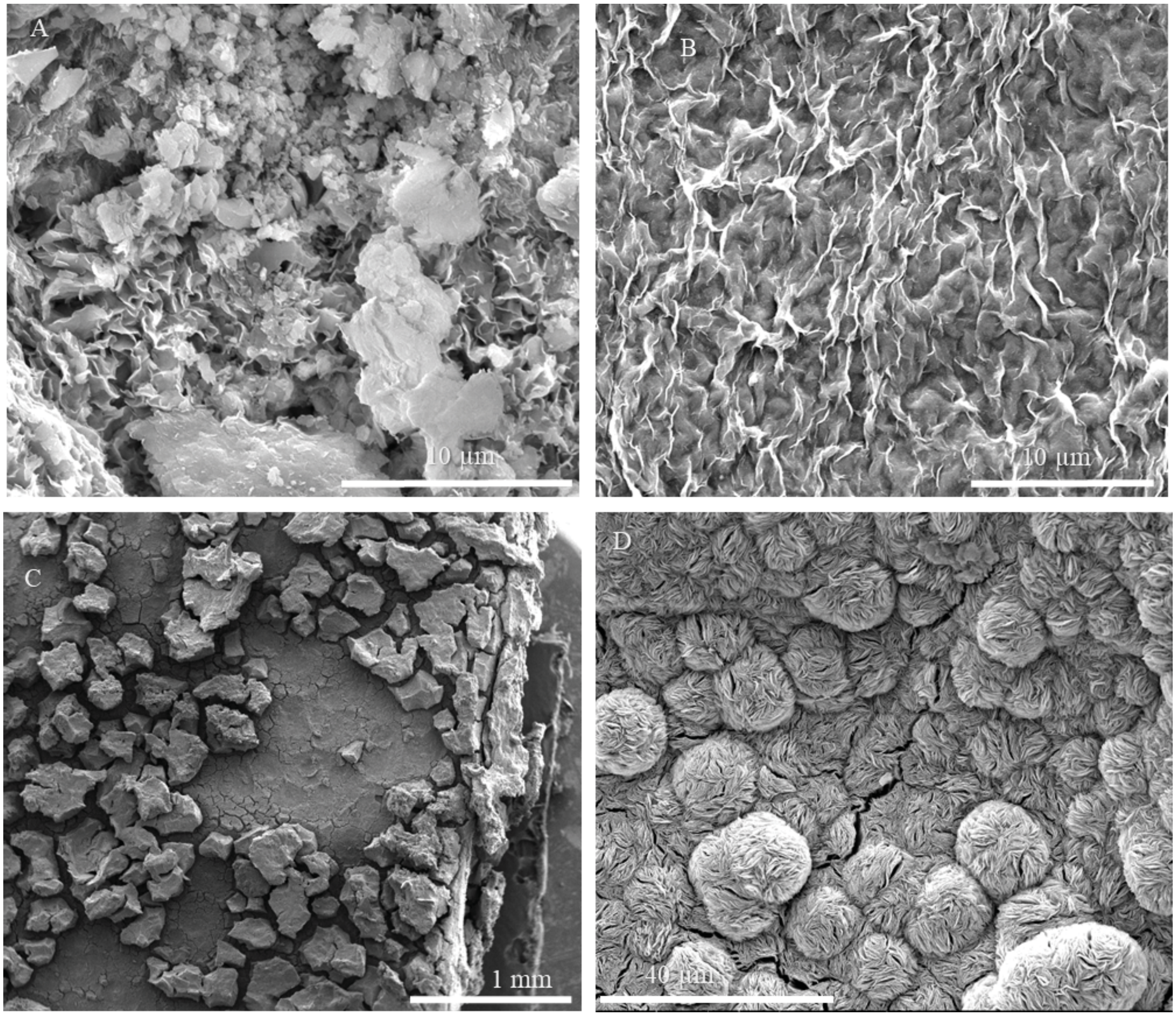

Figure C-8. SE images of IEBS-4 reaction products. [A] Foily-textured Fe-saponite with platey smectite. [B] Texture of dried gel (composed of montmorillonite colloids). [C] Plan view of the edge of a reacted LCS coupon showing smectite attached to underlying Fe-rich clay products. [D] Fe-saponite rosettes formed from the reaction of iron derived from the LCS with the bentonite. Coupon.

C-5. IEBS-5

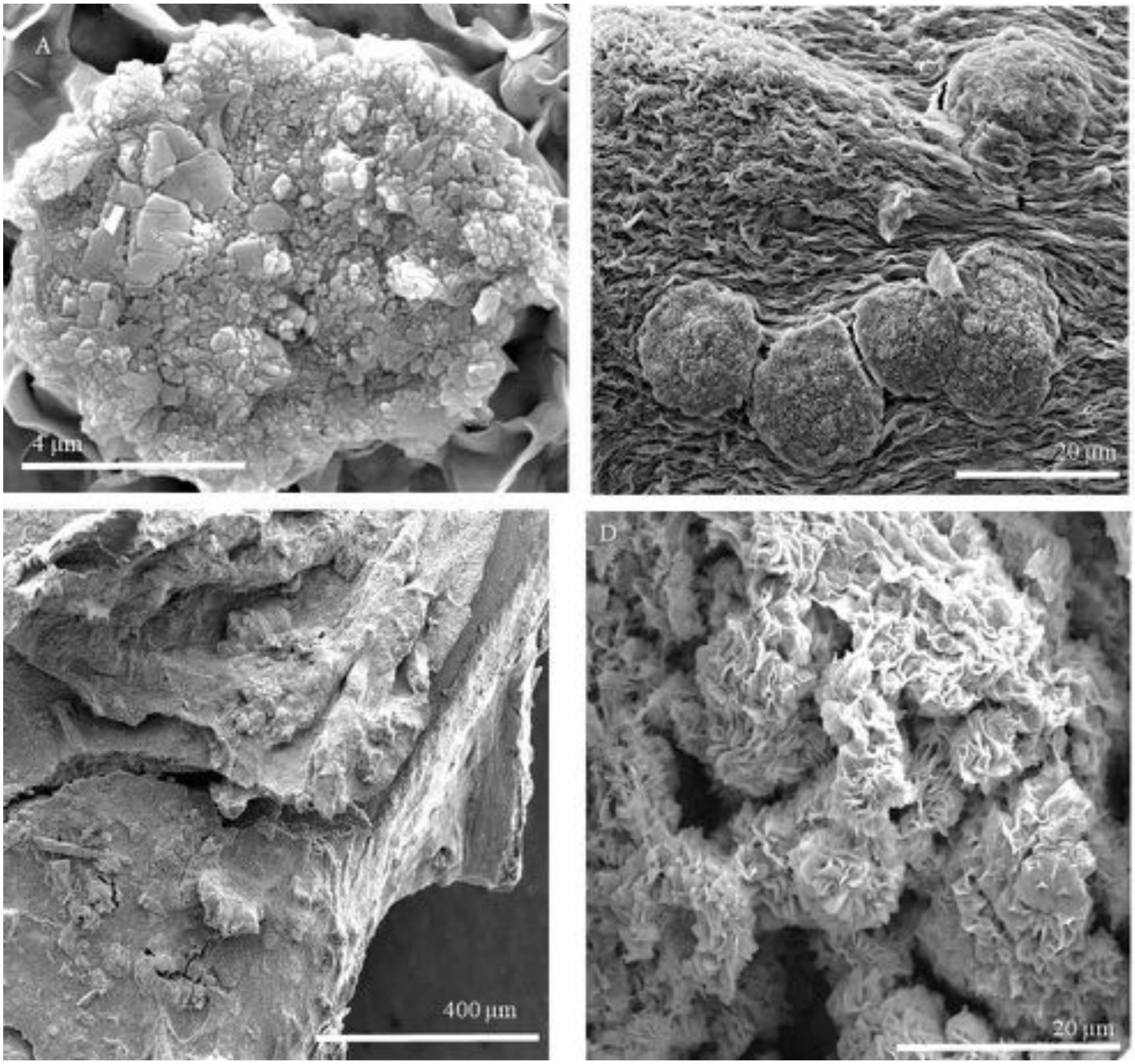

Figure C-9. SE images of IEBS-5 reaction products. [A] C(A)SH mineral and minor carbonate aggregate observed in the dried gel. [B] Carbonate with C(A)SH aggregates embedded in smectite matrix from the dried gel. [C] Overview of the edge of the reacted 316SS coupon showing attached smectite and underlying Fe-rich reaction products. [D] Fe-saponite growth on the surface of the 316SS steel coupon.

C-6. IEBS-6

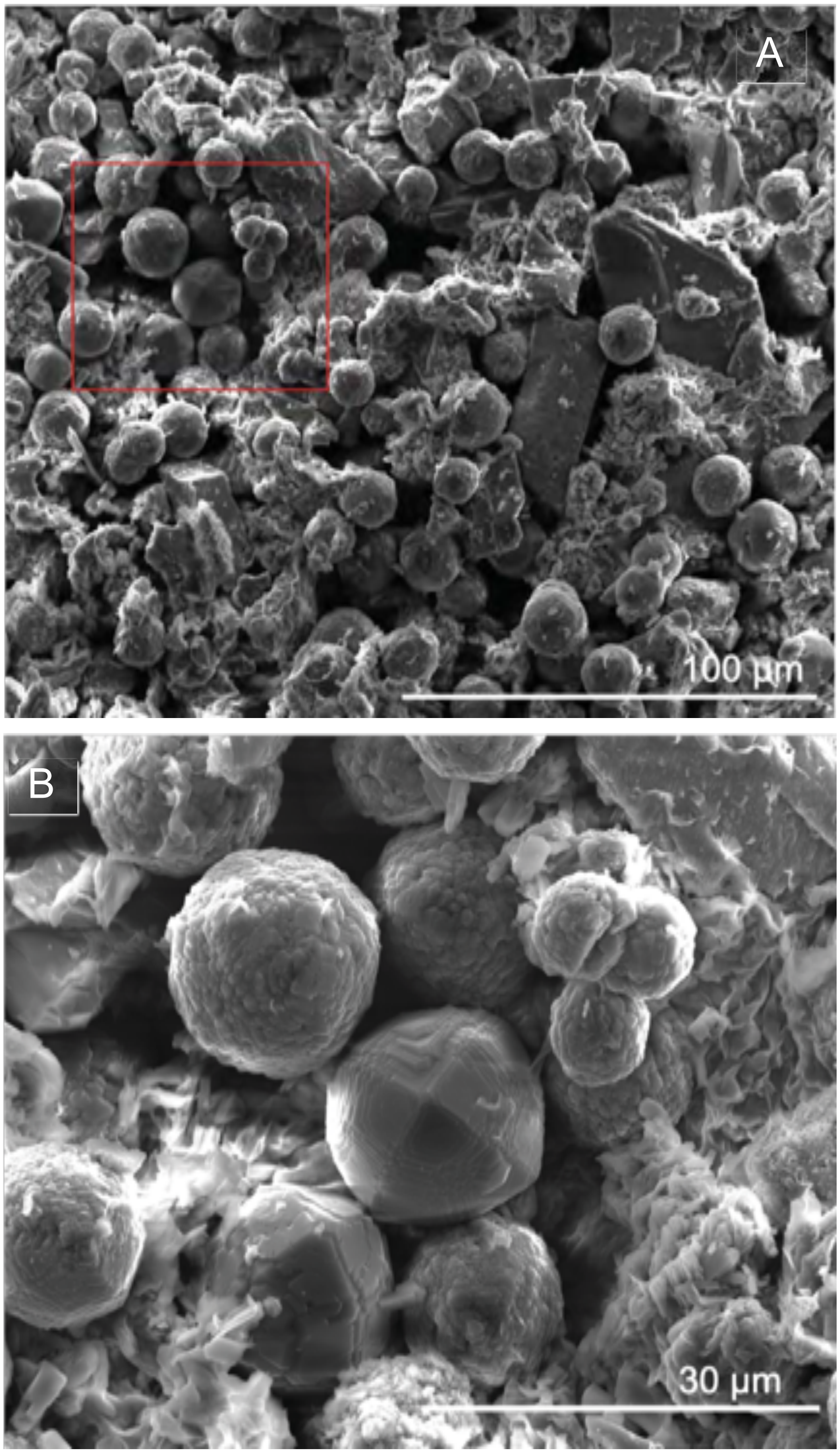

Figure C-10. SE images of particles derived from filtering fluids collected post- experiment from IEBS-6. [A] Clustered of analcime crystals (round) with feldspar (blocky grains) and smectite (fine-grained groundmass). [B] Inset of red box from [A] showing the different crystal forms of the analcime crystals.

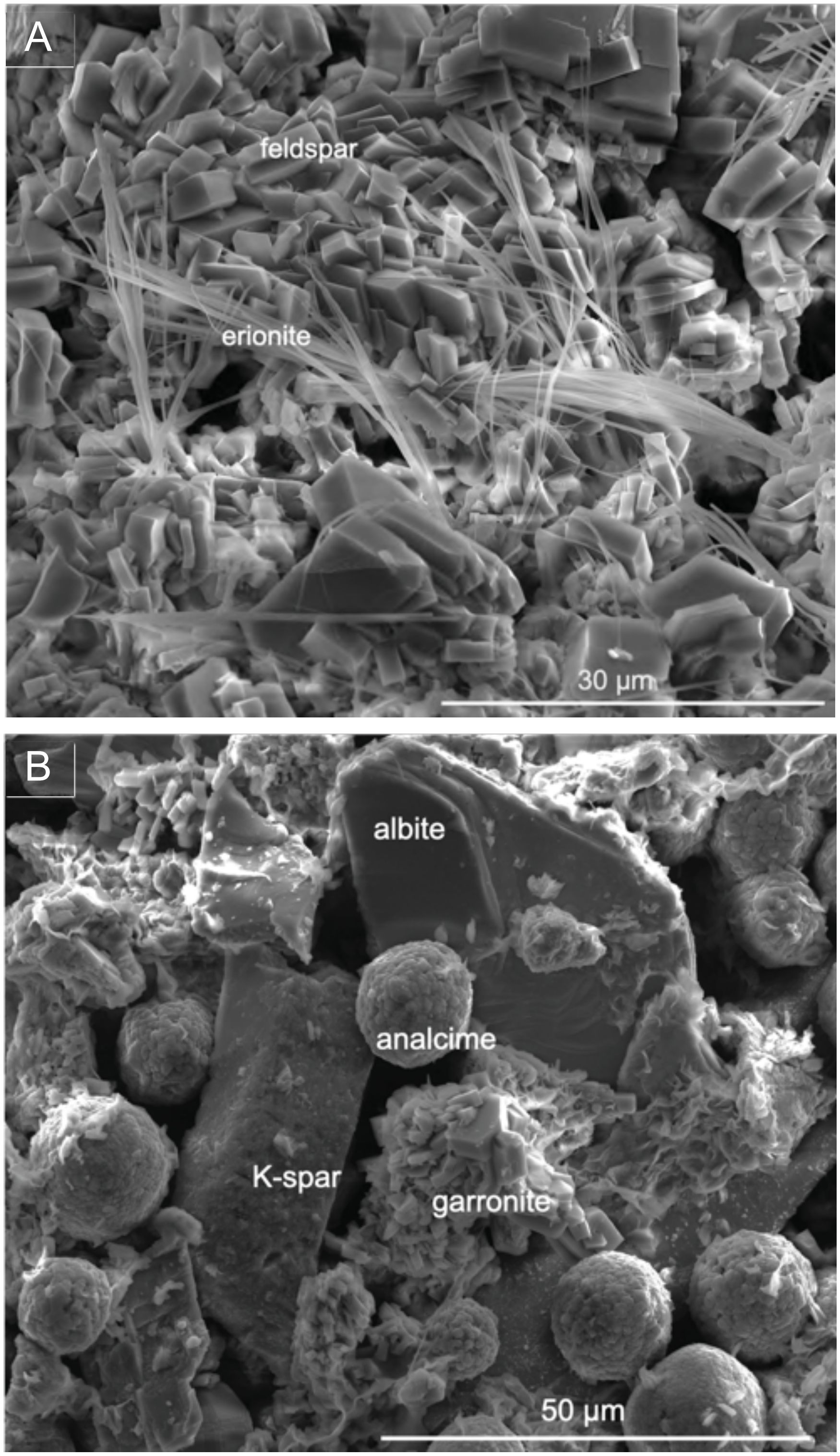

Figure C-11. SE images of IEBS-6 reaction products. [A] Erionite-Ca (fibrous bundles) overlying blocky, Ca-rich feldspars. [B] Feldspar (albite, K-feldspar (K-spar)) and zeolite (analcime, garronite) phases (labelled) embedded in smectite (fine-grained groundmass) matrix.

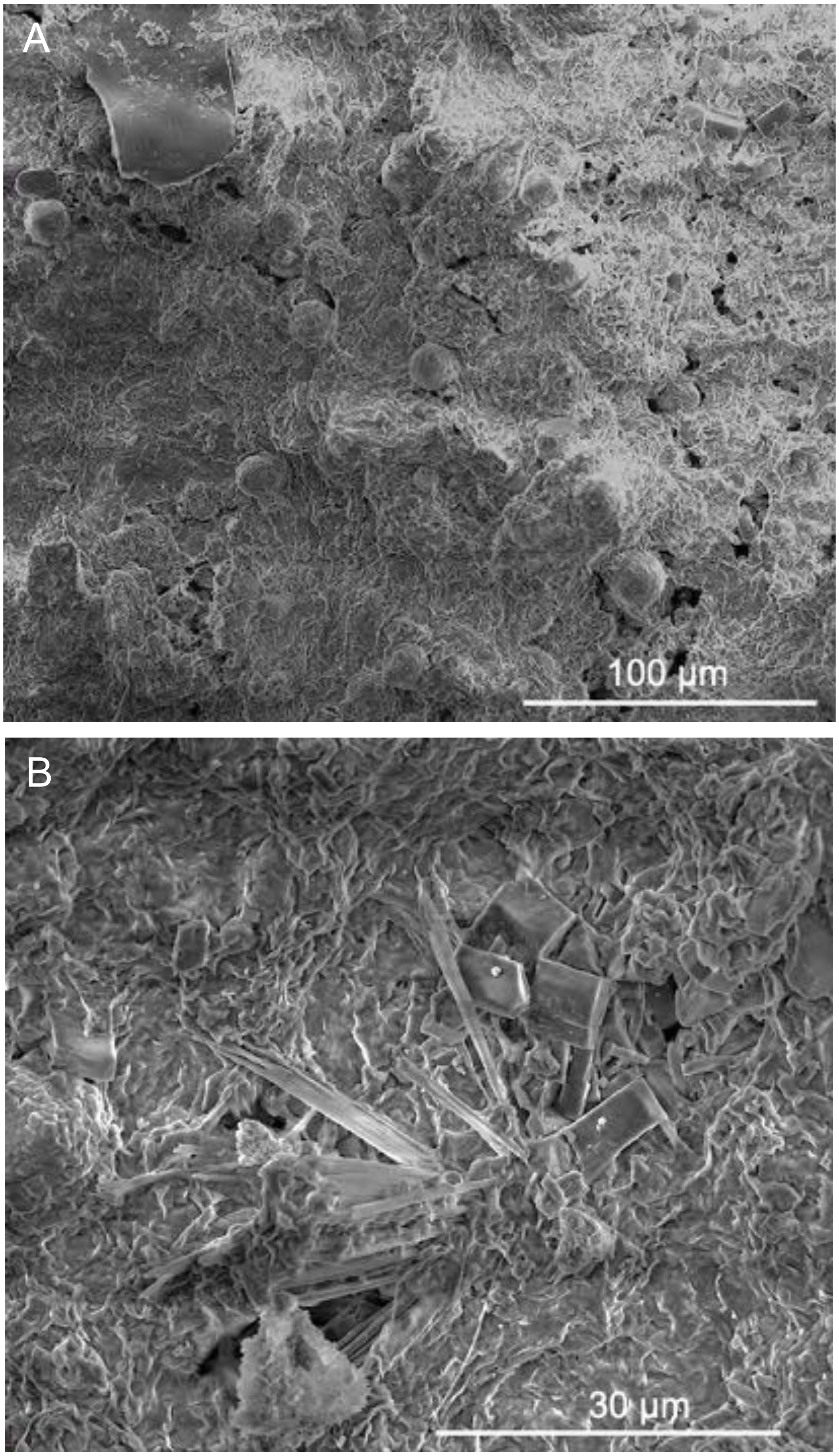

Figure C-12. SE images of the surface of the reacted, cured Portland chip in IEBS-6. No EDS was preformed because the chip was uncoated; mineral identification is based on crystal morphology. [A] Smectite with embedded analcime (round crystals) covering the cement chip surface. [B] Foily smectite with fibrous erionite and blocky feldspar or zeolite crystals.